
PHD THESIS

TAG LOCALIZATION IN PASSIVE UHF RFID

~ Position Aware RFID Systems ~

conducted at the
Signal Processing and Speech Communication Laboratory
Graz University of Technology, Austria

in co-operation with
NXP Semiconductors Austria GmbH Styria
Gratkorn, Austria

by
Daniel Arnitz

Supervisors:
Dr. Klaus Witrissal (Graz University of Technology)
Dr. Ulrich Mühlmann (NXP Semiconductors)

Assessors/Examiners:
Dr. Klaus Witrissal (Graz University of Technology)
Dr. Pavel Nikitin (University of Washington, Intermec Technologies)

Graz, May 2, 2011

Acknowledgment

To all of you who walked with me—this one’s from the heart:

First and foremost, I would like to express my gratitude to Klaus, my supervisor, examiner, and mentor. Thank you for countless discussions, hints, and nudges over the past years. You kept my course steady—I owe you. The same is true for Gernot, who supported me and my PhD studies, and who never failed to derail me during presentations and exams. My heartfelt thanks also to Pavel for being my co-examiner, for his meticulous review of my thesis, and for years of discussions at conferences. You have been my unofficial mentor for three years now. I am honored.

I would like to cordially thank Ulrich for his support and technical advice during all these years as well as NXP for funding and supporting this thesis project. Special thanks also to Hubert and Franz, who have supported me and my work for years now and who gave me the opportunity to make the PARIS framework open-source. My gratitude also goes to the Austrian Research Promotion Agency (FFG), which provided funding for my thesis.

Special and heartfelt thanks to my first-level content filtering team, Andreas, Bernhard, Paul, and Stefan. You kept all these pages tractable and made sure that the proverbial red line is not a dashed one. You also ensured that this thesis meets the unofficial quality criterion for a professional monograph: no jokes whatsoever. Dry reading? Yes, but consistently so!

My deepest gratitude also to Geraldine, Angelika, and Sonja for a tremendously thorough proof-reading and their watchful eye on spelling, grammar, and syntax. You provided a valuable counterpoint to all the technical reviews and a front row view on technical writing style. Respectfully, it’s nonetheless called an upper bound, not an upper limit.

My sincere thanks to Grzegorz for designing the UWB antennas used for measurements, to Albert Angstenberger for providing the substrates as free samples, and to the team of NXP’s Application and System Center, Giuliano, Martin, Gerald, and Alexey for their invaluable help with the measurement setups. I would like to thank Astrid Brodtrager, the far-from-grey eminence for PhD students at the dean’s office, for her leniency regarding certain deadlines. Furthermore, I would like to thank the people at the SPSC, not only for a lot of gruesome discussions, but also for an equal share of laughter during the past four years. This includes, in particular, Thomas, Stefan, Andreas, and Paul, with whom I shared my office and who came up with countless doomsday scenarios all including a certain student and a soldering gun. And, finally, my thanks to Karin, Andreas, and Markus. Your bravery in the face of bureaucracy and your legendary fighting retreats after server failures are an inspiration to us all.

My gratitude to Sir Terry Pratchett, who conceived the Discworld characters of the Librarian and the Death of Rats, who added their comments to this thesis. This gratitude of course extends to Colin Smythe, Sir Terry’s literary agent, who replied to my request for permission with “Ha! of course.”. I can’t tell you how much I appreciated those three words.

Last but not least, I would like to thank my family. It was their support and admirable attitude towards education and self-determination that made my studies possible in the first place. Their efforts gave me the freedom to find my own way, to do what I like best, and, most recently, to write a PhD thesis.

Thank you!

Abstract

Tag localization in passive ultra-high frequency radio frequency identification (UHF RFID) has become something of a holy grail since the system was introduced. First and foremost, it promises improved accuracy for inventory systems, which have to deal with false positive reads outside the intended read zone and the consequent corruption of inventory lists.

This thesis addresses the problem of passive UHF RFID tag localization, with a focus on range finding methods. It shows how typical system setups influence the propagation channel and why this creates a harsh environment for any type of localization. Based on the conclusions drawn in this channel analysis, tag localization approaches are investigated. These investigations cover narrowband through ultra-wideband localization approaches, with three methods discussed in detail: phase-based continuous-wave ranging, frequency-modulation continuous-wave ranging, and ultra-wideband impulse radar.

It is shown that robust and accurate localization of state-of-the-art UHF RFID transponders is possible only in controlled environments. Classification to large read zones such as portals or dock doors, on the other hand, is feasible in principle in the field as well. However, robust classification with low error rates still requires a high number of position estimates. This might be unfeasible in applications with high tag throughput.

Wideband and ultra-wideband methods offer considerably greater robustness and accuracy in typical fields of application for UHF RFID, but come at the cost of increased system complexity. It is shown how state-of-the-art passive RFID tags can be modified to support wideband and even ultra-wideband backscatter localization and also how these methods can be implemented in a reader. Critical system parameters and vulnerabilities with respect to structural and physical properties of UHF RFID installations are discussed in detail and possible countermeasures are provided.

Achievable accuracies depend on the environment, the application scenario, and the localization system in use. Provided that the line-of-sight to the tag is not blocked, errors for a single position estimate range from several tens of centimeters for ultra-wideband systems to several tens of meters for narrowband localization in typical UHF RFID environments. Increased accuracy and robustness with respect to blocked line-of-sights can be achieved by combining several estimates, e.g., by using tracking approaches.

Kurzfassung

Die Lokalisierung von passiven UHF RFID¹ Transpondern (Tags) hat sich seit Einführung des Systems zu einer Art Heiligem Gral entwickelt. Ziel dieser Lokalisierung ist die Identifizierung von unbeabsichtigt gelesenen Transpondern, d.h. Tags, die sich außerhalb des gewünschten Lesebereichs befinden. Durch solch unbeabsichtigte Lesevorgänge werden die entsprechenden Produkte falsch inventarisiert, was ein großes Problem für Logistiksysteme darstellt.

Diese Dissertation beschäftigt sich mit der Lokalisierung passiver UHF RFID Tags und den damit verbundenen Problemen, wobei der Fokus auf Distanzschätzung liegt. Es wird gezeigt, wie typische Systemanordnungen den Übertragungskanal beeinflussen und warum dies die Lokalisierung von Tags erschwert. Basierend auf den in diesen Kanalanalysen gewonnenen Erkenntnissen werden Lokalisierungsverfahren untersucht und bewertet. Die Bandbreite dieser Untersuchungen reicht dabei von schmalbandigen bis hin zu ultra-breitbandigen Verfahren, wobei auf drei Methoden im Detail eingegangen wird: Mehrträger-Dauerstrichradar, Frequenzmodulations-Dauerstrichradar und ultra-breitbandiges Impulsradar.

Es wird gezeigt, dass die fehlerfreie und genaue Lokalisierung von handelsüblichen UHF RFID Tags nur unter Laborbedingungen möglich ist. Klassifikation in größere Lesezonen, wie zum Beispiel Portale oder Ladezonen, ist allerdings auch in typischen Umgebungen möglich. Trotzdem wird auch im Fall der Klassifikation eine hohe Zahl an Positionsschätzungen benötigt, um niedrige Fehlerraten zu erreichen. Speziell in Anwendungen mit hohem Durchsatz an Tags stellt diese Notwendigkeit jedoch ein Problem dar.

Breitbandige und ultra-breitbandige Verfahren erreichen im Vergleich zu deren schmalbandigen Verwandten eine deutlich höhere Robustheit und Genauigkeit in typischen Einsatzgebieten von UHF RFID, sind im Gegenzug jedoch deutlich komplexer. Die für die Verwendbarkeit von breitbandigen und ultra-breitbandigen Lokalisierungsmethoden notwendigen Erweiterungen an handelsüblichen UHF RFID Readern und Tags werden in der Arbeit im Detail beschrieben. Weiters werden kritische Systemparameter und Schwächen der einzelnen Lokalisierungsmethoden hinsichtlich struktureller Eigenschaften von UHF RFID Systemen sowie Umgebungseinflüssen ausführlich diskutiert und Gegenmaßnahmen entwickelt.

Die in der Praxis erreichbaren Genauigkeiten hängen von der Umgebung, dem Anwendungsszenario, sowie dem verwendeten Lokalisierungsverfahren ab. Die Fehler bei vorhandener Sichtverbindung zum Tag reichen hier von einigen zehn Zentimetern für ultra-breitbandige Verfahren bis hin zu Dutzenden von Metern für schmalbandige Methoden. Höhere Genauigkeit und Toleranz gegenüber blockierten Sichtverbindungen können durch die Kombination von mehreren Positionsschätzungen, zum Beispiel durch Nachführungsverfahren, erreicht werden.

¹ ultra-high frequency (UHF) radio frequency identification (RFID) – eine elektronische Form des Strichcodes, die mit Funkwellen im unteren Gigahertzbereich arbeitet

General Layout of this Thesis

Margins

Important passages of this thesis are marked by symbols in the margins. Four different symbols are used:



Marks vital information that must not be ignored, or an important fact that is often misunderstood. Take care: an error here might be impossible to detect.



Indicates that this is harder to understand than it would seem at first glance. Please read carefully: there is a pitfall hidden somewhere.



Marks central results worth looking at.



Indicates an open question or a result that does not make sense (unknown reason).

Reprints of Own Papers

Reprints of all papers published in the course of this thesis project have been added at the end of this document in order to provide the reader with a complete picture of the research conducted. References to these papers are printed in blue, e.g., [0].

Contents

| | | |
|----------|--|-----------|
| 1 | Introduction | 23 |
| 1.1 | A Primer on Passive UHF RFID and Radio Localization | 24 |
| 1.1.1 | Passive UHF RFID | 24 |
| 1.1.2 | Localization: Range vs. Direction | 26 |
| 1.2 | The Difficulties of Localizing Passive UHF RFID Transponders | 28 |
| 1.3 | Motivation and Related Work | 29 |
| 1.4 | Contributions and Outline | 33 |
| 2 | Modeling the UHF RFID Channel | 37 |
| 2.1 | Introduction to Wireless Propagation | 38 |
| 2.1.1 | Basics / Multipath Propagation Mechanisms | 38 |
| 2.1.2 | The Power-Delay-Profile (PDP) | 39 |
| 2.1.3 | Effects of Local Geometry | 40 |
| 2.2 | Channel Models | 42 |
| 2.2.1 | Typical UHF RFID Scenarios and Channels | 42 |
| 2.2.2 | Channel Models in the Literature | 43 |
| 2.2.3 | Applicability of Specific Types of Channel Models to Ranging in UHF RFID | 44 |
| 2.2.4 | Introduction to the Channel Model Implemented in the PARIS Framework | 49 |
| 2.3 | Measurements | 50 |
| 2.3.1 | General Measurement Setup and Description of Performed Analyses | 50 |
| 2.3.2 | Indoor Office/Industrial | 54 |
| 2.3.3 | UHF RFID Gate in an Industrial Environment | 58 |
| 2.4 | Single-Channel Approximation of the Backscatter Channel | 63 |
| 2.5 | Summary of Channel Parameters | 66 |
| 2.5.1 | Channel Basics for Ranging and Localization | 66 |
| 2.5.2 | Recommended Channel Model/Parameters for Simulations | 66 |
| 3 | The PARIS Simulation Framework | 69 |
| 3.1 | Concepts and Basic Framework | 70 |
| 3.1.1 | Basic Structure | 70 |
| 3.1.2 | Logging, Version Management, and Exception Handling | 71 |
| 3.1.3 | Automated Self-Tests | 71 |
| 3.1.4 | Main Simulator Files | 72 |
| 3.2 | Model Overview: Reader, Channel, Tag | 73 |
| 3.2.1 | Reader Model | 74 |
| 3.2.2 | Channel Model Overview | 76 |
| 3.2.3 | Tag Model Overview | 78 |
| 3.2.4 | Limitations of the Implemented Models | 79 |
| 3.3 | The Tag Models in Detail | 81 |
| 3.3.1 | Tag Reflection Coefficient | 81 |
| 3.3.2 | Tag Modulator / Power-Supply Unit | 88 |
| 3.3.3 | Other Modules | 90 |

| | | |
|----------|--|------------|
| 3.4 | The Channel Model in Detail | 91 |
| 3.4.1 | Large-Scale and Directivity Model | 91 |
| 3.4.2 | Deterministic Small-Scale Model: Surfaces and Virtual Transmitters | 91 |
| 3.4.3 | Statistical Small-Scale Model | 96 |
| 3.4.4 | Bringing Everything Together | 101 |
| 3.5 | A Quick Tutorial | 103 |
| 3.5.1 | Where to find... | 103 |
| 3.5.2 | Example Simulation Setup | 103 |
| 4 | Narrowband UHF RFID Tag Localization | 107 |
| 4.1 | Concepts, Overview, and State-of-the-Art | 108 |
| 4.2 | Multi-Frequency Continuous-Wave Ranging | 111 |
| 4.2.1 | Concepts and Theory | 111 |
| 4.2.2 | Performance Bounds / Simulations | 122 |
| 4.2.3 | Measurement Results | 130 |
| 4.3 | Summary | 134 |
| 5 | (Ultra-)Wideband UHF RFID Tag Ranging | 137 |
| 5.1 | Basics and Ranging Methods | 138 |
| 5.1.1 | Signal Analysis Method for Impulse-Radio Ultra-Wideband Ranging | 139 |
| 5.1.2 | Signal Analysis Method for FMCW Radar | 140 |
| 5.1.3 | Semi-Active UHF/UWB Hybrids | 141 |
| 5.2 | Impulse-Radio Ultra-Wideband: Proof-of-Concept | 141 |
| 5.3 | Ranging Accuracy in Portal Applications | 143 |
| 5.4 | Towards an Implementation | 146 |
| 5.4.1 | Tag | 146 |
| 5.4.2 | Reader | 147 |
| 6 | Conclusion | 153 |
| 6.1 | Summary of Scientific Results | 154 |
| 6.2 | Own Contributions | 155 |
| 6.3 | Future Research | 156 |
| A | Polar Gain Patterns | 157 |
| B | Floorplan of SPSC Buildings | 161 |
| C | Simulator Internals | 165 |
| C.1 | Known Issues and To-Do List for Future Builds | 166 |
| C.2 | Available Characteristics Files | 167 |
| C.3 | Example Self-Test Log | 169 |

List of Acronyms and Abbreviations

| | |
|-----------|--|
| 2FCW | Multi-Frequency Continuous-Wave ranging (MFCW) with two carriers |
| 2×3FCW | Multi-Frequency Continuous-Wave ranging (MFCW) with two groups of three carriers |
| A/D | Analog to Digital (conversion) |
| ADC | Analog to Digital Converter |
| AGC | Automatic Gain Control |
| amp | short for amplifier |
| AoA | Angle of Arrival (direction finding localization) |
| APDP | Average Power-Delay-Profile (channel characteristic) |
| ASC | Application and System Center (a research dept. of NXP Semiconductors) |
| ASK | Amplitude Shift Keying (a modulation scheme) |
| AWGN | Additive White Gaussian Noise |
| CDF | Cumulative Distribution Function |
| CIR | Channel Impulse Response (inverse Fourier transform of the CTF) |
| COST | European Co-Operation in the field of Scientific and Technical research |
| CRC | Cyclic Redundancy Check (an error detecting code; CRC-16: 16 bit) |
| CTF | Channel Transfer Function (Fourier transform of the CIR) |
| ctrl | short for control |
| CW | Continuous-Wave (e.g., FMCW: Frequency-Modulation Continuous-Wave) |
| D/A | Digital to Analog (conversion) |
| DAC | Digital to Analog Converter |
| DC | Direct Current; generally referring to 0 Hz |
| DoA | Direction of Arrival (see AoA) |
| DSB | Dual Sideband (e.g., DSB-ASK; a modulation scheme) |
| E(-plane) | electric field plane of linearly polarized antennas |
| EIRP | Equivalent Isotropically Radiated Power |
| EM | ElectroMagnetic |
| EPC | Electronic Product Code |
| EU | European Union |
| EURASIP | European Association for Signal Processing |
| FFT | Fast Fourier Transform (a common method to calculate the spectrum of a signal) |
| FIR | Finite Impulse Response (a type of digital filter) |
| FM | Frequency Modulation (a modulation scheme) |
| FMCW | Frequency-Modulation Continuous-Wave (range finding localization) |
| FR-4 | glass epoxy laminate used for printed circuit boards |
| G2iL | NXP UCODE G2iL, an EPCglobal Class-1 Gen-2 chip manufactured by NXP |
| G2XM | NXP UCODE G2XM, an EPCglobal Class-1 Gen-2 chip manufactured by NXP |
| GNSS | Global Navigation Satellite System |
| GPS | Global Positioning System (GNSS operated by the USA) |
| GS/s | Giga-Samples per second (ADC/DAC sampling rate) |
| H(-plane) | magnetic field plane of linearly polarized antennas |
| HF | High Frequency (3–30 MHz) |
| I/Q | In-phase / Quadrature-phase (e.g., I/Q demodulator; results in a complex signal) |
| IA39B | UHF RFID portal antenna manufactured by Intermec Technologies |
| IC | Integrated Circuit |

| | |
|---------|---|
| IEEE | Institute of Electrical and Electronics Engineers |
| IET | Institution of Engineering and Technology (British organization for engineers and technologists) also: Institute of Electrical Information Technology (dept. of Clausthal Univ. of Techn.) |
| IIR | Infinite Impulse Response (a type of digital filter) |
| IR | Impulse-Radio (IR-UWB: Impulse-Radio Ultra-Wideband) |
| ISM | Industrial, Scientific, Medical (license-free frequency bands) |
| ISO | International Organization for Standardization |
| KTH | Kungliga Tekniska Högskolan (Royal Institute of Technology), Stockholm, Sweden |
| LAN | Local Area Network |
| LF | Low Frequency (30–300 kHz) |
| LNA | Low-Noise Amplifier |
| LOS | Line-Of-Sight (direct propagation path) |
| LSB | Lower Sideband |
| MAE | Mean Absolute Error (average $ \text{true value} - \text{estimate} $) |
| MFCW | Multi-Frequency Continuous-Wave (range-finding localization) |
| MPC | Multipath Component (one component of the channel impulse response) |
| MUSIC | MUltiple SIgnal Classification (an array processing algorithm) |
| NLOS | Non-Line-Of-Sight (reflected propagation path) |
| NWA | Network Analyzer (used in papers; VNA in this thesis) |
| NXP | NXP Semiconductors (company founded by Philips) |
| PAN | Personal Area Network |
| PARIS | Position Aware RFID Systems (title of this thesis project) |
| PDF | Probability Distribution Function (also used for probability mass functions, i.e., discrete PDFs) |
| PDP | Power-Delay-Profile (channel characteristic); used for one realization (instantaneous PDP) |
| PoA | Phase of Arrival (a form of ToA for sinusoidal signals) |
| PR | Phase-Reversal (e.g., PR-ASK; a modulation scheme) |
| pwr | short for power |
| Q | Quality factor (measure for the dampening of resonances) |
| RADAR | Radio Detection and Ranging (used as “radar” in the text) |
| RAM | Random-Access Memory |
| RC | Resistor and Capacitor (e.g., RC lowpass) |
| RF | Radio Frequency (electromagnetic waves; roughly 3 kHz to 300 GHz) |
| RFID | Radio Frequency IDentification (“electronic barcode”) |
| RMS | Root Mean Square (e.g., RMS delay spread) |
| RN16 | 16 bit Random Number (as defined in EPCglobal Class-1 Gen-2, [1]) |
| RSS | Received Signal Strength (RSSI: Received Signal Strength Indicator) |
| RV | Random Variable |
| RX | Receiver |
| SAR/SAS | Synthetic Aperture Radar/Sonar (uses a virtual array created by moving antennas) |
| SAW | Surface Acoustic Wave |
| SDCF | Spaced-Distance Correlation Function (a.k.a. frequency covariance function) |
| SFCF | Spaced-Frequency Correlation Function (a.k.a. frequency correlation function) |
| SIR | Signal-to-Interference Ratio |
| SNR | Signal-to-Noise Ratio |
| SPSC | Signal Processing and Speech Communication Laboratory (dept. of Graz Univ. of Techn.) |
| SSB | Single Sideband (e.g., SSB-ASK; a modulation scheme) |
| SV | Saleh-Valenzuela model (a common (ultra-)wideband channel model) |
| SVN | Subversion (a version control software) |
| TDoA | Time Difference of Arrival (relative form of ToA) |
| ToA | Time of Arrival (range finding localization; a.k.a. triangulation / multilateration) |
| TSSOP | Thin-Shrink Small Outline Package (a small surface mount component package) |
| TUG | Technische Universität Graz (Graz University of Technology) |
| TX | Transmitter |

| | |
|--------|---|
| UHF | Ultra-High Frequency (decimeter waves; 0.3–3 GHz) |
| US | Uncorrelated Scattering (assumption — channel modeling); also: United States (of America) |
| USA | United States of America |
| USB | Upper Sideband |
| UWB | Ultra-Wideband (signal with bandwidth exceeding 500 MHz or 20 % of the center freq.) |
| VCO | Voltage Controlled Oscillator |
| VNA | Vector Network Analyzer (also: NWA) |
| VTX | Virtual Transmitter (a transmitter mirrored in reflective surfaces) |
| WB | Wideband |
| XIXO | arbitrary (“X”) number of Inputs, arbitrary (“X”) number of Outputs |
| ZMCSCG | Zero Mean Circulant Symmetric Complex Gaussian (random variable; used in papers) |

List of Symbols

— General Notation —

| | |
|--------------------------------------|--|
| N, m | mathematical symbol (italics) |
| N, m | index or description (upright) |
| $\mathbf{h}, \mathbf{x}, \mathbf{f}$ | vector (lower case, bold) |
| $\mathbf{H}, \mathbf{X}, \mathbf{F}$ | matrix (upper case, bold) |
| $\mathbf{h} \circ \mathbf{x}$ | element-wise multiplication of vectors \mathbf{h} and \mathbf{x} |
| $x(\cdot)$ | continuous-time signal or function (round brackets) |
| $x[\cdot]$ | discrete-time signal or function (square brackets) |
| Δ | used to indicate a difference, e.g., Δf is a frequency difference |
| $Z_1 \parallel Z_2$ | Z_1 parallel to Z_2 (impedance) |
| \hat{x} | estimate of x |
| x^* | conjugate complex of x |
| \mathbf{x}^T | conjugate complex (Hermitian) transpose of vector \mathbf{x} |
| $:=$ | is defined as |
| \mathbb{R} | real numbers |
| \mathbb{C} | complex numbers |
| $\mathcal{CN}(\mu, \sigma^2)$ | circulant symmetric complex normal distribution with mean μ and variance σ^2 ($\mu, \sigma \in \mathbb{C}$) |

— Operators / Transforms —

| | |
|------------------------|---|
| $\mathcal{F}\{\cdot\}$ | Fourier transform |
| $E\{\cdot\}$ | expected value |
| $\text{var}\{\cdot\}$ | variance |
| $\text{cov}\{\cdot\}$ | covariance |
| $\text{corr}\{\cdot\}$ | correlation |
| $\text{avg}\{\cdot\}$ | average value (time-average) |
| $\text{Re}\{\cdot\}$ | real part (of a complex value/function) |
| $\text{Im}\{\cdot\}$ | imaginary part (of a complex value/function) |
| e^{\cdot} | exponential function (denoted by an upright character) |
| $\log_{10}(\cdot)$ | logarithm base 10 |
| $\lceil \cdot \rceil$ | rounding to the next larger integer (rounding towards infinity) |

— General Symbols (Base) —

| | |
|-----------|---|
| c | speed of light in vacuum / air |
| d | distance |
| x, y, z | axes of the Cartesian coordinate system |
| α | angle |
| t | time |
| τ | propagation delay |
| f | frequency |
| ω | angular frequency ($\omega = 2\pi f$) |
| B | bandwidth |
| λ | wavelength ($\lambda = c/f$) |
| φ | phase shift |
| P | power |

| | |
|-----------------|---|
| v | velocity |
| V | volume (of a 3-dimensional space) |
| O | area (of a 2-dimensional space) |
| $\delta(\cdot)$ | Dirac delta |
| i, j | indices |
| n | sample index (discrete time) |
| N, M | integer numbers (e.g., number of tags, number of transmitters, ...) |

— **General Symbols (Specialized)** —

| | |
|-------------------|---|
| m | index for tag modulation (e.g., tag modulation frequency f_m) |
| s_1, s_K, \dots | signal 1, signal K, ... |
| f_s | sampling frequency |
| T_s | sampling time interval ($T_s = 1/f_s$) |
| f_c | carrier/center frequency (ω_c : angular carrier/center frequency) |
| f_m | tag modulation frequency (ω_m : angular tag modulation frequency) |
| N_{TX} | number of transmitters |
| N_{RX} | number of receivers |
| N_{FFT} | number of FFT samples |
| v_r | radial (centripetal) velocity |
| d_{Ant} | maximum overall antenna size (entire array in case of arrays) |
| SNR | signal-to-noise ratio (SNR) |
| SIR | signal-to-interference ratio (SIR) |

— **Channel Impulse Response (CIR) and Channel Transfer Function (CTF)** —

| | |
|--------------|--|
| $h(\tau)$ | channel impulse response (CIR) over delay τ |
| h_i | channel tap i of a sampled CIR (short for $h[i] = h(\tau_i = iT_s)$) |
| $H(f)$ | channel transfer function (CTF) over frequency f |
| $w(\tau)$ | pulse shape for the continuous-time representation of a band-limited CIR |
| d_{res} | spatial (distance) resolution of a sampled CIR |
| f_{res} | frequency resolution of a sampled channel transfer function or spectrum |
| τ_{grp} | group delay (derivative of the phase w.r.t. frequency) |

— **Power-Delay-Profile (PDP) / Average Power-Delay-Profile (APDP)** —

| | |
|--------------------|--|
| $\psi(\tau)$ | power-delay-profile (PDP) over delay τ |
| $\bar{\psi}(\tau)$ | average power-delay-profile (PDP) over delay τ |
| Φ | spaced-frequency covariance function |
| τ_{LOS} | line-of-sight delay (shortest propagation path) |
| τ_{NLOS} | non-line-of-sight group delay |
| τ_{RMS} | RMS delay spread (square root of the normalized (A)PDP's second central moment) |
| τ_{avg} | average excess delay (first moment of normalized (A)PDP) |
| τ_{max} | maximum excess delay (for truncated (A)PDPs) |
| P_{LOS} | line-of-sight power ((A)PDP at line-of-sight delay τ_{LOS}) |
| P_{NLOS} | non-line-of-sight power (integral over non-line-of-sight part of (A)PDP) |
| $P_{LOS+NLOS}$ | overall power (LOS + NLOS; integral over (A)PDP; also: P_0 , adopted from [2]) |
| K_{LOS} | line-of-sight K-factor (power ratio P_{LOS}/P_{NLOS} ; \sim dominance of LOS path) |
| B_c | coherence bandwidth |
| d_c | coherence distance |
| Γ | multipath decay constant |
| Γ_{dB} | multipath decay in dB/s |

— **Ranging (General, Frequency-Modulation, Impulse-Radio)** —

| | |
|-----------------|---|
| d_{LOS} | true line-of-sight distance (shortest propagation path) |
| \hat{d}_{LOS} | estimated line-of-sight distance |
| e | distance error (estimated to true LOS distance, $\hat{d}_{LOS} - d_{LOS}$) |

| | |
|----------------------------|---|
| μ_e | average distance error (expected value) |
| σ_e | standard deviation of the distance error |
| d_{\max} | maximum unambiguous distance |
| T_{FM} | FMCW sweep duration |
| B_{FM} | FMCW sweep bandwidth |
| $\Delta f_{\text{LOS,FM}}$ | frequency difference corresponding to the (true) LOS distance in FMCW radar |

— **Ranging (Multi-Frequency Continuous-Wave, MFCW)** —

| | |
|--------------------------------------|---|
| N_c | number of MFCW carriers |
| i | MFCW carrier index (carrier at frequency $f_c + f_i$) |
| m_i | index for lower tag modulation sideband of carrier i (“m” indicates tag modulation) |
| im | index for upper tag modulation sideband of carrier i (“m” indicates tag modulation) |
| $s_1 \dots s_6$ | signals in step-by-step MFCW derivation |
| s_m | tag modulation signal in step-by-step MFCW derivation |
| s_K | feedback signal in step-by-step MFCW derivation |
| A_i | complex transmit amplitude of MFCW carrier i |
| \tilde{A}_i | complex amplitude of MFCW carrier i after demodulation (due to partially unknown A_i) |
| ω_i | angular offset frequency of MFCW carrier i |
| ω_m | angular tag modulation frequency |
| ϕ_m | tag modulation phase (uniform between $-\pi$ and π) |
| $\phi_{m,i}$ | tag modulation phase for carrier i in frequency-hopped MFCW (uniform between $-\pi$ and π) |
| H_i | uplink/downlink channel gain for carrier i |
| H_{mi} | uplink/downlink channel gain for lower sideband of carrier i |
| H_{im} | uplink/downlink channel gain for upper sideband of carrier i |
| $\tilde{H}_i, \tilde{H}_{mi}, \dots$ | H_i, H_{mi} , and H_{im} with extracted line-of-sight phase |
| K_i | feedback channel gain for carrier i |
| G_i | reader frontend gain for carrier i |
| G_{mi} | reader frontend gain for lower sideband of carrier i |
| G_{im} | reader frontend gain for upper sideband of carrier i |
| Ψ_{mi} | complex MFCW component, lower modulation sideband of carrier i |
| Ψ_{im} | complex MFCW component, upper modulation sideband of carrier i |
| $\hat{\Psi}_{mi}$ | estimated complex MFCW component, lower modulation sideband of carrier i |
| $\hat{\Psi}_{im}$ | estimated complex MFCW component, upper modulation sideband of carrier i |
| μ_H | expected value of narrowband channel gain for MFCW signals – single-channel |
| σ_H^2 | variance of narrowband channel gain for MFCW signals – single-channel |
| β_H | covariance between narrowband channel gains for MFCW signals – single-channel |
| $\tilde{\mu}_H$ | expected value of narrowband channel gain for MFCW signals – backscatter channel |
| $\tilde{\sigma}_H^2$ | variance of narrowband channel gain for MFCW signals – backscatter channel |
| $\tilde{\beta}_H$ | covariance between narrowband channel gains for MFCW signals – backscatter channel |

— **Channel Model (Large-Scale and Directivity, Noise)** —

| | |
|-----------------------|--|
| ξ | path loss factor (free space propagation) |
| Θ_{LS} | large-scale power gain |
| τ_{LS} | large-scale propagation delay |
| Θ_{dir} | directivity power gain |
| N_0 | single-sided noise spectral density [dBm/Hz] |

— **Channel Model (Surfaces, Virtual Transmitters)** —

| | |
|-----------------------|--|
| χ_r | surface reflection coefficient (amplitude), $\chi_{r\perp}$: perpendicular, $\chi_{r\parallel}$: parallel wave |
| χ_t | surface transmission coefficient (amplitude) |
| χ_a | surface absorption coefficient (amplitude) |
| η_1, η_2 | refractive index of medium 1 and 2 respectively |
| α_{aoi} | angle of incidence on surface (to surface normal) |

| | |
|-----------------------|---|
| d_{POI2edge} | point of incidence to closest surface edge (used for diffraction model) |
| Θ_D | diffraction gain factor ($\Psi_{D,r}$: reflection mode, $\Psi_{D,t}$: transmission mode) |
| β_{blur} | diffraction model blurring factor (user setting) |
| β_{int1} | diffraction model internal setting (blurring factor) |
| β_{int2} | diffraction model internal setting (shift factor) |

— **Channel Model (Statistical Small-Scale)** —

| | |
|--------------------|--|
| $\tilde{\tau}_i$ | delay center of gravity of the i -th segment of the APDP (APDP discretization) |
| f_{res} | channel frequency resolution (setting) |
| B | channel bandwidth (setting) |
| N_{CT} | number of channel taps (discretization of PDP) |
| ε_K | relative tolerable error for LOS K-factor (setting) |
| ε_τ | relative tolerable error for RMS delay spread (setting) |
| \tilde{P}_i | power of channel tap i (discretization of APDP) |
| \tilde{A}_i | amplitude of channel tap i (discretization of APDP) |
| Π | non-line-of-sight power density (of APDP; local usage, adopted from [2]) |
| γ | exponential decay constant (of APDP; local usage, adopted from [2]) |
| ρ^2 | line-of-sight power (of APDP; local usage, adopted from [2]) |

— **Tag Reflection Coefficient Model** —

| | |
|---------------------|--|
| P_{ic} | chip (IC) power |
| P_{in} | input power (available minus reflected power) |
| P_{av} | available (incident) power at the tag's antenna ports |
| P_l | power losses in assembly and modulation impedance |
| P_{bs} | backscattered (reflected) power |
| $P_{\text{ic,min}}$ | minimum operational chip power (tag sensitivity; power-on reset threshold of chip) |
| $P_{\text{av,min}}$ | minimum operational available (incident) power |
| M | modulation state (discrete states modulated \leftrightarrow unmodulated) |
| A | assembly tolerance state (linked to assembly impedance) |
| D | detuning state (antenna detuning near dielectric materials) |
| R_a | antenna resistance (perfectly tuned) |
| X_a | antenna reactance (perfectly tuned) |
| Z_a | complex antenna impedance (perfectly tuned), $Z_a = R_a + jX_a$ |
| Z_{ic} | complex chip impedance in unmodulated state |
| Z_{m} | complex modulation impedance |
| Z_{at} | complex assembly impedance plus tolerances |
| R_{at} | assembly resistance plus tolerances |
| C_{at} | assembly capacitance plus tolerances |
| ρ | tag reflection coefficient |
| $\bar{\rho}$ | linearized reflection coefficient, center value |
| $\Delta\rho$ | linearized reflection coefficient, difference value |

Statutory Declaration

I declare that I have authored this thesis independently, that I have not used other than the declared sources/resources, and that I have explicitly marked all material which has been quoted either literally or by content from the used sources.

date

(signature)

Quoting the Librarian: "Oook!"

1

Introduction

1.1 A Primer on Passive UHF RFID and Radio Localization

1.1.1 Passive UHF RFID

Passive radio frequency identification (RFID) and the well-known barcodes share a common property: They have been designed for and are used for the identification of small goods. In comparison to barcodes, however, RFID systems come with more memory, the ability to modify this memory, and the optional support for authentication and encryption.



(a) a barcode (ISBN/EAN-13)



(b) a UHF RFID self-adhesive label

Figure 1.1: Comparison between barcode and UHF RFID tag (NXP UCODE).

Passive refers to the fact that the mobile device – the so-called tag (the actual replacement for the barcode) – does not have an autonomous energy source like a battery, but is supplied via magnetic or electromagnetic fields by the base station. This based station is called reader or interrogator in RFID. Three different frequency ranges are used for RFID, depending on the application: low frequency (LF) RFID systems operate at around 125 kHz, high frequency (HF) systems at 13.56 MHz, and ultra-high frequency (UHF) RFID uses 860–960 MHz. Apart from these RFID-typical frequency ranges, also other ISM (industrial, scientific, medical) bands are used for RFID devices. Regardless of the frequency band, all passive RFID systems utilize only a few kHz to MHz of bandwidth and are thus classical narrowband systems. Applications range from product identification and tracking, through electronic article surveillance, to secure access cards. There are several textbooks available on RFID and its applications, e.g., [3, 4].

Due to their (comparatively) long range and low cost, passive UHF RFID tags are typically used in supply chain applications, i.e., the tracking of goods. The basic idea here is to attach an RFID tag to all products, like a barcode, and use this tag in all inventory operations (incoming/outgoing goods, warehouse stock, etc.). The general working principle of passive UHF RFID is illustrated in Fig. 1.2: The reader generates a powerful carrier wave that is transmitted by the reader antenna. These reader antennas are typically directive, i.e., they illuminate only a certain volume, the so-called read zone. If a tag is inside this read zone, the power transmitted by the reader activates this tag and it is ready to receive commands. Passive UHF RFID, more precisely EPCglobal Class-1 Gen-2 (adopted as ISO 18000-6C, [1]) UHF RFID, is a “reader-talks-first” protocol, i.e., the tags wait until they are addressed. Upon receipt of a command, which is transmitted via modulation of the carrier wave, the tag sends its identification code or parts of its memory. The tag does not actively transmit this data, but reflects part of the incident reader carrier wave by deliberately detuning its own antenna. This principle is known as backscatter modulation.

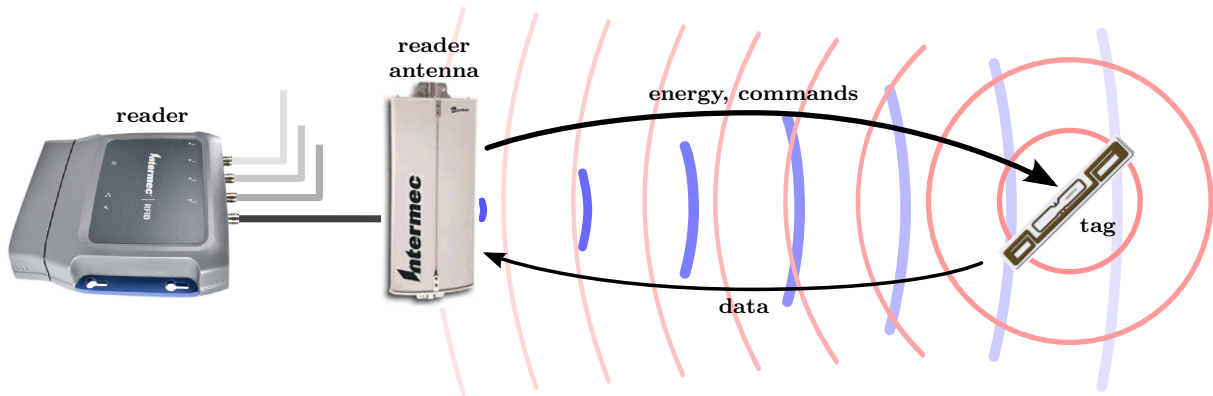


Figure 1.2: Working principle of UHF RFID (Reader, reader antenna: courtesy of Intermec Technologies).

Being a typical supply chain system, passive UHF RFID is mostly used in warehouses, production halls, and salesfloors. Some of these environments are shown in Fig. 1.3. Permanent



Figure 1.3: Typical environments and applications for UHF RFID (courtesy of Intermec Technologies).

installations are mostly used at the loading bays of warehouses or at the exits of shops. They consist of a reader device and typically four reader antennas that are mounted in portals. In Fig. 1.3(a), these antennas are visible at the center portal, where the housing has been removed. In recent years, handheld reader devices have also begun to emerge. Like handheld barcode scanners, they are used for the inventory inside a shop or when individual packages are handled (e.g., delivery of parcels).

Localization of tags becomes an important issue for dock doors and similar scenarios where several parallel portals or conveyor belts are present. Since tags reply to commands whenever they are powered, confining the read zone to a specific area becomes necessary. If, for whatever reason, a tag outside this intended read zone replies to a command, inventory lists are corrupted or false positive alarms are triggered.

Unfortunately, there is no way for a reader to make sure that only tags inside the intended read zone are powered up. In any realistic environment, electromagnetic waves are reflected at all objects in the vicinity and an interference pattern is created, such as the one shown in Fig. 1.4. Blue zones (below roughly -5 dBm) in this measurement indicate that tags are not functional. Conversely, tags in green to red zones are well inside their operational power range. Note that there are “dead zones” inside the portal as well as zones outside the portal where tags are powered. This pattern covers the entire vicinity of the intended read zone. Although the

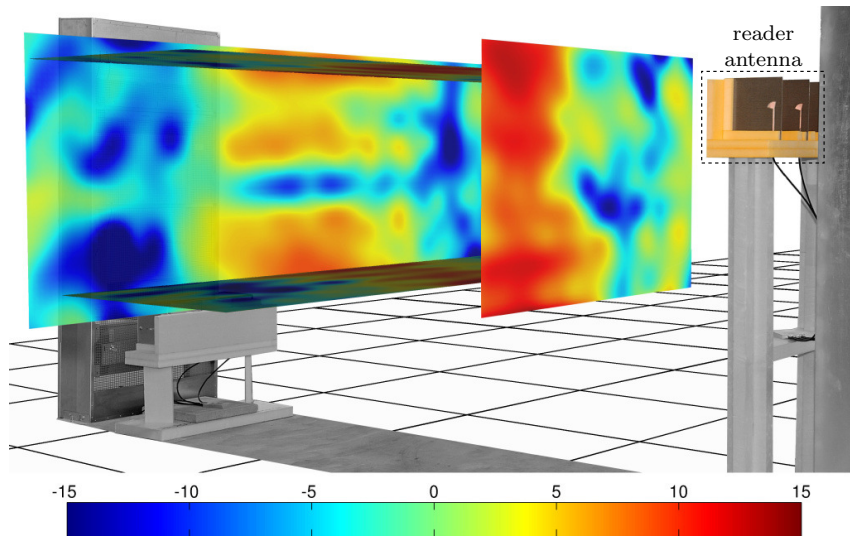


Figure 1.4: Measured receive power distribution [dBm] at the tag inside a UHF RFID portal.

average power decreases with distance from the portal, peaks in this distribution will allow a few tags to reply to a command even far outside the intended read zone. Such stray over-range reads are the reason why tag localization is a desired feature in UHF RFID.

1.1.2 Localization: Range vs. Direction

Essentially, two methods are available to localize an object using base stations at known positions: direction finding and range finding. Both are illustrated in Fig. 1.5.

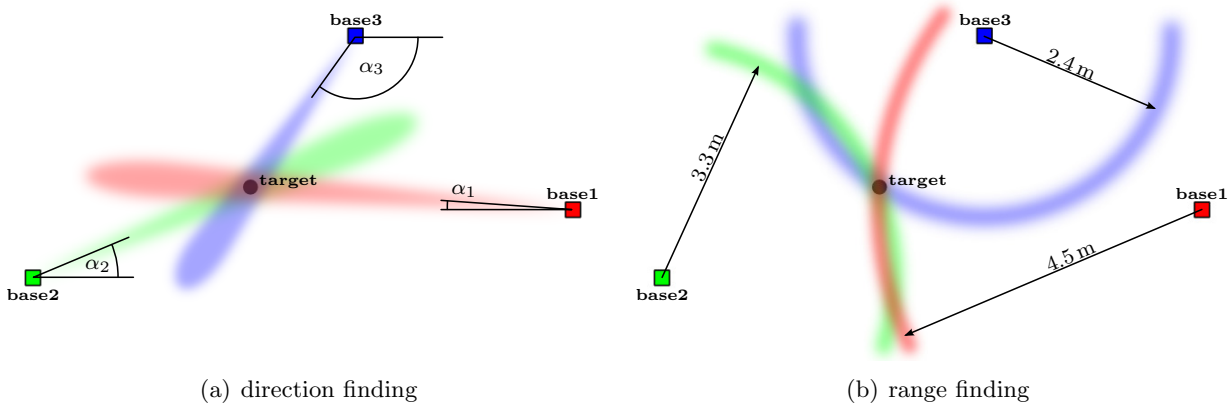


Figure 1.5: Illustration of basic localization methods: direction vs. range finding.

Direction finding is performed by using highly directive base stations. The target can be localized in three dimensions by determining the intersection of beams from at least two base stations. In range finding, each base station independently determines the distance to the target (ranging). The target's location is then calculated by intersecting the resulting circles (2D) or spheres (3D). At least three base stations are necessary to determine the target's location in two dimensions (trilateration), while at least four base stations are necessary to remove all ambiguities in three dimensions (multilateration). A combination of both is used in ground to air radar stations or sonar, where the target's location is determined by measuring range and direction at the same time.

More details on the different types of localization based on electromagnetic or acoustic waves can be found in textbooks, e.g., [5]. Two principles, namely time of arrival and angle of arrival, are used in UHF RFID and thus explained in more detail below.

The ranging principle known as time of arrival (ToA) is straightforward: A transmitter (TX) sends a signal, which in turn is observed at the receiver (RX) τ_1 seconds after the signal was sent, as illustrated in Fig. 1.6(a). The receiver then calculates the distance to the transmitter

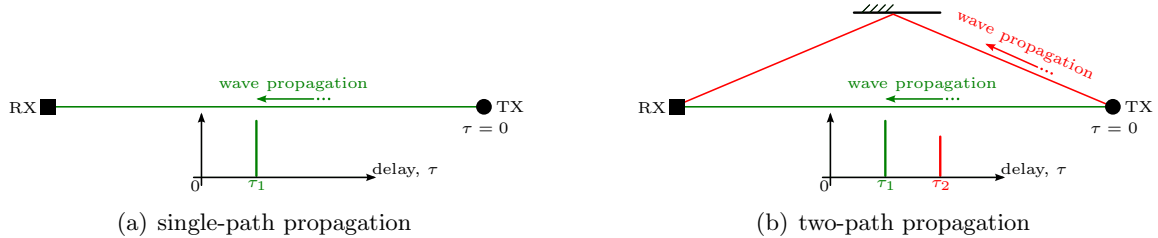


Figure 1.6: Time of arrival (ranging) for single- and two-path propagation.

via $d = c\tau_1$, where c is the speed of light². In any practical scenario, the receiver will also receive additional copies of the signal that are created by reflections in the environment, cf. Fig. 1.6(b). Ideally, the ranging system is able to distinguish those paths (as in the illustration) and thus to lock onto the direct one, called line-of-sight (LOS). This direct path carries the range information. Note that ToA requires transmitter and receiver to be synchronized to the same time base. This synchronization comes for free in classical backscatter radar systems, where transmitter and receiver are located at the base station, while the target is merely a reflector.

In case of a sinusoidal carrier signal, the propagation delay is mapped to a phase shift. For example (neglecting channel attenuation):

$$s_{\text{TX}}(t) = \cos(2\pi ft) \quad \Rightarrow \quad s_{\text{RX}}(t) = s_{\text{TX}}(t - \tau) = \cos(2\pi f(t - \tau_1)), \quad (1.1)$$

where $2\pi f\tau_1$ is the resulting phase shift of the received signal with respect to the transmitted one. This is sometimes referred to as phase of arrival (PoA).

The direction finding method known as angle of arrival (AoA) or direction of arrival (DoA) works by either mechanically rotating antennas or by using an array of two or more receivers (per base station). A classical example for rotating antennas are radar stations, where the angle of arrival is determined by mechanically turning the antenna towards the target. Array-based direction finding, which is commonly used in acoustics, is illustrated in Fig. 1.7(a). Here the

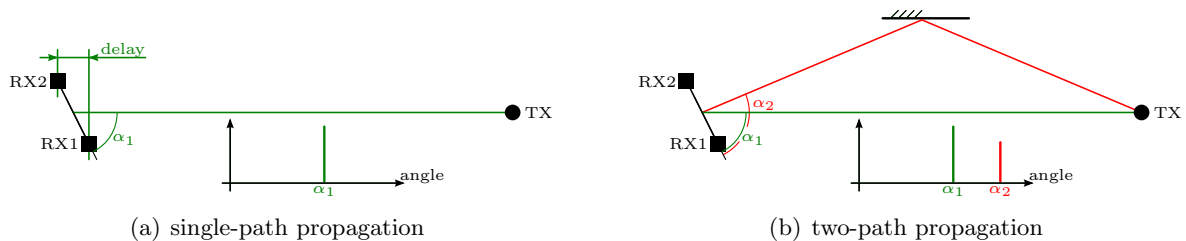


Figure 1.7: Angle of arrival (direction finding) for single- and two-path propagation.

signal sent by the transmitter is received by both receiver antennas of the array, RX1 and RX2. Depending on the angle of arrival there is a small delay between the signals observed by RX1

² more precisely, the group velocity of the wave in the medium

and RX2. This delay is zero if the incoming wavefront is parallel to the array arrangement and maximized if the wave travels along the array. Similar to time of arrival, indirect propagation paths will result in additional copies of the signal at different angles, cf. Fig. 1.7(b). Note that, as opposed to ToA, reflected components can occupy the same angle as the line-of-sight.

AoA assumes a planar wavefront and thus far field conditions, i.e., the LOS distance d_{LOS} between transmitter and receiver has to exceed $2d_{\text{Ant}}^2/\lambda$ by far, where λ is the wavelength of the signal and d_{Ant} is the maximum overall antenna size [6, p. 592]. Below this range, the incoming wavefront has to be considered spherical, with increasing radius for each receiver. Naturally, this massively complicates calculating the direction of arrival. Note that RFID systems do not necessarily operate in the far field (Fraunhofer) region: the Intermec IA39B UHF RFID portal antenna [7], for example, has a dimension of 55×26 cm and is tuned to a frequency of 868 MHz. For this antenna, the Fraunhofer region starts at approximately 2 m distance.



Please note that although Fig. 1.6(b) and Fig. 1.7(b) depict only two paths, any realistic environment features multipath propagation, where “multi” essentially means “infinite”. The number of significant ones among this countless number of paths depends on the environment and the system. In short: two-path propagation may be convenient, but it only rarely reflects reality. See Section 2.2.3 for more details on this topic.

1.2 The Difficulties of Localizing Passive UHF RFID Transponders

Classical radar systems are able to localize a fast-moving plane at distances up to several hundred kilometers. UHF RFID tags, on the other hand, only have to be localized at distances up to a few meters and are quite stationary in comparison. Both are backscatter systems, i.e., they are comparable in their mode of operation. Why, then, is the localization of these small tags so difficult?



Figure 1.8: Air traffic control radar vs. UHF RFID tag localization (Sources: [8] / Intermec Technologies).

There are five major reasons for this:

1. Foremost, the wireless propagation channels of both systems are not even remotely comparable. The echo created by an airplane is usually isolated from all other echoes, i.e., it is not surrounded by considerably larger objects. In contrast, UHF RFID tags are not isolated from their environment and are used indoors, i.e., under massive multipath conditions. The tag here is the proverbial needle in a haystack. Moreover and for the same reason, classical radar always has a clear line-of-sight. Flying the airplane behind a mountain disrupts the ability of the radar station to locate the plane. In UHF RFID, on the other hand, the LOS to the tag is often blocked by the product on which the tag is placed or other obstacles. Any ranging system thus has to deal with these non-line-of-sight (NLOS) conditions.

2. Ground to air radar antennas are pointed at the sky, thus avoiding any reflections in the immediate vicinity. Self-interference caused by such reflections, which are literally a million times stronger than any target echo, cannot be avoided in passive UHF RFID. On the contrary, reader antennas are deliberately pointed at reflecting surfaces in RFID portal setups in order to concentrate energy inside the portal.
3. A radar station has a lot of time to track the airplane (or other targets) and is thus able to learn and predict its behavior. A UHF RFID tag leaves the range of the system within seconds. Constantly tracking a single tag during this time is not possible, since there are tens or even hundreds of tags that have to be processed within this short time frame.
4. Radar stations, especially military ones, use high-end equipment that is a lot more expensive than anything even remotely feasible in RFID.
5. Finally, while “misplacing” an airplane by 10 m is not a problem in air traffic radar, it is a huge problem in passive UHF RFID applications. This is discussed in detail in Section 1.3.

1.3 Motivation and Related Work

Accurate localization of tagged objects could benefit UHF RFID in numerous applications, such as warehouse and point-of-sale portals, salesrooms, or archives. Naturally, the definition of “sufficient accuracy” depends on the application (size of tagged object, environment), and on tolerable error rates.

Two showcase applications for tag localization in UHF RFID are the above-mentioned warehouse portals and the point-of-sale in supermarkets (including electronic article surveillance). Both typically involve several adjacent portals in which tagged items are being registered while moving through. And in both applications, apart from the obvious necessity to distinguish between portals, the system also has to distinguish between “moving through”, “moving by” and “lying somewhere close” with extremely low error rates. For comparison: an error rate of 1‰ at a supermarket point-of-sale would imply that, assuming an average of 50 products per customer, one out of twenty customers will receive an erroneous bill. Taking the typical size of and spacing in-between such portals into account, an accuracy/precision between 30 cm and 1 m at an error rate well below 1‰ for distances up to a few meters would be required for such applications, cf. [5, 9, 10]. Although there has been considerable research on this issue since 2005, this problem remains elusive. There are two major reasons for this: severe multipath propagation, especially inside UHF RFID portals, and the limitations enforced by the general system design (low-power, low-complexity tags; high throughput of tags in portals). The combination of both problems makes tag localization in passive UHF RFID an extremely challenging task.

Hence, the research question addressed and answered by this thesis is:

Is it possible to accurately determine the position of passive UHF RFID tags in typical applications and within the boundary conditions of passive UHF RFID systems?

Most of this thesis deals with ranging (the basis of range finding localization), but also direction finding is discussed to some extent. The central goal is read zone management in typical UHF RFID applications, i.e., the detection of over-range and false positive reads. Apart from having to deal with the UHF RFID channel, any potential system thus has to meet several requirements to ensure compatibility with the established hardware and protocol. From a system point of view, the most important requirements are³:

- compatibility to ISO 18000-6C [1]
- passive, low complexity tags
- backscatter modulation, multiple targets
- target detection time: less than 1 ms
- up to 12 m range
- error: $\leq 10\%$ of the true distance

³ These requirements have been defined by NXP as target specifications for this thesis project [11, 12] (internal).

State-of-the-Art Ranging and Localization Methods in UHF RFID

Localization methods in UHF RFID can be categorized into the following groups, which will be discussed in detail below:

1. localization of the reader using multiple tags (typically conforming to standard)
2. localization of a single tag using one or multiple readers
 - a) methods inside the Gen-2 standard
 - b) methods which require an extension to or coexist with the standard

Localization of the reader using multiple tags is typically used to determine the position of a robot or human inside a room [13–29]. To this end, multiple RFID tags are placed at known positions throughout the room (typically on floor or ceiling) and an RFID reader continuously queries the tags using directional antennas. Depending on the position of the reader, only a certain subset of the tags will reply to the query. The reader’s position is typically obtained from this subset using fingerprinting techniques. The accuracy achieved depends on the spacing between tags and the distance between reader and tags. It is typically in the order of 50 cm for a dense grid (cf. above references). This method is often combined with measurements of the received signal strength (RSS) [13, 16, 17, 21, 22], optimization techniques [13, 17, 20–26, 29], and can also be combined with variable reader output power levels [16, 27, 28]. Robust fingerprinting is feasible in this scenario because several hundred tags can be placed, thus forming a statistically stable base of reference points. A single over-range read or missing tag is thus unlikely to influence the final result. Straightforward application to tag localization using a set of reference readers is theoretically possible (e.g., [26, 30, 31]), but ultimately too expensive.

Localization of a single tag using one or multiple readers is a flagship supply-chain application. As opposed to the above scenario, tags in warehouse- or supply-chain applications can only be ranged a few times (typically only once) before they leave the interrogation zone. The aim is usually classification such as “inside/outside portal 4” (read zone management) or “on shelf 17, 3rd row”. Unlike for the positioning of the robot above, the error rate of each individual estimate has to be very low: While the position estimate for the robot does not depend on a single one out of thousands of reference tags, a truck driver’s boss might not look kindly upon a pallet of expensive goods supposedly (according to the RFID system) loaded onto the truck, but never unloaded at its destination. Process information can be used in order to increase robustness in these scenarios, e.g., [32–34].

A comprehensive overview of (mostly phase-based) narrowband ranging methods for passive UHF RFID can be found in [35], while [36] contains a list of active RFID ranging systems. A more detailed description of different narrowband methods can also be found in Section 4.1.

Several narrowband methods work within the existing standard: Variable reader output power levels or received signal strength in combination with distributed readers can be used to localize a single tag [37–40]. Also combinations with beamsteering [41] are possible. The method reaches a localization error of 60 cm (single-tag, [40]) down to 15 cm (reference tags, [37]), but comes at the cost of a high reader density and the necessity of per-tag calibration in order to reach this accuracy.

RSS-based methods using only one mobile reader on a robot or cart [42–45] reach localization errors down to 10 cm at short distances (approx. 1 m), but need a lot of time to build the virtual array of readers and thus rely on a stationary tag. Like all methods with multiple observations, learning/optimization methods can be used to increase accuracy, e.g. [42].

Another method uses continuous phase measurements of the backscattered carrier, i.e., the rotation in the constellation diagram [46]. This is similar to measuring the Doppler shift [47, 48] and gives an estimate of the radial (centripetal) speed of a tag relative to the reader antenna. No conclusive ranging accuracy is given, although it is likely to be in the range of at least several ten percent of the true distance, cf. Fig. 17 in [35]. Even though this method is not practicable

for ranging in most real-world scenarios (a tag needs to move and be queried continuously to obtain its position), it is currently used to determine if a tag is moving, cf. [49]. However, when combined with synthetic aperture radar techniques (SAR; moving reader), this method yields the position of the tag [50]. Even errors in the low centimeter range can be achieved at short ranges (approx. 1.5 m) [50], provided that tag and environment are stationary for several minutes.

A series of carrier phase measurements in combination with frequency hopping reaches an error of 40 cm and below in anechoic environments [51], but most likely has a considerably higher error in multipath environments. (See Section 4.2 for further details.)

Yet another method uses antenna arrays to determine the angle of arrival from several reader positions [52–57], cf. [58–60]. In idealized simulations [56,57], anechoic rooms [54], and in a light multipath environment [55], accuracy is in the range below 3° using a 2×1 array. Roughly the same accuracy can be reached in dense multipath environments using larger arrays [53]. Last but not least, pseudorandom (pseudo-noise) sequences with well-defined correlation properties (widely used in GPS/GNSS [61], IEEE 802.15.4a-based ranging [62], and a number of other communication systems) have also been applied to the ranging problem in UHF RFID [63]. Using small bandwidths (\sim MHz) and a semi-passive tag, errors in an unspecified multipath environment are in the range of 1.5 m [63].

Methods that require additional transmit signals either coexist with the standard (use a different frequency range) or require an extension to the standard (modification to spectral masks and/or multiple carriers). These are typically multi-carrier systems [64–66] or frequency-modulation continuous-wave (FMCW) systems (up to ultra-wide bandwidths) [67–84]. Both methods are sometimes combined with array processing to mitigate multipath propagation [64, 65]. Ranging accuracy in the absence of multipath propagation⁴ is in the millimeter/centimeter range (see references above), but is likely to reach several meters for practical UHF RFID scenarios, cf. Chapters 4 and 5. Cable-based [73,80,85], AWGN⁴ [66,75,81], and two/three-path wireless channel models [65,86] in particular are overly optimistic representations of the UHF RFID channel, cf. Chapter 2. Notably, active FMCW systems have been tested in industrial environments (under clear LOS) [68, 78, 79, 83], reaching errors below 30 cm at distances up to several hundred meters. Recent publications extend the FMCW approach to semi-passive backscatter systems [67, 71], although it is not yet known if the system is able to deal with the combination of heavy multipath propagation, frequency tolerances [1], and the high tag throughput in UHF RFID application scenarios. See Chapter 5 for a further discussion of this topic.

There are also several commercial passive UHF RFID localization systems available. In contrast to the published scientific results, details concerning the methods used are kept a secret. From a scientific point of view, claims concerning accuracy often seem to be missing an “under ideal conditions and after some manual corrections” note. Active or semi-active RFID tag localization (as implemented by Tagent⁵, for example) is not addressed in this thesis.

Mojix (<http://www.mojix.com>) uses distributed readers (reader antennas) and presumably analyzes the tag responses in the space-time-frequency domain [87]. Accuracy is said to be “within as close as one meter” [88], which can be taken as an accurate claim, since it actually could be interpreted as a lower bound for the error.

RF Controls (<http://www.rfctrls.com>) uses phased arrays for interrogation and localization. Accuracy is said to be 30 cm (1° in the angular domain) [89].

Trolleyscan (<http://trolleyscan.com/>, <http://www.rfid-radar.com>) claims to reach millimeter accuracy at a distance of 40 m using passive tags [90] within the EPC Gen-2

⁴ This includes stationary multipath channels after calibration.

⁵ <http://www.tagent.com>

protocol, without triangulation or fingerprinting, but “using a new method” [91]. This claim seems to be optimistic at best in the light of the results presented in this thesis, but also when compared to high-accuracy ultra-wideband ranging systems [92].

Wirama was a spin-off from the University of California (UC Berkeley and UC Santa Barbara).

Accuracy was supposed to be in the range of 6 inches (15 cm) up to a maximum distance of 10 m [87], solely based on the EPC Gen-2 protocol. The company disappeared in 2008.

Loosely related to the localization methods treated in this thesis are ultra-wideband (UWB) positioning techniques and systems (e.g., [5, 92, 93]). Most prominent among these is the IEEE 802.15.4a standard [94]. An analysis of the ranging capabilities within this standard can be found in [62]. Furthermore, a comprehensive survey of indoor positioning systems (including ultrasound and optical systems) can be found in [95]. UWB technology in general is considered to be a possible successor to current passive RFID technology [96], cf. [97–99].

The exact opposite of ultra-wideband, namely low-frequency near field ranging, is available as well [100]. This technique works at around 1 MHz and evaluates the relation between electric and magnetic near field transmitted from an active transponder about the size of a GPS receiver. It is developed and sold by the US company Q-Track⁶ for localization in rugged environments.

Also loosely related is the topic of indoor and underwater acoustic source localization, e.g., [101–105], including underwater echo localization (sonar), e.g., [106–109]. Both passive and active localization in acoustics almost invariably use large microphone/hydrophone arrays (see [105], for example) or synthetic apertures (e.g., [106]). Moreover, acoustic signals span huge relative bandwidths and are therefore often ultra-wideband (e.g., human speech or an active sonar “ping”). From an electromagnetic point of view, the ease with which large relative bandwidths can be achieved in acoustics, the sampling resolution (above 8 bit), and also the comparatively low hardware costs for huge arrays can only be viewed with envy and amazement.

State-of-the-art simulation and emulation tools in UHF RFID are typically designed for the analysis of the existing EPCglobal Class-1 Gen-2 protocol.

RFIDSim⁷ [110–112] is an open-source protocol simulator for Gen-2 UHF RFID. It features high-level physical models of channel (Rician fading) and tag (nonlinear lookup-table-based reflection coefficient) and is based on a discrete event simulation core (JiST, [113]).

The ASD Kit and Library [114–116] developed and sold by CISC Semiconductor⁸ is a system-level simulation and emulation tool with a focus on the tag model. It uses a chip-level behavioral model of the tag that can also be uploaded to a tag emulator hardware. Emulator testbeds for UHF RFID tags [117–119] and channels [120, 121] are currently also being developed at Vienna University of Technology.

System-level simulators for RFID have been developed at the Auto-ID Labs of Fudan University [122] and at Beijing Jiatong University [123]. The technical focus of both simulators is on the reader. Some resemblance also exists to a WiFi/RFID localization testbed [124] and a system-level simulator for chipless surface acoustic wave (SAW) sensors [125].

Finally, in addition to the publicly available tools listed above, there is likely a high number of proprietary solutions operated by RFID companies around the world.

⁶ <http://www.q-track.com/>

⁷ http://www.matthewjmiller.net/files/rfidsim_doc/html/

⁸ <http://www.cisc.at/>

1.4 Contributions and Outline

Ranging in passive UHF RFID was not even in its infancy at the beginning of this thesis project in 2007. Available work was mostly theoretical and provided only a very high-level view. In order to be able to develop a solution for the ranging problem, two prerequisites had to be met: first of all, an environment for tests and performance benchmarking had to be created and, secondly, a model for the (quite peculiar) UHF RFID wireless channel had to be found.

UHF RFID hardware at that time was not able to support any ranging. Even measurement capabilities for the return link phase (i.e., in-phase/quadrature-phase (I/Q) demodulators) were rare. Furthermore, measurement setups in general are very limited in their capability of switching on/off different physical effects, such as frequency tolerances or multipath propagation. For this reason, a simulation framework was created and gradually refined in the course of this thesis project. In contrast to other UHF RFID simulators (for related work see Section 1.3), it is specifically designed to handle (ultra-)wideband signals and fading channels, as well as nonlinearities and detuning of tags. It also comes with its own exception handling and logging system and an extensive set of self-test routines that ensure the framework's functionality. The first stable version of what would later be called *The PARIS Simulation Framework* was presented at the IEEE RFID conference in 2009:

- [126] Daniel Arnitz, Ulrich Muehlmann, Thomas Gigl, and Klaus Witrisal, “**Wideband system-level simulator for passive UHF RFID,**” in *Proc. IEEE Int RFID Conf*, Orlando, Florida, Apr. 2009, pp. 28-33.

From the beginning, this framework was built for maximum flexibility. The tag model, for example, is based on lookup tables derived from data that can easily be measured, such as antenna- and chip impedances. Simulating different types of tags is thus only a matter of obtaining this data. The currently available tag model is based on data provided by NXP and resembles an NXP UCODE G2XM on an NXP UCODE general purpose reference antenna. The entire simulation tool including all characteristics was made available under the GNU General Public License [127]. It is explained in detail in Chapter 3.

In 2009 and 2010, the *tag reflection coefficient model* has been verified by extensive measurements. The tag reflection coefficient is of paramount importance not only to ranging as a potential source of large errors (cf. Section 4.2), but also to tag-antenna-based sensing. Verification has been done by time-variant scattering (S-) parameter measurements of the modeled NXP UCODE G2XM tag in the field and during modulation, using a vector network analyzer (VNA). The central problem in this measurement is calibration: even with highly directive horn antennas and in an anechoic chamber, environmental reflections and direct coupling (feedback) exceed the tag's reflection coefficient (radar cross section) by several tens of dB. While detecting the change in the reflection coefficient during modulation is an easy task (this is why UHF RFID is so robust), an exact measurement of both modulation states is borderline impossible even using state-of-the-art network analyzers. The reflection coefficient model and the measurement procedure for its verification were published in 2010 at the EURASIP workshop on RFID and won the best paper award:

- [128] Daniel Arnitz, Ulrich Muehlmann, and Klaus Witrisal, “**Tag-based sensing and positioning in passive UHF RFID: Tag reflection,**” in *3rd Int. EURASIP workshop on RFID Techn.*, Cartagena, Spain, Sep. 2010, pp. 51-56.

To our knowledge, this is the first wideband measurement of the tag reflection coefficient in situ and during tag modulation with a standard VNA. A detailed explanation of the tag's reflection coefficient model and its calculation from raw data can be found in Section 3.3.

The second prerequisite mentioned above, the *UHF RFID channel*, was the dominant topic in the third year of the project. During the first two years, the channel was assumed to be not much different from a standard short-range indoor wireless channel. Unfortunately, this is not entirely the case. Common wireless indoor channel models such as the IEEE 802.15.4a model

are not directly applicable due to several peculiarities of UHF RFID setups. These special features include the very short range, several large and possibly strong reflectors in the immediate vicinity of the tag to be ranged (tagged products), and the fact that the channel is degenerate due to its backscatter nature. Following this realization, a UHF RFID measurement setup suitable for ultra-wideband measurements was created and several measurements were conducted. Based on these measurements the channel models implemented in the PARIS framework were corrected and extended, and the candidate ranging systems were re-evaluated. Several publications followed this process. A poster at the IEEE RFID 2010 conference presented our first measurement results with the newly created setup:

- [129] Daniel Arnitz, Ulrich Muehlmann, and Klaus Witrisal, **“Wideband characterization of UHF RFID channels for ranging and positioning,”** Poster at *IEEE Int RFID Conf*, Orlando, Florida, Apr. 2010.

Following this first test measurement and after completing and perfecting the measurement setup, extensive measurements were performed in the UHF RFID gate installation at NXP’s Application and System Center (ASC). The measurement and analysis setup as well as some preliminary results were published at the 11th COST2100 meeting in June 2010, and were also featured in the COST2100 newsletter in July 2010 [130].

- [131] Daniel Arnitz, Grzegorz Adamiuk, Ulrich Muehlmann, and Klaus Witrisal, **“UWB channel sounding for ranging and positioning in passive UHF RFID,”** in *11th COST2100 MCM*, Aalborg, Denmark, Jun. 2010.

The full analysis of those measurements held several unpleasant surprises. The propagation channel inside an RFID portal resembles a severe multipath industrial channel. Additionally, the portal design creates a very deterministic channel, thus also limiting the effects of spatial diversity and invalidating several common assumptions regarding wireless channels. A comprehensive analysis of this channel has been submitted to the IEEE Transactions on Antennas and Propagation:

- [132] Daniel Arnitz, Ulrich Muehlmann, and Klaus Witrisal, **“Wideband characterization and modeling of UHF RFID channels for ranging and localization,”** submitted for publication.

Not part of this analysis is a complete theoretical investigation of the channel’s backscatter property. A derivation of wideband backscatter channel characteristics vital to ranging and localization has been accepted by the IEEE Transactions on Antennas and Propagation:

- [133] Daniel Arnitz, Ulrich Muehlmann, and Klaus Witrisal, **“Wideband characterization of backscatter channels: Derivations and theoretical background,”** accepted for publication.

Finally, a validation of these derivations and the resulting estimators was presented at the European Wireless conference in 2011:

- [134] Daniel Arnitz, Ulrich Muehlmann, and Klaus Witrisal, **“Wideband characterization of backscatter channels,”** in *Proc. Europ. Wireless Conf*, Vienna, Austria, Apr. 2011, pp. 205–211.

This marks the final result of the channel modeling efforts. A summary of the findings published in these papers can be found in Chapter 2.

Naturally, the core topic of this thesis also demanded a lot of effort. In the hope to find a system that could easily fit into current UHF RFID systems, the research on *localization methods for passive UHF RFID* started with narrowband methods⁹. As it was obvious that pure RSS-based methods would never reach the required accuracy and robustness, another approach had to be taken: an evaluation of the relative phase shifts between carriers, usually referred to as continuous-wave (CW) radar. A generalized approach using multiple carriers was published in the IEEE Transactions on Microwave Theory and Techniques in 2009.

- [135] Daniel Arnitz, Ulrich Muehlmann, and Klaus Witrisal, **“Multi-frequency continuous-wave radar approach to ranging in passive UHF RFID,”** *IEEE Transactions Microw. Theory Tech.*, vol. 57, no. 5, pp. 1398–1405, Jul. 2009.

⁹ Tag localization (2-D, 3-D, or quantized into read zones) requires that the underlying range/direction finding problem is solved in the first place. Consequently, most of the thesis deals with ranging. Direction finding is discussed as well, see Section 4.1.

This paper contains the theoretical framework as well as a comprehensive analysis of the ranging error introduced by noise, the tag, and multipath propagation. The main reasons for sending multiple carriers (instead of just two) are the increased robustness to multipath propagation and the possibility to correct some errors created by the tag. Predicted ranging errors are in the range of 10 – 20 % of the true distance for a single carrier pair, with multipath propagation being the most prominent source of errors. In retrospect, this analysis makes an assumption that is too mild for passive UHF RFID: it assumes that the direct path is always the strongest path. A more detailed analysis of this approach, also incorporating the findings of the channel measurements, can be found in Section 4.2.

From the channel measurements performed in the UHF portal, a single conclusion can be drawn regarding ranging methods: only ultra-wideband systems will reach the required error bound within the given measurement time. The small target size in UHF RFID in relation to the massive environmental reflections, however, pose a huge problem for these systems. In essence, UWB-based ranging is comparable to detecting minuscule changes in the environment, namely the change in the tag’s radar cross section ($\sim\text{cm}^2$). To speak from our experience during the measurements, it is a lot simpler to detect the breathing of a person somewhere in the room than to detect the tag modulation. Nonetheless, we managed to prove that UWB-based ranging works in principle by combining the analyses and experience from channel measurements and tag reflection coefficient measurements. Using this approach, we were able to detect a manually emulated tag modulation and pinpoint its source with a median error of 1.5 % of the true distance (maximum error: 7.7 %). These results were obtained in the SPSC’s radio frequency (RF) lab, which resembles an industrial environment from a channel point of view. The measurement-based proof of concept including the method itself was published in 2010 in the *IET Electronics Letters*.

- [136] Daniel Arnitz, Ulrich Muehlmann, and Klaus Witrisal, “**UWB ranging in passive UHF RFID: Proof of Concept,**” *IET Electron. Letters*, vol. 46, no. 20, pp. 1401–1402, Sep. 2010.

Finally, the performance of wideband frequency-modulation continuous-wave radar in the UHF RFID portal environment was analyzed in co-operation with the Institute of Electrical Information Technology of Clausthal University of Technology. The analysis is based on the channel transfer functions recorded in the ASC and shows that wideband radar systems are able to deal with this harsh channel, but also that upper error bounds are reached. The results were published at the IEEE RFID 2010 conference in 2011.

- [137] Gang Li, Daniel Arnitz, Randolf Ebel, Ulrich Muehlmann, Klaus Witrisal, and Martin Vossiek, “**Bandwidth dependence of CW ranging to UHF RFID tags in severe multipath environments,**” in *Proc. IEEE Int RFID Conf*, Orlando, Florida, Apr. 2011, pp. 19–25.

Wideband and ultra-wideband ranging systems are discussed in detail in Chapter 5.

Two more publications as co-author fall within the time period of this thesis. The first paper deals with ranging in IEEE 802.15.4a, which is an ultra-wideband system. It was published at the IEEE Symposium on Personal, Indoor and Mobile Radio Communications in 2009.

- [138] Thomas Gigl, Josef Preishuber-Pfluegl, Daniel Arnitz, and Klaus Witrisal, “**Experimental characterization of ranging in IEEE802.15.4a using a coherent reference receiver,**” in *Proc. IEEE Int Symp. on Personal, Indoor and Mobile Radio Comm.*, Tokyo, Japan, June 2009.

The second paper deals with ultra-wideband channel characterization and is based on the measurement procedures developed for the channel analyses in the context of this thesis. This publication, too, deals with ultra-wideband systems, specifically a channel analysis with respect to specular reflections. It was submitted to the IEEE ultra-wideband conference, ICUWB, in 2011.

- [139] Paul Meissner, Daniel Arnitz, Thomas Gigl, and Klaus Witrisal, “**Analysis of an indoor UWB channel for multipath-aided localization,**” submitted for publication.

2

Modeling the UHF RFID Channel

All wireless communication systems share a common enemy: the channel. Life would be simple (and boring) without its constant (but often time-variant) interference. The subspecies “passive UHF RFID channel” is an assortment of some of the finest wireless channel features, so to speak:

- very short-range (often not fully in the far field)
- reflective materials close to the tag (product on which the tag is placed)
- strong influence of the local geometry (short range, strong specular reflections)
- degenerate (pinhole [140]) channel due to the backscatter nature

This chapter is dedicated to the analysis of typical UHF RFID channels. After introducing some basics in Section 2.1, typical UHF RFID scenarios and the corresponding channels are explained in Section 2.2. This section also includes a discussion of the applicability of common channel models to ranging in UHF RFID. The following channel analysis of the passive UHF RFID channel is based on several measurements in indoor environments, most notably a UHF warehouse portal, and can be found in Section 2.3. Like most channel analyses in the literature, Section 2.3 discusses single-channel parameters. A method to apply wideband single-channel parameters to backscatter systems is provided in Section 2.4. Finally, a summary of recommended channel models and their parameterization is given in Section 2.5.

2.1 Introduction to Wireless Propagation

minor parts of this section have been published in [132]

2.1.1 Basics / Multipath Propagation Mechanisms

The most basic property of wireless channels is multipath propagation, where the time-variant channel impulse response (CIR) between a transmitter (TX) and a receiver (RX) is formed by a countless number of paths. Each path is governed by physical mechanisms: free space loss, reflection/transmission and diffraction at large objects, scattering at small objects and rough surfaces, as well as waveguiding [141, 142]. In its general form, the channel impulse response is multidimensional and thus not a simple construct, cf. [143], [141, p. 113].

Effects of the channel on the received power are categorized into three groups, which are illustrated in Fig. 2.1. The average attenuation (or path loss) is generated mostly by propagation loss. Deviations from this average path loss are called fading and are caused either by large objects between receiver and transmitter (shadowing / large-scale fading; changes slowly) or by interference between paths (small-scale fading; very localized). Both large-scale effects, i.e., the average path loss and shadowing, are typically represented by a log-distance path loss model and log-normal shadowing [142, pp. 138–139]. Small-scale effects are massively frequency-dependent and best understood from the CIR or the channel transfer function (CTF), which is the Fourier transform of the CIR. For narrowband systems, small-scale fading effects can be modeled using a Rayleigh, Rice, or Nakagami distribution [141, 142].

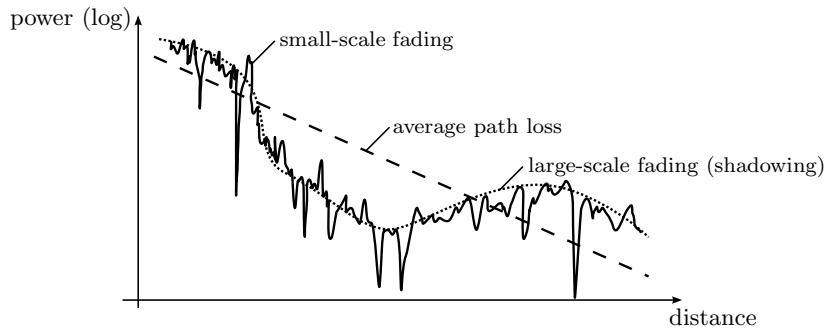


Figure 2.1: Channel basics: comparison of path loss models.

The wave propagation between a transmitter and a receiver can be in line-of-sight (LOS) or non-line-of-sight (NLOS). The definitions of LOS and NLOS, however, are somewhat ambiguous: From a setup/scenario point of view, LOS denotes an unobstructed direct path, i.e., air or other electromagnetically transparent material. Everything else is NLOS. This is the more common definition and the one used in this thesis. It takes into account that any material blocking the direct path will delay the signal due to reduced group velocity in dense materials compared to air. The alternative definition is based on the shape of the CIR. LOS there implies that the direct path can be identified in the CIR regardless of whether there is some object between RX and TX. If the direct path is the strongest component, this is sometimes called direct LOS (DLOS), [144, 145]. For an NLOS CIR the direct path is below the noise floor and thus cannot be identified.



2.1.2 The Power-Delay-Profile (PDP)

As with any linear system, the received signal in wireless communications can be calculated by a convolution of the transmitted signal and the channel impulse response. Unlike the impulse response of linear analog and digital filters, however, the wireless CIR is random and depends on time, position and orientation of transmitter and receiver, polarization, and of course on the environment. It is thus modeled as a stochastic process.

Only a simplified version of the wireless channel impulse response will be used in this thesis, where the CIR $h(\mathbf{p}_{\text{TX}}, \mathbf{p}_{\text{RX}}, \tau)$ depends only on the positions of the transmitter (\mathbf{p}_{TX}) and the receiver (\mathbf{p}_{RX}), and on the propagation delay τ . We will use a band-limited version of the CIR, represented by a filtered tapped delay line model (cf. [141, p. 105])

$$h(\mathbf{p}_{\text{TX}}, \mathbf{p}_{\text{RX}}, \tau) := \sum_{n=0}^N h_n(\mathbf{p}_{\text{TX}}, \mathbf{p}_{\text{RX}}) \cdot w(\tau - nT_s). \quad (2.1)$$

In this representation, $h_n(\mathbf{p}_{\text{TX}}, \mathbf{p}_{\text{RX}})$ is the complex gain factor of the n -th multipath component (MPC) between a transmitter TX at position \mathbf{p}_{TX} and a receiver RX at position \mathbf{p}_{RX} , $w(\tau)$ is a window function (pulse shape) with the appropriate bandwidth, and T_s is the sampling interval. Each MPC (delay bin) in this model combines a large number of physical paths with similar delays. As a consequence and due to the central limit theorem [146], the MPC gain h_n of a NLOS component can typically be modeled as zero-mean Gaussian random variable, cf. [141]. Note that this is not true for deterministic components such as the LOS and deterministic reflections, cf. [133].

Furthermore, we define the (instantaneous) power-delay-profile (PDP) as the squared magnitude of the CIR,

$$S(\mathbf{p}_{\text{TX}}, \mathbf{p}_{\text{RX}}, \tau) := |h(\mathbf{p}_{\text{TX}}, \mathbf{p}_{\text{RX}}, \tau)|^2. \quad (2.2)$$

and the average power-delay-profile (APDP) as the spatial average of PDPs at several positions, e.g., over N_{TX} transmitter and N_{RX} receiver positions

$$\bar{S}(\tau) := \frac{1}{N_{\text{TX}}N_{\text{RX}}} \sum_{i=1}^{N_{\text{TX}}} \sum_{j=1}^{N_{\text{RX}}} S(\mathbf{p}_{\text{TX}i}, \mathbf{p}_{\text{RX}j}, \tau) = \frac{1}{N_{\text{TX}}N_{\text{RX}}} \sum_{i=1}^{N_{\text{TX}}} \sum_{j=1}^{N_{\text{RX}}} |h(\mathbf{p}_{\text{TX}i}, \mathbf{p}_{\text{RX}j}, \tau)|^2 \quad (2.3)$$

Note that these definitions and representations are simplifications. First and foremost, they require ergodicity of the MPCs as well as an absence of correlation between them. Both requirements are easily violated in indoor environments [141, p. 105] or by increasing the bandwidth to UWB [147]. Nonetheless, the implications are sufficiently robust to be useful even in critical environments, as proven on the next few pages. Further details as well as the background theory can be found in [140–142].

With the theory established, we will now take a closer look at the (average) power-delay-profile. Typical UHF RFID wireless channels feature an APDP similar to the one shown in Fig. 2.2. The first arriving component of a PDP or an APDP corresponds to the direct (LOS) path between transmitter and receiver, and all following components correspond to indirect (reflected, NLOS) paths. The NLOS part often features clusters, i.e., distinct groups of reflections that stand out of the general decay. Such clusters are created by multiple reflections and scattering at objects that are spatially close. The decay of APDP and clusters is traditionally modeled as exponential [148]. Note, however, that exponential decay is not a general property of wireless indoor channels, e.g., [149].

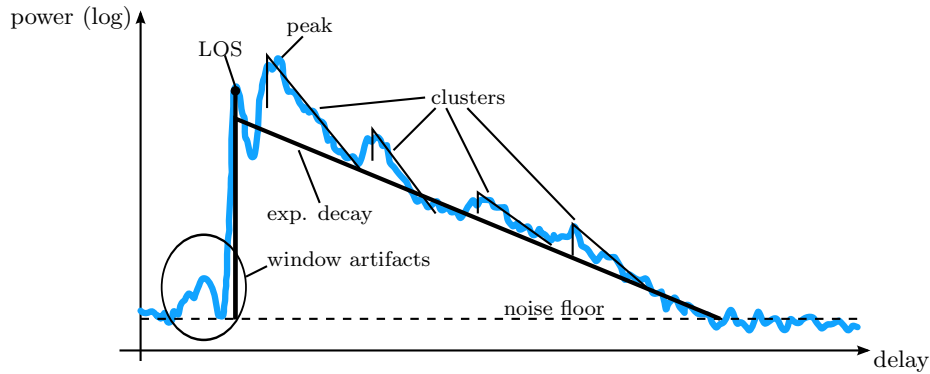


Figure 2.2: Channel basics: typical measured indoor average power-delay-profile (industrial environment).

The shape of the APDP is characterized by several interdependent parameters. The standard deviation¹⁰ of the normalized APDP is called root mean square (RMS) delay spread (τ_{RMS}),

$$\tau_{\text{RMS}} = \sqrt{\frac{\int_{-\infty}^{\infty} (\tau - \tau_{\text{avg}})^2 S(\tau) d\tau}{\int_{-\infty}^{\infty} S(\tau) d\tau}} \quad \text{with the average delay} \quad \tau_{\text{avg}} = \frac{\int_{-\infty}^{\infty} \tau S(\tau) d\tau}{\int_{-\infty}^{\infty} S(\tau) d\tau}, \quad (2.4)$$

while the last significant¹¹ delay is referred to as the maximum excess delay, τ_{max} .

For positioning, the power ratio of the direct (LOS) path to all indirect paths is of paramount importance, as it quantifies the influence of the direct path on the entire delay-profile. This ratio is provided by the K-factor with respect to the LOS path, which is a ratio between the LOS power P_{LOS} and the NLOS power P_{NLOS} ,

$$K_{\text{LOS}} = \frac{P_{\text{LOS}}}{P_{\text{NLOS}}} = \frac{P_{\text{LOS}}}{P_{\text{LOS+NLOS}} - P_{\text{LOS}}}. \quad (2.5)$$

Note that this is not necessarily identical to the definition of the Rician K-factor, which is a power ratio based on the strongest path instead of the direct path [142, pp. 212–214]. Unless explicitly stated otherwise, “K-factor” refers to K_{LOS} in this thesis.

Two more channel properties have a strong influence on ranging accuracy: The *coherence bandwidth* specifies the frequency offset at which the autocorrelation of the CTF (i.e., the spaced-frequency correlation function, SFCF) drops below a specified value. The *coherence distance* (coherence length) is the distance a receiver may move (for a fixed transmitter) before the correlation between the CIRs drops below a given value (typ. 50, 70, or 90 %). The corresponding correlation function is called spaced-distance correlation function (SDCF).

2.1.3 Effects of Local Geometry

While all the above parameters are originally defined for the average PDP and corresponding spectra [141, p. 110], they can of course be calculated for individual (instantaneous) PDPs and CTFs, i.e., single realizations of the wireless channel. This is especially useful in indoor environments, where the shape of the CIR is massively influenced by localized effects such as shadowing, large reflectors, antenna gain patterns, and the distance to the transmitter.

An example is shown in Fig. 2.3. Here the left side of a simple room with concrete walls contains an RFID reader (“transmitter”) with its mainlobe pointed at an absorbing wall. The

¹⁰ more precisely: the square-root of the second central moment of the normalized APDP

¹¹ As always, the definition of “significant” depends on the application.

right side of this room is partially shielded by the absorber which blocks the direct path, but only a small fraction of the reflected and scattered components. An Intermec IA39B [7] is used as a transmitter antenna in this example. Omnidirectional receivers are distributed throughout the room in order to measure and visualize the field distribution. The spatial distribution of K_{LOS} for this setup is shown in Fig. 2.3(a). Since the channel impulse responses at individual positions are random, the shape parameters at these positions become random as well, explaining the “noise” in the plot.

Obviously, the statistics of K_{LOS} depend on location in this room. Behind the absorber, K_{LOS} is in the range of -30 dB and thus very low especially compared to the area in front of the transmitter, where the direct path is very dominant and values up to 25 dB are possible. The fastest changes in K_{LOS} can be observed close to the transmitter and at the border of the absorber’s shadow.

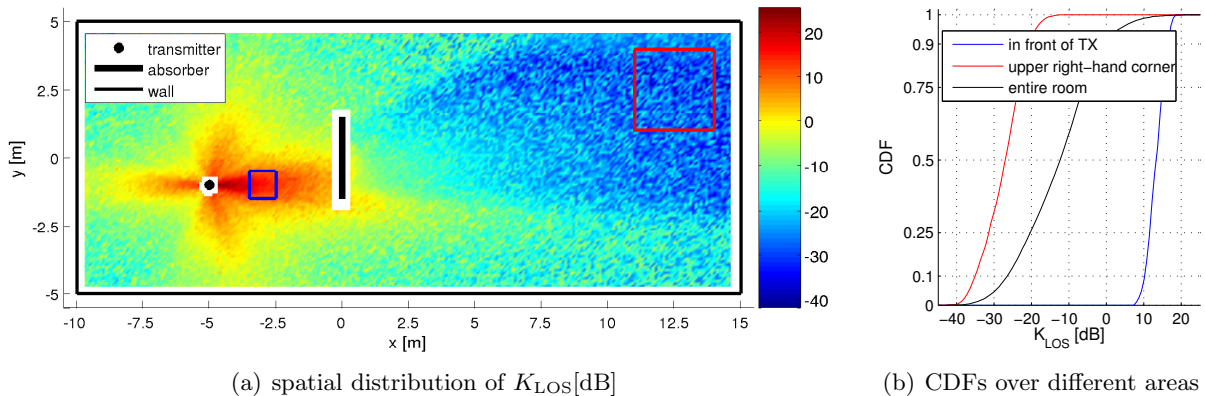


Figure 2.3: Simulation example: K -factor with respect to LOS (K_{LOS}) in a large room. The upper right-hand corner of this room is partially shielded from the transmitter by an absorbing obstacle at $x = 0$ m. CDF plots have been generated for the area in front of the transmitter (blue box), the upper right corner (red box), and the entire room.

Cumulative distribution functions (CDFs) of K_{LOS} are shown in Fig. 2.3(b) for the areas at the upper right corner (red box and line), the area in front of the transmitter (blue box/line), and the entire room (black). Such distribution functions are a very useful tool in evaluating the effects of the wireless channel on a ranging method and will frequently be used in this thesis. If, for example, a ranging method fails for $K_{\text{LOS}} < -12$ dB, it will not work in roughly 50% of the locations in this room. It will, however, always work in front of the transmitter, though never in the upper right-hand corner.

Note that it is hard to find large regions with constant statistics and thus stationary/ergodic PDPs in Fig. 2.3. An exception is the upper right-hand corner, which is characterized mostly by scattered channel components and a negligible LOS path. The PDPs in this region are hence based on the same random process. In close proximity of the transmitter, on the other hand, the LOS path and thus a deterministic component is dominant. At such close ranges, the free space attenuation still changes rapidly with distance, as does the angle dependence created by the antenna gain pattern, cf. [3, 141, 150].

Unfortunately, the concept of APDPs hinges on the approximate ergodicity of the averaged PDPs. Averaging over regions with different statistics will result in a mix of delay-profiles that masks individual characteristics. A proof can be found in Fig. 2.3(b): there is no sign at all of different zones in the CDF over the entire room. Hence, in order to keep this systematic error as small as possible, spatial averaging in indoor environments must be done very carefully.

2.2 Channel Models

2.2.1 Typical UHF RFID Scenarios and Channels

Passive UHF RFID is a classical logistics technology, with main applications in supply chain management and product tracking. As such, two main scenarios arise: a production hall or salesfloor, where small products are identified and tracked, or a portal in which tagged objects are registered while moving through. With the exception of the salesfloor, environments are typically industrial, i.e., they are constructed of highly reflecting materials such as metal and concrete. Additionally, UHF RFID portals are often built with metal shielding. This combination ensures massive multipath propagation.

Similar to anti-theft systems at shop exits, an RFID portal typically consists of two stands to the left and right, holding several antennas connected to the reader (interrogator). Since they are “behind the scenes”, the construction of these portals is often quite crude. The antennas are mounted directly on metal backplanes, which keep the energy inside the portal and also increase the gain of the transmitter antennas, thus maximizing read rates. In combination with multiple antennas at each side, this portal setup ensures the best possible read rates but has devastating effects for narrowband ranging, as will be shown on the following pages and in Chapter 4.

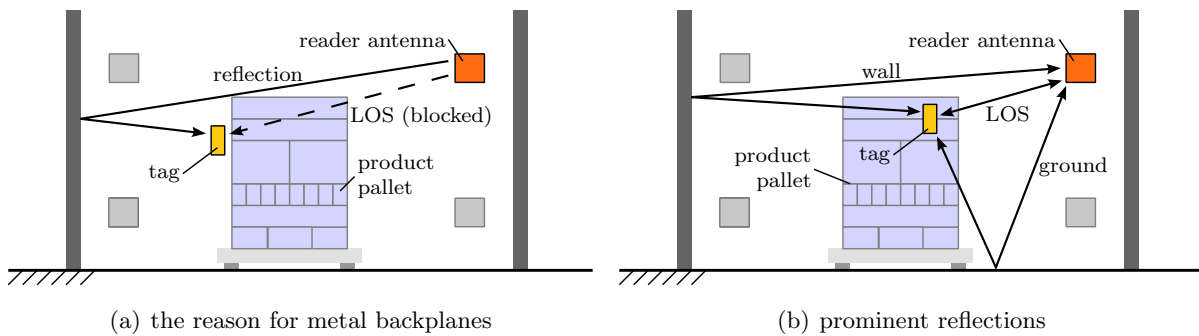


Figure 2.4: Reflections inside the UHF RFID gate (simplified).

Fig. 2.4(a) illustrates why metal backplanes are used in such portals: even though the direct path from the active reader antenna to the tag is blocked by the pallet, the gate reflection is not, hence the tag can still be read. The most prominent multipath components inside the gate are the LOS path, the ground reflection, and the reflection at the opposite gate, as shown in Fig. 2.4(b). It will be demonstrated later that neglecting everything but these three paths is an accurate approximation when calculating receive power levels inside the portal, but is a potentially dangerous oversimplification of the channel when considering ranging, see Section 2.2.3 and [132].

The signal model in Fig. 2.5(a) will be used throughout this thesis. It is a generic signal model that is valid for all backscatter systems. The transmitted signal is sent over the downlink channel to the tag, where it is backscattered and returned via the uplink channel. The feedback channel contains all components of the received signal that have not been modulated by the tag. This includes the antenna mismatch as well as reflections from the environment if receiver and transmitter antenna are identical (monostatic setup). For bistatic setups (distinct TX and RX antennas), the feedback is formed by the multipath channel between TX- and RX-antenna. Both setups are compared in Fig. 2.5(b).

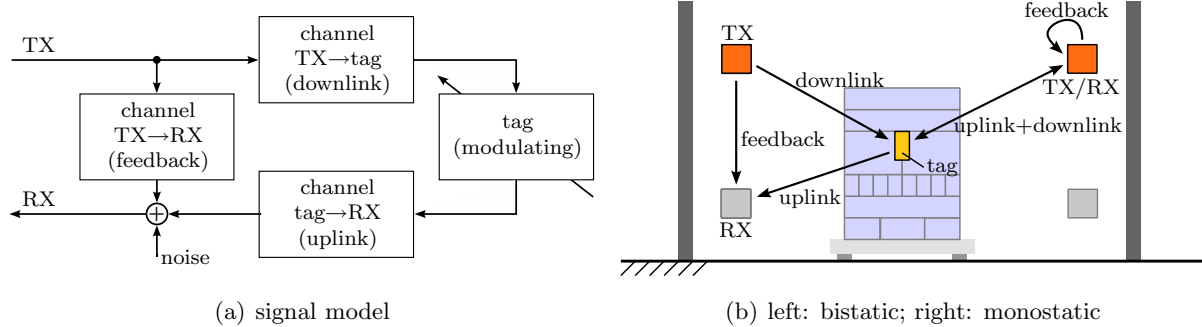


Figure 2.5: Signal model for backscatter systems and simple illustration for bi- and monostatic setups.

2.2.2 Channel Models in the Literature

The literature on channel models is exceptionally rich, ranging from narrowband through wideband to ultra-wideband models, cf. [141, 142]. Channel models for passive UHF RFID are narrowband. Due to the low symbol rates and the short range, dispersion and propagation delay are not an issue [151]. Attenuation and fading, on the other hand, are a vital parameters because of their link to the read rate of passive tags via the minimum required operational power (sensitivity), cf. [3, 152, 153]. Consequently, channel models in UHF RFID deal exclusively with receive power distributions and link budgets. Comprehensive analyses can be found in [151, 154, 155], for example. Furthermore, the channel is degenerate (a.k.a., pinhole, keyhole, dyadic) due to its backscatter nature [154, 156, 157], cf. [158–160], [140, pp. 29–31]. Notably, this is not limited to monostatic antenna configurations, but applies also to bistatic setups [157]. A detailed analysis can be found below, including a measurement-based verification of several of the claimed properties.

Statistical models used in RFID channel modeling are based on Nakagami, Rician, or Rayleigh distributions [157, 161–163] with reference to pioneering works in indoor channel modeling, e.g., [164–166]. Common deterministic RFID channel models are based on single reflections, such as 2-ray models (LOS and ground reflection) [167] or 3-ray models (LOS, ground, and gate reflection, cf. Fig. 2.4(b)) [168], up to 5-ray models [161]. Full-blown ray tracing is sometimes discussed [167] but rarely used in UHF RFID, e.g. [169]. The same applies to large-scale electromagnetic (EM) solvers [167]. Some research has been done towards a hybrid channel model, combining the deterministic 3-ray model and statistical receive power distributions [168].

Most wideband and UWB indoor channel models are based on the assumption of a purely statistical channel in order to remain generic and independent of a specific setup. As such, these models rely on rich and uncorrelated scattering, which causes exponentially decaying APDPs and clusters. Prominent representatives of this group are the Saleh-Valenzuela (SV) model [148] and its derivatives: the proposal for IEEE 802.15.3a [170] (personal area networks, PAN), and the IEEE 802.15.4a channel models [171] (PAN per definition, local area network, LAN, in terms of system design), as well as some similar and/or related models [2, 172, 173]. Deterministic, i.e., site-specific, channel modeling is mostly focused on ray tracing and ray launching algorithms [174–181], but some efforts have also been made towards nonlinear dynamics (chaos theory) [182–184]. A comprehensive list of common UWB channel modeling techniques can be found in [147].

2.2.3 Applicability of Specific Types of Channel Models to Ranging in UHF RFID

The applicability of a specific channel model depends on three vital questions:

1. What is the purpose of the model?
2. What does the physical channel look like?
3. What type of signal is sent over this channel?

The first question is easily answered in the context of this thesis: the channel should be modeled for the purpose of ranging/localization. The second question is treated in detail in Section 2.3, as well as in [132] and [133]. In order to fully understand the third question, it is important to understand how multipath propagation affects signals of different bandwidths. We will thus cover these basics first.

Wideband vs. Narrowband

A very common distinction between signaling schemes for transmission systems is “narrowband vs. wideband”, i.e., is based on the occupied signal bandwidth. The actual border between “narrowband” and “wideband” depends on the channel. A narrowband signal exhibits flat fading, i.e., the CTF magnitude is the same over the entire bandwidth. In other words, the system bandwidth does not exceed the coherence bandwidth of the channel. Conversely, the bandwidth of a wideband signal does exceed the coherence bandwidth.

Effects of Multipath Propagation on Narrowband and Wideband Signals

As wireless channels are linear, the channel impulse response is a generic description of the channel and valid for all signal bandwidths¹². Again due to the linearity, we can split the channel into LOS and NLOS components, as illustrated in Fig. 2.6(a). Each individual sub-channel has its own group delay. For the LOS channel, the group delay is identical to the line-of-sight delay τ_{LOS} . The overall group delay τ_{grp} is a nonlinear mixture of the deterministic LOS delay and the random NLOS group delay τ_{NLOS} . An example PDP is illustrated in Fig. 2.6(a). The stems in this illustration represent a high-resolution sampling of the channel. Note that the LOS component is not necessarily the peak component of the PDP, even if it is dominant in the APDP.

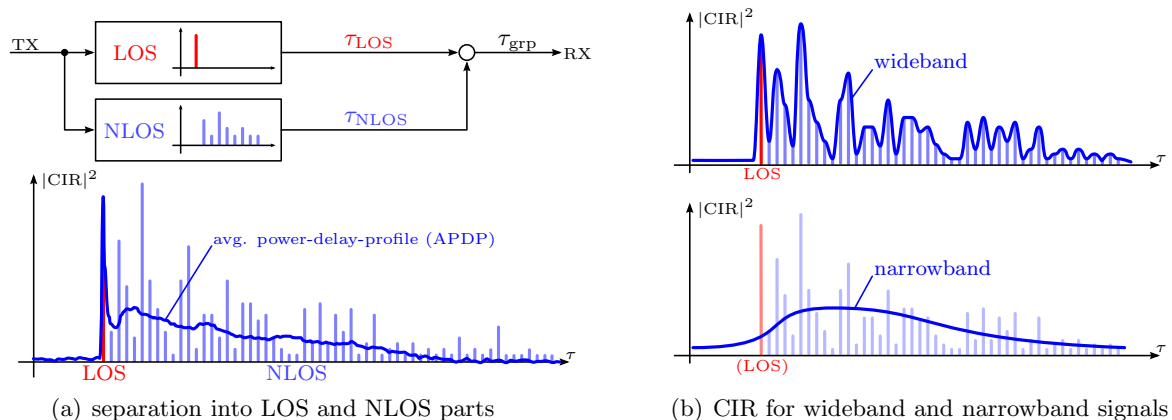


Figure 2.6: Illustration of overall group delay and effects of limited bandwidth on the CIR.

¹² A sampled and truncated CIR is valid up to the bandwidth of the sampling (Nyquist criterion) and also has a limited frequency resolution.

With respect to ranging, the central question is: can the line-of-sight path be identified in the channel impulse response? This question is linked to the physical channel impulse response and the signal bandwidth. If the LOS can be isolated (which is only the case for wideband signals, cf. Fig. 2.6(b)), then the system is able to ignore all NLOS components and the LOS delay estimation yields the true LOS delay, τ_{LOS} .

Limiting the signal bandwidth leads to a smoothed version of the physical CIR due to the uncertainty relation between time and frequency domain¹³, as shown in Fig. 2.6(b). This masks individual components, including the LOS. Consequently, a narrowband signal is delayed by the overall group delay τ_{grp} , not the line-of-sight delay. If the direct path is dominant in the CIR, i.e., if the instantaneous K_{LOS} is large, τ_{LOS} is dominant in τ_{grp} and narrowband ranging will give accurate results. Conversely, the overall group delay is determined mainly by indirect paths in case of low K-factors. Depending on the RMS delay spread and the shape of the CIR, this results in a bias of τ_{grp} towards indirect (i.e., longer) paths. Compare the two smoothed CIRs in Fig. 2.6(b): while the first peak for the wideband example is clearly the LOS component, the same is not true for the narrowband CIR. Here the first peak is somewhere inside the NLOS part. In addition, dominance of random NLOS components leads to high standard deviations of narrowband estimates.

A corresponding example is shown in Fig. 2.7. Here the NLOS part is dominant in the CIR and

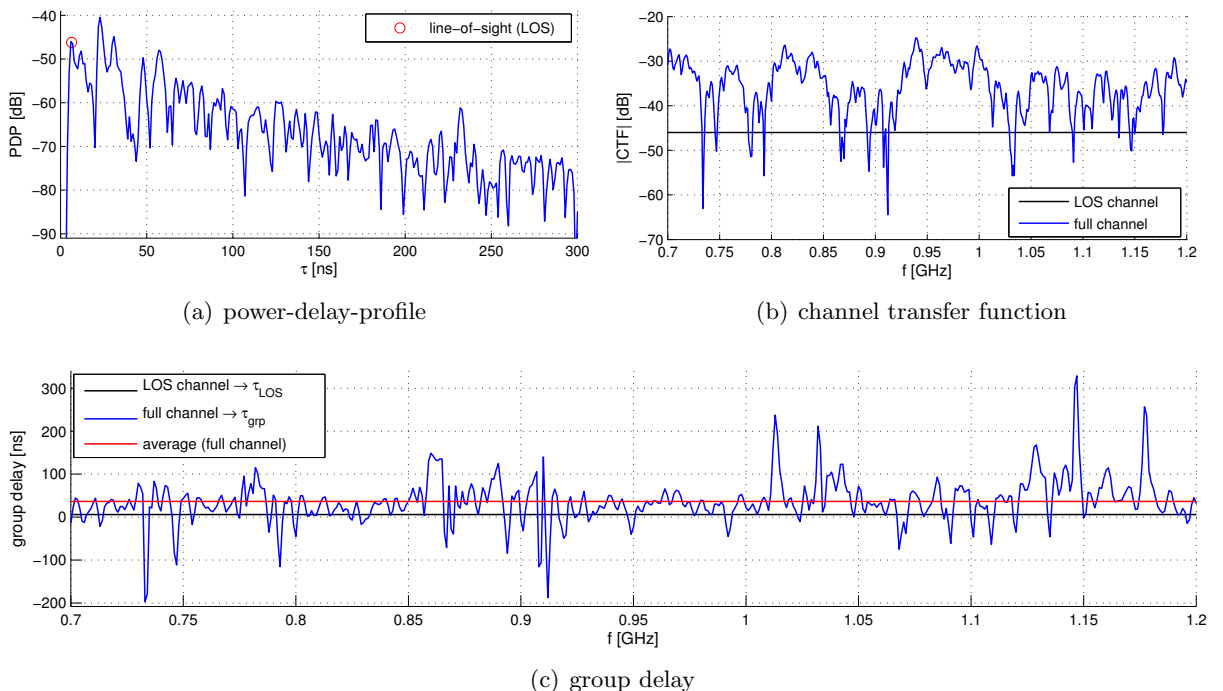


Figure 2.7: Illustration of the relationship between LOS channel and overall (full) channel.

the RMS delay spread is high ($K_{\text{LOS}} = -9.8$ dB, $\tau_{\text{RMS}} = 37.7$ ns). The channel transfer function for the entire channel shows pronounced fading, cf. Fig. 2.7(b). The CTF, on the other hand, is constant over frequency if the LOS component is isolated and the NLOS part is removed. The group delay of the LOS channel is also constant, as can be seen in Fig. 2.7(c). It corresponds to

¹³ As with Heisenberg's uncertainty principle, which limits the level of precision with which momentum and position of a particle can be determined at the same time, the combined precision in time domain and frequency domain is also bounded. The more localized a signal becomes in the frequency domain, the less localized it becomes in the time domain. A perfect impulse is highly localized in the time domain, but has a flat spectrum. Conversely, a sinusoid has only a single frequency, but lasts forever.

the true LOS distance (1.8 m in this example). In contrast, the group delay of the entire channel, τ_{grp} , is largely random. Depending on the frequency at which a narrowband ranging system operates, channel delays between -200 and 350 ns are estimated, corresponding to distances from -60 to 90 m. Note especially that the average of τ_{grp} over frequency is not identical to τ_{LOS} . Averaging over narrowband estimates thus does not yield τ_{LOS} ; the narrowband estimates are highly biased (10.9 m in this example). Multipath propagation is therefore typically the limiting factor for the performance of narrowband systems.

Nonetheless, concluding that wideband and especially ultra-wideband¹⁴ (UWB) localization systems are completely immune to multipath propagation is also incorrect. If – and only if – a wideband system identifies the LOS path correctly, then the error is bounded by the spatial resolution $d_{\text{res}} = c/(2B)$ of the system, where c is the speed of light and B is the signal bandwidth, cf. [5]. Since this is an upper bound, the error is typically well below d_{res} if the LOS is properly identified. If, on the other hand, the LOS detection locked onto the wrong component, the error for ultra-wideband systems is also unbounded and depends solely on indirect (NLOS) components. This can be the case if the LOS component was blocked or otherwise attenuated, or if there are reflections close to the LOS. Unfortunately, since UHF RFID tags are attached to products, reflections close to the LOS path are very likely. Hard-to-detect LOS components are thus not a mere theoretical possibility, but a very real one. See Fig. 5.10 on page 144 for an example based on measurements in a warehouse portal.

With the distinction established between wideband and narrowband in the context of multipath propagation, we can answer the third question above: what type of signal is sent over this channel?

Localization in UHF RFID: Narrowband or Wideband?

In essence, the purpose already defines the signals sent over the channel. In this case, the purpose is localization, so the signals sent are suitable localization signals. Looking at the methods currently under research (listed in Section 1.3), only some employ merely a single carrier modulated by the tag at low frequencies, i.e., a truly narrowband signal. These include methods based on receive power (e.g., [42]), single-carrier angle of arrival (e.g., [53]), and also continuous phase measurements of the carrier [46]. Several other methods employ frequency hopping (e.g., [51]), multiple carriers (e.g., [64]), or frequency modulation (e.g., [67]) and hence may or may not be wideband with respect to the channel.

As discussed above, the central question regarding the type of signal is the bandwidth employed. Unfortunately, this question comes with dangerous pitfalls. Consider an unmodulated carrier that is frequency hopped between 3.1 GHz and 4.1 GHz with 1 MHz step size. For each hop, the phase shift of the received carrier is evaluated and the phase difference between two adjacent carrier phases is used to estimate the propagation distance (see Section 4.2). This set of 1000 pseudo-ranges is subsequently averaged to a single range estimate. The overall estimate thus spans 1 GHz of bandwidth, but using only a single carrier (i.e., a truly narrowband signal).

As to the pitfalls:

1. The overall estimate is not equivalent to an ultra-wideband estimate, for example using impulse radar. Each individual estimate spans 1 MHz, not 1 GHz. The system thus estimates an average of τ_{grp} over frequency, not τ_{LOS} . See Fig. 2.7(c) above for a comparison.
2. The adjacent carrier phases cannot automatically be assumed to be fully coherent, even though the carriers are only spaced by 1 MHz. If the coherence bandwidth is below 1 MHz, this is not a narrowband signal with respect to the channel. Moreover, the phase differences

¹⁴ A signal featuring a bandwidth of at least 500 MHz or a fractional bandwidth exceeding 20 %, according to the FCC definition [5, pp. 25ff]. Note that this is independent of the channel. The UWB property alone is thus insufficient to guarantee that the LOS can be isolated.

will contain significant random components even if the coherence bandwidth is only close to 1 MHz (not below)¹⁵. In any case, assuming full correlation always implies a constant group delay and thus eliminates multipath propagation from the error.

3. The last pitfall relates to channel modeling for this ranging system: Individual estimates cannot be assumed to be fully uncorrelated here, since this would require a coherence bandwidth well below 2 MHz and thus lead to purely random distance estimates (see second item). Naturally, any potential channel model has to cover this correlation as well. More precisely, it has to correctly model the joint density between all estimates, not only the individual (marginal) distributions. This requires that the channel model covers 1 GHz of bandwidth while still keeping the frequency resolution of 1 MHz needed for each individual carrier pair. The combination of both requirements seriously limits the choice of suitable channel models. The 3-ray model typically used in UHF RFID, for example, fails here (see “Discussion of Channel Models” below).

Discussion of Channel Models

The narrowband channel models widely used in UHF RFID are explicitly designed to model receive power distributions. They are thus accurate when predicting the incident power level at the tag [132], [168] but unfortunately produce far too optimistic estimates for channel parameters relevant to ranging, as will be shown below. In particular, the narrowband assumption may lead to the quite erroneous conclusion that all frequency components of the UHF RFID system, including carriers in different channels, are fully correlated and that multipath propagation can thus be neglected, e.g., [65, 66].

The deterministic 2- and 3-ray models, on the other hand, may suggest that multipath propagation can be replaced by two-path propagation in general, e.g., [65]. This assumption is also incorrect.

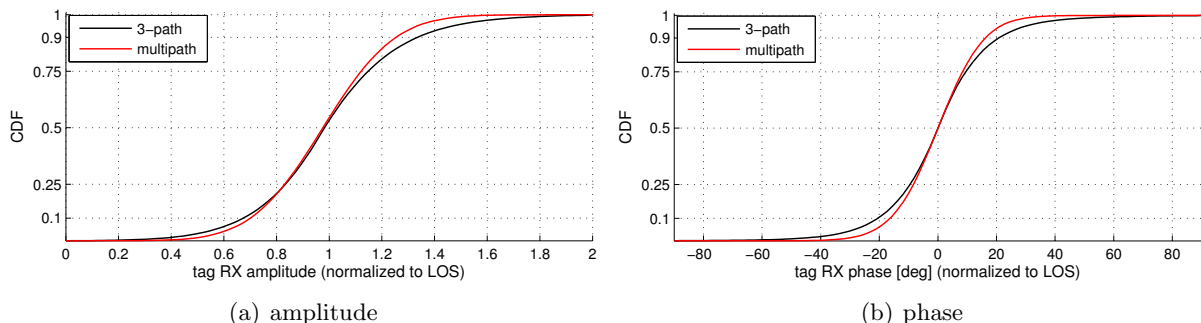


Figure 2.8: Comparison between three-path and full multipath propagation: cumulative distribution functions of narrowband carrier parameters. CDFs have been generated with 10^5 independent realizations.

Consider Fig. 2.8, for example. These two plots compare the amplitude and phase distributions of a single carrier sent over a three-path and a multipath channel (301 paths in this example). Obviously, both distributions match quite well. Now consider the plot in Fig. 2.9, which shows the cross-covariance between two channel gains spaced by Δf for the same channels. This cross-covariance is the central parameter specifying errors caused by multipath propagation for phase-based ranging in the frequency domain, cf. Section 4.2.1. Note that the three-path model predicts a covariance well above the level obtained for full multipath propagation – for example 99.9% instead of roughly 70% for a frequency offset of 3 MHz.

¹⁵ For comparison: the 90% coherence bandwidth for the CTF in Fig. 2.7 is 2.6 MHz. τ_{grp} in this example changes by 26.6 ns on average within a bandwidth of 1 MHz, corresponding to a distance of 8 m.

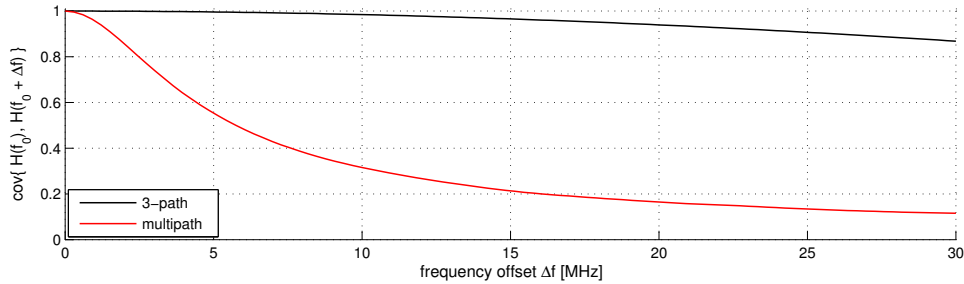


Figure 2.9: Comparison between three-path and full multipath propagation: normalized spaced-frequency covariance function, calculated from 10^5 independent realizations.

The problem here is a statistical one: The marginal distributions, such as amplitude and phase of the individual carriers, do not provide any information on dependencies. Only the joint density can provide such information. Since all localization methods except for RSS-based approaches combine multiple estimates in time, frequency, or space, the corresponding joint densities have to be taken into account. Neglecting such correlations leads to overly optimistic estimates of the error introduced by multipath propagation. For the present example, using two carriers spaced by 3 MHz and evaluating the phase differences, the mean absolute range error is 2.7 m with full multipath propagation taken into account, but only 31 cm are predicted by the three-path model.

Wideband and UWB channel models do not share this failing, since all these models use a high number of paths. However, unlike more common wireless links such as in wireless and cellular networks, the passive UHF RFID channel is very short-range and highly deterministic due to directive antennas and strong reflections in the immediate vicinity [131, 132] and [168]. This creates effects that are not covered by common UWB channel models, including models and analyses for industrial environments such as the IEEE 802.15.4a CM7/8 [149, 171, 185]. For example, the decay of the strongest MPCs inside a UHF RFID portal is not exponential, as assumed by these models, but instead follows a power law [132]. Similar results have been found in industrial environments [149, 186, 187] and reverberant rooms at short distances [188].

In comparison to the stochastic models, purely deterministic UWB channel models are considerably less common. The problems with these models are computational complexity, accuracy in complex environments, and robustness: Currently, calculating the APDP of a simple room takes hours, but reaches a fair level of accuracy when compared to the measured APDP [176]. Unfortunately, by introducing any object large enough to seriously interfere with the wave propagation (starting at roughly one wavelength), the entire calculation is invalidated. For the given UHF/UWB frequency ranges, a human body or a product pallet is definitely a prominent interacting object. Even worse, the predicted delay-profiles in more complex rooms are still far from the measurement results, cf. [178].

A hybrid channel model that has been developed during this thesis project tries to combine both worlds, with a fair degree of success, as will be shown in this chapter and as demonstrated also in [132]. The model combines basic ray tracing along with virtual transmitters and stochastic components. An introduction is given in the following Section 2.2.4. Further details can be found in Section 3.4.

2.2.4 Introduction to the Channel Model Implemented in the PARIS Framework

parts of this section have been published in [132]

The simulation results in the following Section 2.3 have been generated by the PARIS simulation framework [127]. The simulations cover antenna directivities (far field patterns), reflections at walls, floor, ceiling, and other large and flat objects, as well as stochastic components of the CIR. Not modeled are exact geometries, material properties (except for an estimated refractive index), and near field effects.

Reflections are treated by the simulator using a combination of deterministic (ray tracing) and stochastic models. Single reflections in close proximity of transmitters and receivers (e.g., TX→floor→RX) are modeled using reflective surfaces with reflection coefficients derived from the Fresnel equations. Multiple reflections and clusters (e.g., TX→floor→wall→RX), on the other hand, are modeled using reflected versions of the original transmitter, called virtual transmitters (VTX).

The channel impulse response for a single connection between a transmitter and a receiver is assembled from the individual CIRs originating from the transmitter, all virtual transmitters, and all surfaces, as shown in Fig. 2.10. Unlike rays reflected at surfaces, the CIR originating from a TX or VTX contains not only the deterministic LOS path, but stochastic NLOS components as well.

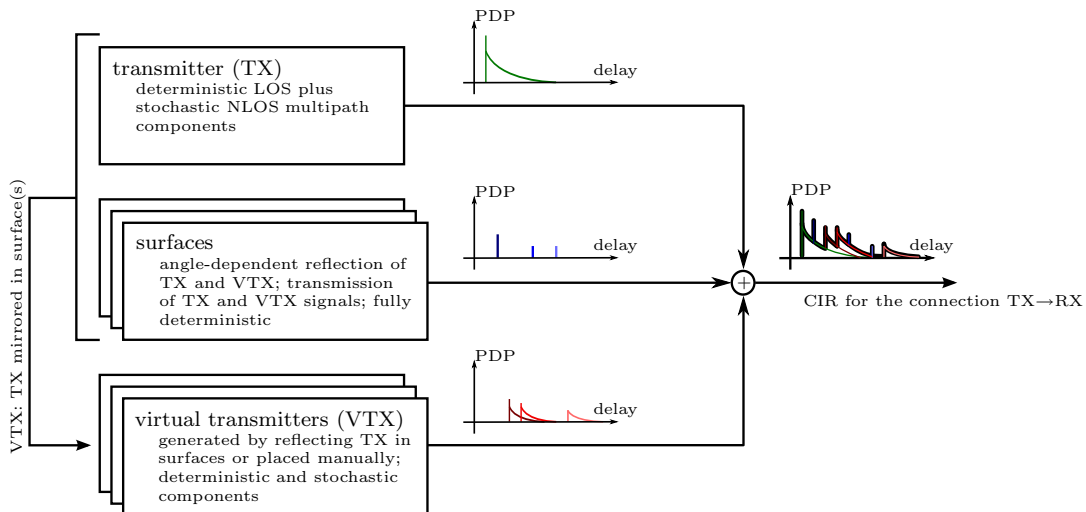


Figure 2.10: Assembly of the CIR for a connection TX-RX; simplified block diagram.

Further details on the handling of surfaces, transmitters and virtual transmitters, the assembly of the CIR and the received signal, and a detailed description of the individual models can be found in Section 3.4.

Fig. 2.11 shows a simulation setup to illustrate the generation and usage of virtual transmitters. For this setup (which is the setup for the example in Section 2.1.3), virtual transmitters are used for all reflections, including 1-fold reflections, in order to illustrate the generation of VTX in detail. The absorbing obstacle between the transmitter TX and the receiver RX blocks the LOS path, but not reflections via the walls or scattered components. The virtual transmitters VTX₂ and VTX₃ are such reflections of TX in the upper and lower wall respectively. A wave that originates from TX and is reflected by the upper wall (blue link in Fig. 2.11) looks as if it was sent from the position of VTX₂. The same is true for the (red) double reflection via the lower and right walls. At the receiver, this connection seems to have its origin at VTX₅, which

is a mirrored version of VTX_3 in the right wall and thus a double reflection of TX in the walls that take part in the reflection. This is why and how multiple reflections can be modeled by virtual transmitters.

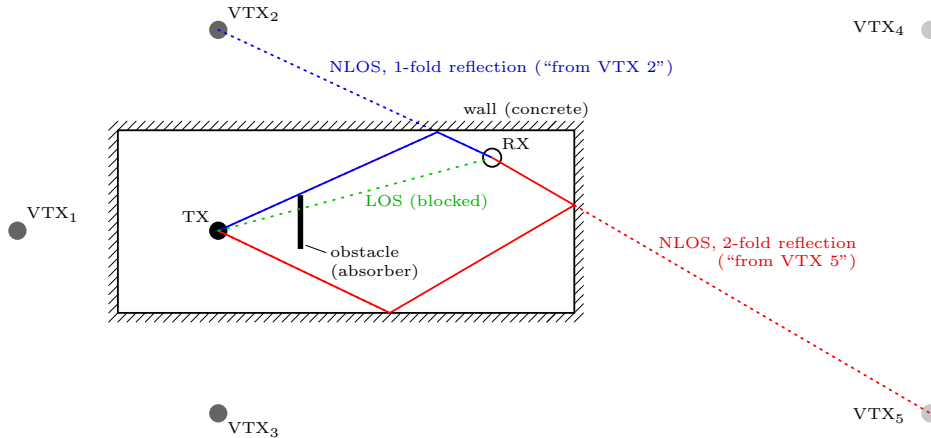


Figure 2.11: TX/VTX setup for the example in Section 2.1.3.

2.3 Measurements

In order to be able to devise and analyze localization methods, first the largest threat – the channel – had to be known. As mentioned above, the subspecies “passive UHF RFID channel” has some special features that are not covered by typical wireless channel models. This section presents an analysis of this channel, including a comparison to model data, as well as the used measurement setup and the applied analysis procedures. Like most of this thesis, the channel analysis focuses on ranging. However, the general results and the recommendations are applicable also to direction finding.

The first three measurement campaigns were used to test and perfect the measurement setup and procedures. They are presented here to cover basic effects and to show some peculiarities. The “real-world” measurements were performed in a warehouse portal (see Section 2.3.3 and [132]). Simulation results are continuously compared to the measurement results in order to show the model accuracy and to point out difficulties in modeling the scenarios.

Unless explicitly stated otherwise, the analyses are based on the individual channels to and from the tag, cf. Fig. 2.5(a). This way, the results remain comparable to the literature and applicable also to non-backscatter systems, such as UHF/UWB hybrids, e.g. [189]. A method to approximate τ_{RMS} and K_{LOS} of the backscatter channel based on the respective values of the individual channels is given in Section 2.4.

2.3.1 General Measurement Setup and Description of Performed Analyses

parts of this section have been published in [131]

All measurements presented in this chapter employ an ultra-wide bandwidth centered around the UHF RFID frequency range (at 860–960 MHz). UWB measurements were chosen for their ability to provide a high-resolution estimate of the channel impulse response. Since the CIR is a generic representation of wireless channels due to their linearity, these measurements are valid for narrowband through ultra-wideband ranging systems. Moreover, the high temporal and spatial resolution of the measurements allows for the identification of individual reflectors and thus for a very detailed analysis of the channel.

The measurement setup consists of a vector network analyzer (VNA), two arrays of four Vivaldi antennas each, as well as two omnidirectional UWB “tag” antennas, cf. Fig. 2.12. The antennas have been designed for an operating frequency range of 0.7 through 1.2 GHz.

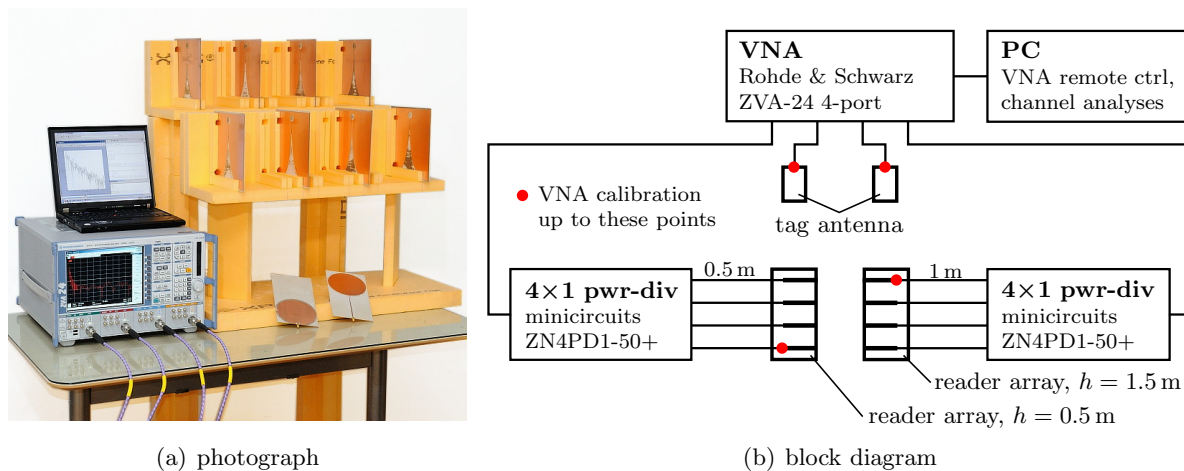


Figure 2.12: Channel measurement setup consisting of a network analyzer, two reader arrays, and two tag antennas. The entire measurement procedure is remote-controlled by a PC or Laptop.

The “tag” antennas employ an elliptic dipole-like structure, see Fig. 2.13(a). This structure maintains its electrical properties largely independent of the surroundings, i.e., it is hard to detune and can be placed close to the products. The antenna has an omnidirectional gain pattern similar to the gain pattern of RFID tags, cf. Fig. 2.14(a).

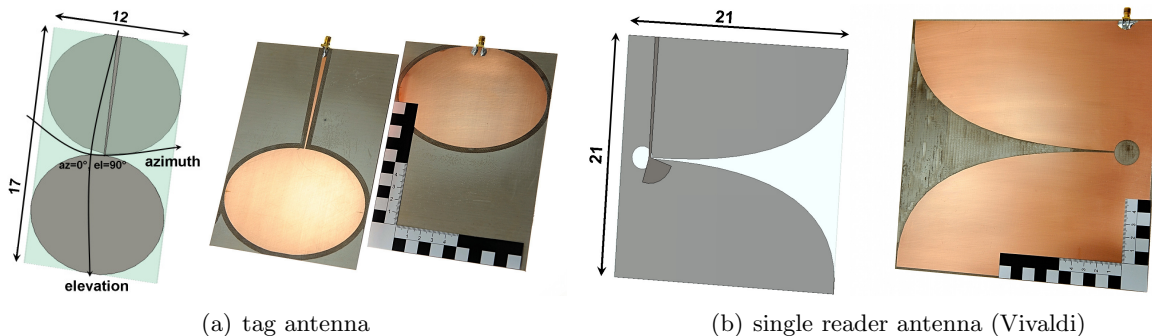


Figure 2.13: Photographs and transparent models of the antennas used (scale is in cm).

The reader antennas consist of tapered slot (Vivaldi) antennas, as shown in Fig. 2.13(b), in a 4×1 array with a separation of 20 cm each (see Fig. 2.12(a)). The average gain pattern of the arrays was designed to emulate an Intermec IA39B RFID antenna [7]. Unfortunately, the mainlobe of the reader arrays is slightly narrower than originally intended, cf. Fig. 2.15(a). Naturally, the UWB gain pattern of the array, shown in Fig. 2.15(b), is not completely independent of frequency. It becomes more directive and develops pronounced grating lobes at higher frequencies. The vertical gain pattern also shows some fluctuations due to weak resonances in the feeding network and the cabling of the array. Polar plots of the gain patterns in E- and H-plane are provided in Appendix A.

The actual measurements were performed using a remote-controlled VNA (Rohde&Schwarz ZVA-24 with 4 ports) measuring CTFs in a frequency range of 0.5–1.5 GHz with 1 MHz step size. Extending the bandwidth to this range allows for proper windowing of the CTF before

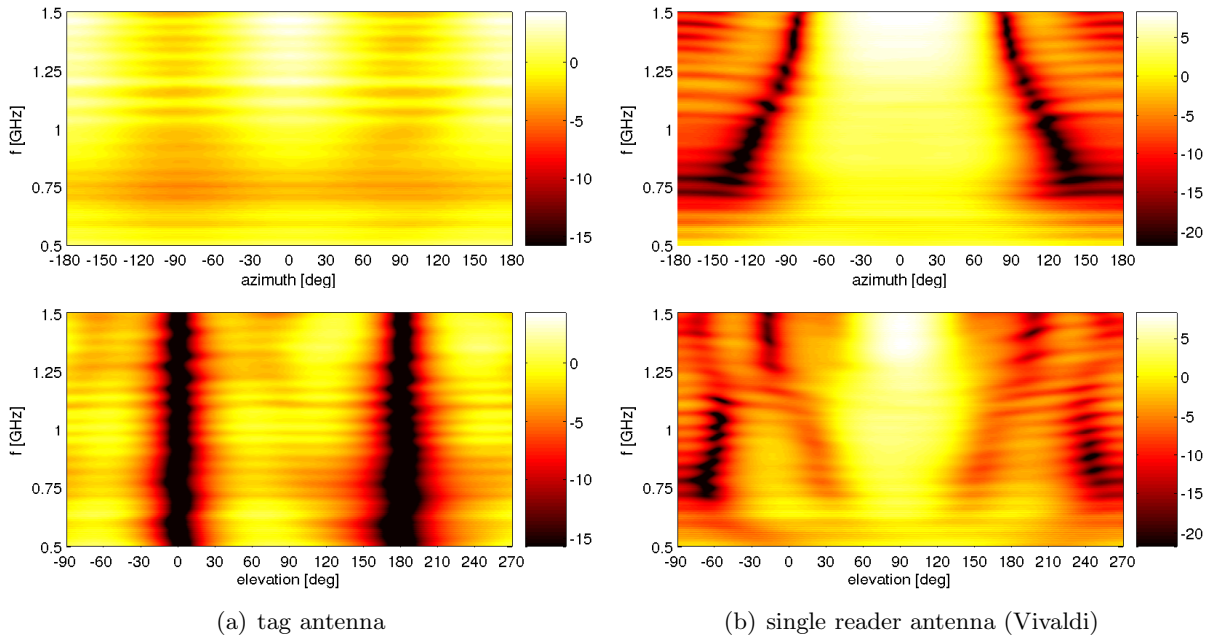


Figure 2.14: Gain patterns [dB] of individual antennas used for the channel measurements. Below 750 MHz, the calibration is extrapolated (no gain for the reference antenna available).

transformation. Due to the windowing (Parzen window, see below), the effective frequency range is roughly truncated to the intended core frequency range of 0.7–1.2 GHz. The chosen step size results in a maximum time delay of roughly 1 μ s, which was found to be sufficient in the given environments (up to smaller halls). The bandwidth resolution of the VNA was set to 10 kHz and the output power varied between 0 and 15 dBm depending on the environment, in order to allow the PDP to reach the noise floor within the given maximum time delay. The resulting effective dynamic range is in the order of at least 100 dB.

A simplified block diagram of the performed analyses can be found in Fig. 2.16. As a first step, the position-dependent CTFs $H(f, \mathbf{p})$ are used to calculate the spaced distance correlation functions (SDCFs) and the coherence distance d_c . (Both consider entire CTFs and are thus implicitly averaged over frequency.) Subsequently, the coherence bandwidth B_c is calculated from each (instantaneous) CTF $H(f)$ via the spaced-frequency correlation function (SFCF). After proper windowing, the CIR $h(\tau)$ is calculated from the CTF via Fourier transform. Several time-domain parameters such as the LOS delay, K-factors, and the RMS delay spread are calculated from the instantaneous PDP $|h(\tau)|^2$. A more detailed description of analysis procedures and measurement setup can be found in [131].

Windowing of the CTF before the time-domain transform is done in order to increase the sidelobe attenuation (better detectability of the LOS slope), and also to mask the AoA-dependent gain patterns of the antennas (especially outside the core frequency range of 0.7–1.2 GHz). A Parzen window [190] as shown in Fig. 2.17(a) was used, mainly for its good performance with the implemented LOS detection, but also for its leakage suppression properties and relatively low bias [191], [192, p. 543]. The window leads to an approximate spatial resolution of ± 50 cm (10 dB mainlobe width) which results in an equivalent “blurring” of the environment’s surfaces, cf. Fig. 2.17(b). The average resolution of the LOS detection is below ± 25 cm (3 dB mainlobe width), and typically in the range of ± 10 cm for the presented measurements.

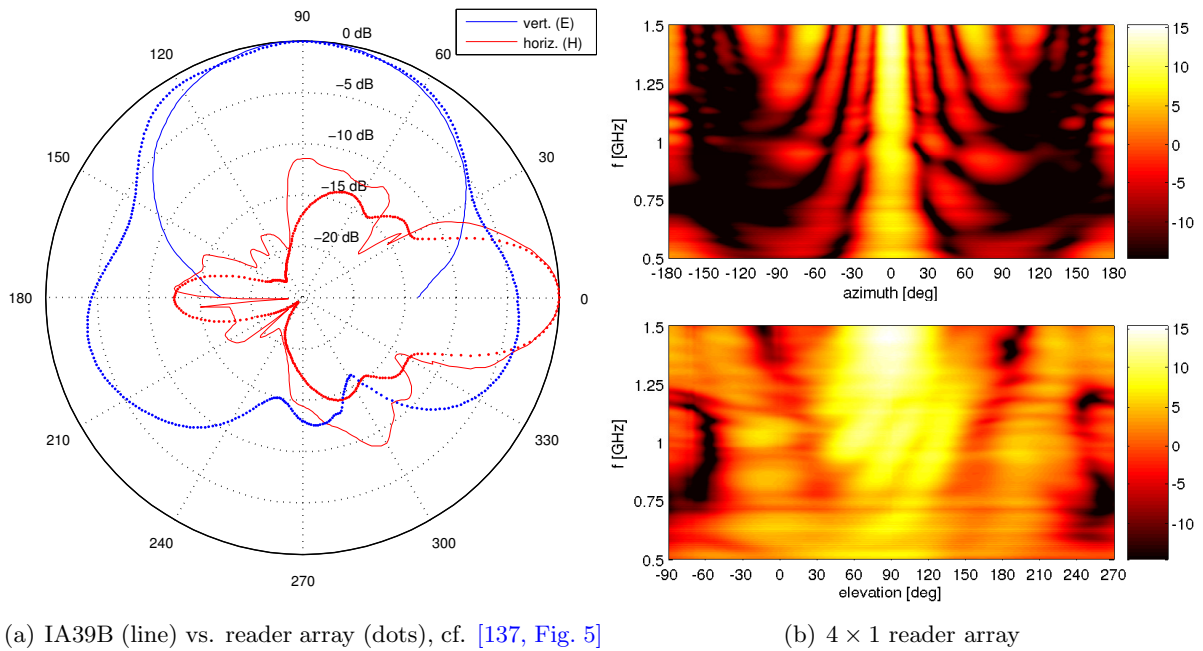


Figure 2.15: Gain patterns [dB] of the reader array used for the channel measurements. The polar plot shows average gain patterns over a frequency range of 0.7–1.2 GHz for the reader array. (Calibration is extrapolated below 750 MHz.)

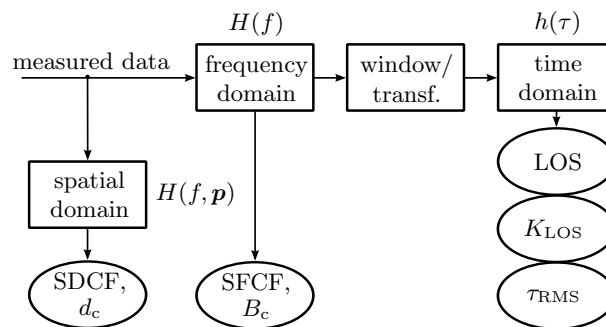


Figure 2.16: Analyses performed in spatial, time, and frequency domain.

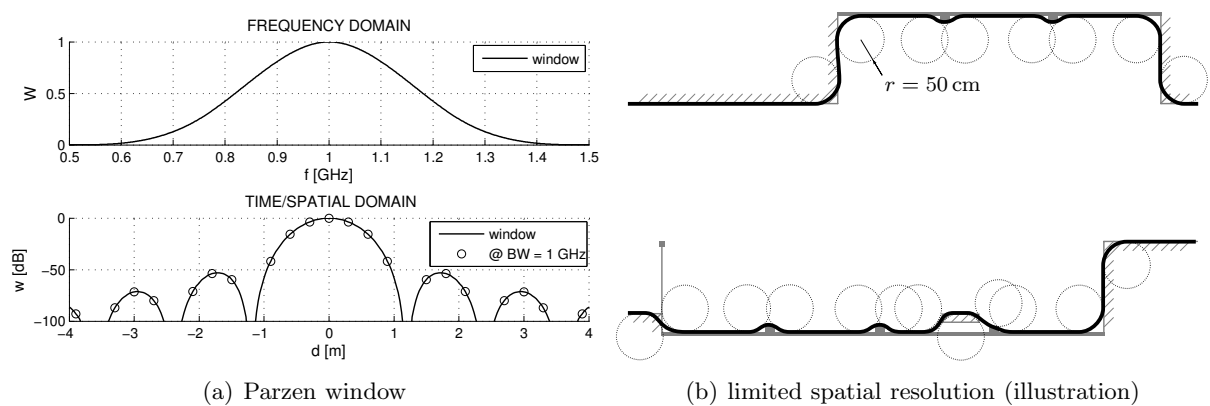


Figure 2.17: Used window function and illustration of the effects of limited spatial resolution on a floorplan (original floorplan in the background: corridor Inffeldgasse 16c; see below).

2.3.2 Indoor Office/Industrial

parts of this section have been published in [129]

Three measurement campaigns were performed at the campus of Graz University of Technology, specifically in Inffeldgasse 16 and 16c, as test measurements for the system. A full floorplan and photographs can be found in the Appendix on page 161. These buildings are made mainly of concrete and metal. Walls, ceiling, and floor are composed of steel-reinforced concrete, doors are made of metal, and the windows are also highly reflective due to metal coating. Judging from their reflection and transmission properties, several outer walls may have embedded metal meshes. The ceilings feature large metal conduits and other large and flat metal surfaces. Thus the interior of these buildings can easily be categorized as industrial in terms of the channel (highly reflective materials, waveguiding effects, ...), even though they are used as office buildings.

The first environment was a small room in Inffeldgasse 16 (“SPSC Salon”), as shown in Fig. 2.18. Apart from the typical style of construction, as described above, the room contains a large circular aluminum strut on the ceiling and a metal cabinet. At the time of this measurement, only one transmitter array was available.

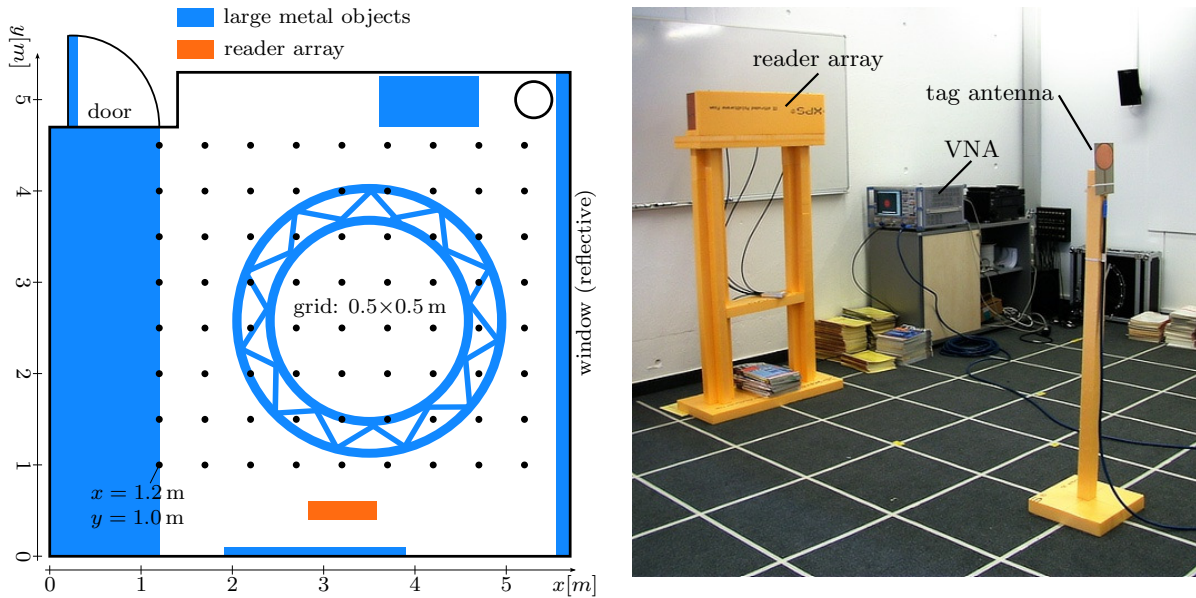


Figure 2.18: Measurement setup “SPSC Salon” (small room; semi-industrial).

✓ The resulting K-factors and RMS delay spreads can be found in Figs. 2.19 and 2.20, along with a comparison to simulation results. Note that the LOS path is the dominant part of the CIR only inside the mainlobe and at very close distances. Even inside the mainlobe, K_{LOS} is rarely above 10 dB. RMS delay spreads in this small room are quite low, with values ranging from 5 ns inside the mainlobe to 20 ns outside. Both channel parameters show evidence of the metal cabinet at the upper right corner. Apart from small mismatches at the top and close to the transmit array, the simulation results match the measurements almost perfectly¹⁶. This is a very surprising result and possible due to very dense scattering with only a few relatively simple reflectors, making this room easy to model. The mismatches at the top are likely caused by a large fridge behind the top wall which is not modeled by the simulation, while the mismatches close to the transmitter are caused by near field effects.

¹⁶ not counting the much higher spatial resolution of the simulation results

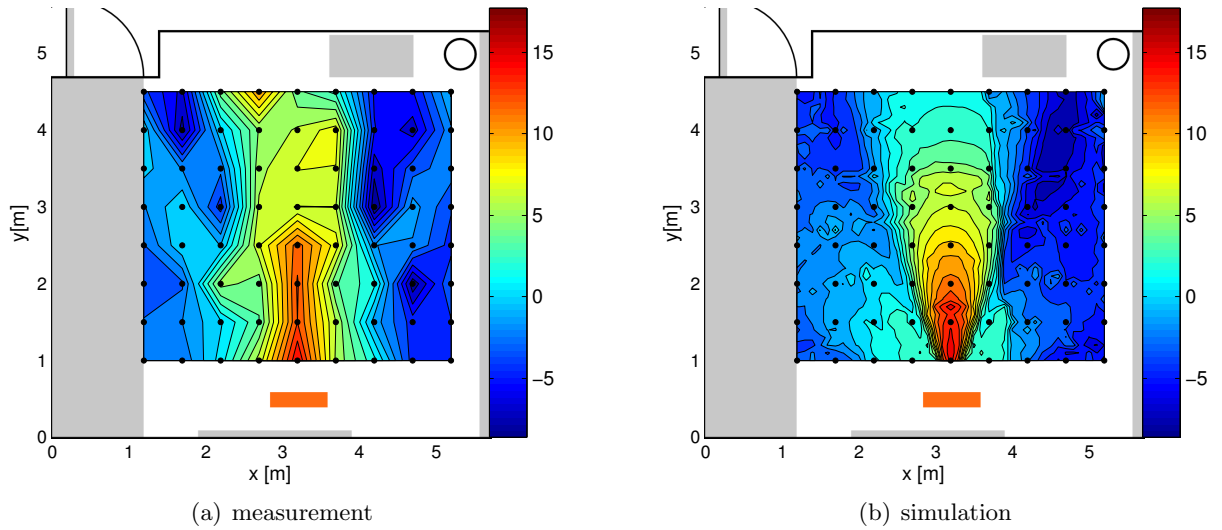


Figure 2.19: K -factor with respect to LOS [dB], “SPSC Salon” (small room; semi-industrial).

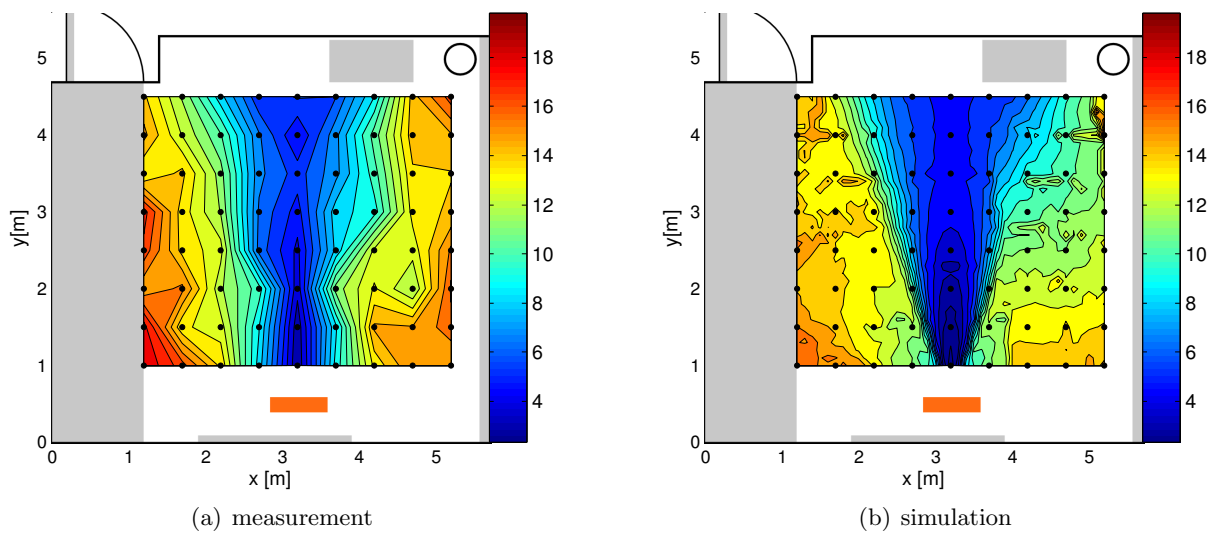


Figure 2.20: RMS delay spread [ns], “SPSC Salon” (small room; semi-industrial).

Two more measurements were taken in a corridor in Inffeldgasse 16c. For the first measurement, the TX array was positioned between two highly reflective windows in a portal-like fashion, as shown in Fig. 2.21. Unfortunately, these windows are not flat; metal beams are mounted in front of the glass. Additionally, there are desks, a large plant, and the measurement setup cluttering the scene. In combination with the blurring effect of the limited spatial resolution, this makes modeling the environment rather challenging. The wave is scattered at the metal beams and focused at other points, for example at the almost parabolic structure between the column and the window to the left and behind the array, cf. Fig 2.17(b) above.

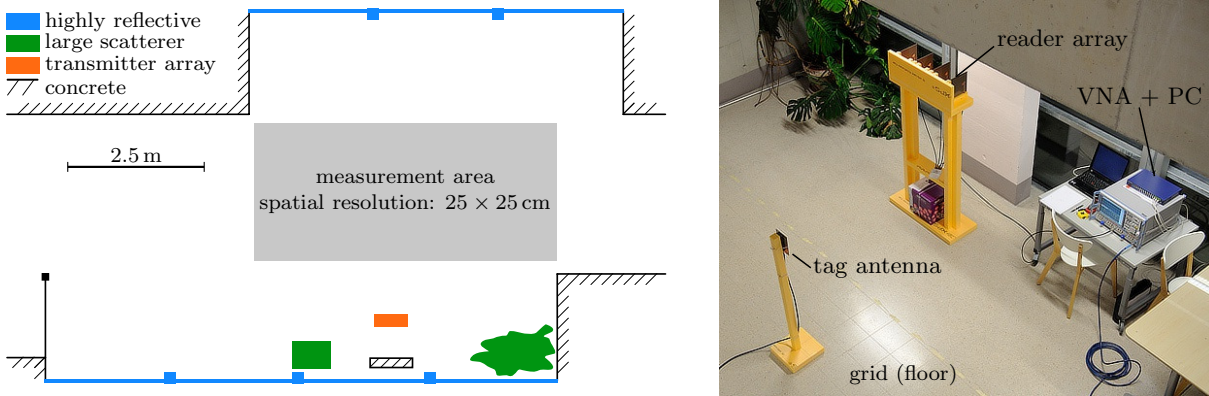


Figure 2.21: Measurement setup: “SPSC Corridor I” (portal-like; semi-industrial).

The resulting K-factor and especially the RMS delay spread are characterized by “grooves” that are created by very localized wave packets traveling through the measurement area once or twice before leaving it, see Figs. 2.22 and 2.23. Videos of the wave propagation can be found online [127] and on the DVD accompanying this thesis. It should be mentioned that the simulation would not be able to predict the fine structure without some manual fine-tuning of the settings. However, the placement of virtual transmitters (cf. Sections 2.2.4 and 3.4) is still done automatically, which explains some of the missing grooves in the RMS delay spread (created by curved and thus unmodeled reflectors).

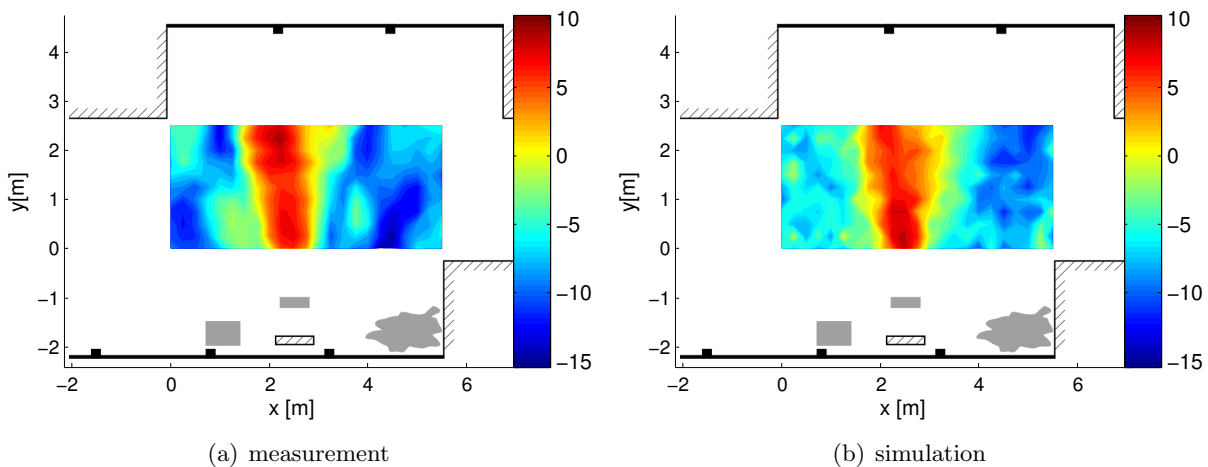


Figure 2.22: K-factor with respect to LOS [dB], “SPSC Corridor I” (portal-like; semi-industrial).

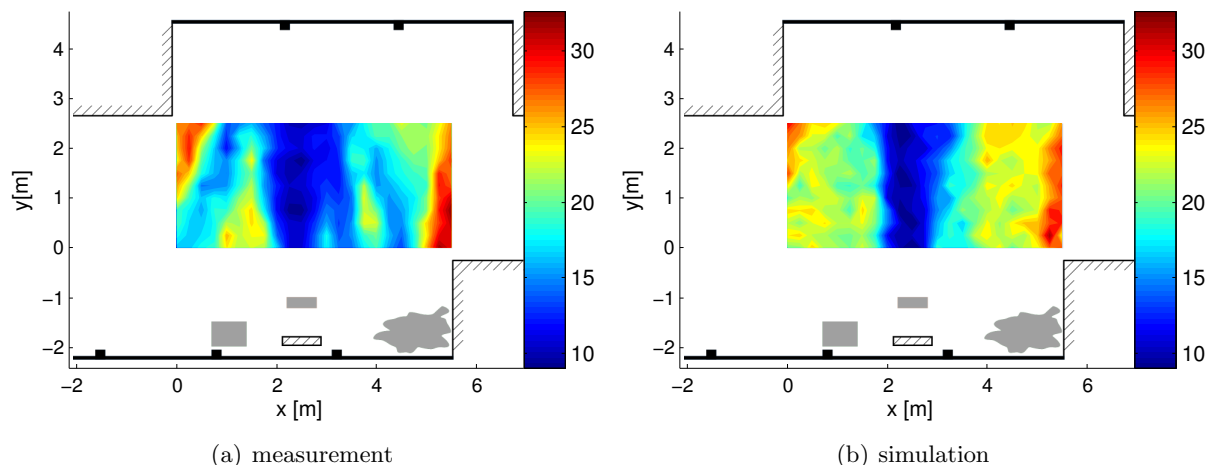
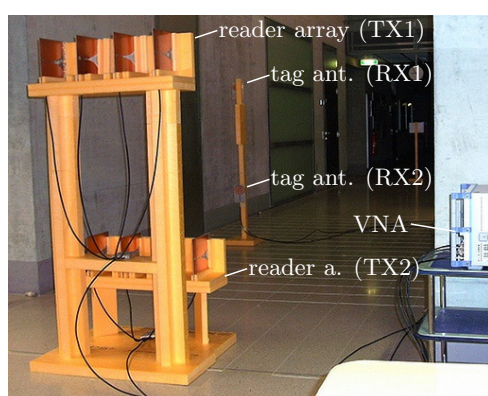


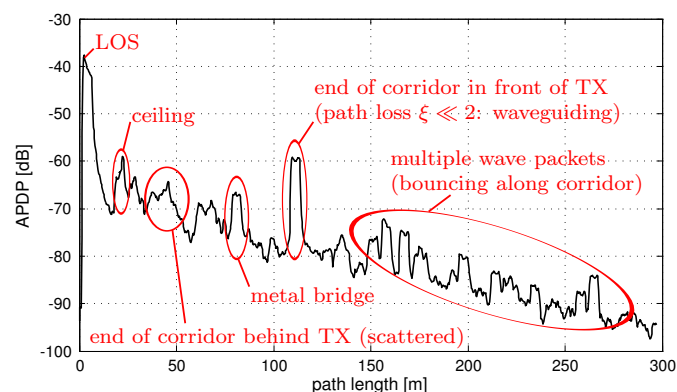
Figure 2.23: RMS delay spread [ns], “SPSC Corridor I” (portal-like; semi-industrial).

Apart from these demonstrations of the local geometry’s massive influence on the CIR at the individual positions, the overall distributions of K-factor and RMS delay spread are unsurprising. Again, K_{LOS} is above 0 dB only when inside the mainlobe and reaches -15 dB outside (i.e., reflected MPCs are 30 times stronger than the LOS component). The RMS delay spread is higher here compared to the measurements in the enclosed room due to the strong reflectors (especially inside the mainlobe) and the larger room dimensions (outside the mainlobe). It is in the range of 10 through 30 ns.

The third measurement within these two buildings already used both reader arrays and two tag antennas, as can be seen in Fig. 2.24(a). The most interesting property of this corridor is intense waveguiding, cf. Fig. 2.24(b). After two initial clusters created by a reflection at the ceiling and scattered reflections at the south-west end of the corridor (behind the arrays), the corridor creates multiple aligned wave packets that travel exclusively along its length. The first of these clusters (a small one) is caused by a metal bridge on the second floor of the building. The most prominent cluster is created by the upper (north-east) end of the corridor. This component is around -60 dB in the APDP, at a path length of 111 m. Compared to the LOS (-40 dB at 4 m) this results in a path loss exponent of $\xi \approx 1.4$, which is less than the free space path loss of $\xi = 2$.



(a) measurement setup



(b) average power-delay-profile

Figure 2.24: Measurement “SPSC Corridor II” (long corridor; semi-industrial).

2.3.3 UHF RFID Gate in an Industrial Environment

parts of this section have been published in [132]

The final set of measurements was aimed directly at measuring the channel in a showcase application for passive UHF RFID: a warehouse portal. For this reason, the entire measurement setup was constructed like a common UHF RFID portal, see Fig. 2.25(a) and [132]. The measurements were performed in NXP’s Application and System Center (ASC) in Gratkorn, Austria, to ensure a realistic warehouse environment. The ASC is located in a converted production hall with corrugated metal walls and ceiling, and a steel-reinforced concrete floor. A simplified schematic of the gate’s surroundings can be found in Fig. 2.25(c). Two different pallets were used: an electromagnetically transparent “free space” pallet as shown in Fig. 2.26(a), constructed of a wooden scaffold and polyurethane slabs, and a challenging products pallet containing liquids and metal-coated packages, as shown in Figs. 2.25(b) and 2.26(b). Receiver antennas were fixed at different x - and z -positions on the pallet, which was incrementally moving through the gate (along y) while recording. The measurements cover an area of ± 1.5 m in the y -direction for the freespace pallet and $y = -1.5 .. 2$ m for the liquids pallet.

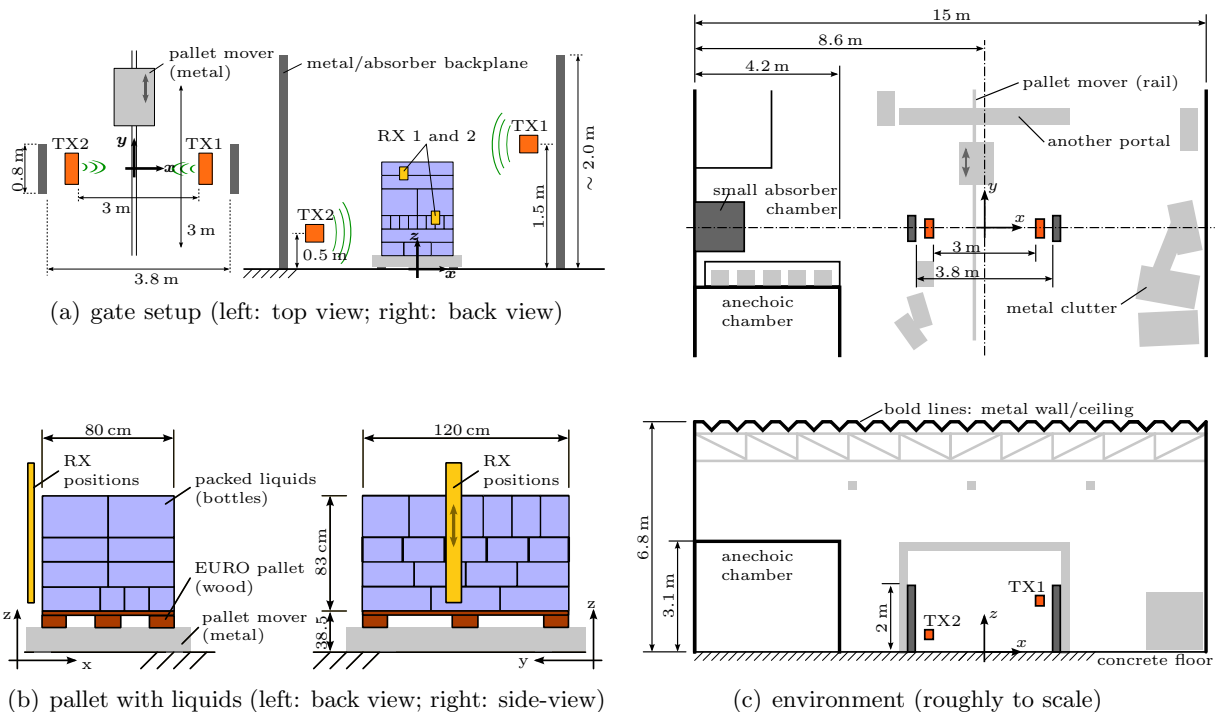


Figure 2.25: Measurement setup: “NXP gate” (portal; industrial).

Two examples of channel transfer functions in this environment are shown in Fig. 2.27. Expectedly, the CTF outside the portal shows more pronounced fading, a lower average power level, and also a considerably more random phase than the CTF inside the portal. Note, however, that tags would receive more than their minimum operational power at both positions for most of the UHF RFID frequency ranges (around 860 MHz and within 902–928 MHz). Consequently, tags at both positions would be functional and localization is necessary.

The following results are a short summary of the most important findings and are also limited to the more common case of metal backplanes. A more detailed analysis of this measurement campaign can be found in [132]. Due to the different channel characteristics inside and outside the portal (cf. Section 2.1.3), some analyses have been split into two regions: the area well in between the backplanes, $|y| \leq 0.5$ m, is defined to be “inside the portal”, while the area for $|y| \geq 1$ m is referred to as “outside” or “in the vicinity of” the portal.

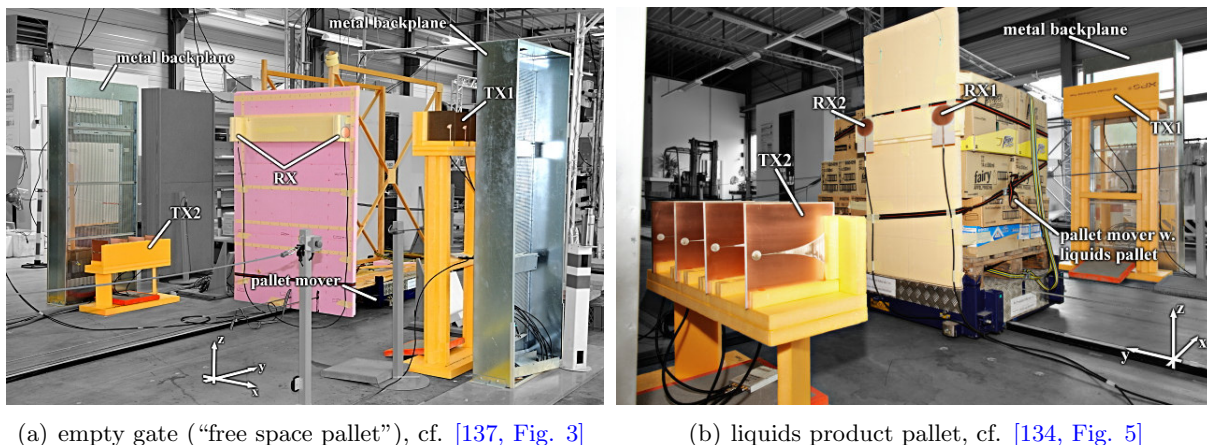


Figure 2.26: Photograph of the measurement setups “NXP gate” (portal; industrial).

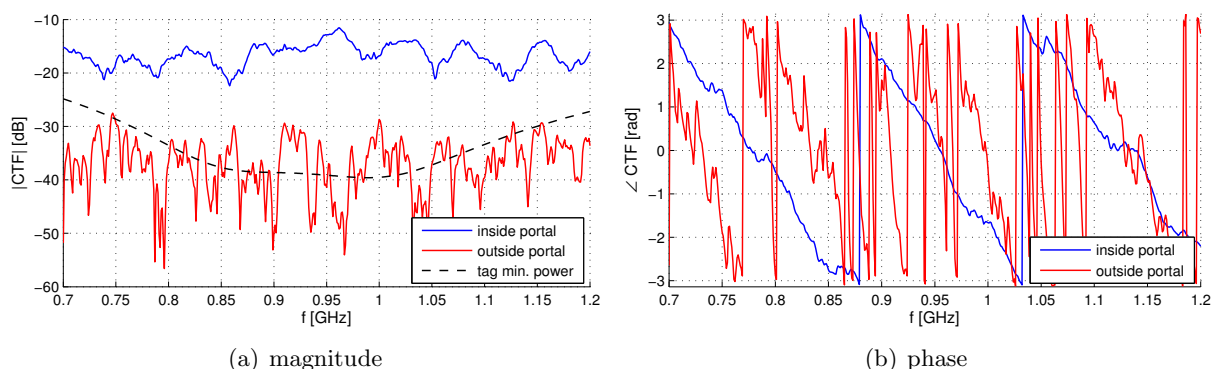


Figure 2.27: Examples of channel transfer functions inside ($K_{LOS} = 8.4$ dB, $\tau_{RMS} = 8$ ns) and outside ($K_{LOS} = -3.9$ dB, $\tau_{RMS} = 45.7$ ns) the portal with metal backplanes. The minimum tag power level shown corresponds to a well-tuned NXP UCODE G2XM on an NXP UCODE general purpose reference antenna at a reader transmit power level of 1 W EIRP (equivalent isotropically radiated power).

Several deterministic components (geometry-dependent reflections) have been identified from the measured APDPs, from videos showing the wave propagation (available online [127] and on the DVD), and from comparison to simulations. The most prominent ones are marked in Fig. 2.28(a). Note that the APDP is dominated by these reflections, hence purely stochastic channel models are insufficient here. Unsurprisingly, the majority of reflections is created by the wave bouncing between the metal backplanes (gate reflections). Up to five bounces can be identified, including multiple reflections between the backplanes and the floor. Reflections at the walls close to the floor are blocked by the gate and scattered by clutter objects. The ceiling, on the other hand, is free of cluttering, thus allowing the wave to bounce between the outer walls of the hall. The APDP shows at least nine reflections of this specific wave packet, six of which are within a path length of 100 m and thus visible in Fig. 2.28(a).

An important observation is illustrated in Fig. 2.28(b): The general shape of the APDP up to path lengths of at least 30 m and the clusters created by the wall reflections close to the ceiling follow a power law $S(\tau) = S_0\tau^{-\Gamma}\tau$, where Γ is the multipath decay constant, instead of the commonly assumed exponential decay. This contradicts standard UWB channel models, but is consistent with a mainly deterministic channel. Similar behavior of the ray power decay in industrial environments has previously been reported in [149]. Outside the portal and for long delays, most of the APDP follows an exponential decay. ✓

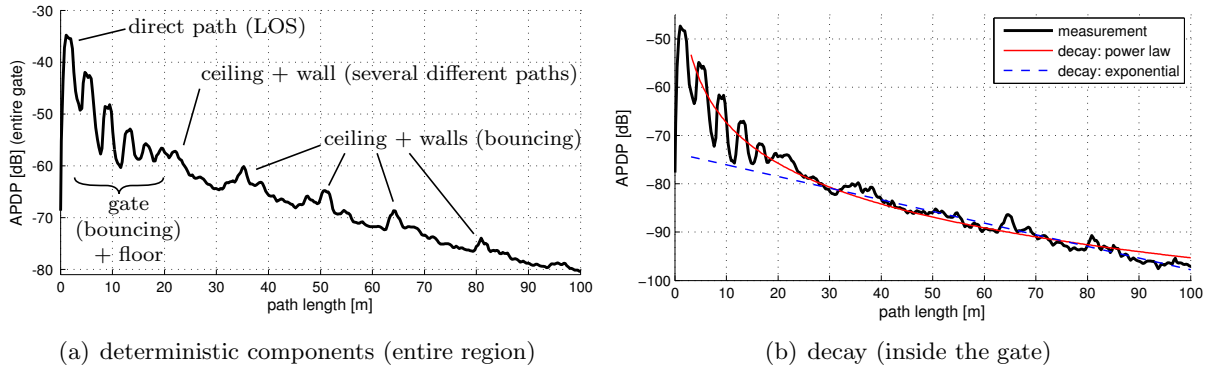


Figure 2.28: Measured APDP with marked clusters and highlighted decay laws (metal backplanes).

The average channel, as shown in Fig. 2.28(a), is dominated by deterministic effects, but also shows considerable stochastic influence that increases with distance from the gate. For this reason, a hybrid channel model combining deterministic and stochastic approaches should be chosen. Simulation results using the model implemented in the PARIS framework [127] are shown in Fig. 2.29. This simulation includes up to 6-fold reflections using 78 automatically placed virtual transmitters. A purely stochastic modeling of the APDP is shown for comparison.

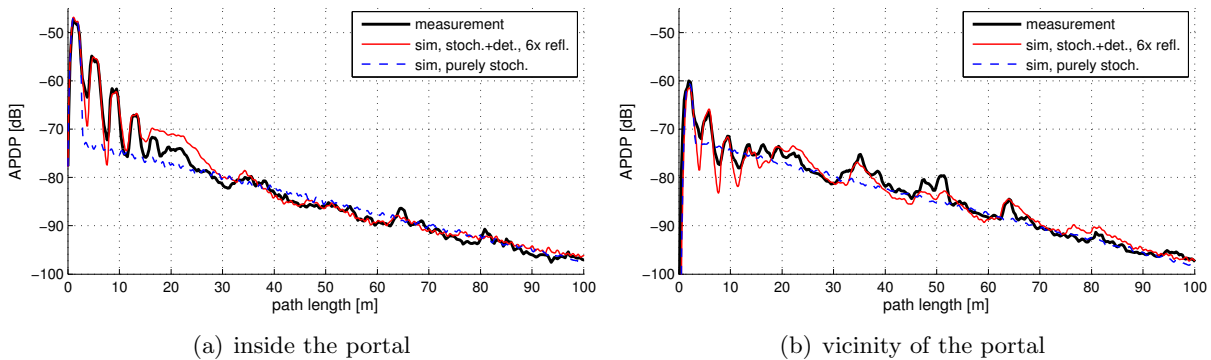


Figure 2.29: Comparison of simulation and measurement results for purely stochastic and hybrid channel model.

One of the major problems for the simulation is the modeling of multiple reflections. Any simulation model is a massive simplification of the environment by necessity. Even though it is imperative to model bouncing reflections in this scenario, the probability of mispredictions increases with the number of reflections (e.g., 1-fold vs. 6-fold). This can for example be seen for the clusters around 15–30 m in Fig. 2.29, which, despite my best efforts, are not modeled 100% correctly.

CDFs of the most important channel parameters can be found in Figs. 2.30 and 2.31. These averages have been taken over the entire area (inside and outside the portal), thus ultimately representing an unknown tag position. A full analysis for the different zones of the portal has been done in [132].

Roughly half the tag positions have $K_{\text{LOS}} < 0$ dB, which means that the direct path cannot be assumed to be dominant in such a scenario even for the individual up- and downlink channels. Coherence bandwidths are mostly in the range of 1 through 100 MHz. Note that especially the UHF RFID frequency range in the United States (US: 902–928 MHz; EU: 865–868 MHz)

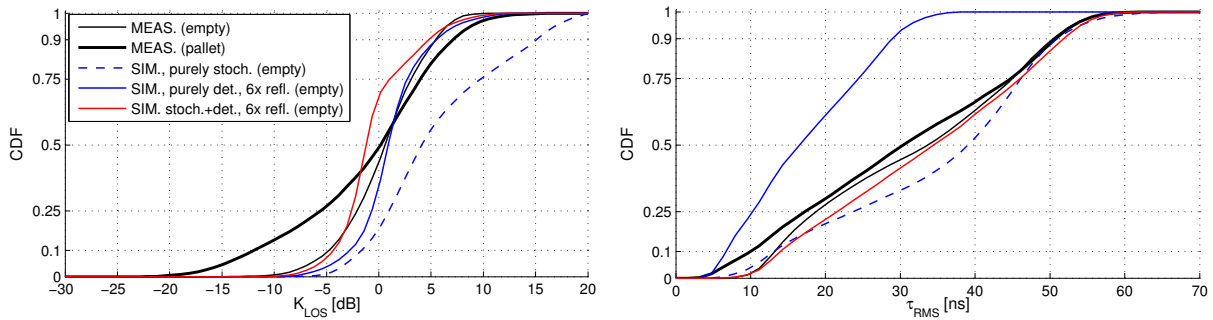


Figure 2.30: K -factor and RMS delay spread for the entire portal (empty and pallet; metal backplanes). The simulation models the empty portal.

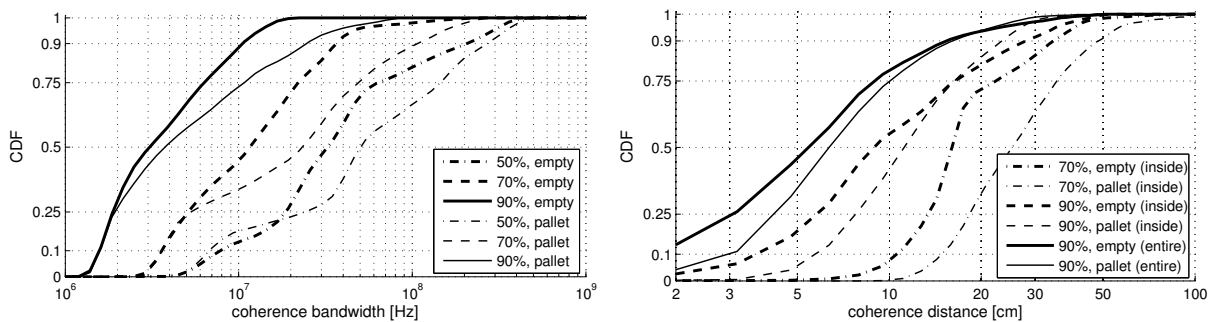


Figure 2.31: Coherence bandwidth and coherence distance for the entire portal (empty and pallet; metal backplanes). Note: coherence distances above 40 cm average over different regions of the portal.

is larger than most coherence bandwidths. Multiple carriers in passive UHF RFID can thus not be assumed to be fully coherent even though the system is called narrowband. Finally, spatial correlation can be very high inside the portal, thus limiting the effect of consecutive range estimates for moving tags (spatial diversity). Note that averaging over different zones of the portal as well as different parts of the reader antenna gain pattern is necessary to cover large coherence distances. This limits the observable/correct coherence distances to roughly 40 cm and truncates the CDFs.

Fig. 2.30 also shows a comparison to different channel models for the empty portal. Neither the purely stochastic nor the purely deterministic model is able to properly predict K_{LOS} and τ_{RMS} properly. Both models produce overly optimistic estimates of K_{LOS} and τ_{RMS} , which are the two most important channel parameters for ranging. The popular 2- and 3-ray models [167, 168] (purely deterministic, 1-fold reflections) produce even less realistic results than the deterministic 6-fold model shown in this plot, cf. [132]. Ultimately, only the hybrid channel model is able to predict both values at the same time. The leftover mismatch for K_{LOS} is caused by the backplanes influencing the transmitter gain pattern and the modeling error for the clusters around 15–30 m (cf. Fig. 2.29).

One of the largest problems in UHF RFID is self-interference due to unmodulated feedback [3, pp. 271ff], especially for a portal with metal backplanes. Any localization system in such scenarios will likely share this problem. The feedback includes unmodulated reflections from the environments for monostatic and bistatic setups as well as antenna mismatches for monostatic antenna configurations, cf. Fig. 2.5(b). Comparisons of the APDPs for feedback and backscatter channels are shown in Fig. 2.32 for both types of setup.

Obviously, the feedback always exceeds the tag signal by several orders of magnitude, especially outside the gate. Required signal-to-interference ratios (SIR) and thus required dynamic



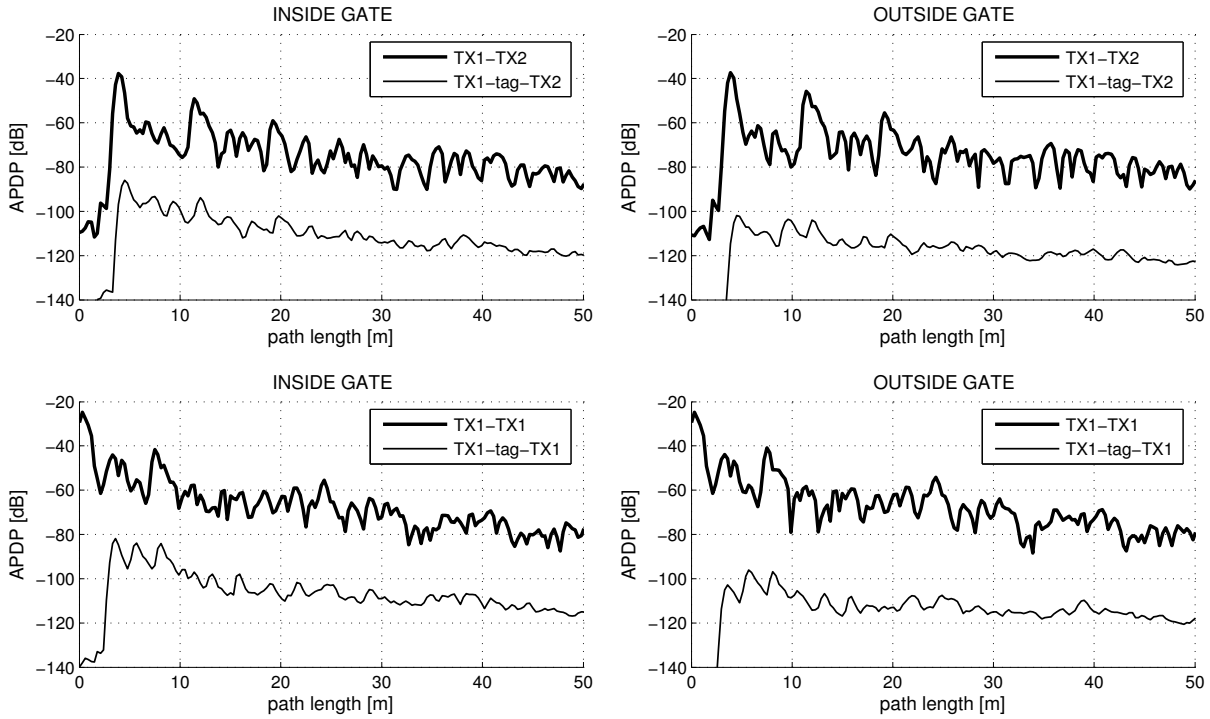


Figure 2.32: Comparison of feedback and backscatter channels for the empty portal (metal backplanes).



ranges without feedback mitigation are in the range of 30 to 70 dB to at least be able to detect the backscatter signal when the tag is inside the portal. This estimate is based on average power levels (narrowband) as well as power levels of the backscatter LOS component and the peak feedback component (UWB). Fig. 2.33 displays bounds for the latter case, i.e., backscatter LOS to peak feedback component (UWB). Note that this is a lower bound: polarization mismatches, nonperfect modulation depth, and an obstructed direct path lead to an additional attenuation of the backscatter link.

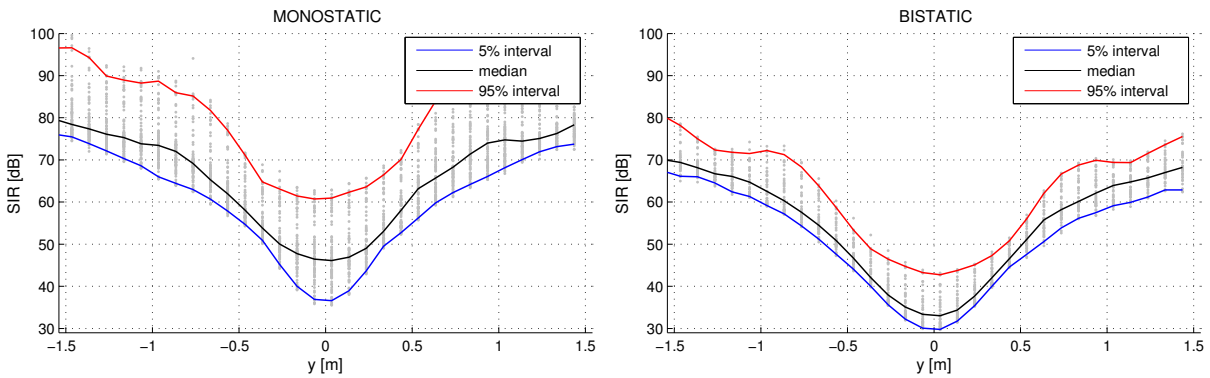


Figure 2.33: Signal-to-interference ratios (SIR) vs. y -position for the empty portal (metal backplanes). For $|y| \leq 0.4$ m, the tag is between the backplanes.

2.4 Single-Channel Approximation of the Backscatter Channel

parts of this section have been published in [133] and [134]

Passive RFID is a backscatter system, where the reader is transmitter and receiver at the same time and the tag is a time-variant part of the wireless CIR. This inevitably results in a degenerate (a.k.a. pinhole, keyhole, or dyadic) channel, where the overall channel is factorized into two individual ones [133, 134], cf. [140, pp. 29–31]. Pinhole in this context refers to the fact that, of all possible paths between TX and RX, only the ones passing the tag are part of the communications channel, as illustrated in Fig. 2.34. All other paths between TX and RX form the feedback channel. See Fig. 2.5(a) for the corresponding signal model.

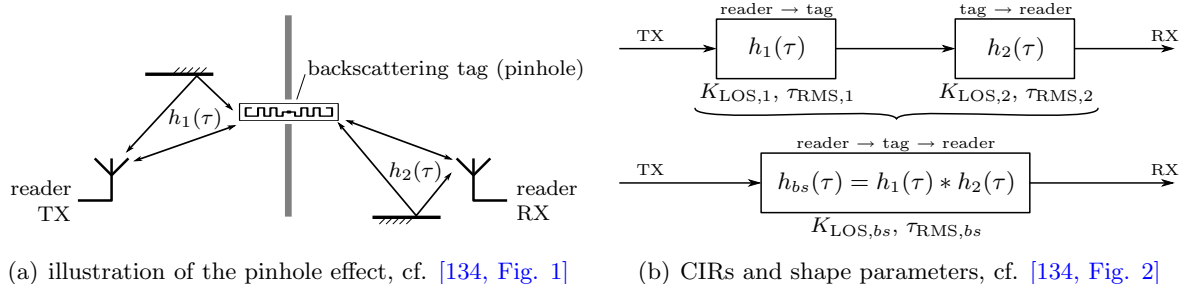


Figure 2.34: Illustration of the pinhole effect in backscatter systems and combination of the individual channels reader→tag (downlink, h_1) and tag→reader (uplink, h_2) to the backscatter channel reader→tag→reader (h_{bs}).

Ranging performance in backscatter systems is determined by the overall backscatter channel and thus depends on the parameters of this channel. However, most analyses are done for the more generic single-channel links, including the analyses in this thesis.

It is straightforward to see from Fig. 2.34(b) that the backscatter CIR $h_{bs}(\tau)$ is the convolution of the CIRs to and from the pinhole, $h_1(\tau)$ and $h_2(\tau)$. However, the connection between the parameters of the backscatter channel and their counterparts of the individual channels (K_{LOS} , τ_{RMS}) is considerably less obvious. Apart from the mathematical point of view (which can be found below) we can make some basic observations regarding the backscatter channel: As a general rule, the combined backscatter channel always has lower K_{LOS} and higher τ_{RMS} than each individual constituent channel. Correlation between the constituent channels, such as in monostatic setups, additionally decreases the K-factor and increases the RMS delay spread compared to the bistatic case. Moreover, the channel gain of a backscatter channel is always the product of both individual gain factors, thus leading to massive attenuation even at close range.

While the exact instantaneous shape parameters of the backscatter channel can only be calculated from the backscatter PDP itself due to the random nature of wireless channels, approximations based on the constituent channels' parameters are possible using the formulas given below. These formulas can be readily applied to instantaneous and averaged PDPs as well as distributions and statistics of the parameters. Derivations for the presented equations can be found in [133, 134].

Apart from helping to avoid the additional complexity of backscatter channel measurements, the given formulas can also be used to evaluate backscatter ranging performance based on existing channel measurements, such as [149, 193, 194], for example.

The backscatter K-factor can be approximated independent of the shapes of the PDPs via

$$K_{\text{LOS},bs} \approx \left(1 - \frac{\alpha_K}{2}\right) \cdot \frac{K_{\text{LOS},1} \cdot K_{\text{LOS},2}}{1 + K_{\text{LOS},1} + K_{\text{LOS},2}}, \quad (2.6)$$

where $0 \leq \alpha_K \leq 1$ represents correlation between the constituent channels. α_K equals zero for uncorrelated channels, while for fully correlated constituent channels $\alpha_K = 1$. If the LOS component is not fully isolated, i.e., reflected paths are mapped to the LOS component due to a limited signal bandwidth, α_K is less than one even in monostatic setups [133].

The RMS delay spread of the backscatter channel can be obtained via

$$\tau_{\text{RMS},bs} \approx \sqrt{\tau_{\text{RMS},1}^2 + \tau_{\text{RMS},2}^2 + 2 \cdot \alpha_\tau \cdot \tau_{\text{RMS},1} \cdot \tau_{\text{RMS},2}}, \quad (2.7)$$

where $0 \leq \alpha_\tau \leq 1$ again represents correlation. Unlike for the K-factor, α_τ depends on the shapes of the constituent channels' PDPs for correlated channels. It approaches $\alpha_\tau = 1$ for high K-factors. For fully correlated up- and downlink channels, i.e., monostatic setups, this parameter is

$$\alpha_{\tau,\text{monostat.}} = \frac{K_{\text{LOS},1}^2 \cdot \left(K_{\text{LOS},1} \cdot (2K_{\text{LOS},1} + 5) - 2\right)}{(1 + 2K_{\text{LOS},1}) \cdot (K_{\text{LOS},1} \cdot (K_{\text{LOS},1} + 4) + 2)^2} \approx \frac{K_{\text{LOS},1}}{10 + K_{\text{LOS},1}}, \quad (2.8)$$

with $K_{\text{LOS},1} = K_{\text{LOS},2}$ due to the full correlation. Although strictly speaking (2.8) is only valid for exponential PDPs [133], the formula works well also for non-exponential ones, such as the channels inside the UHF portal [133, 134].

Figs. 2.35 and 2.36 show cumulative distribution functions of K-factor and RMS delay spread for the constituent channels and the backscatter channel in monostatic and bistatic setups, respectively. These distributions have been calculated from the portal measurements in Section 2.3.3 and cover the entire portal. Plots for the backscatter channel show the CDFs estimated directly from the backscatter channel as well as their approximations using (2.6)–(2.8) on the single-channel CDFs.

Obviously, although based only on relatively simple equations, the backscatter channel parameters can be approximated quite well from the single-channel parameters. This includes the area inside the portal (PDP: power-law, high correlation) and outside the portal (PDP: exponential, low correlation) as well as LOS and NLOS cases (LOS blocked by pallet). The mismatch for the monostatic setups in Fig. 2.35 is caused by a not fully isolated LOS component due to the limited bandwidth and thus limited spatial resolution of the measurements, as well as by false positives in the LOS detection (for extremely low K_{LOS}).

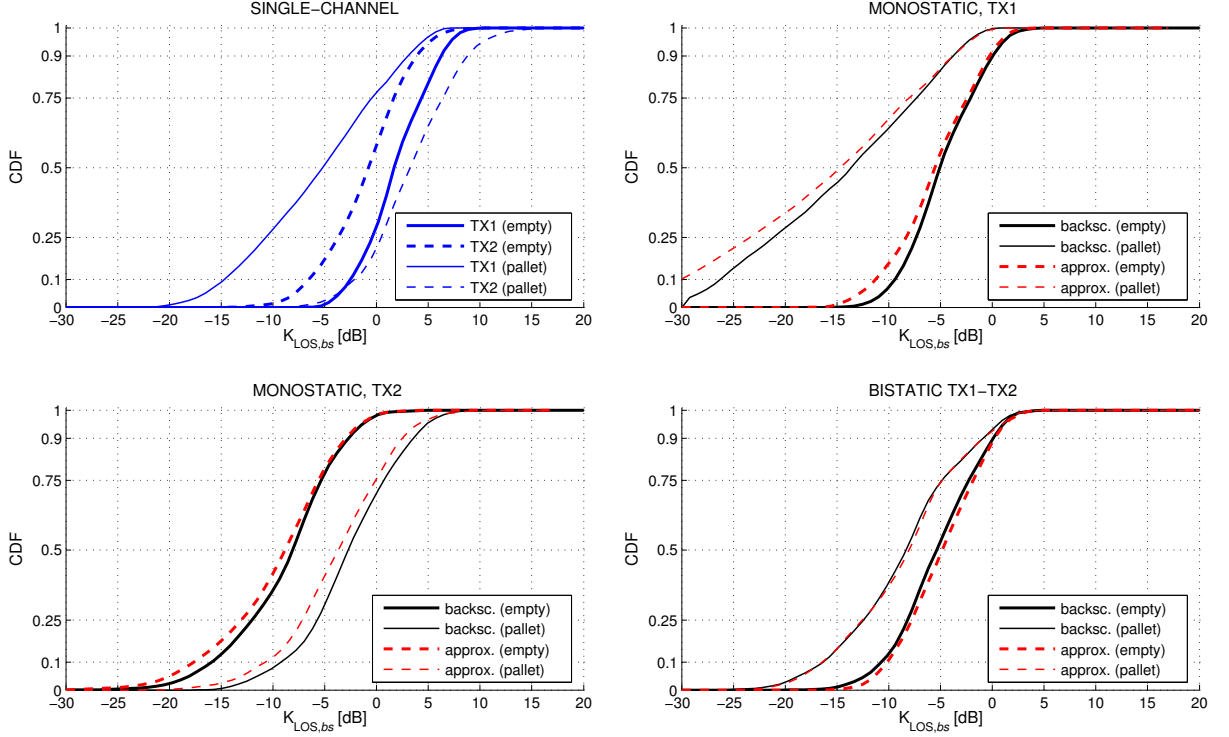


Figure 2.35: Comparison of backscatter parameters to single-channel approximations for monostatic and bistatic setup: K-factor (warehouse portal, metal backplanes, statistics over all measurements).

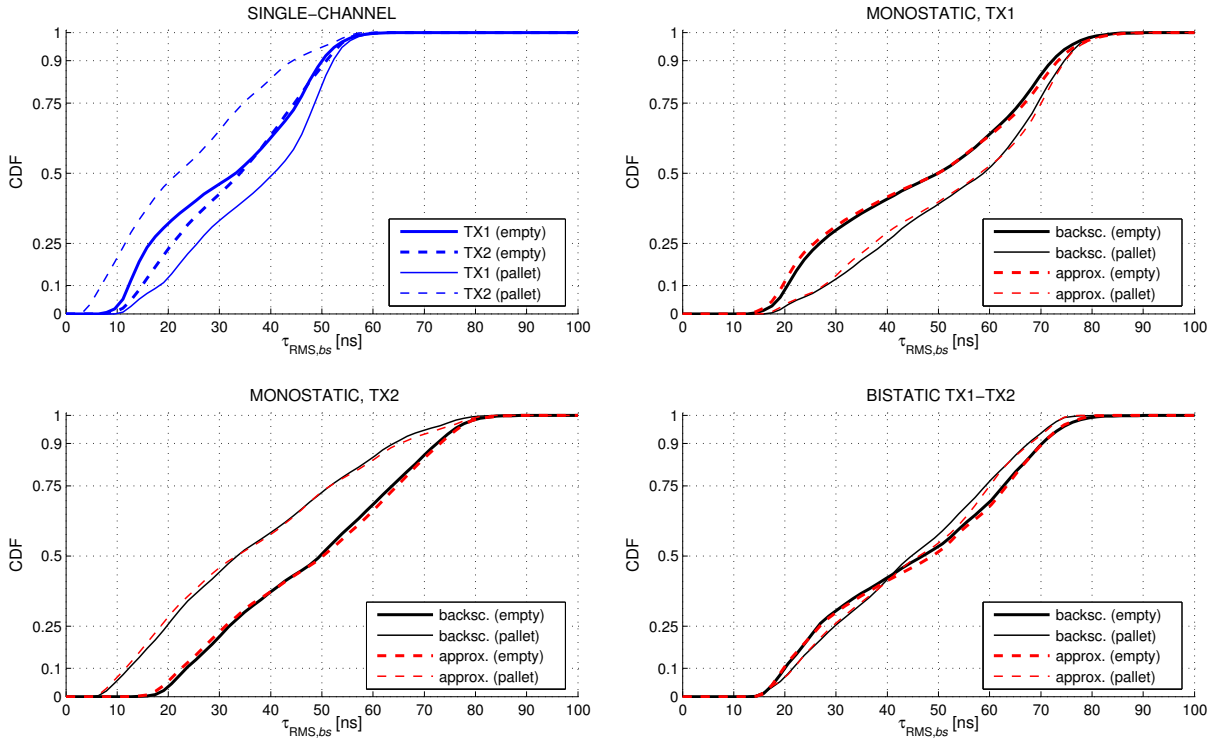


Figure 2.36: Comparison of backscatter parameters to single-channel approximations for monostatic and bistatic setup: RMS delay spread (warehouse portal, metal backplanes, statistics over all measurements). The plot uses the approximation for α_τ , not the full formula.

2.5 Summary of Channel Parameters

parts of this section have been published in [132]

2.5.1 Channel Basics for Ranging and Localization

Passive UHF RFID is a technology that is used mostly in production and supply chain, i.e., in industrial and thus severe multipath environments. Consequently, the channel has to be seen and treated as such and the LOS path cannot be assumed to be the dominant part of the CIR. Warehouse portals with metal backplanes in particular, but also reflecting product pallets, create severe multipath environments. K-factors with respect to the direct path are predominantly below 0 dB on the backscatter link¹⁷, while RMS delay spreads may reach several tens of ns at the same time and even in direct line-of-sight, cf. Figs. 2.35 and 2.36.

2.5.2 Recommended Channel Model/Parameters for Simulations

A hybrid channel model combining deterministic and stochastic elements should be used for simulations. The configuration of these models can be done based on rule-of-thumb values with a fair degree of accuracy. In order to obtain exact results, however, an optimization of the simulation setup based on measurements is necessary.

Reflection/transmission coefficients and refractive indices of surfaces should be chosen according to their structure, composition, and scatterers in front of the surface. Rule-of-thumb values for the PARIS engine can be found in Tab. 2.1. These values originate in the comparison of simulation and measurement results and have been used in the simulations above.

Table 2.1: Rule-of-thumb values for deterministic channel parameters: refractive index (reflection/transmission model) and reflection coefficient (VTX model) of surfaces.

| Material | Refr. Index | VTX Gain |
|----------------------------------|-------------|----------|
| metal (highly reflective) | | |
| unobstructed | 1000 | 0.9–0.95 |
| slightly obstructed / corrugated | 100 | 0.8–0.9 |
| obstructed | 10 | 0.7–0.8 |
| heavily obstructed | — | 0.2–0.5 |
| concrete (cf. [195]) | | |
| unobstructed | 2 – 3 | 0.4–0.6 |
| obstructed | — | 0.2–0.3 |

The *stochastic channel parameters* should be chosen with respect to the environment and the number and influence of virtual transmitters. If, for example, most of the PDP is modeled by clusters and thus VTX, the stochastic part of the channel has only limited influence. In this case, high K_{LOS} and low τ_{RMS} should be chosen. The final choice of stochastic channel parameters is thus hard to generalize, although some rule-of-thumb values and methods can be found in the literature, e.g., [162, 172, 173, 176, 188, 193, 194]. Especially the maximum RMS delay spread (outside the TX antenna’s mainlobe) can be estimated in a scenario-specific way using the electromagnetic reverberation time [172, 173]

$$\tau_{\text{RMS,max}} = \frac{4V}{c \sum_i \chi_{a,i}^2 O_i} \quad (2.9)$$

¹⁷ the link reader → tag → reader, i.e., the convolution of up- and downlink channels

where V is the volume of the reverberant room, c is the speed of light, $\chi_{a,i}^2$ is the power absorption coefficient of the i -th surface, and O_i is the area of the reflecting surface i . The absorption coefficient can be approximated by “one minus reflection coefficient” $\chi_{a,i}^2 = 1 - \chi_{r,i}^2$ for highly reflective surfaces. For the portal in the ASC (see above), this estimate leads to a maximum RMS delay spread of $\tau_{\text{RMS}} \approx 70$ ns, which is fairly close to the highest measured RMS delay spread of roughly 60 ns.

Settings for the stochastic channel model (LOS K-factor and RMS delay spread) used for the above simulations can be found in Fig. 2.37. Both parameters are chosen in a distance-dependent fashion in order to reflect trends reported in the literature [193]. The actual values depend on the scenario: For the test measurements “SPSC Salon”, the TX array was not placed between two highly reflecting surfaces, as it was for all other measurements. This leads to comparably high K_{LOS} and low τ_{RMS} . The second test measurement, “SPSC Corridor”, was done between two reflecting surfaces, but with several scatterers in between. Such a setup leads to a predominantly stochastic channel with low K_{LOS} and relatively high τ_{RMS} . The portal setup, on the other hand, is predominantly deterministic. As such, it was modeled with a great number of VTX, each of which has a comparably high K_{LOS} . RMS delay spreads at high distances, i.e., large path lengths, were chosen according to (2.9). The combination of all VTX then leads to the desired result.

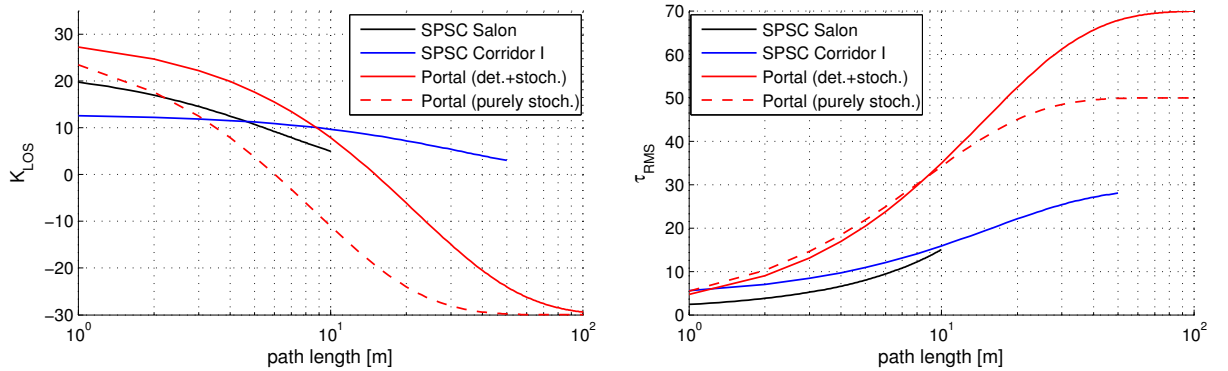


Figure 2.37: Stochastic channel parameters for the simulations presented in Section 2.3.

3

The PARIS Simulation Framework

The PARIS Simulation Framework is a Matlab-based time-domain system-level simulator designed for research on ranging systems in the context of this thesis. It features behavioral models of an NXP UCODE G2XM-based passive UHF RFID tag, a hybrid RF propagation channel model combining ray tracing abilities with stochastic small-scale models, parametric self-tests for most subroutines, characteristics generators to create new behavioral models, and a core framework that performs simple version control, logging, and exception handling.

This chapter deals with the models and concepts behind this simulation tool. Section 3.1 provides an overview and insight into the structure of the framework, while Section 3.2 describes the basic models and their limitations. Detailed descriptions of the implemented tag and channel models are given in Sections 3.3 and 3.4 respectively. Finally, Section 3.5 provides a step-by-step tutorial example explaining how to set up a simulation.

A word of warning: Even though the PARIS framework is an important part of this thesis project, it was not its central task. As a consequence, time to work on the framework was always at a premium. Especially the extension of the framework in 2010 was under very tight time constraints. Non-essential functions and self-tests have not been updated, rendering them inoperable. This also includes the standard (non-field-probe) mode of the 3-D gate simulation. A list of the most prominent known issues can be found in Appendix C.1.

3.1 Concepts and Basic Framework

3.1.1 Basic Structure

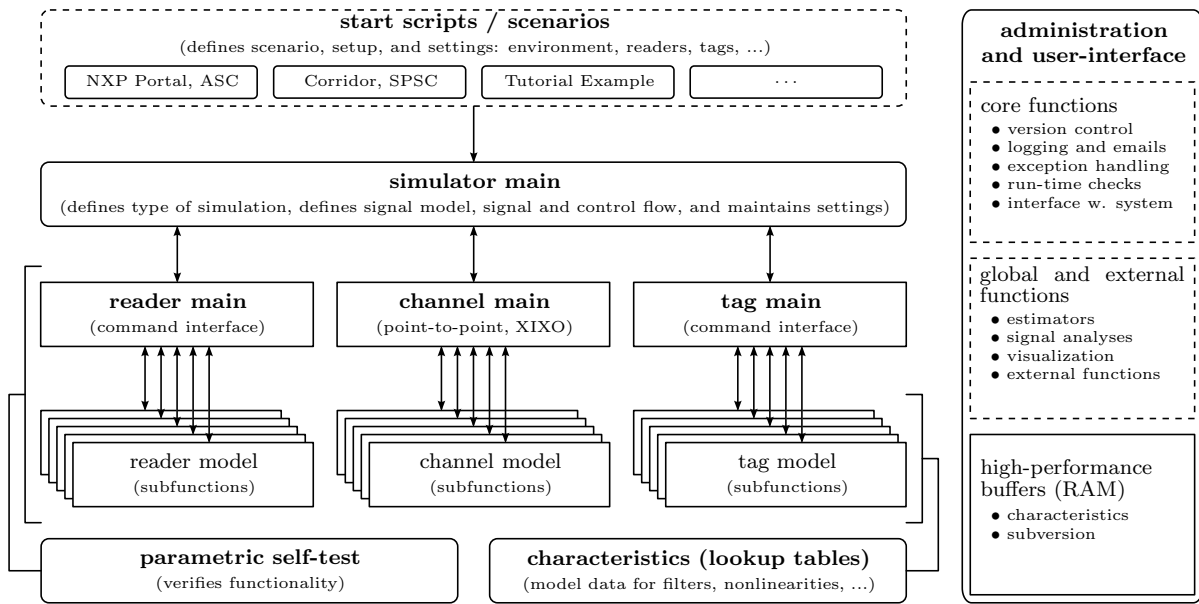


Figure 3.1: Hierarchical structure of the PARIS framework.

The PARIS framework is organized in a hierarchical fashion, shown in Fig. 3.1. The levels of this hierarchy are separated in order to make the framework as modular as possible. Also the different models and functions for reader, channel, and tag are strictly separated. The reader main command interface does not have access to tag subfunctions, models, or settings, for example.

The simulation setup is defined by the user in scripts and provided to the simulator via settings structs. Naturally, these setups are scenario-dependent and also depend on the intended type of simulation (e.g., 3-D simulation including geometries or merely a 1-D ranging simulation). The type of simulation, the signal model, and the signal and control flow are defined by the simulator main function. This function also maintains the settings structs. Readers, channels, and tags are controlled by main functions which provide an easy-to-use interface for the complex underlying models and calculations. Each main function uses and controls a set of model subfunctions implementing clock generators, encoding and decoding blocks, and multi-path propagation models, for example. Model data is stored in lookup tables (generally referred to as characteristics below) and loaded on demand. These characteristics are used by the model subfunctions in order to emulate a modeled device, e.g., a nonlinear power amplifier. A list of characteristics has been compiled in Appendix C.

Administrative functions and user-interface are decoupled from this strict hierarchy. General functions, such as exception handling, have to be available to all functions and models on all levels. These basic functions include version control, logging, the aforementioned exception handling, run-time checks of settings, but also basic estimators and signal analysis functions. A buffer minimizes time-consuming system interaction. This buffer is (optionally) used for characteristics files and version information.

The framework is also equipped with self-tests that check model subfunctions and main control functions using random settings and pre-defined expected results. These self-tests do not compare an output signal with a stored template, but rather analyze the results and verify the parameters against the corresponding settings (\rightarrow parametric self-tests).

The entire simulator is implemented in a procedure-oriented way: a reader, tag, or channel is defined by its settings struct only. These settings also contain the state of an object, such as the volatile memory of a tag. They are maintained by the simulator main function and used and manipulated by the main interface functions of reader, channel, and tag.

3.1.2 Logging, Version Management, and Exception Handling

The framework uses a combination of logging and version management in combination with specialized exception handling functions in order to ensure data integrity and track down corrupted results. Functions and characteristics contain a version number which is registered each time this function or characteristic is used. In addition, m-files¹⁸ also contain a changelog and a to-do list in their header. This header is standardized and can be processed automatically. Each characteristic contains a description field stating when the characteristic was created, by which function/script, and which data files were used in the creation. Any data produced by the simulator can thus be tracked back to the function that created this data and its revision. The framework also provides an interface with subversion in order to detect modified or corrupted files and to collect changelogs and to-do lists when committing changes.

Exception handling and logging functions are provided with several levels of priority, ranging from errors (which immediately stop the simulation), through warnings (these are prominently added to the log but do not interrupt simulation procedures), and finally messages, which are standard log entries. In case of errors, the user is optionally informed by email, stating simulation and error details, including a stack trace. Available types of errors, warnings, and messages are listed in Tab. 3.1. Like most other general settings, the level of verbosity in logging is controlled from `globalinit`.

| Type | Function | Used For |
|------------------|-----------------------|--|
| critical error | <code>criterr</code> | implementation errors that should have been caught (all checks failed to prevent this error) |
| error | <code>err</code> | procedural errors (missing settings, overflows, ...) |
| critical warning | <code>critwarn</code> | configurations that might lead to data corruption (e.g., manual overrides) |
| warning | <code>warn</code> | alteration of settings by housekeeping functions and other low-priority warnings |
| headline | <code>headline</code> | headlines in logs (e.g., start of a new block) |
| message | <code>message</code> | messages in logs (what is done) |

Table 3.1: Types of errors/warnings/messages, sorted by descending priority.

3.1.3 Automated Self-Tests

The PARIS framework is equipped with a series of self-tests in order to ensure its functionality, especially after modifications. The self-tests encompass the model subfunctions of reader, channel, and tag, as well as their controlling main functions. Each model is tested by a specialized self-test function. The concept of these tests is illustrated in Fig. 3.2.

Preparation and execution of self-tests is strictly separated. Settings and expected results are generated by scripts (`results_*.m`) and stored in data files (`results_*.mat`). Each file contains a set of random settings and associated expected results, typically grouped in blocks (e.g., reflection and transmission for the tag modulator). The actual tests are performed by specialized functions (`test_*.m`) which load the stored settings/results file, provide the function

¹⁸ Matlab code files (function or script)

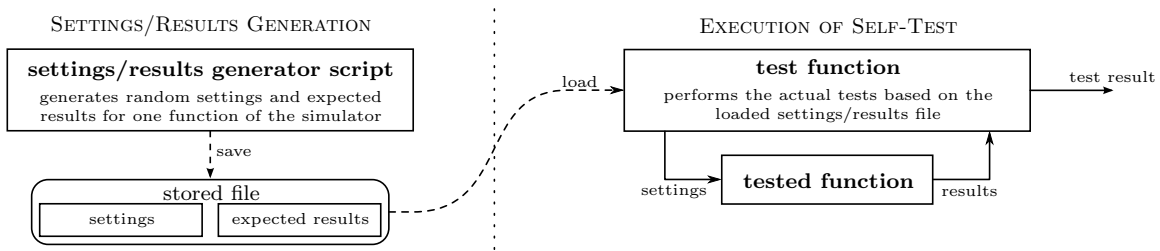


Figure 3.2: Concept for self-tests. Each function of the simulator is tested by a self-test specifically developed for this function. A main self-test script performs all tests in a row and creates a log.

under test with these settings and verify its output. The test functions display the individual test results in Matlab’s command window and return the number of errors found. A main self-test script, `selftest_main`, collects and lists the version information of all scripts/functions and executes all self-tests. An example log created by this main self-test script can be found in Appendix C.



Naturally, although the self-tests provide an additional layer of security, they cannot completely rule out bugs or guarantee proper functioning. First and foremost in the list of possible pitfalls: the expected results have to be defined by the programmer. Typically, this programmer is the person that implemented the function itself (especially if the programming is a one-man show like in a PhD project), so there is a distinct possibility that the test function and the tested function share a common problem. Also, test coverage is typically well below 100% even for randomly selected settings and inputs. Finally, most self-tests use estimators, thus introducing the possibility of false positive and false negative errors.

3.1.4 Main Simulator Files

Two different types of simulator main functions are currently implemented: a 3-D gate simulation and a 1-D ranging simulation. Both functions have been implemented for the narrowband MFCW ranging method (see Section 4.2) and extended on demand. The gate simulation, for example, features a UWB field probe mode, where tags record channel impulse responses. Similar implementations for other ranging methods have been started, but are incomplete.

The gate simulation (`sim_mfcw_gate`) has been used to produce most simulation results presented in this thesis. Although it has originally been developed to model a UHF RFID portal, it can be used for almost arbitrary indoor environments (such as SPSC’s meeting room, for example: see Section 2.3.2). The gate simulation models multiple readers and tags, and implements the signal model shown in Fig. 3.3. Tag positions are modified inside a loop and the distances between readers and tag(s) are continuously estimated. Each reader is activated (transmitting) once for each loop pass while at the same time all readers are receiving and estimating distances. Tags are configured only once using a Query command [1] before the loop in order to speed up the simulation. In a special UWB field probe mode, only channel impulse responses are recorded; all other functionalities are deactivated. This mode was used for the channel simulations in Section 2.3.

The ranging simulation (`sim_mfcw_ranging`) can be used to statistically assess the properties of a ranging system. Recent changes in the channel models have not yet been implemented in this simulation main file, so the development version accompanying this thesis is not operational (version beta 1.0 of the open-source framework is).

3.2 Model Overview: Reader, Channel, Tag

Fig. 3.3 shows the signal flow graph implemented in the simulator. It is an extension of the signal model introduced in Fig. 2.5(a) on page 43. Each communication frame between reader and tag starts with the reader transmitting a signal (modulated or unmodulated carrier, ranging signals, etc.) and ends with either the tag receiving the reader’s signal or with the reader receiving the signal reflected by the tag. Ranging frames for passive and semi-passive tags always encompass the entire signal model, i.e., the reader performs transmission and reception while the tag merely reflects the signal.

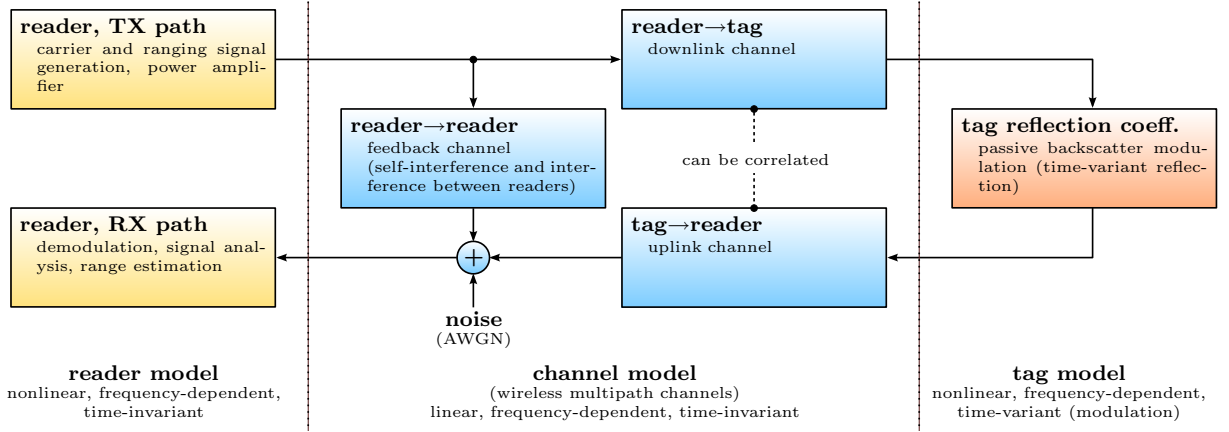



Figure 3.3: Signal model and signal flow graph for the simulator. Time-invariance refers to a single communication frame, i.e., milliseconds (especially for the wireless channels).

The reader model for one such frame is nonlinear due to the power amplifier, frequency-dependent due to channel filters, and time-invariant. The tag model, which is represented in this signal flow graph by its reflection coefficient, is nonlinear, frequency-dependent, and quickly time-variant due to the passive backscatter modulation. All wireless multipath channels are modeled in a linear, frequency-dependent, and time-invariant fashion for one communication frame. Additive white Gaussian noise (AWGN) is added at the receiver; the channel to the tag is assumed to be noiseless. Note that the time-invariance only refers to a single communication frame (\sim milliseconds). 

The signal flow graph in Fig. 3.3 reflects the communication between one reader and one tag. The PARIS framework, on the other hand, supports multiple readers and tags, as does reality. The handling of multiple readers and tags by the framework is illustrated in Fig. 3.4. Each reader and tag interfaces with “the channel”, which is composed of the blocks shown in Fig. 3.3 for each combination of reader and tag. An example for two readers and two tags is illustrated in Fig. 3.4(b). The three channel blocks (reader→tag, tag→reader, reader→reader) use the same channel model, but with different parameters.

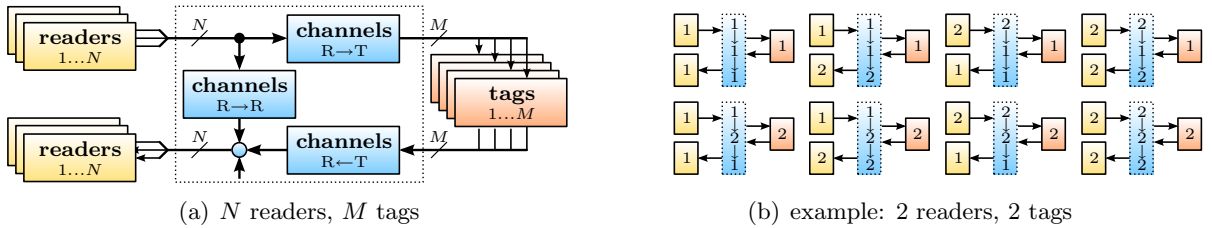


Figure 3.4: Handling of multiple readers and tags. Each blue channel block in (b) consists of feedback, uplink- and downlink channels, and additive noise.

Note that the transmitting reader does not necessarily have to be the receiving one, and that two different readers do not necessarily have to be distinct processing devices. A reader with one transmitter circuit and four receivers circuits, for example, can be connected to four antennas. While only one antenna (“reader”) is transmitting, four antennas (“readers”) are receiving. This is the standard configuration for portal readers and is also reflected in the structure of the UHF gate simulation.

3.2.1 Reader Model

The reader in UHF RFID systems is typically a powerful device, with impressive analog and digital processing capabilities. With respect to research, where costs are a secondary concern, the reader is not the limiting device in UHF RFID. The reader implementation of the PARIS framework is thus generic in comparison to tag or channel model and does not reflect specific types of readers.

Overview

The main reader function, `reader_main`, provides the user with a simple-to-use interpreter interface. This main interface controls an entire set of functions, shown in Fig. 3.5. Details regarding its usage are provided by the simulator help (`help reader_main` in Matlab). The

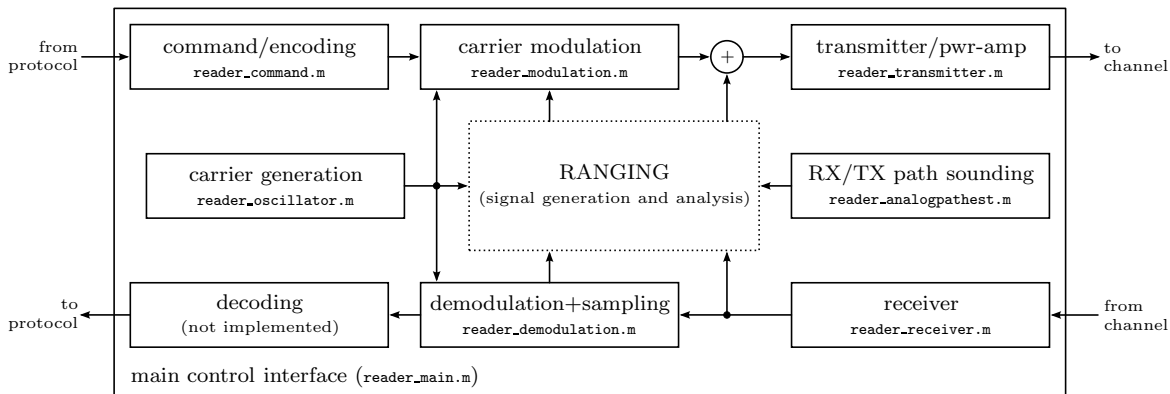


Figure 3.5: Basic structure and functions of the reader model.

central part of the reader structure is the ranging signal generation and analysis. Apart from this block, the reader structure implements a standard communications transceiver. A command is first encoded and then sent to the modulator which in turn modulates the carrier signal provided by the carrier generation block. This signal is sent over the transmitter, after which it enters the channel. The receive path consists of the receiver, an I/Q demodulator, sampling and quantization, and the decoding block. As decoding of the tag signal was not necessary for the work on ranging methods, this last block is not implemented. Last but not least, a linear system estimate of the transmitter and receiver structure of the reader (transmitter, receiver, demodulation) is provided to the ranging algorithm by the RX/TX path sounding block. This data can be used by the ranging algorithm to correct systematic errors introduced by the analog path of the reader.

Transmit Path

Command generation (`reader_command`) and modulation (`reader_modulation`) are implemented according to the EPCglobal Class-1 Gen-2 protocol[1]. Two commands are available: Query and Ack. The modulation function fully implements the timings and waveforms defined in [1], with

the exception of power-up and power-down waveforms. User settings are checked for conformity with these timings and corrected if necessary (forcing settings is of course possible). The created modulation waveform, which uses cosine rolloffs for band limitation, is subsequently modulated onto the reader carrier generated by `reader_oscillator`. Supported modulation schemes are single/dual sideband and phase-reversal amplitude shift keying (SSB-ASK, DSB-ASK, PR-ASK). Carrier generation supports cosine, sine, and complex exponential¹⁹ carriers with arbitrary frequency, phase and amplitude noise, as well as additive white Gaussian noise. The transmitter block (`reader_transmitter`) amplifies and filters the transmitted signal, emulating a nonlinear power amplifier with subsequent bandpass filtering. The pre-defined power amplifier characteristic is shown in Fig. 3.6.

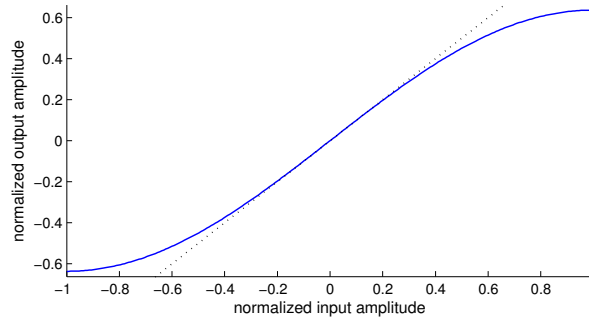


Figure 3.6: Power amplifier characteristic (used by `reader_transmitter`).

Receive Path

On the receive side, the receiver performs bandpass filtering and separates in-phase (I) and quadrature-phase (Q) signals. Demodulation is performed by `reader_demodulation` symmetrically on I and Q channels using a complex exponential carrier generated by `reader_oscillator`. The baseband signal is then filtered (anti-aliasing), resampled to the reader sampling frequency, and linearly quantized. Decoding is not needed for ranging and is thus not implemented.

Ranging

The only fully implemented ranging method is the narrowband multi-frequency continuous-wave (MFCW) Ranging, with three functions shown in Fig. 3.7(a). The MFCW ranging carriers are generated by `mfcw_addseccarriers` and added to the main reader carrier. Received signals are processed by `mfcw_compse1`, extracting carrier phases, and `mfcw_calcdist`, which estimates the distance to the tag based on the extracted phase shifts. Details about MFCW can be found in Section 4.2.

Wideband and ultra-wideband ranging methods (see Chapter 5) are only partially implemented. These methods were analyzed based on the channel measurements in the UHF portal, without the simulator. The evaluation of frequency-modulation continuous-wave (FMCW) ranging was done in co-operation with Clausthal University of Technology, using their simulator (see [137]). The carrier generation for FMCW is fully implemented, however: `mfcw_addfmccarrier` supports several FMCW waveforms (square, sawtooth, triangle, sinusoidal), which are generated in baseband and modulated onto a carrier via single sideband modulation. The FMCW signal analysis, on the other hand, is only partially implemented. Also for Impulse-Radio Ultra-Wideband (IR-UWB) ranging a rudimentary pulse generation function (`uwb_addpulses`) has been implemented, but the analysis function is missing.

¹⁹ used for demodulation (more efficient than independent sine/cosine if a complex baseband is intended anyway)

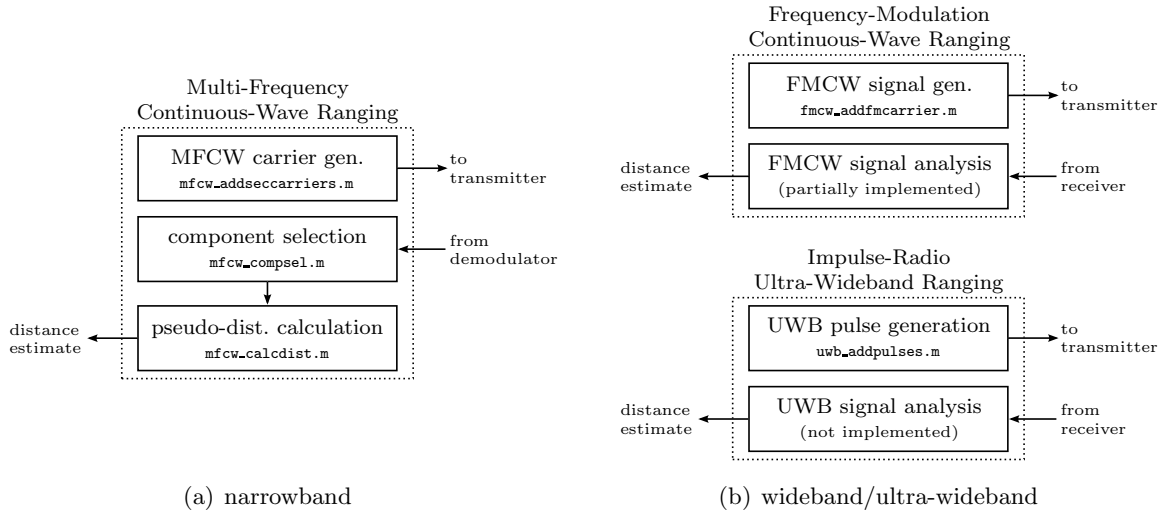


Figure 3.7: Basic structure and functions of ranging blocks.

3.2.2 Channel Model Overview

The channel model of the PARIS framework is optimized for RFID-typical applications such as portals in industrial environments. Indirect propagation paths are modeled by a combination of deterministic and stochastic components, constituting the hybrid channel model. This model combines large-scale path loss, antenna gain patterns (directivity), a deterministic small-scale model consisting of surfaces and virtual transmitters, and a stochastic small-scale model implementing an exponential average power-delay-profile. Noise is modeled as additive white Gaussian noise (AWGN). A detailed description of the individual models can be found in Section 3.4; an overview and the structure of the channel model are given below²⁰.

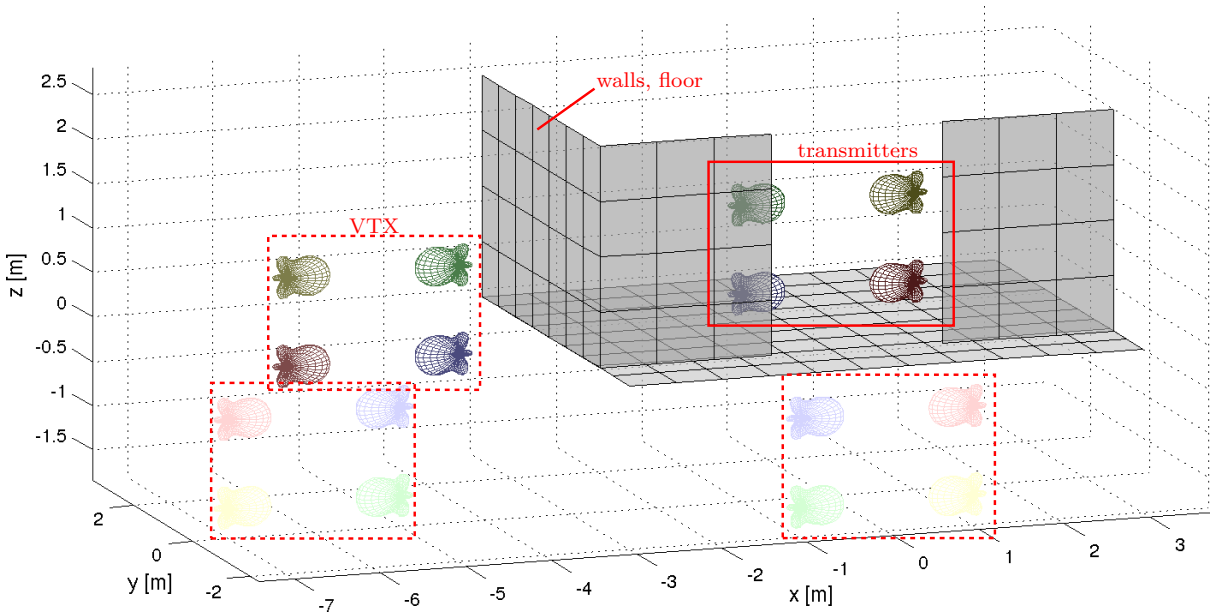


Figure 3.8: Simulation setup example showing TX, VTX (both represented by their gain pattern), and surfaces. Darker surfaces and VTX have higher gain factors (stronger reflection).

²⁰ Another short introduction was provided in Section 2.2.4. However, this introduction was limited to modeled effects. The descriptions in this chapter instead focus on the models and how they should be used.

Fig. 3.8 shows an example setup created by the PARIS framework. This simple example contains four surfaces (three walls plus a floor), four transmitters, and three groups of virtual transmitters. Transmitters and virtual transmitters are represented by colored gain patterns in this illustration. A lighter color signifies a weaker signal. The virtual transmitters (VTX) model double interreflections between surfaces. In this example, the top left (labeled) group of VTX models the interreflection in the corner at the center of the image. Note the different orientation for each group, depending on the reflection the group represents.

The framework creates channel impulse responses based on such geometrical representations and in a step-by-step process. Together with the LOS, reflections at flat surfaces form the purely deterministic parts of a CIR. Surfaces are meant to be used at short range, where the angle of incidence and thus the reflection coefficient changes considerably when either transmitter or receiver changes position (cf. Fig. 3.9; moving receiver), or where there are few scattered components. They provide an efficient way to model strong specular reflections at close range. Like the LOS, multipath components created by the surface model are deterministic peaks in the CIR. Apart from creating deterministic reflections, the surfaces also feature as a simple transmission model.

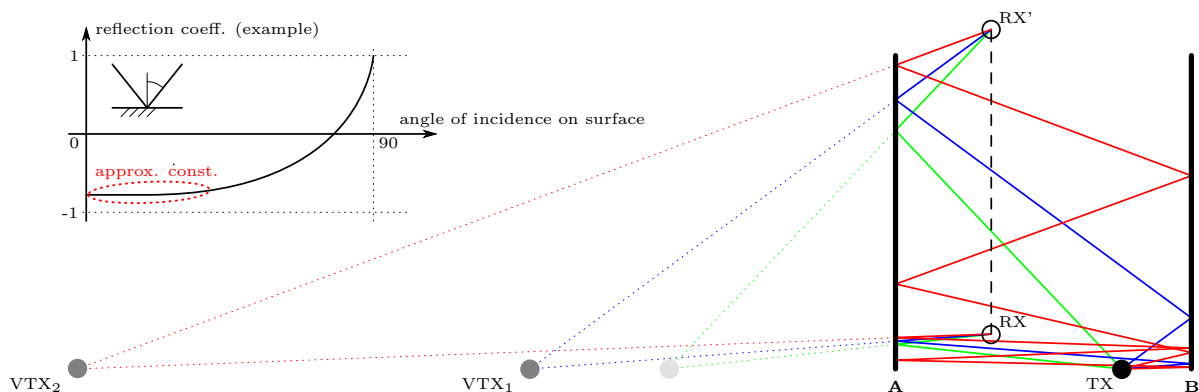


Figure 3.9: Angle dependence of reflection coefficients and comparison of VTX and surface model for a moving receiver. Note that higher-order reflections generally have smaller angles of incidence to the surface normals and that the angles change more slowly with the receiver movement in this example. This translates to largely movement-invariant surface reflection coefficients, justifying fixed gains for virtual transmitters.

Specular interreflections (reflections involving more than one surface), diffuse reflections and scattering, as well as clusters are modeled by virtual transmitters. A virtual transmitter is a reflected version of the original transmitter. VTX₁ in Fig. 3.9, for example, is a double reflection of the transmitter (TX) in surfaces B and A. Diffuse and random components are incorporated by a stochastic small-scale model which is (optionally) included in any channel impulse response from transmitters and virtual transmitters.

The basic structure of the implemented channel model is shown in Fig. 3.10. Unlike the main reader and tag functions, `channel_main` does not provide an interpreter interface, but merely calculates the output signals for a given set of input signals, subject to the channel settings. The function is designed to handle an arbitrary number of transmitters (inputs) and receivers (outputs), N_{TX} and N_{RX} , respectively.

The channel between a transmitter and a receiver is formed by piecewise assembly of the channel impulse response. The LOS component is created by the combined results of large-scale model (gain and delay), directivity model (antenna gain pattern), and surface model (transmission gain) for the LOS link. Large-scale and directivity gains are calculated by `channel_large` and `channel_directivity` respectively, and the surface transmission gain is calculated by

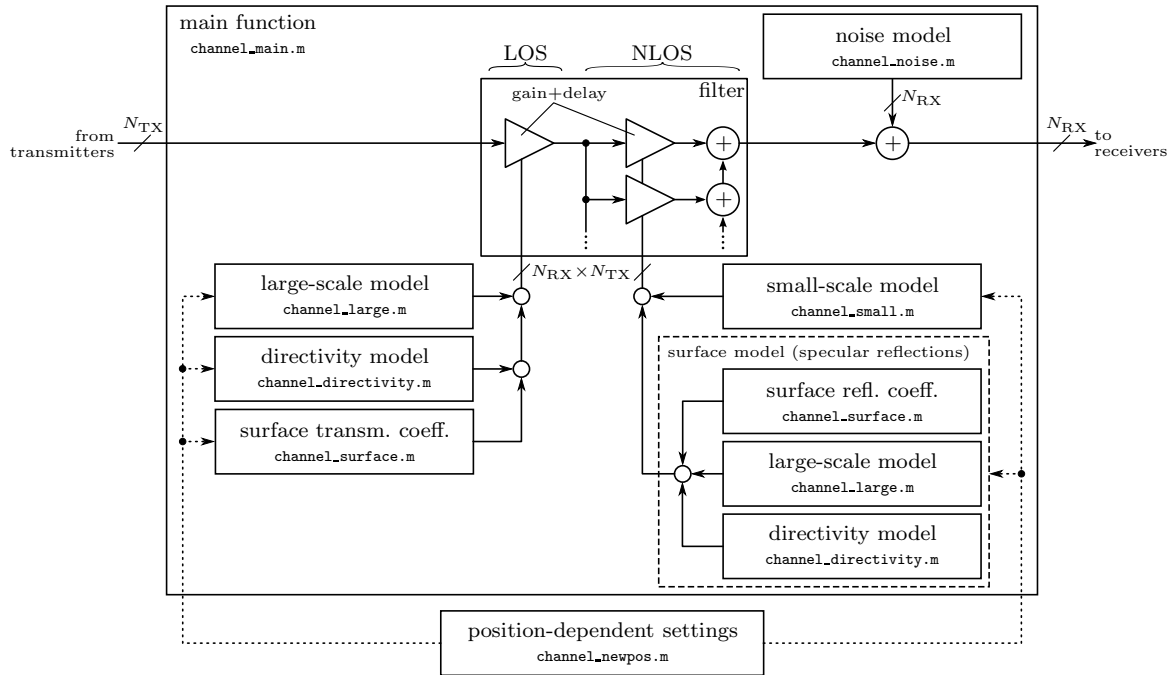


Figure 3.10: Basic structure and functions of the channel model. Virtual transmitters (VTX) are treated like normal transmitters in this structure.

channel_surface. The NLOS part of the CIR is created by a stochastic small-scale model plus deterministic reflections in surfaces. The latter each employ large-scale and directivity model, as well as a surface reflection coefficient. The stochastic NLOS components created by **channel_small** are scaled by the large-scale LOS gain and (optionally) by the directivity gain.

Geometric and position-dependent settings (distances, angles for directivity patterns, angles of incidence on surfaces, distance-dependent small-scale parameters, etc.) are provided by **channel_newpos**. This function is not controlled by **channel_main** in order to separate the channel models from any environment-specific considerations (the channel model is controlled by settings, not the environment).

After the CIR assembly is complete, channel output signals are calculated by summing the input signals filtered by the respective CIRs. In the final step, additive white Gaussian noise (AWGN) is added. The variance of the added noise floor considers resampling by the receiver and is controlled via the single-sided noise spectral density N_0 ([W/Hz]).

3.2.3 Tag Model Overview

The structure of the tag model is shown in Fig. 3.11. Unlike the reader model, the tag model is designed to simulate specific tags. Simulations in this thesis are based on the model of an NXP UCODE G2XM chip soldered onto an NXP UCODE general purpose reference antenna, see Fig. 3.12.

The most important part of the tag with respect to localization is the interface between tag and channel: the tag reflection coefficient. The reflection coefficient of a passive UHF RFID tag is highly nonlinear, frequency-dependent, and time-variant during tag modulation. It is intertwined with the tag (backscatter) modulator and the power supply unit, and provided by **tag_modulation** in the model. This function is by far the most complex tag module, based on several physical tag characteristics and a large filterbank structure. On the receive path, the part of the incoming signal that is neither reflected nor lost in the modulator circuitry or parasitics is

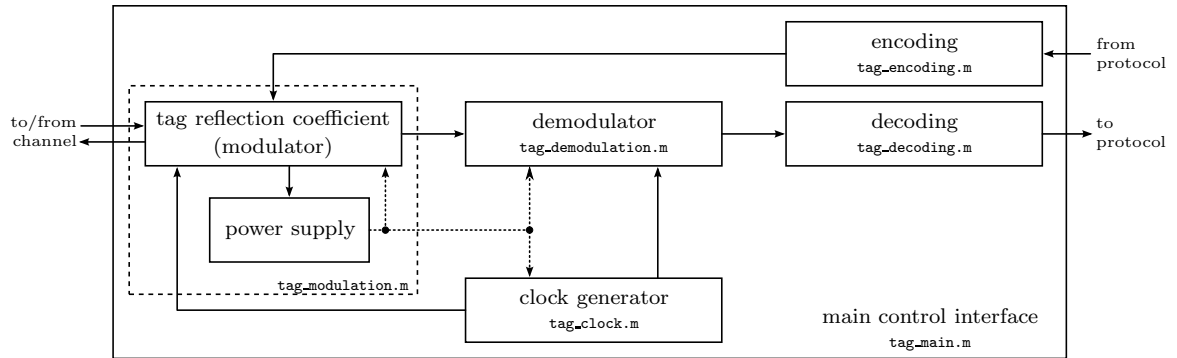


Figure 3.11: Basic structure and functions of the tag model.

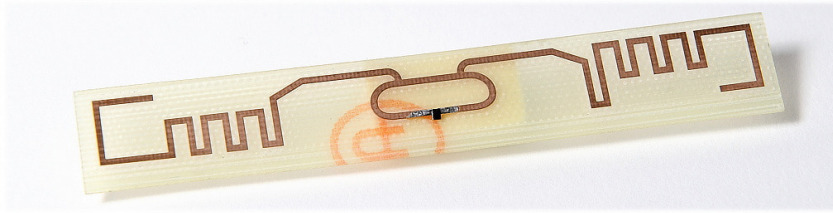


Figure 3.12: NXP UCODE G2XM on NXP UCODE general purpose reference antenna.

sent to the demodulator (`tag_demodulation`), where it is amplitude-demodulated and resampled to the tag clock rate. Decoding (`tag_decoding`) is implemented according to [1] (for a limited set of commands). The transmit path consists of the encoding block (`tag_encoding`), which sends the encoded data directly to the modulator. Extensive descriptions of the tag models can be found in Section 3.3, including a detailed description of the tag reflection coefficient and its calculation.

The entire set of tag subfunctions can be difficult to handle, especially if implementational issues such as group delays, shared settings, or shared states have to be considered. In order to simplify the usage of the tag model, the main control function `tag_main` provides a simple interpreter interface for the user.

3.2.4 Limitations of the Implemented Models



The implemented models have several limitations of which a user should be aware. These limitations originate in the trade-off between accuracy, implementational effort, and computational complexity. The most prominent limitations are:

1. Channel Model

- All deterministic models (large-scale, directivity, surfaces, VTX) are bandwidth-independent and thus strictly speaking not valid for UWB signals.
- Surfaces are limited to xy -, xz -, or yz -plane, and their refractive indices are limited to real values. Absorption and changes in propagation delay are not considered (pure surfaces; no volumes).
- The geometry model governing VTX activity only considers the last reflection.
- Specular reflections in surfaces are not affected by other surfaces, i.e., they are neither reflected, nor blocked.

- There is no connection between the VTX gain and the corresponding angle-dependent reflection coefficients.
- Antenna gain patterns have to be symmetrical with respect to xy and xz , where x is the mainlobe direction.
- The VTX/surface setup is not fool-proof. If a user neglects to mark a surface as “covered by VTX” (see Section 3.4), the direct path of the VTX created by this surface is reflected even though this maps the reflection to the original TX. Checks done by the framework cannot cover all combinations (this would require full ray tracing).
- Scattered reflections (stochastic NLOS components) are not reflected by the environment, but rather sent by each transmitter. As such, the entire stochastic NLOS CIR originates from the transmitter, i.e., a single point in space. Geometrically diffuse components are not featured/supported. They can, however, be modeled by a high number of VTX with deactivated direct paths placed at the positions of scatterers (cf. [139, 196]).
- Narrowband correlations are only asymptotically correct for a large number of taps (stochastic small-scale model).
- Polarization is not modeled.

2. Tag Model

- The implemented reflection coefficient model assumes short-time stationary power (stationary for one frame). A nonlinear selection of the time-variant reflection coefficient during modulation is possible in principle but not implemented for performance reasons.
- There is an inevitable trade-off between accuracy and time-resolution for the reflection coefficient filterbank (\rightarrow time-frequency localization).
- The antenna detuning model does not support massive detuning (not valid if tag is closer than roughly 1 cm to metal or water).
- The tag clock does not feature frequency drift.

3. Self-Tests

- The test coverage is typically well below 100%: checking all possible combinations of settings and input signals is rarely feasible.
- Expected results have to be created and defined by the programmer along with the checks. Naturally, this is not error-proof.
- False positive and false negative errors are possible (parameter estimators).

3.3 The Tag Models in Detail

3.3.1 Tag Reflection Coefficient

parts of this section have been published in [128]

A tag's reflection coefficient is the only physical tag parameter visible to the reader. This makes it the most important tag parameter for backscatter-based sensing [197–203] and tag localization.

The following section provides a detailed description of the reflection coefficient model implemented in the PARIS framework, how it is calculated, and how it was verified. The model uses impedance data of an EPCglobal Class-1 Gen-2 [1] chip in modulated and unmodulated states, as well as assembly- and antenna-impedances in order to calculate the reflection coefficient of the fully assembled Gen-2 tag. These impedances can be obtained via conducted measurements [152, 204] or simulations, whereas measuring the reflection coefficient directly requires an anechoic environment and comparatively complex measurement procedures [205].

Overview

The reflection coefficient of passive tags is highly frequency-dependent, nonlinear, and fast time-variant due to the modulation. The implemented model of this physical behavior is based on the equivalent circuit shown in Fig. 3.13. Similar equivalent circuits are well established in RFID [3, 4, 206, 207]. Not included in this model are the antenna gain pattern and polarization mismatches. This is a very common and useful simplification; both factors can, however, be added at any later time, cf. [208–211].

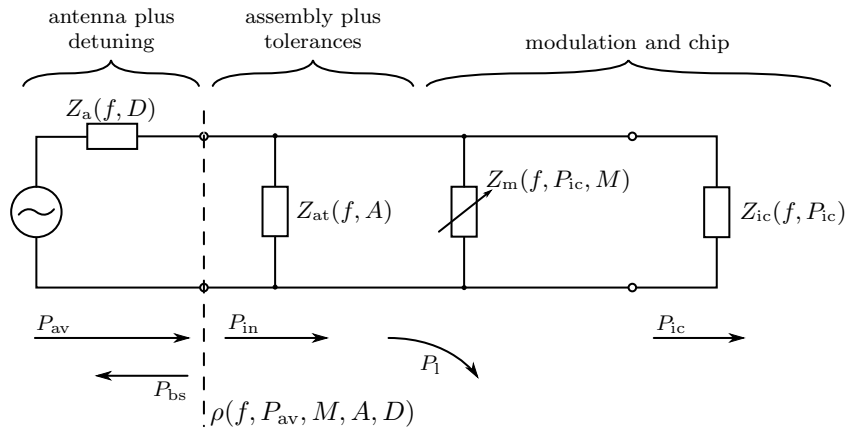


Figure 3.13: Equivalent circuit model of the tag reflection coefficient, cf. [128, Fig. 1]; antenna impedance Z_a , assembly impedance Z_{at} , modulation impedance Z_m , and unmodulated chip impedance Z_{ic} . Parts of the available (incident) power P_{av} are backscattered (P_{bs}). The input power P_{in} is partially lost in assembly and modulation impedance (losses P_l); the remaining power is the chip input power P_{ic} . The model has three state variables: modulation state M , assembly state A , and detuning state D .

For simulations, the reflection coefficient (ρ) is implemented as a multidimensional lookup table, representing the nonlinear reflection coefficient over frequency and power for different “states” of a tag. These states consist of the modulation state M (e.g., modulated and unmodulated), the assembly state A , and the detuning state D . The assembly state here represents the value of the parasitic assembly impedance Z_{at} , whereas the detuning state covers the changes of the tag in proximity to dielectric materials. Of these states, only the modulation state is fast

time-variant, while the assembly and detuning states will likely be fixed during a single communication with the tag. A lookup table used for such a communication frame thus has to contain only the reflection coefficient over frequency, power, and the modulation state, i.e., $\rho(f, P_{\text{av}}, M)$. A set of lookup tables (one file per table) spans different assembly and detuning states. The files also contain lookup tables for power levels and several other data fields which are regularly used in simulations. The mapping from detuning and assembly states to actual model parameters is done based on another lookup table, see Appendix C. Although this may sound cumbersome, it is a very flexible and simple way to cover an arbitrary set of states, depending on the type of tag and/or the application.

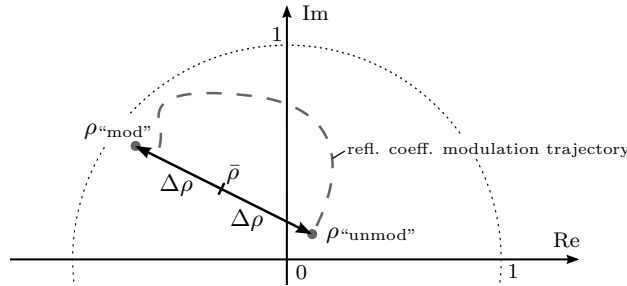


Figure 3.14: Linear model of the tag reflection coefficient (intended for derivations) with average reflection coefficient $\bar{\rho}$ and difference value $\Delta\rho$, cf. [128, Fig. 3]. Only the end points of the original trajectory are preserved.

Linearized Model of the Tag Reflection

Although multidimensional lookup tables are simple to handle in simulations, they are rather bulky in mathematical derivations. For this purpose, the model offers a simple and straightforward version of the reflection coefficient. This linearized model is a simplification of the quite complex reflection coefficient trajectory during modulation (cf. Fig. 3.14) and uses the fact that the tag modulation is almost perfectly binary, i.e., switching quickly between only two modulation states (modulated and unmodulated). The model replaces the trajectory by a fictive center $\bar{\rho}$ and a difference $\Delta\rho$, where

$$\rho^{\text{mod}} = \bar{\rho} + \Delta\rho \quad \text{and} \quad \rho^{\text{unmod}} = \bar{\rho} - \Delta\rho \quad (3.1)$$

This approach is loosely linked to differential radar cross sections, cf. [212]. Note that the end points of the trajectory are power- and frequency-dependent, hence the parameters of the linear model also depend on frequency and power, i.e., $\bar{\rho} = \bar{\rho}(f, P)$ and $\Delta\rho = \Delta\rho(f, P)$. The benefit of this model is its simplicity when it comes to modulation. The complex reflection coefficient during modulation can be expressed by

$$\rho(f, P, t) = \underbrace{\bar{\rho}(f, P)}_{\text{center}} + \underbrace{s_m(t)}_{\text{modulation}} \cdot \underbrace{\Delta\rho(f, P)}_{\text{difference}} \quad (3.2)$$


with $-1 \leq s_m(t) \leq 1$ being the modulation waveform. This modulation model is especially useful for multiple frequency components if the power level is roughly constant and hence the superposition principle holds, cf. Section 4.2.1 and [135].

Calculation of the Model

Pre-Processing of Measurement Data: Most of the processing is done for the chip impedance data, which is obtained via conducted measurements [204]. Approximation and median filtering are used to remove the ripple in the measured chip impedance created by the tag’s power-up procedures (cf. [152]), as well as the ripple typically created by stepped-frequency measurements with network analyzers (cf. Fig. 2.14 on page 52). Moreover, power losses and impedance mismatches are taken into account and removed from the measurements, thus aligning the power vectors between modulated and unmodulated state to the chip power P_{ic} . The modulation impedance Z_m is obtained using a combination of brute-force search and nonlinear optimization, finding the optimal parallel impedance to turn the unmodulated into the modulated chip impedance.

1. Base Data: As a first step in the calculation of the reflection coefficient, necessary data is loaded and the base vectors for power and frequency are generated. This process starts with the perfectly tuned antenna impedance in free space Z_a and the frequency vector f . The created frequency vector has a non-homogeneous resolution, with a denser grid inside the UHF frequency bands. Next, the minimum power characteristic over frequency, $P_{ic,min}$, is loaded and interpolated to the frequency vector (second step).

The third step is a little more complex: After loading the unmodulated chip impedance Z_{ic} , this impedance is inter- and extrapolated to the frequency vector via polynomial approximation. This approach relies on the flatness of the chip impedance over frequency and removes any measurement ripple generated by line-by-line VNA measurements that has not been removed by pre-processing of the impedance data. Moreover, the logarithmic chip power base vector P_{ic} is also generated in this step.

A similar approach is taken for the modulation impedance Z_m in the fourth step. After aligning it with the frequency base using polynomial approximation and interpolation to the chip power basis, a version of the modulation impedance depending on the modulation state M is created by linear weighting of Z_m (“on-impedance”) and a user-defined “off-impedance”. The result is the final modulation impedance $Z_m(f, P_{ic}, M)$. The user has several choices here: The modulation impedance can either be made active, i.e., modulation below $P_{ic,min}$ is made possible by holding Z_m at the minimum power $P_{ic,min}$, or kept passive by setting $Z_m(P_{ic} < P_{ic,min}, \dots)$ to the “off-impedance”. This can be done in a frequency-dependent fashion using $P_{ic,min}(f)$ or frequency-independent based on $\max\{P_{ic,min}(f)\}$. Note that the frequency-dependent mode will introduce discontinuities in Z_m due to the limited power/frequency resolution in combination with subsequent interpolation. Replacing Z_m below the minimum power threshold is necessary in any case, as the chip typically cannot be forced to the modulated state in hardware. For the NXP G2XM, this mode has to be set by sending a command, which is of course only possible for a working chip. Furthermore, it is reset if the chip falls below its operational power. As a consequence, the measured modulation impedance is unreliable near the power threshold and completely unusable below. 

2. Assembly Matching and Tolerances: The assembly impedance Z_{at} takes the mounting of the chip on the antenna (flip-chip, TSSOP plus soldering, ...) and associated tolerances into account. This parasitic impedance is modeled by a parallel RC circuit [207] for simplicity. Assembly tolerances are a major problem in the manufacturing of RFID tags: A performance degradation of more than 90 % is easily reached in case of a bad assembly [207].

For the model, the parasitic capacity is chosen depending on the assembly tolerance state A . The Ohmic part is then calculated using Q-matching (e.g., [213,214]) between antenna and load impedance at the intended frequency of operation and the tag’s power threshold $P_{ic,min}$ [152]. This approach reflects the effort of a manufacturer to match the tag “as well as possible” for

a given assembly process. The actual matching is done numerically by linear optimization and subsequent checking of the resulting Q-factor. If an exact match is impossible, the next best match is chosen and a warning is issued. As the assembly tolerance will also affect the resistance, the optimally tuned resistor is subsequently multiplied by a scalar factor which, like the chosen capacity, depends on the assembly tolerance state A . By using a factor instead of a constant resistance, the results stay independent of the actual matching point.

3. Antenna Detuning is the effect of dielectric materials on the antenna impedance. Detuning typically results in an increased quality factor and thus an amplification of the antenna self-resonance as well as in a shift of the resonance towards lower frequencies. Near metal, very high Q-factors can be reached before a significant frequency shift occurs. If the antenna is placed very close to the material, i.e., for high levels of detuning, the frequency shift reaches several hundred MHz while the resonance vanishes (low Q), see Fig. 3.15.

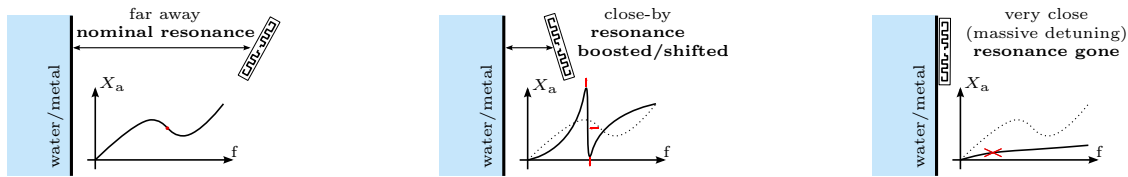


Figure 3.15: Illustration of the effects of close-by dielectric materials on the antenna impedance.

Unfortunately, the effects of detuning depend massively on the antenna type and the offending material [3, pp. 336ff] as well as the relative orientation of antenna and dielectric object, making a generic model a challenging task. Detuning is thus usually modeled as simple gain penalty and/or performance degradation in RFID, cf. [153, 215]. This simplification, however, is not feasible for ranging, since it removes the frequency dependence, which is a primary source of errors in narrowband ranging (see Section 4.2). Hence a wideband detuning model had to be found.

The implemented model modifies the antenna impedance in free space by changing the quality factor and shifting the antenna self-resonance in frequency, as shown in Fig. 3.16. This heuristic model is based on nonlinear interpolation of the antenna impedance Z_a to emulate the effects of close-by water and metal objects. It has been derived from impedance measurements of an NXP UCODE general purpose reference antenna (see Fig. 3.19(b)) and is controlled by two parameters: percent enhancement and frequency shift of the antenna self-resonance. The first parameter controls a compression of the frequency axis around the resonance and an expansion of R - and X -axes. The second parameter controls the frequency shift along the shift axis of R_a and X_a , as well as the increasing attenuation of the resonance for large frequency shifts, see Fig. 3.16. The combination of both parameters forms the detuning state D .

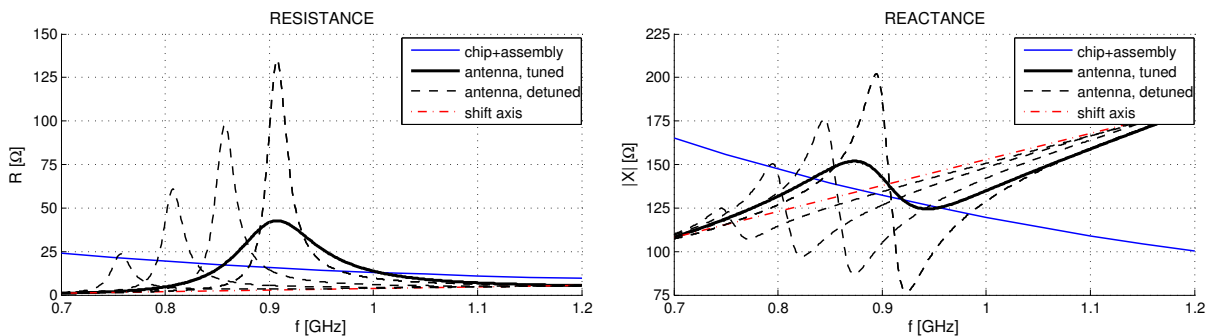



Figure 3.16: Examples of chip impedance (flip-chip assembly) and antenna impedance (tuned and detuned), cf. [128, Fig. 2]. Increased detuning leads to more pronounced changes in the impedance.

Note that this method will only give qualitatively correct results. Specifically, it does not consider additional resonances created by close coupling, the alteration and shifting of resonances other than the main antenna self-resonance, the effects of different orientations of the antenna relative to the offending material, or compound materials. A comparison of the reduction in read range due to detuning found in experiments [153] suggests that the used detuning model is valid if the tag is separated from water/metal by at least 1 cm [128]. However, these limitations apply only to the modeling of detuning, not to the entire equivalent circuit model. If high accuracy is required, measured impedances of detuned antennas can easily be used. 

4. Input Reflection Coefficient: With all the necessary data available, the reflection coefficient $\rho(f, P_{ic}, M, A, D)$ can be calculated using the impedance mismatch at the antenna ports

$$\rho(f, P_{ic}, M, A, D) = \frac{Z_a - (Z_{at} \parallel Z_m \parallel Z_{ic})^*}{Z_a + (Z_{at} \parallel Z_m \parallel Z_{ic})}, \quad (3.3)$$

where \parallel denotes the parallel impedance and $*$ is the complex conjugate. The input power is calculated from the impedances by considering the power loss in assembly and modulation impedance:

$$P_{in}(f, P_{ic}, M, A, D) = P_{ic} \cdot \left(1 + \frac{\text{Re}\{(Z_{at} \parallel Z_m)\} \cdot |Z_{ic}|^2}{\text{Re}\{Z_{ic}\} \cdot |(Z_{at} \parallel Z_m)|^2} \right) \quad (3.4)$$

Finally, the available (incident) power level at the tag antenna ports can easily be calculated using P_{in} and the reflection coefficient:

$$P_{av}(f, P_{ic}, M, A, D) = P_{in} / (1 - |\rho|^2). \quad (3.5)$$

Naturally, the calculated power levels are functions of frequency f , chip power P_{ic} , modulation state M , assembly state A , and detuning state D .

5. Re-Interpolation to the Incident Power Level: So far, the power levels and the reflection coefficient are functions of the chip power P_{ic} . A more practical dependence would be the incident power level P_{av} here, which is the power output of the channel and independent of any tag parameter (as opposed to P_{ic}). This gives the tag reflection coefficient model a well-defined interface.

Hence, as a next step, the power base vector P_{av} (available/incident power) is created. This vector is designed to be linear with distance under the assumption of free-space propagation with some arbitrary large-scale path loss exponent. The path loss exponent should be chosen slightly higher than the free-space path loss ($\xi = 2$) here in order to increase the resolution around the tag's minimum power threshold (which is typically the area with the fastest changes).

Using this vector and the connection between available and chip power levels $P_{av}(f, P_{ic}, \dots)$, the reflection coefficient is re-interpolated using linear interpolation along the power axis. This interpolation inescapably results in “out-of-range” values, i.e., areas of the warped reflection coefficient where no source data is available. The entire procedure of selecting the power vector and re-interpolating the reflection coefficient is done iteratively to minimize these areas. Avoiding them entirely, however, is impossible. The result of this procedure is the reflection coefficient over frequency, available (incident) power, modulation, assembly, and detuning $\rho(f, P_{av}, M, A, D)$.

6. Extrapolation of the Reflection Coefficient to DC and the Nyquist frequency is necessary to make the model usable in digital filters. This extrapolation in the frequency domain is done by fitting an infinite impulse response (IIR) band-stop filter in the frequency dimension for all P_{av} , M , A , and D . The actual optimization is performed by altering the gain factors for all

poles and zeros of the IIR using nonlinear optimization. The cost function includes the border values of the existing reflection coefficient (magnitude and slope) as well as a penalty term for active reflection coefficients $|\rho| > 1$, and leads to a smooth transition of the magnitude at the borders. Because of the different shapes of ρ for different assembly and detuning states, this optimization is done for a set of different IIR configurations. Several other measures (median filters, alignment of the phase, ...) are in place to ensure a smooth transition at the border regions. Note, however, that the cost function optimizes only the magnitude of the reflection coefficient, not the phase. Although discontinuities in the phase are unlikely due to the accompanying measures, special care should be taken when using extrapolated parts of the characteristic in combination with methods that are sensitive to discontinuities in the phase.

7. A Full Reverse Check – i.e., a recalculation of the original chip impedance Z_{ic} from reflection coefficient data for randomly chosen combinations of frequency and power – is performed to double-check the above calculations. This check is done in two ways: the first way uses the connection between the lookup tables $P_{in}(f, P_{ic}, \dots)$ and $Z_{ic}(f, P_{ic})$ to index the chip impedance directly, while the second way inverts the entire set of calculations. Naturally, the results of both methods have to match. Although this check does not cover every part of the calculation, the most complex parts are included. Plots can be generated in order to facilitate manual checks of steps that are not covered by this automated verification.

8. Filling of the Leftover Gaps created by the warping of $\rho(P_{ic}, \dots)$ to $\rho(P_{av}, \dots)$ is the last step in the calculation of the reflection coefficient characteristic. This is done by simple interpolation subject to a smoothness condition.

An example reflection coefficient generated by the above calculations can be found in Fig. 3.17. The plot shows the unmodulated magnitude of a perfectly tuned NXP UCODE G2XM mounted by flip-chip assembly on an NXP UCODE general purpose reference antenna (see Fig. 3.12). The colored areas indicate that source data was available; the grid represents extrapolated areas.

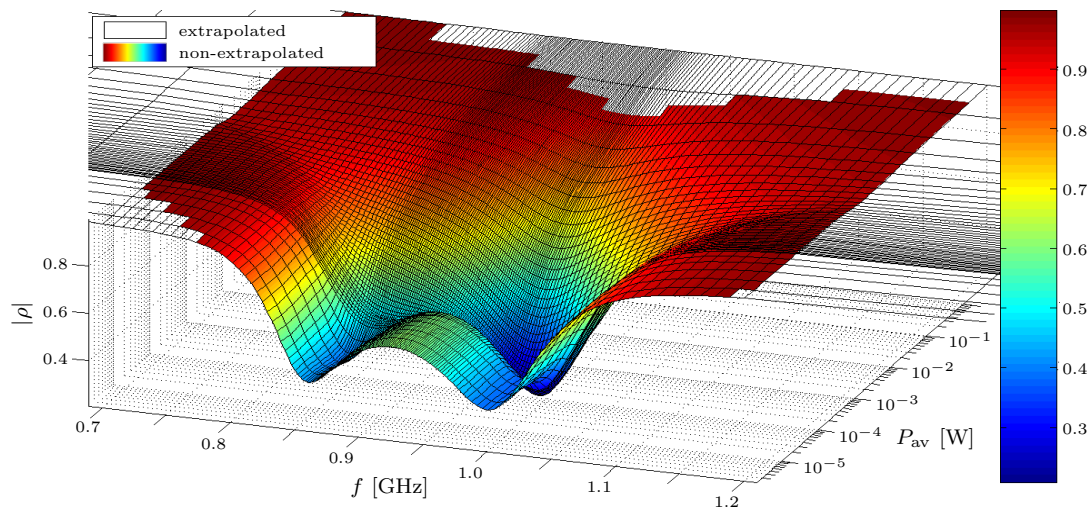


Figure 3.17: Example reflection coefficient magnitude (unmodulated; perfectly tuned flip-chip assembly).

Measurement-Based Verification

The calculations leading to the reflection coefficient rely on several simplifications, foremost the relatively simple equivalent circuit. A validation measurement was conducted in order to verify the reflection coefficient model and its calculation, as well as the linearized version of the model. These measurements used the same type of tag that has been modeled for the simulator.

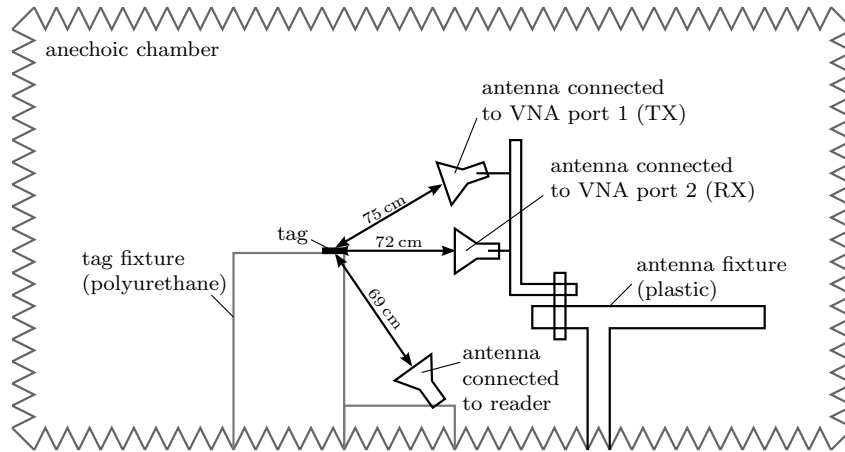
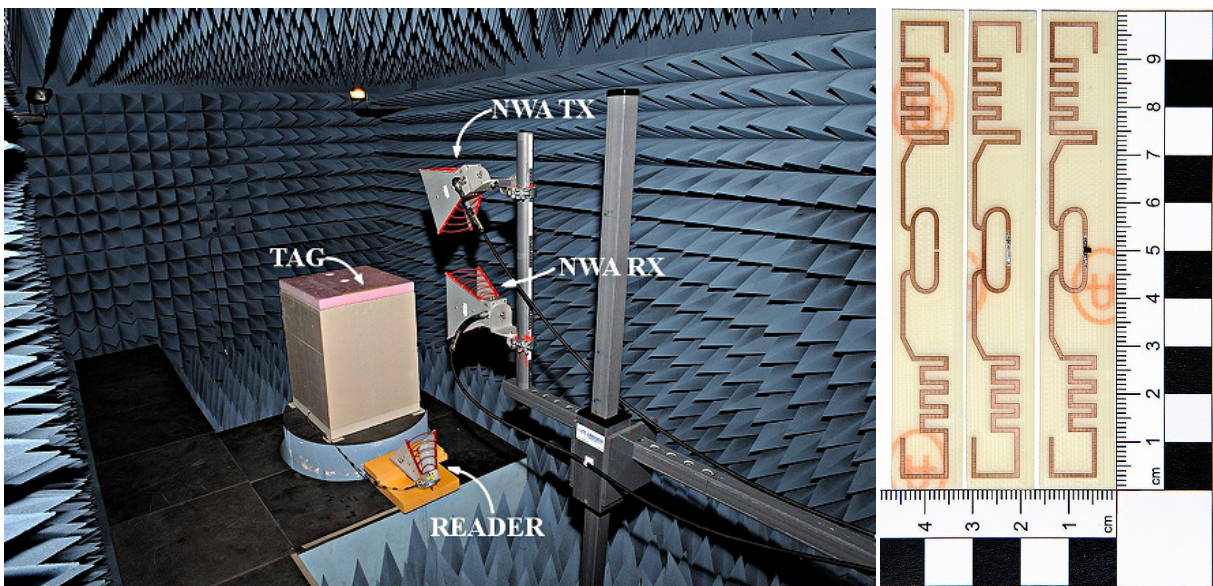


Figure 3.18: Bistatic VNA measurement setup used for tag reflection coefficient measurements (not to scale). The UHF reader (bottom antenna) is used as a power source for the tag and to send commands, while the VNA measures the reflection coefficient during tag modulation. (©2010 IEEE, [128])



(a) interior of the anechoic chamber (©2010 IEEE, [128])

(b) open / short / G2XM

Figure 3.19: Photographs of the tag reflection coefficient measurement setup and used references/tag.

The used measurement procedure is based on a bistatic VNA setup in an anechoic chamber, and is designed to obtain the time-variant reflection coefficient of a UHF RFID tag during modulation in the field. The measurement setup is shown in Figs. 3.18 (schematic) and 3.19 (photographs) respectively. It combines several approaches [204, 205, 216] in order to obtain the complex reflection coefficient during modulation. Details can be found in [128].

Unlike for conducted measurements [204], assembly tolerances and detuning are covered by this setup. The major drawback is calibration: environmental reflections exceed the reflection of the antenna outside its resonance even in an anechoic chamber, making measurements outside its center frequency unreliable. Moreover, a full calibration did not lead to the expected results, even though the reduction in signal-to-noise ratio (SNR) due to the rather ill-conditioned calibration matrix should not cause any problems. The reason for this is an open question. A possible explanation is numerical instability due to the similarity of the calibration references for open and short. As a consequence of the problems with full calibration, the absolute phase could not be reconstructed and the measurement result is limited to magnitudes, similar to [205] (VNA-based) or [217] (using a spectrum analyzer).

A comparison between the measured reflection coefficient and the model can be found in Fig. 3.20. Note that the measured reflection coefficient slightly exceeds $|\rho| = 1$ outside 900 through 1000 MHz due to the above mentioned environmental reflections. The reconstructed magnitude is a good match, with a residual mean absolute error of 0.022 ($|\rho| \in [0, 1]$) in the center frequency range of 910–970 MHz (area with best calibration). Furthermore, the assembly state of the model, $R_{\text{at}} = 235 \Omega$ parallel to $C_{\text{at}} = 475 \text{ fF}$, corresponds well with soldering the G2XM on milled FR-4, according to NXP. The same is true for the detuning state, which shows a nominal resonance shifted by 20 MHz. This frequency shift may have been caused by a slight redesign of the antenna after the model data was calculated; a verification measurement of the antenna impedance showed the same frequency shift.

These results in combination with the well-established theory of equivalent circuits for antenna systems indicate the validity of the equivalent circuit model and the linear model described above.

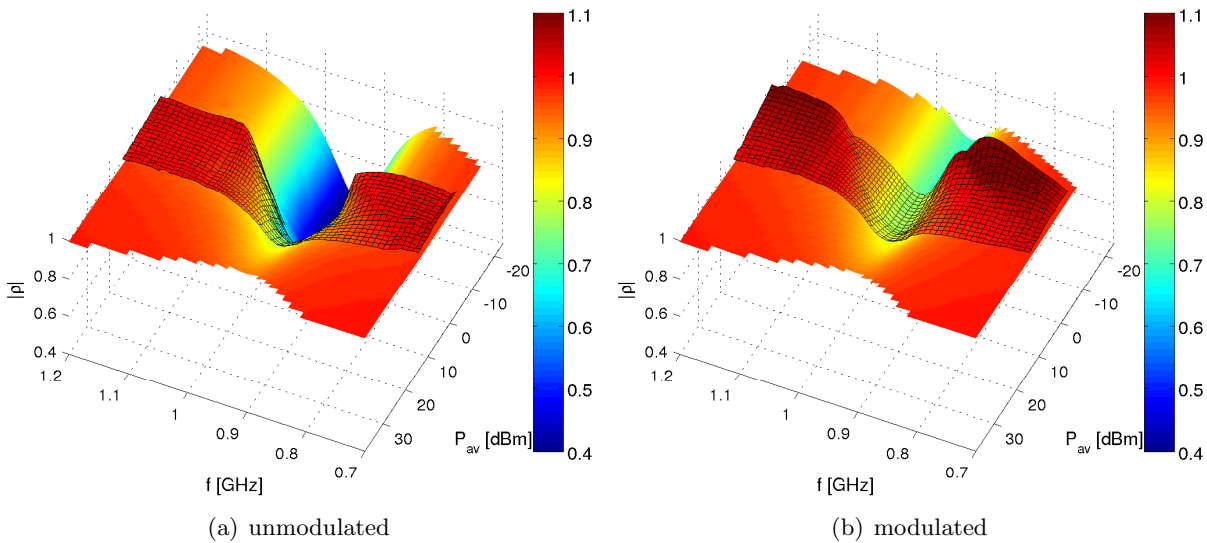


Figure 3.20: Comparison of reconstructed reflection coefficient magnitudes (gridlines) to model data, cf. [128, Fig. 7].

3.3.2 Tag Modulator / Power-Supply Unit

The tag modulator calculates the backscattered signal as well as the input signal of the tag, and is one of the most complex modules of the simulator. For historical reasons and for simplicity, it also contains the tag power supply unit, which calculates the power supply voltage of the tag. The function has two main modes: the first mode is used for calculation of the modulated backscatter (modulation) while the second mode is used to calculate the input signal of the tag's demodulator (transmission).

As a first step in backscatter (modulation) mode, the function calculates the length of the modulation signal at the carrier level for a given modulation bitstream provided by the encoding function. This also includes group delays of carrier and modulation signal as well as block-processing effects created by the used polyphase filterbank (see below). This information is used by the framework to determine the carrier length necessary for modulation. After the length calculations are complete, the function generates the modulation signal at the tag clock level.

The second step is related mainly to the tag power supply functionality and applies to reflection and transmission mode. After loading the reflection coefficient characteristic (see Section 3.3.1), the average carrier power level during modulation/transmission is calculated. Using the average power level here implicitly assumes short-time stationary power and thus short-time stationary characteristics of the tag²¹.

Using the incident carrier power level, the tag reflection coefficient, and the modulation signal, the function then calculates the chip power level and determines whether the tag is functional, i.e., above its minimum power threshold. The chip power calculation has a bias towards the unmodulated state in order to take into account the supply buffer, which, for a real tag, is loaded for a long time in the unmodulated state before the modulation starts. This simplification is a weakness of the current implementation and should be corrected in order to support long tag replies as well as different power consumption for each command (cf. [218]).



Nonfunctional tags are handled differently for the two modes of operation: In transmission mode, a nonfunctional tag will anyway not be able to decode the information, so the time-consuming filter operation is skipped and a vector containing zeros is returned. Nonfunctional tags in backscattering (modulation) mode are set to continuous unmodulated reflection. Optionally, the tag modulation can also be maintained even below the minimum power threshold, thus essentially generating an active tag with the nonlinear characteristic of a passive one.

As a last step before filtering, the filter coefficients are extracted from the reflection coefficient data and re-interpolated to the homogeneous resolution needed for the used filterbank implementation. Transmission, i.e., calculation of the chip input signal, is implemented as $\sqrt{1 - |\rho|^2}$, where ρ is the reflection coefficient. The phase information can be discarded without a problem here because passive UHF tags only use narrowband envelope demodulation.

Filtering is performed by a polyphase filterbank [219]. After the analysis step and before re-synthesis, each block is multiplied independently by a transfer function selected out of the tag reflection coefficient characteristic. The filterbank thus performs a block-by-block approximation of the tag's time-variant reflection coefficient in frequency and in time. This creates a trade-off between time and frequency resolution: a high frequency resolution requires a large number of filter channels and thus a large block size which in turn reduces the time resolution of the filterbank²². At the time of this documentation, the standard setup used a 4096-channel filterbank with 32 taps per channel for the finite impulse response (FIR) synthesis and analysis filters.

In transmission mode, the demodulator input signal is calculated after the filtering by multiplying the transmitted signal by the appropriate input impedance, thus resulting in the voltage at the demodulator ports.

²¹ During the reflection coefficient measurements, the tag has shown the ability to buffer one RN16 (16 bit random number [1]) reply even if the current power level is too low. This supports the assumption of a well-buffered and thus short-time stationary power supply.

²² This is a fundamental principle created by the interrelation between time and frequency domain and cannot be avoided. The more localized a signal becomes in the frequency domain, the less localized it becomes in the time domain and vice versa. A pulse, for example, is very narrow in the time domain, but occupies an ultra-wide bandwidth. This is very similar to Heisenberg's uncertainty principle and is thus sometimes referred to as "Heisenberg-box".

3.3.3 Other Modules

Demodulation The demodulator implements an adaptive threshold-based amplitude demodulator [220]. The input signal is rectified, filtered by an RC lowpass, and amplified according to an automatic gain control (AGC) characteristic. An example AGC characteristic is shown in Fig. 3.21(a). These processing steps create a normalized envelope signal which is subsequently downsampled for performance reasons²³.

The amplitude modulated command sent by the reader is then demodulated by comparing the envelope amplitude with a threshold level that is generated by a feedback loop. The non-linearity of the feedback loop prevents a simple modeling, hence the threshold generation has been approximated by a sample-by-sample nonlinear filter with saturated slew-rates and levels. The modeling is not perfect. In particular, overshoots at very high power levels are not reproduced properly. Nonetheless, considering that the demodulator is vital to ranging only in terms of robustness to the ranging signals sent by the reader, the accuracy of the implemented model should be more than appropriate. A comparison between a circuit simulation and the implemented model for a moderate burst of the input signal can be found in Fig. 3.21(b).

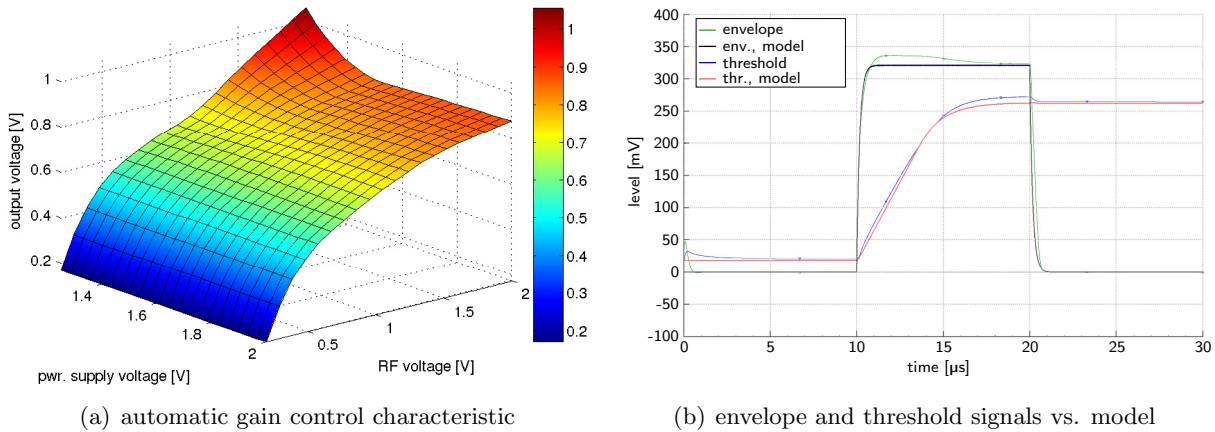


Figure 3.21: Demodulator characteristics and models.

Tag Clock The tag clock module is a relatively simple block that generates a vector of clock events. The function is able to handle clock offsets (tolerances) and clock jitter. Clock drift is currently not implemented.

Decoding The decoding block analyzes a demodulated reader command, calculates its timing (Tari, RTcal, and TRcal [1]), and performs a simple threshold-based decoding. Naturally, the entire decoding block operates at the tag clock level and is thus subject to its timing, including tolerances. So far, only Query and Ack commands are implemented for the decoding, cf. [1].

Encoding is done as defined for EPCglobal Class-1 Gen-2 tags [1] using a generic state-machine implementation. The function also performs the subcarrier encoding (Miller encoding), and optionally adds the cyclic redundancy check block (CRC-16) as well as the preamble sequences [1].

²³ The downsampling is optional and generates a warning since it may change clock characteristics.

3.4 The Channel Model in Detail

3.4.1 Large-Scale and Directivity Model


The large-scale channel power gain is calculated via the Friis equation (log-distance model)


$$\Theta_{\text{LS}} = \left[\frac{c}{4\pi f_c d} \right]^\xi \quad (3.6)$$

and the large-scale propagation delay is calculated via


$$\tau_{\text{LS}} = \text{round} \left(\frac{f_s d}{c} \right), \quad (3.7)$$

where c is the speed of light, f_s and f_c are sampling and carrier/center frequency respectively, d is the path length, and ξ is the path loss factor. Adding log-normal shadowing is easily possible but has not yet been implemented, since shadowing is calculated in a site-specific and thus deterministic manner (see Section 3.4.2).

Directivity patterns are implemented using lookup tables. These characteristics are loaded from files and can either contain 2×2-D (horizontal and vertical) or full 3-D gain patterns. Predefined characteristics include the Intermec IA39B portal antenna [7], $\lambda/2$ and $\lambda/4$ dipoles, as well as the UWB antennas used for the channel measurements (see Section 2.3). The patterns can be arbitrarily rotated, but not mirrored²⁴. As a consequence, only symmetrical gain patterns are handled correctly by the surface model and virtual transmitters. 

The bandwidth-independent implementation of large-scale and directivity gain was chosen mainly for reasons of computational complexity. An extension to ultra-wide bandwidths would require additional channel taps while the current implementation only scales existing taps. Since large-scale and directivity gains are used in almost all channel taps²⁵, this extension would drastically increase the overall number of taps per link and therefore the computational complexity. The model is thus a simplification and care should be taken when using the framework for ultra-wideband signals. 

3.4.2 Deterministic Small-Scale Model: Surfaces and Virtual Transmitters

Reflection and Transmission Coefficient: Reflection coefficients for surfaces are calculated from the Fresnel equations, cf. [6, pp. 248ff]. For a wave with an angle of incidence α_{aoi} to the surface normal and refractive indices η_1 and η_2 according to Fig. 3.22(b), the reflection coefficient at a surface is 

$$\chi_{r\perp} = \frac{\eta_1 \cos \alpha_{\text{aoi}} - \eta_2 \sqrt{1 - \left(\frac{\eta_1}{\eta_2} \sin \alpha_{\text{aoi}} \right)^2}}{\eta_1 \cos \alpha_{\text{aoi}} + \eta_2 \sqrt{1 - \left(\frac{\eta_1}{\eta_2} \sin \alpha_{\text{aoi}} \right)^2}} \quad (3.8)$$

²⁴ Since all predefined antenna characteristics are symmetrical (i.e., can be mirrored in xy or xz , where x is the direction of the mainlobe), implementing a mirroring function was never necessary. This functionality in connection with an improved ray tracing model is part of the roadmap for future builds, cf. Appendix C.1.

²⁵ except for directivity gains in ‘room’ mode, where the directivity model is only applied to LOS paths and reflections; see Section 3.4.4

if the polarization of the wave is perpendicular to the surface, and

$$\chi_{r\parallel} = \frac{\eta_1 \sqrt{1 - \left(\frac{\eta_1}{\eta_2} \sin \alpha_{\text{aoi}}\right)^2} - \eta_2 \cos \alpha_{\text{aoi}}}{\eta_1 \sqrt{1 - \left(\frac{\eta_1}{\eta_2} \sin \alpha_{\text{aoi}}\right)^2} + \eta_2 \cos \alpha_{\text{aoi}}} \quad (3.9)$$

if the incoming wave is polarized parallel to the surface. Transmission is modeled as “1–reflection” for power, i.e., absorption and scattering (diffuse reflections) are neglected. The transmission coefficient of surfaces is calculated via $\chi_t = 1 - \chi_r^2$ (air→material→air). Example reflection and transmission coefficients for a concrete surface ($\eta_1 \approx 2.5$) in air ($\eta_1 = 1$) are plotted in Fig. 3.22(c). The transmitter antenna in this example is z -polarized, i.e., perpendicular to the floor and parallel to the walls.

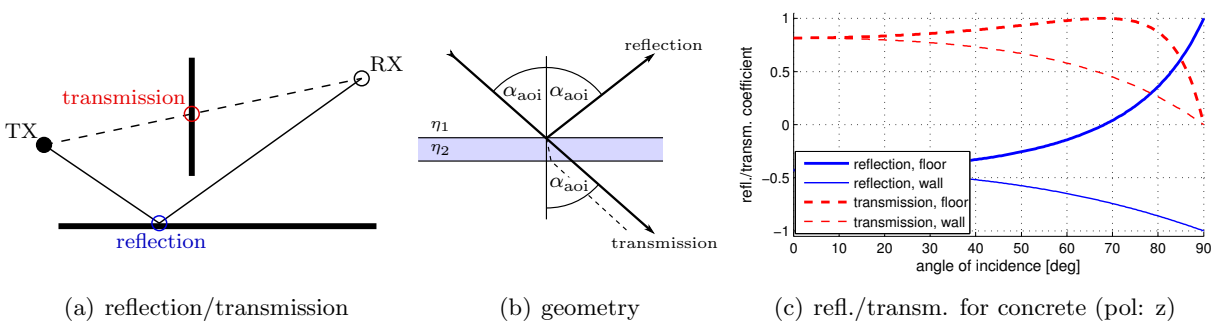


Figure 3.22: Reflection and transmission at surfaces. Note that the geometry model makes some simplifications for the transmitted wave and that absorption and scattering are neglected.

The surface model makes several simplifications: First of all, surfaces are assumed to be completely flat and homogeneous, without scattered components or changes in material properties. Moreover, only rectangular surfaces parallel to the xy -, xz -, or yz -plane are implemented²⁶. Diffraction at the surface edges is considered in a qualitative fashion, i.e., without an underlying physical diffraction model (see below). Also the transmission model for surfaces is a very rudimentary add-on. It does not consider the reduced group velocity inside the dense material, which causes an additional delay and refraction in reality. Finally, the refractive indices of the surface materials are assumed to be real and independent of frequency.

Diffraction Coefficient: Diffraction at surface edges and rounded edges is only modeled to some extent. If the wave (ray) passes a surface near to its edge, the observed amount of power behind the surface will be higher than is suggested by the transmission coefficient. Conversely, a reflected wave can be observed even if the point of incidence is slightly outside the surface. This creates a gradual change of the reflection/transmission coefficient at a surface edge. The corresponding rolloff factor is calculated via

$$\Psi_{D,r} = e^{-\max\left(0, \frac{\beta_{\text{int}2} \cdot \beta_{\text{blur}} - d_{\text{POI}2\text{edge}}}{\beta_{\text{int}1} \cdot \beta_{\text{blur}}}\right)} \quad (3.10)$$

for reflections, and

$$\Psi_{D,t} = e^{-\max\left(0, \frac{\beta_{\text{int}2} \cdot \beta_{\text{blur}} + d_{\text{POI}2\text{edge}}}{\beta_{\text{int}1} \cdot \beta_{\text{blur}}}\right)} \quad (3.11)$$

²⁶ The basic functionality for arbitrarily oriented surfaces has been implemented by Anna Jöbstl during her internship at the SPSC in 2010. As this module requires several changes in antenna characteristics, setup structure, and the surface model itself, it has not yet been added to the framework.

for transmissions, where d_{POI2edge} is the distance from the point of incidence to the surface edge in wavelengths at the center frequency f_c . β_{int1} and β_{int2} are parameters according to Tab. 3.2. The amount of blurring can be controlled by the user via a blurring factor, $0 \leq \beta_{\text{blur}} \leq 1$.

The rolloff created by this model is shown in Fig. 3.23. For a diffraction gain factor of $\Psi_{D,r,t} \rightarrow 0$, reflection and transmission coefficients of a surface also go towards zero. For a gain factor of one, reflection and transmission coefficients are as calculated via the Fresnel equations.

| | reflection | transmission |
|--|------------|--------------|
| decay constant β_{int1} [wavelengths at f_c] | 8 | 2 |
| shift constant β_{int2} [wavelengths at f_c] | 1 | 0 |

Table 3.2: Internal settings for diffraction model (in `channel_main`).

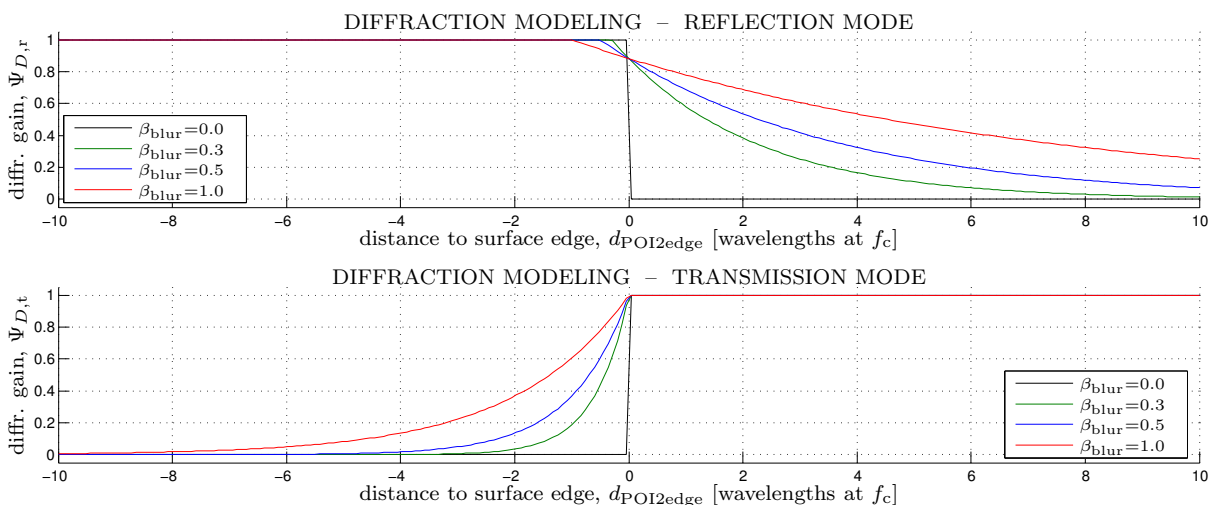


Figure 3.23: Diffraction gain factor close to surface edges for different blurriness settings (β_{blur}). If the diffraction gain factor approaches zero, the reflection/transmission coefficients of the surface are also close to zero. For a gain factor close to one, reflection/transmission coefficients approach those calculated via the Fresnel equations. A negative distance to the edge translates to the point of incidence being inside the surface.

Virtual Transmitters (VTX) are used by the framework to model clusters and interreflections (double-, triple-, ... -reflections). Apart from a few special features of VTX (described below), virtual transmitters are treated like normal transmitters. The channel between a VTX and a receiver thus contains a “direct” path, a stochastic small-scale part, as well as reflections in all surfaces that have not been marked as “covered by a VTX” (explanations provided below). VTX are pure transmitters by definition, i.e., they cannot receive any signal.

The geometry involved in the creation of virtual transmitters is illustrated in Fig. 3.24. In this example, a transmitter (TX) is placed in a corner created by two perpendicular surfaces A and B. The first-order reflections, VTX_a and VTX_b , are created by mirroring TX in A and B respectively. The second-order virtual transmitter, VTX_{ab} , can either be created by mirroring VTX_a in surface B or by reflecting VTX_b in surface A. Note that the mirror axes are not confined to the surfaces for interreflections, i.e., VTX_{ab} is a valid reflection even though neither VTX_a nor VTX_b are mirrored directly in a surface²⁷.

²⁷ VTX_{ab} is created by VTX_a mirrored in the reflection of surface B in surface A, for example.

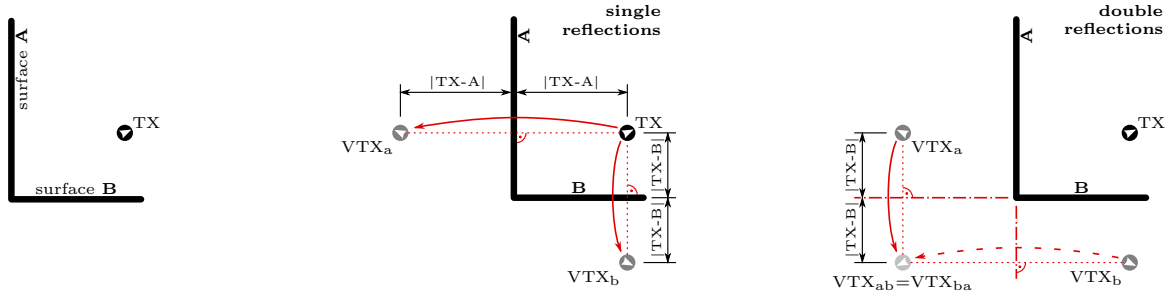


Figure 3.24: Creation of virtual transmitters (VTX) for single and double reflections.

The process of creating virtual transmitters is semi-automatic. Basic functionalities to mirror objects (transmitters, receivers, surfaces) in the creation of the setup are provided by the framework. The process of determining possible reflections and appropriate gain factors for the corresponding VTX, on the other hand, is up to the user. These factors account for reflection coefficients at surfaces (including scattering) and scale the transmitted power of VTX relative to the originating TX.

Unlike transmitters, virtual transmitters can be linked to a surface. This link is used by the framework to determine if the VTX is active for a given receiver position, i.e., if the reflection is possible. The direct path between a receiver and a virtual transmitter either has to pass the surface or must not pass it, depending on a setting. Consider the situation illustrated in Fig. 3.25, where VTX_{ba} and VTX_{bc} are both linked to surface A. In Fig. 3.25(a), the direct path between VTX_{ba} and the receiver has to pass the surface, so VTX_{ba} is only active at RX2, not at RX1. This setting is used to link a virtual transmitter to the last surface that took part in its creation, in this case surface A. In Fig. 3.25(b), on the other hand, the situation is reversed. Here the smaller surface A blocks a reflection in the much larger surface C, modeled by VTX_{bc} . In this case the virtual transmitter is linked to a surface that is between the reflecting surfaces that created the VTX.

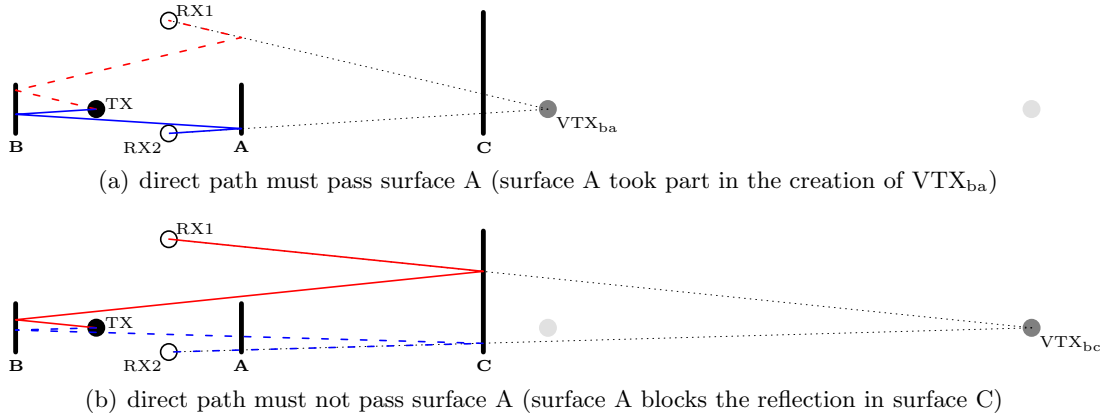


Figure 3.25: Linking a VTX to a surface: VTX_{ba} and VTX_{bc} are both linked to surface A, but with different link conditions.

Like most of the deterministic channel model, the concept of linking a VTX to a single surface was designed for geometrically simple environments such as parallel walls. Like any model designed for simplicity, it has its limits: If two facing surfaces have different dimensions, for example, then the VTX might be active even though the reflection is geometrically impossible.

A corresponding scenario is shown in Fig. 3.26: From the receiver's viewpoint, the red link (a triple reflection) originates from VTX_{abab} . This virtual transmitter is created by the transmitter being reflected four times in the facing surfaces²⁸. Because the last reflection was in surface B, the VTX is linked to this surface and the only requirement to activate the VTX is that the link $\text{VTX}_{\text{abab}} \rightarrow \text{RX}$ passes surface B, which it does. As a consequence, the VTX is active even though it would not be there in reality because the necessary reflection in surface A is not possible.

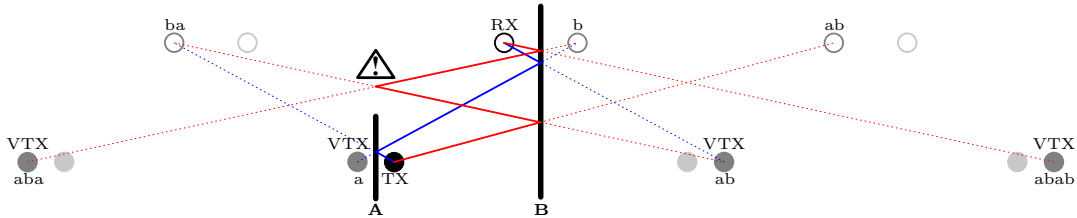


Figure 3.26: Limitations of VTX model when transmitter (TX) and receiver (RX) are placed between two reflecting walls of different width.

Regardless of its limitations, the deterministic small-scale model was of great value in the modeling of UHF RFID channels due to their predominantly deterministic nature, cf. Section 2.3. An example VTX and surface setup is shown in Fig. 3.27. This simulation setup has been used to simulate the warehouse portal in the ASC, see Section 2.3.3.

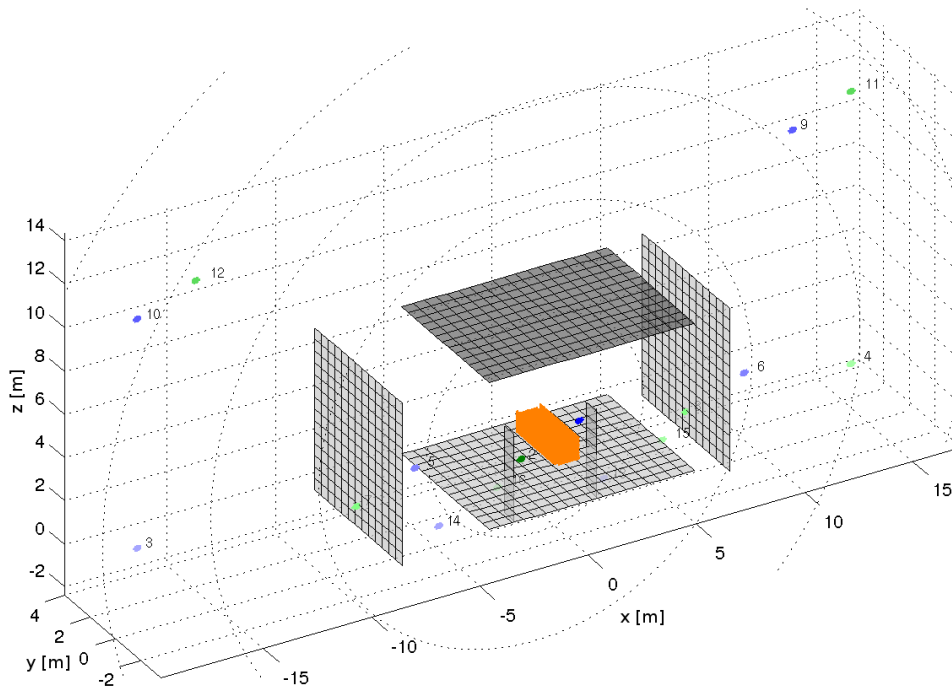


Figure 3.27: Simulation setup for the portal environment (cf. Section 2.3.3) with double reflections. Shown are surfaces (gate, walls, floor, ceiling), TX1 and its set of VTX (blue), TX2 and its set of VTX (green), as well as receivers (orange). Darker surfaces and VTX have higher gain factors (stronger reflection).

²⁸ TX reflected in surface A \rightarrow VTX_a reflected in B \rightarrow VTX_{ab} reflected in A \rightarrow VTX_{aba} ... \rightarrow VTX_{abab}

3.4.3 Statistical Small-Scale Model

Theoretical Background

Statistical parts of the multipath channel are implemented via a sampled version of an exponentially decaying continuous short-range indoor wireless average power-delay-profile [2]. The APDP of this model is defined by [2]

$$\bar{\psi}(\tau) = \begin{cases} 0 & \tau < 0 \\ \rho^2 \delta(\tau) & \tau = 0, \\ \Pi e^{-\gamma\tau} & \tau > 0 \end{cases}, \quad (3.12)$$

where τ is the delay, ρ^2 is the LOS power, $\delta(\tau)$ is the Dirac delta, and Π is the NLOS power density. As the overall gain and the LOS delay are handled by the large-scale model, the APDP is normalized to an LOS delay of $\tau_{\text{LOS}} = 0$ and to unit power,

$$P_{\text{LOS+NLOS}} = \int_{-\infty}^{\infty} \bar{\psi}(\tau) d\tau = \rho^2 + \frac{\Pi}{\gamma} = 1. \quad (3.13)$$

K-factor and RMS delay spread of this APDP are

$$K_{\text{LOS}} = \frac{P_{\text{LOS}}}{P_{\text{NLOS}}} = \frac{\rho}{\int_{-\infty}^{\infty} \bar{\psi}(\tau) d\tau - \rho} = \frac{\rho^2 \gamma}{\Pi} \quad (3.14)$$

and

$$\tau_{\text{RMS}} = \sqrt{\frac{\int_{-\infty}^{\infty} \tau^2 \bar{\psi}(\tau) d\tau}{\int_{-\infty}^{\infty} \bar{\psi}(\tau) d\tau} - \left(\frac{\int_{-\infty}^{\infty} \tau \bar{\psi}(\tau) d\tau}{\int_{-\infty}^{\infty} \bar{\psi}(\tau) d\tau} \right)^2} = \sqrt{\frac{\Pi(\Pi + 2\gamma\rho^2)}{\gamma^2(\Pi + \gamma\rho^2)^2}} = \frac{1}{\gamma} \cdot \frac{\sqrt{2K_{\text{LOS}} + 1}}{K_{\text{LOS}} + 1} \quad (3.15)$$

respectively, cf. [2]. For simulation purposes, a truncation of the APDP to a maximum delay τ_{max} is necessary in order to allow implementation. Naturally, the truncated APDP has a slightly higher K-factor,

$$K_{\text{LOS},trunc.} := \frac{\rho}{\int_{-\infty}^{\tau_{\text{max}}} \bar{\psi}(\tau) d\tau - \rho} = \frac{\rho^2 \gamma}{\Pi(1 - e^{-\gamma\tau_{\text{max}}})}, \quad (3.16)$$

and also a slightly smaller RMS delay spread,

$$\begin{aligned} \tau_{\text{RMS},trunc.} &:= \sqrt{\frac{\int_{-\infty}^{\tau_{\text{max}}} \tau^2 \bar{\psi}(\tau) d\tau}{\int_{-\infty}^{\tau_{\text{max}}} \bar{\psi}(\tau) d\tau} - \left(\frac{\int_{-\infty}^{\tau_{\text{max}}} \tau \bar{\psi}(\tau) d\tau}{\int_{-\infty}^{\tau_{\text{max}}} \bar{\psi}(\tau) d\tau} \right)^2} \\ &= \sqrt{\frac{\Pi(\Pi + e^{2\gamma\tau_{\text{max}}}(\Pi + 2\gamma\rho^2) - e^{\gamma\tau_{\text{max}}}(2(\Pi + \gamma\rho^2) + \gamma^2\tau_{\text{max}}(2\rho^2 + \tau_{\text{max}}(\Pi + \gamma\rho^2))))}{\gamma^2(\Pi - e^{\gamma\tau_{\text{max}}}(\Pi + \gamma\rho^2))^2}}. \end{aligned} \quad (3.17)$$

Sampling is done by replacing a given range in the NLOS power density by a bin at the range's center of gravity $\tilde{\tau}$, as illustrated in Fig. 3.28. The sampled model thus concentrates the power of a theoretically infinite number of physical paths to one bin (tap) in the sampled model. The LOS-component at $\tilde{\tau}_0 = 0$ has a power-level of $\tilde{P}_0 = \rho^2$, while the i -th NLOS-component has a power level of

$$\tilde{P}_i := \int_{\tau_i}^{\tau_{i+1}} \bar{\psi}(\tau) d\tau = \frac{\Pi}{\gamma} (e^{-\gamma\tau_i} - e^{-\gamma\tau_{i+1}}) \quad i = 1, 2, \dots \quad (3.18)$$

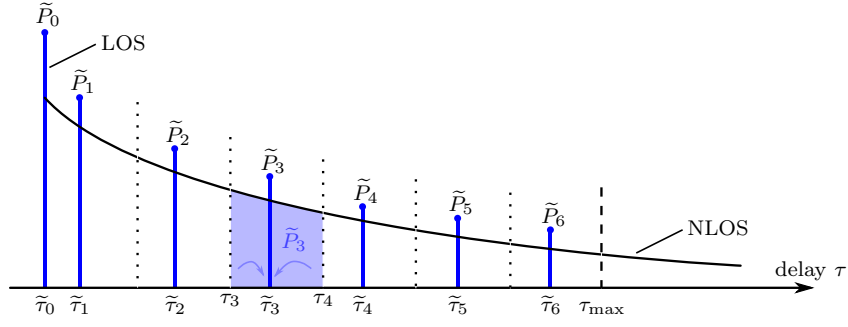


Figure 3.28: Small-scale model: discretization of the average power-delay-profile.

and is located at a delay of

$$\tilde{\tau}_i := \frac{\int_{\tilde{\tau}_i}^{\tilde{\tau}_{i+1}} \tau \bar{\psi}(\tau) d\tau}{\int_{\tilde{\tau}_i}^{\tilde{\tau}_{i+1}} \bar{\psi}(\tau) d\tau} = \frac{e^{-\tilde{\tau}_i \gamma} (\tilde{\tau}_{i+1} \gamma + 1) - e^{-\tilde{\tau}_{i+1} \gamma} (\tilde{\tau}_i \gamma + 1)}{\gamma \cdot (e^{-\tilde{\tau}_i \gamma} + e^{-\tilde{\tau}_{i+1} \gamma})} \quad i = 1, 2, \dots \quad (3.19)$$

A major problem with this approach is the tap spacing between $\tilde{\tau}_0$ (LOS) and $\tilde{\tau}_1$ (first NLOS). This spacing is smaller than all other spacings, as can be seen in Fig. 3.28. This prevents equidistant spacing of the channel taps, which would be simpler to handle and which is also more efficient, since the required sampling frequency is determined by the smallest spacing.

Individual channel impulse responses are finally generated from this sampled APDP by replacing the created bins with independent Gaussian random variables (RVs), where the variance of each RV is taken from the corresponding bin of the APDP. This reflects two basic assumptions: The Gaussianity implies that each channel tap is created by a high number of physical paths. Under this assumption, the distribution of the generated tap is Gaussian regardless of the distribution of the physical paths due to the central limit theorem [146, 192]. Uncorrelatedness between paths, which automatically implies independence for Gaussian RVs, essentially occurs if there are no deterministic paths and is commonly referred to as uncorrelated scattering (US) [141, p. 103], [221, 222]. Due to the fact that deterministic reflections are handled by different functions of the simulator (cf. Section 3.4.2), this is a reasonable assumption for the purely stochastic small-scale model.

Implementation

The function `channel_small` takes K_{LOS} and τ_{RMS} along with associated maximum relative errors ε_K and ε_τ , as well as the one-sided channel bandwidth B and the minimum frequency resolution f_{res} . It calculates and returns one or more CIRs featuring these parameters (on average) along with calculated statistics. The function works in three steps: calculation of necessary parameters (power levels, delays, number of taps, ...), creation of the (deterministic) APDP, and creation of an arbitrary number of CIRs by randomization of the APDP.

Step 1 – Calculation of Parameters: First, the parameters of the continuous APDP are calculated according to [2], with $P_{\text{LOS+NLOS}} = P_0 = 1$:

$$\Pi = \frac{\gamma}{K_{\text{LOS}} + 1} \quad (3.20)$$

$$\gamma = \frac{1}{\tau_{\text{RMS}}} \cdot \frac{\sqrt{2K_{\text{LOS}} + 1}}{K_{\text{LOS}} + 1} \quad (3.21)$$

$$\rho^2 = \frac{K_{\text{LOS}}}{K_{\text{LOS}} + 1} \quad (3.22)$$

As a next step, the required maximum delay τ_{\max} is calculated. This delay depends on the frequency resolution f_{res} as well as the tolerable errors for K_{LOS} and τ_{RMS} , ε_K and ε_τ respectively. The first lower bound for τ_{\max} is taken from the LOS K-factor. Inserting ε_K into (3.16) and solving for τ_{\max} leads to

$$K_{\text{LOS},\text{trunc}} := K_{\text{LOS}}(1 + \varepsilon_K) \quad \Rightarrow \quad \tau_{\max,K} = -\frac{1}{\gamma} \cdot \ln\left(\frac{\varepsilon_K}{\varepsilon_K + 1}\right). \quad (3.23)$$

Solving (3.17) in a similar fashion, thus calculating the bound for τ_{RMS} and ε_τ , is unfortunately not possible. It can be shown, however, that the relative error for the RMS delay spread,

$$\varepsilon_\tau := \frac{\tau_{\text{RMS}} - \tau_{\text{RMS},\text{trunc}}}{\tau_{\text{RMS}}}, \quad (3.24)$$

for $\tau_{\max} = \tau_{\max,K}$ does not depend on τ_{RMS} and is furthermore bounded by

$$\varepsilon_\tau|_{K_{\text{LOS}} \rightarrow \infty} \leq \varepsilon_\tau \leq \varepsilon_\tau|_{K_{\text{LOS}} \rightarrow 0} \quad (3.25)$$

with

$$\varepsilon_\tau|_{K_{\text{LOS}} \rightarrow \infty} = 1 - \sqrt{\frac{2 + \varepsilon_K \ln\left(1 + \frac{1}{\varepsilon_K}\right) \left(2 + \ln\left(\frac{\varepsilon_K}{\varepsilon_K + 1}\right)\right)}{2(1 + \varepsilon_K)}} \quad (3.26)$$

and

$$\varepsilon_\tau|_{K_{\text{LOS}} \rightarrow 0} = 1 - \sqrt{1 - \varepsilon_K(1 + \varepsilon_K) \cdot \left[\ln\left(\frac{\varepsilon_K}{\varepsilon_K + 1}\right)\right]^2}. \quad (3.27)$$

This is done by evaluating (3.24) and (3.17) for $\tau_{\max} = \tau_{\max,K}$ and substituting (3.20)–(3.22). The result is shown in Fig. 3.29 for comparison. The implementation inverts an approximation of the upper bound of ε_τ ,

$$\varepsilon_\tau|_{K_{\text{LOS}} \rightarrow 0} \approx 3 \cdot \varepsilon_K^{\frac{1}{\sqrt{2}}}, \quad (3.28)$$

which is roughly valid for $10^{-4} \leq \varepsilon_K \leq 10^{-2}$, cf. Fig. 3.29(b). This approximation is used in combination with (3.23) in order to obtain the second bound for τ_{\max} ,

$$\tau_{\max,\tau} = -\frac{1}{\gamma} \cdot \ln\left(\frac{\varepsilon_K}{\varepsilon_K + 1}\right) \Big|_{\varepsilon_K = (\varepsilon_\tau/3)\sqrt{2}} = \frac{1}{\gamma} \ln\left(1 + 3\sqrt{2}\varepsilon_\tau^{-\sqrt{2}}\right). \quad (3.29)$$

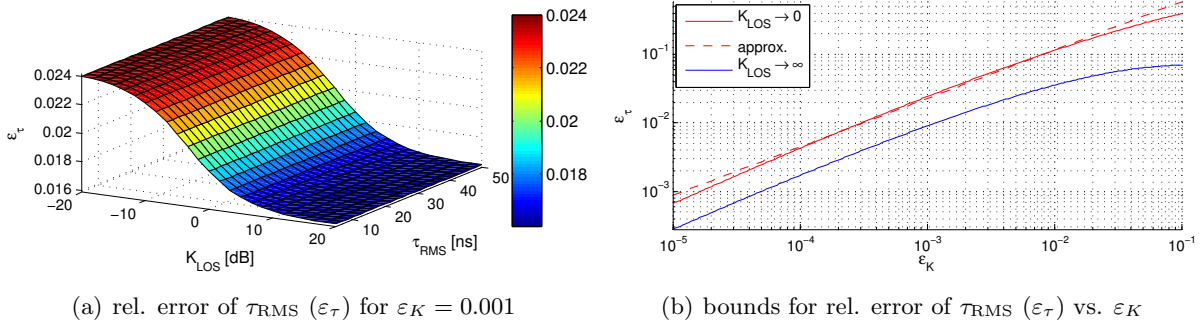


Figure 3.29: Comparison of relative error bounds for K-factor and RMS delay spread.

Finally, the maximum delay is also bounded by the necessary frequency resolution via

$$\tau_{\max,f} = \frac{1}{f_{\text{res}}} \cdot \frac{N_{\text{CT}} - 1}{N_{\text{CT}}}, \quad (3.30)$$

where N_{CT} is the number of channel taps (bins of the APDP) and is calculated by

$$N_{\text{CT}} = \left\lceil \frac{2B}{f_{\text{res}}} \right\rceil + 1. \quad (3.31)$$

Combining these requirements, we obtain

$$\tau_{\max} := \max(\tau_{\max,K}, \tau_{\max,\tau}, \tau_{\max,f}) \quad (3.32)$$

as lower bound for the maximum delay in order to reach f_{res} , ε_K , and also (approximately) ε_τ . The maximum delay also has a theoretical upper bound created by the numerical accuracy in the calculation of (3.18) and (3.19). This bound, however, is of no practical relevance in the implementation (double-precision float).

Step 2 – Creation of the APDP: The sampling of the continuous APDP is done according to (3.18) and (3.19) for equidistantly spaced τ_i . The function subsequently checks K-factor and RMS delay spread of the sampled APDP. If the relative error of the delay spread does not meet ε_τ , the function increases the number of taps. Moreover, if the bins are packed too densely, τ_{\max} is also increased. This is done iteratively until either ε_τ is met or a maximum number of iterations is reached.

Step 3 – Creation of CIR(s) from the APDP: The CIR(s) are then created from the APDP by randomizing amplitudes and delays of the NLOS part, as illustrated in Fig. 3.30. The taps are replaced by zero-mean Gaussian random variables with amplitude

$$\tilde{A}_i \sim \mathcal{N}(0, \tilde{P}_i) \quad i = 1, 2, \dots, N_{\text{CT}}, \quad (3.33)$$

and their position is shifted uniformly within a delay interval of $\pm\Delta\tau$. The randomization of the delay-axis mitigates the impact of its discretization on frequency correlation, especially for near-critical sampling. Naturally, this randomization may not exchange taps, i.e.,

$$\Delta\tau < \min(\tilde{\tau}_i - \tilde{\tau}_{i-1}) \quad \forall i = 1, 2, \dots, N_{\text{CT}}. \quad (3.34)$$

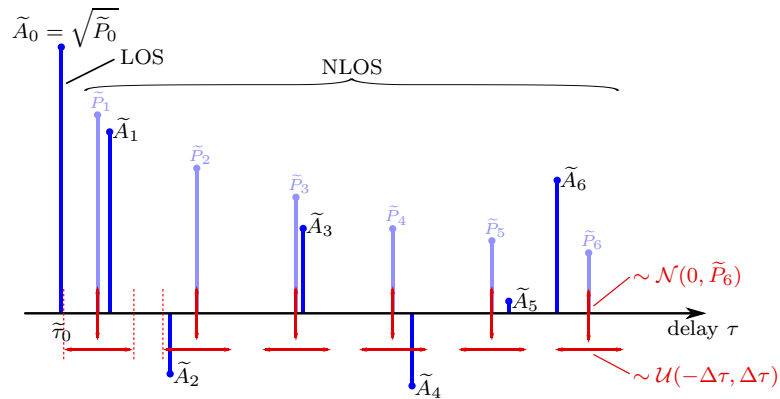


Figure 3.30: Small-scale model: randomization of the average power-delay-profile in order to create independent channel impulse responses.

Analysis of the Results

The implemented sampling optimizes K_{LOS} and τ_{RMS} , which are wideband parameters of the APDP. Narrowband parameters, i.e., correlations between narrowband signals, are not explicitly considered in the creation of the CIRs. Nonetheless, these correlations are a vital parameter in narrowband ranging methods, cf. Section 4.2.

Cross-covariances at a frequency spacing equal to the set bandwidth ($\Delta f = B$) are shown in Fig. 3.31 for several combinations of K_{LOS} and τ_{RMS} , while Fig. 3.32 presents correlations over frequency for NLOS scenarios. The settings for the presented results have been chosen deliberately near to critical sampling, with a sampling frequency of $f_s = 1.5$ GHz and bandwidths of up to ± 500 MHz around a center-frequency of 1 GHz. Theoretical values for the cross-covariances are taken from the spaced-frequency covariance function²⁹ of the APDP [2],

$$\begin{aligned} \Phi(\Delta f) &:= \mathcal{F}\{\mathbb{E}\{h(t)h(t-\tau)^*\} - \mathbb{E}\{h(t)\}\mathbb{E}\{h(t)\}^*\} = \mathcal{F}\{\overline{\psi}(\tau)\} - \mathcal{F}\{\mathbb{E}\{h(t)\}\}^2 \\ &= \frac{\Pi}{\gamma + j2\pi\Delta f}, \end{aligned} \quad (3.35)$$

where $\mathcal{F}\{\cdot\}$ denotes the Fourier transform $\tau \circlearrowleft \Delta f$. As with any sampling, the resulting CIRs have asymptotically correct statistics for a high number of taps. This is especially true for the narrowband statistics and puts a lower bound on the number of taps for $B \approx f_{\text{res}}$.

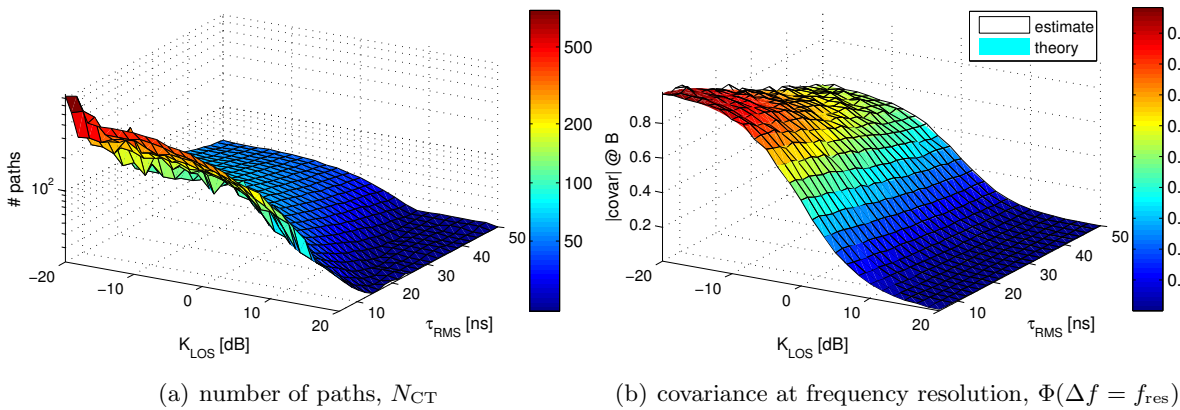


Figure 3.31: Resulting number of paths and narrowband correlation for a range of K_{LOS} and τ_{RMS} .

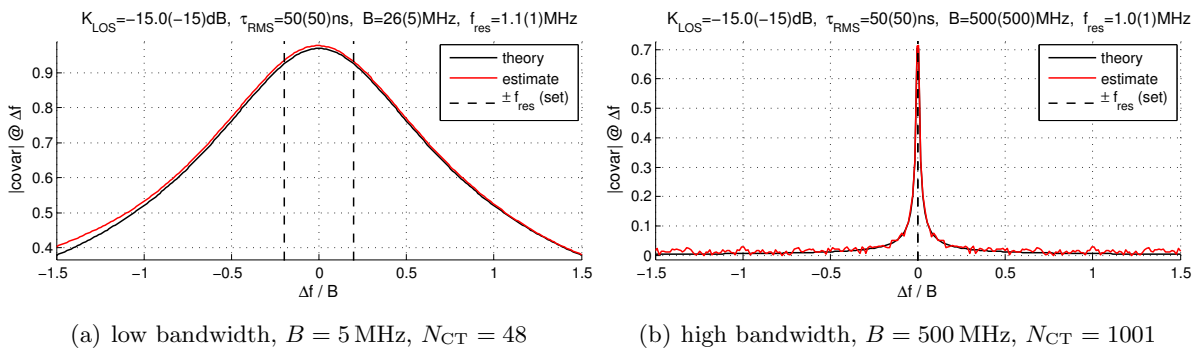


Figure 3.32: Narrowband correlations, NLOS scenario (values in brackets are the original user settings). The function prioritizes K_{LOS} and τ_{RMS} over B and f_{res} ; see Important Remarks below.

²⁹ cf. (time-)frequency correlation function, [141, p. 106], [221, 222]

Important Remarks



- The implemented small-scale model is a short-range indoor model. As a consequence, it does not work well for combinations of K_{LOS} and τ_{RMS} that are highly unlikely in indoor environments, such as $K_{\text{LOS}} = 20$ dB in combination with $\tau_{\text{RMS}} = 50$ ns.
- Narrowband correlations are only asymptotically correct for a large number of taps (N_{CT}), i.e., for $f_s/2 \gg B \gg f_{\text{res}}$ (see above). They are quite delicate and should be double-checked even after minor changes in the behavior of `channel_small`.
- The function generally prioritizes K_{LOS} and τ_{RMS} over B and f_{res} .
 - Most of the time the number of taps has to be increased in order to reach ε_τ , so the channel bandwidth B is typically higher than is required by the setting. A high tolerable error for the RMS delay spread should be chosen if the number of taps and thus computational performance is an important consideration.
 - For the same reason, the frequency resolution (f_{res}) can be slightly off for a small number of taps, cf. (3.30).
- The function provides a struct with statistics and warnings along with the generated impulse response(s). Users should check these values before using the created CIR(s). It cannot be guaranteed that the settings, including K_{LOS} and τ_{RMS} , are met.



3.4.4 Bringing Everything Together

The above models are controlled by and combined in the main channel function, `channel_main`. This function assembles the individual CIRs between transmitters and receivers and calculates the output signals as shown in Fig. 3.33.

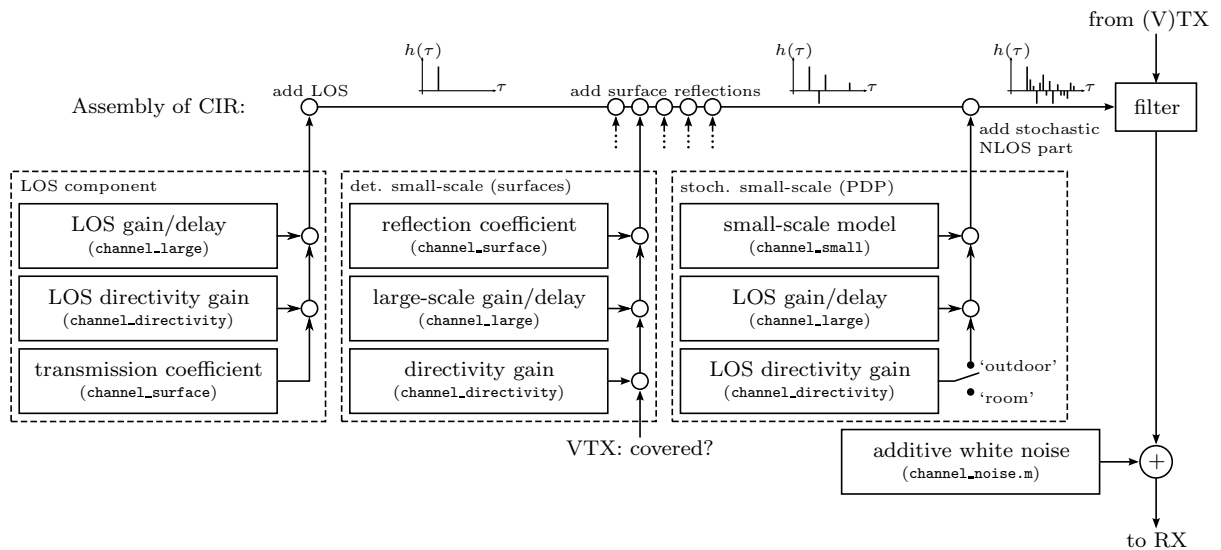


Figure 3.33: Functionality of `channel_main` for a channel between one transmitter and one receiver.

The process of assembling a CIR is started with the LOS component, which incorporates large-scale gain and delay, directivity gains of receiver and transmitter, and a transmission coefficient for all surfaces through which the LOS path passes. Alternatively, the large-scale model can be replaced by directly setting the large-scale gain and delay. This is useful for the feedback channel in monostatic setups, where there is no explicit LOS component. Next, specular reflections in surfaces are added. These components of the CIR incorporate gain and delay of the reflected component (large-scale model), directivity gains, and the surface reflection coefficients. As a last step, the stochastic channel components are created and added to the CIR. These final

components are created by the small-scale model and are scaled and shifted by the LOS gain and delay before adding them to the CIR. Optionally, the LOS directivity gain can also be applied to the stochastic NLOS part. This setting, ‘outdoor’, is the long-range setting and assumes that scattered reflections are mostly generated in the vicinity of the receiver and thus subject to the transmitter’s LOS directivity. For UHF RFID, the ‘room’ setting (indoor short-range) is more appropriate. In this mode, the scattered components created by the small-scale model are not influenced by the gain patterns of transmitter and receiver.

A channel involving a virtual transmitter (VTX) is treated in a slightly different manner. Reflections from surfaces marked as “covered by a VTX” are switched off if the transmitter is virtual. This prevents the addition of reflections of a VTX in surfaces that took part in its creation, which would map the reflection to an already existing reflection or transmitter. Moreover, VTX with a linked surface are only considered if the link condition is met (see Section 3.4.2). Finally, VTX are always in the long-range ‘outdoor’ mode, since clusters are a directional phenomenon and thus subject to directivity patterns.

Note that there is a general limitation regarding shadowing by surfaces (transmission model): only the direct path between transmitter and receiver is influenced by surfaces in transmission mode. Indirect components are thus not affected by surfaces. A surface behind another should therefore always be modeled with virtual transmitters. Complete shielding is not supported.



Output (received) signals are calculated by summing the signals from all transmitters after filtering them by the respective CIRs. As the created CIRs are typically sparse vectors (i.e., consisting of a small number of distinct bins with large gaps between them), filtering is performed by a straightforward tapped delay line structure. If a CIR is not sparse, filtering is performed using Matlab’s `filter` command. The sparsity threshold below which `filter` is preferred depends on the host machine and is determined by `syschar_sparsefir` (characteristic, see Appendix C).

In addition to the received signals, `channel_main` also provides channel statistics, including the CIR for each connection. These statistics are used in the ‘UWB field probe mode’ of the gate simulation, cf. Section 3.1.4.

3.5 A Quick Tutorial

3.5.1 Where to find...

The main startup scripts defining scenarios and initializing the simulator are located in the `simulator/main` subdirectory. The 3-D simulator used in the tutorial below is started by `mfcw_gate3d.m`. Characteristics generators can be found in the `characteristics` directory of the framework, while the main self-test script can be found in the `simulator` directory.

Global settings like the verbosity level in logging or buffer settings are defined in `globalinit.m`, located in the root directory. This function also contains the email address that is contacted if an error occurs during a simulation. The second file in this directory, `collect_changelogs.m`, collects version information, changelogs, and to-do lists of all modified files and provides the corresponding commit command for subversion (SVN).

The full directory structure with short descriptions of the contents is listed in Tab. 3.3:

| | |
|------------------------------|---|
| <code>characteristics</code> | <i>Characteristics files and generators.</i> Most simulator characteristics (<code>*char*</code>) are calculated out of external data (<code>meas*</code>). |
| <code>channel</code> | <code>channelchar_*</code> ; antenna directivity data (gain patterns) |
| <code>reader</code> | <code>readerchar_*</code> ; power amplifier gain characteristic |
| <code>system</code> | <code>syschar_*</code> ; speed characteristics for the host (use <code>syschar_sparsefir.m</code> to generate) |
| <code>tag</code> | <code>tagchar_*</code> ; tag modulator, demodulator, and power supply characteristics |
| <code>tagmod</code> | <code>tagchar_modulator_*</code> ; tag reflection coefficient data |
| <code>concepts</code> | Strictly speaking not a part of the framework. Contains a theory simulator for MFCW. |
| <code>core</code> | Basic framework; version control, exception handling, and control flow. |
| <code>external</code> | External and plot helper functions. |
| <code>simulator</code> | Main simulator directory. Contains the <i>main self-test script</i> , <code>selftest_main.m</code> , as well as the simulator functions, <code>sim_*</code> . |
| <code>channel</code> | channel model subfunctions |
| <code>main</code> | <i>start scripts for simulator functions</i> |
| <code>other</code> | small helper and data conversion functions used exclusively by simulator functions |
| <code>ranging</code> | ranging algorithms and functions (signal generation and analysis) |
| <code>reader</code> | reader model subfunctions |
| <code>selftest</code> | Self-test functions. All tests use random setups generated along with expected results by <code>results_*</code> . Actual testing is done by <code>test_*</code> functions. Do not modify these files unless you are absolutely sure you know what you are doing. Carefully check expected results! |
| <code>tag</code> | tag model subfunctions |

Table 3.3: Directory structure of the PARIS Simulation Framework.

3.5.2 Example Simulation Setup

This section contains a short tutorial on how simulation setups are created for the PARIS framework. The setup in Fig. 3.34 serves as an example for this purpose. This setup resembles a loading bay for trucks, where tags move through a portal (along y) and are registered by the portal readers in the process. The ceiling is non-reflective in this example and has thus been removed for simplicity. This tutorial example is also included in the framework (`mfcw_gate3d.m`, rev. beta 3.0).

We will start by evaluating the environment: The setup allows for four single reflections per reader (floor and all walls), two groups of double reflections (floor-walls and wall-wall in the left corner), and one group of triple reflections (floor-wall-wall in the left corner). Reader and tag setup in this example are quite straightforward, as is the definition of the surfaces. We will thus

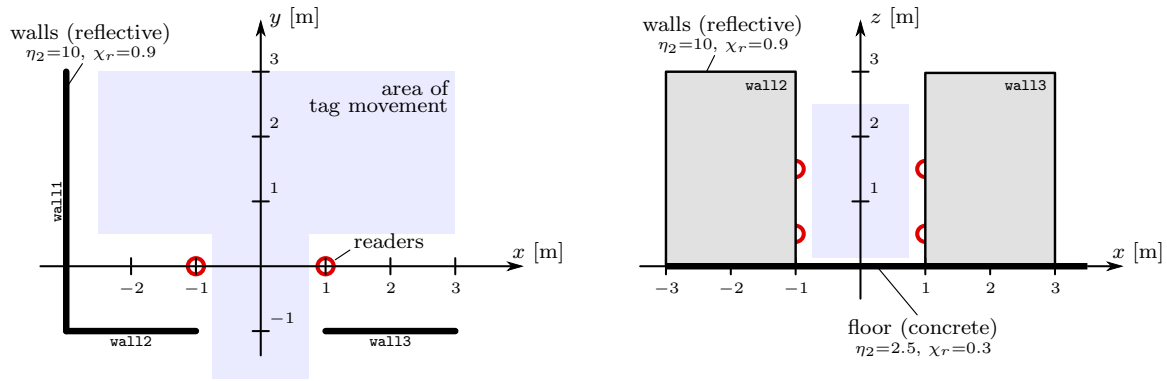


Figure 3.34: Tutorial example — a portal behind a door (reader positions are marked red, areas of possible tag movement are marked by a light blue).

focus on the creation of virtual transmitters. The vital parts of the corresponding Matlab code are shown in Listing 3.1. This part is discussed in the following paragraphs. Feel free also to look up the full code in `mfcw_gate3d.m`.

```

1 % create a template VTX pool
2 settings.vtxpool = replicate(create_stdrr(settings.specials.probemode, 1), settings.readerpool.n);
3 % [REMOVED: configure VTX like TX and link them to the originating TX]
4
5 % wall1-wall2
6 settings.readerpool = add2pool(settings.readerpool, settings.vtxpool);
7 for i = settings.readerpool.n - settings.vtxpool.n + 1 : settings.readerpool.n
8     % mirror
9     settings.readerpool = mirror_obj(settings.readerpool, i, settings.channel_global_surfaces.wall1);
10    settings.readerpool = mirror_obj(settings.readerpool, i, settings.channel_global_surfaces.wall2);
11    % complete VTX setup [REMOVED: set gain factor and reflection number]
12    settings.readerpool.virt_surf{i} = 'wall2'; % has to pass the side wall (smaller than wall1)
13 end
14
15 % floor-wall*
16 % every reflection from now on includes floor => mirror entire vtxpool in floor
17 for i = 1 : settings.vtxpool.n
18    settings.vtxpool = mirror_obj(settings.vtxpool, i, settings.channel_global_surfaces.floor);
19 end
20 % mirror in walls
21 for s = {'wall1', 'wall2', 'wall3'}
22    settings.readerpool = add2pool(settings.readerpool, settings.vtxpool);
23    % mirror
24    for i = settings.readerpool.n - settings.vtxpool.n + 1 : settings.readerpool.n
25        settings.readerpool = mirror_obj(settings.readerpool, i,
26            settings.channel_global_surfaces(cell2mat(s)));
27        % complete VTX setup [REMOVED: set gain factor and reflection number]
28        settings.readerpool.virt_surf{i} = cell2mat(s); % link to wall
29    end
30 end
31 % floor-wall1-wall2 (copied from above)
32 settings.readerpool = add2pool(settings.readerpool, settings.vtxpool);
33 for i = settings.readerpool.n - settings.vtxpool.n + 1 : settings.readerpool.n
34    % mirror
35    settings.readerpool = mirror_obj(settings.readerpool, i, settings.channel_global_surfaces.wall1);
36    settings.readerpool = mirror_obj(settings.readerpool, i, settings.channel_global_surfaces.wall2);
37    % complete VTX setup [REMOVED: set gain factor and reflection number]
38    settings.readerpool.virt_surf{i} = 'wall2';
39 end

```

Listing 3.1: Creating virtual transmitters for this tutorial example: corresponding Matlab code.

It is often useful to define a template pool with virtual transmitters that are already linked to their respective transmitters and properly configured. Such a template can be manipulated as needed in order to create the entire set of VTX, as done with `vtxpool`³⁰ in this example. For the first cluster of double reflections, `vtxpool` is appended to the list of readers (`readerpool`) and subsequently mirrored in `wall1` and `wall2` using `mirror_obj()`, a function provided by the framework. The virtual transmitters in this cluster are linked to `wall2` in order to activate them only if the corresponding reflection is possible. `wall2` is preferred over `wall1` here because the former ends inside the setup and because tag positions can be on both sides of `wall2`.

³⁰ `vtxpool` is short for `settings.vtxpool`, `readerpool` for `settings.readerpool`, `wall2` is short for `settings.channel_global_surfaces.wall2`, and so on.

Merely linking the virtual transmitters to `wall12` is not enough, however, as can be seen in Fig. 3.35. Obviously, the links to both receivers are geometrically possible reflections, but only the link `TX`→`RX1` passes `wall12`. A simple trick corrects this problem: Even though the link to `RX2` does not pass the original wall, it passes the reflection of `wall12` in `wall11`. Hence only the extension of `wall12` is required to include this reflection and keep the model valid. The same is done for the floor reflections.

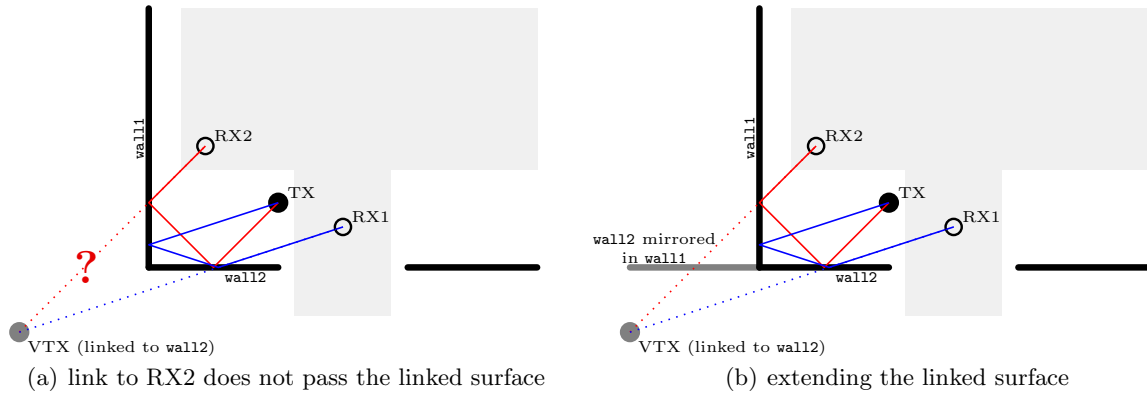
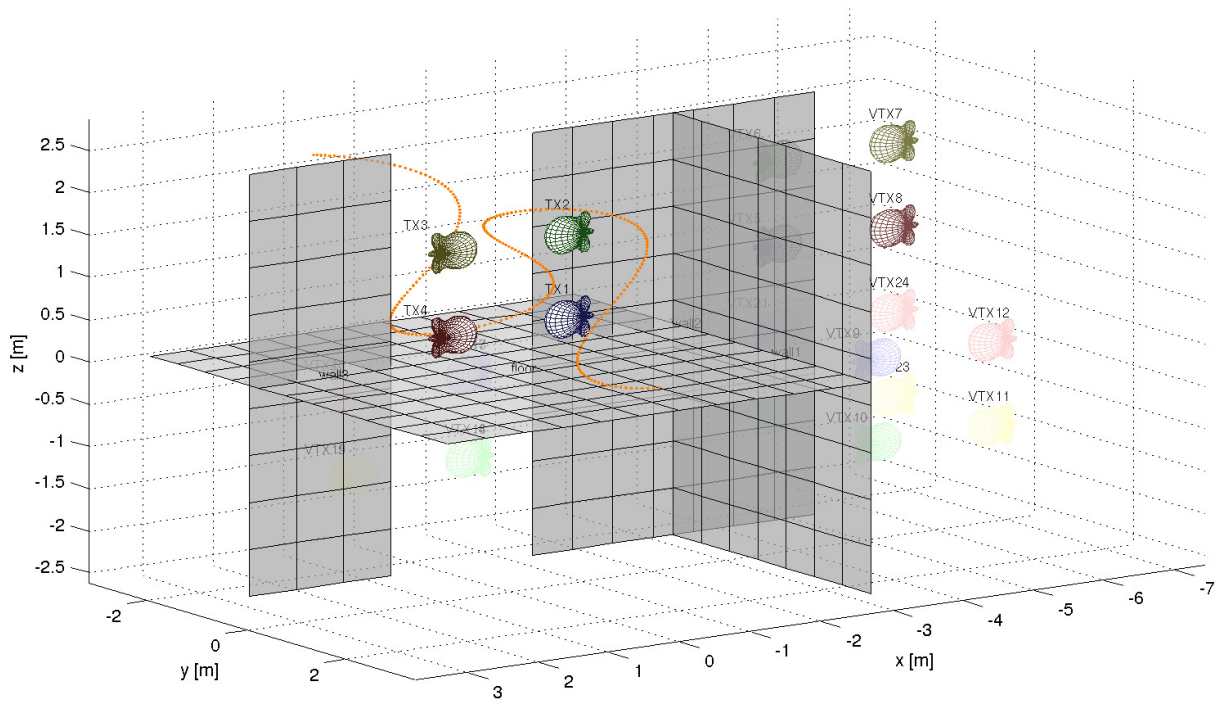


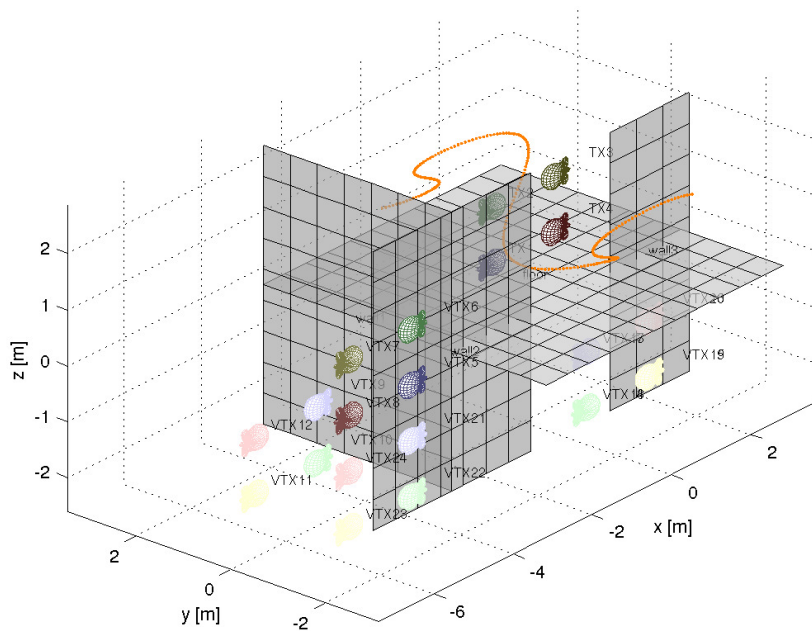
Figure 3.35: Possible problem in modeling double reflections with linked virtual transmitters.

This concludes the modeling of the double reflection in the lower left corner. All the remaining clusters include the floor reflection. Consequently, the entire pool of virtual transmitters is mirrored in the floor (lines 17–19 in Listing 3.1) before the remaining `VTX` are created using the same method as described above.

The final setup is shown in Fig. 3.36. The readers in these images are represented by their gain patterns. A brighter gain pattern for virtual transmitters indicates a lower transmit power, i.e., a weaker reflection. The orange curve passing through the gate is the tag movement—possibly a tagged bumblebee in this example. Note that all walls have been extended to below the floor level, and that `wall12` also includes its mirror image in `wall11`. Note further that the lower left group of `VTX` in Fig. 3.36(b) consists of two groups of four `VTX` each, created by floor-wall reflections involving `wall12` and `wall13`, respectively. Even though these two groups of reflections share their `VTX`-locations, they are different reflections and the corresponding `VTX` are linked to two different surfaces.



(a)



(b)

Figure 3.36: Final simulator setup from two different points of view (orange curve is the tag movement).

4

Narrowband UHF RFID Tag Localization

EPCglobal Class-1 Generation-2 UHF RFID [1] is a classical narrowband system, with channel bandwidths in the range of 1 MHz. Apart from the EPC standard, a complex set of local regulations exists governing allocated bands, transmit power levels, and behavioral issues such as “reader-talks-first”. The system is defined for identification only; tag localization is not an intended functionality of Gen-2. Nonetheless, as large-scale deployment of the system began and false positive reads increasingly corrupted inventories and inadvertently triggered false alarms in article surveillance systems, localization became a focus of research. Scientists and engineers all over the world started to work on methods to localize UHF RFID tags. Since the entire system design and signaling scheme is narrowband, a narrowband localization method seems the most obvious choice.

This chapter starts with an overview of narrowband localization methods in Section 4.1, including a feasibility study in light of the requirements stated in the introduction to this thesis. Section 4.2 focuses on continuous-wave radar using multiple carriers, a method that is potentially able to provide the speed and location of a (semi-)passive UHF RFID tag in classical UHF RFID scenarios. This section covers the basic working principles, theoretical derivations, a discussion of error sources, simulation-based performance analyses, and measurements inside a UHF RFID warehouse portal. Finally, a summary is provided in Section 4.3.

4.1 Concepts, Overview, and State-of-the-Art

Methods Overview

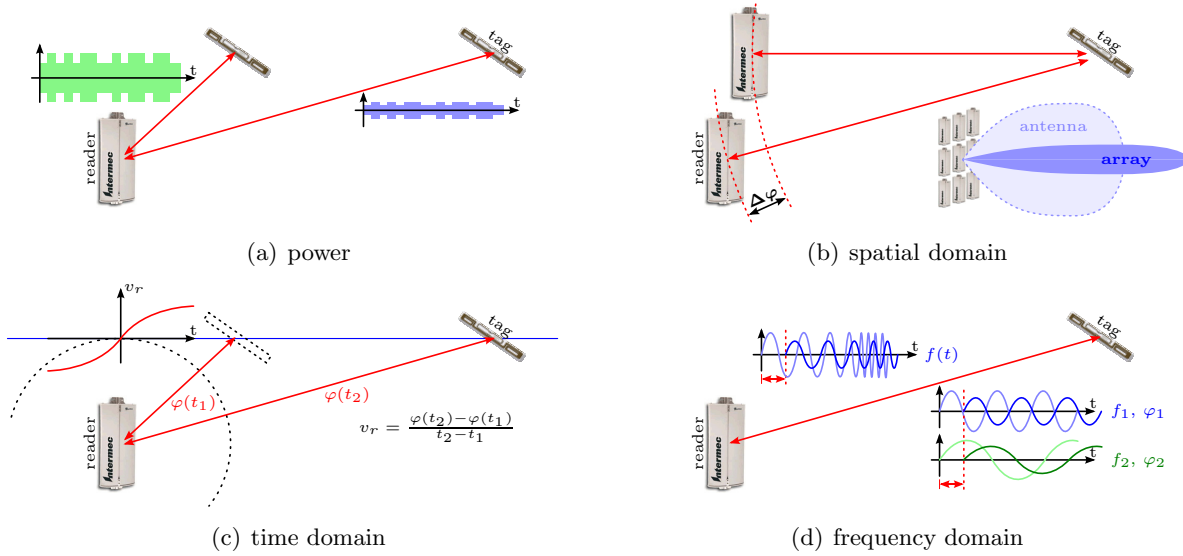


Figure 4.1: Narrowband localization methods (Reader antenna: courtesy of Intermec Technologies).

Fig. 4.1 illustrates the four most common narrowband localization methods, ranging from received signal strength measurements through array processing and time-domain phase measurements to phase-based ranging approaches in the frequency domain. A discussion of the spatial-, time-, and frequency-domain methods can also be found in [35].

Measuring the received signal strength (RSS), as shown in Fig. 4.1(a), is likely the simplest method. Unfortunately, it is also the least accurate, since narrowband signals experience high levels of fading caused by multipath propagation. Fig. 4.2 shows the receive power at the tag inside a UHF RFID portal. Note that the receive power changes by 20 dB within a few centimeters even inside the portal. This fading corresponds to a factor of ten in terms of distance (doubling the distances increases the attenuation by 6 dB). Consequently, RSS-based narrowband localization is not a feasible option.

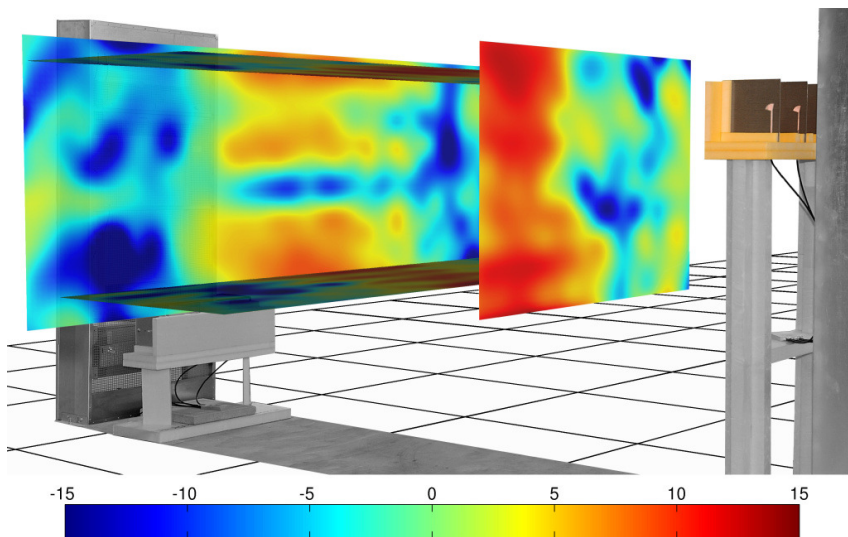


Figure 4.2: Measured (incident) receive power distribution [dBm] at the tag for the portal with metal back-planes (see Section 2.3.3). The orange transmitter array on the right-hand side is active.

Beamforming and array processing is the current method of choice for localization in UHF RFID, cf. Fig. 4.1(b). The signal backscattered by the tag is recorded by several reader antennas connected to the same reader device. The time delay between the observations can be used to determine the angle of arrival (AoA, a.k.a. direction of arrival, DoA) of the received signal [223]. Several algorithms have been proposed to solve this problem. MUSIC (MUltiple SInal Classification) and its derivatives are among the most popular, see [53, 58].

The principle of AoA measurements can also be applied to the transmitter side. Instead of receiving time-shifted signals, the transmitted signal is deliberately delayed at some antennas, thus transmitting the signal in a certain direction. More precisely, the gain pattern of the entire array can be shaped and directed using controllable phase shifts at each antenna input [60]. Such phased arrays can therefore be used to scan an area, similar to radar. This is, for example, done by the US company RF Controls, changing the mode of operation “*from nodal (portal) to zonal monitoring, covering a wide area (or volume) using strategically placed integrated antenna arrays*”³¹.

Continuous phase measurements in the constellation diagram are used by the time-domain method in Fig. 4.1(c) to determine the radial velocity (v_r) of a tag relative to the reader antenna [46]. This method essentially determines the Doppler shift caused by the moving tag, cf. [47, 48]. The position of the tag can be inferred in post-processing by using zero crossings of the radial velocity from several (synchronized) reader positions. Even though this method is not practicable for localization in most real-world scenarios (a tag needs to move and be queried continuously to obtain its position), it is currently used to determine whether a tag is moving, cf. [49].

The last group of methods, shown in Fig. 4.1(d), uses phase estimates at different frequencies rather than in time or space. Three possibilities arise: frequency modulation of the carrier, transmission of several carriers, or frequency hopping.

Frequency modulation ranging – commonly referred to as frequency-modulation continuous-wave (FMCW) radar – works by transmitting a chirped carrier. Since in the ideal case the received signal is merely a delayed version of the transmitted signal, a frequency offset can be observed at the transmitter between the currently transmitted and the received signal. The range to the backscattering target is calculated from this frequency offset [73, 78].

Transmitting several carriers is another option to determine the range in the frequency domain. Since a constant time delay leads to different phase shifts for carriers at different frequencies, a comparison of the phase shifts between the received carriers can be used to determine the range to the backscattering tag [224]. This method (multi-frequency continuous-wave radar, MFCW) is discussed in detail in Section 4.2. Frequency hopping instead of parallel transmission of carriers can also be employed in time-invariant environments.

On the Feasibility of Different Narrowband Ranging/Localization Methods

Among the methods presented above, receive power-based ranging from a single reader antenna is likely the most inaccurate (see description above). Narrowband RSS-based ranging has thus been discarded as a viable standalone option for the ranging problem. Nonetheless, the received signal’s amplitude can be used in other methods, for example in a weighted combining of carrier phases.

Antenna arrays, i.e., AoA-based methods, are currently the most accurate option but come at the price of large and expensive arrays. Fig. 4.3 shows images of a direction finding system developed at Louvain University of Technology (MUSIC-based AoA with parallel receivers [53]). Reported accuracies are in the range of 3° , which translates to roughly ± 25 cm at a range of 5 m. However, this assumes a dominant direct path. Like any narrowband system, AoA approaches

³¹ <http://www.rf-controls.com/>, overview description of RF Controls’ ITCS (March 20, 2011)

are prone to lock onto a reflection if the LOS is attenuated or blocked. Consequently, several arrays have to be used in order to robustly determine the location of a tag. This increases costs and space requirements tremendously. Beamsteering techniques (as used by RF Controls) additionally come at the cost of a high detection time for a tag at an unknown position, since the array has to scan the entire volume if no prior information is available. Depending on the beam width, this may take up to several seconds for a single tag.

These properties of AoA approaches conflict with the maximum target detection time defined for this thesis project (millisecond range) and its aim of read zone management in portal and portal-like applications (tight space constraints due to parallel portals). Beamsteering and other AoA approaches were thus discarded at an early stage of the project³².



(a) antenna array

(b) direction finding in a warehouse

Figure 4.3: Photographs of an antenna array used for UHF RFID tag localization. Hislop et. al., “A prototype 2D direction finding system with passive RFID tags”, *EuCAP 2010*. (©2010 IEEE, [53]).

Also the time-domain approach is not directly applicable as a ranging method, since a tag would have to move and be queried constantly in order to locate it. Moreover, the tag position can only be determined in post-processing. The radial velocities can, on the other hand, be used as an input to tracking algorithms (see Section 4.3).

Frequency-domain methods are able to determine the range (and speed) of the tag using a single communication with the tag. Unfortunately, they also use a resource that is scarce and subject to regulation: radio spectrum.

Narrowband FMCW ranging has been discarded because it lacks the required target detection speed. Following [73, eq. 9], a sweep bandwidth of $B_{\text{FM}} = 1.2 \text{ MHz}$ within a sweep time of $T_{\text{FM}} = 1 \text{ ms}$ (single sweep within the maximum target detection time) leads to a frequency offset of

$$\Delta f_{\text{LOS,FM}} = \frac{4B_{\text{FM}}}{cT_{\text{FM}}} = 16 \text{ Hz/m}. \quad (4.1)$$

This frequency offset is impossible to detect robustly within $T_{\text{FM}} = 1 \text{ ms}$, since the available frequency resolution of the corresponding spectrum is

$$f_{\text{res}} = \frac{f_s}{N_{\text{FFT}}} = \frac{f_s}{T_{\text{FM}} \cdot f_s} = \frac{1}{T_{\text{FM}}} = 1 \text{ kHz}, \quad (4.2)$$

³² in retrospect and considering the zonal monitoring concept, unjustly so

where f_s is the sampling frequency and N_{FFT} is the fast Fourier transform (FFT) window size in samples. Super-resolution methods surpassing (4.2) are available [225], but require low noise levels and are vulnerable to dense multipath propagation.

A sweep time of at least 62.5 ms is necessary to range a tag at 1 m distance in the above example. Note that this sweep already violates the spectral masks defined by the Gen-2 standard [1]. Making the system even more narrowband, i.e., lowering the sweep bandwidth B_{FM} , will further reduce $\Delta f_{\text{LOS,FM}}$, thus making even longer sweep times necessary. Wideband FMCW ranging, on the other hand, is a viable option and is discussed in detail in Chapter 5. Section 5.1.2 also contains a more detailed explanation of the FMCW ranging principle, including an explanation of (4.1).

4.2 Multi-Frequency Continuous-Wave Ranging

4.2.1 Concepts and Theory

parts of this section have been published in [135]

Basic Principles of Phase-Based Continuous-Wave Radar

The principle of continuous-wave (CW) radar with two carriers is illustrated in Fig. 4.4. The phase shift between two carriers with slightly different frequencies increases with distance from the transmitter. If transmitter and receiver are synchronized³³, i.e., if the receiver knows the

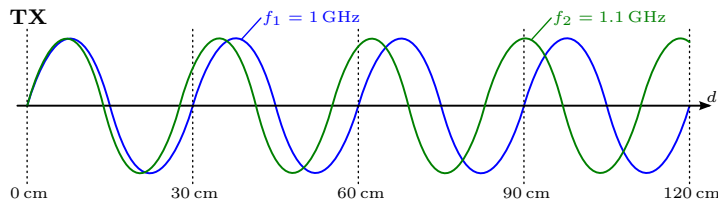


Figure 4.4: Basic principle of operation of two-frequency continuous-wave radar: phase shift between two carriers observed at different distances from the transmitter (TX).

phase shift between the transmitted carriers at the exact instant it receives the signal, the distance between both units can be calculated [224]. This distance estimate is based on the phase difference introduced by the channel, $\varphi_2 - \varphi_1$:

$$d_{\text{LOS}} = -\frac{c}{2\pi} \cdot \frac{\varphi_2 - \varphi_1}{f_2 - f_1} = -\frac{c}{2\pi} \cdot \frac{\Delta\varphi}{\Delta f} = -c \cdot \frac{\Delta\varphi}{\Delta\omega} \quad (4.3)$$

In this calculation c is the speed of light, $\Delta\varphi$ is the phase difference between the carriers in radians, and Δf is the frequency offset (beat frequency). Note that (4.3) contains a secant approximation of the group delay, $\tau_{\text{grp}}(\omega) = -\partial\varphi(\omega)/\partial\omega$. CW radar is thus based on a direct estimate of the channel's group delay.

The backscatter property of the system, however, also has major drawbacks for phase-based CW ranging. First and foremost, the degenerate nature of backscatter channels introduces large (randomly) frequency-dependent phase shifts ($\rightarrow \tau_{\text{grp}}(\omega)$; see Section 2.2.3). Secondly, the tag reflection coefficient's frequency dependence also introduces different phase shifts for each

³³ No special synchronization is necessary between transmitter and receiver for backscatter systems like UHF RFID, since transmitter and receiver are both located in the reader.

carrier, as illustrated in Fig. 4.5. Since this changes the phase relation between the carriers, the differential tag phase shift translates directly to a bias of the estimated distance.

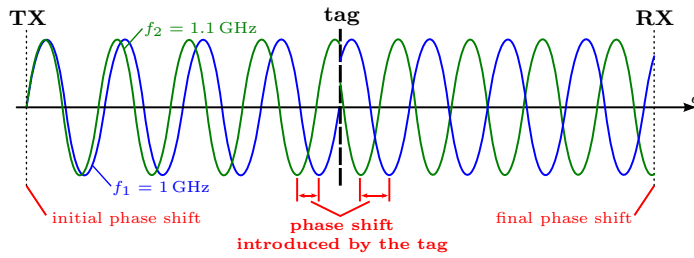


Figure 4.5: Effect of a frequency-dependent reflector (tag) in the signal path for two-frequency continuous-wave radar.

An example spectrum for 4-carrier continuous-wave radar (4FCW) is shown in Fig. 4.6. The powerful carrier at f_c supplies the tag with energy and is used to send commands to the tag (standard UHF RFID functionality). All additional carriers have considerably less power in order to avoid creating an overall envelope a tag might mistake for a reader command. These carriers can for example be placed in free channels in the UHF RFID band, the 2.45 GHz ISM band, or any other frequency range, provided that the tag is able to modulate in this band (see Chapter 5).

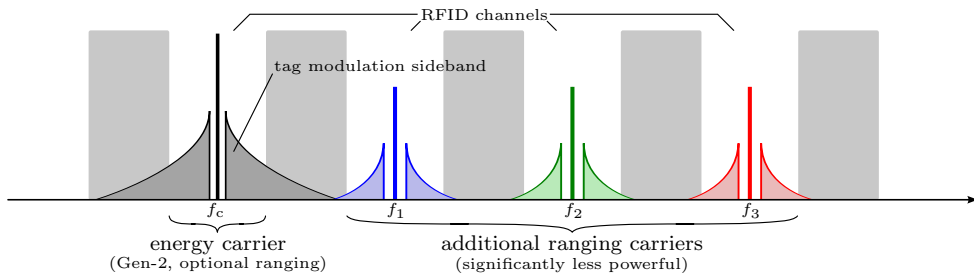


Figure 4.6: Spectrum of the received MFCW signal for four carriers placed in UHF RFID channels.

Apart from the carriers, the received signal also contains the modulation sidebands created by the tag's backscatter modulation. The distance information is embedded in these sidebands for the modulating tag.

In order to extract the distance information, the reader dissects the spectrum after reception. Fig. 4.7 shows a block diagram of transmitter and receiver for multi-frequency continuous-wave ranging. The MFCW signal is digitally generated in the baseband and modulated onto the energy carrier (f_c) after digital to analog conversion. The resulting baseband signal is subsequently amplified, filtered, and transmitted.

After transmission, the bulk of the signal travels over the feedback channel directly to the receiver. Only the part that travels via the tag is modulated. The signal received at the reader is thus composed of the unmodulated direct feedback as well as the modulated tag backscatter. This signal is filtered, amplified, demodulated, and sampled. The resulting spectrum contains all carriers as well as their tag modulation sidebands. Complex amplitudes for the fundamental frequencies of upper and lower sidebands are extracted by digital filters. This is done after down-converting the signal with each carrier frequency f_i in order to simplify the filter design. Fig. 4.7 shows this process for a periodic rectangular modulation for simplicity. Adding another down-conversion with the tag reply allows for arbitrary tag modulation signals (e.g., the electronic product code, EPC).

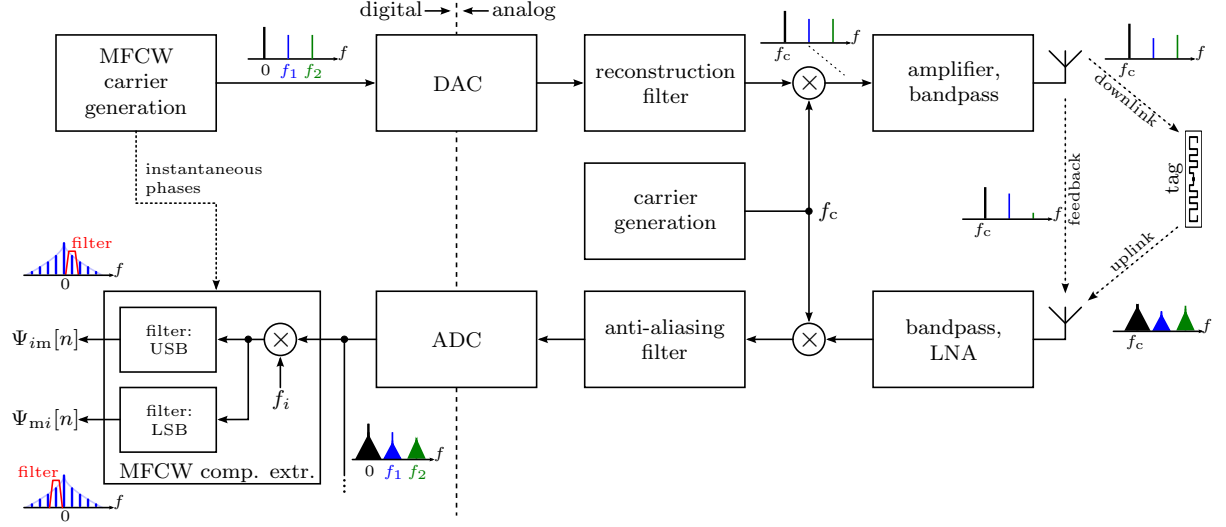


Figure 4.7: Block diagram of multi-frequency continuous-wave ranging (MFCW).

Analysis of Multi-Frequency Continuous-Wave (Backscatter) Ranging

The derivations below have been copied from our publication [135], but use a slightly modified notation and also neglect noise (insignificant compared to multipath propagation; see [135]). They are based on the signal model and the linear reflection coefficient model shown in Fig. 4.8, and are done in the complex baseband. Details of the tag reflection coefficient, including the linearized model, can be found in Section 3.3.1. The entire derivation assumes short-time stationarity.

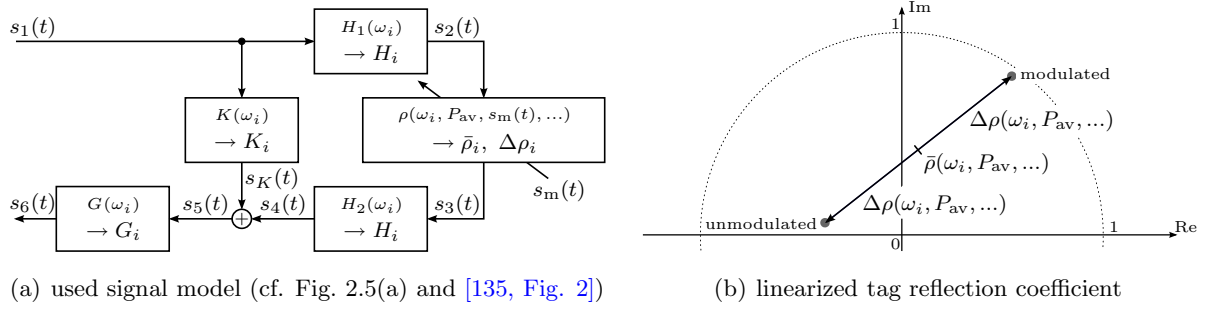


Figure 4.8: Signal model and linearized tag reflection coefficient model: feedback channel $K(\omega_i)$, reader \leftrightarrow tag channels $H_1(\omega_i)$ and $H_2(\omega_i)$, tag reflection coefficient $\rho(\omega_i, P_{av}, s_m, \dots)$ with (artificial) center value $\bar{\rho}(\omega_i, P_{av}, \dots)$ and (artificial) difference value $\Delta\rho(\omega_i, P_{av}, \dots)$, reader frontend $G(\omega_i)$, modulation signal $s_m(t)$, signals $s_1(t)$ through $s_6(t)$, and feedback signal $s_K(t)$; ω is the angular frequency, t is the time variable, and i is the carrier index.

The transmitted multi-carrier signal $s_1(t)$ is composed of N_c carriers at frequency offsets ω_i from the center carrier, with complex amplitudes A_i :

$$s_1(t) := \sum_{i=1}^{N_c} A_i e^{j\omega_i t} \quad (4.4)$$

Downlink and uplink channels are assumed to be linear and are modeled by frequency-dependent

gain factors H_i for the sinusoidal carriers. Hence the incident signal at the tag is

$$s_2(t) = \sum_{i=1}^{N_c} A_i H_i e^{j\omega_i t}. \quad (4.5)$$

The tag modulation is introduced using the linear model discussed in Section 3.3.1 and shown in Fig. 4.8(b). The tag backscatter signal for the i -th carrier is calculated via

$$s_{3,i}(t) = s_{2,i}(t) \cdot (\bar{\rho}_i + s_m(t) \cdot \Delta\rho_i), \quad (4.6)$$

where $\bar{\rho}_i$ is the center tag reflection coefficient at the carrier frequency ω_i , $\Delta\rho_i$ is the corresponding difference value, and $s_m(t)$ is the tag modulation signal. We assume a periodic cosine modulation³⁴

$$s_m(t) := \cos(\omega_m t + \phi_m) = \frac{1}{2} e^{j(\omega_m t + \phi_m)} + \frac{1}{2} e^{-j(\omega_m t + \phi_m)}, \quad (4.7)$$

where ω_m is the tag modulation frequency and ϕ_m is an arbitrary phase shift, $-\pi \leq \phi_m < \pi$. Note that ϕ_m is not the phase shift introduced by the tag for each carrier as discussed in the introduction, but the phase of the modulation waveform. We use the superposition principle to calculate the tag backscatter signal from (4.6) for all carriers

$$s_3(t) = \sum_{i=1}^{N_c} A_i H_i \bar{\rho}_i e^{j\omega_i t} + \frac{1}{2} \sum_{i=1}^{N_c} A_i H_i \Delta\rho_i e^{j((\omega_i + \omega_m)t + \phi_m)} + \frac{1}{2} \sum_{i=1}^{N_c} A_i H_i \Delta\rho_i e^{j((\omega_i - \omega_m)t - \phi_m)}. \quad (4.8)$$

This signal consists of unmodulated components at the carrier frequencies as well as upper and lower modulation sidebands. It is sent over the uplink channel to the reader as a next step:

$$s_4(t) = \sum_{i=1}^{N_c} A_i H_i^2 \bar{\rho}_i e^{j\omega_i t} + \frac{1}{2} \sum_{i=1}^{N_c} A_i H_i H_{im} \Delta\rho_i e^{j[(\omega_i + \omega_m)t + \phi_m]} + \frac{1}{2} \sum_{i=1}^{N_c} A_i H_i H_{mi} \Delta\rho_i e^{j[(\omega_i - \omega_m)t - \phi_m]}. \quad (4.9)$$

The index im here denotes the i -th carrier's upper sideband (UWB) while the lower sideband (LSB) index is mi . For example, the channel gain H_{4m} is the gain for the upper sideband of carrier $i = 4$. Uplink and downlink channels are assumed to be identical for simplicity, but can easily be separated in the results.

The signal received at the reader, $s_5(t)$, consists of the signal reflected by the tag, $s_4(t)$, and the unmodulated feedback $s_K(t)$. The feedback term $s_K(t)$ models direct coupling caused by parasitics and non-ideal devices as well as reflections by the environment. Like up- and downlink channels, it is decomposed into frequency-dependent gain factors K_i for sinusoidal signals.

$$s_K(t) = \sum_{i=1}^{N_c} A_i K_i e^{j\omega_i t} \quad (4.10)$$

Finally, also the reader frontend (combined transmit and receive stage) introduces a frequency-

³⁴ The factor $4/\pi$ for the fundamental wave of a rectangular modulation signal can easily be included in the differential reflection coefficient, $\Delta\rho$. More complex modulation signals are also possible, but would needlessly complicate these derivations.

dependent gain factor, denoted G . Hence

$$\begin{aligned}
s_6(t) &= \sum_{i=1}^{N_c} A_i G_i (K_i + H_i^2 \bar{\rho}_i) e^{j\omega_i t} + \frac{1}{2} \sum_{i=1}^{N_c} A_i H_i H_{im} G_{im} \Delta \rho_i e^{j[(\omega_i + \omega_m)t + \phi_m]} \\
&\quad + \frac{1}{2} \sum_{i=1}^{N_c} A_i H_i H_{mi} G_{mi} \Delta \rho_i e^{j[(\omega_i - \omega_m)t - \phi_m]}.
\end{aligned} \tag{4.11}$$

The frequency components of $s_6(t)$ are separated in the receiver by shifting each component to DC and applying a lowpass filter (direct conversion receiver). The range information, which is buried in the channel gains in (4.11), is subsequently calculated from these components. In order to make the range information visible, we extract the deterministic line-of-sight channel delay τ_{LOS} from these gains. For instance,

$$H_{im} = \tilde{H}_{im} e^{-j(\omega_c + \omega_i + \omega_m)\tau_{\text{LOS}}} \tag{4.12}$$

with ω_c being the center carrier frequency. The phase of the remaining channel gain \tilde{H}_{im} is defined by NLOS components only and is thus purely stochastic. With this slight alteration, we define the complex amplitude of the i -th carrier's upper sideband as

$$\Psi_{im} := \frac{1}{2} \tilde{A}_i \tilde{H}_i \tilde{H}_{im} G_{im} \Delta \rho_i e^{j[\phi_m - \tau_{\text{LOS}} \cdot (2\omega_c + 2\omega_i + \omega_m)]} \tag{4.13}$$

and the complex amplitude of the corresponding lower sideband as

$$\Psi_{mi} := \frac{1}{2} \tilde{A}_i \tilde{H}_i \tilde{H}_{mi} G_{mi} \Delta \rho_i e^{-j[\phi_m + \tau_{\text{LOS}} \cdot (2\omega_c + 2\omega_i - \omega_m)]} \tag{4.14}$$

for $i=1, \dots, N_c$. The term \tilde{A}_i is the mismatch between the transmitted complex carrier amplitude and the demodulation signal, including any mismatch created by frequency conversion from baseband to the UHF RFID frequency range and back. If the MFCW carrier demodulation is done perfectly, the carrier amplitude \tilde{A}_i equals one.

Time-series of Ψ_{im} and Ψ_{mi} are isolated by the last step in the receiver chain, cf. Fig. 4.7. These signal components (denoted MFCW components) are used to estimate the LOS distance to the modulating tag. Time-series are used even in the complex baseband case in order to be able to compensate for frequency drifts (time-variant complex amplitudes).

As a first step in the range calculation, phases of the MFCW components are determined. The resulting sets of estimated lower and upper sideband phases, $\{\angle \Psi_{mi}\}$ and $\{\angle \Psi_{im}\}$, form a system of equations that is subsequently solved for the desired delay τ_{LOS} . However, because $\omega_c \gg \omega_i \gg \omega_m$, a direct solution of this system of equations leads to an ill-conditioned problem. Moreover, the tag modulation phase shift ϕ_m is unknown and uniformly distributed between $-\pi$ and π (cf. timings in [1]). We therefore subtract the phase shifts beforehand in order to eliminate ϕ_m and ω_c . This cannot be achieved by combining upper and lower sidebands, hence $\{\Psi_{im}\}$ and $\{\Psi_{mi}\}$ are used independently. Fig. 4.9 illustrates this process for two-frequency continuous-wave ranging.

A phase comparison between the sidebands at two different carriers i and j leads to

$$\begin{aligned}
\angle \Psi_{im} \Psi_{jm}^* &= \angle \Psi_{im} - \angle \Psi_{jm} \\
&= 2\tau_{\text{LOS}} (\omega_j - \omega_i) + \angle \Delta \rho_i \Delta \rho_j^* + \angle \tilde{H}_i \tilde{H}_{im} \tilde{H}_j^* \tilde{H}_{jm}^* + \angle \tilde{A}_i \tilde{A}_j^* + \angle G_{im} G_{jm}^*
\end{aligned} \tag{4.15}$$

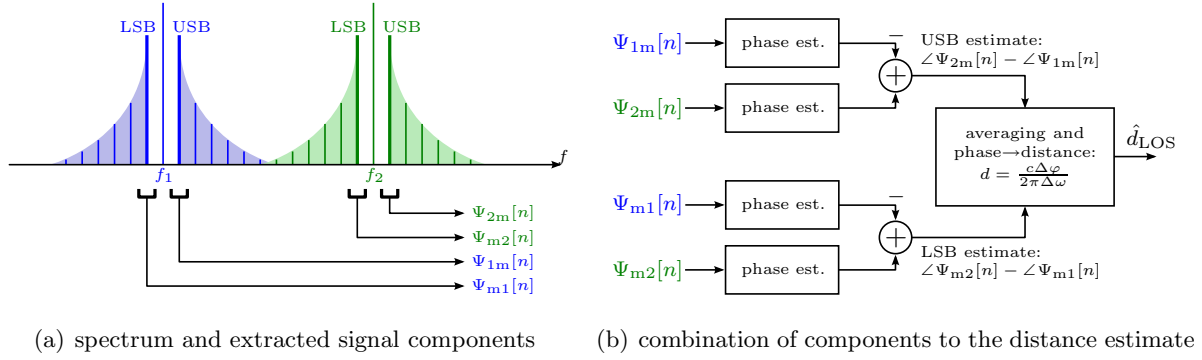


Figure 4.9: Distance extraction from modulation sidebands for 2FCW.

for the upper sideband and

$$\begin{aligned} \angle \Psi_{mi} \Psi_{mj}^* &= \angle \Psi_{mi} - \angle \Psi_{mj} \\ &= 2\tau_{\text{LOS}} (\omega_j - \omega_i) + \angle \Delta \rho_i \Delta \rho_j^* + \angle \tilde{H}_i \tilde{H}_{mi} \tilde{H}_j^* \tilde{H}_{mj}^* + \angle \tilde{A}_i \tilde{A}_j^* + \angle G_{mi} G_{mj}^* \end{aligned} \quad (4.16)$$

for the lower sideband (* denotes the complex conjugate). Note that directly subtracting the sideband phases assumes parallel transmission of carriers i and j . For frequency hopping the time-variance of all parameters has to be taken into account, especially the time-variance of the tag modulation phase ϕ_m . Details are provided in the error analysis below.

Finally, the LOS distance is calculated from time-averaged estimates of these components, i.e.,

$$\angle \hat{\Psi}_{mi} \hat{\Psi}_{mj}^* = \text{avg} \{ \angle \Psi_{mi}[n] \Psi_{mj}^*[n] \} \quad \text{and} \quad \angle \hat{\Psi}_{im} \hat{\Psi}_{jm}^* = \text{avg} \{ \angle \Psi_{im}[n] \Psi_{jm}^*[n] \} \quad (4.17)$$

for all $i, j = 1 \dots N_c$, $i \neq j$. Averaging at this point increases robustness to frequency drifts and also removes noise (processing gain). It does not, however, mitigate the error terms in (4.15) and (4.16), since these errors are typically not zero-mean time-variant. The LOS distances estimated from the averages

$$\hat{d}_{\text{LOS},ij,\text{LSB}} = \frac{c}{2(\omega_j - \omega_i)} \angle \hat{\Psi}_{mi} \hat{\Psi}_{mj}^* = d_{\text{LOS}} + e_{ij,\text{LSB}} \quad (4.18)$$

and

$$\hat{d}_{\text{LOS},ij,\text{USB}} = \frac{c}{2(\omega_j - \omega_i)} \angle \hat{\Psi}_{im} \hat{\Psi}_{jm}^* = d_{\text{LOS}} + e_{ij,\text{USB}} \quad (4.19)$$

thus consist of the true LOS distance d_{LOS} as well as error terms $e_{ij,\text{LSB}}$ and $e_{ij,\text{USB}}$. These error terms incorporate all errors, including noise. All upper and lower sideband estimates are subsequently combined to obtain the overall distance estimate. This can be done by simply averaging the distance estimates or by some form of weighted average (higher weights for good estimates).

Sources of Errors

Distance estimates based on phase shifts between simultaneously transmitted narrowband carriers suffer from five error sources: the frequency dependence of the tag reflection coefficient, multipath propagation, unknown phase/frequency offsets between the carriers (including I/Q

imbalances), filters in the signal path (frequency-dependent phase shift), and noise. Except for the noise, all errors are directly represented in (4.15) and (4.16). For example

$$\angle\Psi_{im}\Psi_{jm}^* = \underbrace{2\tau_{\text{LOS}}(\omega_j - \omega_i)}_{\text{true LOS path}} + \underbrace{\angle\Delta\rho_i\Delta\rho_j^*}_{\text{tag reflection coeff.}} + \underbrace{\angle\tilde{H}_i\tilde{H}_{im}\tilde{H}_j^*\tilde{H}_{jm}^*}_{\text{multipath propagation}} + \underbrace{\angle A_i A_j^* + \angle G_{im} G_{jm}^*}_{\text{systematic errors (reader)}}.$$

The last two terms, $\angle A_i A_j^*$ and $\angle G_{im} G_{jm}^*$, are systematic influences and can be kept small by careful reader design and reference measurements at known distances. Multipath propagation channels are represented by $\angle\tilde{H}_i\tilde{H}_{im}\tilde{H}_j^*\tilde{H}_{jm}^*$. This term is zero in anechoic environments, i.e., for AWGN channels. It can be minimized to some extent by careful system design³⁵, but cannot be fully avoided. Likewise, the differential phase shift introduced by the tag, $\angle\Delta\rho_i\Delta\rho_j^*$, can only be mitigated to a certain extent. Only in anechoic environments can this error be fully removed by careful calibration [51]. Noise is a minuscule problem in comparison to multipath propagation and the tag’s reflection coefficient, even if the power of ranging carriers is chosen below 1 mW, see [135].

Two additional error sources arise for frequency hopping multi-carrier systems. The first source is time-variance, especially of the channel. The second and dominant source is the tag modulation phase shift ϕ_m . Since carrier hopping requires a re-initialization of the carrier according to the Gen-2 standard [1], the tag is powered down. The uniform random variable ϕ_m is thus re-initialized and no longer cancels in the phase comparison between upper and lower sidebands ($\rightarrow\phi_{m,i}$). Consequently, it has to be estimated at each hop. This can be done by comparing the phase of upper and lower sidebands for one carrier,

$$\angle\Psi_{im}\Psi_{mi}^* = 2\phi_{m,i} - 2\tau_{\text{LOS}}\omega_m + \angle\tilde{H}_{im}\tilde{H}_{mi}^* + \angle G_{im}G_{mi}^*. \quad (4.20)$$

This system of equations is added to the system formed by the phase comparisons between upper and lower sideband phases. The systematic phase shift $\angle G_{im}G_{mi}^*$ in (4.20) is again removed by calibration measurements. The only error source that cannot be compensated for is the phase shift introduced by multipath propagation, $\angle\tilde{H}_{im}\tilde{H}_{mi}^*$. It can, however, be kept small by choosing a low tag modulation frequency. Note that frequency hopping also requires that the averaging is done before the phase comparisons due to the unstable tag modulation. This decreases robustness to frequency drifts.

Finally, the maximum unambiguous range is also a potential source of error. Since the carriers are periodic, a phase shift of $2\pi + \varphi$ is mapped to φ (phase ambiguity). Hence a tag at 11 m looks like a tag at 1 m distance to the phase-based ranging system with a maximum unambiguous range of 10 m. Naturally, this also includes errors introduced by multipath propagation. A positive error of 2 m at a true distance of 9 m, for example, again maps the tag to 1 m. The offset frequency thus has to be chosen carefully [135] in order to avoid classification of over-range reads as short-range. For two carriers, the maximum unambiguous range is

$$d_{\text{max},2\text{FCW}} = c/(2\Delta f) \quad (4.21)$$

where c is the speed of light and Δf is the frequency spacing between the two carriers. The factor of two here originates from the fact that the backscatter distance is twice the range of the tag (“there and back again”). The maximum unambiguous range for multi-carrier systems can be extended over (4.21) by unwrapping the respective phases [66,226]. Carriers at $f_1 = 902$ MHz, $f_2 = 908$ MHz, and $f_3 = 928$ MHz, for example, lead to a maximum unambiguous range of 75 m [66]. This is obtained from the least common divisor of all frequencies and a fairly common approach in synthetic aperture radar (SAR), e.g., [226,227].

³⁵ avoiding parallel reflecting surfaces, using non-reflective and scattering materials whenever possible, avoiding pointing directive antennas straight at reflecting surfaces, etc.

Analysis with respect to Multipath Propagation

In case of multipath propagation, the stochastic channel phase terms in (4.15) and (4.16) are potentially the largest source of error. Each channel gain in these terms is complex Gaussian and circularly symmetric around the LOS gain μ_H , e.g., $H_i \sim \mathcal{CN}(\mu_H, \sigma_H^2)$. This assumption implies dense scattering and a predominantly stochastic channel, i.e., negligible specular reflections.

Even under the simplifying assumption of Gaussianity, the effects of multipath propagation on the range error are very complex, since four mutually dependent channel gains are multiplied, e.g., $H_i H_{im} H_j^* H_{jm}^*$ for the USB. Calculating the phase of these terms additionally introduces a nonlinearity, as this requires the inverse tangent. Several simplifications have therefore to be made in order to render an analytic derivation feasible³⁶:

- Channel gains for carrier i and j are identically distributed, $H_i, H_j \sim \mathcal{CN}(\mu_H, \sigma_H^2)$. The covariance between both gain factors is $\text{cov}\{H_i, H_j^*\} = \beta_H$. This implies that second order statistics of the CTF depend only on the frequency difference, not the absolute frequency. As a consequence, uncorrelated scattering is required, cf. [141, p. 104].
- The modulation sidebands experience the same channel gains as the carriers themselves, e.g., $H_{mi} = H_i = H_{im}$. This requires modulation frequencies f_m well inside the coherence bandwidth ($f_m \ll B_c$) and that the average channel delay is well below $1/f_m$. In essence and for practical implementations, this translates to $\omega_m \ll \omega_j - \omega_i$.
- The multiplication of Gaussian random variables is also assumed to be approximately Gaussian at several points in the derivations, cf. [135]. This presumes a dominant LOS path, i.e., $|\mu_H| \gg \sigma_H$. In addition, dominance of the LOS path is necessary also to replace inverse tangent and expectation operators and thus be able to use spaced-frequency correlation and covariance functions. Simulations have shown that $K_{\text{LOS}} \geq 10$ dB is required per channel in order to fulfill these requirements.
- Finally, we assume identical K-factors and RMS delay spreads for up- and downlink (identical / identically parameterized channels). Considering arbitrary channels is possible using the analyses in [133], but of course doubles the number of parameters and thus the complexity of the results.

Mean value, variance, and covariance of the Gaussian distributions can be calculated from K_{LOS} and τ_{RMS} . The mean value corresponds to the normalized LOS amplitude,

$$|\mu_H|^2 = P_{\text{LOS}} = \frac{K_{\text{LOS}}}{1 + K_{\text{LOS}}}. \quad (4.22)$$

Variance and covariance can be calculated from the spaced-frequency covariance function³⁷. For exponentially decaying channels, this function is [2]

$$\Phi(\Delta\omega) = \frac{\Pi}{\gamma + j\Delta\omega} = \frac{\sqrt{1 + 2K_{\text{LOS}}}}{(1 + K_{\text{LOS}})(\sqrt{1 + 2K_{\text{LOS}}} + j\Delta\omega(1 + K_{\text{LOS}})\tau_{\text{RMS}})}, \quad (4.23)$$

where Π is the NLOS power density, γ is the multipath decay constant, and $\Delta\omega$ is the frequency offset. Hence

$$\sigma_H^2 = \Phi(0) = \frac{1}{1 + K_{\text{LOS}}} \quad (4.24)$$

³⁶ These assumptions, including the assumption of Gaussian channel gains, are of course not made for the simulations.

³⁷ cf. (time)-frequency correlation function, [141, p. 106], [221, 222]

and

$$\beta_H = \Phi(\omega_j - \omega_i) = \frac{\sqrt{1 + 2K_{\text{LOS}}}}{(1 + K_{\text{LOS}}) (\sqrt{1 + 2K_{\text{LOS}}} + j(\omega_j - \omega_i)(1 + K_{\text{LOS}})\tau_{\text{RMS}})}. \quad (4.25)$$

Under the above assumptions, variance σ_e^2 and bias μ_e of the error for a single-channel link can be approximated by

$$\mu_e = \frac{c}{2(\omega_j - \omega_i)} \text{E}\{\angle H_i H_j^*\} \approx \frac{c}{2(\omega_j - \omega_i)} \angle \text{E}\{H_i H_j^*\} = \frac{c}{2(\omega_j - \omega_i)} \angle (|\mu_H|^2 + \beta_H) \quad (4.26)$$

and

$$\begin{aligned} \sigma_e^2 &= \frac{c}{2(\omega_j - \omega_i)} \text{var}\{\angle H_i H_j^*\} \approx \frac{c}{2(\omega_j - \omega_i)} \angle \text{var}\{H_i H_j^*\} \\ &= \frac{c}{2(\omega_j - \omega_i)} \arctan\left(\frac{\text{Re}\{\sigma_H^4 - \beta_H^2 + 2|\mu_H|^2(\sigma_H^2 - \beta_H)\}}{2\text{Re}\{\beta_H + |\mu_H|^2\}^2}\right), \end{aligned} \quad (4.27)$$

cf. [135]. Note that we replace the angle operator \angle and the expected value $\text{E}\{\cdot\}$ here. This assumes approximate linearity of the inverse tangent, which is true for small angles only and thus presumes a dominant LOS path. This step is by far the most critical simplification.

The mean absolute error (MAE) can be expressed by mean and standard deviation under the assumption of a Gaussian distribution for the error [135],

$$\text{E}\left\{\left|\hat{d}_{\text{LOS}} - d_{\text{LOS}}\right|\right\} = \frac{1}{\sigma_e \sqrt{2\pi}} \int_{-\infty}^{\infty} |x - \mu_e| e^{-\frac{x^2}{2\sigma_e^2}} dx = \sqrt{\frac{2}{\pi}} \sigma_e e^{-\frac{\mu_e^2}{2\sigma_e^2}} + \mu_e \text{erf}\left\{\frac{\mu_e}{\sqrt{2}\sigma_e}\right\}, \quad (4.28)$$

where $\text{erf}\{\alpha\}$ is the error function [228, p. A56]

$$\text{erf}\{\alpha\} = \frac{2}{\sqrt{\pi}} \int_0^{\alpha} e^{-x^2} dx. \quad (4.29)$$

The backscatter property is taken into account by either modifying K_{LOS} and τ_{RMS} as discussed in Section 2.4 on page 63 (see also [133] and [134]) or by modifying μ_H , σ_H , and β_H as suggested in [135]:

$$\tilde{\mu}_H = \mu_H^2, \quad \tilde{\sigma}_H^2 = 2\sigma_H^2 (\sigma_H^2 + 2\mu_H^2), \quad \tilde{\beta}_H = 2\beta_H (\beta_H + 2\mu_H^2) \quad (4.30)$$

for identical up- and downlink channels and

$$\tilde{\mu}_H = \mu_H^2, \quad \tilde{\sigma}_H^2 = \sigma_H^2 (\sigma_H^2 + 2\mu_H^2), \quad \tilde{\beta}_H = \beta_H (\beta_H + 2\mu_H^2) \quad (4.31)$$

for independent channels. Simulations have shown that the modification of μ_H , σ_H , and β_H leads to slightly better results, especially for the bias term. The reason is frequency correlation: using (4.23) with modified K_{LOS} and τ_{RMS} implies that the overall backscatter channel is assumed to be exponentially decaying, which is not the case (cf. [133, Fig. 3]). Since the frequency correlation function depends on the shape of the PDP, the approach in [135] is better suited here.

A third alternative, namely the calculation of $\Phi(\Delta\omega)$ for the overall backscatter channel using the methodology in [133] leads to no more accurate a result than the modification of μ_H , σ_H , and β_H . Like (4.26) and (4.27), this method relies on replacing the nonlinear inverse tangent and the expectation operator. This is the most severe simplification in the above derivations and hence responsible for most of the mismatch. Consequently, there is no benefit in this alternative.

A comparison between the theoretical results derived above and simulations is shown in Fig. 4.10. This comparison validates the theoretical results and also illustrates their limits. K-factors and RMS delay spreads here are typical for UHF RFID, cf. Section 2.3.

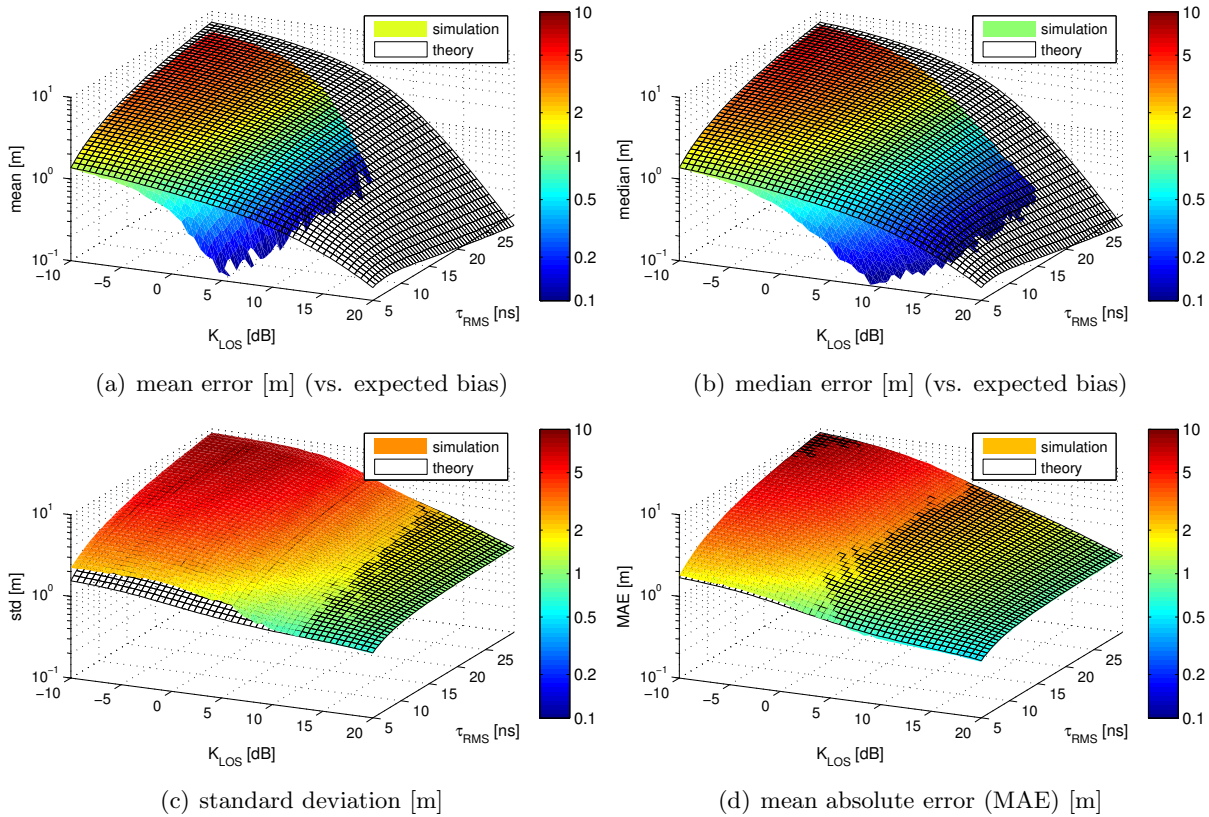


Figure 4.10: Errors [m] caused by multipath propagation: comparison between theory and simulation for a frequency offset of $\Delta f = 3$ MHz and independent up-/downlink channels. Configuration for the simulation: $f_1 = f_c = 910$ MHz, $f_2 = 913$ MHz, $f_m = 48$ kHz, 10^5 realizations per point.

The bias term is generally over-estimated by the derived theory, especially for high K-factors. The theory thus represents an upper bound in case of the bias. The predicted standard deviation matches the simulation results for K-factors larger than 10 dB (as discussed above). For lower K-factors, the standard deviation is higher than predicted by the theory. Surprisingly, the theoretical results for the mean absolute error according to (4.28) match the simulated errors almost perfectly over the entire range of K_{LOS} and τ_{RMS} . This is not limited to this example; the MAE shows a good match for all frequency offsets with identical and with independent channels.

Mean absolute errors as predicted by theory can be found in Figs. 4.11 and 4.12 for frequency spacings of 1 and 10 MHz respectively. These plots cover typical (single-channel) K-factors and RMS delay spreads³⁸, cf. Section 2.3. The upper end of the colormaps in the plots (dark red color) corresponds to the highest possible MAE for the given frequency spacing. This bound of the MAE is obtained for a uniform distribution of the distance estimate over the entire unambiguous range. All distance information is lost in this case.

Predictably, the highest error can be observed at low K-factors and high RMS delay spreads. The system with 1 MHz reaches an MAE of 12 m within the given interval of K_{LOS} and τ_{RMS} , while the system with 10 MHz carrier spacing reaches only about 3 m. In addition, the minimum

³⁸ Note that high K_{LOS} in combination with high τ_{RMS} is unlikely in indoor environments. The same is true for low K-factors in combination with low RMS delay spreads.

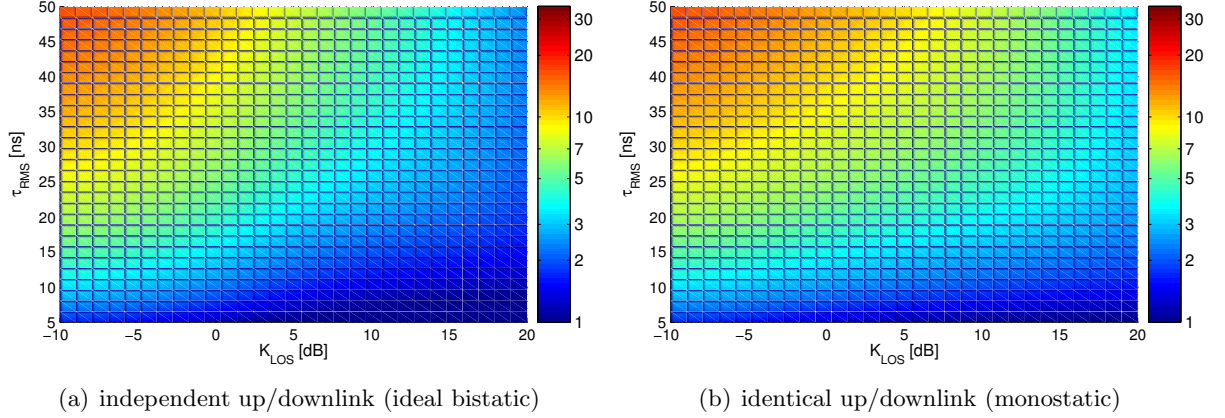


Figure 4.11: Mean absolute error (MAE) [m] for 2FCW with a frequency spacing of $\Delta f = 1$ MHz.

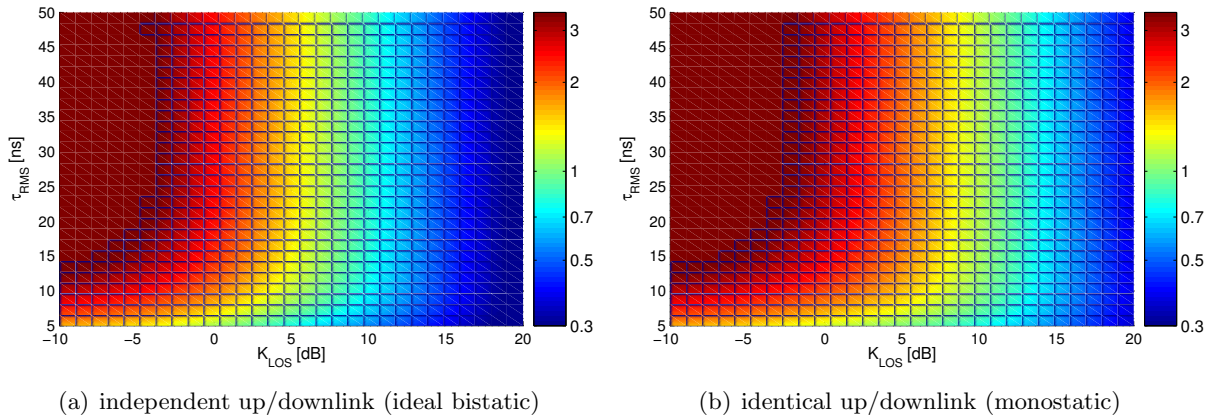


Figure 4.12: Mean absolute error (MAE) [m] for 2FCW with a frequency spacing of $\Delta f = 10$ MHz.

error is smaller for $\Delta f = 10$ MHz. Note, however, that the MAE for $\Delta f = 1$ MHz is still well below its upper bound. This is not the case for the system with $\Delta f = 10$ MHz, which reaches the upper bound of the MAE for K-factors below -3 dB and RMS delay spreads above 10 ns. In this area, the carriers are fully decorrelated and all distance information is lost.

The performance in bistatic setups generally exceeds the performance in monostatic setups (lower MAE). Finally, note that the MAE for 2FCW with $\Delta f = 10$ MHz depends solely on the K-factor for $\tau_{\text{RMS}} > 20$ ns. In this region the CIR is already long enough to create a uniformly distributed phase difference for $\Delta f = 10$ MHz. Increasing the length thus changes nothing. This is not the case for $\Delta f = 1$ MHz, where the MAE depends on both K_{LOS} and τ_{RMS} for the displayed range of both parameters.

4.2.2 Performance Bounds / Simulations

parts of this section have been published in [128]

In this section, the performance of MFCW ranging is analyzed under fully controlled conditions, i.e., simulation-based. Since it was shown in [135] that noise is a secondary problem for MFCW ranging, while multipath propagation and tag detuning potentially cause extremely large errors, the simulations are limited to the latter two effects.

Errors Caused by Multipath Propagation

Let us start with the dominant source of errors: multipath propagation. Unless otherwise stated, the simulations with respect to multipath propagation below are based on the exponential small-scale channel model of the PARIS framework (see Section 3.4.3) with a main carrier frequency of $f_1 = f_c = 910$ MHz and a tag modulation frequency of $f_m = 48$ kHz.

Mean absolute errors (MAE) for two-frequency continuous-wave (2FCW) ranging with frequency spacings of 1 and 10 MHz are displayed in Fig. 4.13 for mono- and bistatic setups respectively. As a point of reference: the K-factor inside UHF RFID portals ranges from -5 through 15 dB and the RMS delay spread reaches 30 ns [132] (see also Section 2.3.3).

The MAE is smaller for the larger carrier spacing and ranges from 30 cm for high K-factors ($\Delta f = 10$ MHz, bistatic) to 12 m for low K_{LOS} and high τ_{RMS} ($\Delta f = 1$ MHz, monostatic). Also note that the error is always larger for the monostatic setup (i.e., identical up- and downlink channels) than for the bistatic case.

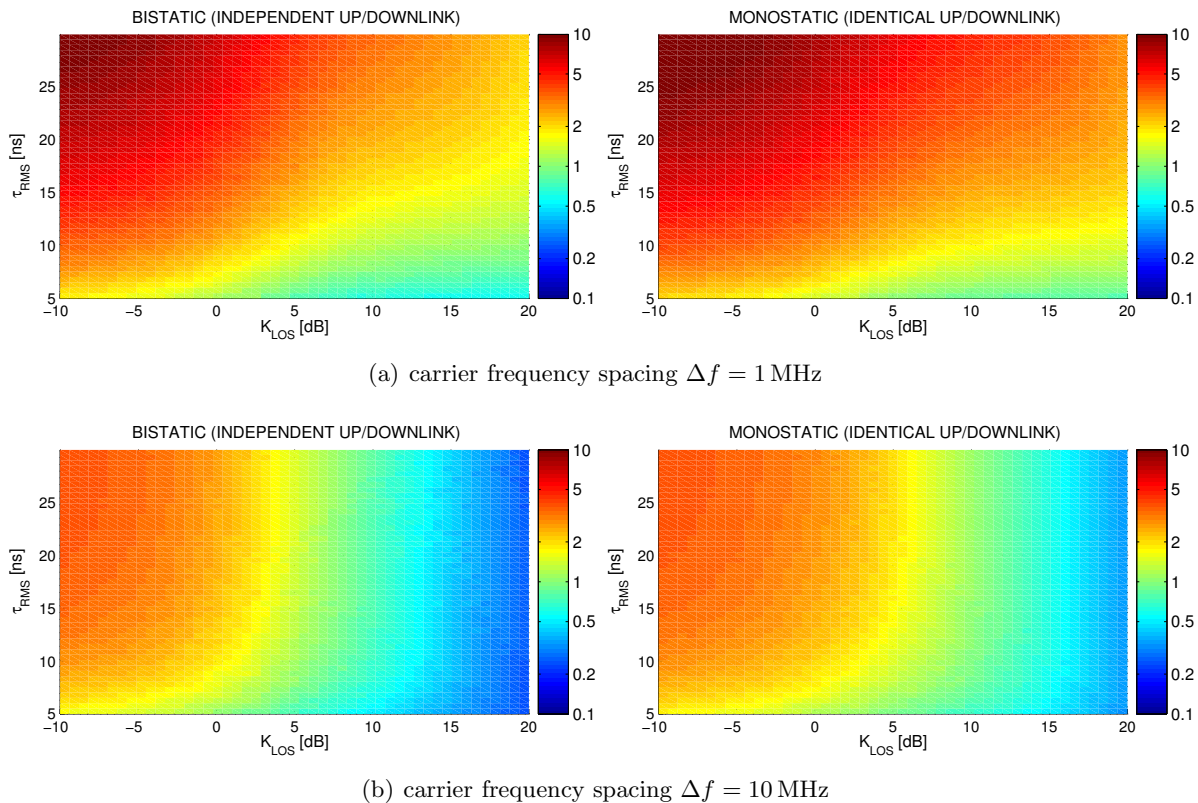


Figure 4.13: Mean absolute error (MAE) [m] vs. typical LOS K-factors and RMS delay spreads for two different carrier spacings (10^5 realizations per point).

The bias is shown in the next group of plots, Fig. 4.14. For $K_{\text{LOS}} > 5$ dB, the LOS is still dominant and the bias is negligible. For low K-factors, on the other hand, the bias reaches up

to 8 m for the system with 1 MHz carrier spacing. The system with higher spacing again shows better performance.

A peculiarity can be seen in Fig. 4.14(b): the bias decreases for increasing RMS delay spread at low K-factors although it should increase due to the longer impulse response associated with higher delay spreads. Unfortunately, this only shows an increasingly uniform distribution over the entire range – which is unbiased but no longer carries any distance information.

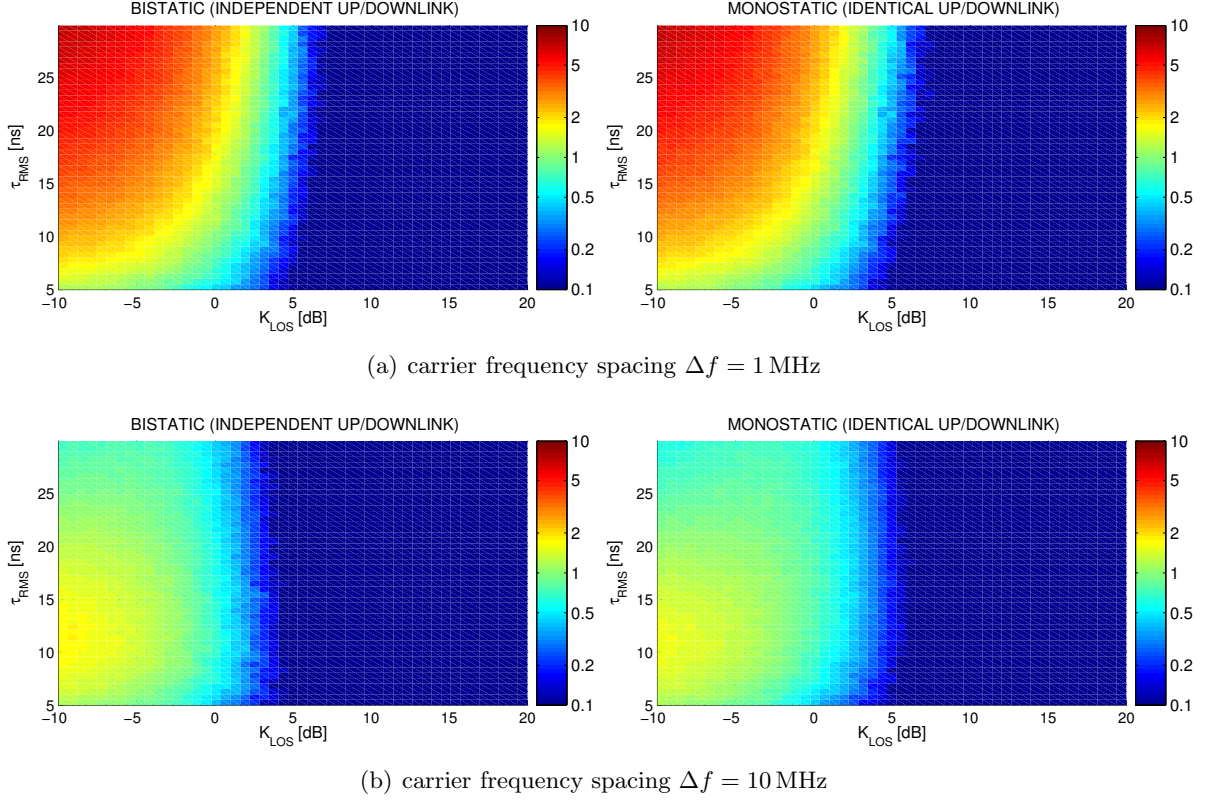


Figure 4.14: Bias [m] vs. typical LOS K-factors and RMS delay spreads for two different carrier spacings (10^5 realizations per point).

Looking at the probability distribution functions (PDFs) of the range error for different channel configurations and carrier spacings (i.e., bandwidths) in Fig. 4.15, the suspicion regarding the type of distribution is confirmed. The error is indeed almost uniform at frequency spacings of 10 MHz and above for low K-factors and the corresponding medium to high RMS delay spreads.

Apart from the PDFs, the plots also show the bias obtained from (4.26) (circular marker) and the unambiguous range of a system (dashed lines). The largest errors can be observed for the most narrowband system, with high bias and high variance over the entire range of channels. This is caused by the long wavelength of 300 m for 1 MHz offset (beat frequency). Even a minuscule phase error leads to a high distance error at such a long wavelength. Increasing the frequency offset from 1 to 10 MHz decreases the error, especially for high K-factors and high RMS delay spreads. Note, however, that the error relative to the wavelength increases with frequency offset in all multipath channels. This is especially visible when comparing the errors for 10 and 30 MHz with their respective maximum unambiguous ranges. The increase can be explained by looking at the error introduced by multipath propagation to the received MFCW signal amplitudes (4.15) and (4.16), e.g.,

$$\angle H_i H_{im} H_j^* H_{jm}^* = \angle H_i H_{im} - \angle H_j H_{jm} \approx \angle H_i^2 - \angle H_j^2. \quad (4.32)$$



This phase shift increases with carrier spacing $f_j - f_i$ because the correlation between channel gains H_i and H_j decreases with frequency spacing, cf. (4.25). Note that the tails of the distributions already reach the ambiguity range for $\Delta f = 10$ MHz and $K_{\text{LOS}} = 0$ dB while this is not the case for $\Delta f = 1$ MHz. Lowering the K-factor even further, the error becomes increasingly uniform for any significant RMS delay spread at $\Delta f = 10$ MHz and especially at $\Delta f = 30$ MHz. Based on the results in Fig. 4.15, a frequency offset in the range of 10 MHz seems to be the most reasonable choice for ranging *inside* a UHF RFID portal.

The (analytically calculated) bias marks the most likely error in Fig. 4.15, i.e., the peak of the PDF³⁹. Note that it decreases for a fixed K-factor when increasing the frequency offset between the carriers (Fig. 4.15). Again, this can be linked to the correlation between the channel gains: increasing the carrier spacing decreases the correlation between the range errors, as can be seen in Fig. 4.16. This figure is based on a three-carrier (3FCW) system, where carriers 1 and 2 are spaced by 1 MHz and the spacing to carrier 3 is continuously increased, starting at the same offset as carrier 2. Distances are extracted from carriers 1-2 and 1-3 in this example.

The correlation between the errors of these two distance estimates decreases with the frequency offset between carriers 2 and 3, but also with increasing multipath propagation, see Fig. 4.16(a). The three curves correspond to negligible multipath propagation (blue), typical multipath propagation inside the transmitter antenna’s mainlobe and at short range (green), and multipath propagation outside the mainlobe (red), cf. Section 2.3. Correlation between the carriers causes similar errors for each estimate and thus reduces the usefulness of the additional estimate. For three carriers uniformly spaced by 1 MHz, for example, only 3–60% of the second distance estimate is “new information”, depending on the channel. Increasing the spacing between carriers 2 and 3 to 15 MHz decreases this correlation to below 20% (>80% is new).

One might thus conclude that increasing the carrier spacing is a good idea to reduce the correlation of the error and thus the bias. This is not the case, as illustrated in Fig. 4.16(b). This plot shows the closeness of the resulting variance to the limiting case: a uniform distribution over the entire range. As can be seen, the decrease in correlation is accompanied by an increase in randomness of the estimates. Increasing the carrier spacing decreases the error in “nice” channels but, at the same time, massively increases it in more common “not so nice” environments⁴⁰. Consequently, there is a trade-off between the error at close range and inside the mainlobe, and the error outside the mainlobe.

Multiple carriers with different frequency spacings can be used to overcome this problem and thus detect and classify over-range reads. Such stray reads are outside the normal read zone per definition. This implies that the K-factor is extremely low and the RMS delay spread is at a maximum. Hence a low frequency spacing is required, since the error for higher spacings reaches a uniform distribution under these conditions. The bias here will additionally increase the estimated distance, thus helping in the classification of such a stray read as “outside the intended read zone”. Unfortunately, a low carrier spacing causes high errors inside the read zone, where K-factors are high. These effects can be observed in Fig. 4.15. Intelligently combining the estimates of multiple carriers with different frequency spacings (cf., [66]) can be used to overcome this problem. However, making this approach robust will likely require several independent estimates in order to determine proper weights for the combination.

³⁹ This is the case because the bias has been calculated under the assumption of a Gaussian error. Since peak and expected value are identical for this type of distribution, the bias points at the peak. The increasingly uniform distribution, on the other hand, is generated by the mapping of the tails of the Gaussian PDF to the unambiguous range. Hence, provided that the peak is still visible above the uniform shape, and accounting for some skewness due to asymmetrical mapping, the bias still approximately points at the peak of the PDF.

⁴⁰ Note that this does not take into account the fact that closely spaced carriers also experience the same amplitude fading, i.e., noise becomes a problem if all ranging carriers experience high fading levels at the same time.

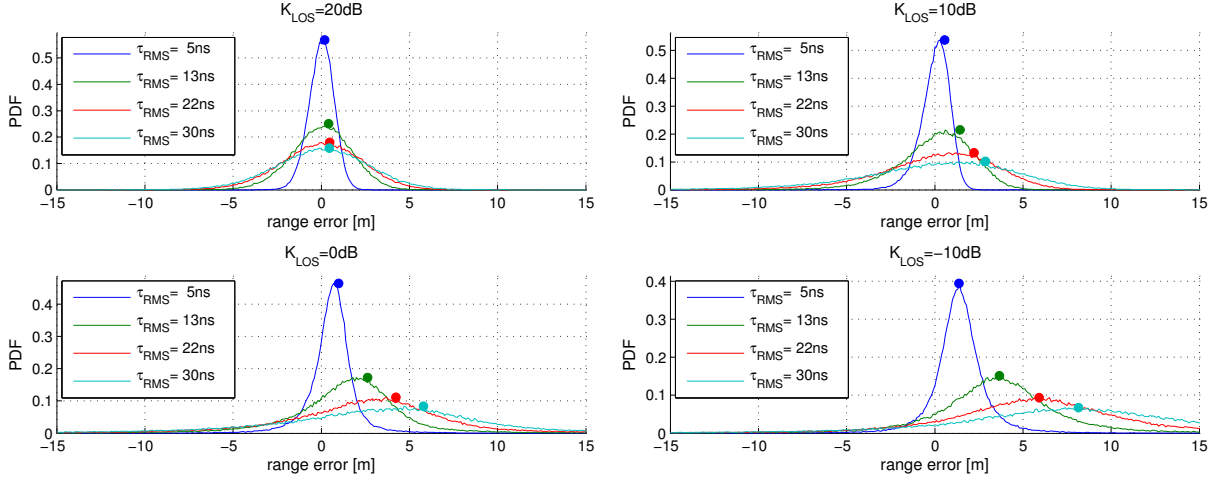
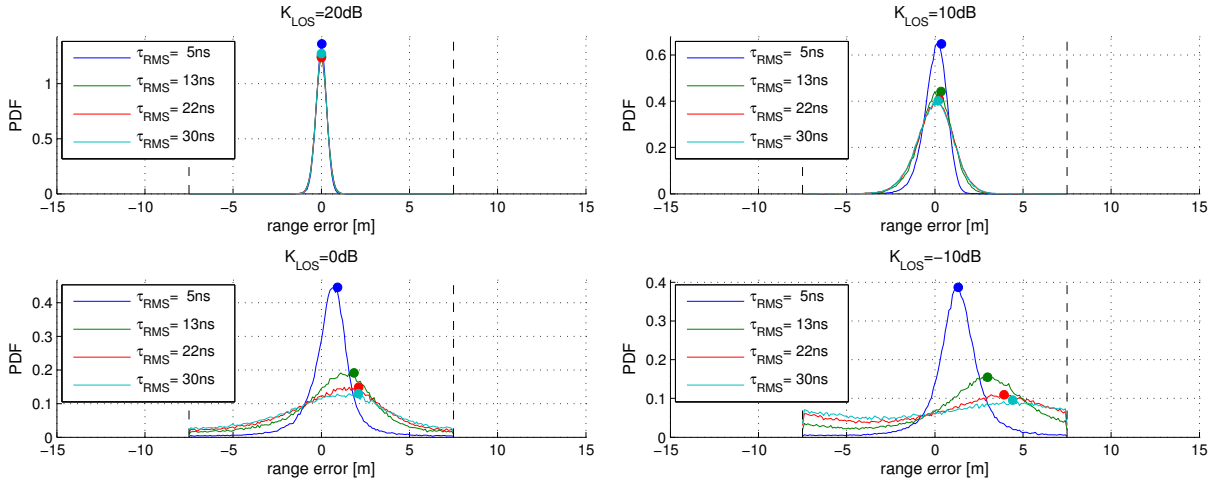
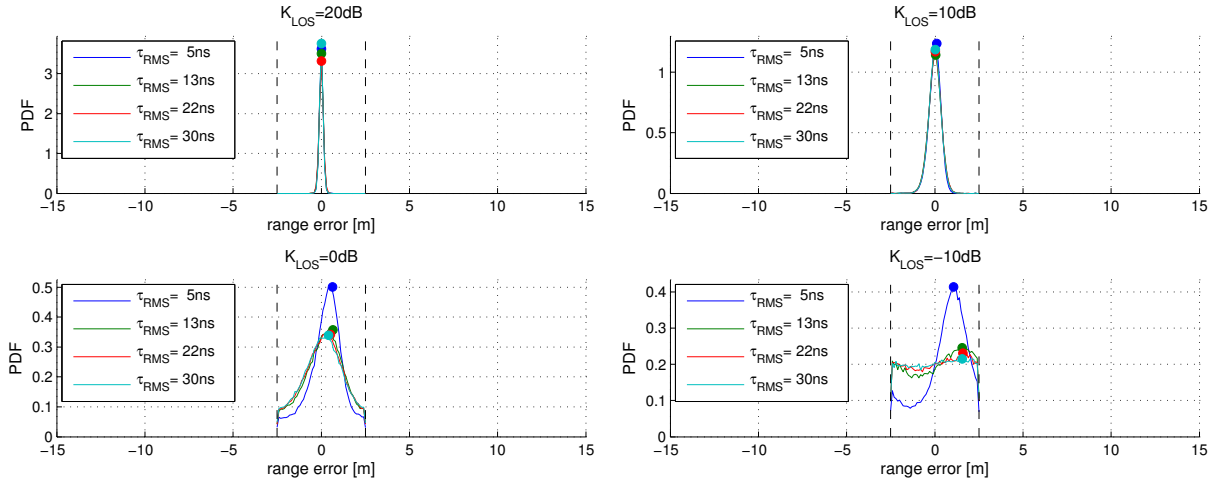
(a) carrier frequency spacing $\Delta f = 1$ MHz (bound due to max. unambiguous range: ± 75 m)(b) carrier frequency spacing $\Delta f = 10$ MHz (bound due to max. unambiguous range: ± 7.5 m)(c) carrier frequency spacing $\Delta f = 30$ MHz (bound due to max. unambiguous range: ± 2.5 m)

Figure 4.15: Range error distributions for 2FCW with three different bandwidths and for different K -factors and RMS delay spreads. Dots show the expected bias; dashed lines indicate the bound due to the maximum unambiguous range. (Independent up- and downlink channels with identical configuration, frequency offset Δf as indicated in the subfigure captions. PDFs have been generated with 10^5 realizations.)

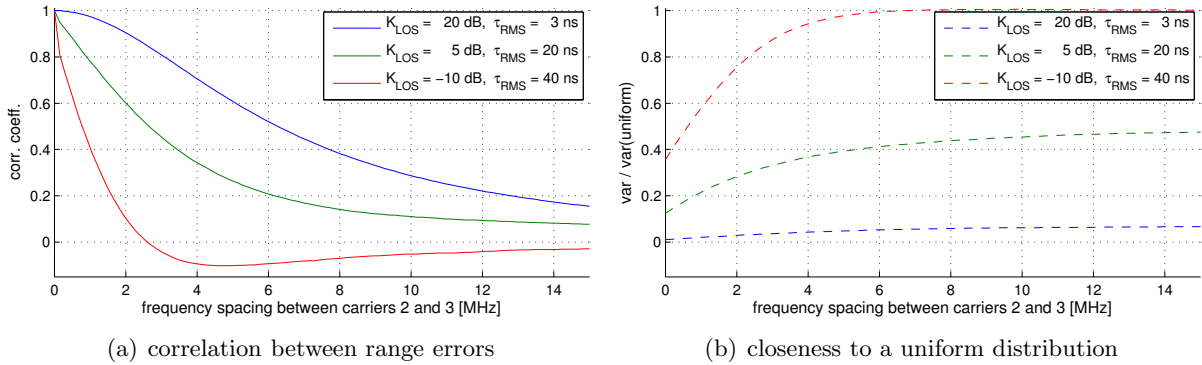


Figure 4.16: Correlation between range errors for closely spaced carriers (3FCW) and similarity of the error to a uniform distribution (10^6 realizations).

Errors Caused by Tag Detuning

The error introduced by the tag is represented in (4.15) and (4.16) by the term

$$\angle \Delta \rho_i \Delta \rho_j^* = \angle \Delta \rho_i - \angle \Delta \rho_j.$$

It is minimized if the tag’s differential reflection coefficient (“modulated minus unmodulated”, cf. Fig. 4.8(b)) does not vary over frequency. Unfortunately, this requirement clashes with the resonant design of UHF RFID tag antennas, cf. [208]. Moreover, the reflection coefficient is massively influenced by tolerances in the assembly process of a tag as well as by antenna detuning near conductive materials. In addition, it is highly nonlinear.

Compare Figs. 4.17 and 4.18, for example. These plots show the phase of the differential reflection coefficient during modulation vs. available power P_{av} and carrier frequency f_c . The left-hand plots (a) display the phase, while the right-hand plots (b) show the gradient of the phase with respect to frequency. The higher the gradient, the larger the error introduced in multi-carrier phase estimates. All plots also display the minimum tag power threshold in fully unmodulated and fully modulated state⁴¹ as a reference level, as well as the UHF RFID frequency range of 860–960 MHz. The values shown have been calculated from the model of the NXP UCODE G2XM on NXP’s UCODE general purpose reference antenna (see Section 3.3.1).

High gradients in the phase are limited to a few “hot spots” for this tag. In case of a perfectly tuned tag these hot spots are mostly outside the RFID frequency ranges, as can be seen in Fig. 4.17.

Unfortunately, as mentioned above, the reflection coefficient is affected by any modification in the assembly impedance and/or the antenna impedance. Especially antenna detuning in the vicinity of water and metal tends to increase the quality factor of the antenna’s self-resonance and thus makes the tag more resonant. This can be observed in Fig. 4.18, where the same tag is located a few centimeters from metal. Apart from the apparent shift in frequency, changes in the differential reflection coefficient phase happen much faster in this scenario, leading to steeper gradients. Moreover, one of the hot spots was shifted in frequency and is now inside the European UHF RFID frequency band (865–868 MHz). As a consequence, MFCW-based ranging inside the EU bands will now be biased⁴².

Since there are only a few such hot spots in the gradient, most errors due to detuning will be small. If a tag hits such an “unlucky detuning”, however, the error can reach several meters.

⁴¹ Modulation transistor switched off (unmodulated; matched state) or on (modulated; mismatched) permanently.

⁴² A shift of 7° corresponds to an error of roughly $c/(2\Delta f) \cdot 7/360 \approx 3 \text{ m}$ at a frequency spacing of $\Delta f = 1 \text{ MHz}$, for example.

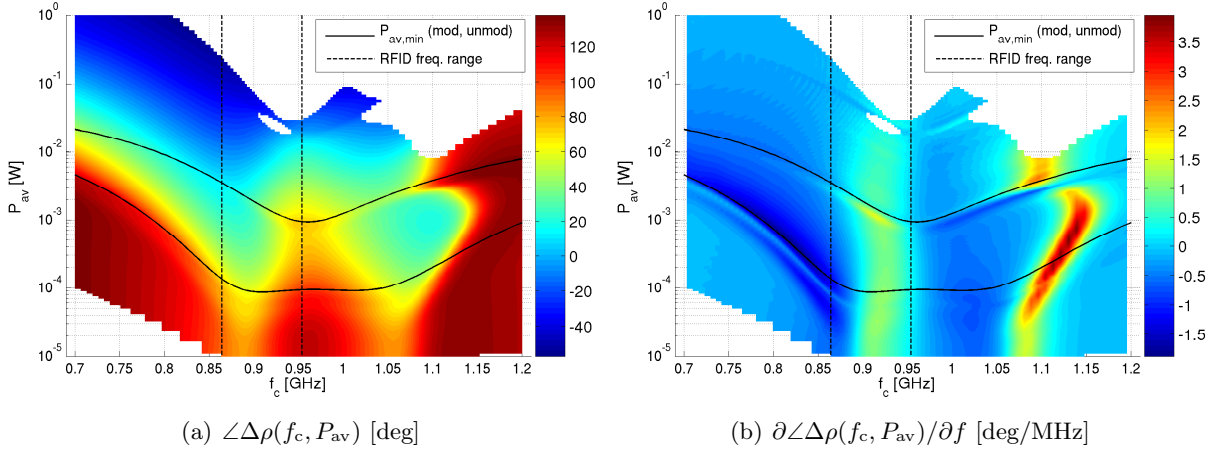


Figure 4.17: Differential tag reflection coefficient phase $\angle\Delta\rho$ (linear model) and its gradient over frequency (well-tuned; resonance boosted 0 % and shifted by 0 MHz).

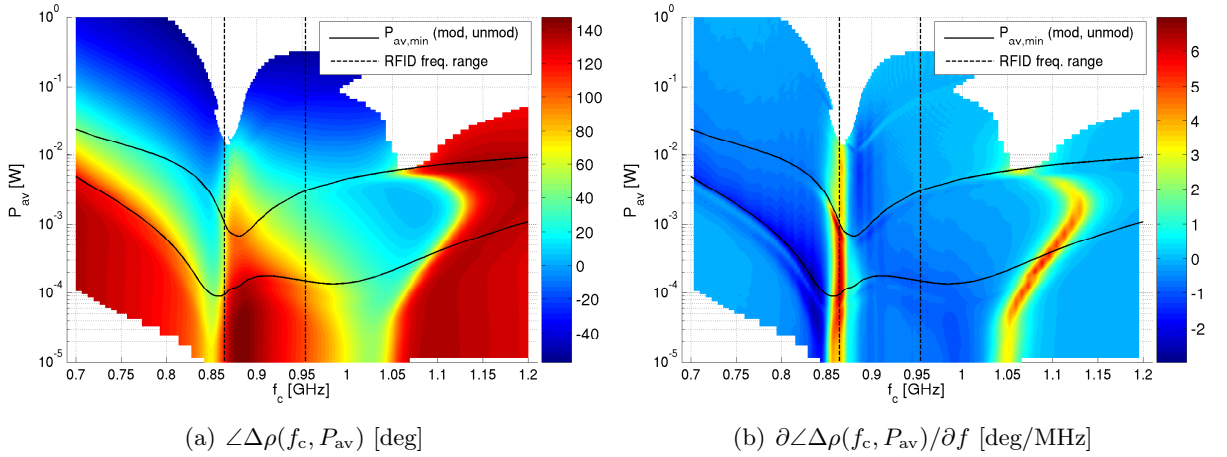


Figure 4.18: Differential tag reflection coefficient phase $\angle\Delta\rho$ (linear model) and its gradient over frequency (detuned; resonance boosted 50 % and shifted by 75 MHz).

In order to assess the influence of assembly tolerances and tag detuning on the error of MFCW ranging, several parameter sweeps have been performed and published in [128] along with the validation of the reflection coefficient model. Two of these sweeps are briefly discussed below. The first sweep varies the assembly impedance over the range shown in Fig. 4.19(a) and covers perfect assemblies through completely messed-up ones. The second sweep investigates typical tags with good to medium flip-chip assemblies in combination with detuning up to levels that occur if tags are placed in the vicinity of water. The corresponding model parameters are shown in Fig. 4.19(b). A description of these parameters and their effect on the reflection coefficient (model) can be found in Section 3.3.1.

The simulations assume a transmit power level of 3.28 W EIRP (limit for the EU; EIRP: equivalent isotropically radiated power) and a reader sensitivity of -80 dBm⁴³. The employed channel model is a free-space path loss model (path loss factor $\xi = 2$) and the frequency spacing used is $\Delta f = 10$ MHz.

⁴³ It is important to limit the receiver sensitivity here, since the phase of a complex value is subject to extremely fast changes at zero crossings of the magnitude.

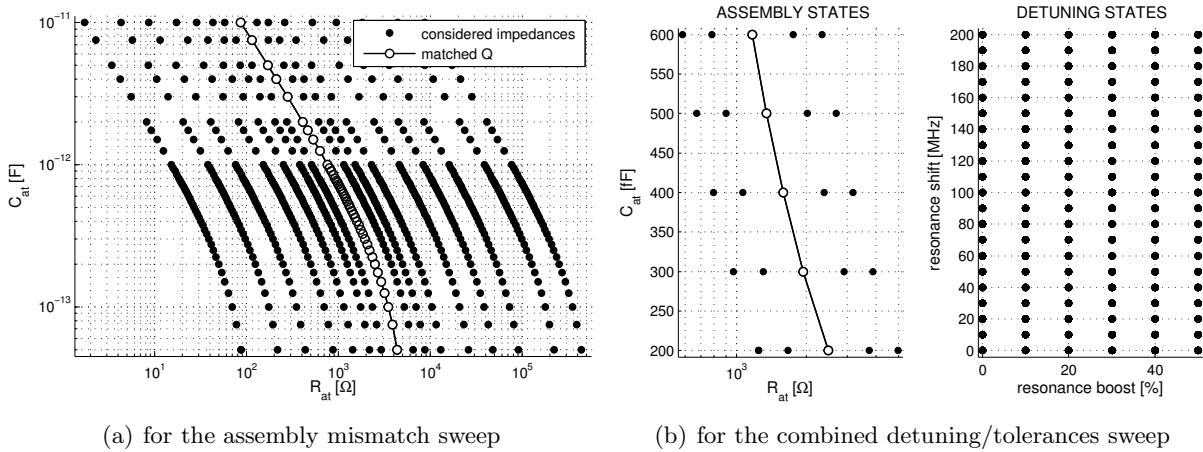


Figure 4.19: Simulated assembly mismatch and antenna detuning states. (©2010 IEEE, [128])

Fig. 4.20 shows cumulative distribution functions of the mean absolute error over frequency for both sweeps. The error has a distinct minimum around 960 MHz if only assembly tolerances are considered, see Fig. 4.19(a). At this point the shapes of antenna and chip reactance are similar, thus creating a flat phase that is virtually independent of assembly mismatches (cf. Fig. 3.16 on page 84). Conversely, the largest errors can be observed at frequencies well above and below the UHF RFID frequency ranges. This is consistent with the location of the hot spots in Figs. 4.17(b) and 4.18(b) and proves that the range error introduced by the tag can be minimized by proper tag design (wideband matches). Also using less resonant tags will decrease the error, cf. [135, Fig. 3].

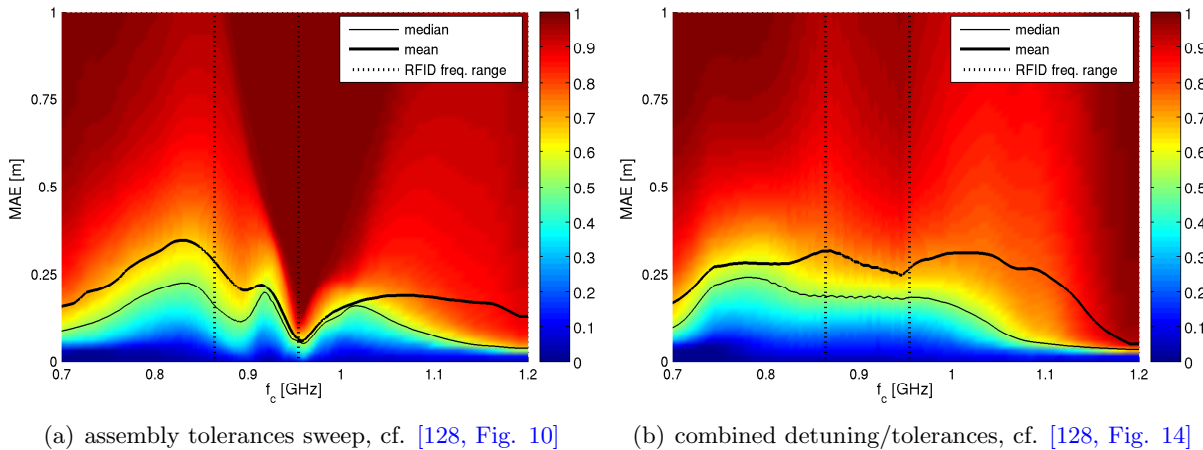


Figure 4.20: CDFs of the mean absolute ranging error (MAE) over frequency (for all distances). 2FCW carrier frequency offset $\Delta f = 10$ MHz.

Detuning near metal/water in combination with a resonant tag design, on the other hand, potentially causes large errors over the entire frequency range due to frequency shifts introduced by antenna detuning. The bulk of tags will experience up to medium detuning (close to water) as well as some assembly mismatches. This combination was simulated for the CDF in Fig. 4.20(b). Since detuning is able to shift the hot spots all over the frequency range, the error is largely

uniform over all RFID frequency bands. While median and mean value of the error are below 30 cm within 860–960 MHz in this scenario, the peak errors are well above one meter.

The overall CDFs for the three most common UHF RFID frequency bands⁴⁴ are shown in Fig. 4.21(a). For the simulated NXP tag and the considered range of detuning and assembly mismatches, errors caused by detuning are mostly below 60 cm, with (very unlikely) peak errors of a few meters. The error caused by the tag’s reflection coefficient phase is also virtually independent of the carrier frequency offset, cf. Fig. 4.21(b). This holds for offset frequencies at which the differential phase is still approximately linear with frequency, cf. (4.15)–(4.19).

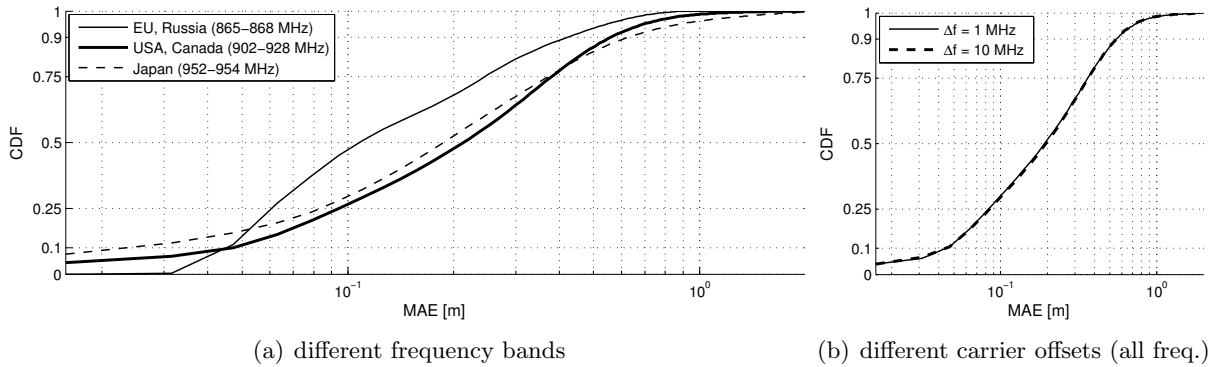


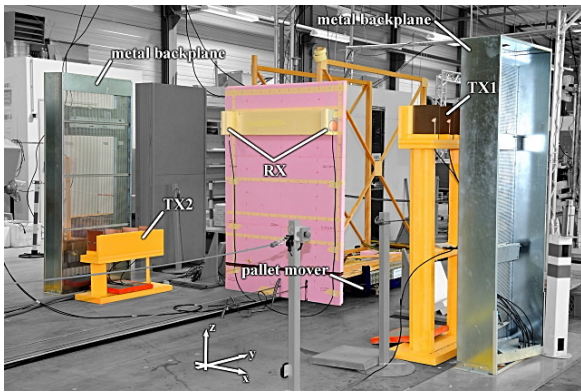
Figure 4.21: Overall CDFs of the mean absolute ranging error (MAE) for the combined detuning/tolerances simulation.

To sum up, the error caused by detuning is considerably smaller than the error caused by multipath propagation, with the exception of “unlucky detuning”, where the MFCW carriers hit a peak in the differential reflection coefficient’s phase. Mean and median of the mean absolute error are well below 50 cm and within limits independent of the frequency offset.

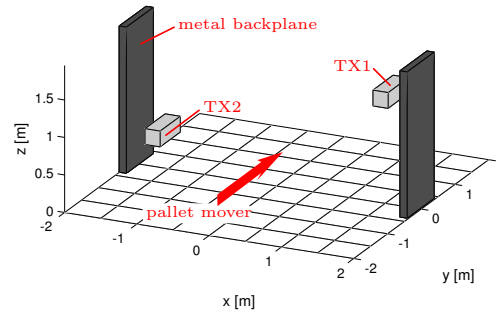
⁴⁴ This is not a weighting with respect to importance; the shown bands simply cover the worldwide UHF RFID bands, e.g., 920–925 MHz for Thailand, 918–926 MHz for Australia, ... [3, p. 34].

4.2.3 Measurement Results

The performance of multi-frequency-based ranging was also evaluated based on measurements. Since multipath propagation is the dominant source of errors and thus the main limiting factor for MFCW ranging, a detailed analysis with respect to multipath propagation is presented below. The base data for this analysis are the channel transfer functions obtained during the portal measurements discussed in Section 2.3.3. A photograph along with a generic schematic of the measurement setup is shown in Fig. 4.22. See Section 2.3.3 and [132] for channel-specific analyses of this environment, also with respect to narrowband ranging. Please note that the carriers and the tag modulation sidebands are assumed to be fully coherent here, i.e., $H_{mi} = H_i = H_{im}$. This requires very low modulation frequencies (low kHz range).



(a) photograph (empty portal), cf. [137, Fig. 3]



(b) schematic (viewpoint of plots below)

Figure 4.22: Photograph and schematic of the “NXP gate” measurements (see Section 2.3.3).

Theory and simulations suggest that MFCW (like any other narrowband method) requires a dominant LOS path and as little multipath propagation as possible – two prerequisites that are far from being met in UHF RFID portals, cf. Section 2.3.3. Let us thus start this analysis with the most obvious question: will a straightforward implementation work? Fig. 4.23 shows the corresponding range errors for a single 2FCW estimate per position (10 MHz carrier spacing).

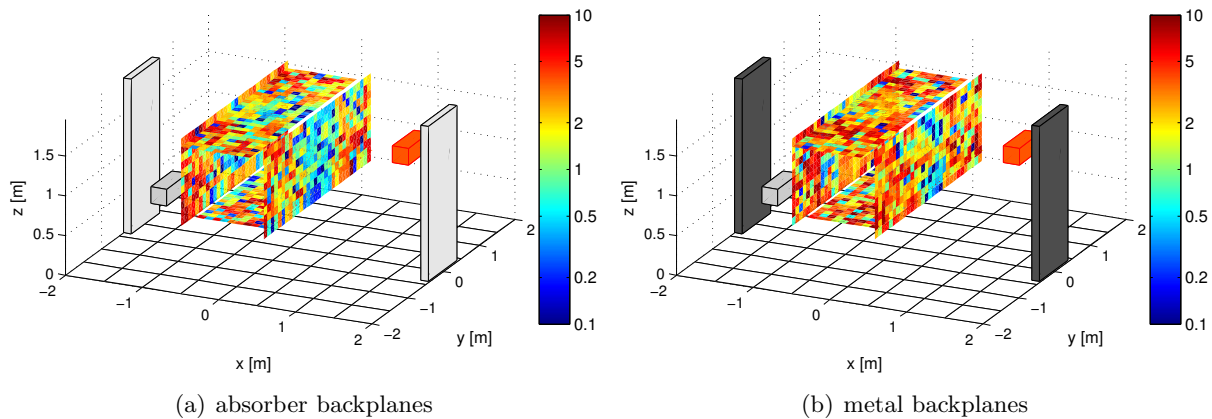


Figure 4.23: Absolute error [m] for a single 2FCW range estimate per position for metal and absorber backplanes ($f_1 = 915$ MHz, $f_2 = 925$ MHz). The top right transmitter is active (marked orange).

Obviously, the error is considerable. It ranges from below 0.5 m inside the portal with absorber backplanes when the tag is directly in front of the active transmitter to 10 m outside the portal. Switching to metal backplanes decreases the performance inside the portal to the point where only a few “sweet spots” are consistently below an error of 1 m. The error then appears to be almost uniform over the entire portal, with distance estimates ranging from 10 cm to 10 m (for the true distances below 3 m).

To answer the question: no, a single 2FCW range estimate is obviously not sufficient in the portal environment. Consequently, several estimates have to be combined in order to reduce the influence of multipath propagation and thus to reach acceptable levels for the error. This can be achieved with carriers at different frequencies, over time, or from different positions. Since MFCW already works with multiple carriers in the frequency domain, the most obvious choice here is frequency diversity, i.e., the combination of several 2FCW estimates obtained at different frequencies. Regardless of the type of diversity employed, the achievable overall error depends on the statistics of the individual estimates, provided that they are largely independent. We will thus have a closer look at the statistics of such 2FCW estimates.

Fig. 4.25 shows the bias of 2FCW estimates for metal and absorber portal setups (frequency spacing: 10 MHz). As predicted by the simulations, the ranging error is unbiased up to medium K-factors and RMS delay spreads (such as the values inside the portal, cf. [132]). A slight bias of roughly 50 cm can be observed outside the absorber portal. This bias is increased to up to 2 m when installing metal backplanes instead of the absorbers. Note that also the width of the bias-free zone inside the portal decreases in comparison to the absorber portal.

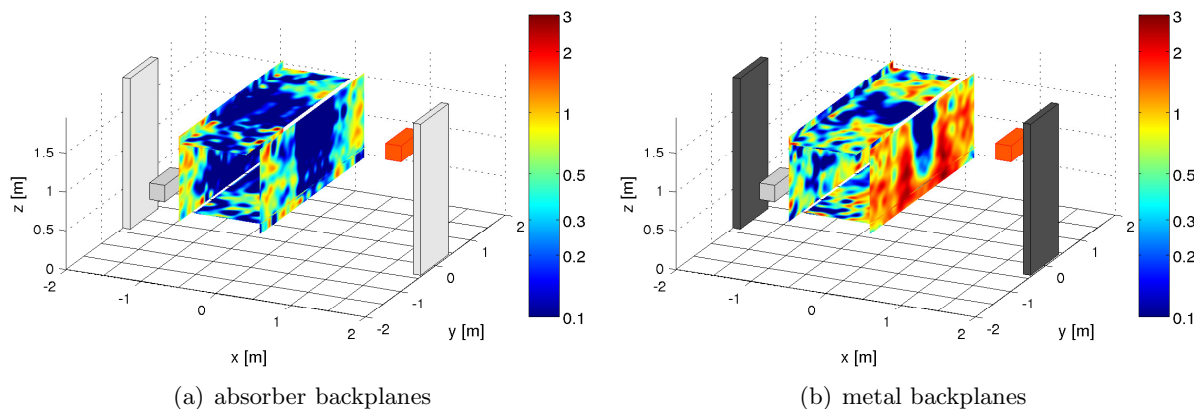


Figure 4.24: Bias [m] of 2FCW range estimates for metal and absorber backplanes. Carrier frequency spacing $\Delta f = 10$ MHz. The top right transmitter is active (marked orange).

The standard deviation in Fig. 4.25 shows an even more pronounced difference in performance between the metal and the absorber portal. The standard deviation increases from 0.75–1.5 m at the center of the absorber portal to above 2–3 m for the metal one. Reducing the standard deviation to below 50 cm inside the portal thus requires $(1.5/0.5)^2 = 9$ independent estimates for the absorber portal and at least $(3/0.5)^2 = 36$ estimates for the metal gate⁴⁵. The standard deviation outside the portal is consistently in the range of 5 m, which indicates an almost uniform distribution of the error⁴⁶. Averaging over multiple estimates again reduces the standard deviation, but does not result in an unbiased overall estimate. For comparison: Fig. 4.24 shows the average of 400 (not fully independent) estimates.

⁴⁵ Averaging over N estimates with independent errors reduces the variance by a factor of N .

⁴⁶ $1/\sqrt{12} \cdot c/\Delta f = 8.6$ m is the standard deviation of a uniform distribution for this frequency spacing (cf. [192])

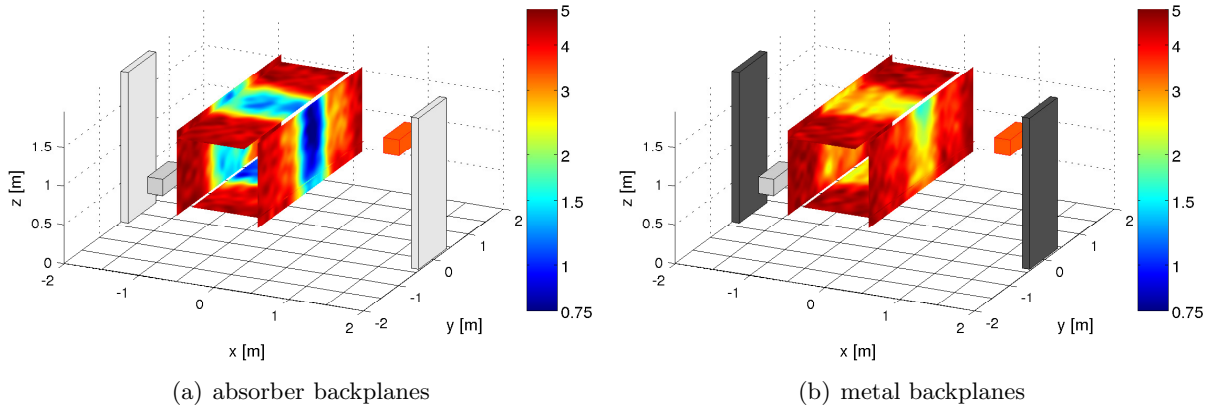


Figure 4.25: Standard deviation [m] of 2FCW range estimates for metal and absorber backplanes. Carrier frequency spacing $\Delta f = 10$ MHz. The top right transmitter is active (marked orange).

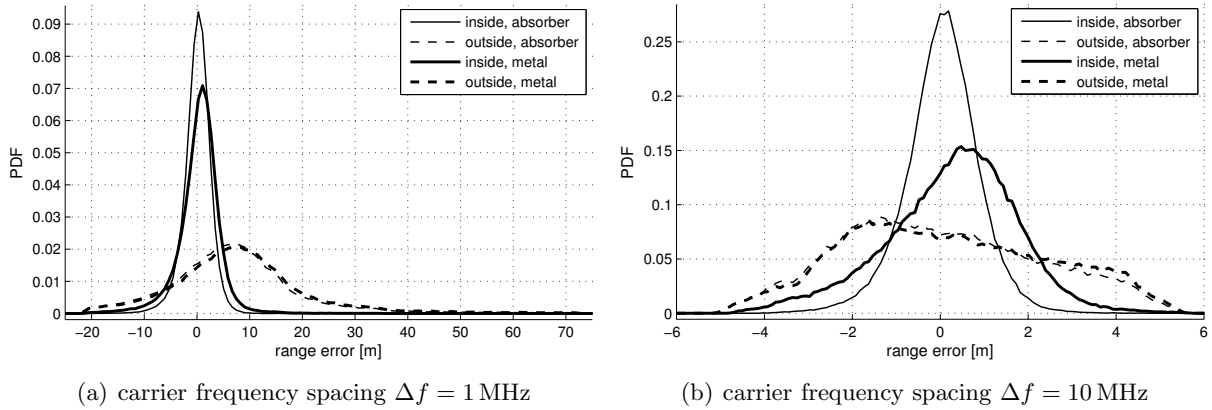


Figure 4.26: Probability distribution functions (PDFs) of the error for a single 2FCW estimate inside/outside the portal for absorber/metal backplanes and for different carrier frequency offsets (TX1).

Overall distributions of the error are shown in Fig. 4.26 for carrier spacings of 1 and 10 MHz. Several observations can be made based on these distributions:

1. The errors are too high to use a single 2FCW estimate for ranging purposes in this environment. Nonetheless, accurate localization inside the portal is possible if several estimates can be combined. This is not possible outside the portal, where the bias prevents accurate pinpointing of the tag. In theory, the bias can be corrected if K_{LOS} and τ_{RMS} are known or if calibration measurements are available. This will, however, be hard to achieve in any practical scenario due to time-variance and location dependence of all parameters.
2. While the bias may prevent localization, it helps in classification: The distributions of the error inside and outside the portal can be fully separated if their standard deviations are reduced. Since the bias of approximately 7 m is larger than the portal width, even tags at close range to the transmitter can be properly classified into inside/outside the portal.
3. The type of backplane has negligible influence on ranging performance outside the portal. This can be tied directly to K_{LOS} and τ_{RMS} , on which the choice of backplanes has only a minor effect [132]. Inside the portal, on the other hand, both bias and standard deviation increase considerably for metal backplanes compared to absorbing material. Again, this is connected to K-factor and RMS delay spread, cf. [132].



4. As already predicted by the simulations, the estimates for small carrier spacings are highly biased and have a considerable standard deviation, also inside the portal. Higher frequency spacings (10 MHz) lead to a smaller standard deviation inside the portal, at the cost of an almost uniformly distributed error outside (cf. Fig. 4.15). All this can be traced back to the coherence bandwidth: outside the portal, the 90% coherence bandwidth is below 3 MHz even for the individual channels to/from the tag [132]. Essentially, the two carriers with $\Delta f = 10$ MHz thus experience two different channels, making a comparison between their phase shifts useless. Conversely, the coherence bandwidth inside the portal is mostly well above 10 MHz for the absorber portal, making range estimation at $\Delta f = 10$ MHz feasible.
5. The error is indeed roughly Gaussian for measured channels as well, provided of course that the maximum unambiguous range is not reached (high K-factor, low RMS delay spread).

All plots above have been generated for the top right transmitter, TX1. Compared to the transmitter near the floor (TX2), TX1 better illuminates the measurement planes and projects less energy towards the floor, see Fig. 4.27. As a consequence, TX1 is better suited to ranging than TX2. This is illustrated in Fig. 4.28, where CDFs of bias and standard deviation inside the portal are shown for both transmitters. The error is considerably higher for TX2 than for TX1.

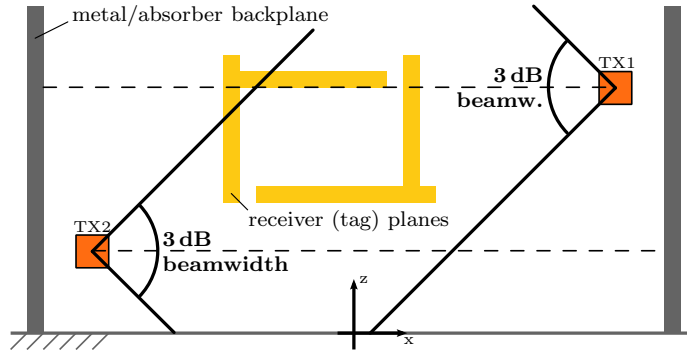


Figure 4.27: Illustration of the portal with receiver planes and transmitter directivity (roughly to scale).

To sum up, the measured bias for the 10 MHz spacing is below 1 m for the absorber portal, but increases considerably for the metal backplanes. In the worst case, it reaches 5 m (TX2). The standard deviation is mostly above 1 m, with an additional increase by a factor of two on average for the metal portal compared to the absorber backplanes. Nonetheless, the critical limit of a uniform distribution (8.6 m for this configuration) is not reached inside the portal. It is, however, reached outside, cf. Fig. 4.26.

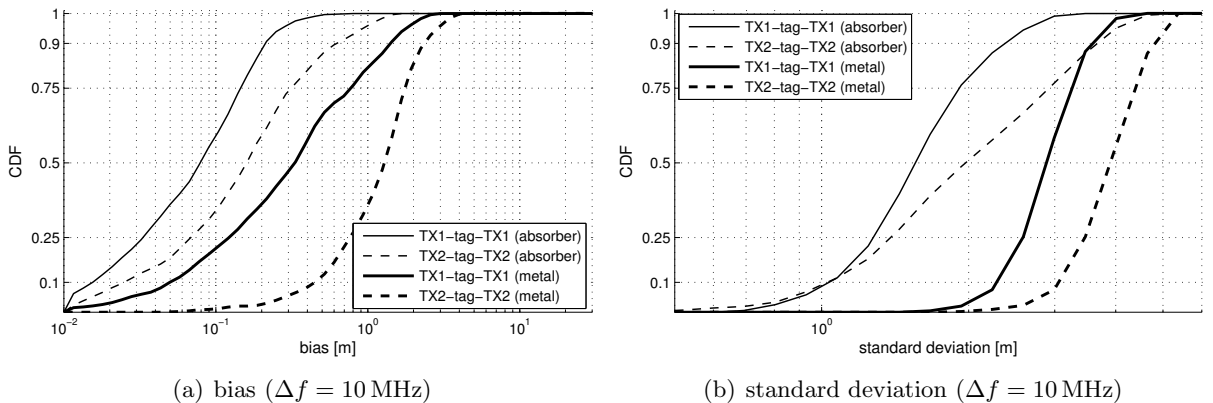


Figure 4.28: Cumulative distribution functions (CDFs) of the error for a single 2FCW estimate *inside* the portal for absorber/metal backplanes and for different transmitters (cf. Fig. 4.27).

4.3 Summary

Narrowband methods are relatively easy to implement and maintain, and are (optionally) able to work within the existing UHF RFID standard and spectral masks. This includes RSS-based methods, phase-based methods using the rotation of the constellation diagram, phased arrays, and stepped-frequency continuous-wave radar. Additional transmit signals (multiple or frequency-modulated carriers) violate the standard but deliver better instantaneous range/position estimates.

The main drawback of all narrowband methods is their vulnerability to multipath propagation. In order to reach acceptable levels of errors in indoor multipath environments, several range estimates have to be combined. This can be done in the time domain (tracking), in the frequency domain (multiple carriers / carrier groups), or in the spatial domain (several receiver antennas).

Among the narrowband methods, multi-frequency continuous-wave (MFCW) radar has been discussed in detail. The system evaluates the phase between multiple carriers in order to determine the range to the tag. An implementation using frequency hopping instead of parallel transmission of multiple carriers is also possible, although this requires estimating the tag modulation phase shift and introduces additional errors. To sum up, the narrowband MFCW system is;

- + simple and (relatively) cheap to implement. Frequency hopping enables its application within Gen-2 (but at the cost of robustness and speed);
- + (within limits) immune to tag modulation frequency instabilities, since only the component selection filters have to be widened to compensate (at the price of an increased noise floor). Frequency drifts can also be easily compensated if the carriers are transmitted in parallel;
- + (within limits) robust to feedback, since any unmodulated feedback is mapped to DC (direct current; 0 Hz) and can be filtered. In addition, active feedback suppression systems such as the ones used for UHF RFID (e.g., [229–231]) are effective;
- + robust to noise, because high processing gains can be achieved (long averaging times with respect to the narrow bandwidth);
- vulnerable to differential phase shifts introduced by the tag, since a model-based compensation is not possible in practical scenarios (cf. [135]);
- vulnerable to multipath propagation, since the LOS component cannot be isolated, i.e., the estimated range is based on the instantaneous group delay and thus depends on the entire channel impulse response; and
- vulnerable to stray and over-range reads, since these reads are typically outside the main-lobe of the transmitter(s) and thus have extremely low K-factors and high RMS delay spreads. (This leads to high errors with any narrowband localization method.)

A practical implementation in multipath environments like warehouses or salesfloors thus has to use averaging and tracking in order to gain robustness. A possible (suggested) implementation combining all available methods of averaging is as follows. The base of this system is multi-carrier ranging using distributed carrier triplets, as illustrated in Fig. 4.29. Each triplet provides two distance estimates (one for each carrier spacing). Different carrier spacings are used in order to account for different multipath conditions (as discussed in Section 4.2.2). Estimates of different triplets are uncorrelated due to the large frequency spacing between the groups (exceeding the coherence bandwidth). This provides independent estimates in the frequency domain. In addition, the signal is received by several antennas deployed throughout the read zone, thus providing spatial diversity. Using the 2.45 (or 5.8) GHz ISM bands for ranging carriers would allow for cheap and small reader antennas; arrays are also considerably cheaper in this frequency

range than in the UHF RFID bands⁴⁷. Tracking covers the last remaining dimension: time. A speed estimate using the method discussed in [46] can be used as an additional input for the tracking algorithm. Finally, all estimates are combined using particle filtering.

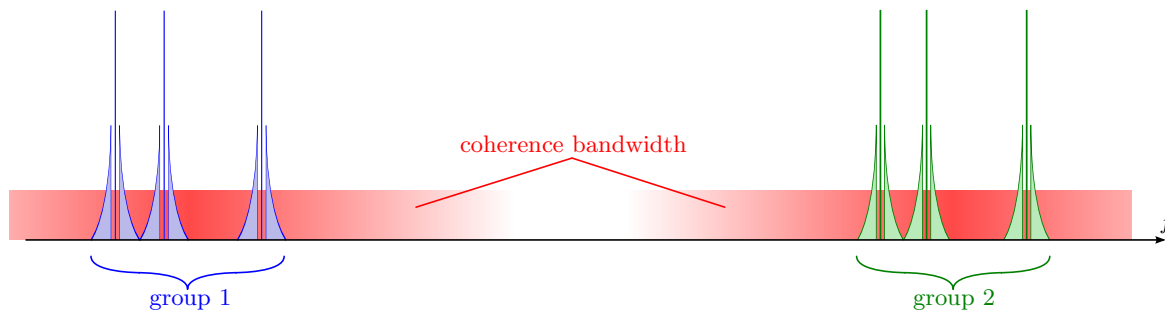


Figure 4.29: Distributed carrier triplets: 2×3 FCW spectrum.

⁴⁷ The high(er) attenuation/noise in license-free ISM bands should not pose a critical problem, since transmit power levels are high for RFID applications in all ISM bands and long-term averaging over the entire tag response is possible.

5

(Ultra-)Wideband UHF RFID Tag Ranging

Wideband and ultra-wideband (UWB) ranging methods are a big step from classical UHF RFID and are thus often viewed with suspicion. The potential reward is extremely accurate ranging, an inherent resilience to multipath propagation especially for ultra-wide bandwidths, and almost complete decoupling of protocol and ranging signals. On the downside, wideband and UWB ranging come at the cost of complex hardware for reader and tag. The reader needs to be able to generate and receive signals with (ultra-)wide bandwidths, which is more complex and more expensive than transmitting/receiving narrowband signals. At the same time, the tag needs to be able to modulate this signal, i.e., the reflection coefficient has to be controlled in a suitable frequency band and over a large bandwidth. This requires a new tag design, since classical UHF RFID tags do not meet these requirements.

This chapter discusses the possibility of using wideband and UWB ranging methods for the localization of passive UHF RFID tags. Section 5.1 gives an overview and discusses methods and properties. A basic proof of concept for impulse-radio (IR) UWB ranging using lab equipment is provided in Section 5.2. Measurement-based accuracy bounds for wideband and ultra-wideband ranging in a UHF RFID portal are given in Section 5.3. Finally, implementation issues and possible obstacles and pitfalls are discussed in Section 5.4.

5.1 Basics and Ranging Methods

parts of this section have been published in [136]

Wideband and ultra-wideband ranging methods work in a frequency range different to the one occupied by Gen-2 UHF RFID. Typical frequency bands for (ultra-)wideband systems are the 2.45 GHz or 5.8 GHz ISM bands, or the UWB frequency range of 3.1–10.6 GHz⁴⁸ (as opposed to 860–960 MHz for Gen-2 UHF RFID). The lower transmit power levels and the completely different frequency bands ensure that tags (and standard Gen-2 readers) are not affected by the ranging signals in any way. As a consequence, wideband and ultra-wideband ranging methods are able to operate in parallel to the established Gen-2 protocol.

The basic principle of operation for wideband and UWB ranging is shown in Fig. 5.1 using IR-UWB as an example. The radar setup emits an (ultra-)wideband signal which is reflected

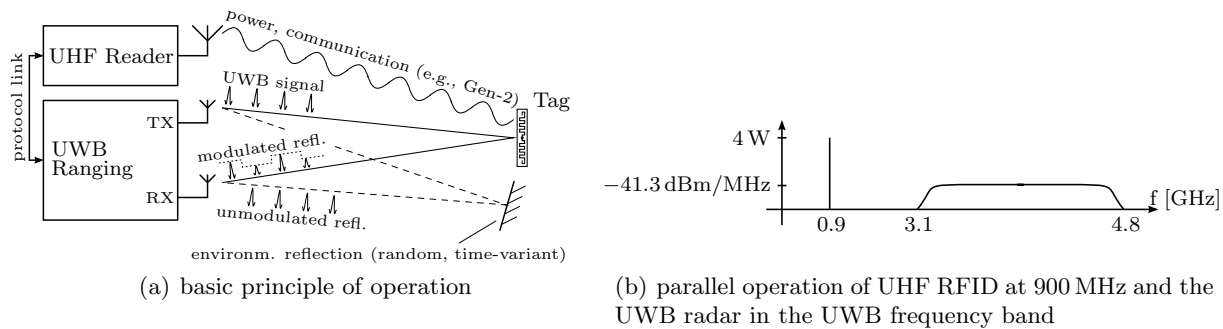


Figure 5.1: Basic principle of operation for UWB ranging systems using an impulse-radio UWB radar as example. (©2010 IEEE/IET, [136])

by the tag during normal operation. Separation from the generally time-variant environment (decluttering) is performed by detecting the backscatter modulation in the received UWB signal. Tag modulation in the UWB frequency range can be enabled by using two distinct antennas and modulation transistors for UHF and UWB, as shown later in this chapter. It is important to note that the tag does not process the UWB signal sent by the reader in any way. Consequently, the system requires only minimal changes in tag design and does not drain the tag’s power supply. Note that this method is different from semi-active UHF/UWB tags, which actively transmit a UWB signal. See Section 5.1.3 for a short overview of such UHF/UWB hybrids.

Candidate frequency ranges for wideband and ultra-wideband UHF RFID tag localization are listed in Tab. 5.1, including permitted transmit power levels, bandwidths, and the corresponding spatial resolutions.


| Frequency Band [MHz] | BW [MHz] | Resolution [m] | TX Power [dBm/MHz] | System |
|-------------------------|-------------|-------------------|-----------------------|--------------|
| 2400 – 2480 | 80 | 1.8 | –9 | FMCW |
| 5725 – 5875 | 150 | 1.0 | –8 | FMCW |
| 3100 – 10600 | ≥500 | ≤0.6 | –41.3 | IR-UWB, FMCW |

Table 5.1: Frequency bands and spatial resolution for wideband and ultra-wideband ranging. Permitted TX power levels are simplifications; see [232, 233] for details on spectral regulations in Europe and the United States.

⁴⁸ subject to local regulations

In contrast to narrowband ranging methods, the spatial resolution of (ultra-)wideband methods is typically below the maximum range of UHF RFID systems. This resolution is an upper bound on the ranging error if (and only if) the LOS component is correctly identified. It can be calculated via

$$d_{\text{res}} = c/(2B) \quad (5.1)$$

where c is the speed of light and B is the signal bandwidth. Considerably lower errors than suggested by this bound can be reached if the LOS is well isolated and the noise level is low, cf. [76, 82]. Unfortunately, as there are reflectors within a few centimeters of the tags (e.g., the products on which the tags are placed), the LOS is rarely fully isolated in UHF RFID systems even with several GHz of bandwidth (see Section 5.3). Consequently, d_{res} is not necessarily an upper bound on the error in UHF RFID ranging. See Section 5.3 and [137] for details. 

5.1.1 Signal Analysis Method for Impulse-Radio Ultra-Wideband Ranging

IR-UWB ranging works by detecting the time variance caused by tag modulation in the channel impulse response (CIR), as illustrated in Fig. 5.2. While modulating, the tag essentially switches

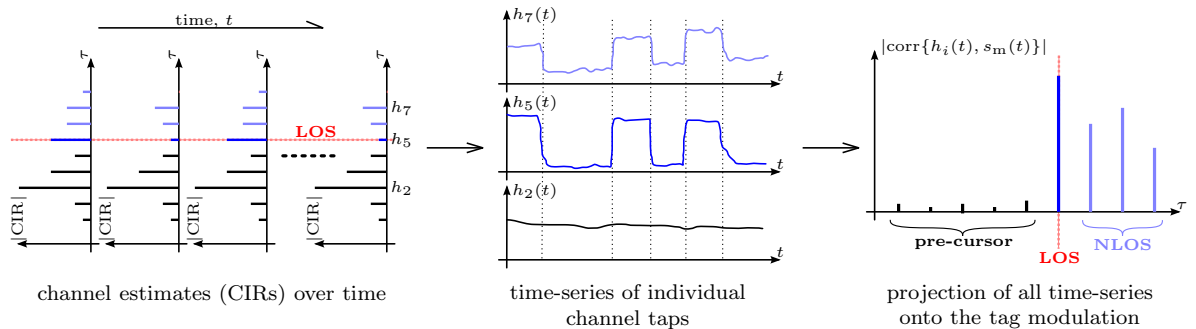


Figure 5.2: Analysis method for IR-UWB ranging. The development of each channel tap over time $h_i(t)$ is correlated with the known tag modulation signal $s_m(t)$. The first arriving component that shows this modulation is the LOS distance.

between match (little reflection) and mismatch (large reflection). As a consequence of this backscatter modulation, the tap of the CIR that corresponds to the shortest path to the tag and subsequent taps (multipath propagation on the return link) will show the modulation. This known time-variance can be detected by evaluating each multipath component over time. The protocol link to the reader ensures that the tag reply is known to the UWB radar and thus can be used for the detection of the backscatter modulation in the CIR, cf. Fig. 5.1(a). The detection of the tag reply can for example be performed by filtering (correlating) the recorded channel taps over time with the known tag reply. Any time-variance that is not caused by the tag modulation is attenuated by the filtering. No special ranging signals are necessary for this method, since the correlation can be performed with any tag reply. Finally, because the recorded tag reply is used for the correlation, the tag's frequency instability (cf. [1]) does not pose a problem.

Preliminary proof-of-concept measurements for this method can be found in Section 5.2. Fig. 5.3 shows an example based on these measurements. The left plot shows the recorded PDPs for matched and unmatched states of the tag antenna while the right plot shows the extracted differences. The dashed line in both plots marks the true backscatter path length. As can be seen, the profiles start to differ at the shortest path to the tag.

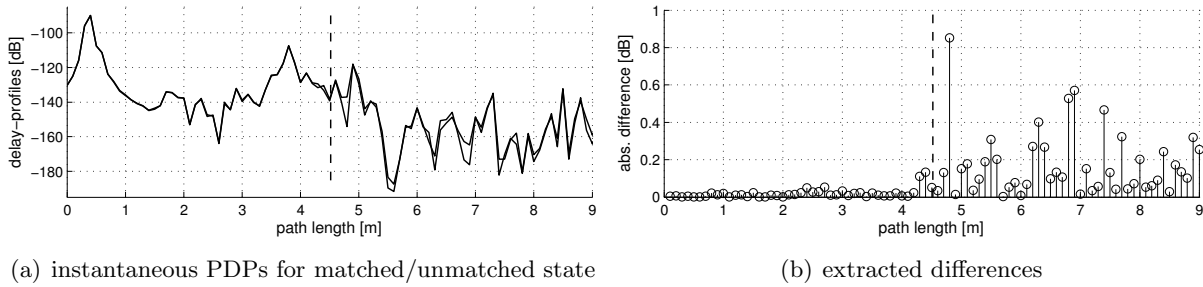


Figure 5.3: Example PDPs and modulation extraction for the IR-UWB method, based on the proof-of-concept measurements discussed in Section 5.2. The difference in the PDP plot (a) has been increased by a factor of 20 to increase visibility; plot (b) shows the true difference.

5.1.2 Signal Analysis Method for FMCW Radar

Frequency-modulation continuous-wave (FMCW) systems operate by sending a chirped carrier that is at the same time used for demodulation of the received signal. The propagation delay for the received signal creates a frequency offset between the demodulation signal and the received signal, with longer propagation delays leading to a higher frequency offset. This principle is illustrated in Fig. 5.4. The power-delay-profile is thus mapped to a frequency range of a few

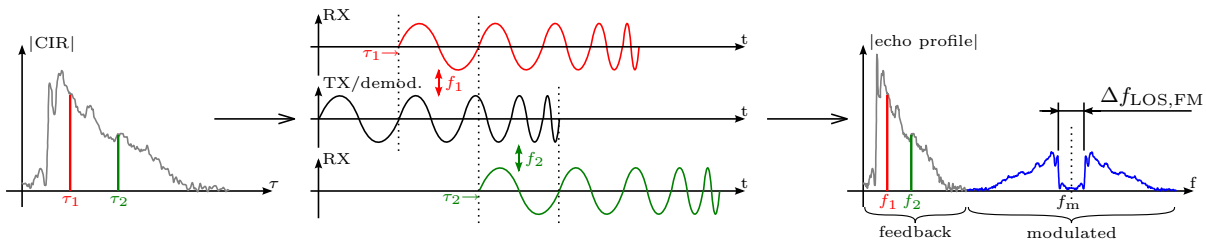


Figure 5.4: Principle of FMCW ranging. The chirped signal maps propagation delay (τ) to the frequency domain, forming the echo profile. Modulation creates “sidebands” of the backscatter CIR in the echo profile, centered around the modulation frequency f_m . The spacing between the upper and the lower “sideband” corresponds to the LOS distance.

kHz (depending on the sweep properties), forming the echo profile. Assuming, for example, a linear (sawtooth or triangle) frequency sweep covering a bandwidth of $B_{\text{FM}} = 100$ MHz within a sweep time of $T_{\text{FM}} = 1$ ms, the mapping of delay τ to frequency f is

$$\Delta f / \Delta \tau = B_{\text{FM}} / T_{\text{FM}} = 100 \text{ Hz/ns}. \quad (5.2)$$

The corresponding time-domain signal can be sampled with high resolution, since only sampling frequencies in the MHz-range are required for feasible sweep rates and indoor propagation delays, cf. [80, 193]. A continuous sinusoidal backscatter modulation creates two “sidebands” of the backscatter channel impulse response in the echo profile, centered around the backscatter modulation frequency f_m . The spacing between the upper and the lower “sideband” corresponds to the LOS distance between the transmitter/receiver antenna and the tag [73, 78],

$$d_{\text{LOS}} = \frac{c \Delta f_{\text{LOS,FM}} T_{\text{FM}}}{4 B_{\text{FM}}}. \quad (5.3)$$

Both sidebands are used here because the modulation frequency of the tag has high tolerances (up to 22%, [1]) and is thus unknown.

A thorough derivation of FMCW radar can for example be found in [78]. Extensions to semi-passive UHF backscatter transponders have been published in [67, 71, 73]⁴⁹.

⁴⁹ The transponders in these papers feature a stable continuous modulation. This is not possible with fully passive UHF RFID transponders, cf. [1]. [73] additionally uses a cable as channel to the transponder.

5.1.3 Semi-Active UHF/UWB Hybrids

Semi-active tags obtain their power from the field, but transmit actively, i.e., not by backscatter modulation⁵⁰. Typically the uplink (tag→reader) is replaced by the UWB link, while energy harvesting and the downlink (reader→tag) remain in the RFID band. A UHF/UWB hybrid system is currently being developed at the KTH in Sweden [97–99, 189, 234, 235], for example. A similar system is also used by the US company Tagent⁵¹ (first announced 2009). Tagent’s chips have integrated antennas and harvest energy at 5.8 GHz, while transmitting data in an ultra-wide bandwidth at 6.7 GHz.

5.2 Impulse-Radio Ultra-Wideband: Proof-of-Concept

The first proof-of-concept measurement for the above-mentioned IR-UWB method has been performed in the SPSC’s RF-lab, an enclosed room similar to the SPSC Salon, cf. Fig. 2.18. The room has three concrete and one plasterboard wall, and contains several highly reflective surfaces such as large metal conduits, reflective windows, and a large whiteboard. A floorplan and a photograph of the setup can be found in Fig. 5.5. The antennas used for this measurement

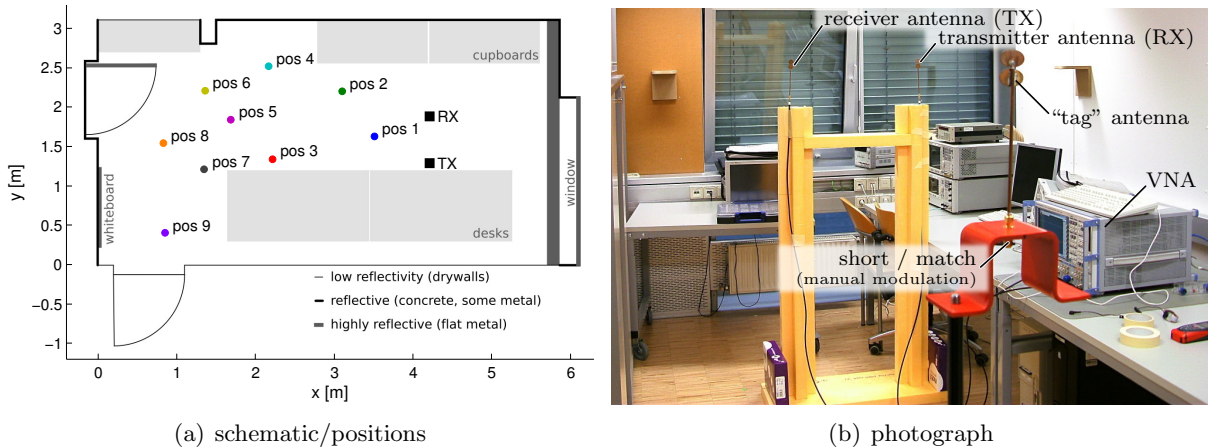


Figure 5.5: Measurement setup for IR-UWB proof of concept. Nine “tag” positions inside SPSC’s RF-lab are analyzed using a network-analyzer-based setup (small room; semi-industrial).

are omnidirectional UWB batch antennas, see [236, Fig. B.5(a) on p. 86]. Two such antennas are connected to a VNA, functioning as transmitter and receiver (3–6 GHz). A third patch antenna acts as the “tag” antenna. As UHF RFID tags with an additional UWB antenna were not available at the time of the measurements, the tag modulation was simulated by manually switching between short and match at the “tag” antenna port.

Measuring short and match independently is not an ideal setup. The ever-present slow time-variance of wireless channels (small movement, temperature drifts, ...) cannot be suppressed in the extracted multipath components for such measurements. Moreover, the necessity to exchange short and match terminators at the antenna ports makes entering the room and long measurement cycles necessary. Both increase the noise caused by time-variance. On the other hand, the VNA features a dynamic range that cannot be reached with UWB receivers (see Section 5.4.2). The presented measurements should thus be seen as qualitative results only.

⁵⁰ Conversely, semi-passive tags are battery-supplied, but transmit data via backscatter modulation.

⁵¹ <http://www.tagent.com>

The extracted modulation information for the first six positions is shown in Fig. 5.6. As explained above, the estimated LOS distance corresponds to the first component that shows the modulation and is thus significantly above the noise floor. The choice for the first two positions is obvious and the error is minimal. For all the other positions, the chosen component would likely not be the true LOS path. For position 5, for example, the component at 5.5 m would likely be chosen, thus leading to an error of 40 cm (8%). Note that this error exceeds the spatial resolution of this system (3 GHz bandwidth \Rightarrow 10 cm resolution).

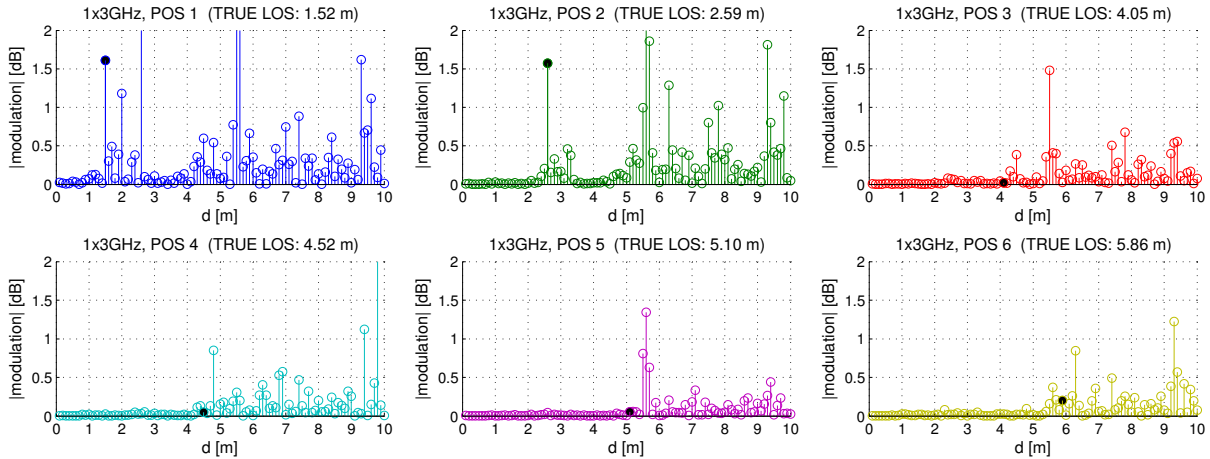


Figure 5.6: UWB signal analysis for positions 1–6 (good to medium K_{LOS}). The first significant component is the estimated distance; the true LOS distance is marked by a filled stem. Bandwidth: 3 GHz.

A benefit of IR-UWB ranging is the possibility to trade resolution for robustness. Positions 8 and 9, for example, are close to two major reflectors (whiteboard and door); the LOS to position 9 is additionally blocked in part by a computer screen. As a consequence, the LOS to position 9 in particular is hard to detect with the full bandwidth of 3 GHz, cf. Fig. 5.7 (upper row). Reducing resolution solves this problem, as demonstrated by the lower row of Fig. 5.7. Here the

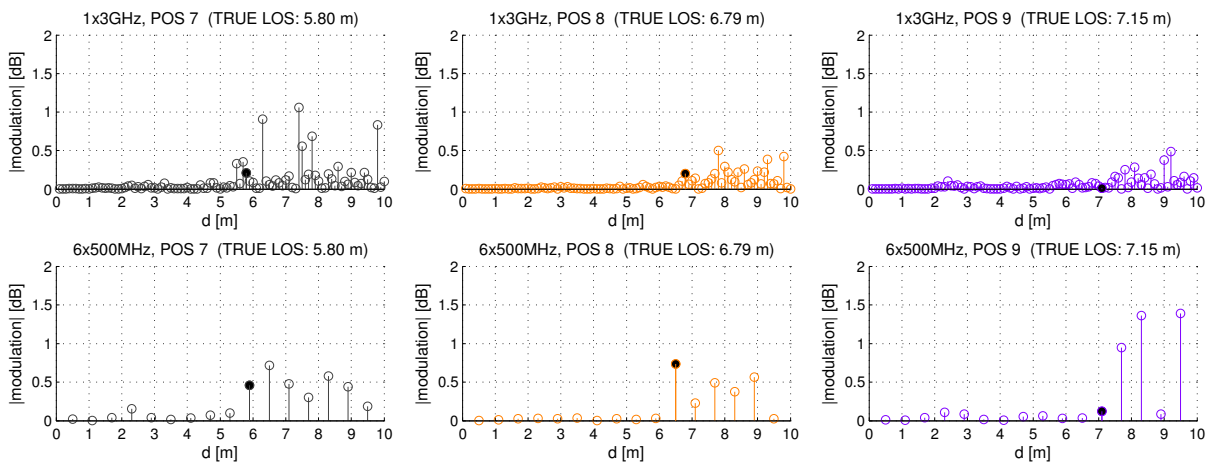


Figure 5.7: UWB signal analysis for positions 7 through 9 (bad K_{LOS}). The first significant component is the estimated distance; the true LOS distance is marked by a filled stem. Upper row plots: bandwidth 3 GHz. Lower row plots: average of six sub-channels with 500 MHz each.

full bandwidth of 3 GHz (10 cm resolution) is separated into six sub-channels with 500 MHz each (resolution: 60 cm). The sub-channels are subsequently averaged, which boosts the modulation components. In essence, the system can adaptively increase its dynamic range by sacrificing resolution.

5.3 Ranging Accuracy in Portal Applications

The following performance analyses for FMCW and IR-UWB ranging are based directly on the portal measurements discussed in Section 2.3.3. A photograph and a generic schematic of the measurement setup are shown in Fig. 5.8. See Section 2.3.3 and [132] for channel-specific analyses of this environment.

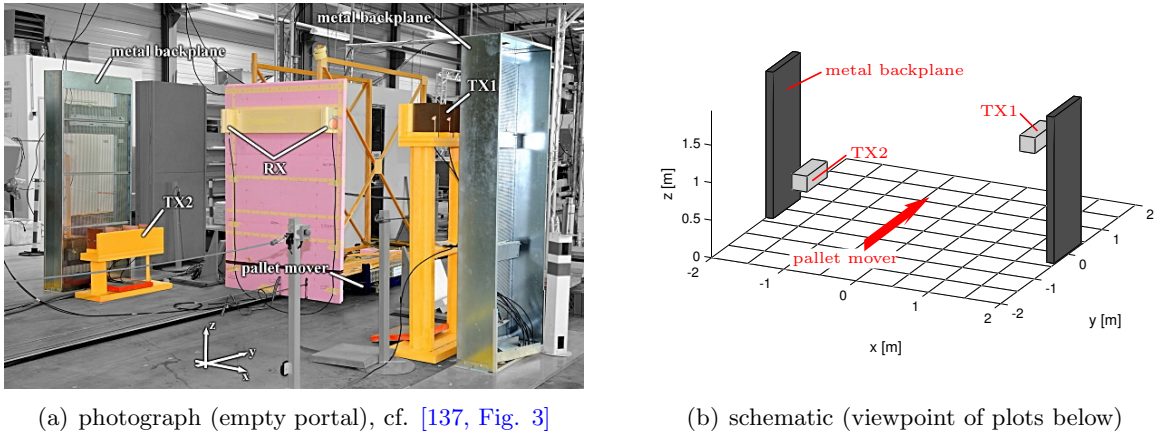


Figure 5.8: Photograph and schematic of the “NXP gate” measurements (see Section 2.3.3).

The channel measurements have an extremely high dynamic range of at least 100 dB (max. 125 dB, see [237]) and also a very low noise floor (around -150 dBm), cf. Section 2.3.1. The presented results should thus be seen as lower bound for the error that is reached for long-term averaging (high processing gain) and perfect feedback suppression. Results for IR-UWB ranging have been taken directly from the LOS detection on the backscatter channel, cf. [131], while results for FMCW ranging are simulation-based, using the measured transfer functions but neglecting noise. The simulations have been performed by Gang Li, a PhD student at the Institute of Electrical Information Technology (IET) of Clausthal University of Technology⁵². Further results have been published in a joint paper between IET and SPSC [137].

The portal environment is characterized by strong reflections close to the tag. The most prominent reflectors are the backplanes (especially in case of metal backplanes) and the floor, cf. Sections 2.2.1 and 2.3.3. The minimum distance⁵³ of tags to these reflectors is roughly 25 cm. This results in a path length difference of 50 cm between the LOS and the strong NLOS component created by the gate reflection, see Fig. 5.9(a).

The floor reflection, on the other hand, can be as close as 2 cm to the LOS path, as illustrated in Fig. 5.9(b). Resolving this reflection would thus require at least 7.5 GHz of bandwidth, according to (5.1). Another reflection that is extremely close to the LOS path (down to a few millimeters) is created by the product to which the tag is attached. Even though resolving such reflections is not necessary in terms of spatial resolution, strong and dense reflections close to the tag might cause the LOS detection of any (ultra)-wideband system to miss the actual LOS path and lock onto the next strongest reflection instead. This is particularly the case if the LOS is attenuated in some way (e.g., by the transmitter gain pattern), cf. Fig. 5.10. As the LOS condition of a stray read cannot be predicted beforehand (it could even be NLOS), the ranging/localization system also has to deal with such hard-to-detect LOS components.

⁵² <http://www.iei.tu-clausthal.de>

⁵³ safety distance to backplanes/antennas for reflections in the backplanes and/or the height of a EURO pallet plus some margin in case of floor reflections

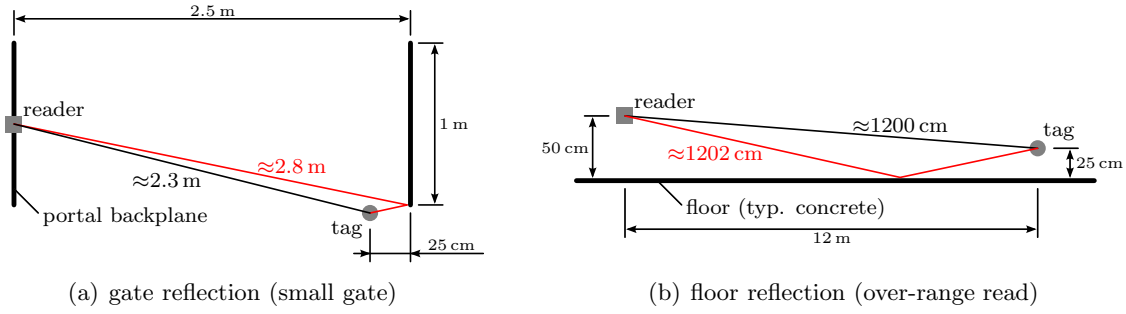


Figure 5.9: Illustration of LOS and closest NLOS path lengths (strong reflectors).

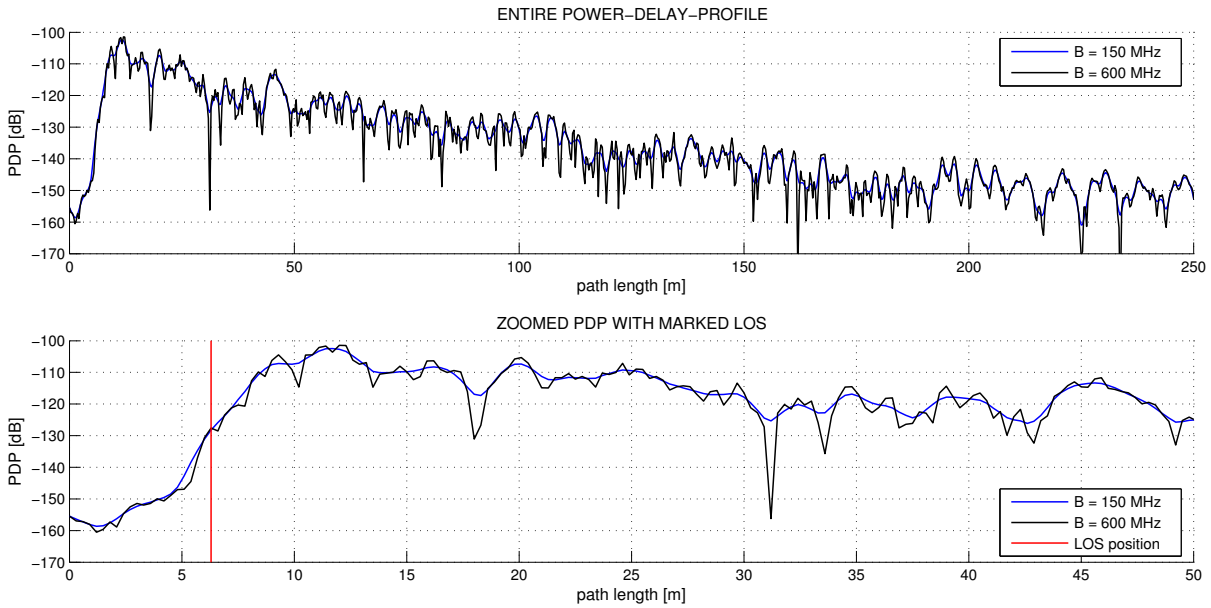


Figure 5.10: Hard-to-detect LOS (reflections close to an attenuated LOS plus strong gate reflections). Note that the LOS is no longer visible at $B = 150$ MHz.

The resulting ranging errors for the empty portal and different systems/bandwidths are shown in Fig. 5.11. The bottom left transmitter is active for these plots. The upper left quadrant of the portal in particular is poorly illuminated by this transmitter (gain patterns can be found in Fig. 2.14 on page 52). Consequently, the error is largest in this area. Note that the spatial resolution is reached for all methods, but also that the error is considerably smaller than this bound when the tag is directly in front of the transmitter.

Similar results can be observed if the tag antennas are attached to the liquids pallet, see Fig. 5.12. The pallet even has a positive effect on the ranging errors for smaller bandwidths, because it blocks the extremely strong gate reflection. This can be seen by comparing the plane closest to the transmitter in Fig. 5.11(a) to the plane in Fig. 5.12(a). (The relatively constant error of 50 cm for the 80 MHz bandwidth is likely caused by the floor reflection.)

Cumulative distribution functions of the absolute ranging error for all methods and bandwidths are provided in Fig. 5.13(a) for the empty portal and Fig. 5.13(b) for the portal with the liquids pallet. Only TX2 has been considered for the pallet measurements, since TX1 does not have a clear line-of-sight⁵⁴. Note that some ranging errors exceed the respective spatial resolutions for all methods except the IR-UWB ranging. This is not an inherent flaw of the

⁵⁴ This would lead to an unfair comparison due to the NLOS bias.

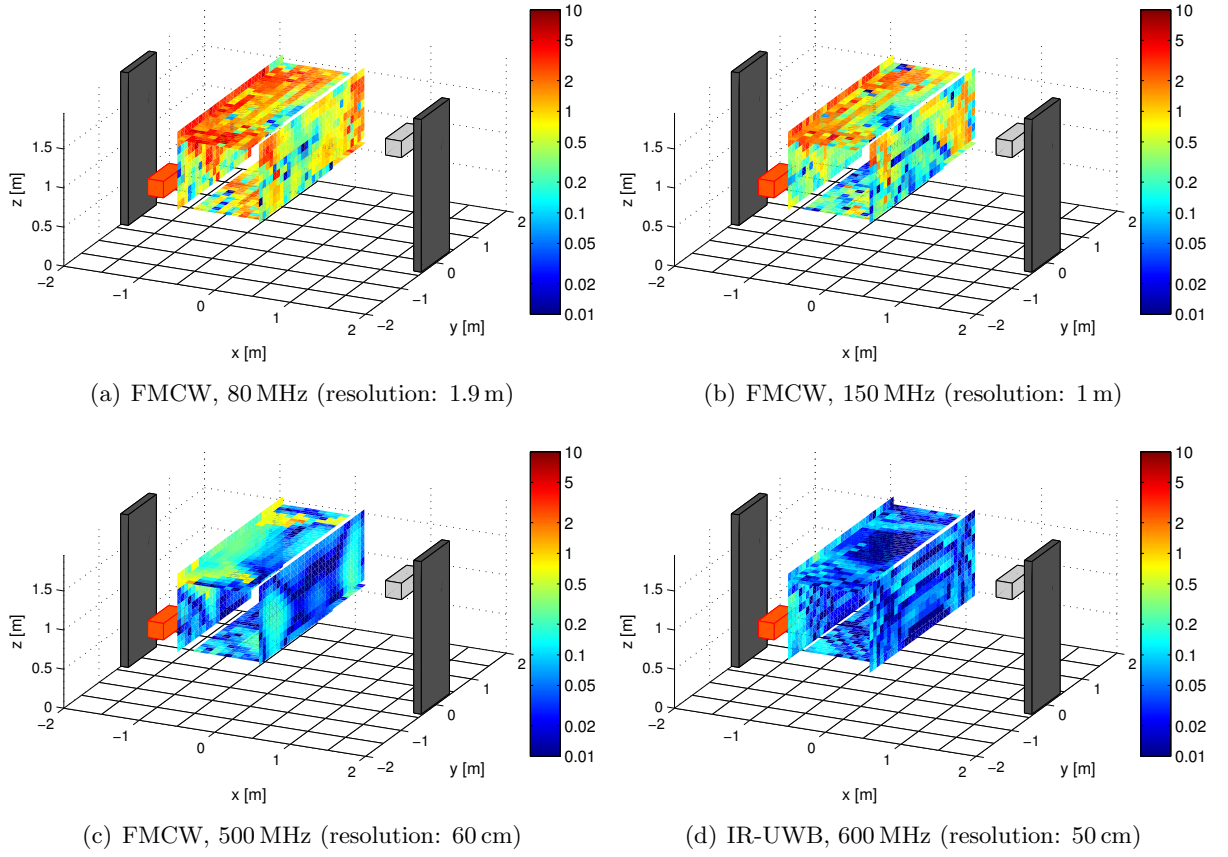


Figure 5.11: Absolute range error [m] for different methods/bandwidths inside the empty portal with metal backplanes. The bottom left transmitter is active (marked orange).

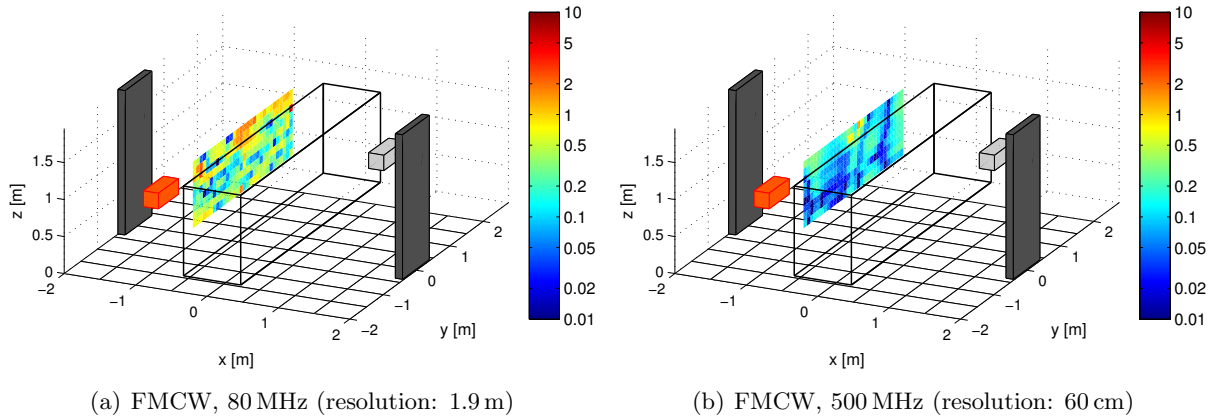


Figure 5.12: Absolute range error [m] for different bandwidths inside the portal with metal backplanes and tags attached to the liquids pallet (pallet indicated by the mesh). The bottom left transmitter is active (marked orange).

FMCW method, but simply a matter of LOS detection. The IR-UWB method uses the LOS detection implemented for the analysis of these measurements and is thus specifically designed to deal with hard-to-detect LOS components such as the one in Fig. 5.10. The FMCW system's LOS detection, on the other hand, was designed for directive links, cf. [78]. It assumes a strong LOS, which is often not the case in the UHF RFID gate environment, cf. Section 2.3.3.

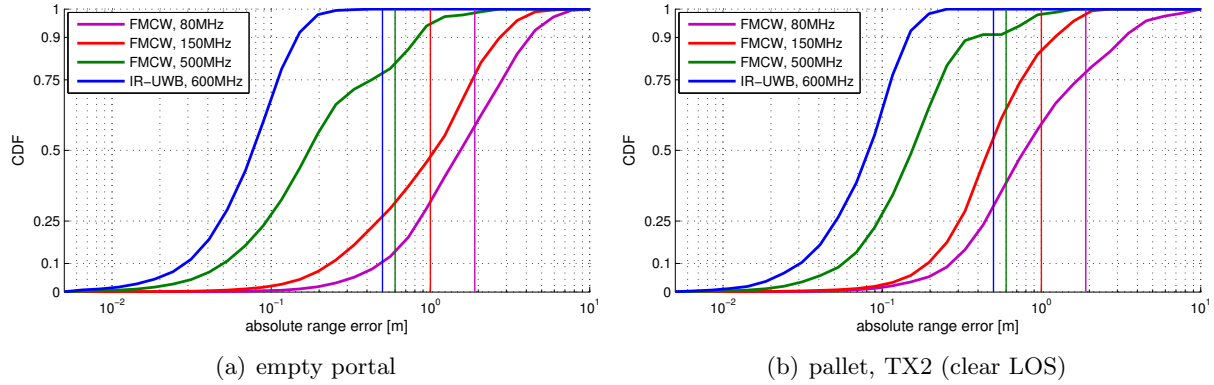


Figure 5.13: Cumulative distribution functions of the absolute range error for different methods/bandwidths. The vertical lines mark the spatial resolutions.

Ranging errors of below 1 m are necessary in order to correctly classify a tag to the portal⁵⁵. Errors exceeding this value might cause a tag to be falsely classified to the adjacent portal. In theory, this maximum error corresponds to a bandwidth of at least 150 MHz. Note, however, that only 50 % of the measured positions in the empty portal fulfill this requirement at 150 MHz bandwidth. This is caused by false positives in the LOS detection for hard-to-detect LOS components, cf. Fig. 5.10. While the LOS can still be identified in this PDP with UWB signals, the initial slope is already completely flat for 150 MHz, making a correct LOS detection impossible. Since a correctly identified LOS component implicitly requires that the spatial resolution (d_{res}) forms an upper bound on the error, 50 % of the assumed LOS positions are incorrect for 150 MHz FMCW.

Systems with ultra-wide bandwidths are still able to isolate the LOS component under these conditions, leading to a considerably better performance. In contrast to FMCW with 80 and 150 MHz bandwidth, almost 100 % of the errors for ultra-wideband FMCW are below 1 m and 80 % are below the spatial resolution. A LOS detection method better suited to this environment will likely set this to 100 %, just like for the IR-UWB method.

5.4 Towards an Implementation

5.4.1 Tag

From a tag's point of view, the most important requirement for wideband and ultra-wideband ranging is the ability to backscatter the ranging signal in a modulated way. This can be done either by creating a second impedance matching between chip and antenna or by integrating a second modulation structure on the tag. Either way, it is imperative that the respective loads are as perfectly matched as possible in the used frequency range in order to maximize the tag's differential radar cross section, cf. [238]. This maximizes the backscattered signal while at the same time minimizing the required dynamic range (modulated vs. non-modulated parts of the channel impulse response).

Since the tag's input impedance is highly nonlinear due to the energy harvesting (cf. Section 3.3 or [152, 204]), creating such a perfect match may be extremely hard to achieve using only a single modulation structure. Adding a second modulation structure as shown in Fig. 5.14, on the other hand, enables close to perfect loads. The main drawbacks of this approach are the

⁵⁵ assuming 50 cm spacing between the portals plus 25 cm safety distance of a tag to each portal wall

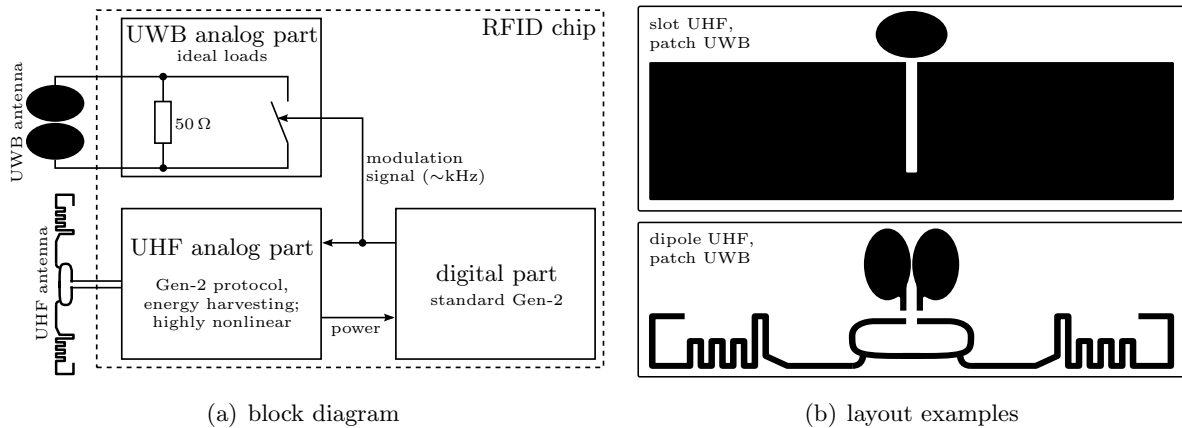


Figure 5.14: Block diagram and layout examples for a UHF RFID tag with UWB backscatter capabilities.

additional space required for the UWB antenna (tag size) and the increased number of ports (at least three instead of two). Both increase the cost of a tag. In order to minimize at least the space lost, the UHF dipole can also be folded around the UWB antenna, cf. [239].

A photograph of a UHF RFID tag with independent UWB antenna is shown in Fig. 5.15. This prototype has been built by NXP Semiconductors and is designed for the 3.1–4.8 GHz band.

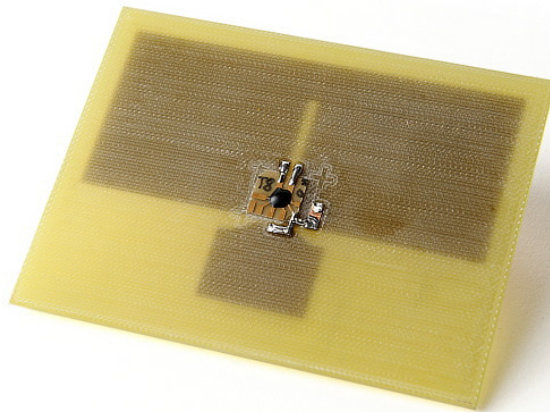


Figure 5.15: Photograph of the UHF/UWB prototype tag (based on an NXP UCODE G2iL chip).

5.4.2 Reader

Most of the complexity for localization in UHF RFID lies with the reader. Unfortunately, the combination of (ultra-)wide bandwidths and unstable backscatter modulation increases the complexity to a particularly high level. The pinhole (double fading) property of the channel also leads to high attenuations, as can be seen in Tab. 5.2. The attenuation of a 5.8 GHz backscatter system at 10 m range, for example, corresponds to a distance of 25 km for a single-channel link⁵⁶.

Since narrowband filters cannot be applied for (ultra-)wideband signals, noise is also a problem here. As a general rule, multipath propagation becomes less important with increasing

⁵⁶ The free space propagation loss in dB is $-20\log_{10}(c/(4\pi df)) = 68$ dB at $f = 5.8$ GHz and $d = 10$ m for a single-channel link, 74 dB at $d = 20$ m, and 136 dB at $d = 25$ km. A backscatter channel with $10 + 10$ m has an attenuation of $68 + 68 = 136$ dB, cf. [3, pp. 87].

bandwidth, while noise becomes more of a problem. The short tag reply (\sim ms) in combination with time-variance (moving tags) also limits achievable processing gains (long-term averaging) in UHF RFID localization. Depending on the used method and the bandwidth, unmodulated feedback (dynamic range) and the unstable tag modulation also pose critical problems for wide-band and ultra-wideband ranging. Details are provided below and a summary can be found in Tab. 6.1 on page 154.

| | | at 3 m | at 5 m | at 10 m |
|-----------|-----|--------|--------|---------|
| 2.45 GHz, | ISM | 106 dB | 114 dB | 126 dB |
| 4 GHz, | UWB | 114 dB | 123 dB | 135 dB |
| 5.8 GHz, | ISM | 121 dB | 129 dB | 141 dB |
| 7.5 GHz, | UWB | 125 dB | 134 dB | 146 dB |

Table 5.2: Overall channel attenuation [dB] assuming 3 dB TX antenna gain, 3 dB RX antenna gain, 1 dB tag antenna gain, -1 dB for polarization mismatch, -3 dB modulation loss, -3 dB implementation loss, and -6 dB fading margin (high bandwidths). Channel attenuation assumes free space propagation (see (3.6) on page 91) with a path loss exponent of $\xi = 2$.

Impulse-Radio Ultra-Wideband (IR-UWB) Ranging IR-UWB ranging suffers mostly from noise and self-interference due to unmodulated feedback. Signal-to-interference ratios (SIRs) in portal applications are in the range of -30 to -70 dB for bistatic setups and -40 to -100 dB for monostatic setups, see Fig. 2.33. Since the ultra-high speed analog to digital converters (ADCs) required for sampling UWB signals lack the necessary resolution to sample this signal directly⁵⁷, feedback suppression techniques have to be applied.

Fig. 5.16 shows the block diagram of the IR-UWB reader. Transmission is performed similarly to any UWB transceiver, cf. [62], consisting of pulse generation, pulse shaping, up-conversion, bandpass filtering and amplification. The receive path starts with bandpass filtering and (low-noise) signal amplification, followed by anti-alias filtering, sampling (ADC), matched filtering and despreading of the pulse train, cf. [62].

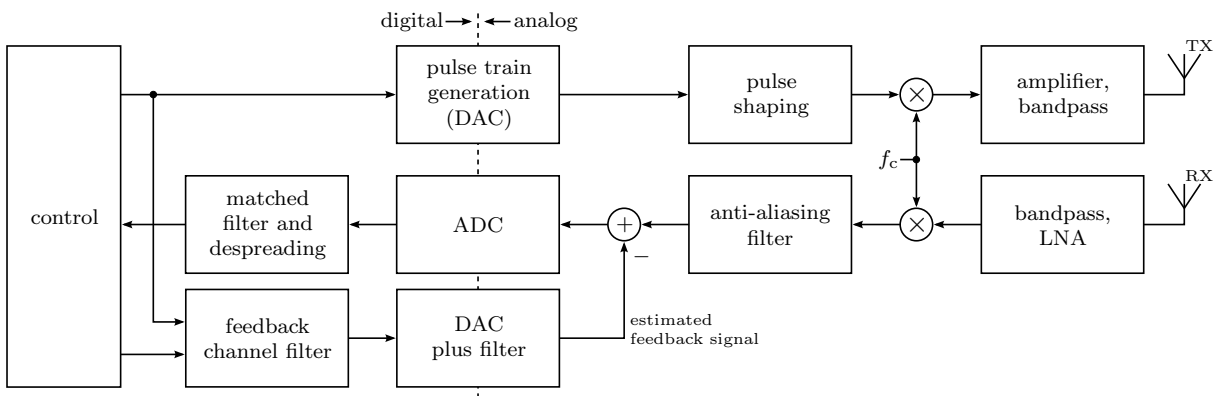


Figure 5.16: Reader block diagram for IR-UWB ranging.

Feedback suppression is performed by subtracting an estimated feedback signal before analog to digital conversion. In order to obtain this estimate, the recorded channel impulse responses (cf. Fig. 5.2) are averaged over a short period of time (\sim ms). This eliminates the tag response in the averaged CIR, since the modulated part of the CIR is quickly time-varying. The created

⁵⁷ Currently, the National ADC12D1800 reaches an SNR of 58.5 dB and a spurious free dynamic range of 73 dB at a sampling frequency of 3.6 GS/s, <http://www.national.com/ds/DC/ADC12D1800.pdf>.

average CIR is subsequently used to calculate an estimate of the feedback signal. The influence of the feedback's time-variance can be minimized by updating the feedback filter coefficients before each tag reply (\sim ms).

One possibility for the design of the IR-UWB ranging systems is to use IEEE 802.15.4a [94] preambles as ranging signal. Since transmitter and receiver are implemented in the same device for passive backscatter ranging, coherent processing does not require carrier synchronization. The maximum channel attenuation with coherent processing is roughly 130 dB with achievable signal-to-noise ratios using 1024 IEEE 802.15.4a ranging preambles⁵⁸ [62]. Comparing this to the link budget in Tab. 5.2, it becomes clear that channel attenuation is only a problem at large distances and in the higher frequency ranges⁵⁹. However, this assessment assumes an interference-free environment. Since interference is dominant in this environment, the effective SNR will likely be well below the one assumed in [62], depending on the effectiveness of (and also the amount of noise added by) the feedback suppression.

A final benefit of IR-UWB is the ability to select a different code sequence for each reader in environments with dense reader placement. If these codes are orthogonal to each other, reader-to-reader interference is suppressed (cf. code division multiple access [141]).

To sum up, the IR-UWB system is:

- + immune to instabilities of the tag modulation and does not need a special tag response (see Section 5.1.1);
- + (within limits) immune to multipath propagation, since UWB bandwidths can be reached;
- + robust to reader-to-reader interference for dense reader placement;
- vulnerable to unmodulated feedback (self-interference). The feedback suppression is complex and might be ineffective; and
- vulnerable to noise due to the high attenuation of the backscatter channel in combination with strong self-interference (feedback).

Frequency-Modulation Continuous-Wave (FMCW) Ranging In contrast to IR-UWB, feedback is not the primary issue in FMCW ranging — at first glance. FMCW is inherently robust to unmodulated feedback, since feedback and backscatter channel are mapped to different frequencies and can thus be separated using analog filters before sampling, cf. Section 5.1.2. The only prerequisite is a sufficiently high backscatter modulation frequency in order to avoid in-band interference, as illustrated in Fig. 5.17(a). It should be possible to meet this prerequisite

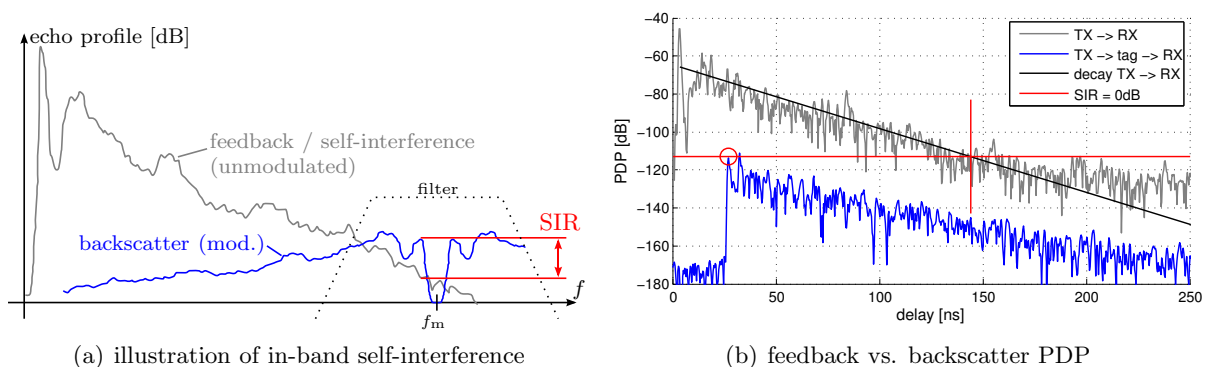


Figure 5.17: In-band interference for FMCW radar due to strong feedback.

⁵⁸ assuming a tag reply length of roughly 2 ms and a preamble length of 2 μ s

⁵⁹ On a sidenote: Ultra-wideband signals experience only very little fading. Classification as over-range read can thus be based on the fact that the UWB signal is below the noise floor, provided that this noise floor is constant and not caused by interference, and provided that the LOS is not blocked by some obstacle.

with RFID systems at short ranges and in smaller rooms/halls, although it is increasingly difficult to achieve for high sweep rates, large distances to the tag, and in large halls. A sweep rate of 150 MHz/ms, for example, maps to 150 Hz/ns according to (5.2). Now consider the (instantaneous) PDPs for feedback and backscatter channel shown in Fig. 5.17(b). These are the channels for position 9 of the UWB test measurements presented in Section 5.2. The feedback decays faster in this environment than in a UHF RFID portal, with RMS delay spreads in the range of 7 ns compared to up to 25 ns in the gate, see Section 2.3.3 and [132]. The resulting minimum modulation frequency for the channels in Fig. 5.17(b) is roughly 40 kHz in order to achieve an average SIR of 30 dB, as will be shown below.

The lowest feasible modulation frequency in order to reach a certain SIR can be calculated from the channel parameters of backscatter and feedback channel following the illustration in Fig. 5.17(a). The decay of the feedback channel and the relation between feedback and backscatter channel LOS attenuation are of particular interest for this purpose.

The feedback decay can be calculated from K-factor and RMS delay spread assuming an exponentially decaying NLOS APDP [2]

$$S_{\text{NLOS,fb}}(\tau) \sim e^{-\Gamma\tau} \quad (5.4)$$

where Γ is the NLOS decay constant. Using

$$\Gamma = \frac{1}{\tau_{\text{RMS}}} \cdot \frac{\sqrt{2K_{\text{LOS}} + 1}}{K_{\text{LOS}} + 1}, \quad (5.5)$$

cf. [2, Table I], the decay of the feedback APDP is

$$\Gamma_{\text{dB,fb}} = \frac{d}{d\tau} 10 \cdot \log_{10}(S_{\text{NLOS,fb}}(\tau)) = -10 \cdot \log_{10}(e) \cdot \Gamma = -\frac{10 \cdot \log_{10}(e)}{\tau_{\text{RMS,fb}}} \cdot \frac{\sqrt{2K_{\text{LOS,fb}} + 1}}{K_{\text{LOS,fb}} + 1} \quad [\text{dB/s}]. \quad (5.6)$$

From this decay, the minimum tag modulation frequency can be calculated using the geometry shown in Fig. 5.18.

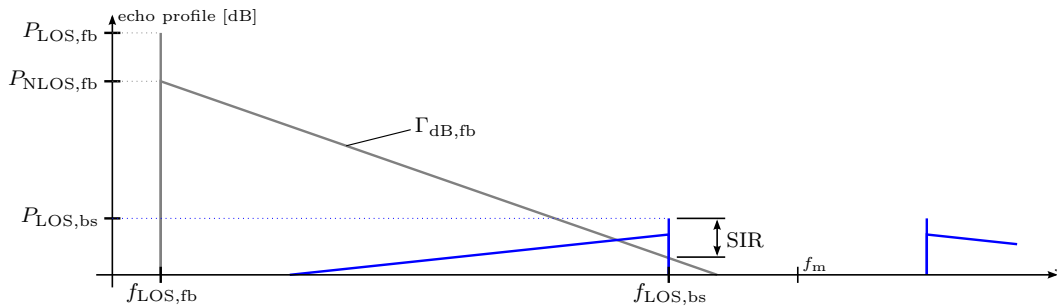


Figure 5.18: Minimum tag modulation frequency for FMCW ranging in order to reach a specific SIR.

The feedback channel starts at a frequency of

$$f_{\text{LOS,fb}} = \tau_{\text{LOS,fb}} \cdot \frac{B_{\text{FM}}}{T_{\text{FM}}} \quad (5.7)$$


in the echo profile, where $\tau_{\text{LOS,fb}}$ is the delay of the first arriving feedback component and $B_{\text{FM}}/T_{\text{FM}}$ is the sweep rate of the FMCW chirp. The delay is generated by the distance between TX and RX antenna *plus the delay in cables*⁶⁰. The backscatter LOS component is located near

⁶⁰ The latter is often dominant.



the modulation frequency f_m , at a frequency of

$$f_{\text{LOS,bs}} = f_m - \tau_{\text{LOS,bs}} \cdot \frac{B_{\text{FM}}}{T_{\text{FM}}}, \quad (5.8)$$


where the backscatter LOS delay $\tau_{\text{LOS,bs}}$ is the propagation delay TX→tag→RX plus delays in cables (not only the propagation delay of the LOS path to the tag). 

The LOS power levels of backscatter and feedback channel are $P_{\text{LOS,bs}}$ and $P_{\text{LOS,fb}}$ respectively, and the feedback decays with $\Gamma_{\text{dB,fb}}$ over delay and thus with $\Gamma_{\text{dB,fb}} \cdot T_{\text{FM}}/B_{\text{FM}}$ in the echo profile. The start point of this decay, $P_{\text{NLOS,fb}}$, can be calculated using the formulas provided in [2, Table I] for exponentially decaying feedback channels,

$$P_{\text{NLOS,fb}} = \frac{P_{\text{LOS,fb}}}{B_{\text{FM}} \cdot \tau_{\text{RMS,fb}}} \cdot \frac{\sqrt{2K_{\text{LOS,fb}} + 1}}{K_{\text{LOS,fb}}^2 + K_{\text{LOS,fb}}}, \quad (5.9)$$


where $1/B_{\text{FM}}$ is the delay resolution of the measurement. Hence, based on the geometry in Fig. 5.18, the minimum modulation frequency in order to achieve a given *average* SIR is

$$f_m \geq \frac{B_{\text{FM}}}{T_{\text{FM}}} \cdot \left(\frac{P_{\text{NLOS,fb}} - P_{\text{LOS,bs}} + \text{SIR}}{\Gamma_{\text{dB,fb}}} + \tau_{\text{LOS,bs}} + \tau_{\text{LOS,fb}} \right). \quad (5.10)$$

Note that the necessary modulation frequency increases with sweep rate, distance to the tag, and feedback RMS delay spread and is thus environment- and system-dependent. For the example in Fig. 5.17, the decay of the feedback channel is 0.33 dB/ns starting from 65 dB, and the backscatter LOS is at −113 dB. An average SIR of 30 dB is reached at 250 ns, which corresponds to a minimum modulation frequency of approximately 40 kHz. This is the lower bound for the return link frequency range in passive UHF RFID [1]. Since the feedback RMS delay spread in this example is extremely low ($\tau_{\text{RMS,fb}} = 6.5$ ns) and will be exceeded by factors in large halls or a UHF RFID gate (cf. [132]), in-band self-interference has to be considered in the design of FMCW backscatter ranging systems, especially for ultra-wide bandwidths. 

The primary drawback of FMCW, however, is its vulnerability to frequency instabilities. Any frequency instability of the modulation frequency “smears” the echo profile, thus making the LOS detection impossible. Assuming a sweep bandwidth of $B_{\text{FM}} = 150$ MHz within a sweep time of $T_{\text{FM}} = 1$ ms, for example, the resulting distance instability is

$$e_{\text{f-inst.}} = \frac{c \cdot T_{\text{FM}}}{B_{\text{FM}}} = 2 \text{ m/kHz}. \quad (5.11)$$

If the tag modulation frequency jitters by ± 1 kHz during tag modulation, for example, the echo profile’s effective resolution is reduced to ± 2 m by the smearing effect. As UHF RFID tags “feature” up to 2.5% clock jitter and 22% frequency drift at modulation frequencies up to 640 kHz [1], the effective resolution for the FMCW configuration above is reduced to ± 32 m by the jitter alone for a tag modulation frequency of 640 kHz. Increasing the modulation frequency, as may be necessary to avoid in-band self-interference, thus increases the systematic error created by the unstable tag modulation. 

Notably, ranging results using FMCW radar in the 2.45 GHz band with a passive multistandard tag reached acceptable accuracies in an anechoic environment [240]. However, as only the sweep bandwidth is given in this paper (and other papers by this group) and not the sweep duration, an assessment with respect to frequency instabilities is not possible⁶¹.

⁶¹ On a sidenote: the anechoic nature of the environment used for the measurements in [240] also suppresses feedback, which would allow for extremely low tag modulation frequencies, thus minimizing instability issues.

As a countermeasure, the received FMCW signal could theoretically be demodulated by the received tag modulation signal. This removes the frequency instability of the tag and also allows for arbitrary tag responses (no longer limited to continuous modulation). On the downside, it places harsh stability restrictions also on the UHF carrier (radar grade; like for the FMCW signal) and also requires careful alignment between RFID and FMCW part. In essence, the combined frequency instability for the above example must not exceed 500 Hz during the tag response in order to reach an effective spatial resolution of ± 1 m for the echo profile.

Finally, also reaching UWB bandwidths is difficult with fast (\sim ms) frequency sweeps. The current limit is roughly 1 GHz/ms, cf. [73, 75, 80, 81], although this likely comes at the cost of considerable frequency instability (phase noise). In addition, extremely high sweep rates decrease the SIR caused by in-band self-interference (noise and interference). In essence, ultra-wideband FMCW most likely “imports” all problems of IR-UWB systems (noise and self-interference), while at the same time keeping the inherent problems of FMCW ranging (vulnerability to unstable clocks). FMCW is thus an ideal option for the 2.45 GHz and 5.8 GHz ISM bands, but likely not for ultra-wideband ranging.

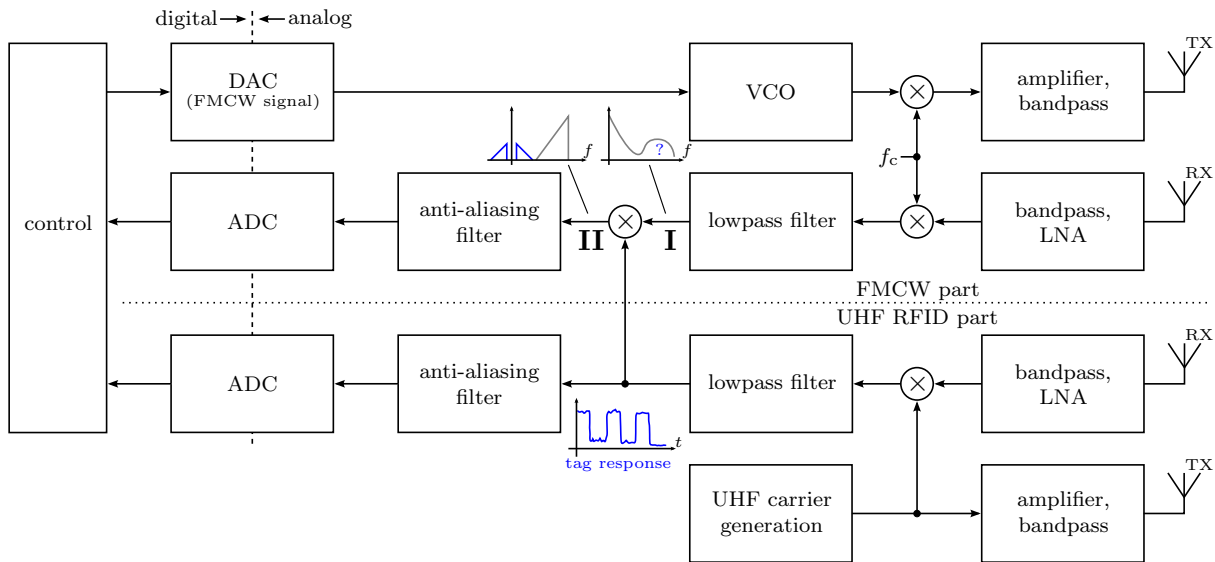


Figure 5.19: Reader block diagram for FMCW ranging.

Fig. 5.19 shows the block diagram of the FMCW ranging system. FMCW signal generation is performed by a voltage controlled oscillator (VCO) with subsequent up-conversion to the proper frequency band, filtering and amplification. On the receiver side, the FMCW signal is amplified, filtered, and down-converted. At this point, marked by **I** in Fig. 5.19, the echo profile is distorted by the tag’s unstable modulation frequency. Hence, as a next step, the signal is down-converted with the tag reply demodulated in the UHF reader part. This clears the echo profile and also puts the tag response around DC (point **II**). The signal at **II** is subsequently filtered in order to remove the direct feedback component and is finally sampled.

In summary, the FMCW system is:

- + robust to feedback, provided that the tag modulation frequency is sufficiently high;
- + within limits robust to multipath propagation, since high bandwidths can be reached;
- vulnerable to noise, since only a single sweep is possible within the given target detection time (no processing gain; see Section 1.3);
- extremely vulnerable to unstable tag modulation during the sweep time (see above); and
- vulnerable to reader-reader interference for dense reader placement if the frequency band is fixed (e.g., 2.45 GHz ISM).

6

Conclusion

6.1 Summary of Scientific Results

The central conclusion, after almost four years of research on tag localization in UHF RFID, is: UHF RFID is not designed for localization. Narrowband signaling, massive multipath propagation, unstable backscatter modulation, and high tag throughput are all conflicting with vital requirements for accurate localization.

Within the limits of EPCglobal Class-1 Gen-2, zonal classification using large arrays, as implemented by RF Controls⁶² or Mojix⁶³, is the only feasible option. However, accurate localization of a single tag at an unknown position requires careful calibration, several arrays, and a lot of time. Both companies are quite cagey when it comes to performance measures, so it is ultimately unknown how accurate and also how robust their respective systems are.

If a tag should be located within $\pm 10\%$ of the true range and within 1 ms in typical UHF RFID scenarios (as defined in the requirements for this thesis project), an extension of the system is necessary, using dedicated and more wideband ranging signals. Candidates for this extension are listed and evaluated in Tab. 6.1.

| | MFCW | FMCW-WB | FMCW-UWB | IR-UWB |
|-------------------------|-----------------|-----------------|-----------------|------------------|
| multipath propagation | critical | robust | immune | immune |
| unmodulated feedback | robust | problem | critical | critical |
| unstable tag modulation | immune | critical | critical | immune |
| noise | immune | robust | problem | critical |
| tag complexity | low | moderate | moderate | moderate |
| reader complexity | low | moderate | high | very high |

— Legend —

| | | | |
|------------------|---------------------------------|-------------------|---|
| immune: | method is inherently immune | problem: | countermeasures are complex or semi-effective |
| robust: | countermeasures are effective | critical: | might be impossible to solve (no-go) |
| low: | state-of-the-art RFID equipment | high: | lab/radar equipment |
| moderate: | state-of-the-art, but expensive | very high: | lab/radar equipment, complex to implement |

Table 6.1: Summary — vulnerability of ranging methods to channel and system properties.

The narrowband MFCW, discussed in Section 4.2, can be implemented at low cost and is immune to most system properties, but requires an environment with little multipath propagation. It is, furthermore, the only method capable of ranging standard Gen-2 tags in realistic environments.

Wideband FMCW is the best option for robust portal classification. However, the vulnerability of FMCW radar to unstable backscatter modulation has to be addressed first. Ultra-wide bandwidth FMCW is likely not a feasible option, since it essentially combines the vulnerabilities of FMCW and UWB systems. Both versions of FMCW-based ranging are analyzed in Chapter 5.

Impulse-Radio UWB is the method of choice if highly accurate localization is desired. It is discussed in detail in Chapter 5. Unfortunately, this method is likely to be complex to implement. Moreover, its vulnerability to self-interference and noise limits its applicability. Installing IR-UWB ranging systems in portals, which combine high levels of feedback and the necessity for fast measurements, may not be feasible from today's point of view.

In order to achieve robustness under realistic conditions, several estimates of the tag's location have to be combined for all localization methods. These estimates can be obtained by consecutive measurements (tracking), by combining different methods (concurrent estimates of range and angle of arrival, for instance), or by incorporating prior information (floorplans, statistics).

⁶² <http://www.rfctrls.com>

⁶³ <http://www.mojix.com>

To sum up and to answer the central research question of this thesis: *Is it possible to accurately determine the position of passive UHF RFID tags in typical applications and within the boundary conditions of passive UHF RFID systems?*

No, it is not. Not within the limits of UHF RFID. It is, however, possible to accurately localize a UHF RFID tag if the system is extended to facilitate (ultra-)wideband localization. Essentially, tag localization in UHF RFID is feasible. It just does not come for free...

6.2 Own Contributions

The main contributions of this work are outlined by the chapter structure: wideband channel modeling, the PARIS simulation framework, an in-depth discussion of multiple/stepped-frequency continuous-wave radar, and the extension of localization in UHF RFID to (ultra-)wide bandwidths.

Channel modeling in UHF RFID has never before been seen from a wideband point of view. EPCglobal Class-1 Gen-2 is narrowband, so why deal with the complexities of wideband or even ultra-wideband channel modeling? Being part of an ultra-wideband group provided me with a unique perspective and of course also access to high-end lab equipment. First and foremost, we have been able to show that established channel models in UHF RFID are insufficient for localization purposes, especially when considering bandwidths exceeding a few MHz. It has also been shown that the line-of-sight path is not dominant in classical UHF RFID scenarios, invalidating the most common assumption regarding UHF RFID tag localization. Moreover, apart from modeling the UHF RFID channel in detail, we have also been able to extend the theory of wideband backscatter channels. This extension includes expressions for the backscatter average power-delay-profile as well as approximations for wideband parameters of the backscatter channel based on their counterparts in the constituent channels.

The PARIS simulation framework is also a contribution to the scientific community. The hybrid channel model and the tag reflection coefficient model in particular are highlights within this framework. It is our hope that these models will be useful and valuable to other groups working on indoor localization or in the field of UHF RFID. As an open-source software, it can be used and continuously developed by researchers all over the world. Currently, ten research institutes and one company on three continents are registered users.

Multi-frequency continuous-wave radar was the first analyzed ranging method in the context of this thesis. Even though the idea of phase-based continuous-wave ranging is of course not a new one, the detailed analysis with respect to indoor ranging is. Note that we, too, assumed that the LOS path is dominant in this first analysis. Unfortunately, UHF RFID is not used in medium to light multipath environments, but in severe ones which are challenging even for wideband and ultra-wideband localization. Following this realization, the research on more wideband methods was intensified.

Within this thesis, requirements have been defined for wideband and ultra-wideband tag localization based on channel and system properties, challenges and limiting factors have been identified, and possible solutions have been provided. Based on measurements, it has been shown that UWB-based passive tag localization is feasible in principle. The same measurements have, however, also shown that the UHF RFID channel is challenging even for UWB ranging methods, and that the (ultra-)wideband property alone is insufficient to guarantee accurate localization even when noise is negligible.

The research on (ultra-)wideband passive tag localization using FMCW or IR-UWB is still in its initial stage. The contribution of this work is the analysis of wideband and ultra-wideband ranging from an RFID perspective, thus also taking into account the challenging scenarios in UHF RFID as well as inherent system properties such as the extreme instability (from a radar point of view) of the tag clock.

6.3 Future Research

Tag localization in passive UHF RFID was in its infancy at the beginning of this thesis project. Even though it has definitely grown in the meantime, it is still immature. As a consequence, challenging research on passive tag localization is still possible and necessary. Suggested topics for future research can be categorized into three groups: reader and tag design, system design, and simulator design.

Among these groups, reader/tag design is the most obvious, but also the most complex and thus the riskiest choice. From today's perspective, open research questions regarding tag design include the ability for ultra-wideband backscattering as well as increasing clock stability (for FMCW-based ranging). Research opportunities in reader design include an analysis of FMCW-based ranging with respect to tag clock jitter and drift, and a feasibility study of IR-UWB ranging. Both methods are critically vulnerable to at least one system or channel property that cannot fully be compensated for. Hence reader design should ideally be accompanied by system (re)design.

We suggest that the focus of system design should be on backend processing and (re)design of the environment. Tag localization in passive UHF RFID is difficult not only because the environment and the necessary tag throughput are challenging, but also because the entire system design is devastating for localization. As such, a (partial) redesign of the portal concept should be considered. The concept of zonal monitoring introduced by RF Controls and Mojix may lead the way in this area.

Moreover, computational intelligence and classification is a field that did not receive a lot of attention during the work on this thesis. Nonetheless, such backend processing offers a potentially huge increase in robustness by suppressing poor estimates. Sensor fusion is another keyword in this field. Most ranging systems can be combined, like UWB time difference of arrival and UWB received signal strength, for instance. This, too, increases robustness, provided that the estimates are not linearly dependent.

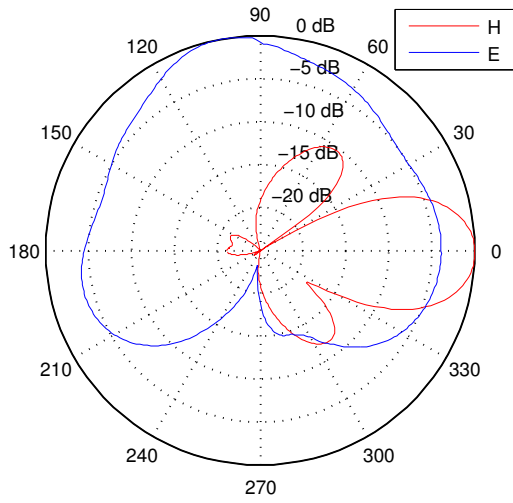
A lot of problems in UHF RFID are caused by the backscatter property of the system. In the long run, addressing this core property might thus also be worth considering. Active transmission of ultra-wideband pulses, for example, would almost instantly solve the ranging and thus the localization problem in UHF RFID (while certainly introducing new ones). Hybrid UWB long-range tags with UHF energy harvesting are currently under research, but still use way too much power to be a real option. Removing the backscatter property is thus primarily a problem of low-power tag design and highly efficient energy buffering on the tag.

The final group of topics, simulator design, offers synergetic effects especially when combined with reader or system design. The framework was explicitly designed for research on tag localization, so the models cover all effects that make this a challenging task. As such, the framework is an ideal option for testing a ranging method without actually having to implement it on real-time hardware. Further research on FMCW, for instance, can benefit from the unstable clock generator already implemented.

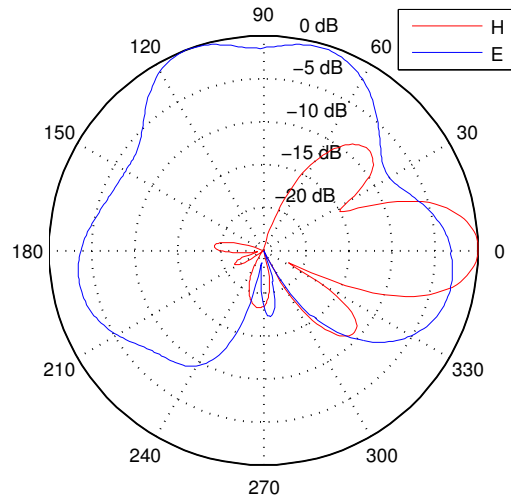
The central models of the framework, especially the hybrid channel model and the tag detuning model, are potential topics of research as well. A list of limitations of the currently implemented models is provided in Section 3.2.4. These limitations are (mostly) hard to overcome, thus providing an interesting challenge.



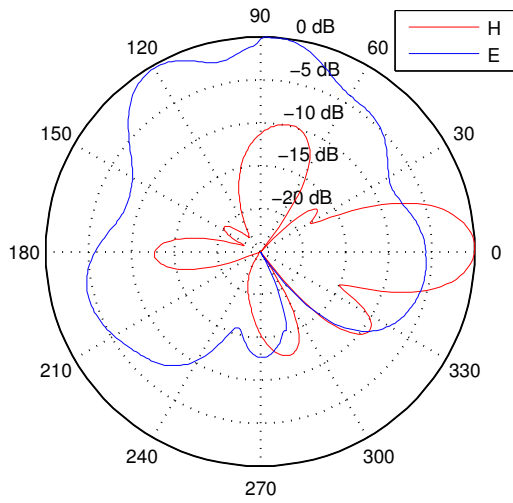
Polar Gain Patterns



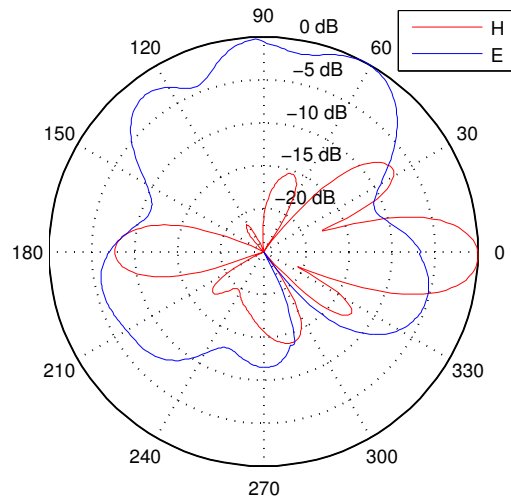
(a) $f = 700$ MHz



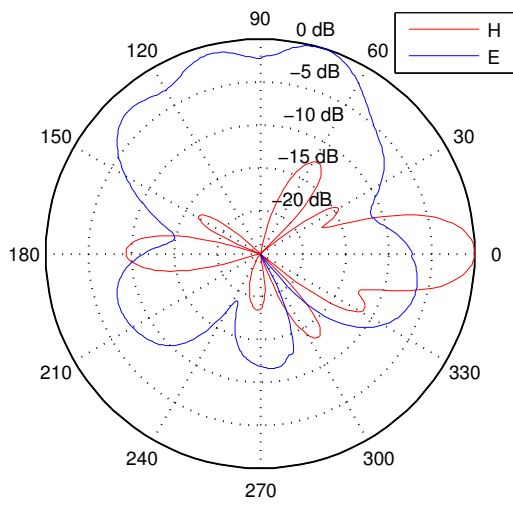
(b) $f = 800$ MHz



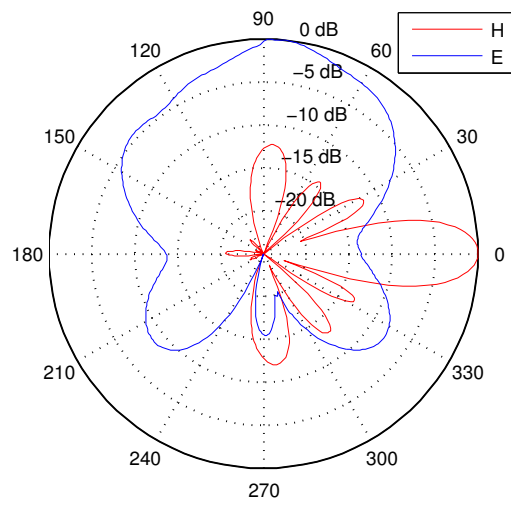
(c) $f = 900$ MHz



(d) $f = 1000$ MHz

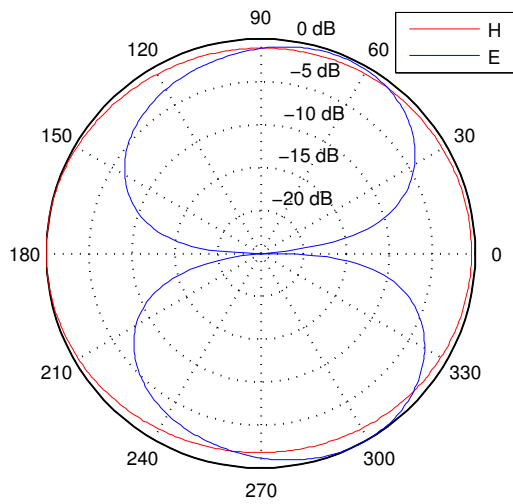


(e) $f = 1100$ MHz

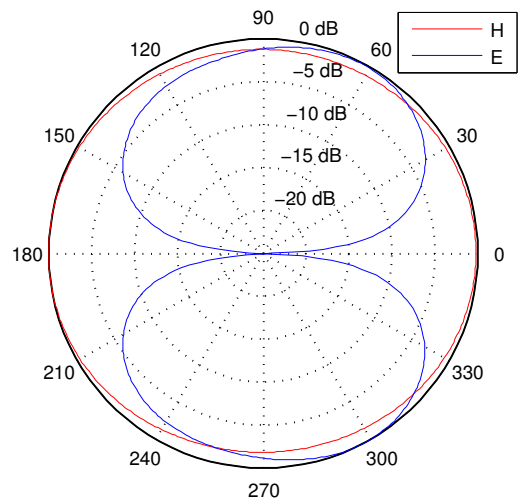


(f) $f = 1200$ MHz

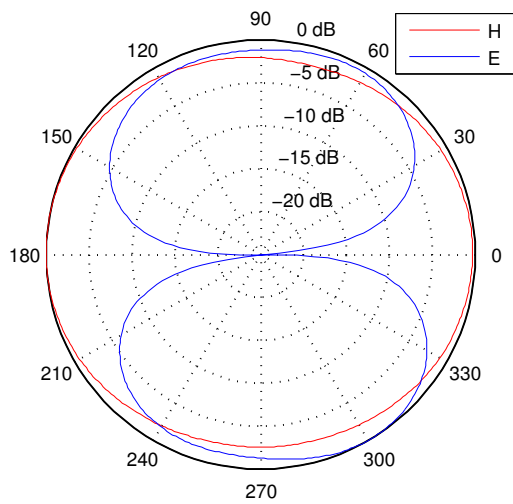
Figure A.1: Measured gain patterns of the UWB reader arrays used for measurements (TX1).



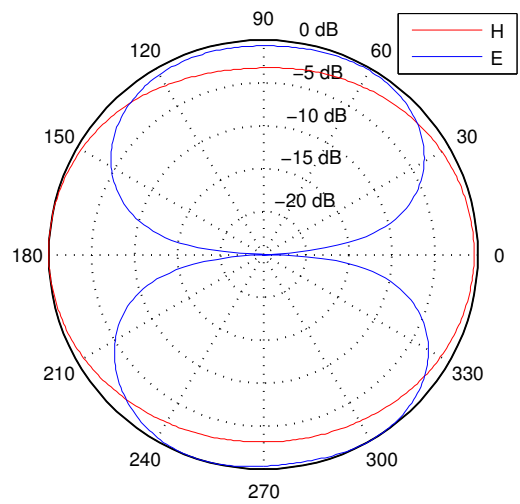
(a) $f = 700$ MHz



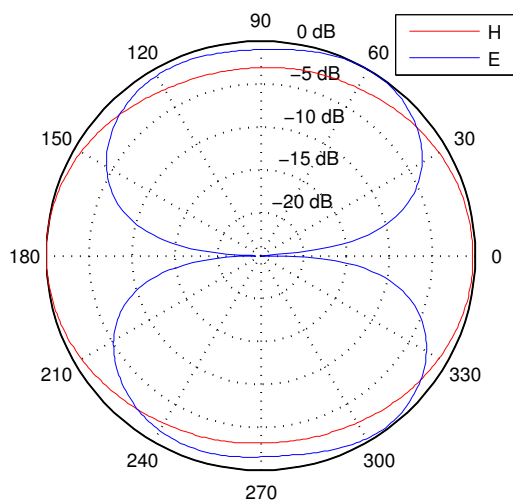
(b) $f = 800$ MHz



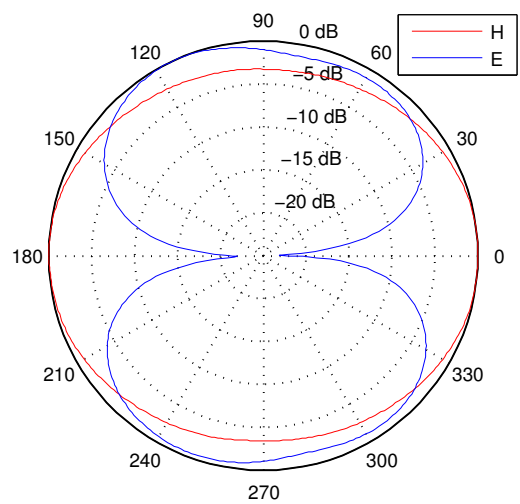
(c) $f = 900$ MHz



(d) $f = 1000$ MHz



(e) $f = 1100$ MHz



(f) $f = 1200$ MHz

Figure A.2: Measured gain patterns of the omnidirectional UWB tag antenna used for measurements.

B

Floorplan of SPSC Buildings

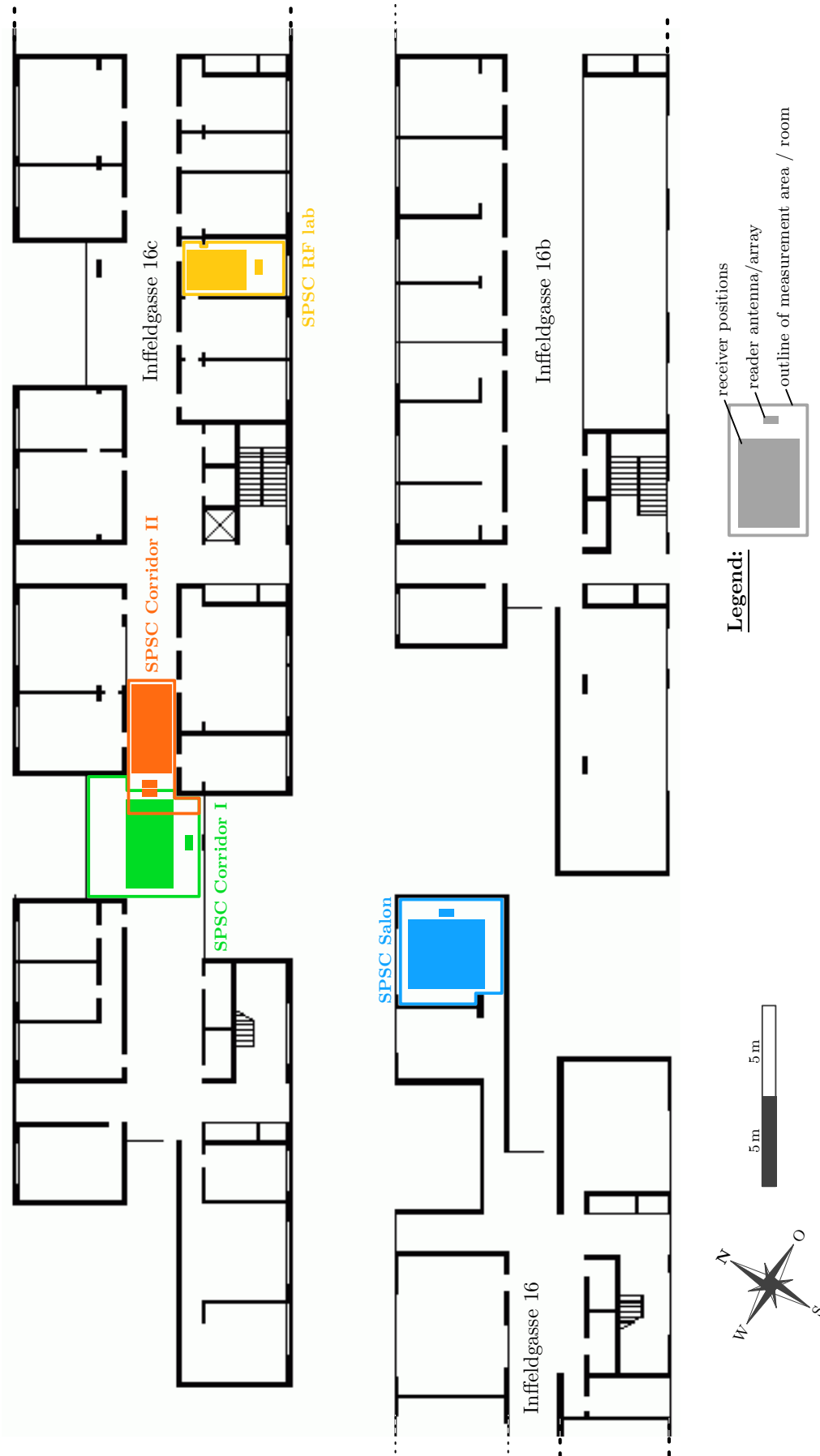


Figure B.1: Floorplan of the buildings Inffeldgasse 16, 16b, and 16c (Graz Univ. of Technology) with marked measurement campaigns. Source of floorplan: <https://online.tugraz.at> (Apr. 2011).

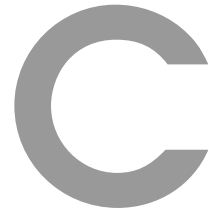


(a)



(b)

Figure B.2: Photographs of the building Inffeldgasse 16c (Graz University of Technology)



Simulator Internals

C.1 Known Issues and To-Do List for Future Builds

There are several known issues with the most current (development) version of the framework (version prefix: alpha), listed below. As the self-tests have not been updated to include the most current models, additional unknown bugs seem likely, especially in rarely used functionalities. The list also contains nice-to-have features for future builds. For the full to-do list, please refer to the commit logs of the SVN repository and/or the function headers.



- MAJOR ISSUES
 - Virtual transmitters are not treated correctly by the gate simulation (`sim_mfcw_gate`) in non-probemode. This problem affects the return link (tag→reader), the feedback link (reader→reader), and the control flow (VTX is not activated with corresponding TX). The CIRs of TX and corresponding VTX should be flattened in `channel_main`, and `sim_mfcw_gate` should be updated accordingly.
 - The directivity gain of the receiver is not excluded in ‘outdoor’ mode.
 - Self-tests for the following functions are not up-to-date and have been deactivated: `channel_newpos`, `channel_surface`, `channel_main`, `reader_main`, `tag_main`, and `mfcw_*`.
- MINOR ISSUES / MISSING FEATURES
 - Channel model
 - ability to use measured channel impulse responses loaded from file (this feature was prepared, but never fully implemented)
 - transmission model (absorption, delay)
 - support for arbitrarily oriented surfaces
 - support for asymmetrical gain patterns (“mirror” functionality)
 - trace VTX and calculate gains automatically
 - wideband/UWB extension of large-scale and directivity model
 - version of `channel_small` with equidistant sampling
 - Tag model
 - time-variant implementation of the tag power supply
 - nonlinear implementation of the filterbank
 - Reader model
 - implement missing ranging functions
 - implement decoding
 - single-sideband reader modulation creates overshoots
 - Core framework / other functions
 - `version_system`: extract function version from function header (changelog)
 - ripple measurement and time-variant modulation depth in `linktiming_reader`

The open-source versions of the framework are partial branches of the development version. Version beta 1.0 is stable and self-tests cover the entire framework. Beta 1.0, on the other hand, does not feature virtual transmitters or the antenna detuning model (see below). Version beta 2.0 and 3.0, released in September 2010 and at the end of this thesis work respectively, are unstable testing releases. A list of known issues for the open-source framework can be found on the simulator homepage [127].

C.2 Available Characteristics Files

Characteristics are lookup tables stored in `.mat`-files. They are used to describe the output behavior of a modeled component for some input. Characteristics should always be loaded by `loadmat`. Apart from loading the `.mat`-file, this function maintains the buffer used to speed up processing and collects version information from the loaded files.

Underlying data (mostly measurements, but also electromagnetic solver results, etc.) is stored in `.mat`-files starting with `meas`. This data is used by the simulator's characteristics generators. There are four groups of characteristics: Tag (`tagchar_*`), channel (`channelchar_*`), reader (`readerchar_*`), and system (`syschar_*`). A complete list of characteristics and measurement data files can be found in Tabs. C.1 and C.2 respectively.

Note that some pre-calculated characteristics are not part of the open-source framework due to their file size (several gigabytes). However, these characteristics can be recalculated without a problem if needed, since all characteristics generators and the underlying data sets are included.

| File | Models | Description |
|--------------------------------|---------------------|---|
| <code>meas_antenna_*</code> | antenna directivity | directivity patterns for all used antennas (Intermec IA39B, Vivaldi and Vivaldi arrays, UWB tag antenna, dipoles) |
| <code>meas_tag_agc</code> | tag demodulator | internal demodulator signals (envelope and peak) for NXP UCODE G2XM; generated by circuit simulations |
| <code>meas_tag_picmin</code> | tag pwr supply | minimum operational power of a NXP UCODE G2XM chip (tag sensitivity); measurement data |
| <code>meas_tag_vdda</code> | tag pwr supply | power supply / limiter characteristic for three different versions of the G2XM chip; measurement data |
| <code>meas_tag_za_*</code> | tag modulator | antenna impedance of the modeled NXP UCODE general purpose reference antenna (different versions); generated by an electromagnetic field simulation software |
| <code>meas_tag_zic</code> | tag modulator | chip impedance of the modeled NXP UCODE G2XM over frequency and power (unmodulated state); measurement data |
| <code>meas_tag_zmod-act</code> | tag modulator | modulation impedance of the modeled NXP UCODE G2XM over frequency and power, simulating an active tag (modulation possible below the minimum power threshold); measurement data |
| <code>meas_tag_zmod-psv</code> | tag modulator | modulation impedance of the modeled NXP UCODE G2XM over frequency and power, passive tag (modulation not possible below the minimum power threshold); measurement data |

Table C.1: List of measurement data files and their origin.

| File | Description |
|--|---|
| <code>channelchar_directivity_*</code> | antenna directivity patterns for all used antennas (Intermec IA39B, Vivaldi and Vivaldi arrays, UWB tag antenna, $\lambda/2$ and $\lambda/4$ dipoles) |
| <code>readerchar_transmitter</code> | power amplifier characteristic (nonlinearity) |
| <code>tagchar_demodulator</code> | automatic gain control (AGC) characteristic and RC lowpass filter coefficients |
| <code>tagchar_modulator_adsm</code> | mapping of assembly and detuning states for tag reflection coefficient characteristics to settings of detuning and assembly mismatch model (see Section 3.3.1); generated by <code>tagchar_modulator_basevectors.m</code> |
| <code>tagchar_modulator_fb</code> | channel filter coefficient vectors for tag reflection coefficient filterbank (see [219]); generated by <code>tagchar_modulator_filterbank.m</code> |
| <code>tagchar_power</code> | tag power supply characteristic (power supply voltage vs. chip power) |
| <code>tagchar_modulator_b-p2a-sim_*</code> | tag reflection coefficient intended for the simulator; low-Q antenna; for a mapping of detuning/assembly states to values see <code>tagchar_modulator_adsm</code> |
| <code>tagchar_modulator_c-p2a-sim_*</code> | tag reflection coefficient intended for the simulator; high-Q antenna; for a mapping of detuning/assembly states to values see <code>tagchar_modulator_adsm</code> |
| <code>tagchar_modulator_c-p2a_a-light</code> | tag reflection coefficient used for the analyses in [128] (assembly mismatch); not suitable for the simulator |
| <code>tagchar_modulator_c-p2a_d-light</code> | tag reflection coefficient used for the analyses in [128] (antenna detuning); not suitable for the simulator |
| <code>tagchar_modulator_c-p2a_ad-light*</code> | tag reflection coefficient used for the analyses in [128] (antenna detunings and assembly mismatch); not suitable for the simulator |
| <code>syschar_sparsefir_<host></code> | performance characteristics of a host machine regarding the sparse-FIR filtering operation performed by <code>channel_main</code> (see Section 3.4) |

Table C.2: List of characteristics files.

C.3 Example Self-Test Log

```

1 Created on 05-Feb-2011 17:24:20
2
3 *****
4 * Versions:
5 This is version_system.m (rev.: alpha 1.11 | svn-rev.: 183 | svn-status: " ")
6 ... SVN is available (version 1.5.1)
7
8 Printing status of all .m-files in /afs/spsc.tugraz.at/user/arnitz/spr/simulator and subdirectories
9 sorted by filename (85 files total):
10 channel_directivity.m (rev.: alpha 1.2 | svn-rev.: 183 | svn-status: " ")
11 channel_large.m (rev.: alpha 1.5 | svn-rev.: 183 | svn-status: " ")
12 [...]
13
14 *****
15 * Reader:
16 = reader_oscillator **
17 Using results_reader_oscillator.mat (created by results_reader_oscillator.m, rev.: alpha 2.0)
18 - 100 setup(s) "clean carrier"
19 checking frequency +/-0.01%, phase +/-0.01deg, and amplitude +/-0.1%
20 ... passed
21 - 100 setup(s) "frequency instability"
22 checking frequency instability +/-2%
23 ... passed
24 - 100 setup(s) "additive noise"
25 checking SNR +/-0.5dB
26 ... passed
27 [...]
28
29 *****
30 * Channel:
31 = channel_newpos **
32 checking distances +/-0.01%, angles +/-0.0001deg,
33 Using results_channel_newpos.mat (created by results_channel_newpos.m, rev.: alpha 1.0)
34 - 200 setup(s) "LOS/Direct"
35 additional check: K-factor and RMS delay spread +/-0.01%
36 ... passed
37 - 100 setup(s) "NLOS"
38 ... passed
39 [...]
40
41 *****
42 * Tag:
43 = tag_modulation **
44 checking power levels and supply voltage (pav, pin, pic, vdda) +/-5%
45 checking [avg +/-, std <=]: magnitude [0.01, 0.005], phase [0.1, 0.05]deg, LF [1% + nfft, 0.1%]
46 checking leading t0 +/-5% + nfft/2 and trailing t0 +/-5% + nfft/2 + tclk (jitter)
47 Using results_tag_modulation.mat (created by results_tag_modulation.m, rev.: alpha 2.5)
48 - 20 setup(s) "modulate"
49 ... passed
50 - 20 setup(s) "filter"
51 additional check: checking chip input impedance Zic +/-1%
52 ... passed
53 - 7 setup(s) "exception handling"
54 ... passed
55 [...]
56
57 *****
58 * Ranging:
59 = multi-frequency-continuous-wave ranging (mfcw_addseccarrier, mfcw_compsel, and mfcw_calcdist) ***
60 checking estimated distance +/-5%
61 Using results_mfcw.mat (created by results_mfcw.m, rev.: alpha 1.1)
62 - 25 setup(s) "ideal carrier modulation"
63 ... passed
64
65 *****
66 * Main:
67 = reader_main and tag_main (top-level functionality) ***
68 Using results_main_reader_tag.mat (created by results_main_reader_tag.m, rev.: alpha 1.3)
69 - 5 setup(s) "data R->T"
70 checking sent data for equality and decoded timings (tari, rtcval, and trcal) +/-5%
71 ... passed
72 - 5 setup(s) "data T->R"
73 checking type of encoding and presence of pilot tone; checking LF +/-5% + nfft
74 Warning: no checks of sent data (reader_decoding not yet implemented)
75 ... passed
76 - 3 setup(s) "MFCW"
77 checking distance +/-5% (compensating expected tag phase shift)
78 ... passed
79
80 *****
81 * RESULT:
82 Reader: 0 error(s)
83 Channel: 0 error(s)
84 Tag: 0 error(s)
85 Ranging: 0 error(s)
86 Main: 0 error(s)
87
88 Legend:
89 ** statistical test (not all possible setup combinations covered)
90 *** low test coverage (not all parameters tested)

```

Listing C.1: Example log created by main self-test script, *selftest_main.m* (abridgement).

Bibliography

- [1] *ISO/IEC 18000-6C (EPCglobal Class-1 Gen-2)*, EPCglobal/ISO Std., 2004, version 1.0.9.
- [2] K. Witrisal, Y.-H. Kim, and R. Prasad, "A new method to measure parameters of frequency-selective radio channels using power measurements," *IEEE Trans. Commun.*, vol. 49, no. 10, pp. 1788–1800, Oct. 2001.
- [3] D. M. Dobkin, *The RF in RFID*. Elsevier, 2007, ISBN-13: 978-0750682091.
- [4] K. Finkenzeller, *RFID Handbook: Fundamentals and Applications in Contactless Smart Cards and Identification*, 2nd ed. Wiley & Sons, 2003, ISBN-13: 978-0470844021.
- [5] Z. Sahinoglu, S. Gezici, and I. Guvenc, *Ultra-wideband Positioning Systems: Theoretical Limits, Ranging Algorithms, and Protocols*. Cambridge University Press, 2008, ISBN-13: 978-0521873093.
- [6] S. J. Orfanidis, *Electromagnetic Waves and Antennas*, rev. August 31, 2010. [Online]. Available: <http://www.ece.rutgers.edu/~orfanidi/ewa/>
- [7] Intermec. (2005) IA39B Rugged Antenna. [Online]. Available: http://www.intermec.com/products/rfid_ant_ia39b/index.aspx
- [8] Wikimedia, Uploader: Peripitus. License: Creative Commons Attribution-Share Alike 3.0 Unported. Downloaded March 29, 2011. [Online]. Available: http://commons.wikimedia.org/wiki/File:HMAS-Adelaide_FFG01_main_radar_Dish.jpg
- [9] S. J. Ingram, D. Harmer, and M. Quinlan, "Ultrawideband indoor positioning systems and their use in emergencies," in *Proc. Position Location and Navigation Symp. PLANS 2004*, 2004, pp. 706–715.
- [10] K. Siwiak and J. Gabig, "802.15.4iGa informal call for application response, contribution #11," IEEE Tech. Rep. IEEE 802.15-04/266r0, Jul. 2003. [Online]. Available: <http://www.ieee.org>
- [11] "Position Aware RFID Systems (PARIS)," Project Description, Graz Univ. of Techn. / NXP Semicond., Dec. 2008, (internal document).
- [12] "Signal Processing for Ranging (SPR)," Project Description, Graz Univ. of Techn. / NXP Semicond., Aug. 2007, (internal document).
- [13] S. Saab and S. Nakad, "A standalone RFID indoor positioning system using passive tags," *IEEE Trans. Ind. Electron.*, no. 99, p. 1, 2010, early Access.
- [14] T. Jingwangsa, S. Soonjun, and P. Cherntanomwong, "Comparison between innovative approaches of RFID based localization using fingerprinting techniques for outdoor and indoor environments," in *Proc. 12th Int Advanced Communication Technology (ICACT) Conf*, vol. 2, 2010, pp. 1511–1515.
- [15] S. Jeon, M. Choi, G. Kim, and B. Hong, "Localization of pallets based on passive RFID tags," in *Proc. Seventh Int Information Technology: New Generations (ITNG) Conf*, 2010, pp. 834–839.
- [16] F. Manzoor, Y. Huang, and K. Menzel, "Passive RFID-based indoor positioning system, an algorithmic approach," in *Proc. IEEE Int RFID-Technology and Applications (RFID-TA) Conf*, 2010, pp. 112–117.
- [17] D. Lieckfeldt, J. You, and D. Timmermann, "Exploiting RF-scatter: Human localization with bistatic passive UHF RFID-systems," in *Proc. IEEE Int. Conf. Wireless and Mobile Computing, Networking and Communications WIMOB 2009*, 2009, pp. 179–184.
- [18] S. Park and S. Hashimoto, "Indoor localization for autonomous mobile robot based on passive RFID," in *Proc. IEEE Int. Conf. Robotics and Biomimetics ROBIO 2008*, 2009, pp. 1856–1861.
- [19] S. Soonjun, D. Boontri, and P. Cherntanomwong, "A novel approach of RFID based indoor localization using fingerprinting techniques," in *Proc. 15th Asia-Pacific Conf. Communications APCC 2009*, 2009, pp. 475–478.
- [20] P. Vorst and A. Zell, "Particle filter-based trajectory estimation with passive UHF RFID fingerprints in unknown environments," in *Proc. IEEE/RSJ Int. Conf. Intelligent Robots and Systems IROS 2009*, 2009, pp. 395–401.
- [21] T. Deyle, C. C. Kemp, and M. S. Reynolds, "Probabilistic UHF RFID tag pose estimation with multiple antennas and a multipath RF propagation model," in *Proc. IEEE/RSJ Int. Conf. Intelligent Robots and Systems IROS 2008*, 2008, pp. 1379–1384.

- [22] S. P. Subramanian, J. Sommer, S. Schmitt, and W. Rosenstiel, "RIL — reliable RFID based indoor localization for pedestrians," in *Proc. 16th Int. Conf. Software, Telecommunications and Computer Networks SoftCOM 2008*, 2008, pp. 218–222.
- [23] P. Yang, W. Wu, M. Moniri, and C. C. Chibelushi, "SLAM algorithm for 2D object trajectory tracking based on RFID passive tags," in *Proc. IEEE Int RFID Conf*, 2008, pp. 165–172.
- [24] T. Shiraishi, N. Komuro, H. Ueda, H. Kasai, and T. Tsuboi, "Indoor location estimation technique using UHF band RFID," in *Proc. Int. Conf. Information Networking ICOIN 2008*, 2008, pp. 1–5.
- [25] A. Milella, P. Vanadia, G. Cicirelli, and A. Distanto, "RFID-based environment mapping for autonomous mobile robot applications," in *Proc. IEEE/ASME International Conference Advanced Intelligent Mechatronics*, 2007, pp. 1–6.
- [26] C. Wang, H. Wu, and N.-F. Tzeng, "RFID-based 3-D positioning schemes," in *Proc. INFOCOM 2007. 26th IEEE Int. Conf. Computer Communications*, 2007, pp. 1235–1243.
- [27] P. Wilson, D. Prashanth, and H. Aghajan, "Utilizing RFID signaling scheme for localization of stationary objects and speed estimation of mobile objects," in *Proc. IEEE Int RFID Conf*, 2007, pp. 94–99.
- [28] R. C. Luo, C.-T. Chuang, and S.-S. Huang, "RFID-based indoor antenna localization system using passive tag and variable RF-attenuation," in *Proc. 33rd Annual Conf. of the IEEE Industrial Electronics Society IECON 2007*, 2007, pp. 2254–2259.
- [29] D. Hahnel, W. Burgard, D. Fox, K. Fishkin, and M. Philipose, "Mapping and localization with RFID technology," in *Proc. IEEE Int. Conf. Robotics and Automation ICRA '04*, vol. 1, 2004, pp. 1015–1020.
- [30] M. Bouet and G. Pujolle, "L-VIRT: A 3-D range-free localization method for RFID tags based on virtual landmarks and mobile readers," in *Proc. 6th IEEE Consumer Communications and Networking Conf. CCNC 2009*, 2009, pp. 1–5.
- [31] —, "L-VIRT: Range-free 3-D localization of RFID tags based on topological constraints," *Computer Communications*, vol. 32, no. 13-14, pp. 1485 – 1494, 2009. [Online]. Available: <http://www.sciencedirect.com/science/article/B6TYP-4WBK7C5-1/2/a3d1f38ba5e30de901c79ca1573ddd33>
- [32] M. Goller and M. Brandner, "Improving classification performance of RFID gates using hidden Markov models," in *IEEE Int Instrumentation and Measurement Technology Conf*, Hangzhou, China, May 2011.
- [33] —, "Increasing the robustness of RFID systems using a probabilistic business process model," Poster at IEEE Int RFID Conf, Orlando, Florida, Apr. 2011.
- [34] M. Goller, "Localization and tracking of UHF RFID tags using probabilistic models," Master thesis, Graz Univ. of Techn., Austria, 2010.
- [35] P. V. Nikitin, R. Martinez, S. Ramamurthy, H. Leland, G. Spiess, and K. V. S. Rao, "Phase based spatial identification of UHF RFID tags," in *Proc. IEEE Int RFID Conf*, 2010, pp. 102–109.
- [36] M. Bouet and A. L. dos Santos, "RFID tags: Positioning principles and localization techniques," in *Proc. 1st IFIP Wireless Days WD '08*, 2008, pp. 1–5.
- [37] K. Chawla, G. Robins, and L. Zhang, "Object localization using RFID," in *Proc. 5th IEEE Int Wireless Pervasive Computing (ISWPC) Symp*, 2010, pp. 301–306.
- [38] J. S. Choi, H. Lee, R. Elmasri, and D. W. Engels, "Localization systems using passive UHF RFID," in *Proc. Fifth Int. Joint Conf. INC, IMS and IDC NCM '09*, 2009, pp. 1727–1732.
- [39] W. Li, J. Wu, and D. Wang, "A novel indoor positioning method based on key reference RFID tags," in *Proc. IEEE Youth Conf. Information, Computing and Telecommunication YC-ICT '09*, 2009, pp. 42–45.
- [40] C. Alippi, D. Cogliati, and G. Vanini, "A statistical approach to localize passive RFIDs," in *Proc. IEEE Int. Symp. Circuits and Systems ISCAS 2006*, 2006.
- [41] A. Almaaitah, K. Ali, H. S. Hassanein, and M. Ibnkahla, "3D passive tag localization schemes for indoor RFID applications," in *Proc. IEEE Int Communications (ICC) Conf*, 2010, pp. 1–5.
- [42] D. Joho, C. Plagemann, and W. Burgard, "Modeling RFID signal strength and tag detection for localization and mapping," in *Proc. IEEE Int. Conf. Robotics and Automation ICRA '09*, 2009, pp. 3160–3165.
- [43] T. Wada, N. Uchitomi, Y. Ota, T. Hori, K. Mutsuura, and H. Okada, "A novel localization scheme for passive RFID tags; communication range recognition (CRR)," in *Proc. IEEE Int RFID Conf*, 2009, pp. 163–169.
- [44] —, "A novel scheme for spatial localization of passive RFID tags; communication range recognition (CRR) scheme," in *Proc. IEEE Int. Conf. Communications ICC '09*, 2009, pp. 1–6.
- [45] Y. Ota, T. Hori, T. Onishi, T. Wada, K. Mutsuura, and H. Okada, "Localization of passive RFID tags with robot using adaptive likelihood distribution algorithm," in *Proc. Australasian Telecommunication Networks and Applications Conf. ATNAC 2007*, 2007, pp. 163–168.

- [46] B. Yanakiev, P. Eggers, G. F. Pedersen, and T. Larsen, "Assessment of the physical interface of UHF passive tags for localization," in *Proc. 1st Int EURASIP RFID Workshop*, 2007, pp. 1–4.
- [47] B. Kusy, A. Ledeczki, and X. Koutsoukos, "Tracking mobile nodes using RF Doppler shifts," in *SenSys '07: Proceedings of the 5th international conference on Embedded networked sensor systems*. New York, NY, USA: ACM, 2007, pp. 29–42.
- [48] H. Jingyu, S. Bin, and Y. Xiaohu, "The phase probability distribution of general Clarke model and its application in Doppler shift estimator," *IEEE Antennas Wireless Propag. Lett.*, vol. 4, pp. 373–377, 2005.
- [49] D. A. M. I. Broer, "RFID tag movement determination," Patent US20 100 156 651, June, 2010. [Online]. Available: <http://www.freepatentsonline.com/y2010/0156651.html>
- [50] R. Miesen, F. Kirsch, and M. Vossiek, "Holographic localization of passive UHF RFID transponders," in *Proc. IEEE Int RFID Conf*, 2011, pp. 32–37.
- [51] V. Viikari, P. Pursula, and K. Jaakkola, "Ranging of UHF RFID tag using stepped frequency read-out," *IEEE Sensors J.*, vol. 10, no. 9, pp. 1535–1539, 2010.
- [52] S. Azzouzi, M. Cremer, U. Dettmar, and R. Kronberger, "New measurement results for the localization of UHF RFID transponders using an angle of arrival (AoA) approach," in *Proc. IEEE Int RFID Conf*, 2011, pp. 155–161.
- [53] G. Hislop, D. Lekime, M. Drouguet, and C. Craeye, "A prototype 2D direction finding system with passive RFID tags," in *Proc. Fourth European Conf. Antennas and Propagation (EuCAP)*, 2010, pp. 1–5.
- [54] C. Angerer, R. Langwieser, and M. Rupp, "Direction of arrival estimation by phased arrays in RFID," in *3rd Int. EURASIP workshop on RFID Techn.*, Cartagena, Spain, 2010.
- [55] C. Hekimian-Williams, B. Grant, X. Liu, Z. Zhang, and P. Kumar, "Accurate localization of RFID tags using phase difference," in *Proc. IEEE Int RFID Conf*, 2010, pp. 89–96.
- [56] Y. Zhang, M. G. Amin, and S. Kaushik, "Localization and tracking of passive RFID tags based on direction estimation," *Hindawi Int Journal of Antennas and Propagation*, 2007, article ID 1742.
- [57] J. Wang, M. Amin, and Y. Zhang, "Signal and array processing techniques for RFID readers," in *SPIE Wireless Sensing and Processing*, vol. 6248, 2006.
- [58] R. Schmidt, "Multiple emitter location and signal parameter estimation," *IEEE Trans. Antennas Propag.*, vol. 34, no. 3, pp. 276–280, 1986.
- [59] L. Brennan, "Angular accuracy of a phased array radar," *IRE Transactions on Antennas and Propagation*, vol. 9, no. 3, pp. 268–275, 1961.
- [60] W. H. Von Aulock, "Properties of phased arrays," *Proceedings of the IRE*, vol. 48, pp. 1715–1727, 1960.
- [61] E. D. Kaplan and C. J. Hegarty, Eds., *Understanding GPS: Principles and Applications*, 2nd ed. Artech House, 2006, ISBN-13: 978-1580538947.
- [62] T. Gigl, "Low-complexity localization via impulse radio ultra-wideband signals," PhD thesis, Graz Univ. of Techn., Austria, 2010.
- [63] T. wen Xiong, J. juan Liu, Y. qing Yang, X. Tan, and H. Min, "Design and implementation of a passive UHF RFID-based real time location system," in *Proc. Int VLSI Design Automation and Test (VLSI-DAT) Symp*, 2010, pp. 95–98.
- [64] Y. Zhang, X. Li, and M. G. Amin, "Target localization in multipath environment through the exploitation of multi-frequency array," in *Int Waveform Diversity and Design Conference*, 2010.
- [65] —, "Array processing for RFID tag localization exploiting multi-frequency signals," in *SPIE Symposium on Defense, Security, and Sensing*, 2009.
- [66] X. Li, Y. Zhang, and M. G. Amin, "Multifrequency-based range estimation of RFID tags," in *Proc. IEEE Int RFID Conf*, 2009, pp. 147–154.
- [67] S. Kungel, M.-S. Huang, R. Bieber, and M. Vossiek, "SAR-like localization of RFID tags for non-uniform trajectory," 2010.
- [68] M. Vossiek, R. Miesen, and J. Wittwer, "RF identification and localization - recent steps towards the internet of things in metal production and processing," in *Proc. 18th Int Microwave Radar and Wireless Communications (MIKON) Conf*, 2010, pp. 1–8.
- [69] F. Ali and M. Vossiek, "Detection of weak moving targets based on 2-D range-Doppler FMCW radar fourier processing," in *Proc. German Microwave Conf*, 2010, pp. 214–217.
- [70] J. Heidrich, D. Brenk, J. Essel, S. Schwarzer, K. Seemann, G. Fischer, and R. Weigel, "The roots, rules, and rise of RFID," *IEEE Microw. Mag.*, vol. 11, no. 3, pp. 78–86, 2010.
- [71] S. Kunkel, R. Bieber, M.-S. Huang, and M. Vossiek, "A concept for infrastructure independent localization and augmented reality visualization of RFID tags," in *Proc. IEEE MTT-S Int. Microwave Workshop Wireless Sensing, Local Positioning, and RFID IMWS 2009*, 2009, pp. 1–4.

- [72] T. Ussmueller, M. Jung, and R. Weigel, "Synthesizer concepts for FMCW based locatable wireless sensor nodes," in *Proc. IEEE MTT-S Int. Microwave Workshop Wireless Sensing, Local Positioning, and RFID IMWS 2009*, 2009, pp. 1–4.
- [73] J. Heidrich, D. Brenk, J. Essel, G. Fischer, R. Weigel, and S. Schwarzer, "Local positioning with passive UHF RFID transponders," in *Proc. IEEE MTT-S Int. Microwave Workshop Wireless Sensing, Local Positioning, and RFID IMWS 2009*, 2009, pp. 1–4.
- [74] R. Mosshammer, B. Waldmann, R. Eickhoff, R. Weigel, and M. Huemer, "A comparison of channel access concepts for high-precision local positioning," in *Proc. 6th Workshop Positioning, Navigation and Communication WPNC 2009*, 2009, pp. 37–41.
- [75] B. Waldmann, A. Goetz, and R. Weigel, "An ultra wideband positioning system enhanced by a short multipath mitigation technique," in *Proc. IEEE MTT-S Int. Microwave Workshop Wireless Sensing, Local Positioning, and RFID IMWS 2009*, 2009, pp. 1–4.
- [76] S. Scheiblhofer, S. Schuster, M. Jahn, R. Feger, and A. Stelzer, "Performance analysis of cooperative FMCW radar distance measurement systems," in *Proc. IEEE MTT-S Int. Microwave Symp. Digest*, 2008, pp. 121–124.
- [77] S. Max, M. Vossiek, and P. Gulden, "Fusion of FMCW secondary radar signal beat frequency and phase estimations for high precision distance measurement," in *Proc. European Radar Conf. EuRAD 2008*, 2008, pp. 124–127.
- [78] S. Roehr, P. Gulden, and M. Vossiek, "Precise distance and velocity measurement for real time locating in multipath environments using a frequency-modulated continuous-wave secondary radar approach," *IEEE Trans. Microw. Theory Tech.*, vol. 56, no. 10, pp. 2329–2339, 2008.
- [79] A. Stelzer, M. Jahn, and S. Scheiblhofer, "Precise distance measurement with cooperative FMCW radar units," in *Proc. IEEE Radio and Wireless Symp*, 2008, pp. 771–774.
- [80] B. Waldmann, R. Weigel, and P. Gulden, "Method for high precision local positioning radar using an ultra wideband technique," in *Proc. IEEE MTT-S Int. Microwave Symp. Digest*, 2008, pp. 117–120.
- [81] B. Waldmann, R. Weigel, P. Gulden, and M. Vossiek, "Pulsed frequency modulation techniques for high-precision ultra wideband ranging and positioning," in *Proc. IEEE Int. Conf. Ultra-Wideband ICUWB 2008*, vol. 2, 2008, pp. 133–136.
- [82] S. Roehr, M. Vossiek, and P. Gulden, "Method for high precision radar distance measurement and synchronization of wireless units," in *Proc. IEEE/MTT-S Int. Microwave Symp*, 2007, pp. 1315–1318.
- [83] S. Roehr, P. Gulden, and M. Vossiek, "Novel secondary radar for precise distance and velocity measurement in multipath environments," in *Proc. European Microwave Conf*, 2007, pp. 1461–1464.
- [84] M. Vossiek, R. Roskosch, and P. Heide, "Precise 3-D object position tracking using FMCW radar," in *Proc. 29th European Microwave Conf*, vol. 1, 1999, pp. 234–237.
- [85] S. Scheiblhofer, S. Schuster, M. Jahn, R. Feger, and A. Stelzer, "Performance analysis of cooperative FMCW radar distance measurement systems," in *Proc. IEEE MTT-S Int. Microwave Symp. Digest*, 2008, pp. 121–124.
- [86] T. Sollenberger, "Multipath phase errors in CW-FM tracking systems," *IRE Transactions on Antennas and Propagation*, vol. 3, no. 4, pp. 185–192, 1955.
- [87] IDTechEx. Article "Real Time Locating Systems Using Passive Tags - High Volume RTLS". (Jul 22, 2008). [Online]. Available: http://www.idtechex.com/research/articles/real_time_locating_systems_using_passive_tags_high_volume_rtls_00001005.asp
- [88] Mojix. (2009) Mojix EPC Compliant Real-Time Location System. [Online]. Available: http://www.mojix.com/products/documents/RTLS_brochure.pdf
- [89] RF Controls / Businesswire. Article "RF Controls' ITCS Delivers 3D Tag Location with a Single Antenna". (Nov 09, 2009). [Online]. Available: <http://www.businesswire.com/news/home/20091109005167/en>
- [90] Trolleyscan. Newsletter No. 82 (2009). [Online]. Available: <http://trolleyscan.com/newslett.html>
- [91] ——. How it works (Aug. 2010). [Online]. Available: <http://www.rfid-radar.com/howworks.html>
- [92] C. Zhang, M. J. Kuhn, B. C. Merkl, A. E. Fathy, and M. R. Mahfouz, "Real-time noncoherent UWB positioning radar with millimeter range accuracy: Theory and experiment," *IEEE Trans. Microw. Theory Tech.*, vol. 58, no. 1, pp. 9–20, 2010.
- [93] S. Gezici, Z. Tian, G. B. Giannakis, H. Kobayashi, A. F. Molisch, H. V. Poor, and Z. Sahinoglu, "Localization via ultra-wideband radios: a look at positioning aspects for future sensor networks," *IEEE Signal Process. Mag.*, vol. 22, no. 4, pp. 70–84, 2005.
- [94] *IEEE 802.15.4a*, IEEE Std., 2007.

- [95] H. Liu, H. Darabi, P. Banerjee, and J. Liu, "Survey of wireless indoor positioning techniques and systems," *IEEE Trans. Syst., Man, Cybern. C*, vol. 37, no. 6, pp. 1067–1080, 2007.
- [96] D. Dardari, R. D'Errico, C. Roblin, A. Sibille, and M. Z. Win, "Ultrawide bandwidth RFID: The next generation?" *Proc. IEEE*, vol. 98, no. 9, pp. 1570–1582, 2010.
- [97] Z. Zou, T. Deng, Q. Zou, M. D. Sarmiento, F. Jonsson, and L.-R. Zheng, "Energy detection receiver with TOA estimation enabling positioning in passive UWB-RFID system," in *Proc. IEEE Int Ultra-Wideband (ICUWB) Conf*, vol. 2, 2010, pp. 1–4.
- [98] L.-R. Zheng, M. B. Nejad, Z. Zou, D. S. Mendoza, Z. Zhang, and H. Tenhunen, "Future RFID and wireless sensors for ubiquitous intelligence," in *Proc. NORCHIP*, 2008, pp. 142–149.
- [99] M. Baghaei-Nejad, Z. Zou, H. Tenhunen, and L.-R. Zheng, "A novel passive tag with asymmetric wireless link for RFID and WSN applications," in *Proc. IEEE Int. Symp. Circuits and Systems ISCAS 2007*, 2007, pp. 1593–1596.
- [100] H. G. Schantz, "Near field phase behavior," in *Proc. IEEE Antennas and Propagation Society Int. Symp*, vol. 3, 2005, pp. 134–137.
- [101] K. Yan, H.-C. Wu, and S. S. Iyengar, "Robustness analysis and new hybrid algorithm of wideband source localization for acoustic sensor networks," *IEEE Trans. Wireless Commun.*, vol. 9, no. 6, pp. 2033–2043, 2010.
- [102] J. S. Rogers and J. L. Krolik, "Passive broadband source localization in shallow-water multipath acoustic channels," in *Proc. OCEANS 2008*, 2008, pp. 1–4.
- [103] J. H. DiBiase, "A high-accuracy, low-latency technique for talker localization in reverberant environments using microphone arrays," PhD thesis, Brown University, USA, 2000.
- [104] M. Hawkes and A. Nehorai, "Wideband source localization using a distributed acoustic vector-sensor array," *IEEE Trans. Signal Process.*, vol. 51, no. 6, pp. 1479–1491, 2003.
- [105] M. S. Brandstein, J. E. Adcock, and H. F. Silverman, "A closed-form location estimator for use with room environment microphone arrays," *IEEE Trans. Speech Audio Process.*, vol. 5, no. 1, pp. 45–50, 1997.
- [106] A. Bellettini and M. Pinto, "Design and experimental results of a 300-kHz synthetic aperture sonar optimized for shallow-water operations," *IEEE J. Ocean. Eng.*, vol. 34, no. 3, pp. 285–293, 2009.
- [107] Q. Chen, W. Xu, X. Pan, and J. Li, "Wideband multipath rejection for shallow water synthetic aperture sonar imaging," *IET Radar, Sonar & Navigation*, vol. 3, no. 6, pp. 620–629, 2009.
- [108] B. J. Davis, P. T. Gough, and B. R. Hunt, "Modeling surface multipath effects in synthetic aperture sonar," *IEEE J. Ocean. Eng.*, vol. 34, no. 3, pp. 239–249, 2009.
- [109] S. Pawar and S. Subbaraman, "Passive multipath ranging in sonars using auto-correlation processing," in *Proc. Int. Conf. Industrial and Information Systems ICIIS 2007*, 2007, pp. 491–496.
- [110] C. Floerkemeier and S. Sarma, "RFIDSim—A physical and logical layer simulation engine for passive RFID," *IEEE Trans. Autom. Sci. Eng.*, vol. 6, no. 1, pp. 33–43, 2009.
- [111] C. Floerkemeier and R. Pappu, "Evaluation of RFIDSim - a physical and logical layer RFID simulation engine," in *Proc. IEEE Int RFID Conf*, 2008, pp. 350–356.
- [112] K. K.-W. Yu, "RFIDSim - A discrete event simulator for radio frequency identification systems," PhD thesis, Massachusetts Institute of Technology, USA, 2003.
- [113] R. Barr, "An efficient, unifying approach to simulation using virtual machines," PhD thesis, Cornell University, USA, 2004.
- [114] V. Derbek, C. Steger, R. Weiss, D. Wischounig, J. Preishuber-Pfluegl, and M. Pistauer, "Simulation platform for UHF RFID," in *Proc. Design, Automation & Test in Europe Conf. & Exhibition DATE'07*, 2007, pp. 1–6.
- [115] V. Derbek, J. Preishuber-Pfluegl, C. Steger, and M. Pistauer, "Architecture for model-based UHF RFID system design verification," in *Proc. European Conf. Circuit Theory and Design*, vol. 2, 2005.
- [116] V. Derbek, C. Steger, S. Kajtazovic, J. Preishuber-Pfluegl, and M. Pistauer, "Behavioral model of UHF RFID tag for system and application level simulation," in *Proc. IEEE Int. Behavioral Modeling and Simulation Workshop BMAS 2005*, 2005, pp. 60–63.
- [117] M. Winkler, T. Faseth, and H. Arthaber, "Implementation of an EPC tag emulator for reproduction of worst case test scenarios," in *3rd Int. EURASIP workshop on RFID Techn.*, Cartagena, Spain, Sep. 2010.
- [118] M. Winkler, T. Faseth, H. Arthaber, and G. Magerl, "An UHF RFID tag emulator for precise emulation of the physical layer," in *Proc. European Microwave Conf. (EuMC)*, 2010, pp. 1750–1753.
- [119] —, "An UHF RFID tag emulator for precise emulation of the physical layer," in *Proc. European Wireless Technology Conf. (EuWIT)*, 2010, pp. 273–276.

- [120] H. Arthaber and C. Schuberth, "A UHF RFID channel emulator hardware for playback of measured link-scenarios," in *Proc. IEEE Int RFID Conf*, 2009, pp. 34–41.
- [121] —, "A channel emulator for UHF RFID systems," in *Proc. IEEE Radio and Wireless Symp. RWS '09*, 2009, pp. 518–521.
- [122] Y. Han and H. Min, "System modeling and simulation of RFID," in *Auto-ID Labs Whitepaper*, 2005. [Online]. Available: <http://www.autoidlabs.org/uploads/media/AUTOIDLABS-WP-HARDWARE-010.pdf>
- [123] J. Li and C. Tao, "Analysis and simulation of UHF RFID system," in *Proc. 8th Int Signal Processing Conf*, vol. 4, 2006.
- [124] M. A. Assad, M. Heidari, and K. Pahlavan, "Effects of channel modeling on performance evaluation of WiFi RFID localization using a laboratory testbed," in *Proc. IEEE Global Telecommunications Conf. GLOBECOM '07*, 2007, pp. 366–370.
- [125] J. M. Pavlina and D. C. Malocha, "Chipless RFID SAW sensor system-level simulator," in *Proc. IEEE Int RFID Conf*, 2010, pp. 252–259.
- [126] D. Arnitz, U. Muehlmann, T. Gigl, and K. Witrals, "Wideband system-level simulator for passive UHF RFID," in *Proc. IEEE Int RFID Conf*, Orlando, Florida, Apr. 2009, pp. 28–33. [Online]. Available: <http://www.spsc.tugraz.at/publications>
- [127] The PARIS Simulation Framework. Graz University of Technology / NXP Semiconductors. Open-Source (GNU GPL v3). [Online]. Available: <http://www.spsc.tugraz.at/tools/paris-osf>
- [128] D. Arnitz, U. Muehlmann, and K. Witrals, "Tag-based sensing and positioning in passive UHF RFID: Tag reflection," in *3rd Int. EURASIP workshop on RFID Techn.*, Cartagena, Spain, Sep. 2010, pp. 51–56. [Online]. Available: <http://www.spsc.tugraz.at/publications>
- [129] —, "Wideband characterization of UHF RFID channels for ranging and positioning," Poster at IEEE Int RFID Conf, Orlando, Florida, Apr. 2010. [Online]. Available: <http://www.spsc.tugraz.at/publications>
- [130] COST2100. (2010, Jul.) Newsletter No. 9. [Online]. Available: http://www.cost2100.org/uploads/File/Newsletters/COST2100_Newsletter_No9.pdf
- [131] D. Arnitz, G. Adamiuk, U. Muehlmann, and K. Witrals, "UWB channel sounding for ranging and positioning in passive UHF RFID," in *11th COST2100 MCM*, Aalborg, Denmark, Jun. 2010. [Online]. Available: <http://www.spsc.tugraz.at/publications>
- [132] D. Arnitz, U. Muehlmann, and K. Witrals, "Wideband characterization and modeling of UHF RFID channels for ranging and localization," submitted for publication. [Online]. Available: <http://www.spsc.tugraz.at/publications>
- [133] —, "Wideband characterization of backscatter channels: Derivations and theoretical background," accepted for publication. [Online]. Available: <http://www.spsc.tugraz.at/publications>
- [134] —, "Wideband characterization of backscatter channels," in *Proc. Europ. Wireless Conf*, Vienna, Austria, Apr. 2011, pp. 205–211. [Online]. Available: <http://www.spsc.tugraz.at/publications>
- [135] —, "Multi-frequency continuous-wave radar approach to ranging in passive UHF RFID," *IEEE Trans. Microw. Theory Tech.*, vol. 57, no. 5, pp. 1398–1405, Jul. 2009. [Online]. Available: <http://www.spsc.tugraz.at/publications>
- [136] —, "UWB ranging in passive UHF RFID: Proof of concept," *IET Electron. Letters*, vol. 46, no. 20, pp. 1401–1402, Sep. 2010. [Online]. Available: <http://www.spsc.tugraz.at/publications>
- [137] G. Li, D. Arnitz, R. Ebel, U. Muehlmann, K. Witrals, and M. Vossiek, "Bandwidth dependence of CW ranging to UHF RFID tags in severe multipath environments," in *Proc. IEEE Int RFID Conf*, Orlando, Florida, Apr. 2011, pp. 19–25. [Online]. Available: <http://www.spsc.tugraz.at/publications>
- [138] T. Gigl, J. Preishuber-Pfluegl, D. Arnitz, and K. Witrals, "Experimental characterization of ranging in IEEE802.15.4a using a coherent reference receiver," in *Proc. IEEE 20th Int Personal, Indoor and Mobile Radio Communications Symp.*, Tokyo, Japan, Jun. 2009, pp. 92–96. [Online]. Available: <http://www.spsc.tugraz.at/publications>
- [139] P. Meissner, D. Arnitz, T. Gigl, and K. Witrals, "Analysis of an indoor UWB channel for multipath-aided localization," submitted for publication. [Online]. Available: <http://www.spsc.tugraz.at/publications>
- [140] A. Paulraj, R. Nabar, and D. Gore, *Introduction to Space-Time Wireless Communications*. Cambridge University Press, 2003, ISBN-13: 9-780521826150.
- [141] A. Molisch, *Wireless Communications*. John Wiley & Sons, 2005, chapters 4–7, ISBN-13: 978-0470848876.
- [142] T. S. Rappaport, *Wireless Communications*, 2nd ed. Prentice Hall International, 2002, chapters 4–5, ISBN-13: 978-0130422323.
- [143] W. Wiesbeck, G. Adamiuk, and C. Sturm, "Basic properties and design principles of UWB antennas," *Proc. IEEE*, vol. 97, no. 2, pp. 372–385, 2009.

- [144] K. Pahlavan, X. Li, and J. P. Makela, "Indoor geolocation science and technology," *IEEE Commun. Mag.*, vol. 40, no. 2, pp. 112–118, 2002.
- [145] K. Pahlavan, P. Krishnamurthy, and A. Beneat, "Wideband radio propagation modeling for indoor geolocation applications," *IEEE Commun. Mag.*, vol. 36, no. 4, pp. 60–65, 1998.
- [146] H. Cramér, *Mathematical Methods of Statistics*. Princeton University Press, 1946, ISBN-13: 978-0691005478.
- [147] A. F. Molisch, "Ultrawideband propagation channels-theory, measurement, and modeling," *IEEE Trans. Veh. Technol.*, vol. 54, no. 5, pp. 1528–1545, 2005.
- [148] A. Saleh and R. Valenzuela, "A statistical model for indoor multipath propagation," *IEEE J. Sel. Areas Commun.*, vol. 5, no. 2, pp. 128–137, 1987.
- [149] J. Karedal, S. Wyne, P. Almers, F. Tufvesson, and A. F. Molisch, "A measurement-based statistical model for industrial ultra-wideband channels," *IEEE Trans. Wireless Commun.*, vol. 6, no. 8, pp. 3028–3037, 2007.
- [150] D. C. Hogg, "Fun with the Friis free-space transmission formula," *IEEE Antennas Propag. Mag.*, vol. 35, no. 4, pp. 33–35, 1993.
- [151] P. V. Nikitin and K. V. S. Rao, "Antennas and propagation in UHF RFID systems," in *Proc. IEEE Int RFID Conf*, 2008, pp. 277–288.
- [152] P. V. Nikitin, K. V. S. Rao, R. Martinez, and S. F. Lam, "Sensitivity and impedance measurements of UHF RFID chips," *IEEE Trans. Microw. Theory Tech.*, vol. 57, no. 5, pp. 1297–1302, 2009.
- [153] S. R. Aroor and D. D. Deavours, "Evaluation of the state of passive UHF RFID: An experimental approach," *IEEE Systems Journal*, vol. 1, no. 2, pp. 168–176, 2007.
- [154] J. D. Griffin and G. D. Durgin, "Complete link budgets for backscatter-radio and RFID systems," *IEEE Antennas Propag. Mag.*, vol. 51, no. 2, pp. 11–25, 2009.
- [155] P. V. Nikitin and K. V. S. Rao, "Performance limitations of passive UHF RFID systems," in *Proc. IEEE Antennas and Propagation Society Int. Symp. 2006*, 2006, pp. 1011–1014.
- [156] J. D. Griffin and G. D. Durgin, "Multipath fading measurements for multi-antenna backscatter RFID at 5.8 GHz," in *Proc. IEEE Int RFID Conf*, 2009, pp. 322–329.
- [157] —, "Link envelope correlation in the backscatter channel," *IEEE Commun. Lett.*, vol. 11, no. 9, pp. 735–737, 2007.
- [158] —, "Gains for RF tags using multiple antennas," *IEEE Trans. Antennas Propag.*, vol. 56, no. 2, pp. 563–570, 2008.
- [159] T. Taniguchi, Y. Karasawa, and M. Tsuruta, "An analysis method of double fading MIMO channels including LOS environments," in *Proc. IEEE 19th Int. Symp. Personal, Indoor and Mobile Radio Communications PIMRC 2008*, 2008, pp. 1–5.
- [160] J. D. Griffin and G. D. Durgin, "Reduced fading for RFID tags with multiple antennas," in *Proc. IEEE Antennas and Propagation Society Int. Symp.*, 2007, pp. 1201–1204.
- [161] W. Su, K. M. Beilke, and T. T. Ha, "A reliability study of RFID technology in a fading channel," in *Proc. Conf. Record of the Forty-First Asilomar Conf. Signals, Systems and Computers ACSSC 2007*, 2007, pp. 2124–2127.
- [162] D. Kim, M. A. Ingram, and J. Smith, W. W., "Measurements of small-scale fading and path loss for long range RF tags," *IEEE Trans. Antennas Propag.*, vol. 51, no. 8, pp. 1740–1749, 2003.
- [163] D. Kim, M. A. Ingram, and W. W. Smith, "Small-scale fading for an indoor wireless channel with modulated backscatter," in *Proc. VTC 2001 Fall Vehicular Technology Conf. IEEE VTS 54th*, vol. 3, 2001, pp. 1616–1620.
- [164] T. S. Rappaport and C. D. McGillem, "UHF fading in factories," *IEEE J. Sel. Areas Commun.*, vol. 7, no. 1, pp. 40–48, 1989.
- [165] T. S. Rappaport, "Characterization of UHF multipath radio channels in factory buildings," *IEEE Trans. Antennas Propag.*, vol. 37, no. 8, pp. 1058–1069, 1989.
- [166] R. Bultitude, "Measurement, characterization and modeling of indoor 800/900 MHz radio channels for digital communications," *IEEE Commun. Mag.*, vol. 25, no. 6, pp. 5–12, 1987.
- [167] G. Marrocco, E. Di Giampaolo, and R. Aliberti, "Estimation of UHF RFID reading regions in real environments," *IEEE Antennas Propag. Mag.*, vol. 51, no. 6, pp. 44–57, 2009.
- [168] U. Muehlmann, G. Manzi, G. Wiednig, and M. Buchmann, "Modeling and performance characterization of UHF RFID portal applications," *IEEE Trans. Microw. Theory Tech.*, vol. 57, no. 7, pp. 1700–1706, 2009.
- [169] P. Bosselmann, "Planning and analysis of UHF RFID systems for consumer goods logistics using ray tracing predictions," in *Proc. 1st Annual RFID Eurasia*, 2007, pp. 1–7.

- [170] A. F. Molisch, J. R. Foerster, and M. Pendergrass, "Channel models for ultrawideband personal area networks," *IEEE Wireless Commun. Mag.*, vol. 10, no. 6, pp. 14–21, 2003.
- [171] A. F. Molisch, D. Cassioli, C.-C. Chong, S. Emami, A. Fort, B. Kannan, J. Karedal, J. Kunisch, H. G. Schantz, K. Siwiak, and M. Z. Win, "A comprehensive standardized model for ultrawideband propagation channels," *IEEE Trans. Antennas Propag.*, vol. 54, no. 11, pp. 3151–3166, 2006.
- [172] J. B. Andersen, J. O. Nielsen, G. F. Pedersen, G. Bauch, and M. Herdin, "Room electromagnetics," *IEEE Antennas Propag. Mag.*, vol. 49, no. 2, pp. 27–33, 2007.
- [173] C. L. Holloway, M. G. Cotton, and P. McKenna, "A model for predicting the power delay profile characteristics inside a room," *IEEE Trans. Veh. Technol.*, vol. 48, no. 4, pp. 1110–1120, 1999.
- [174] I. Kashiwagi, T. Taga, and T. Imai, "Time-varying path-shadowing model for indoor populated environments," *IEEE Trans. Veh. Technol.*, vol. 59, no. 1, pp. 16–28, 2010.
- [175] M. Thiel and K. Sarabandi, "3D-wave propagation analysis of indoor wireless channels utilizing hybrid methods," *IEEE Trans. Antennas Propag.*, vol. 57, no. 5, pp. 1539–1546, 2009.
- [176] G. Tiberi, S. Bertini, W. Q. Malik, A. Monorchio, D. J. Edwards, and G. Manara, "Analysis of realistic ultrawideband indoor communication channels by using an efficient ray-tracing based method," *IEEE Trans. Antennas Propag.*, vol. 57, no. 3, pp. 777–785, 2009.
- [177] G. Tiberi, S. Bertini, A. Monorchio, F. Giannetti, and G. Manara, "Computationally efficient ray-tracing technique for modelling ultrawideband indoor propagation channels," *IET Microwaves, Antennas & Propagation*, vol. 3, no. 3, pp. 395–401, 2009.
- [178] M. Porebska, T. Kayser, and W. Wiesbeck, "Verification of a hybrid ray-tracing/FDTD model for indoor ultra-wideband channels," in *Proc. European Conf. Wireless Technologies*, 2007, pp. 169–172.
- [179] J. H. Tarng, W.-S. Liu, Y.-F. Huang, and J.-M. Huang, "A novel and efficient hybrid model of radio multipath-fading channels in indoor environments," *IEEE Trans. Antennas Propag.*, vol. 51, no. 3, pp. 585–594, 2003.
- [180] W. K. Tam and V. N. Tran, "Propagation modelling for indoor wireless communication," *Electronics & Communication Engineering Journal*, vol. 7, no. 5, pp. 221–228, 1995.
- [181] U. Dersch and E. Zollinger, "Propagation mechanisms in microcell and indoor environments," *IEEE Trans. Veh. Technol.*, vol. 43, no. 4, pp. 1058–1066, 1994.
- [182] S. Bug, "Charakterisierung von Mobilfunkkanälen auf Basis der nichtlinearen Dynamik," PhD thesis, TU Darmstadt, Germany, 2006, ISBN-13: 978-3832254414.
- [183] S. Bug, A. Nazarov, K. Kastell, and R. Jakoby, "Characterizing the mobile radio channel by a conservative dynamical system," in *Proc. VTC 2006-Spring Vehicular Technology Conf. IEEE 63rd*, vol. 6, 2006, pp. 2772–2776.
- [184] S. Bug and R. Jakoby, "Modeling the mobile radio channel using theory of dynamics – reconstruction of dynamics by differential equations," in *Proc. VTC2004-Fall Vehicular Technology Conf. 2004 IEEE 60th*, vol. 1, 2004, pp. 28–32.
- [185] T. Gigl, T. Buchgraber, A. Adalan, J. Preishuber-Pfluegl, M. Fischer, and K. Witrisal, "UWB channel characterization using IEEE 802.15.4a demonstrator system," in *Proc. IEEE Int. Conf. Ultra-Wideband ICUWB 2009*, 2009, pp. 230–234.
- [186] J. Karedal, S. Wyne, P. Almers, F. Tufvesson, and A. F. Molisch, "Statistical analysis of the UWB channel in an industrial environment," in *Proc. VTC2004-Fall Vehicular Technology Conf. 2004 IEEE 60th*, vol. 1, 2004, pp. 81–85.
- [187] —, "UWB channel measurements in an industrial environment," in *Proc. IEEE Global Telecommunications Conf. GLOBECOM '04*, vol. 6, 2004, pp. 3511–3516.
- [188] G. Steinboeck, T. Pedersen, and B. H. Fleury, "Model for the path loss of in-room reverberant channels," in *Proc. IEEE Int. Conf. Global Comm. GLOBECOM*, Dec. 2010.
- [189] M. B. Nejad, "Ultra wideband impulse radio for wireless sensing and identification," PhD thesis, Royal Institute of Techn., Sweden, 2008.
- [190] E. Parzen, "Mathematical considerations in the estimation of spectra," *Technometrics*, vol. 3, no. 2, pp. 167–190, 1961.
- [191] F. J. Harris, "On the use of windows for harmonic analysis with the discrete Fourier transform," *Proc. IEEE*, vol. 66, no. 1, pp. 51–83, 1978.
- [192] A. Papoulis and S. U. Pillai, *Probability, Random Variables, and Stochastic Processes*, 4th ed. McGraw-Hill, 2002, ISBN-10: 0-07-366011-6.

- [193] M. K. Awad, K. T. Wong, and Z.-b. Li, "An integrated overview of the open literature's empirical data on the indoor radiowave channel's delay properties," *IEEE Trans. Antennas Propag.*, vol. 56, no. 5, pp. 1451–1468, 2008.
- [194] M. S. Varela and M. G. Sanchez, "RMS delay and coherence bandwidth measurements in indoor radio channels in the UHF band," *IEEE Trans. Veh. Technol.*, vol. 50, no. 2, pp. 515–525, 2001.
- [195] K. Sato, T. Manabe, J. Polivka, T. Ihara, Y. Kasashima, and K. Yamaki, "Measurement of the complex refractive index of concrete at 57.5 GHz," *IEEE Trans. Antennas Propag.*, vol. 44, no. 1, pp. 35–40, 1996.
- [196] E. G. Araujo and R. A. Grupen, "Feature detection and identification using a sonar-array," in *Proc. IEEE Int Robotics and Automation Conf*, vol. 2, 1998, pp. 1584–1589.
- [197] R. Bhattacharyya, C. Floerkemeier, and S. Sarma, "Low-cost, ubiquitous RFID-tag-antenna-based sensing," *Proc. IEEE*, vol. 98, no. 9, pp. 1593–1600, 2010.
- [198] S. Capdevila, L. Jofre, J.-C. Bolomey, and J. Romeu, "RFID multiprobe impedance-based sensors," *IEEE Trans. Instrum. Meas.*, no. 99, pp. 1–9, 2010, early Access.
- [199] R. Bhattacharyya, C. Floerkemeier, and S. Sarma, "RFID tag antenna based temperature sensing," in *Proc. IEEE Int RFID Conf*, 2010, pp. 8–15.
- [200] —, "RFID tag antenna based sensing: Does your beverage glass need a refill?" in *Proc. IEEE Int RFID Conf*, 2010, pp. 126–133.
- [201] —, "Towards tag antenna based sensing - an RFID displacement sensor," in *Proc. IEEE Int RFID Conf*, 2009, pp. 95–102.
- [202] S. Capdevila, M. M. Massud, R. Serrano, A. Aguiasca, S. Blanch, J. Romeu, J. C. Bolomey, and L. Jofre, "RFID based probes for EM-field measurements," in *Proc. 3rd European Conf. Antennas and Propagation EuCAP 2009*, 2009, pp. 2787–2790.
- [203] S. Capdevila, L. Jofre, J. C. Bolomey, and J. Romeu, "RFID array probe for EM-field measurements," in *Proc. IEEE Antennas and Propagation Society Int. Symp. APSURSI '09*, 2009, pp. 1–4.
- [204] L. W. Mayer and A. L. Scholz, "Sensitivity and impedance measurements on UHF RFID transponder chips," in *Int EURASIP Workshop on RFID Techn., Vienna, Austria*, 2007. [Online]. Available: http://publik.tuwien.ac.at/files/PubDat_165917.pdf
- [205] P. V. Nikitin and K. V. S. Rao, "Theory and measurement of backscattering from RFID tags," *IEEE Antennas Propag. Mag.*, vol. 48, no. 6, pp. 212–218, 2006.
- [206] E. Colin, A. Moretto, C. Ripoll, and S. A. Chakra, "Delta RCS of UHF RFID taking into account the shunt resistance in the tag model," in *Proc. Joint IEEE North-East Workshop Circuits and Systems and TAISA Conf. NEWCAS-TAISA '09*, 2009, pp. 1–4.
- [207] U. Muehlmann, "UHF RFID System Requirements – Tag Scattering Properties (Part I)," NXP Semiconductors, Tech. Rep., rev. 1, Apr. 2006, (internal document).
- [208] K. V. S. Rao, P. V. Nikitin, and S. F. Lam, "Antenna design for UHF RFID tags: a review and a practical application," *IEEE Trans. Antennas Propag.*, vol. 53, no. 12, pp. 3870–3876, 2005.
- [209] Y. Tikhov, "Comments on antenna design for UHF RFID tags: a review and a practical application," *IEEE Trans. Antennas Propag.*, vol. 54, no. 6, 2006.
- [210] P. V. Nikitin and K. V. S. Rao, "Reply to comments on antenna design for UHF RFID tags: A review and a practical application," *IEEE Trans. Antennas Propag.*, vol. 54, no. 6, pp. 1906–1907, 2006.
- [211] W. Wiesbeck, G. Adamiuk, and C. Sturm, "Basic properties and design principles of UWB antennas," *Proc. IEEE*, vol. 97, no. 2, pp. 372–385, 2009.
- [212] P. V. Nikitin, K. V. S. Rao, and R. D. Martinez, "Differential RCS of RFID tag," *Electronics Letters*, vol. 43, no. 8, pp. 431–432, 2007.
- [213] J.-W. Lee, H. Kwon, and B. Lee, "Design consideration of UHF RFID tag for increased reading range," in *Proc. IEEE MTT-S Int. Microwave Symp. Digest*, 2006, pp. 1588–1591.
- [214] K. V. S. Rao, P. V. Nikitin, and S. F. Lam, "Impedance matching concepts in RFID transponder design," in *Proc. Fourth IEEE Workshop Automatic Identification Advanced Technologies*, 2005, pp. 39–42.
- [215] J. D. Griffin, G. D. Durgin, A. Haldi, and B. Kippelen, "RF tag antenna performance on various materials using radio link budgets," *IEEE Antennas Wireless Propag. Lett.*, vol. 5, no. 1, pp. 247–250, 2006.
- [216] S. Hu, C. L. Law, and W. Dou, "Measurements of UWB antennas backscattering characteristics for RFID systems," in *Proc. IEEE Int. Conf. Ultra-Wideband ICUWB 2007*, 2007, pp. 94–99.
- [217] P. Pursula, M. Hirvonen, K. Jaakkola, and T. Varpula, "Antenna effective aperture measurement with backscattering modulation," *IEEE Trans. Antennas Propag.*, vol. 55, no. 10, pp. 2836–2843, 2007.

- [218] U. Karthaus and M. Fischer, "Fully integrated passive UHF RFID transponder IC with $16.7\mu\text{W}$ minimum RF input power," *IEEE J. Solid-State Circuits*, vol. 38, no. 10, pp. 1602–1608, 2003.
- [219] W. Lubberhuizen, "Near perfect reconstruction polyphase filterbank," 2007, licensed under 2-clause BSD. [Online]. Available: <http://www.mathworks.com/matlabcentral/fileexchange/authors/28947>
- [220] R. Entner, "Ucode QL Demodulator," NXP Semiconductors, Tech. Reports and eMails, Aug./Sept. 2007, (internal documents).
- [221] R. Kattenbach, "Statistical modeling of small-scale fading in directional radio channels," *IEEE J. Sel. Areas Commun.*, vol. 20, no. 3, pp. 584–592, 2002.
- [222] P. Bello, "Characterization of randomly time-variant linear channels," *IEEE Transactions on Communications Systems*, vol. 11, no. 4, pp. 360–393, 1963.
- [223] J. Fuhl, J.-P. Rossi, and E. Bonek, "High-resolution 3-D direction-of-arrival determination for urban mobile radio," *IEEE Trans. Antennas Propag.*, vol. 45, no. 4, pp. 672–682, 1997.
- [224] U. Muehlmann and A. Salfelner, "Two-frequency CW RADAR approach to ranging in UHF RFID systems," in *Proc. Europ. Microw. Assoc.*, vol. 4, Dec. 2007, pp. 317–322.
- [225] X. Li and K. Pahlavan, "Super-resolution TOA estimation with diversity for indoor geolocation," *IEEE Trans. Wireless Commun.*, vol. 3, no. 1, pp. 224–234, 2004.
- [226] W. Xu, E. C. Chang, L. K. Kwok, H. Lim, W. Cheng, and A. Heng, "Phase-unwrapping of SAR interferogram with multi-frequency or multi-baseline," in *Proc. Int. Geoscience and Remote Sensing Symp. IGARSS '94. Surface and Atmospheric Remote Sensing: Technologies, Data Analysis and Interpretation*, vol. 2, 1994, pp. 730–732.
- [227] V. Pascazio and G. Schirinzi, "Estimation of terrain elevation by multifrequency interferometric wide band SAR data," *IEEE Signal Process. Lett.*, vol. 8, no. 1, pp. 7–9, 2001.
- [228] E. Kreyszig, *Advanced Engineering Mathematics*, 8th ed. Wiley, 1999, ISBN-10: 0-471-33328-X.
- [229] T. wen Xiong, X. Tan, J. tian Xi, and H. Min, "High TX-to-RX isolation in UHF RFID using narrowband leaking carrier canceller," *IEEE Microw. Wireless Compon. Lett.*, vol. 20, no. 2, pp. 124–126, 2010.
- [230] V. Derbek, J. Preishuber-Pfluegl, M. Pistauer, and T. Holtstiege, "Method of receiver sensitivity improvement for RFID measurement and test instruments," in *3rd Int. EURASIP workshop on RFID Techn.*, Cartagena, Spain, Sep. 2010.
- [231] G. Lasser, R. Langwieser, and A. L. Scholtz, "Broadband suppression properties of active leaking carrier cancellers," in *Proc. IEEE Int RFID Conf*, 2009, pp. 208–212.
- [232] ETSI EN 302-208-1, "Electromagnetic compatibility and Radio spectrum Matters (ERM): Radio frequency identification equipment operating in the band 865 MHz to 868 MHz with power levels up to 2 W, Part 1: Technical requirements and methods of measurement", ETSI Std., Jul. 2007.
- [233] FCC Title 47, Part 15, "Operation within the bands 902–928 MHz, 2435–2465 MHz, 5785–5815 MHz, 10500–10550 MHz, and 24075–24175 MHz", FCC Std.
- [234] M. Baghaei-Nejad, D. S. Mendoza, Z. Zou, S. Radiom, G. Gielen, L.-R. Zheng, and H. Tenhunen, "A remote-powered RFID tag with 10Mb/s UWB uplink and -18.5dBm sensitivity UHF downlink in $0.18\mu\text{m}$ CMOS," in *Proc. IEEE Int. Solid-State Circuits Conf. - Digest of Technical Papers ISSCC 2009*, 2009, pp. 198–199.
- [235] Z. Zou, M. Baghaei-Nejad, H. Tenhunen, and L.-R. Zheng, "An efficient passive RFID system for ubiquitous identification and sensing using impulse UWB radio," *Elektrotechnik und Informationstechnik*, vol. 124, pp. 397–403, 2007, 10.1007/s00502-007-0483-y. [Online]. Available: <http://dx.doi.org/10.1007/s00502-007-0483-y>
- [236] C. Krall, "Signal processing for ultra wideband transceivers," PhD thesis, Graz Univ. of Techn., Austria, 2008.
- [237] *R&S ZVA Vector Network Analyzer Specifications*, Rohde & Schwarz, Oct. 2010, version 09.00. [Online]. Available: http://www2.rohde-schwarz.com/file/ZVA_dat-sw_en.pdf
- [238] A. Aleksieieva and M. Vossiek, "Design and optimization of amplitude-modulated microwave backscatter transponders," in *Proc. German Microwave Conf*, 2010, pp. 134–137.
- [239] T. Deleruyelle, P. Pannier, J. Alarcon, M. Egels, and E. Bergeret, "Multi-standard UHF and UWB antennas for RFID applications," in *Proc. Fourth European Conf. Antennas and Propagation (EuCAP)*, 2010, pp. 1–4.
- [240] J. Heidrich, D. Brenk, J. Essel, M. Heinrich, G. Hofer, G. Holweg, S. Schwarzer, J. Meyer, R. Herschmann, B. Geck, R. Weigel, and G. Fischer, "Multifunctional reference cells for multistandard RFID transponders," *IEEE Trans. Microw. Theory Tech.*, no. 99, 2011, early Access.

SQUEAK.*

* The End.

Reprints of Published Papers

(in the order of citation)

Wideband System-Level Simulator for Passive UHF RFID

Daniel Arnitz[†], Ulrich Muehlmann[‡], Thomas Gigl[†], and Klaus Witrisal[†]

[†] Signal Processing and Speech Communication Laboratory, Graz University of Technology, Graz, Austria
{daniel.arnitz, thomas.gigl, witrisal}@tugraz.at

[‡] NXP Semiconductors, Gratkorn, Austria
ulrich.muehlmann@nxp.com

Abstract—A chip manufacturing process requires extensive support of CAD-tools in order to predict the behavior of the embedded circuitry and to ensure the intended system functionality. Past experience shows that the overall performance of UHF RFID systems is mainly limited by multipath propagation and detuning. In this context, system-level simulations are vital to assess the overall performance and improve the embedded circuit. We present a simulator framework capable of handling chip-level tag models, fading MIMO radio channels, and interrogator building blocks on signal level. It is based on highly flexible behavioral tag-models instead of highly accurate but static ASIC models. In contrast to other UHF RFID simulators, it is explicitly designed to handle wideband signals, fading channels, nonlinearities, and detuning effects. The simulator is currently used to develop and evaluate the performance of ranging and realtime channel estimation systems. The presented results emphasize the feasibility of our framework in the evaluation of a range estimation approach between a standard UHF RFID transponder and an interrogator.

Index Terms—UHF RFID, system modeling, nonlinear systems, simulation, wideband channel, multipath channel, detuning, ranging

I. INTRODUCTION

Current developments in UHF RFID are mostly driven by cheaper transponder chip implementations and by increasing the read range (cf. [1]). These are market relevant aspects, since in 2005 and 2006 major retailers announced to replace barcodes by RFID tags [2]. It is an open secret that multipath propagation and detuning are significant challenges in this process. Consequently, average performance in multipath environments became a major issue.

In order to estimate the performance of existing implementations and to accelerate and simplify development processes, simulation tools for passive UHF RFID [3]–[5] were explicitly designed to analyze state-of-the-art systems. As spectral masks and permitted frequency bands are quite strict ([2], [6]), these simulation architectures only feature narrowband models. Furthermore, just the simulator presented in [4] supports fading channels. Although a narrowband assumption is an obvious choice for the analysis of today's systems, next generation RFID might take advantage of the benefits of wideband and multiband systems in multipath environments.

The presented simulator framework is specifically designed to support the development and verification of wideband and

ultra-wideband (UWB) system components in fading environments. Furthermore, it is designed to handle arbitrary tag properties, which cannot be provided by ASIC simulators like the architecture described in [3].

This document is organized as follows: Section II gives an overview over the simulator structure and its purpose, while Section III lists more specific details about the implementation and limitations. Current simulation examples can be found in Section IV. This Section also contains a signal model used for these simulations and a brief outlook on future improvements. Note that some parts of Section IV-A, including Fig. 7, appear in [7].

II. OVERVIEW: GENERAL STRUCTURE / FRAMEWORK

A. Field of Application

The presented simulator is primarily designed to study new system components that are far beyond state-of-the-art technology or require reader/tag performance that can not be achieved yet. As a key differentiator to other simulators as proposed in [3]–[5], it is designed to handle wideband signals in the presence of nonlinearities, fading, and detuning. Sophisticated approaches like combined frequency-/time-domain simulation [3] are difficult to handle and provide little gain in terms of simulation performance under such circumstances. Accordingly, our simulator is based on a straightforward sampled time-domain approach written in Matlab.

Complexity is the major drawback of this implementation: Due to the UHF (\sim GHz) carrier and low data rates (\sim kHz), RAM usage is extensive. Block processing (cf. Fig. 1) is applied to mitigate this drawback. The blocksize is variable and typically chosen to be one data burst (e.g., a single command). Performance problems limit the use of this architecture for protocol simulations (e.g., anticollision). However, such simulations are not the primary field of application for this simulator.

Currently the system is used to develop and test realtime channel estimation systems in fading and nonfading environments; examples can be found in Section IV. Connected to that problem is a major issue of the past years: ranging.

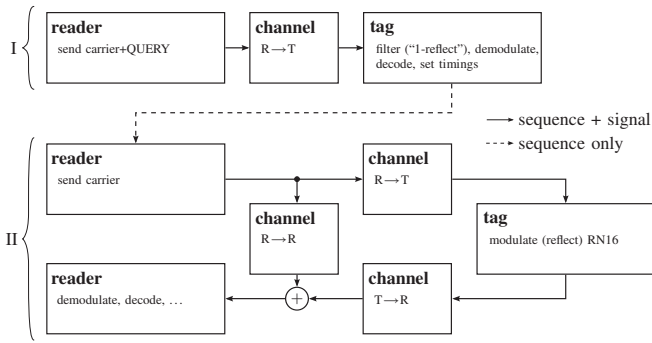


Fig. 1. Block processing example (EPCglobal Class-1 Gen-2 protocol [8]). Block I: The interrogator (reader) sends a QUERY command to the tag. Block II: The tag answers with RN16, i.e., modulates a carrier that has been generated by the reader. The signals are transmitted over reader→reader and reader←→tag channels. In general, multiple readers/channels/tags are handled.

B. Structure Overview

The simulator is organized in two abstraction levels (see Fig. 2) to simplify its handling. Top-level functions ($*_main$) provide a simple interface for the user to build custom simulation setups (e.g., a EPCglobal Gen-2 [8] protocol simulation in a dense reader environment), while bottom-level functions ($reader_*$, $channel_*$, tag_*) perform the actual operations. In that fashion even complex protocols and/or simulation setups can be simplified to a few lines of code, making the creation of new setups a matter of minutes. The main script for the sequence shown in Fig. 1, for example, might look like this:

```
% issue QUERY command
r_tx = reader_main('query');
t_rx = channel_main('r->t', r_tx);
tag_main(t_rx, 'query');

% reply RN16
r_tx = reader_main('carrier');
t_rx = channel_main('r->t', r_tx);
t_tx = tag_main(t_rx, 'rn16');
r_rx = channel_main('r->r', r_tx)+channel_main('t->r', t_tx);
reader_main('rn16', r_rx);
```

Most components, especially the tag building blocks, use lookup tables to model their behavior. These tables form the characteristics library. The library is able to support different reader/tag types, although currently, it only holds the characteristics of one type of tag and a basic reader.

Administrative work is done by several background modules of the simulator, called core functions. This set of functions handles exceptions, and performs version control and logging. Furthermore, all major functions contain a parametric selftest. These tests verify that all functions work within a set of predefined parameters and thus ensure proper functionality of the entire simulator, for example, after modifications.

III. IMPLEMENTATION DETAILS

The presented simulation environment has originally been designed for ranging simulations, without emphasis on the implementation details of an interrogator. Hence, most effort has been spent on tag and channel models.

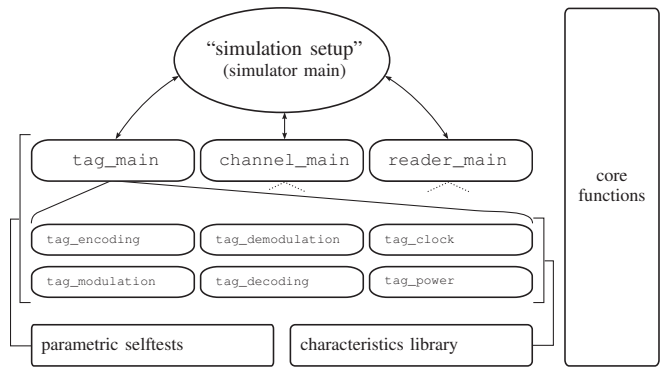


Fig. 2. Basic simulator structure: The complex bottom-level functions ($reader_*$, $channel_*$, tag_*) are handled by simple top-level interfaces ($*_main$); the user can construct the "simulation setup" in an interpreter fashion. All modules are verified by parametric selftests; core functions manage function/characteristic versions, logging and exceptions.

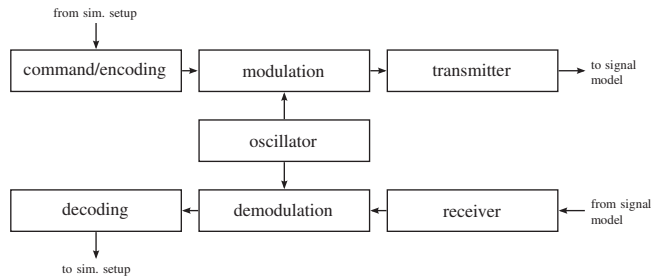


Fig. 3. Reader block diagram. Each reader in multireader environments is treated separately. Signal model and simulation setup are defined by the user in the "simulator main" script. A possible signal model is shown in Fig. 6.

In this Section, the "simulation setup" represents an overall metalevel of a specific simulation, defined in the simulator main script (cf. Fig. 2). Hence "sim. setup" in Figs. 3 and 5 is a synonym for the simulated physical setup (e.g., tags moving through a gate), the communications protocol (e.g., EPCglobal Gen-2), additional signal processing algorithms (e.g., ranging) and other high-level functions like user interaction.

A. Interrogator (see Fig. 3)

As mentioned above, the interrogator is implemented in a simple and straightforward manner. The oscillator produces a sine wave with arbitrary amplitude and phase instability, plus additive noise. This signal can be modulated according to the EPCglobal Class-1 Gen-2 standard [8] with cosine rolloffs. Arbitrary wideband carrier signals are also possible. The transmitter contains a nonlinear power amplifier and a linear bandpass model of the antenna.

The receive path consists of a bandpass filter plus a power splitter (receiver), and a standard zero-IF IQ demodulator with complex output. This output is filtered, re-sampled, and quantized (anti-aliasing-filter plus analog to digital conversion).

Encoding and decoding do not necessarily imply a communications protocol like EPC Gen-2 in this context. For example, these blocks could also represent a ranging method like the modulation and analysis of UWB pulses.

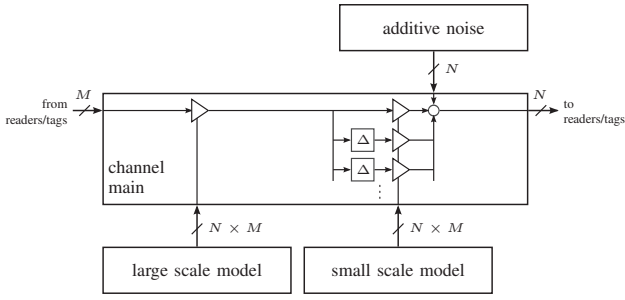


Fig. 4. Channel block diagram. Unlike reader and tag, the channel is XIXO per definition (e.g. M readers, N tags). Also the reader to reader channel $K(\omega, i)$ in Fig. 6 is modeled in this fashion ($M = N$ readers).

B. Channel (see Fig. 4)

In order to allow the application of standard wireless models, a linear channel has to be isolated. Spectral shaping by the reader may be (partially) located before the nonlinear power amplifier in the transmit path and is thus not included in the channel model. In order to keep the symmetry, spectral shaping in the reader's receive path is also excluded. Finally, the tag's reflection coefficient is also nonlinear and thus not covered by the channel model. Accordingly, the downlink channel starts after the power amplifier and stops at the reflection coefficient. The other direction – the uplink channel – starts at the reflection coefficient and ends at the reader's power splitter. As mentioned above, all channel models and their implementations are XIXO (arbitrary number of inputs and outputs) and wideband.

More precisely, the channel between two devices (e.g., reader/tag or reader/reader) consists of additive noise, a large-scale and a small-scale model. The large-scale channel consists of a log-distance model with optional log-normal shadowing. The small-scale model implements a sampled version of the average power-delay-profile described in [9] (model for short-range indoor radio channels) with $\tau_1 = 0$. This model creates Ricean fading characteristics for a single narrowband carrier. The small-scale channel can be configured to use a randomized or fixed power delay profile to model time-variant or time-invariant environments.

C. Tag (see Fig. 5)

The entire observable behavior of the tag at signal level is based on its reflection properties. This is why the reflection coefficient model is considered to be the most important part for the assembly of an accurate tag model. It is calculated using measured and simulated chip and antenna data and encompasses chip input impedance, modulation impedance, antenna impedance, as well as detuning. This nonlinear (incident power dependent), time-variant (modulation) and frequency dependent (resonances) reflection coefficient is implicitly linearized for one block by the assumption of a short-time stationary power, and modeled by a time-variant linear filter using a polyphase filterbank [10]. A more detailed study of a nonlinear implementation is currently conducted. Note

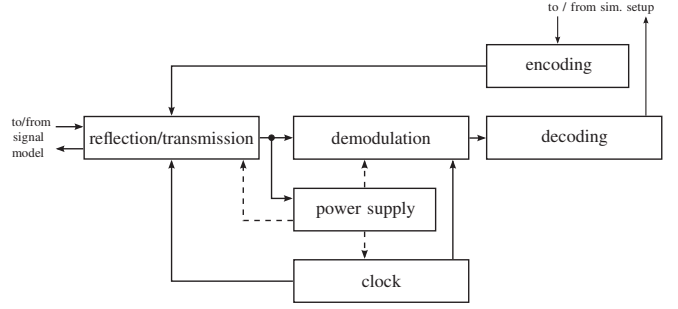


Fig. 5. Tag block diagram. Each tag in multitag environments is treated separately. Signal model and simulation setup are defined by the user in the “simulator main” script. A possible signal model is shown in Fig. 6.

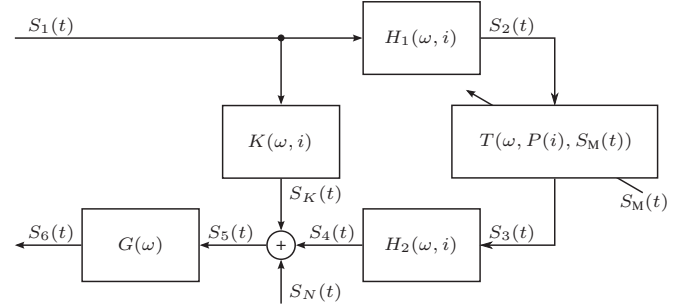


Fig. 6. Used signal model: Reader to reader channel $K(\omega, i)$, reader to tag channels $H_1(\omega, i)$ and $H_2(\omega, i)$, tag reflection coefficient $T(\omega, P, S_M)$, reader input stage $G(\omega)$, modulation signal $S_M(t)$, carrier level signals $S_1(t)$ through $S_6(t)$, noise $S_N(t)$; i is the block index (\rightarrow block processing), ω is the angular frequency, t is the time variable within one block

that detuning is not covered directly by the simulator, but implicitly by selecting an appropriate reflection coefficient data set. This way the functionality of the simulation framework is independent of a specific detuning model.

Demodulator and power supply unit are based on lookup tables stored in the characteristics library. The clock source features arbitrary frequency instability and random initial phase. Decoding and encoding are implemented according to the Gen-2 protocol [8]; all other blocks have been modeled using data provided by NXP Semiconductors.

IV. SIMULATION EXAMPLES / FUTURE WORK

A. Signal Model and Linearized Tag Model

The signal model currently used for simulations is shown in Fig. 6. This drawing is limited to the communication between one reader and one tag for simplicity; the simulator supports multiple interrogators and multiple tags. Note that the signal model is a part of the simulator main script and thus defined by the user. All blocks except the tag reflection coefficient are assumed to be short-time stationary for one block index i (\rightarrow block processing).

The reader to reader channel $K(\omega, i)$ and the uplink and downlink channels $H_2(\omega, i)$ and $H_1(\omega, i)$, respectively, are modeled as linear filter channels; ω is the angular frequency. $K(\omega, i)$ includes direct coupling as well as multipath feedback. The tag reflection coefficient $T(\omega, P(i), S_M(t))$ is modulated

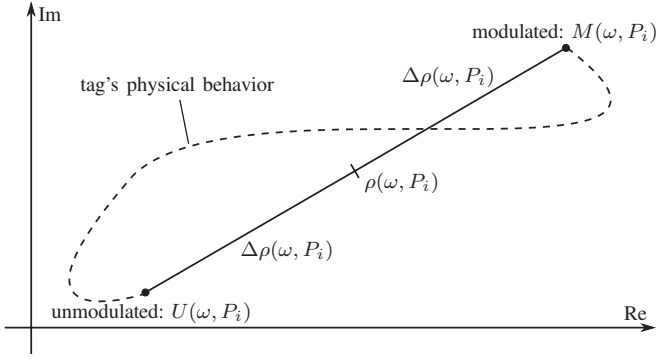


Fig. 7. Tag reflection coefficient linearization: The tag's physical behavior during modulation is a nonlinear, time-variant, frequency- and power-dependent curve. The linearized model assumes a fictive center value $\rho(\omega, P_i)$ and a difference value $\Delta\rho(\omega, P_i)$; only the endpoints are identical to the original curve. The assumption of short-time stationary power $P(i)=P_i$ completes the linearization.

by $S_M(t)$ and, due to the assumption of short-time stationary power $P(i)$, implicitly linearized as follows:

On a physical level, the tag modulates data by varying a modulation impedance. The reflection coefficient during this process depends on the chip impedance, which itself depends on the chip input power. This dependence causes the reflection coefficient to be nonlinear. Furthermore, the interaction between the time-variant impedances creates a curved transition trajectory in the complex plane (cf. Fig. 7). The linearization now first neglects everything but the end points of this curve, introducing a center value $\rho(\omega, P)$ and a difference value $\Delta\rho(\omega, P)$. The end points are more important here than the trajectory itself, because of the nearly square tag modulation (either modulated or unmodulated).

$$\begin{aligned} \text{modulated: } M(\omega, P) &= \rho(\omega, P) + \Delta\rho(\omega, P) \\ \text{unmodulated: } U(\omega, P) &= \rho(\omega, P) - \Delta\rho(\omega, P) \end{aligned} \quad (1)$$

Assuming an arbitrary modulation signal $S_M(t)$ satisfying $-1 \leq S_M(t) \leq 1$ we can approximate the time-variant tag reflection coefficient $T(\omega, P, t)$ by

$$T(\omega, P, S_M(t)) \approx \rho(\omega, P) + S_M(t) \cdot \Delta\rho(\omega, P) \quad (2)$$

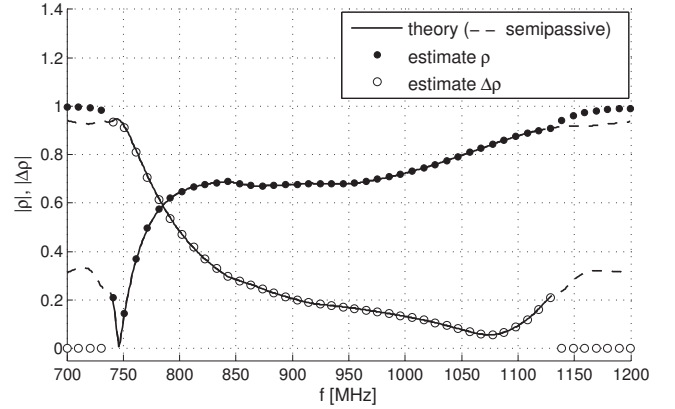
which is a simplified trajectory, but still power-dependent and thus nonlinear. Assuming short-time-stationary power (one block) $P \rightarrow P(i)$, the linearization is complete

$$T(\omega, P(i), S_M(t)) \approx \rho_i(\omega) + S_M(t) \cdot \Delta\rho_i(\omega) \quad (3)$$

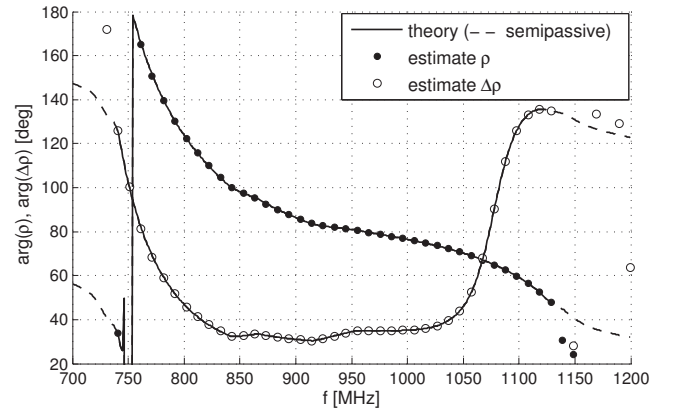
By assuming a symmetrical and zero-mean modulation (like, for instance, a cosine), the center value ρ is identical to the average reflection coefficient. As mentioned above, the tag's reflection coefficient is implicitly linearized by the assumption of short-time stationary power.

B. Signal (+ Channel) Model Estimation

A typical characterization of the UHF RFID channel is focused on narrowband signal analyses and receive power



(a) magnitude



(b) phase

Fig. 8. Example: Signal model estimation. A linear model of the tag's reflection coefficient is estimated for one power level. Estimation window 2 ms per frequency, 100 kHz modulation frequency, AWGN channels with known distances, feedback attenuation 32 dB, additive noise -82 dBm/Hz, passive tag (functional, i.e., powered and continuous modulation possible within approx. 740–1125 MHz), typical assembly/detuning.

measurements (e.g., [11]–[14]). Short-range (< 10 m) wide-band channel measurements in the UHF frequency band are rare ([15], cf. [16]–[18]). To our knowledge, wideband channel measurements with typical UHF RFID setups (like gates) are not publicly available in the literature.

Although a narrowband model is sufficient for product development based on current standards and regulations, it is limiting for research on next generation products. For instance, ranging methods typically require a significant amount of bandwidth to mitigate multipath interference effects. As a consequence, narrowband models are not suitable, hence the creation of a wideband channel model for UHF RFID is of vital importance to this simulator and all related applications. For example, the distance between interrogator and tag is an inherent channel property. Estimating this distance (ranging) is therefore identical to a channel estimation.

Currently, and as a pilot test prior to measurements, the simulator is used to test methods to estimate and separate channel from tag characteristics. A challenge for such an

estimation is the nonlinearity of the reflection coefficient and the fact that power measurements on passive tags are not feasible, especially during normal operation. Any outside observer, for instance, the interrogator, can only measure incident plus reflected power. As the reflection coefficient and thus the reflected power depends on the incident power, the inference from observed on incident power levels is ambiguous. For example, an observed power level of 1 mW could be created by 1 mW incident power without reflection (perfect matching) or by 0.5 mW incident plus 0.5 mW reflected power.

These simulations are based on the signal model shown in Fig. 6; a first result is shown in Fig. 8: Assuming known AWGN channels, the linear model of the tag's reflection coefficient, consisting of the average reflection coefficient ρ and the difference value $\Delta\rho$, is estimated by hopping the carrier frequency. The hopping creates short-time stationary power levels, thus eliminating the nonlinearity of the reflection coefficient. Subsequently the linear model is a perfect match, which is underlined by the simulation results in Fig. 8; the effect of additive noise is negligible for the used window size of 2 ms. The modulation stops outside 740–1125 MHz, indicating that the tag reflects too much power to stay operational. Detuning would diminish this frequency range and shift it towards lower frequencies, thus the result corresponds well with the intended minimal frequency range of 840–960 MHz for moderately detuned tags.

Once its reflective properties are known, the tag is placed into a multipath environment. By continuously estimating the frequency response of the system, wideband channel properties can be obtained.

C. Ranging

The first application to test the capabilities of the simulator was multi-frequency continuous-wave radar ranging [7], a generalization of [19].

As an example, a tag is placed at a distance of 0.5, 1, 1.5, . . . 4 m from the interrogator. This range is then estimated multiple times per distance setting using two-frequency continuous-wave radar. The theoretical bounds for the distance error's variance and the expected average error are derived in [7]. Under the assumption of an AWGN channel and a perfectly calibrated reader input stage, we can write

$$\begin{aligned} E\{\tilde{d}\} &= \frac{c}{2\omega_1} (\angle\Delta\rho_2 - \angle\Delta\rho_1) \\ \text{var}\{\tilde{d}\} &\approx \frac{c^2 N_0}{16N\omega_1^2} \cdot \frac{1}{|A_1|^2 |H_1|^4 |\Delta\rho_1|^2} \\ &\quad + \frac{c^2 N_0}{16N\omega_1^2} \cdot \frac{1}{|A_2|^2 |H_2|^4 |\Delta\rho_2|^2} \end{aligned} \quad (4)$$

for the distance error \tilde{d} , where c is the speed of light, N_0 is the single-sided noise density, N is the number of averaged samples, ω_1 is the offset frequency between main and secondary carrier, H is the channel gain, A is the carrier amplitude and $\Delta\rho$ is the differential linearized reflection coefficient. Index 1 denotes the main carrier while 2 indicates the secondary carrier. The simulation result is shown in Fig. 9.

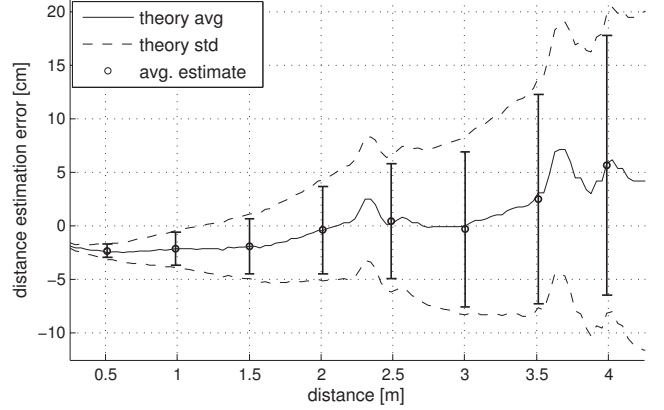


Fig. 9. Example: Two-frequency continuous-wave radar ranging; AWGN channel, single-sided noise density $N_0 = -82$ dBm/Hz, isotropic carrier power 1 W/10 mW for primary/secondary carrier, frequency spacing 1 MHz, typical tag/assembly. Errorbars represent mean and standard deviation of 500 realizations per distance setting (0.5, 1, 1.5, . . . , 4 m).

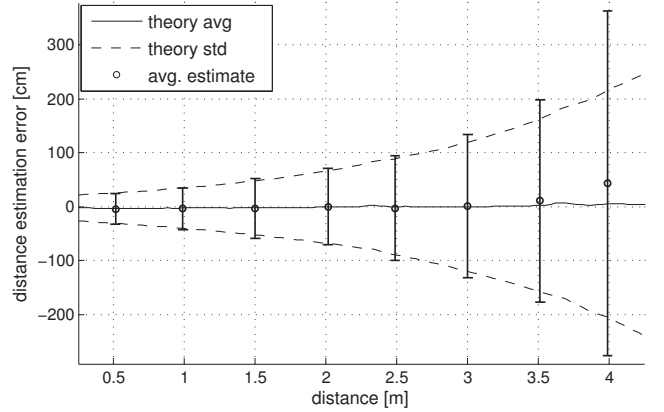


Fig. 10. Example: Two-frequency continuous-wave radar ranging; noiseless fading channel, logarithmic trends for Ricean K-factor $K = 30 \dots 10$ dB and RMS delay spread $\tau_{RMS} = 1 \dots 20$ ns within distance 0 . . . 5 m (per channel). Isotropic carrier power 1 W/10 mW for primary/secondary carrier, frequency spacing 1 MHz, typical tag/assembly. Errorbars represent mean and standard deviation of 500 realizations per distance setting (0.5, 1, 1.5, . . . , 4 m). Note that the exponential behavior is mainly due to the logarithmically changing K and τ_{RMS} .

Using the same ranging approach in a multipath environment, shown in Fig. 10, the standard deviation increases significantly. Like any narrowband system, two-frequency continuous-wave ranging is not able to mitigate multipath propagation effects. The only mitigating factor is the correlation between the channel frequency responses H_1 and H_2 at primary and secondary carrier frequency, respectively. The theoretical variance is [7]

$$\text{var}\{\tilde{d}\} \approx \frac{c^2}{8\omega_1^2} \cdot \frac{\text{Re}\{\sigma^4 - \beta^2 + 2|m|^2(\sigma^2 - \beta)\}}{\text{Re}\{\beta + |m|^2\}^2} \quad (5)$$

where σ^2 is the variance of the channel gains, β is the cross-covariance and m the expected value. This result assumes i.i.d. circular symmetric complex Gaussian channel gains for

primary and secondary carrier $H_1, H_2 \sim \mathcal{CN}(m, \sigma^2)$, which reflects a Ricean fading channel. Moreover, this approximation is only true for LOS-scenarios (high K-Factor).

D. Modifications to the Simulator

The present simulation architecture is still under development, adding and/or improving components on a need-to-have basis.

One of the weaknesses of the current implementation is the assumption of short-time stationary power conditions. Although fast changes in the incident power are filtered by the tag's power supply buffer, relatively slow changes w.r.t. the time constants of the tag power supply are not covered by this stationary model. Accordingly, the current reflection coefficient implementation will be replaced by a time-variant nonlinear approximation, allowing time-variant power levels.

Other future issues are more efficient implementations of filter channels and tag modulation, and of course the incorporation of the findings of the signal model and channel measurements described above.

V. CONCLUSION

In this paper, a system-level UHF RFID simulator based on behavioral models is described. This simulator is the first UHF RFID simulator to the authors' knowledge that supports (ultra)wideband signals as well as fading channels, different tag models, detuning, and nonlinearities at carrier level. Self-test routines ensure that all modules work within a predefined set of parameters and guarantee proper functionality of the complex simulator framework.

The simulator's tag-models are based on simulated and measured data of commercial UHF transponder chips. The most important signal-level property of the tag – the reflection coefficient – encompasses chip input impedance, modulation impedance, antenna impedance, and detuning. The channel is based on a wireless indoor power-delay-profile.

Two simulation examples are presented. The first example is a narrowband range estimation system based on a second carrier, the second example is a preliminary test simulation prior to channel/signal model measurements. The simulation results agree with wireless communications theory in both examples, underlining the validity of the simulator.

VI. ACKNOWLEDGMENTS

The authors would like to thank NXP Semiconductors, Gratkorn, Austria, for funding this project and for providing data for the tag library. This work is supported by the national Austrian Research Promotion Agency (FFG) under the grant number 818072, for which we are also very grateful.

REFERENCES

[1] "The RFID benchmark report - finding the technology's tipping point," Aberdeen Group, Dec. 2005.
 [2] D. M. Dobkin, *The RF in RFID*. Elsevier, 2007, ISBN-13: 978-0750682091.
 [3] V. Derbek, J. Preishuber-Pfluegl, C. Steger, and M. Pistauer, "Architecture for model-based UHF RFID system design verification," in *European Conference on Circuit Theory and Design (ECCTD05)*, vol. 2, Sept. 2005, pp. 181–184, 10.1109/ECCTD.2005.1523023.

[4] C. Floerkemeier and R. Pappu, "Evaluation of RFIDSim - a physical and logical layer RFID simulation engine," in *International Conference on RFID (RFID2008)*, Apr. 2008, pp. 350–356, 10.1109/RFID.2008.4519374.
 [5] J. Li and C. Tao, "Analysis and simulation of UHF RFID system," in *International Conference on Signal Processing (ICSP2006)*, vol. 4, 2006, pp. 16–20, 10.1109/ICOSP.2006.346107.
 [6] K. Finkenzeller, *RFID Handbook: Fundamentals and Applications in Contactless Smart Cards and Identification*, 2nd ed. Wiley & Sons, 2003, ISBN-13: 978-0470844021.
 [7] D. Armitz, K. Witrisal, and U. Muehlmann, "Multi-frequency continuous-wave radar approach to ranging in passive UHF RFID," to be published in *IEEE Trans. Microwave Theory Tech.*
 [8] *ISO/IEC 18000-6C (EPCglobal Class 1 Gen 2)*, ISO Std., 2004.
 [9] K. Witrisal, Y.-H. Kim, and R. Prasad, "A new method to measure parameters of frequency-selective radio channels using power measurements," *IEEE Trans. Commun.*, vol. 49, no. 10, pp. 1788–1800, Oct. 2001, 10.1109/26.957401.
 [10] W. Lubberhuizen. (2007) Near perfect reconstruction polyphase filterbank. Matlab Central. [Online]. Available: <http://www.mathworks.com/matlabcentral/fileexchange/15813>
 [11] D. Kim, M. A. Ingram, and W. W. Smith, "Measurements of small-scale fading and path loss for long range RF tags," *IEEE Trans. Antennas Propagat.*, vol. 51, no. 8, pp. 1740–1749, Aug. 2003, 10.1109/TAP.2003.814752.
 [12] R. J. C. Bultitude, "Measurement, characterization and modeling of indoor 800/900 MHz radio channels for digital communications," *IEEE Commun. Mag.*, vol. 25, no. 6, pp. 5–12, June 1987.
 [13] T. S. Rappaport and C. D. McGillem, "UHF fading in factories," *IEEE J. Select. Areas Commun.*, vol. 7, no. 1, pp. 40–48, Jan. 1989, 10.1109/49.16842.
 [14] P. N. Nikitin and K. V. S. Rao, "Antennas and propagation in UHF RFID systems," in *International Conference on RFID (RFID2008)*, Apr. 2008, pp. 277–288, 10.1109/RFID.2008.4519368.
 [15] M. S. Varela and M. G. Sánchez, "RMS delay and coherence bandwidth measurements in indoor radio channels in the UHF band," *IEEE Trans. Veh. Technol.*, vol. 50, no. 2, pp. 515–525, Mar. 2001, 10.1109/25.923063.
 [16] T. Takeuchi, M. Sako, and S. Yoshida, "Multipath delay estimation for indoor wireless communication," in *Vehicular Technology Conference (VETEC1990)*, 1990, pp. 401–406, 10.1109/VETEC.1990.110355.
 [17] T. S. Rappaport, *Wireless Communications*, 2nd ed. Prentice Hall International, 2002, ISBN-13: 978-0130422323.
 [18] D. M. J. Devasirvatham, M. J. Krajin, D. A. Rappaport, and C. Banerjee, "Radio propagation measurements at 850 MHz, 1.7 GHz and 4 GHz inside two dissimilar office buildings," *Electronics Letters*, vol. 26, no. 7, pp. 445–447, Mar. 1990, 10.1049/el:19900289.
 [19] U. Muehlmann and A. Salfelner, "Two-frequency CW RADAR approach to ranging in UHF RFID systems," in *Proceedings of the European Microwave Association (EuMA07)*, vol. 4, Dec. 2007, pp. 317–322.

Tag-Based Sensing and Positioning in Passive UHF RFID: Tag Reflection

Daniel Arnitz

Signal Proc. and Speech Comm. Lab
Graz Univ. of Technology, Austria
daniel.arnitz@tugraz.at

Ulrich Muehlmann

NXP Semiconductors
Gratkorn, Austria
ulrich.muehlmann@nxp.com

Klaus Witrisal

Signal Proc. and Speech Comm. Lab
Graz Univ. of Technology, Austria
witrisal@tugraz.at

Abstract - We present a comprehensive model of the complex reflection coefficient of UHF RFID tags during modulation. The model is based on an equivalent circuit and validated using measurements of an NXP UCODE G2XM on an NXP UCODE general purpose reference antenna in an anechoic chamber. Using this model, we conduct an analysis of the influence of assembly tolerances and antenna detuning on accuracy in a frequency-domain phase-based ranging approach. The tools used in this analysis are also applicable to tag antenna based sensing and are available under GNU GPL as part of the PARIS simulation framework, a simulation tool intended to serve in the development and testing of backscatter-based sensing and positioning.

I. INTRODUCTION

UHF RFID has come a long way since its early stages in the 1970s and the first standardization in the early 2000s [1]. Since then, it has become ubiquitous in various applications from supply chain management to laundry services. Even though UHF RFID is now a widespread technology, reliable positioning is a feature that is not yet available. There has been considerable research on UHF RFID positioning during the last years, but no conclusive breakthrough [2].

Foremost in the list of reasons for this are the need to keep the tag simple (power consumption, costs) and the strict bandwidth limits of the UHF RFID frequency band(s). As a consequence, the used ranging methods are based on narrowband parameters such as return link phases and thus especially vulnerable to multipath propagation. A comprehensive overview of such phase-based ranging and positioning systems currently under research can be found in [2]. Even though the error for phase-based ranging methods in typical supply chain management applications such as portals is dominated by multipath propagation [2–4], the error caused by tag phase shifts can become significant in light multipath environments. This error depends on the detuning of the tag and is thus a parameter that typically cannot be controlled. Detuning is a major issue in conventional RFID systems [5], but also offers opportunities when it is used for tag-based sensing [6–8].

In Section II we will introduce two models of the tag reflection that will subsequently be used in Section IV to investigate the effects of detuning on a phase-based ranging system [4]. In Section III the used models are validated using reflection coefficient measurements of a Gen-2 tag in situ, i.e., during its normal operation in the electromagnetic field.

II. TAG MODELING

The only physical tag parameter visible to the reader is the tag's reflection coefficient, which makes it the most important tag parameter for backscatter-based sensing and positioning. The reflection coefficient of passive tags is highly frequency dependent, nonlinear, and time-variant.

The presented model uses impedance data of chip (modulated and unmod.), assembly, and antenna to calculate the reflection coefficient of the fully assembled tag. These impedances can be obtained via conducted measurements [9, 10] or simulations, while measuring the reflection coefficient directly requires an anechoic environment [11].

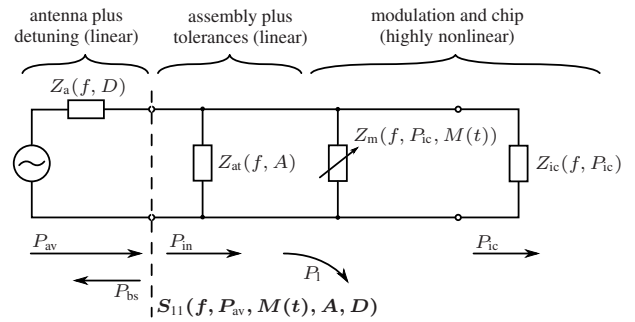


FIGURE 1 - EQUIVALENT CIRCUIT MODEL

2.1 Equivalent Circuit Model

The equivalent circuit model shown in Fig. 1 is applied to keep the complexity manageable. Similar equivalent circuits are well established in RFID [1, 12, 13].

As a first step in the calculation of the tag's reflection coefficient, modulation and chip impedance are combined for different modulation states, forming a three-dimensional matrix (over frequency f , chip power P_{ic} , and modulation state M).

As a next step the assembly impedance Z_{at} is computed (parallel RC). This impedance models the mounting of the chip on the antenna (flip-chip, TSSOP plus soldering, ...), including tolerances. The parallel capacity is chosen depending on the assembly tolerance state A , and the Ohmic part is calculated using Q-matching (e.g., [14, 15]) between antenna and load impedance at the intended frequency of operation (typ. 915 MHz) and the tag's power threshold $P_{ic,min}$, [10]. This approach reflects the effort of a manufacturer to still match the tag "as well as possible" for a given assembly process. As the assembly is not fully predictable and will also affect the resistance, the optimally tuned resistor is subsequently multiplied by a scalar factor which, like the chosen capacity, depends on the assembly tolerance state A . By using a factor instead of a constant resistance the results stay independent of the actual matching point. Using the assembly impedance Z_{at} the power losses in modulation impedance and assembly can be calculated, thus making the input power P_{in} known:

$$P_{in} = P_{ic} \cdot \left(1 + \frac{R_{at||m} \cdot |Z_{ic}|^2}{R_{ic} \cdot |Z_{at||m}|^2} \right) \quad (1)$$

The third step takes detuning of the antenna near objects into account. Especially near metal, the antenna self-resonance is considerably boosted. Detuning will also shift this resonance to lower frequencies. A detuning model has been implemented that modifies the antenna impedance in free space by increasing the quality factor and shifting the antenna self-resonance in frequency, as shown in Fig. 2. This heuristic model is based on nonlinear interpolation of the antenna impedance to emulate the effects of close-by water and metal objects. It has been derived from impedance measurements of an NXP UCODE general purpose antenna and is controlled by two

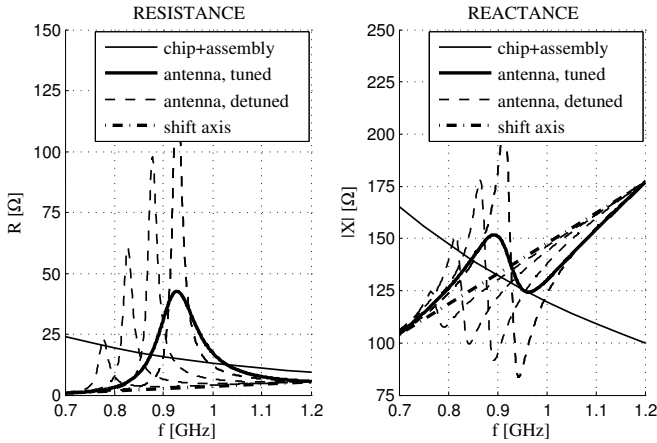


FIGURE 2 - EXAMPLES FOR IMPEDANCES OF CHIP (FLIP-CHIP ASSEMBLY) AND ANTENNA (TUNED AND DETUNED).

parameters: percent enhancement and frequency shift of the antenna self-resonance. The first parameter controls a compression of the frequency axis around the resonance and an expansion of R - and X -axes. The second parameter controls the frequency shift along the shift axis of R_a and X_a , as well as the increasing attenuation of the resonance for large frequency shifts (cf. Fig. 2). The combination of both parameters forms the detuning state D . Note that this method will only give qualitatively correct results. Specifically, it does not consider additional resonances created by close coupling, the alteration and shifting of resonances other than the main antenna self-resonance, the effects of different orientations of the antenna relative to the offending material, or compound materials. However, these limitations only apply to the modeling of detuning, not the entire equivalent circuit model. If high accuracy is required, measured impedances of detuned antennas can easily be used instead.

As a final step, the reflection coefficient (S_{11}) at the connection between antenna and combined tag impedance

$$S_{11} = \frac{Z_a - Z_{at||m||ic}^*}{Z_a + Z_{at||m||ic}} \quad (2)$$

as well as the incident/available power level P_{av} are computed (* denotes the complex conjugate)

$$P_{av} = P_{in} / (1 - |S_{11}|^2). \quad (3)$$

So far, the combined impedances and the reflection coefficient are functions of the chip power P_{ic} . A more practical dependence would be P_{av} here, as it is a value that can be directly derived from channel models, thus giving the tag (reflection coefficient) model a well-defined interface. For this reason the reflection coefficient is re-interpolated using the connection between available (incident) and chip power levels $P_{av}(f, P_{ic}, \dots)$, forming the final reflection coefficient over frequency, incident power, modulation, assembly, and detuning $S_{11}(f, P_{av}, M, A, D)$. Note that antenna gain pattern and polarization mismatch are not included in this model. This is a very common and useful simplification; they can, however, be factored in at any later time, cf. [16–19].

2.2 Linear Model of the Tag Modulation

This linear model is a simplification of the quite complex reflection coefficient trajectory during modulation, cf. Fig. 3. A more detailed description can be found in [4]. The model replaces the trajectory by a fictive center ρ and a difference $\Delta\rho$, where

$$\text{“mod”} = \rho + \Delta\rho \quad \text{and} \quad \text{“unmod”} = \rho - \Delta\rho \quad (4)$$

This approach is loosely linked to differential radar cross sections, cf. [20]. Note that the end points of the trajectory are power and frequency

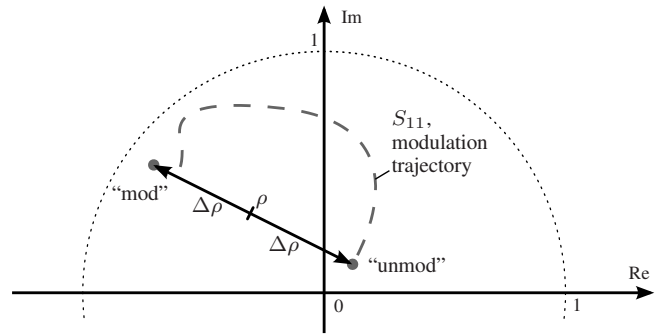


FIGURE 3 - LINEAR MODEL OF THE REFLECTION COEFFICIENT: ONLY THE END POINTS OF THE MODULATION TRAJECTORY ARE PRESERVED.

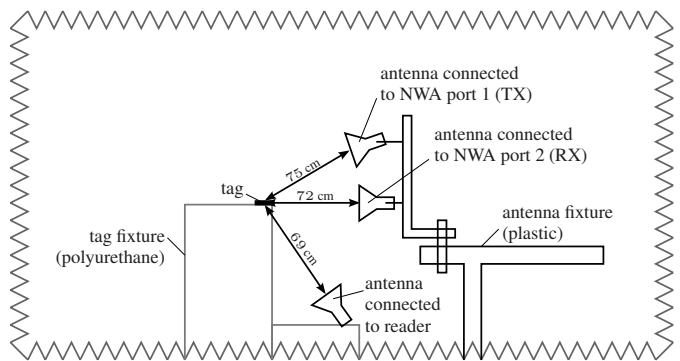


FIGURE 4 - BISTATIC NWA MEASUREMENT SETUP WITH A UHF RFID READER FOR POWER SUPPLY (NOT TO SCALE).

dependent, hence also the parameters of the linear model depend on frequency and power, i.e., $\rho = \rho(f, P)$ and $\Delta\rho = \Delta\rho(f, P)$.

The benefit of this model is its simplicity when it comes to modulation. The complex reflection coefficient during modulation can be expressed by

$$S_{11}(f, P, t) = \underbrace{\rho(f, P)}_{\text{center}} + \underbrace{s_M(t)}_{\text{modulation}} \cdot \underbrace{\Delta\rho(f, P)}_{\text{difference}} \quad (5)$$

with $-1 \leq s_M(t) \leq 1$. The modulation model in (5) is especially useful for multiple frequency components if the power level is roughly constant and hence the superposition principle holds, cf. [4].

2.3 Underlying Data

The above models are implemented as part of the tag model in the PARIS simulation framework [21, 22], which is available under the GNU General Public License¹. There are also several predefined lookup tables available with the framework, including the ones we have used in Section IV. Modulation and chip impedance of these tables are based on conducted measurements performed by NXP Semiconductors using the method in [9]. The antenna impedance was calculated using CST and verified using a network analyzer during the validation measurements.

III. MODEL VALIDATION (MEASUREMENTS)

The above models are based on well-established theory and, with the exception of the antenna impedance, on measured data. Nonetheless, the calculations leading to the reflection coefficient rely on several simplifications, thus making validation necessary. For this reason we have measured the reflection coefficient of the tag during modulation in an anechoic chamber. In order to also validate the linear model

¹<http://www.gnu.org/licenses/gpl.html>

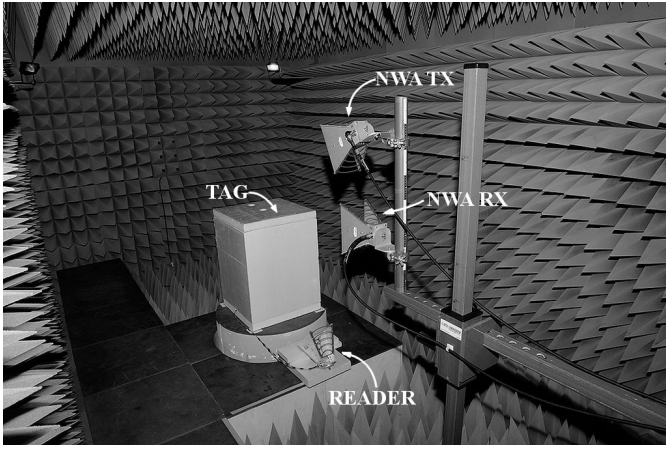


FIGURE 5 - PHOTOGRAPH OF THE ANECHOIC CHAMBER'S INTERIOR WITH THE MEASUREMENT SETUP.

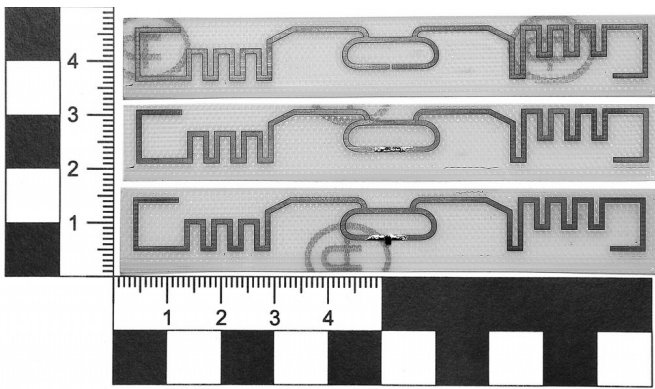


FIGURE 6 - PHOTOGRAPH OF USED CALIBRATION REFERENCES OPEN (TOP) AND SHORT (MIDDLE), AND USED TAG (NXP UCODE G2XM; BOTTOM). SCALE IS IN CM.

of the tag reflection, the calculation of the reflection coefficient from measured data is based on this model.

The used measurement procedure combines several approaches [9, 11, 23] to obtain the complex reflection coefficient of a UHF RFID tag during modulation in the field. To this end, we adapted the procedure in [9], which is a well established procedure for conducted measurements of the chip impedance during modulation: The tag was placed in an anechoic chamber at a short distance from three ETS Lindgren Model 3115 horn antennas (cf. Figs. 4 and 5). The bottom antenna was connected to a Sirit IN510 reader. This reader was used to supply the tag during measurements and to send a custom command setting the tag to continuous modulation at 80 kHz. Middle and uppermost antenna were connected directly to a Rohde&Schwarz ZVA-24 network analyzer (NWA), which was recording S_{21} in a time sweep at an effective sampling frequency of 248.6 kHz. We chose the bistatic setup for its superior isolation compared to directional couplers and circulators. The short distance at the lower end of the far-field ($2D^2/\lambda \approx 73$ cm) minimizes calibration issues.

The major drawbacks of the used method are speed and calibration: Even though the reader carrier is attenuated by the measurement procedure because its period is shorter by factors than the measurement time, changes in the noise floor are considerable. This makes the recording of several thousand periods of the modulation necessary. Furthermore, the environmental reflections exceed the reflection of the antenna outside its resonance even in an anechoic chamber, making measurements outside its center frequency unreliable.

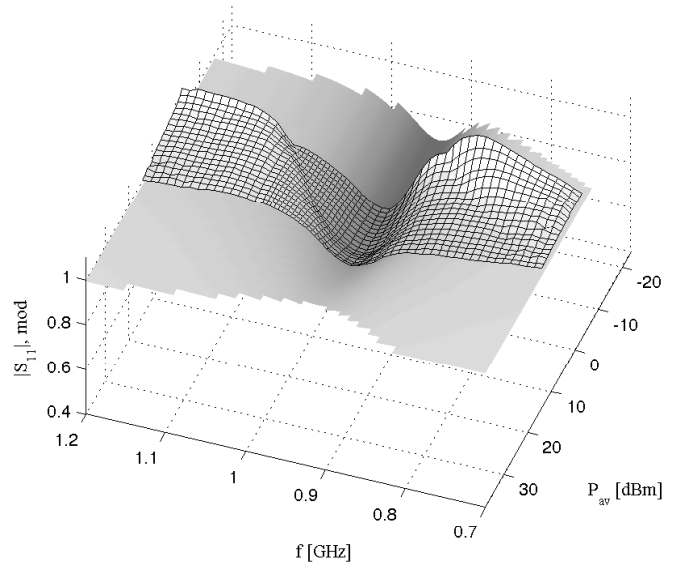
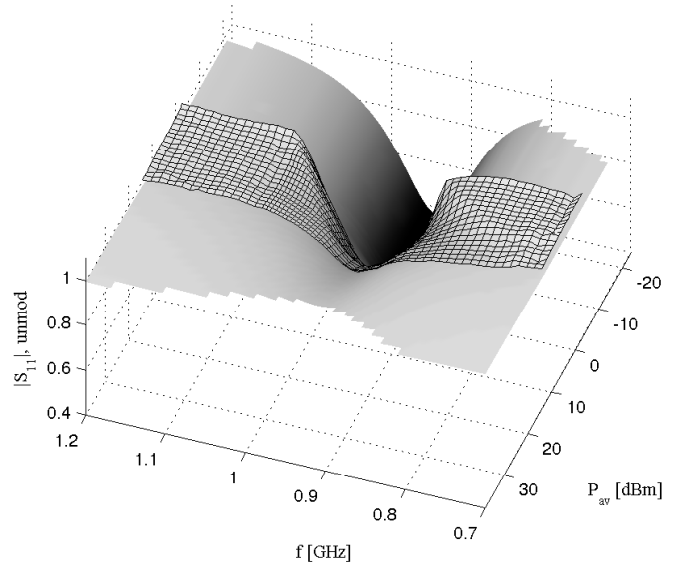


FIGURE 7 - COMPARISON OF UNMODULATED (TOP) AND MODULATED (BOTTOM) REFLECTION COEFFICIENT MAGNITUDES: SIMULATION MODEL VS. MEASUREMENT (GRIDLINES).

Calibration was performed by measuring open- and short-references (Fig. 6). The match reference was produced by measuring the reflection of the empty chamber. Time-sweeps with 10,000 samples were recorded for 59 points between 0.7 GHz and 1.2 GHz and power levels from 13 to 30 dBm in 1 dBm steps at the reader output port. Correction of the measured S_{21} was performed to short $S_{21,s}$ and match $S_{21,m}$ references [23]:

$$S_{11,corr} = S_{21,corr} = \frac{S_{21} - S_{21,m}}{S_{21,s} - S_{21,m}} \quad (6)$$

A full calibration, also taking the open-reference into account, was discarded due to numerical instabilities.

The backscatter modulation is subsequently extracted from $S_{11,corr}$ via the linear model using (4) and (5). A comparison between this measured reflection coefficient and its model can be found in Fig. 7. Note that the measured reflection coefficient slightly exceeds $|S_{11}| = 1$ outside 900–1000 MHz due to the above mentioned calibration problems. Furthermore, we were not able to reconstruct the reflection coefficient phase for the same reason; a full calibration is too instable. The reconstructed magnitude on the other hand is

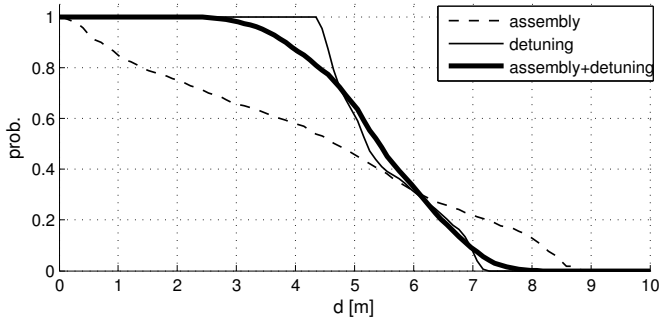


FIGURE 8 - CDFs OF THE MAXIMUM READ RANGE (EU BAND) FOR ALL SCENARIOS.

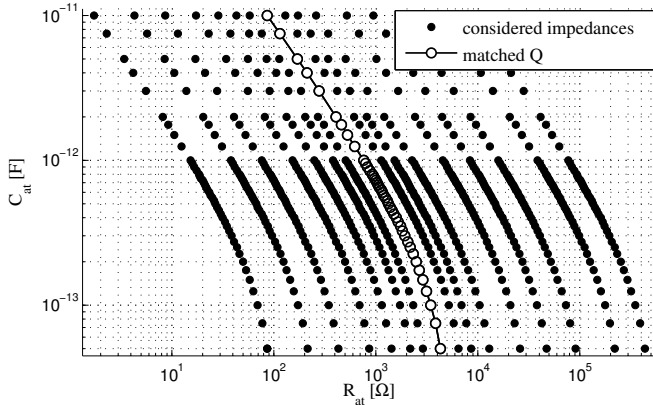


FIGURE 9 - USED ASSEMBLY IMPEDANCES FOR THE ASSEMBLY MISMATCH SIMULATION.

a near-perfect match, with a residual mean absolute error of 0.022 ($|S_{11}| \in [0, 1]$). Also the calculated “best fit” assembly, $R_{at}=235 \Omega$ parallel to $C_{at}=475$ fF, corresponds well with soldering the G2XM on milled FR-4.

Hence, in combination with the well established theory of equivalent circuits for antenna systems, this result indicates the validity of the equivalent circuit model and the linear model described above.

IV. IMPACT OF ASSEMBLY TOLERANCES AND DETUNING ON PHASE-BASED RANGING

4.1 Introduction and Used Setup

We have used the above model in a parameter sweep simulation in order to investigate the effects of assembly and detuning on the ranging error of [4], which is a phase-based ranging approach for passive UHF RFID. For the presented investigation we have evaluated three different scenarios: Assembly mismatch (well-matched to complete mismatch), antenna detuning (well-tuned to near-metal), and combined (typical combinations of mismatch and detuning). The chip/antenna combination is again the NXP G2XM on the UCODE general purpose reference antenna. Power levels are varied from 3.28 W EIRP (limit for EU) to the tag minimum power threshold level for all simulations; the reader sensitivity is assumed to be -80 dBm. The employed channel model is a free-space path loss model (pathloss factor 2).

Cumulative distribution functions (CDFs) of the maximum read range in the EU frequency band are given in Fig. 8. The maximum read ranges for well-tuned and well-matched tags approach 10 m, which fits previous findings for this chip ($P_{min} \approx -13$ dBm) [10]. The maximum read range for detuned tags, on the other hand, is in the range of 3 m (assembly+detuning).

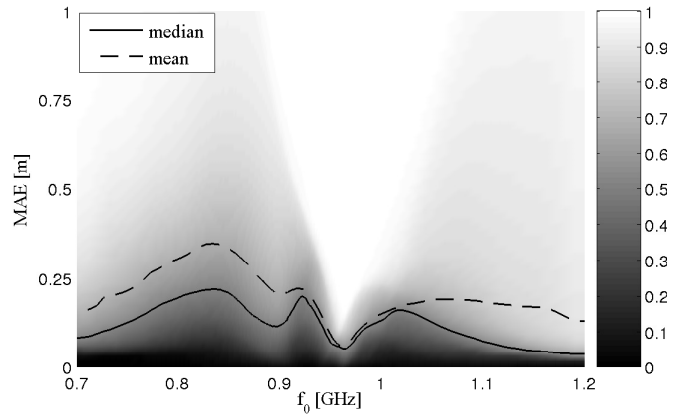


FIGURE 10 - CDF OF THE MEAN ABSOLUTE RANGING ERROR (MAE) FOR A SINGLE CARRIER PAIR OVER FREQUENCY (ALL DISTANCES); ASSEMBLY TOLERANCES.

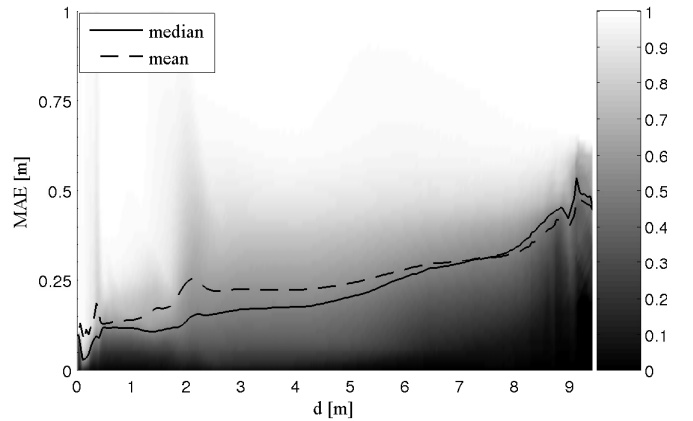


FIGURE 11 - CDF OF THE MEAN ABSOLUTE RANGING ERROR (MAE) OVER DISTANCE FOR ALL UHF RFID FREQUENCIES; ASSEMBLY TOLERANCES.

4.2 Assembly Mismatch

For the presented investigation the assembly capacity has been varied from 50 fF to 10 pF, while the assembly resistance was varied between 2 and 10,000 % of the ideal (Q-matched) value, cf. Fig. 9. This covers perfect assemblies as well as completely messed-up ones.

Fig. 10 shows the cumulative distribution function (CDF) of the mean absolute ranging error (MAE) for one carrier pair (2-frequency continuous wave ranging 2FCW, cf. [4]) with a frequency spacing of $\Delta f=1$ MHz at different center frequencies. The error is smallest around 960 MHz, which is the upper turning point of the antenna self-resonance, cf. Fig. 2. At this point the shapes of antenna and chip reactance are similar, thus creating a flat phase that is virtually independent of assembly mismatches. The largest errors are created at transitions between areas where the unmodulated state is better matched to the antenna impedance than the modulated impedance and areas where this matching is reversed. At these crossings the phase of $\Delta \rho$ is subject to fast changes which result in large ranging errors.

A CDF for a carrier placement uniformly distributed over the UHF RFID frequency ranges (865–868 MHz, 902–928 MHz, and 952–954 MHz) can be found in Fig. 11. For high power levels, i.e., short distances, the tag is mismatched by design because the incident power level is considerably higher than the needed chip power. This creates a flat phase and limits the effects of any additional mismatch. With decreasing power, the tag impedance gets closer to the matching

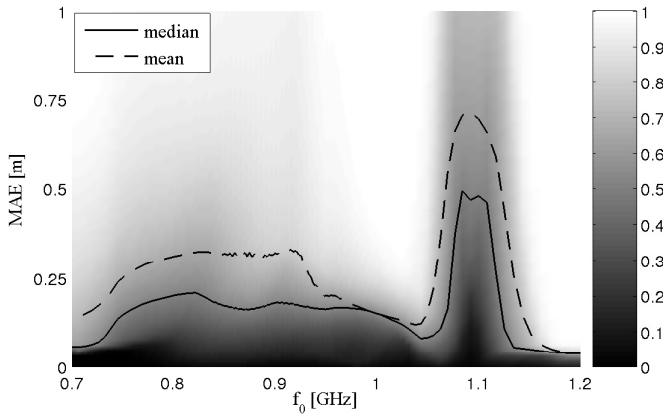


FIGURE 12 - CDF OF THE MEAN ABSOLUTE RANGING ERROR (MAE) FOR A SINGLE CARRIER PAIR OVER FREQUENCY (ALL DISTANCES); ANTENNA DETUNING.

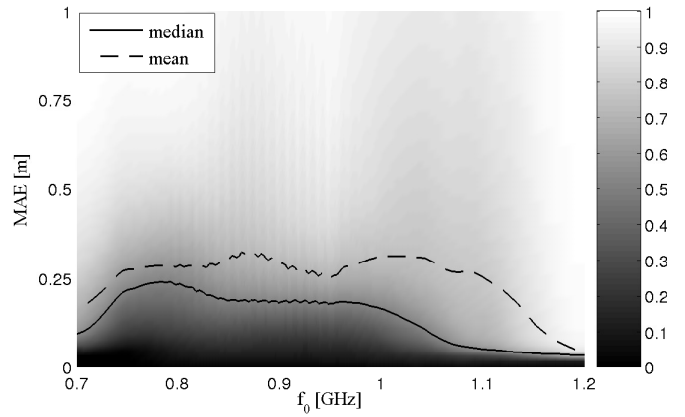


FIGURE 14 - CDF OF THE MEAN ABSOLUTE RANGING ERROR (MAE) FOR A SINGLE CARRIER PAIR OVER FREQUENCY (ALL DISTANCES); COMBINED MISMATCH/DETUNING.

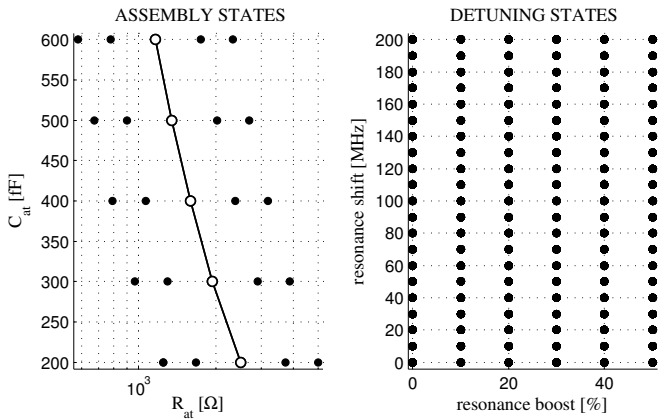


FIGURE 13 - USED ASSEMBLY / DETUNING STATES FOR THE COMBINED MISMATCH SIMULATION.

point, increasing the quality factor of the entire system, i.e., making it more resonant. For this reason, the error increases for higher distances.

4.3 Antenna Detuning

For this study we have boosted the resonance of a perfectly matched tag (flip-chip assembly) between -30% (slightly weaker resonance) up to 100% (near-metal). The frequency of the resonance was reduced by up to 200 MHz in 5 MHz steps. This selection of parameters corresponds to tags in free space as well as tags that are separated from metal by roughly one centimeter (e.g., two sheets of corrugated fiberboard). Tags directly on metal are not covered by this simulation.

Fig. 12 shows the MAE over frequency for antenna detuning. The errors below 1 GHz are caused by the boosted resonance leading to steeper gradients in the tag's phase. This error decreases for massive detuning, as the resonance is shifted towards lower frequencies and attenuated in magnitude. The error around 1.1 GHz is caused by near-zero modulation depth. Just like for the assembly mismatch, areas with near-zero modulation depth cause steep gradients in the modulation phase and thus large errors.

4.4 Combined Assembly Mismatch / Antenna Detuning

The values chosen here are meant to represent the bulk of used tags. Assembly capacities are varied from 200 fF to 600 fF , the assembly resistance is varied from 50% to 100% of the Q-matched value. These assembly impedances cover good to medium flip-chip assemblies. The antenna self-resonance is varied from 100% to 150% of its original

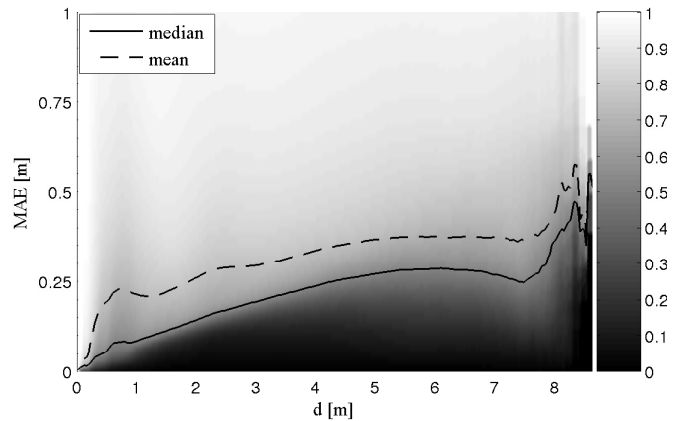


FIGURE 15 - CDF OF THE MEAN ABSOLUTE RANGING ERROR (MAE) OVER DISTANCE FOR ALL UHF RFID FREQUENCIES; COMBINED MISMATCH/DETUNING.

shape and shifted by up to 200 MHz in 10 MHz steps. The maximum detuning corresponds to tags that are in the vicinity of water. A summary of assembly and detuning states can be found in Fig. 13.

Fig. 14 shows the frequency dependence of the ranging error for this scenario. The combination of detuning and mild assembly tolerances generates an almost uniformly distributed MAE over frequency, with the exception of the frequency range above the antenna self-resonance, where errors are considerably smaller. Even though the average MAE also does not exceed 0.5 m for the chosen mismatch/detuning states in the UHF RFID frequency bands, the peak errors are well above one meter.

The same is true for the errors over distance: While averages (mean and median) do not exceed 0.5 m , the error bound is again in the meter range. The error increases with distance up to the point where heavily detuned and mismatched tags fail. At extreme distances the error is dominated by a relatively small group of well-matched but detuned tags with increased quality factor and small frequency shifts.

V. CONCLUSION

We have presented a simulation model of the complex reflection coefficient of a UHF RFID tag based on its equivalent circuit, as well as a simple linear model that can be used in derivations to describe the tag modulation. Both models have been verified using time-variant reflection coefficient measurements of an NXP UCODE G2XM Gen2 chip

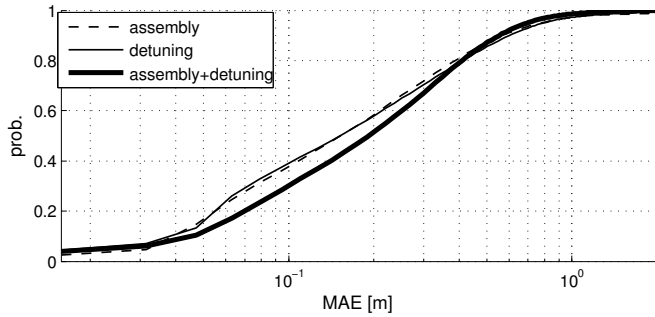


FIGURE 16 - CDFs OF THE MEAN ABSOLUTE RANGING ERROR (MAE) IN THE UHF RFID FREQUENCY BANDS FOR ALL SCENARIOS.

on an NXP UCODE general purpose reference antenna.

Using these models, we have investigated the influence of assembly tolerances and tag detuning on a frequency-domain phase-based ranging system. Although the average mean absolute error (MAE) for this system is below 50 cm, the maximum error may exceed 2 m. A summary CDF for all MAE distance errors in the UHF RFID frequency bands can be found in Fig. 16. Differences between errors caused by assembly mismatches, detuning, or combined mismatch/detuning are minimal.

The reduction in read range due to detuning found in experiments [5] was slightly more pronounced than in the presented simulations. A comparison suggests that the used detuning model is valid if the tag is separated from water/metal by at least 1 cm.

Although the underlying methods and databases [21] have originally been developed to support research on ranging and positioning systems, we hope that they also prove useful for other applications, such as tag-based sensing [6–8].

VI. ACKNOWLEDGMENTS

The authors would like to thank NXP Semiconductors, Gratkorn, Austria, for funding this project and for providing the environment for all measurements. We would also like to thank Giuliano Manzi and Martin Rampetsreiter for their help with the tag models and the measurement setup. This work was supported by the Austrian Research Promotion Agency (FFG) under the grant number 818072.

REFERENCES

- [1] D. M. Dobkin, *The RF in RFID*. Elsevier, 2007, ISBN-13: 978-0750682091.
- [2] P. V. Nikitin, R. Martinez, S. Ramamurthy, H. Leland, G. Spiess, and K. V. S. Rao, “Phase based spatial identification of UHF RFID tags,” in *Proc. IEEE Int RFID Conf*, 2010, pp. 102–109.
- [3] D. Arnitz, G. Adamiuk, U. Muehlmann, and K. Witrisal, “UWB channel sounding for ranging and positioning in passive UHF RFID,” in *11th COST2100 MCM*, Aalborg, Denmark, Jun. 2010.
- [4] D. Arnitz, K. Witrisal, and U. Muehlmann, “Multi-frequency continuous-wave radar approach to ranging in passive UHF RFID,” *IEEE Trans. Microw. Theory Tech.*, vol. 57, no. 5, pp. 1398–1405, Jul. 2009.
- [5] S. R. Aroor and D. D. Deavours, “Evaluation of the state of passive UHF RFID: An experimental approach,” *IEEE Systems Journal*, vol. 1, no. 2, pp. 168–176, 2007.
- [6] R. Bhattacharyya, C. Floerkemeier, and S. Sarma, “RFID tag antenna based temperature sensing,” in *Proc. IEEE Int RFID Conf*, 2010, pp. 8–15.
- [7] —, “RFID tag antenna based sensing: Does your beverage glass need a refill?” in *Proc. IEEE Int RFID Conf*, 2010, pp. 126–133.
- [8] —, “Towards tag antenna based sensing - an RFID displacement sensor,” in *Proc. IEEE Int RFID Conf*, 2009, pp. 95–102.
- [9] L. W. Mayer and A. L. Scholz, “Sensitivity and impedance measurements on UHF RFID transponder chips,” in *Int EURASIP Workshop on RFID Techn., Vienna, Austria, 2007*. [Online]. Available: http://publik.tuwien.ac.at/files/PubDat_165917.pdf
- [10] P. V. Nikitin, K. V. S. Rao, R. Martinez, and S. F. Lam, “Sensitivity and impedance measurements of UHF RFID chips,” *IEEE Trans. Microw. Theory Tech.*, vol. 57, no. 5, pp. 1297–1302, 2009.
- [11] P. V. Nikitin and K. V. S. Rao, “Theory and measurement of backscattering from RFID tags,” *IEEE Antennas Propag. Mag.*, vol. 48, no. 6, pp. 212–218, 2006.
- [12] K. Finkeneller, *RFID Handbook: Fundamentals and Applications in Contactless Smart Cards and Identification*, 2nd ed. Wiley & Sons, 2003, ISBN-13: 978-0470844021.
- [13] E. Colin, A. Moretto, C. Ripoll, and S. A. Chakra, “Delta RCS of UHF RFID taking into account the shunt resistance in the tag model,” in *Proc. Joint IEEE North-East Workshop Circuits and Systems and TAISA Conf. NEWCAS-TAISA '09*, 2009, pp. 1–4.
- [14] J.-W. Lee, H. Kwon, and B. Lee, “Design consideration of UHF RFID tag for increased reading range,” in *Proc. IEEE MTT-S Int. Microwave Symp. Digest*, 2006, pp. 1588–1591.
- [15] K. V. S. Rao, P. V. Nikitin, and S. F. Lam, “Impedance matching concepts in RFID transponder design,” in *Proc. Fourth IEEE Workshop Automatic Identification Advanced Technologies*, 2005, pp. 39–42.
- [16] —, “Antenna design for UHF RFID tags: a review and a practical application,” *IEEE Trans. Antennas Propag.*, vol. 53, no. 12, pp. 3870–3876, 2005.
- [17] Y. Tikhov, “Comments on antenna design for UHF RFID tags: a review and a practical application,” *IEEE Trans. Antennas Propag.*, vol. 54, no. 6, 2006.
- [18] P. V. Nikitin and K. V. S. Rao, “Reply to comments on antenna design for UHF RFID tags: A review and a practical application,” *IEEE Trans. Antennas Propag.*, vol. 54, no. 6, pp. 1906–1907, 2006.
- [19] W. Wiesbeck, G. Adamiuk, and C. Sturm, “Basic properties and design principles of UWB antennas,” *Proc. IEEE*, vol. 97, no. 2, pp. 372–385, 2009.
- [20] P. V. Nikitin, K. V. S. Rao, and R. D. Martinez, “Differential RCS of RFID tag,” *Electronics Letters*, vol. 43, no. 8, pp. 431–432, 2007.
- [21] The PARIS Simulation Framework. Graz University of Technology / NXP Semiconductors. Open-Source (GNU GPL v3). [Online]. Available: <http://www.spsc.tugraz.at/research-topics/wireless-communications/paris-os/>
- [22] D. Arnitz, U. Muehlmann, T. Gigl, and K. Witrisal, “Wideband system-level simulator for passive UHF RFID,” in *Proc. IEEE Intl. Conf. on RFID, RFID'09*, Orlando, Florida, Apr. 2009.
- [23] S. Hu, C. L. Law, and W. Dou, “Measurements of UWB antennas backscattering characteristics for RFID systems,” in *Proc. IEEE Int. Conf. Ultra-Wideband ICUWB 2007*, 2007, pp. 94–99.

Wideband Characterization of UHF RFID Channels for Ranging and Positioning

DANIEL ARNITZ, ULRICH MUEHLMANN, AND KLAUS WITRISAL

daniel.arnitz@tugraz.at, ulrich.muehlmann@nxp.com, witrisal@tugraz.at
Graz University of Technology / NXP Semiconductors, Austria

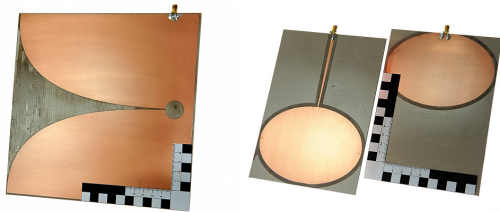
Abstract

- **Positioning** is a much-desired feature in UHF RFID: Methods using **phase shifts between multiple carriers** have been proposed (fit into spectral masks)
- Unfortunately, the phase shifts are **heavily affected by multipath propagation**.
- As a consequence, **wideband properties** of UHF RFID channels are **imperative for positioning**, yet not well understood and rarely taken into account
- **This work presents the first (ultra)wideband channel characterization for typical UHF RFID setups (indoor, short-range, suitable TX antennas, ...)**

1. Measurement Setup

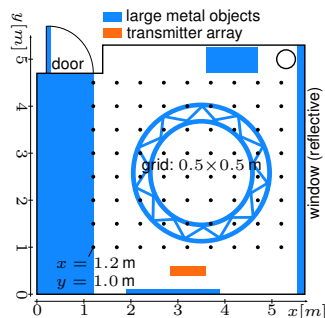
Measurement Description

- 500..1500 MHz using a Vector Network Analyzer
- TX antenna: custom 4×1 Vivaldi array (left photo; gain pattern resembling a typical UHF RFID reader antenna)
- RX antenna: custom omnidirectional UWB antenna (right photo; gain pattern resembling a typical UHF RFID tag antenna)



Measurement Environment: Semi-Industrial

- reinforced concrete floor, walls, and ceiling
- large window with highly reflective coating
- large metal objects (metal platings, large circular strut mounted on ceiling, large cabinet, ...)



2. Channel Model, Simulation Setup

Channel Model

- deterministic largescale: log-distance line-of-sight (LOS)
- deterministic smallscale: reflections using simple ray-tracing
- stochastic smallscale (scattering)

Simulation Setup

Simulation results have been created by [1] with some enhancements. Modeled are:

- RX-antenna and TX-array directivity (far field)
- reflections on walls, floor, and ceiling (simple ray-tracing)
- statistical model of scattering

Explicitly NOT modeled are:

- exact room geometry and/or materials
- TX antenna array size / near-field effects

3. Measurement and Simulation Results

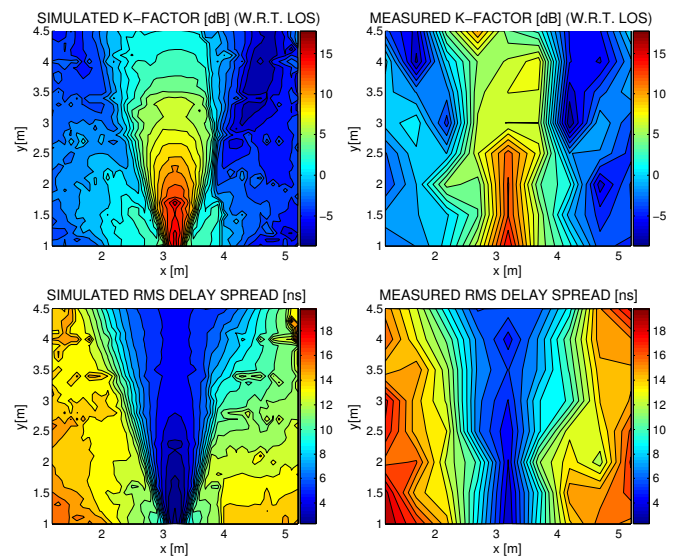
In a Nutshell...

- surprisingly low K-factor: max. 10..15 dB within main lobe
- coverage (tag powered) approx. 15% of meas. area
- local influence of metal objects evident

Simulation (left) vs. Measurement (right):

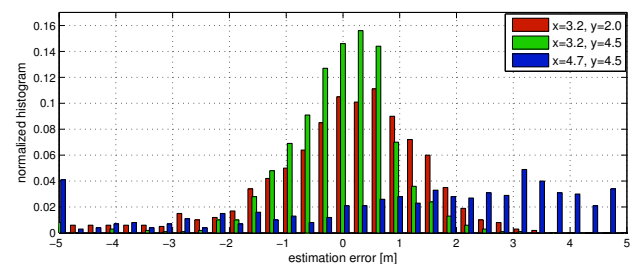
Differences mainly due to:

- point source vs. 60×21×21 cm array (close to TX)
- local influence of complex metal objects (top and right side)



Example: Phase-Difference-Based Ranging TX→RX

- two carriers at 0.5..1.5 GHz, offset $\Delta f = 1$ MHz
- dist. estimate TX→RX: $\hat{d} = \Delta \hat{\varphi} / (2\pi) \lambda = c \Delta \hat{\varphi} / (2\pi \Delta f)$



- ranging even in main lobe not a simple task (low K-factor)
- close to uniform phase outside main lobe (\Rightarrow random \hat{d})
- 90% coh. BW: ≈ 50 MHz inside main lobe, ≈ 4 MHz outside

4. Conclusion

- Multicarrier positioning methods without taking the wideband channel parameters into account will fail under realistic indoor conditions
- Simulations using the wideband UHF RFID simulator match the measurement results
- Future Work: Industrial environments / gates

REFERENCES

- [1] D. Arnitz, U. Muehlmann, T. Gigl, and K. Witrisal. Wideband system-level simulator for passive UHF RFID. In *IEEE Intl. Conf. on RFID, RFID'09*, Orlando, Florida, April 2009.

UWB Channel Sounding for Ranging and Positioning in Passive UHF RFID

Daniel Arnitz*, Grzegorz Adamiuk**, Ulrich Muehlmann***, and Klaus Witrisal*

* Signal Processing and Speech Communication Laboratory, Graz University of Technology, Austria
{daniel.arnitz, witrisal}@tugraz.at

** Institut für Hochfrequenztechnik und Elektronik, Karlsruher Institut für Technologie, Germany
grzegorz.adamiuk@kit.edu

*** NXP Semiconductors, Gratkorn, Austria
ulrich.muehlmann@nxp.com

Abstract—The market of passive UHF RFID has reached a state where it is mainly cost-driven, although there are desired features that remain elusive. Positioning, for example, has seen a lot of research in the past years, but no conclusive breakthrough. Due to limitations enforced by tag design and regulations, such positioning systems are inherently narrowband and thus vulnerable to multipath propagation. Despite that, the UHF RFID channel is not well-understood with respect to channel parameters such as K-factor or RMS delay spread, which are vital parameters for ranging accuracy.

We present an ultra-wideband channel measurement setup aimed at the UHF RFID frequency range around 900 MHz and extending over a bandwidth of 1 GHz. Based on channel measurements in a UHF-RFID warehouse gate, we will also show the challenges positioning systems have to face in such scenarios.

Index Terms—UHF RFID, ultra-wideband, channel sounding, multipath propagation, warehouse portal, ranging, positioning

I. INTRODUCTION

UHF RFID has come a long way since its early stages in the 1970s and the first standardization in the early 2000s [1]. Since then, it has become ubiquitous in various applications from supply chain management to laundry services. Even though UHF RFID is now a widespread technology, reliable positioning is a feature that is not yet available. There has been considerable research on UHF RFID positioning during the last years, but no conclusive breakthrough [2].

Foremost in the list of reasons for this are the need to keep the tag simple (power consumption, costs) and the very strict bandwidth limits of the UHF RFID frequency band(s). As a consequence, the used ranging methods are based on narrowband parameters such as return link phases and thus especially vulnerable to multipath propagation. A very good overview of such phase-based ranging and positioning systems currently under research can be found in [2].

Registering tagged objects moving through a portal is a very common application of UHF RFID [3]. The

design of these gates is optimized to concentrate energy within the gate, with devastating effects on narrowband ranging systems. In this paper we present an ultra-wideband measurement setup aimed at the UHF RFID frequency range and show what challenges positioning systems have to face in everyday portal applications.

This paper is organized as follows: Section II addresses the design of the ultra-wideband (UWB) antennas that are necessary for UWB measurements in the UHF frequency range. The measurement setup is described in Section III, while the analyses methods of the measured channels is explained in detail in Section IV. Finally, measurement results are presented in Section V, including ranging error estimates for a phase-based ranging approach [4].

II. ANTENNA DESIGN

A. Tag Antenna

The tag antenna (receiver-/RX-antenna in the following sections) is intended to be placed on a pallet with different goods, of which dielectric properties may vary. For that reason an antenna which preserves its properties (such as impedance matching in a wide frequency range, radiation pattern, ...), independent of the dielectric permittivity of the surroundings must be applied. Since the direction to the reader is a-priori unknown, such an antenna must maintain an omnidirectional radiation pattern.

In the presented approach a broadband dipole antenna for an operational frequency range of 0.7–1.2 GHz is used. The schematics of the antenna, as well as the photograph are shown in Fig. 1. It consists of two ellipses which are arranged in a dipole-like structure on the opposite sides of the substrate. As a substrate the Taconic RF-33 with $\epsilon_r=3.3$ is used. The antenna is fed by a microstrip line, for which one of the ellipses serves as a ground plane. The connector is soldered to the microstrip line and the ground plane (cf. Fig. 1). The end of the microstrip is connected to the second ellipse. A tapering

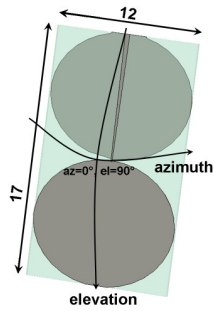


Fig. 1. Transparent model (left) and a photograph (right) of an omnidirectional tag antenna (RX). Units are in cm.

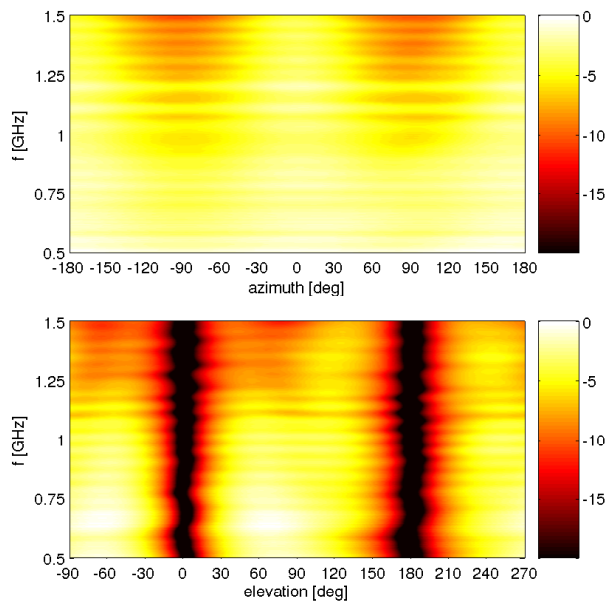


Fig. 2. Normalized horizontal/vertical gain pattern in dB: omnidirectional tag antenna.

of the microstrip line's width is used for the impedance matching.

The measured gain patterns of the antenna in horizontal plane (E-plane, elevation) and vertical plane (H-plane, azimuth) are shown in Fig. 2. It can be noted that the antenna exhibits an ultra broadband radiation. In the E-plane two maxima, which are oriented perpendicular to the antenna surface, are present. In the H-plane a nearly omnidirectional radiation pattern over a wide frequency range is achieved. In the higher frequency range the antenna becomes larger w.r.t. the wavelength and some discrepancy from the omnidirectional pattern is observed. The results show that the antenna possesses a dipole-like radiation over a very wide frequency range.

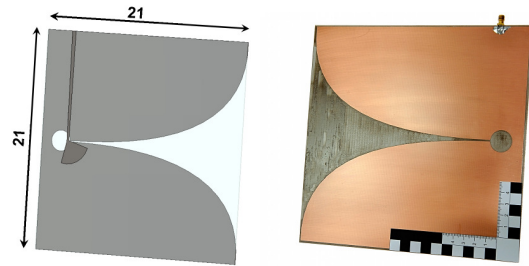


Fig. 3. Transparent model (left) and a photograph (right) of a single reader antenna. Units are in cm.

B. Reader Antenna

The reader antenna characteristics must maintain a directional radiation pattern. The operational frequency range is, as in the case of the tag antenna, from 0.7 GHz to 1.2 GHz. An ultra-wideband radiation with directive pattern is achieved by the application of a tapered slot antenna (also called Vivaldi antenna), which is shown in Fig. 3. As a substrate the Taconic RF-30 with $\epsilon_r=3$ is used. It is fed by an SMA connector, which is soldered to the microstrip line at the top of the structure (see Fig. 3). The electromagnetic wave is coupled to the slot line by an aperture coupling. The slot is widened and the structure is formed to the tapered slot, which fulfils radiation conditions in a wide frequency range (according to the traveling wave principle). The lower cut-off frequency depends on the maximal opening of the slot, i.e., on the height of the antenna.

The antenna exhibits a directive radiation behavior. The main beam direction is conformal with the direction pointed by the slot opening. The 3 dB-beamwidth is approx. $60-80^\circ$ in the E-plane and approx. $130-160^\circ$ in the H-plane, depending on frequency. In order to assure spatial selectivity of the system in the application (e.g., a gate), the beam in the H-plane should be narrowed. For that purpose a 4×1 linear antenna array is used (transmitter-/TX-antenna in the following sections). The schematics of the antenna is shown in Fig. 4. Four Vivaldi antennas are placed next to each other in the distance of 20 cm. The extension plane of the array is in the H-plane of the single antenna, i.e., the horizontal plane. Such an arrangement concentrates the radiation in the respective plane and allows for the suppression of the grating lobes. The measured radiation characteristics for the elevation plane (E-plane) and the azimuth plane (H-plane) are shown in Fig. 5. A very directive radiation pattern in the azimuth plane is observed in the desired frequency range. Aside from the main beam direction, some side lobes and grating lobes are present. Their amplitude is suppressed by approx. 13 to 16 dB w.r.t. the maximal gain at 0° . In the elevation plane a wider beam is observed. Within the main beam in this plane

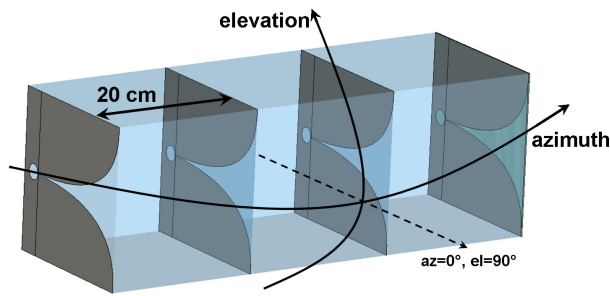


Fig. 4. Schematic of the linear 4×1 Vivaldi-array (TX).

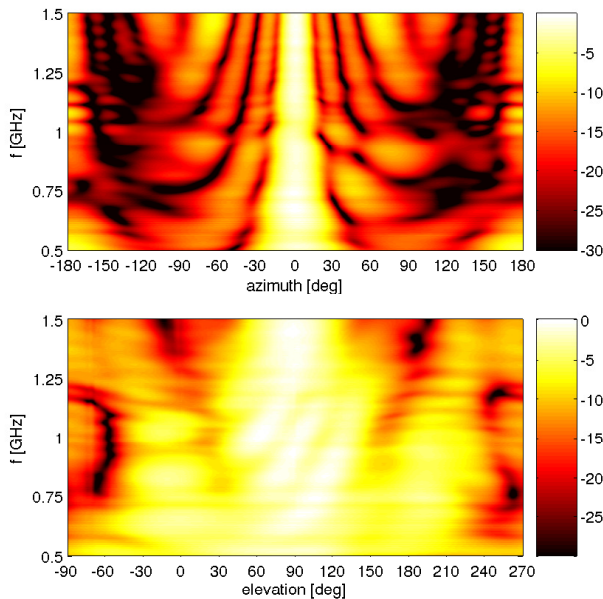


Fig. 5. Normalized horizontal/vertical gain pattern in dB: Vivaldi 4×1 array.

some small fluctuations of the gain values are present, which are due to the coupling between the elements in the array and weak resonances in the feeding network. The form of the beam in the elevation plane is conformal with the one of the single antenna.

III. MEASUREMENT SETUP

A. Description of the Environment

All measurements were performed in NXP's Application and System Center (ASC) in Gratkorn, Austria, to ensure a realistic environment. The ASC is located in a converted production hall with (partially) corrugated metal walls and ceiling, and a steel-reinforced concrete floor. Among other setups, the ASC is equipped with a pallet mover that passes through several UHF RFID gates, one of which was replaced by the presented measurement setup. The entire hall is cluttered with

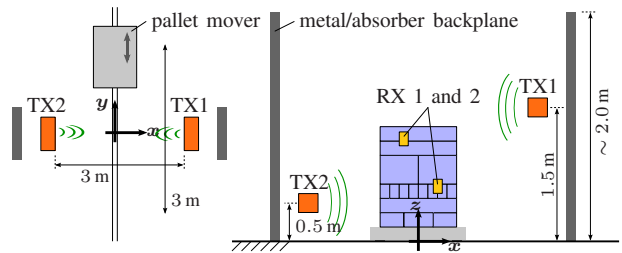


Fig. 6. Gate setup (left: top view, right: back view): A product pallet is placed on a pallet mover and transported through the gate while recording channel transfer functions (pallet was stopped for each recording).

metal objects of different sizes (from boxes with screws to a room-sized anechoic chamber).

It is also a busy environment, both physically and electrically: During the measurements, people were moving around (not within the gate), creating a time-variant and thus realistic environment. Also, as the ASC is a test center for RFID, several UHF-readers were active throughout the entire hall and cell phones were used close to the gate setup. Tests have shown that cell phones and UHF readers increase the noise floor by approximately 20 to 30 dB for individual measurements. Even though these changes in the noise floor are quickly time-varying due to modulation, there was no perceivable influence on the presented analyses.

B. Description of the Gate Setup

The entire setup outlined in Fig. 6 was constructed like a UHF-RFID portal: The transmitter arrays were positioned 3 m apart (front to front) to the left and right of the pallet mover. The antenna heights (floor to center) were 0.5 m (TX2) and 1.5 m (TX1), respectively. The backplanes behind the transmitter antennas (80×195 cm) are made of metal. This setup is designed to concentrate as much energy as possible within the gate and to be able to use the gate reflection to read a tag even when the direct path is blocked by the pallet. All measurements were also performed with absorber¹ backplanes of similar size to assess the influence of the metal backplanes.

Measurements with two different pallets were done: The first pallet consisted of a wooden scaffold with a polyurethane foam slab for receiver antenna mounting that was kept at a safe distance from the metal pallet mover (Fig. 7). This setup ensures wave propagation close to free space, thus forming a baseline for changes created by product pallets. The second pallet consisted of packed liquid cleaning agents in bottles, as well as some aluminum-packed candies (Fig. 8) and is considered a reference for strong distortions by NXP. A detailed

¹Emerson & Cuming ECCOSORB AN-79; reflectivity approx. -20 dB

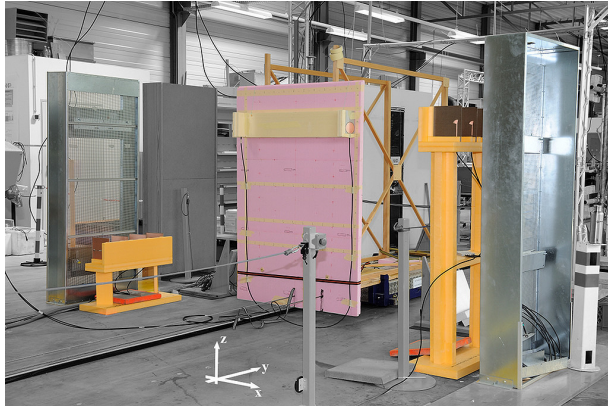


Fig. 7. Photograph of a gate setup with “free space” pallet and metal backplanes. The transmitter arrays are positioned on the stands to the left and right of the pallet mover, while the receiver antennas are mounted on the polyurethane foam slab. Note that the coordinate system is not at its origin.



Fig. 8. Photograph of a gate setup with “ETSI” pallet (liquid cleaning agents in bottles) and absorber backplanes. The receiver antennas are mounted on the polyurethane foam slab left of the pallet. Note that the coordinate system is not at its origin.

schematic of this pallet (not to scale) along with receiver antenna positions can be found in Fig. 9.

The receiver antennas were fixed at different x - and z -positions on polyurethane foam slabs, which were mounted on the pallet. The pallet was incrementally moved through the gate while recording. After each pass through the gate, the receivers were re-positioned, and the pallet was transported through the gate again. The spacing between two adjacent measurements in x , y , and z was chosen to be 10 cm to have a sufficiently high resolution within the gate while keeping the measurement time manageable. The entire set of all measurements for one receiver (lines in y) thus forms a plane in xy or yz .

All antennas were vertically polarized. Because the tag antenna gain has a minimum along this dimension, the floor reflection is considerably attenuated for some positions. It is also important to note that the cables to

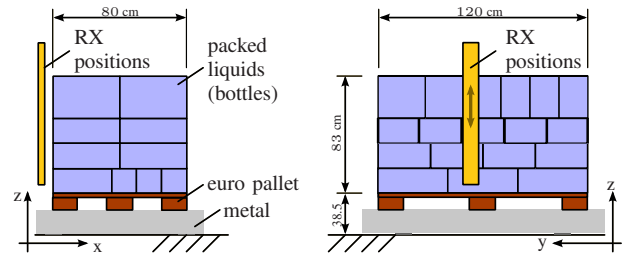


Fig. 9. Pallet with liquid cleaning agents: Back view (left) and side-view from TX2 (right). The pallet is considered a reference pallet for heavy distortions (“ETSI pallet”). A photograph can be found in Fig.8. The upper part of the receiver plane is visible to both transmitter antennas, while the lower part is visible only to TX2. Receiver antennas were kept at a distance of 10 cm from the liquids.

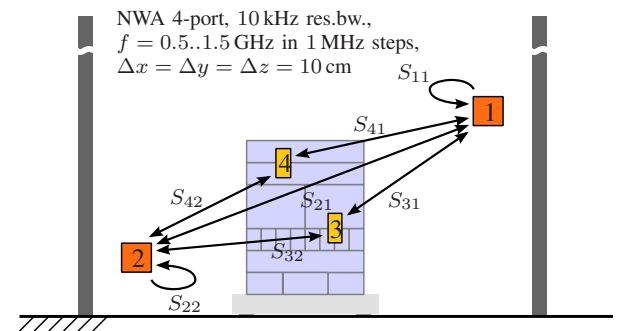


Fig. 10. Measured channels: TX at ports 1 and 2, RX at ports 1 through 4. Feedback might also be a problem for ranging systems, thus also S_{11} and S_{22} have been recorded. Shadowing properties of a product pallet and feedback for bistatic ranging setups can be analyzed via S_{21} . As tag to tag communication/ranging is not an issue in UHF RFID, receiver to receiver channels have not been recorded.

the receiver antennas are very critical in such setups; they have to be placed and fixed very carefully to minimize their influence on the measurement results.

The channels shown in Fig. 10 were measured for each position and in the frequency range of $f=0.5..1.5$ GHz with 1 MHz stepsize using a Rohde&Schwarz ZVA-24 network analyzer (NWA) with 4 ports. This stepsize results in a maximum time delay of roughly $1 \mu\text{s}$ (maximum path length 300 m), which was found to be fully sufficient in this environment. The bandwidth resolution of the NWA was 10 kHz and conducted power set to 0 dBm, resulting in a noise floor of roughly -100 dBm and thus an effective dynamic range of 100 dB.

IV. DESCRIPTION OF PERFORMED ANALYSES

The recorded complex S-parameters for all receiver positions are analyzed as shown in Fig. 11. The individual analyses are described in detail in the following subsections.

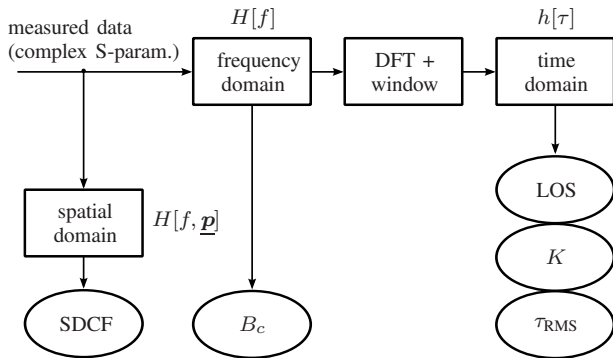


Fig. 11. Performed analyses in spatial domain, frequency domain, and time domain.

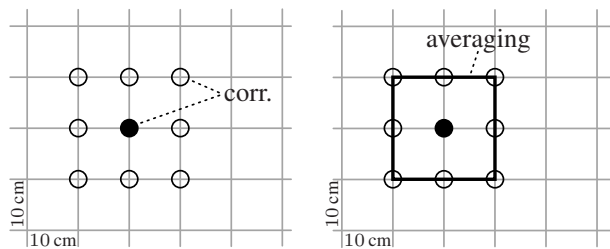


Fig. 12. Correlations in the spatial domain: The transfer function at each point is correlated with its neighbors and the resulting correlation coefficients are averaged to obtain a single coefficient.

A. Spatial Domain

Calculation of the average spaced-distance correlation function (SDCF), i.e., the correlation of the channel transfer function at each point with its nearest neighbors, is performed by averaging the correlation coefficients between the center and all its neighbors (Fig. 12). Note that this averaging neglects the inherent direction-dependence of the correlation.

B. Frequency Domain

The frequency domain analysis consist solely of calculating the coherence bandwidth B_c (cf. [5]) at several thresholds (50, 70, and 90 %). We have also implemented moment-based estimates of the K-factor [6], [7] and estimates of the RMS delay spread τ_{RMS} based on level crossing rates [7]. However, for our measurements, these estimators have been found to be unreliable due to the unknown and considerably angle-dependent (and thus position-dependent) gain patterns of the used RX and TX antennas.

C. Time-Domain

To obtain the channel impulse response (CIR) out of the channel transfer function (CTF), the spectrum is windowed by a Parzen window and transformed using

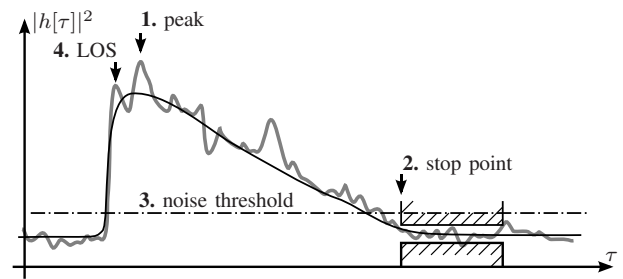


Fig. 13. Sequence of operations on the power-delay-profile: Peak detection (1), stop point detection (2), noise floor and -threshold calculation (3), and LOS detection (4).

a discrete Fourier transform (DFT). The CIR is subsequently truncated to remove artifacts created by cyclic convolution and re-normalized to the correct power level.

All calculations done for the time-domain analysis are based solely on the squared magnitude of the CIR, the power-delay-profile (PDP). The central part of the analysis is the partitioning of the PDP, as illustrated in Fig. 13: After simple peak (maximum) detection, a heavily filtered version of the PDP is created in order to detect the delay τ where the profile drops below the noise floor (max. excess delay; denoted stop point here). To ensure a robust detection, the noise floor is considered to be reached if the filtered version does not change by more than 3 dB for at least 200 ns. The choice of these values is arbitrary, but should reflect the shape of the PDP. As all measurements were performed in an enclosed hall without connecting corridors to other halls, clusters are not an issue. Thus, as a third step, everything after the stop point is considered noise and averaged to create the noise threshold, which is calculated using mean and standard deviation of the noise, the dispersive properties of the used window, and an additional margin of 10 dB. This margin takes the slightly higher noise level prior to the LOS component into account. The LOS path is defined to be the first component at or above this noise threshold. If the maximum peak is below the threshold, the recorded impulse response is considered noise-only. In a last step, interpolation around the detected LOS path is used to increase resolution.

Following the partitioning of the channel impulse response, several values are calculated (cf. [5]):

- LOS power and delay, taking the deformations by the used window's main lobe into account (see below)
- K-factor w.r.t. the LOS component (important for ranging) and w.r.t. the peak component ("Ricean K-factor")
- RMS delay spread with correction of the bias created by windowing (see below)

It is of vital importance here to consider the effects

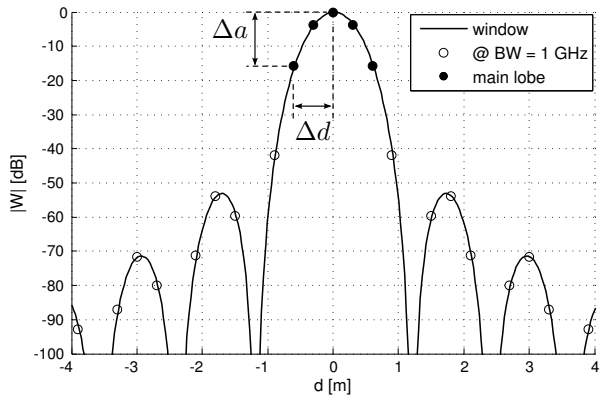


Fig. 14. Used Parzen window (circles): Max. mainlobe attenuation Δa , mainlobe width $2\Delta d$. The considered mainlobe for the presented measurements consists of 5 points, hence $> 99.99\%$ of the window power is within the main lobe.

of the used window on all calculations: Not only will the window's main lobe broaden the LOS peak (if there is a peak in the first place), but the strongest sidelobe will also shift energy from the possibly very strong LOS peak to the noise floor that precedes the LOS path. If this sidelobe is sufficiently pronounced and not considered in the threshold calculation, the artifact will be identified as LOS component. These distortions introduced by windowing are factored in at four different points (cf. Fig. 14):

- 1) The noise threshold is increased by the gain difference of minimum and maximum mainlobe sample (Δa).
- 2) The true LOS position is assumed to be close to Δd after the threshold crossing.
- 3) For K-factor calculations, ± 2 samples around the LOS position are considered to be part of the LOS component.
- 4) The bias for the RMS delay spread created by windowing [8] is corrected. It should be noted though that this bias is merely 0.75 ns for the used Parzen window.

V. MEASUREMENT RESULTS

For the sake of brevity, the majority of measurement results shown here are limited to the most realistic setup: The gate with metal backplanes and the liquids ("ETSI") pallet. As mentioned above, this pallet is considered a reference and is thus also a good benchmark for ranging and positioning. Photograph and schematic of the setup can be found in Figs. 8 and 9, respectively.

We will start our analysis with the incident power level at the tag. This is the single most important value for the analysis of state-of-the-art UHF RFID systems,

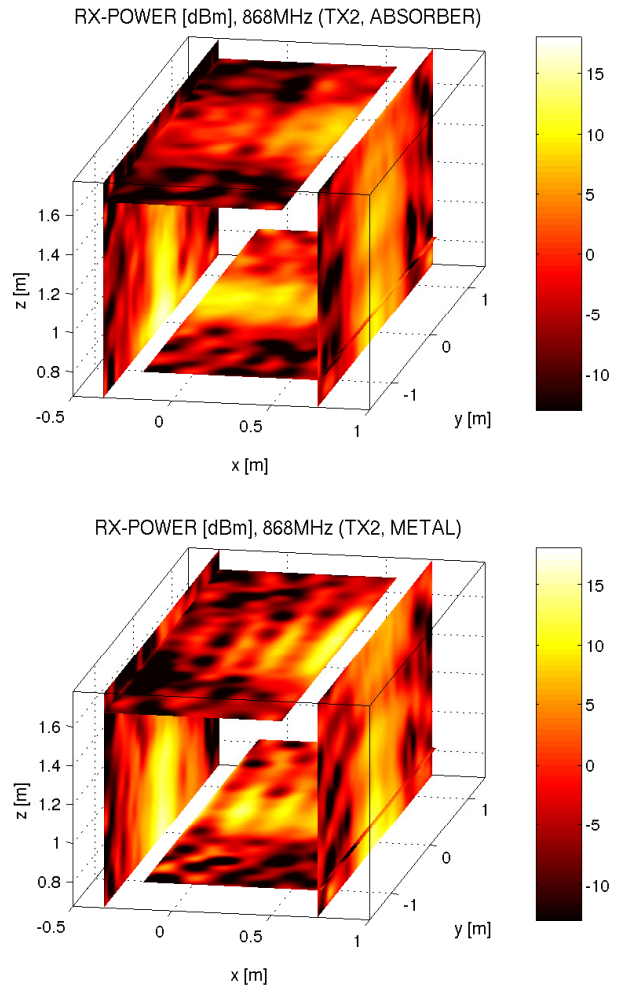


Fig. 15. Incident power level [dBm] at the tag for 35.2 dBm (EIRP) conducted power at 868 MHz and TX2; empty gate with absorber/metal backplanes

as it is directly connected to read rates and thus to the most important performance metric for RFID users. A comprehensive analysis of the incident power distribution in a portal application can be found in [3]. The circular line structure created by standing waves within the empty gate predicted by simulations in [3] and [9] can also be observed here: Fig. 15 shows some vertical circles created by the floor reflection for the absorber backplanes, as well as pronounced standing waves in horizontal and vertical planes for the metal backplanes.

Things change considerably when a pallet enters the gate: Fig. 16 shows the power distribution for TX1 and TX2. The standing wave pattern is destroyed by the moving pallet (which is highly reflective itself). A slight circular structure (created by the floor reflection) can be observed after the pallet has left the gate ($y > 1$ m).

Even though the incident power level at a certain frequency is a vital metric for UHF RFID, its importance

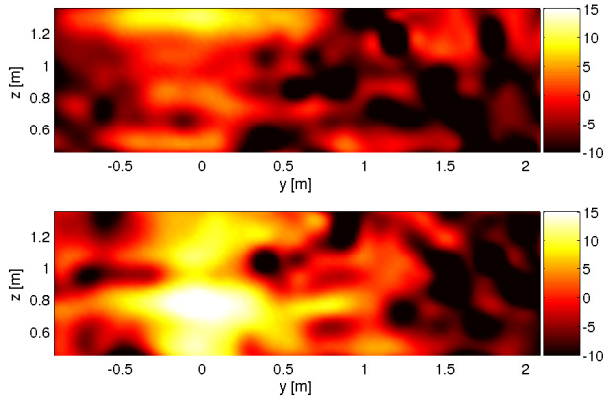


Fig. 16. Incident power level [dBm] at the tag; 35.2 dBm (EIRP) conducted power at 868 MHz; TX1 (top) and TX2 (bottom); “ETSI pallet”, metal backplanes; view from TX1.

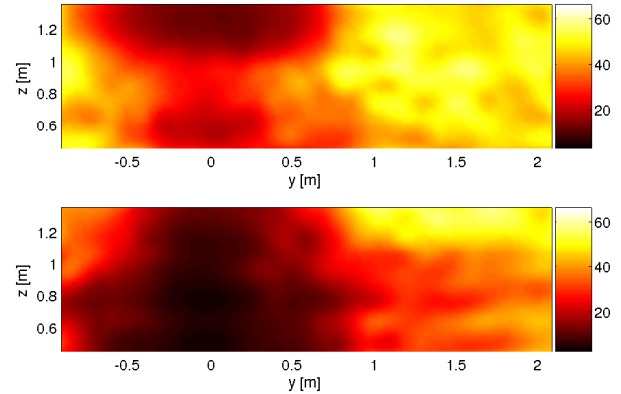


Fig. 18. RMS delay spread [ns] for TX1 (top) and TX2 (bottom); “ETSI pallet”, metal backplanes; view from TX1.

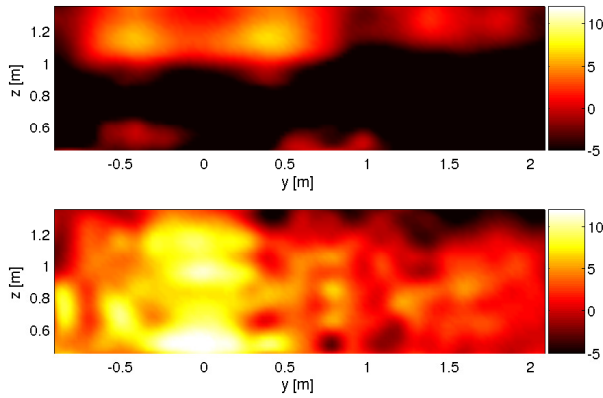


Fig. 17. K-Factor [dB] w.r.t. the LOS component for TX1 (top) and TX2 (bottom); “ETSI pallet”, metal backplanes; view from TX1.

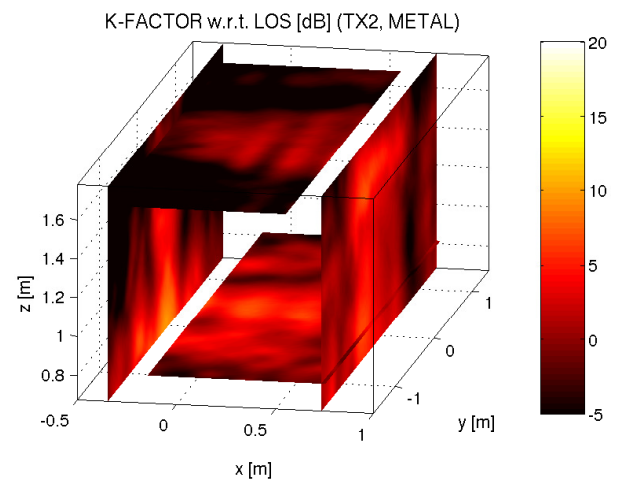
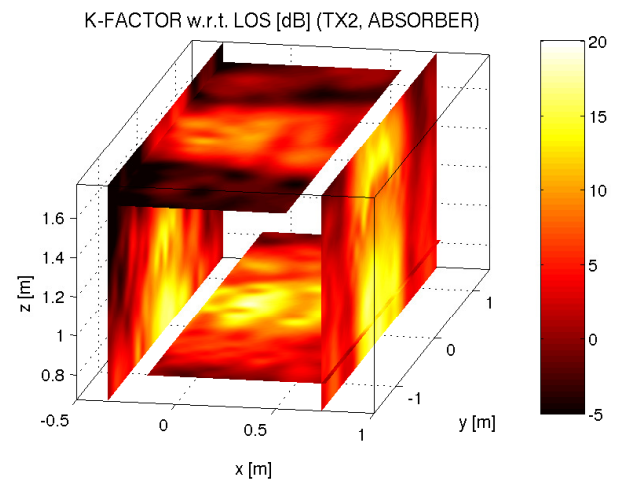


Fig. 19. K-Factor [dB] w.r.t. the LOS component for TX2; empty gate with absorber/metal backplanes

to ranging and positioning is minimal. On the other hand, the K-factor w.r.t. the direct (LOS) path and the RMS delay spread are of paramount importance here, and shown for the liquids pallet in Figs. 17 and 18, respectively. Considering the reflective properties of the used materials (metal backplanes, a metal pallet mover, a steel-reinforced concrete floor, and a cubic meter of liquids), it comes at no surprise that the K-factor only exceeds $K \approx 5$ dB when the receiver is directly in front of the transmitter array ($y = -30..30$ cm). Still, considering that the distance to the array in this case is less than one meter, K-factors are surprisingly low. The same is true for the RMS delay spread, which is above 10 ns for almost the entire gate. For comparison, this delay of 10 ns corresponds to a path length of 3 m in free space.

Fig. 19 shows a comparison of the K-factor w.r.t. the direct path for metal and absorber backplanes. As can be seen, the K-factor inside the gate drops considerably for the metal backplanes.

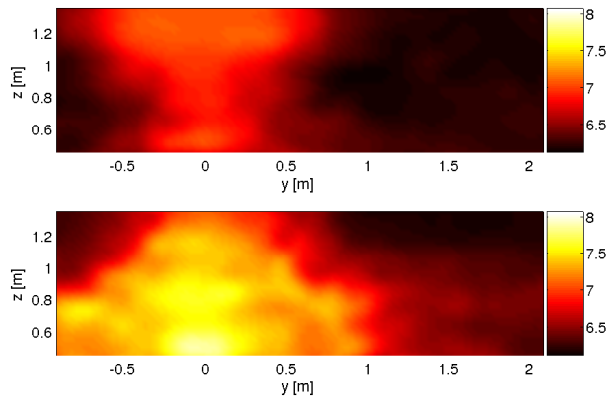


Fig. 20. 90 % coherence bandwidth [$\log_{10}(\text{Hz})$] for TX1 (top) and TX2 (bottom); “ETSI pallet”, metal backplanes; view from TX1.

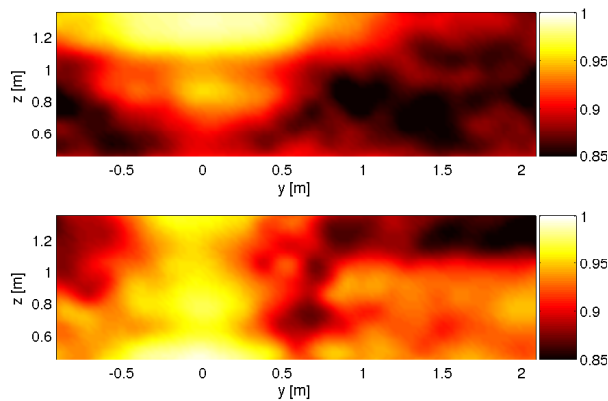


Fig. 21. Spaced-distance correlation function at $\Delta = 12$ cm for TX1 (top) and TX2 (bottom); “ETSI pallet”, metal backplanes; view from TX1.

The coherence bandwidth (correlation in frequency domain) is shown in Fig. 20, while the spaced-distance correlation function (correlation in spatial domain) can be found in Fig. 21. As can be seen, the 90 % coherence bandwidth is in the range of 50 MHz inside the gate when in direct line of sight, and around 1 MHz outside the gate. Correlations at a length (distance) of 12 cm, which is 20..60 % of a wavelength for the given frequency range, are above 90 % for most of the gate. The estimated coherence length (70 %) is around 1..2 wavelengths outside the gate, if the direct path is blocked by the pallet, and several wavelengths inside the gate. Curiously, the coherence distance is almost independent of the used backplane.

Last, but not least, the error for a phase-based ranging method [4] with a frequency spacing of 1 MHz is shown in Figs. 22 and 23. Note that these are the errors for the path TX→RX and a single ranging estimate.

Fig. 22 shows the expected value (bias) of this estimate. Outside the gate, the combined non-line-of-sight

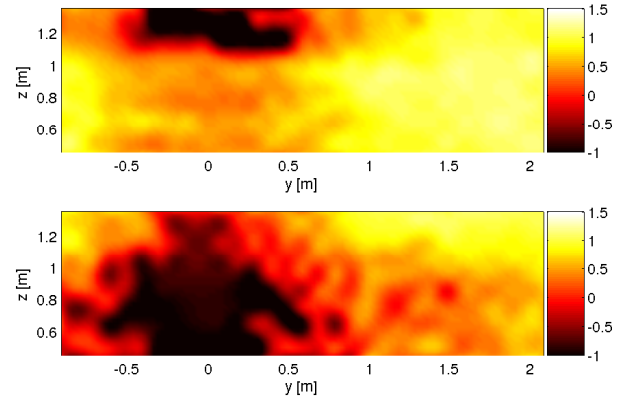


Fig. 22. Expected value (bias) $\log_{10}(\text{[m]})$ of a single 2FCW estimate w. $\Delta f = 1$ MHz for TX1 (top) and TX2 (bottom); “ETSI pallet”, metal backplanes; view from TX1.

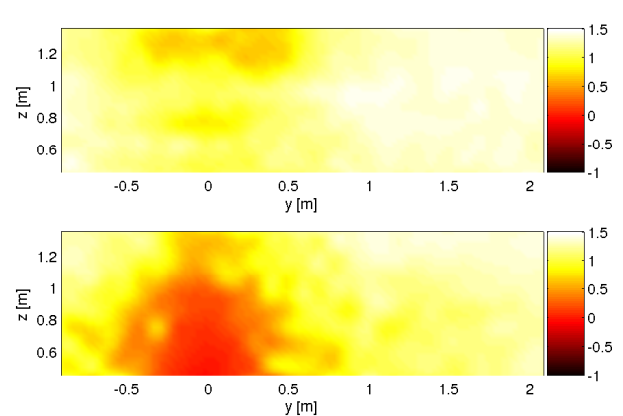


Fig. 23. Standard deviation $\log_{10}(\text{[m]})$ of a single 2FCW estimate w. $\Delta f = 1$ MHz for TX1 (top) and TX2 (bottom); “ETSI pallet”, metal backplanes; view from TX1.

(NLOS) paths are stronger than the direct LOS path by far, leading to a heavily biased estimate. Said bias ranges from below 10 cm inside the gate provided the LOS path is not blocked by the pallet, and reaches up to 20 m outside the gate. The standard deviation for a single estimate (Fig. 23) ranges from roughly 1.5 m in front of the transmitter (at a distance of less than a meter!) to 30 m outside the gate. Note that the wavelength of the offset frequency (1 MHz) is 300 m; thus the phase difference is still non-ambiguous. As the standard deviation can be reduced by successive/independent range estimates, classification “inside/outside gate” still might be possible. In fact, the bias will help for such a classification, as it will quickly shift the range estimate to outside the gate (note the almost linearly increasing bias in this logarithmic plot).

VI. CONCLUSION

We have presented a measurement setup for channel sounding in the UHF RFID frequency band. Using

this setup, we have done extensive measurements in a UHF RFID portal scenario under realistic conditions. The presented measurements are widely consistent with previous measurements in this portal [3] in terms of narrowband power levels.

The design of UHF RFID portals is optimized for best possible read rates, employing metal backplanes to concentrate energy within the portal. This design has devastating effects on narrowband ranging systems, as it reduces K-factors w.r.t. the LOS component by more than 10 dB and increases the RMS delay spread by factors. It should also be noted that the channel inside such a portal is highly deterministic [2], [3]. Any ranging system has to deal with K-factors w.r.t. the direct path in the range of 5..10 dB at best, and RMS delay spreads above 10 ns even at distances below one meter.

RMS delay spreads outside the gate (but still with an unobstructed direct path) reached 60 ns in our measurements, while K-factors dropped well below 0 dB. In this aspect our results correspond well with measurements at distances up to 20 m in an industrial environment [10]. It follows that the exterior of the gate, i.e., everything outside the space spanned by the metal backplanes, has to be treated as non-line-of-sight, even if the direct path is unobstructed. Furthermore, we find that previous short-range measurements in the UHF band [8] and other short-range channel models like IEEE 802.15.3a [11] (based on meas. [12], [13]) are too optimistic for UHF RFID gates even when considering the worst case scenario of these models.

VII. ACKNOWLEDGMENTS

The authors would like to thank NXP Semiconductors, Gratkorn, Austria, for funding this project and for providing the environment for all measurements. We would also like to thank Giuliano Manzi, Gerald Wiednig, Martin Rampetsreiter, and Alexey Nazarov for manufacturing all used antennas and for their help with the measurement setup, as well as Albert Angstenberger from Taconic for providing the substrate for the antennas. This work was supported by the Austrian Research Promotion Agency (FFG) under the grant number 818072.

REFERENCES

- [1] D. M. Dobkin, *The RF in RFID*. Elsevier, 2007, ISBN-13: 978-0750682091.
- [2] P. V. Nikitin, R. Martinez, S. Ramamurthy, H. Leland, G. Spiess, and K. V. S. Rao, "Phase based spatial identification of UHF RFID tags," in *Proc. IEEE Int RFID Conf*, 2010, pp. 102–109.
- [3] U. Muehlmann, G. Manzi, G. Wiednig, and M. Buchmann, "Modeling and performance characterization of UHF RFID portal applications," *IEEE Trans. Microw. Theory Tech.*, vol. 57, no. 7, pp. 1700–1706, 2009.
- [4] D. Arnitz, K. Witrisal, and U. Muehlmann, "Multi-frequency continuous-wave radar approach to ranging in passive UHF RFID," *IEEE Trans. Microw. Theory Tech.*, vol. 57, no. 5, pp. 1398–1405, Jul. 2009.
- [5] A. Molisch, *Wireless Communications*, 1st ed. John Wiley & Sons, 2005, ISBN-13: 978-0470848876.
- [6] C. Tepedelenlioglu, A. Abdi, and G. B. Giannakis, "The rician K factor: estimation and performance analysis," *IEEE Trans. Wireless Commun.*, vol. 2, no. 4, pp. 799–810, 2003.
- [7] K. Witrisal, Y.-H. Kim, and R. Prasad, "A new method to measure parameters of frequency-selective radio channels using power measurements," *IEEE Trans. Commun.*, vol. 49, no. 10, pp. 1788–1800, Oct. 2001, 10.1109/26.957401.
- [8] M. S. Varela and M. G. Sánchez, "RMS delay and coherence bandwidth measurements in indoor radio channels in the UHF band," *IEEE Trans. Veh. Technol.*, vol. 50, no. 2, pp. 515–525, Mar. 2001, 10.1109/25.923063.
- [9] G. Marrocco, E. Di Giampaolo, and R. Aliberti, "Estimation of UHF RFID reading regions in real environments," *IEEE Antennas Propag. Mag.*, vol. 51, no. 6, pp. 44–57, 2009.
- [10] T. Gigl, T. Buchgraber, A. Adalan, J. Preishuber-Pfluegl, M. Fischer, and K. Witrisal, "UWB channel characterization using IEEE 802.15.4a demonstrator system," in *Proc. IEEE Int. Conf. Ultra-Wideband ICUWB 2009*, 2009, pp. 230–234.
- [11] A. F. Molisch, J. R. Foerster, and M. Pendergrass, "Channel models for ultrawideband personal area networks," *IEEE Wireless Commun. Mag.*, vol. 10, no. 6, pp. 14–21, 2003.
- [12] J. R. Foerster and Q. Li, "UWB channel modeling contribution from intel," IEEE Tech. Rep. P802.15 02/279SG3a, 2002, IEEE P802.15 SG3a Contribution.
- [13] M. Pendergrass and W. Beeler, "Empirically based statistical ultra-wideband (UWB) channel model," IEEE Tech. Rep. P802.15 02/240SG3a, 2002, IEEE P802.15 SG3a Contribution.

Wideband Characterization and Modeling of UHF RFID Channels for Ranging and Localization

Daniel Arnitz, *Student Member, IEEE*, Ulrich Muehlmann, *Member, IEEE*, and Klaus Witrisal, *Member, IEEE*

Abstract—This paper presents a comprehensive characterization and modeling of the UHF RFID channel for narrowband through ultra-wideband tag localization systems. The analyses are based on ultra-wideband channel measurements in a warehouse portal, centered around the 900 MHz RFID band. Measured scenarios include an electromagnetically transparent pallet and a pallet containing liquids, each for a portal shielded by metal backplanes and a portal shielded by absorbing material. The presented analyses include the individual channels to and from the tag, the feedback channel, and the backscatter channel, for bi- and monostatic reader setups, respectively.

We find that for the more commonly used portal with metal shielding the direct path is rarely dominant on the backscatter link. K-factors w.r.t. the line-of-sight path range from -20 through 5 dB and RMS delay spreads are in the range of $10-80$ ns even the case of an unobstructed direct path. This combination of low K-factors and high RMS delay spreads causes biased estimates and high standard deviations for all localization methods that cannot isolate the line-of-sight. Classical channel models in UHF RFID, although predicting the incident power level at the tag accurately, produce far too optimistic estimates of all channel parameters relevant to ranging and localization.

Index Terms—ultra-high-frequency (UHF) RF identification (RFID), channel characterization, ranging, positioning, localization, narrowband, wideband, ultra-wideband

I. INTRODUCTION

Localization in UHF RFID has seen a lot of research in the past years, but no conclusive breakthrough [1]. Due to limitations enforced by tag design and regulations, employed ranging systems are mostly narrowband and thus share a common property: They cannot distinguish individual multipath components (MPCs), i.e., the range estimate is based on an “average path”. This generally results in biased estimates and high standard deviations if the direct path is not the dominant MPC. As opposed to ultra-wideband (UWB) localization [2], the ranging error for narrowband systems depends on the shape of the entire channel impulse response (CIR), and especially on the power ratio between the direct and indirect paths. Unfortunately, there is little information available regarding the CIR of UHF RFID channels, because wideband parameters are usually not treated in the context of the narrowband RFID system. This is a major problem for theoretical and simulation-based ranging analyses, where the influence of the direct (line-of-sight, LOS) path is usually overestimated.

D. Arnitz and K. Witrisal are with the Signal Processing and Speech Communication Laboratory, Graz University of Technology, Graz, Austria (e-mail: daniel.arnitz@tugraz.at, witrisal@tugraz.at).

U. Muehlmann is with NXP Semiconductors, Gratkorn, Austria (e-mail: ulrich.muehlmann@nxp.com).

This work has been funded by NXP Semiconductors, Gratkorn, Austria, and by the Austrian Research Promotion Agency (FFG) under the grant number 818072.

We hope to fill this gap by presenting comprehensive analyses of the UHF RFID channel in a warehouse portal, including an evaluation of deterministic and stochastic models for this channel.

This paper is organized as follows: Common multipath channel models are briefly discussed in Section II, while a short summary of channel parameters and their influence on (narrowband) ranging is given in Section III. Section IV sketches the measurement setup and used simulation models and their parameterization are given in Section V. Analyses of the empty gate are presented in Section VI, while Section VII is dedicated to the analysis of the gate with a pallet containing liquids passing through. These analyses are mostly based on point-to-point measurements between reader and tag; a simple method to apply the results on backscatter channels is presented in Section VIII.

II. DISCUSSION OF CHANNEL MODELS

Channel models in UHF RFID are commonly based on single reflections, such as two-path (floor reflection) or three-path models (floor and gate/wall reflection) [1], [3], [4]. Full-blown raytracing is sometimes mentioned, but ultimately rarely used, e.g., [5]. Hybrid models like [3] are uncommon, too. As read rates in UHF RFID are directly connected to the power received by the tags, the aim of UHF RFID channel models is exclusively the modeling of the receive power at the tag; all other considerations are secondary.

(Ultra-)wideband channel models, such as the IEEE 804.15.4a channel model [6], on the other hand, do not focus exclusively on the overall receive power, but on individual multipath components instead. Because they essentially describe the CIR and thus the most generic channel characteristic, they are suitable for the analyses of any ranging method, including narrowband approaches. Unfortunately, as opposed to more common wireless links such as in cellular or wireless networks, the UHF RFID channel is very short-range and highly deterministic due to directive antennas and strong reflections in the immediate vicinity [3], [7]. As a consequence, well-known channel models and characterizations such as [6], [8], [9], including models and analyses for industrial environments [6], [10], [11], are not directly applicable to UHF RFID channels due to the dominant effects of the local geometry. Furthermore, the UHF RFID channel is a degenerate (pinhole) channel due to its backscatter nature, cf. [12].

From the viewpoint of ranging, the channel is structured as shown in Fig. 1. The feedback incorporates all parts of the received signal that have not been modulated by the tag,

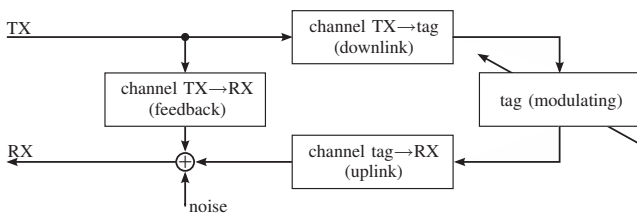


Fig. 1. Channels from the viewpoint of ranging. Note that all channels are time-variant and may only be assumed to be short-time-stationary.

i.e., mismatches at the antenna port for monostatic¹ setups, direct coupling for bistatic setups, as well as unmodulated environmental reflections. The backscatter channel comprises downlink (TX→tag) and uplink (tag→RX) channel, as well as the tag (time-variant reflection coefficient). This combined channel is the basis for any backscatter-based localization system; individual channels are not accessible.

For the presented analyses, we will neglect the tag and focus on the wireless channels. These analyses are based on measurements conducted in a frequency range of 0.5–1.5 GHz, thus including the UHF RFID frequency range at 860–960 MHz. The UWB bandwidth of 1 GHz was chosen in order to obtain generic results that are valid for all ranging methods currently under research (narrowband through UWB), and to be able to assess the channel in detail and identify major components in the CIR. The measurement setup itself was designed like a UHF portal, with UWB reader antennas having a gain pattern similar to an Intermec IA39B [13] and omnidirectional UWB tag antennas. A more detailed description of the setup can be found in [7].

III. CHANNEL PARAMETERS AND THEIR INFLUENCE ON RANGING AND LOCALIZATION

As opposed to UHF RFID systems, the fine time resolution of UWB signals allows for the separation of individual propagation paths, i.e., the observation of the CIR. This gives a more thorough insight into the channel and its effects on any system that relies on channel-based estimates, such as ranging and localization. From the viewpoint of narrowband systems, on the other hand, the channel is a single complex gain factor with random attenuation and phase shift, and some group delay.

Typical wireless channels feature an exponentially decaying power-delay-profile (PDP; essentially the squared magnitude of the average CIR). The first arriving component corresponds to the direct (LOS) path between transmitter and receiver and all following components to indirect (reflected) paths. The square root of the second central moment of the normalized PDP is called RMS delay spread (τ_{RMS}), while the last significant delay is referred to as the maximum excess delay [14]. For localization, the power ratio of the direct (LOS) path to all indirect paths is of vital importance, as it quantifies the influence of the direct path on the entire delay-profile. This ratio is provided by the K-factor w.r.t. the LOS path, K_{LOS} . Note that this is not necessarily identical to the definition of

¹monostatic: TX=RX-antenna, bistatic: separate TX and RX antennas

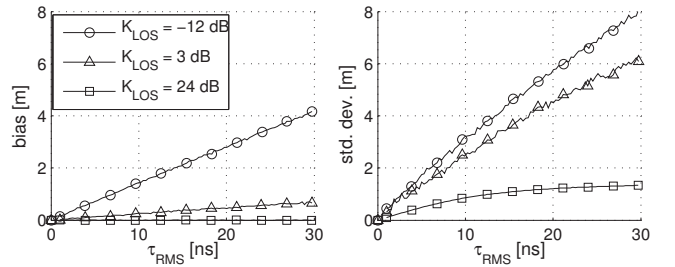


Fig. 2. Influence of wideband channel parameters (K_{LOS} and τ_{RMS}) on ranging accuracy (TX→tag only, 10^5 ensembles). The plots show bias and standard deviation for a phase-based ranging method with 1 MHz bandwidth.

the Ricean K-factor, which uses the strongest path instead of the direct path [15]. We will use the term “K-factor” (K_{LOS}) for the K-factor w.r.t. the LOS component in this paper.

For high K-factors, the direct path is dominant in the complex gain factor of a narrowband signal and narrowband ranging will give accurate results. For low K_{LOS} , the gain factor is mainly determined by indirect paths. Depending on the RMS delay spread and the shape of the CIR, this results in a bias of the gain factor towards indirect (i.e., longer) paths. Also, the dominance of random NLOS components leads to high standard deviations of narrowband range estimates for low K_{LOS} . This dependence is illustrated in Fig. 2. As can be seen, the bias increases with the RMS delay spread but is close to zero for high K-factors. At the same time, the standard deviation increases with K_{LOS} and τ_{RMS} .

Depending on the ranging method, also correlation in spatial and frequency domain have a strong influence on ranging accuracy. This correlation is described by the coherence distance and the coherence bandwidth, respectively. The coherence distance (coherence length) is the distance a receiver may move for a fixed transmitter before the correlation between the instantaneous CIR and the CIR at the original position drops below a given value (typ. 50, 70, or 90%). This value is important for all ranging approaches that use the difference between two channel-based estimates in order to remove the influence of multipath propagation, e.g. [16]. The coherence bandwidth specifies the frequency offset at which the autocorrelation of the channel transfer function (CTF) drops below a specified value and is important for all ranging methods that work in the frequency domain, for example by evaluating the phase shift between carriers [17]–[19]. A similar definition exists for the time dimension (coherence time).

IV. MEASUREMENT SETUP

A. Environment Description

All measurements were performed in NXP’s Application and System Center (ASC) in Gratkorn, Austria, to ensure a realistic warehouse environment. The ASC is located in a converted production hall (approx. $40 \times 15 \times 7$ m) with corrugated metal walls and ceiling, and a steel-reinforced concrete floor. The entire hall is cluttered with metal objects of different sizes (from boxes with screws to a room-sized anechoic chamber).

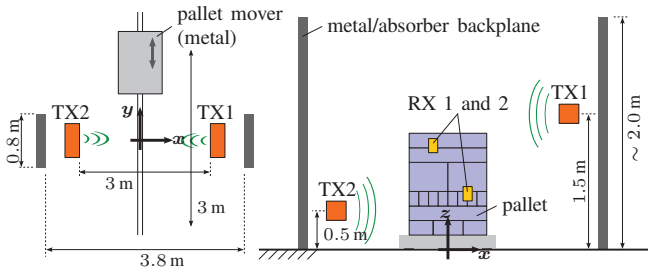


Fig. 3. Gate setup with TX array positions (left: top view, right: back view).

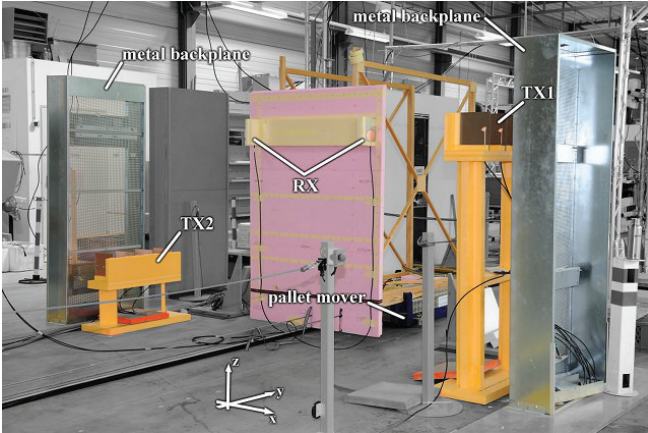


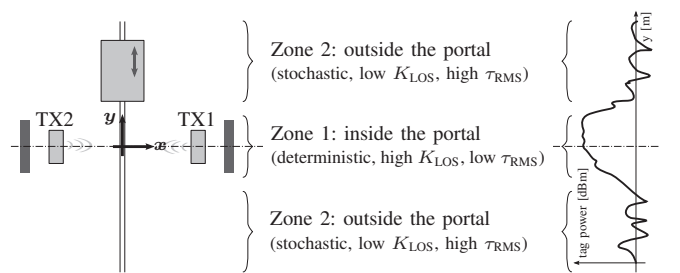
Fig. 4. Photograph of the gate setup with “free space” pallet and metal backplanes. The transmitter arrays are positioned on the orange stands to the left and right of the pallet mover, while the receiver antennas are mounted on the pink polyurethane foam slab.

B. Gate Setup

The measurement setup (see Fig. 3) was constructed like a UHF-RFID portal: The transmitter arrays were positioned 3 m apart (front to front) to the left and right of a pallet mover. The antenna heights (floor to center) were 0.5 m (TX2) and 1.5 m (TX1), respectively. The backplanes behind the transmitter arrays (80×195 cm, 22 cm from the back of the transmitter arrays) spanned a portal of 3.8 m width. Measurements were done with metal backplanes (typ. for portals, cf. [3]) and with absorber backplanes (reflectivity approx. -20 dB). A picture of the setup is shown in Fig. 4. All antennas were vertically polarized.

Receiver antennas were fixed at different x - and z -positions on polyurethane foam slabs, which were themselves mounted on the pallet. The pallet was then incrementally moved through the gate (along y) while recording. This was done for several positions on the pallet with a spacing of 10 cm between two adjacent measurements in x , y , and z . The entire set of recorded receiver positions is used as a virtual array in the analyses below.

The channel measurements were performed in a frequency range of 0.5 through 1.5 GHz with 1 MHz stepsize, using a Rohde&Schwarz ZVA-24 network analyzer with 4 ports. This stepsize results in an ambiguity range of roughly $1 \mu\text{s}$ (maximum path length 300 m), which was found to be sufficient in this environment. The bandwidth resolution of the network analyzer was set to 10 kHz and the conducted power was

Fig. 5. Definition of zones for the portal. Zone 3 covers the area far from the portal (purely stochastic, very low K_{LOS} , high τ_{RMS}).

0 dBm, resulting in an effective dynamic range of 100 dB (high noise floor due to active UHF RFID readers and mobile phones in the vicinity). The system was calibrated up to the antenna ports. Calibration of the remaining delay and gain was done using the known line-of-sight distance and power. A more detailed description of the measurement setup, including full UWB directivity patterns of the used antennas, can be found in [7].

For the following analysis, the portal has been separated in three zones as shown in Fig. 5. As UHF RFID uses directive antennas and often metal portals, it can be expected that “the typical UHF RFID channel” shows different behavior inside and outside the portal. Within the portal (Zone 1, $|y| \leq 0.5$ m) the channel is dominated by the portal’s geometry and thus highly deterministic, especially for metal backplanes. In the vicinity of the portal (Zone 2, $|y| \geq 1.0$ m) the portal’s influence is smaller but still present. Zone 3, which is not covered by the presented measurements, spans the remaining space outside the vicinity of the portal and can most likely be modeled in a purely stochastic fashion (industrial non-line-of-sight).

C. Pallet Description

All measurements were conducted with two different pallets: An electromagnetically transparent “free space” pallet (Fig. 4) constructed of a wooden scaffold and polyurethane foam slabs was used to measure the channels inside the empty portal. Measurements with this pallet were done in four planes, two horizontal and two vertical, forming a three-dimensional virtual array of 1364 receivers that can be used to pinpoint major sources of reflections (see Section VI). These “free space” measurements are also used to establish a baseline for the second pallet, containing liquids and metal-coated packages. This pallet (cf. Fig. 6) is considered a reference pallet for heavy field distortions and hard-to-read tags, and acts as a challenging example for ranging here.

V. SIMULATION SETUP

In order to check the validity of channel models and to identify the source of multipath clusters, the measurements presented in this paper are compared to simulations. The simulations were performed using the PARIS simulation framework, which is open-source and available online [20]. Since the first publication, [21], several new features were

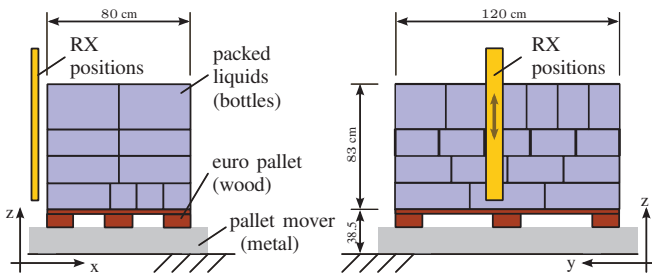


Fig. 6. Pallet with liquid cleaning agents: Back view (left) and side-view from TX2 (right). The upper part of the receiver plane is visible to both transmitter antennas, while the lower part is visible only to TX2. Receiver antennas were kept at a distance of 10 cm from the liquids.

TABLE I
REFRACTIVE INDEX (REFLECTION/TRANSMISSION MODEL) AND REFLECTION COEFFICIENT (VTX MODEL) OF SURFACES.

| Refractive Index | Value | Description |
|-------------------|-------|--|
| floor | 2.5 | concrete |
| gate | 10 | metal mesh w. antennas/cables in front |
| Reflection Coeff. | Value | Description |
| floor | 0.5 | concrete |
| gate | 0.75 | metal mesh w. antennas/cables in front |
| ceiling | 0.85 | metal, triangular structure (scatters) |
| wall | 0.4 | close to floor: obstructed by clutter |
| wall + ceiling | 0.85 | close to ceiling: unobstructed |

added. This includes reflective surfaces, simple ray-tracing abilities, and a UWB field probe mode in which the tags record channel impulse responses. Antenna directivity patterns were taken from previous measurements [7]. Reflections are treated by this simulator using a combination of deterministic (ray-tracing) and stochastic models:

Single reflections in close proximity of transmitters and receivers (e.g., TX→floor→RX) are modeled using reflective surfaces with reflection coefficients derived from the Fresnel equations. Apart from spatial properties (size, position, orientation), reflective surfaces are defined by their refractive indices only. Imaginary parts and any frequency dependence of the refractive indices are neglected. Values used for the presented simulations are shown in Table I. The chosen values account for the reflective properties of the respective surfaces as well as some margin for dispersion by non-ideal surfaces and clutter objects.

Multiple reflections (e.g., TX→floor→gate→RX) are modeled using virtual transmitters (VTX), i.e., reflected versions of the original transmitters. The contribution of a virtual transmitter is controlled by the product of the gain factors of all surfaces that take part in the creation of the VTX, independent of the angle of incidence on each surface. This approximation works for close to perpendicular angles of incidence to the surface planes (cf. Fresnel equations). Transmitted power is modeled as difference to reflected power, thus neglecting absorption. Clusters² are modeled using a combination of virtual transmitters and a stochastic small-scale model (see below) rather than in a purely statistical fashion in order to account for predictable path geometries, cf. [22]. The parameterization

²A cluster is a group of reflections that belong together. Clusters are usually created by multiple reflections and scattering at objects that are spatially close.

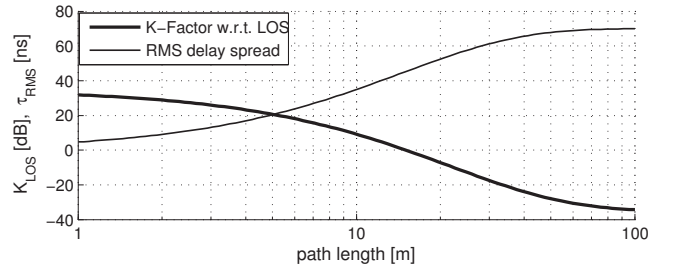


Fig. 7. Used distance-dependent small-scale model parameters.

for the presented simulations can be found in Table I.

The channel from all transmitters, including VTX, feature a stochastic small-scale model [23]. The small-scale model is globally parameterized by distance-dependent K-factors and RMS delay spreads. K_{LOS} and τ_{RMS} for each transmitter are chosen according to the path length, as shown in Fig. 7. This approach makes sure that the deterministic channel dominates at small distances, while at large distances the stochastic part is dominant. The treatment of virtual transmitters is slightly different here: Virtual transmitters inherit the RMS delay spread of the originating transmitter; the K-factor is again chosen according to Fig. 7. This creates a similar decay for all clusters in logarithmic scale, cf. [11], [23]. The general shape of these parameters in combination with the deterministic model has proven quite useful for industrial and semi-industrial scenarios, e.g., [24].

VI. IN-DEPTH ANALYSES: EMPTY GATE

As mentioned above, the measurements in the empty gate form a reference for the channel. The results can be used to test localization algorithms in a best-case scenario, i.e., with an unobstructed direct path. The results for the gate with absorber backplanes can also be taken as reference for applications in light multipath environments (direct LOS, no reflectors in the immediate vicinity).

We will start this in-depth analysis with an investigation of the effects of absorber and metal backplanes, followed by the identification of major reflectors / clusters (deterministic parts of the channel), a comparison to established UHF RFID channel models, and finish with the analysis of the channel for ranging and localization. In order to mitigate the error introduced by spatial averaging of PDPs in such an environment, cf. [11], we use cumulative distribution functions (CDFs) of instantaneous channel parameters to complement the “average channel” shown in the APDPs. A description of the used estimators and calculations behind these analyses can be found in [7].

A. Metal vs. Absorber Backplanes

Three-dimensional plots of the spatial distribution of K_{LOS} and τ_{RMS} are shown in Figs. 8 and 9, respectively, for metal and absorber backplanes. The influence of the backplane on K_{LOS} and τ_{RMS} is quite drastic: The K-factor drops by 8 dB inside and 3 dB outside the portal for metal backplanes compared to absorbing material, cf. Fig. 10. At the same time

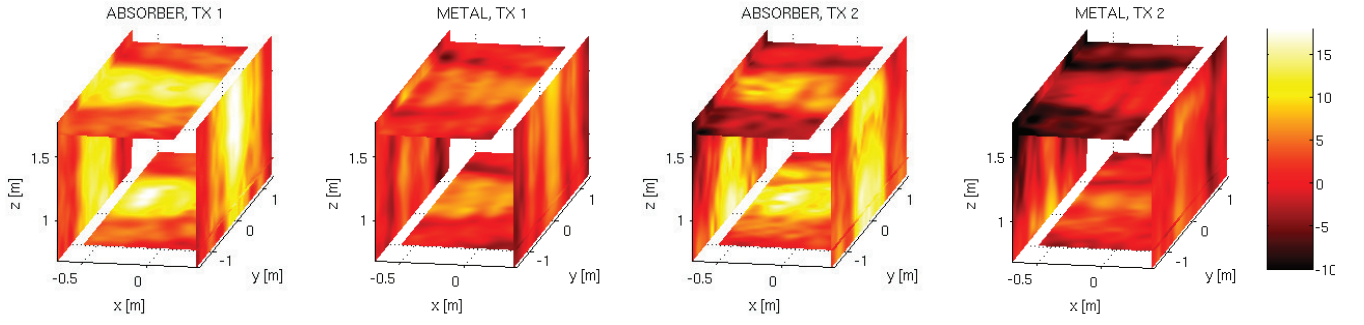


Fig. 8. K-factor [dB], comparison between absorber and metal backplanes for TX1 and TX2 (coordinate system origin: center of the gate at floor level).

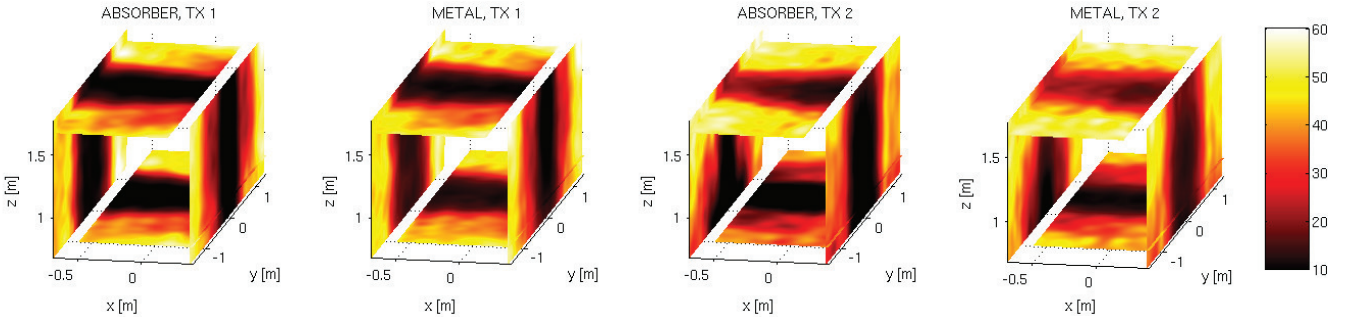


Fig. 9. RMS delay spread [ns], comparison between absorber and metal backplanes for TX1 and TX2 (coord. system origin: center of the gate at floor level).

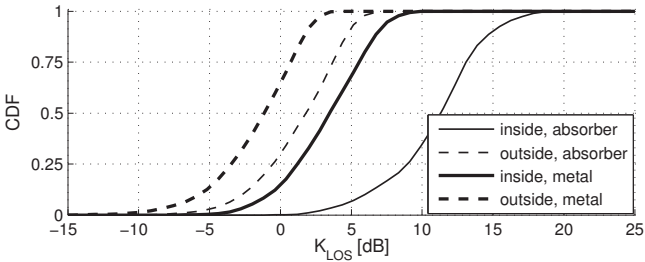


Fig. 10. CDFs of the K-factor for metal and absorber backplanes (inside and outside the portal).

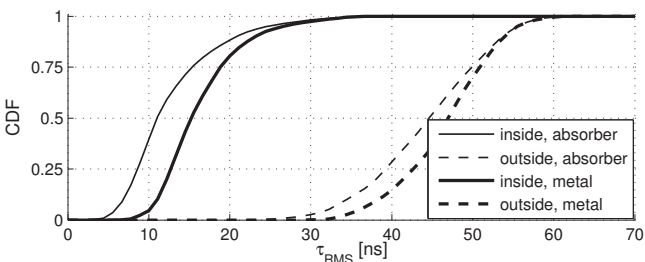


Fig. 11. CDFs of the RMS delay spread for metal and absorber backplanes (inside and outside the portal).

the RMS delay spread at the center of the portal increases by 40% to roughly 15 ns (Fig. 11).

The following analyses are limited to metal backplanes, which are more commonly used in UHF portals [3].

B. Source of Major Reflections / Clusters

Major reflectors were identified using the measured average power-delay-profiles (APDPs) and videos showing the wave propagation³. A comparison to simulated power-delay-profiles with placement of virtual transmitters according to the portal/hall geometry shown in Fig. 12 was used to verify the presence of a certain reflection in a cluster. These simulations cover multiple reflections (bounces) between the gate backplanes, walls, the ceiling, and the floor.

Unsurprisingly, the metal backplanes are the dominant source of reflections. Up to five bounces can be identified, including multiple reflections between backplanes and the floor, see Fig. 13. Reflection at the walls close to the floor are blocked by the gate and scattered by clutter objects, thus making wall reflections relatively insignificant. This is, on the other hand, not true for a double reflection via the ceiling close to the walls, which is not obstructed by the backplanes for either transmitter. Unlike the floor, the ceiling is free of cluttering, thus allowing the wave to bounce between the outer walls of the hall several times. The APDP shows at least nine reflections of this specific wave packet, six of which are within 100 m and thus visible in Fig. 13.

The general shape of the APDP inside the gate (see Fig. 14) follows a power law [11]

$$P(\tau) = P_0 \tau^{-\alpha} \quad (1)$$

instead of the commonly assumed exponential decay. In (1) $P(\tau)$ is the average power of all MPCs arriving at a delay of τ and α is a decay constant. This formula is similar to

³Available online: <http://www.tinyurl.com/paris-osf/examples>

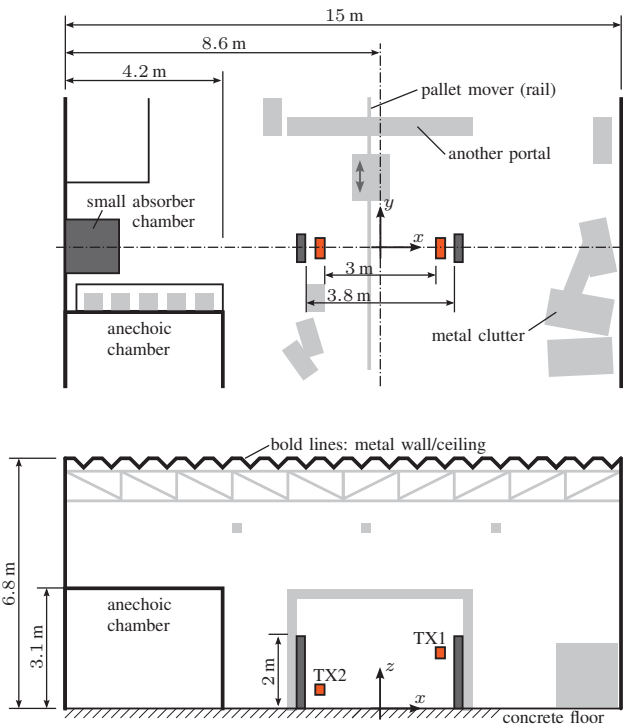


Fig. 12. Environment (roughly to scale). Reflections at the walls near the floor are mostly blocked by clutter objects. Above 3 m and within the portal, wave packets can bounce freely.

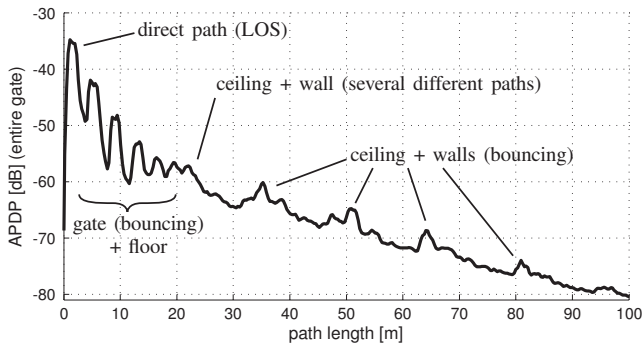


Fig. 13. Average power-delay-profile (APDP) for TX1 with marked clusters.

the free space path-loss (i.e., the Frijs equation, [25]) and thus consistent with a mainly deterministic channel, cf. [26]. Note that not only the main shape of the PDP shows this decay: The clusters created by the wall-reflections close to the ceiling have a distinctly linear decay in a double-logarithmic scale, i.e., they also follow (1) both for peak power and cluster decay. A similar behavior of the ray power decay in industrial environments has previously been reported in [11]. Outside the portal, most of the APDP follows an exponential decay.

Finally, a comparison between the measured and simulated APDPs is shown in Fig. 15. As can be seen, the simulated PDP (up to the fifth reflection) follows the measured one quite well, except for the region outside the gate around path lengths of 10 to 20 m, where a cluster is not modeled properly. Note

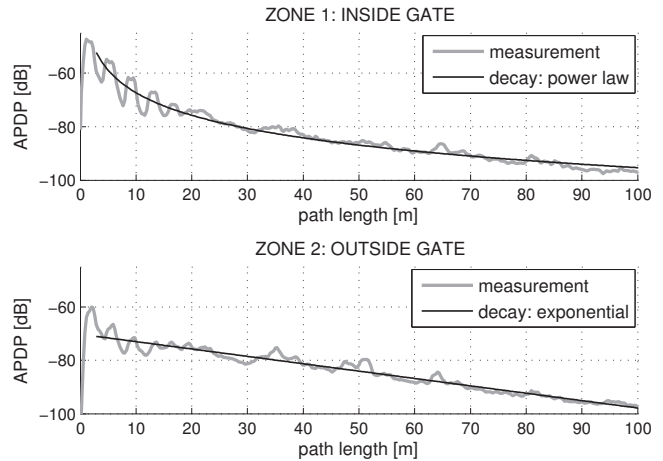


Fig. 14. Average power-delay-profile (APDP) for TX1 inside and outside the portal. The APDP inside the gate follows a power law instead of the commonly assumed exponential decay.

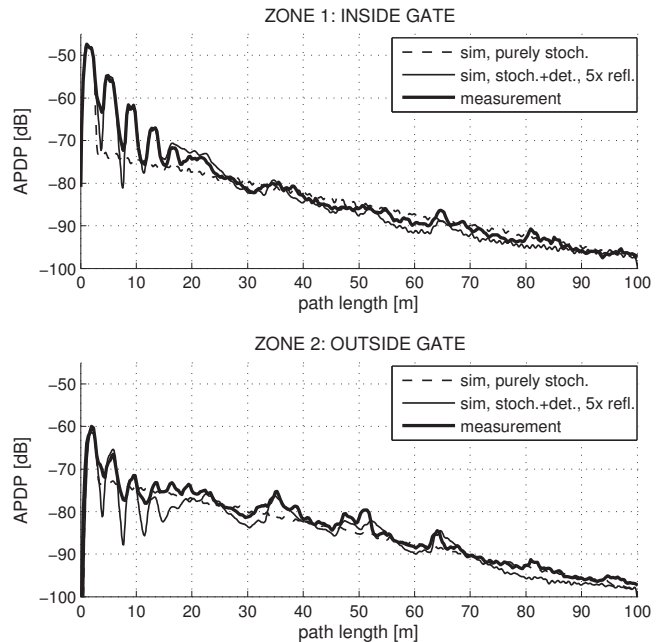


Fig. 15. Comparison between measured and simulated average power-delay-profile inside and outside the gate.

that the purely stochastic channel model only fits the general shape of the APDP for large path lengths. The hybrid model (stochastic plus deterministic up to the fifth reflection), on the other hand, fits the shape until the cluster at 80 m, which is a sixfold reflection.

C. Comparison to Common UHF RFID Propagation Models

The most important performance metric for UHF RFID in a portal is the ratio of tags that can be read while passing through the read zone. As the range of UHF RFID is typically limited by the tags' power requirements, this ratio depends mostly on the incident power level at the tag (neglecting polarization and detuning here) [4], [27], [28]. As a consequence, channel

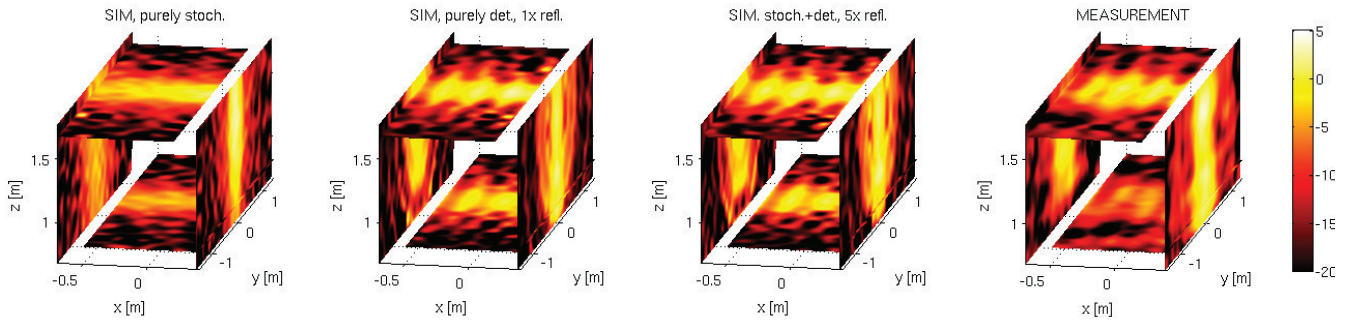


Fig. 16. Incident power level [dBm] at the tag; carrier frequency 915 MHz, transmit power 3.28 W EIRP. Comparison between models of different complexity and the measurement (inside and outside gate). The coordinate system origin is at the center of the gate at floor level.

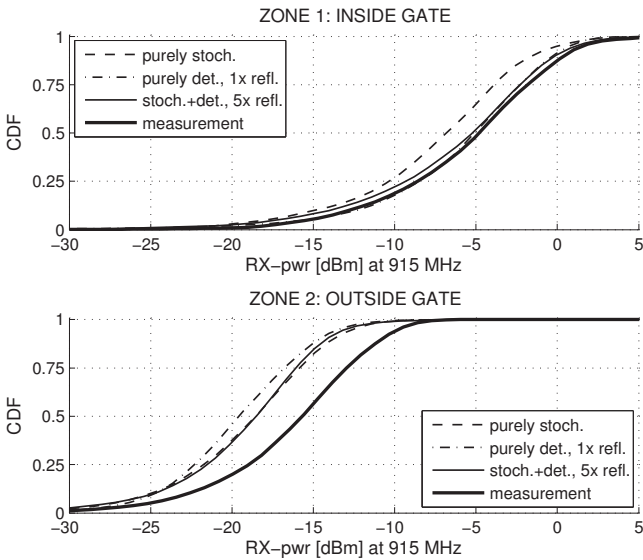


Fig. 17. CDFs of the incident power level at the tag (inside and outside the portal; 915 MHz, 3.28 W EIRP TX-pwr).

models for UHF RFID focus on carrier power distributions.

It was suggested in [3] to decompose the channel model into two components which are represented by two planes: The first plane spans the portal (xz here) and consists of the average power distribution calculated by deterministic models. It is usually calculated using a three-ray model consisting of the direct path, the floor reflection, and the reflection at the opposite side of the gate, cf. [3], [29]. The second plane is in the dimension of the tag movement (yz) and modeled in a stochastic fashion by a bimodal distribution.

Inside the gate, very simple models already sufficiently describe the incident power at some frequency in terms of distribution and shape, as can be seen in Figs. 16 and 17. This validates the usage of a three-ray model (which is a single-reflection model) when calculating average power distributions inside the portal.

Outside the gate, on the other hand, the mismatch is more pronounced. This includes the more complex models due to the above mentioned modeling problem of the multipath cluster (missing power) in the range of 10–20 m (path length). Also the purely stochastic model, which by design does not model

geometry dependent parts of the APDP, shows an offset of about 3 dB. The stochastic model is also not able to reproduce effects created by deterministically interacting waves, such as the standing wave pattern visible for the measurement in Fig. 16.

Based on these results it seems safe to assume that considering single-point reflections is sufficient to fully model the RFID channel inside the gate for ranging and localization. This very common assumption is wrong, as will be shown in the next Section.

D. Analysis of the Channel for Ranging and Localization

It has already been mentioned in the introduction that the shape of the channel impulse response, and thus shape parameters such as K-factor and RMS delay spread, are the most important parameters for ranging (narrow-, wide-, and ultra-wideband). Also the coherence bandwidth (which is loosely coupled to the RMS delay spread [14], [30]) and the coherence distance are of vital importance.

A comparison between measurements and different models for the two most common parameters (K_{LOS} and τ_{RMS}) is shown in Figs. 18 and 19. Even though the simple models (1-pt deterministic and purely stochastic) were able to predict the tag receive power inside the gate almost perfectly, K-factor and RMS delay spread are off by factors. The mismatch is especially drastic for the K-factor predicted by the purely stochastic model inside the gate (off by approx. 10 dB for the median) and the RMS delay spread inside and outside the gate predicted by the deterministic three-ray model (off by a factor of five). Considering that the three-ray model already considers two one-point (single) reflections (floor and gate), it is safe to assume that the mismatch would be even more dramatic if only the floor reflection was modeled. Even the complex simulation employing deterministic and stochastic models is not able to predict the shown channel parameters perfectly, although the mismatch is miniscule in comparison. Moreover, the hybrid model overestimates the multipath propagation slightly instead of underestimating it, which is preferable.

As the model parameters for the presented simulations have been optimized manually, an exhaustive optimization of all parameters could lead to slightly better results for all models. Nonetheless, a model that neglects important parts of the channel, such as the single-reflection deterministic or

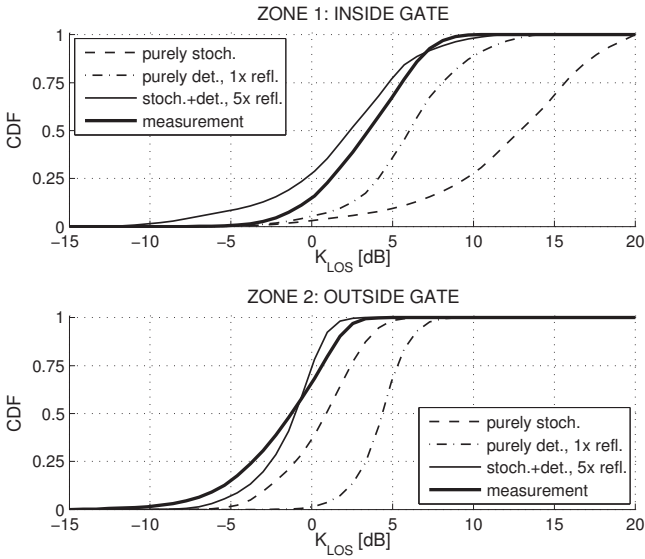


Fig. 18. CDFs of K_{LOS} [dB] (metal portal). Comparison between models of different complexity and the measurement.

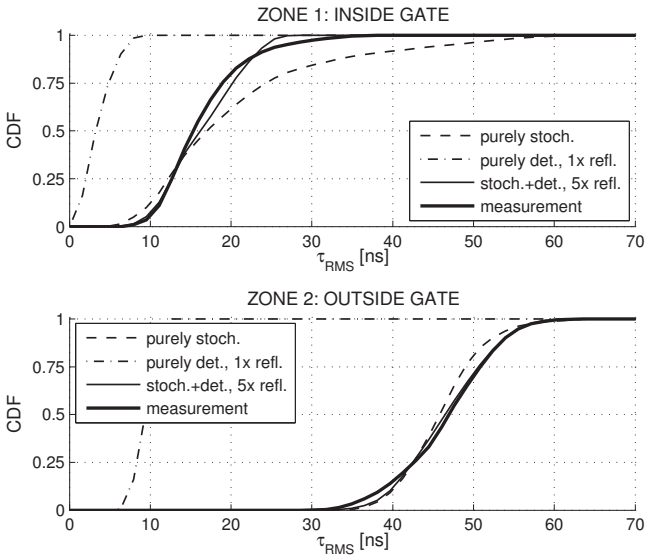


Fig. 19. CDFs of the RMS delay spread [ns] (metal portal). Comparison between models of different complexity and the measurement.

the purely stochastic model, cannot be optimized to fit all parameters at the same time.

Distributions of K_{LOS} and τ_{RMS} for metal and absorber backplanes in terms of spatial distribution and CDF as well as APDPs can be found in the previous Sections (Figs. 10 through 9, and 15). The K-factors for metal backplanes are in the range of -10 through 5 dB outside and -5 through 10 dB inside the gate, while the RMS delay spreads range from roughly 10 ns inside the gate to 60 ns outside. Although in the APDPs the direct path is always the strongest path, this is not true for the instantaneous PDPs, especially outside the gate.

Cumulative distribution functions of the 90% coherence bandwidth and the correlation at a spacing of 12 cm (the average distance for a rectangle with 10 cm spacing, see [7])

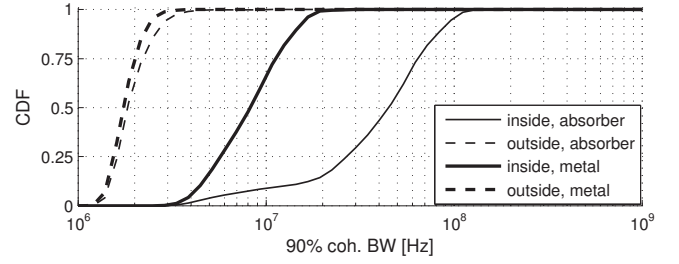


Fig. 20. CDFs of the 90% coherence bandwidth (empty gate).

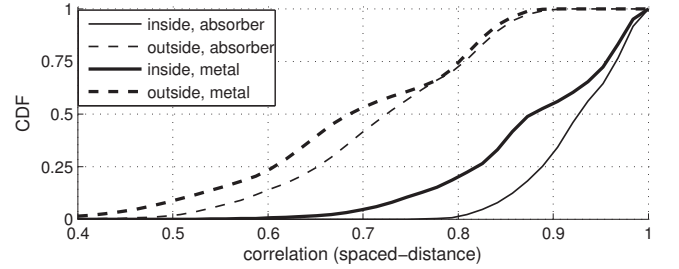


Fig. 21. CDFs of the channel coherence at a spacing of 12 cm from the original position (empty gate).

for details) are provided in Figs. 20 and 21, respectively. The correlation at a fixed spacing is used instead of the coherence distance because it only needs averaging over a small area and thus keeps the systematic error caused by the position- and direction dependence of the spaced-distance correlation function (SDCF) [30] at a minimum, cf. [7], [11]. The coherence bandwidth ranges between 1 and 3 MHz outside and reaches 20 MHz inside the gate for metal backplanes and 100 MHz for absorbing material. At a distance of 12 cm, the measurements show an average (median) correlation of roughly 90% inside the gate and 70% outside. Note that the influence of the portal setup (metal/absorber) on coherence bandwidth and correlation distance is relatively small in the region outside the gate.

VII. IN-DEPTH ANALYSES: GATE WITH PALLET

The analyses in this Section are intended to complement the measurements in the empty gate and to assess the influence of a highly reflective pallet on the wave propagation. To this end, the receiver antennas have been attached to the left side (closer to TX2) of the liquids pallet at heights of 0.5 through 1.3 m (the pallet has an approximate height of 1.2 m, cf. Fig. 6). As a result, the upper part of the virtual receiver array is visible to both transmitters, while the lower part has a clear line-of-sight only to TX2.

A. Analysis of the Channel for Ranging and Localization

Cumulative distribution functions for the most important channel parameters can be found in Figs. 22 through 25. Compared to the empty gate, almost all parameters span wider ranges.

While the pallet has predominantly adverse effects on the channel parameters for the absorber gate (dropping K_{LOS} ,

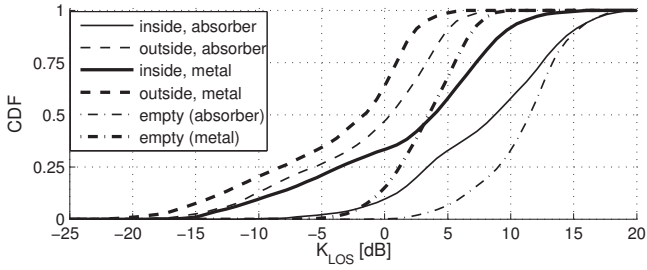


Fig. 22. CDFs of the K-factor [dB] (liquids pallet; CDFs for the inside of the empty gate are displayed for comparison.).

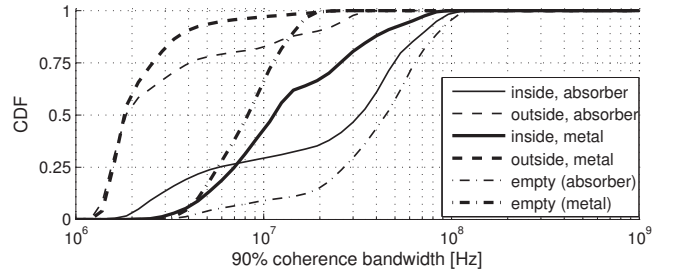


Fig. 24. CDFs of the 90% coherence bandwidth (liquids pallet; CDFs for the inside of the empty gate are displayed for comparison.).

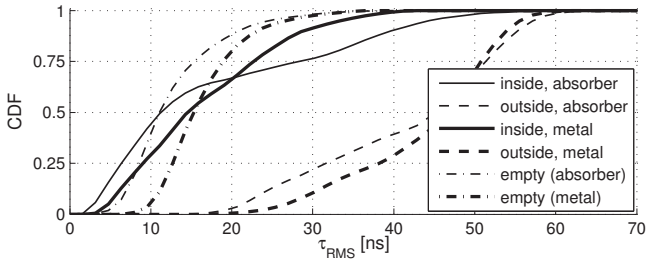


Fig. 23. CDFs of the RMS delay spread [ns] (liquids pallet; CDFs for the inside of the empty gate are displayed for comparison.).

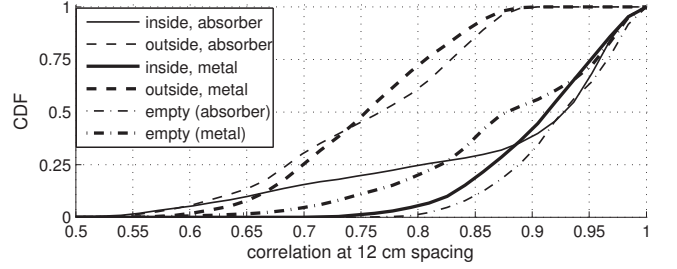


Fig. 25. CDFs of the channel coherence at a spacing of 12 cm from the original position (liquids pallet; CDFs for the inside of the empty gate are displayed for comparison.).

increased probability for high RMS delay spreads, ...) it also blocks strong gate reflections for the metal gate, thus improving the situation in some measurements. Nonetheless the pallet blocks the LOS path from TX1 for most tag positions, which results in K-factors down to -15 dB and thus values that are typical for the region outside the gate.

Figs. 26 and 27 show the actual spatial distribution of K_{LOS} and the spatial coherence. The liquids contained in the pallet block the line-of-sight to TX1, especially at a height of $z=0.8$ m. The bottom of the pallet on the other hand consists of a wooden (EURO) pallet which creates a narrow space between the liquids and the metal pallet mover that acts as a conduit for the signal sent by TX1. This effect can be seen in the higher K-factor at $z=0.6$ m in Fig. 26 (top). Another effect of the pallet can be seen in the right part of the correlation for TX2: The pallet keeps the correlation at roughly 80% by blocking several indirect paths when outside the gate ($y > 1$ m).

Figs. 28 and 29 show the errors (bias and standard deviation) of narrowband range estimates [17], for monostatic and bistatic antenna setups, respectively. Inside the portal, the monostatic setup using TX2, which has a clear line-of-sight, reaches a bias in the range of 10 cm at a standard deviation of 3 m for a single range estimate. Using absorber backplanes, the standard deviation is roughly 1 m (not shown in the plots). The true range from TX2 is between 0.5 and 2.3 m, hence the error for a single estimate is larger than the true distance, even at such short range and in direct line-of-sight. Note though that at least the standard deviation can be considerably reduced by combining several estimates.

B. Feedback Channels

Feedback limits the available dynamic range and might thus also be a problem for ranging systems. The feedback includes unmodulated backscattering from the channel (paths that did not go via the tag) for mono- and bistatic setups as well as antenna mismatches for monostatic setups (cf. Fig. 1). While narrowband feedback can be massively attenuated using active carrier cancellation techniques, this may not be possible for more wideband signals because of the time-variant nature of the feedback.

A major goal of ranging and localization in UHF RFID is to eliminate stray reads created by tags far outside the gate.

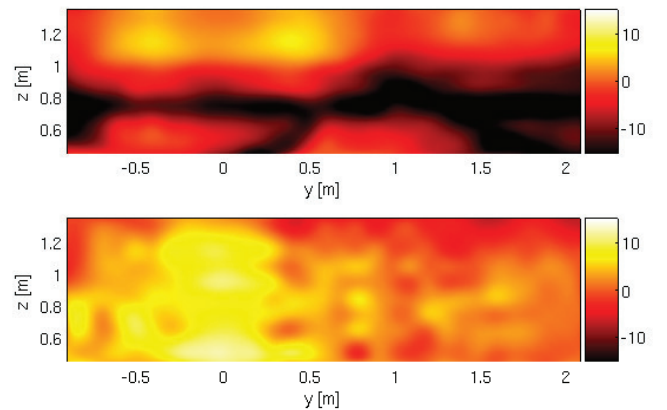


Fig. 26. Recorded K-factors while moving through the portal for TX1 (top) and TX2 (bottom); liquids pallet, metal backplanes; view from TX1. The tag is attached to the left side (closer to TX2) of the pallet (height approx. 1.2 m).

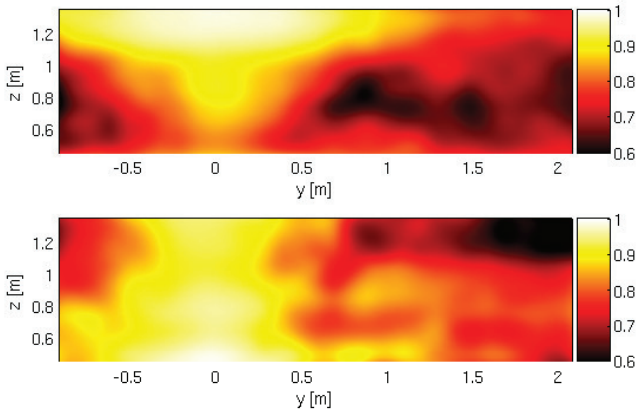


Fig. 27. Correlations at a spacing of 12 cm while moving through the portal for TX1 (top) and TX2 (bottom); liquids pallet, metal backplanes; view from TX1. The tag is attached to the left side (closer to TX2) of the pallet (height approx. 1.2 m).

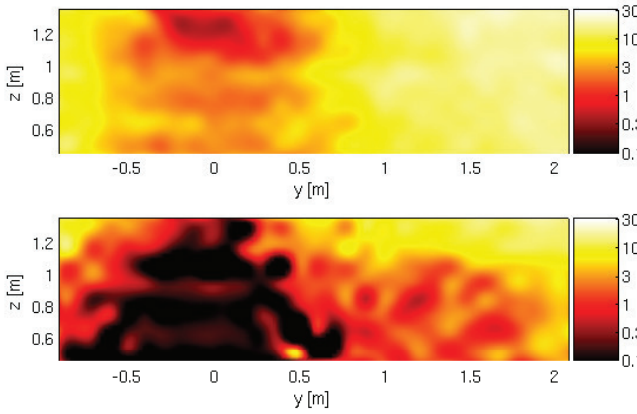


Fig. 28. Expected value (bias) [m] of a single 2FCW [17] estimate w. $\Delta f = 1$ MHz for bistatic setup TX1-TX2 (top) and monostatic setup TX2-TX2 (bottom); liquids pallet, metal backplanes; view from TX1.

These tags are powered by constructive interference caused by multipath propagation, cf. [3]. A potential ranging system has to be able to range such tags or at least be able to detect that the distance to the tag is larger than the intended read zone (classification). Such a tag is the worst case scenario for ranging: It is outside the main beam of the TX antennas and possibly far from the portal, which typically results in massive multipath propagation (and might cause phase ambiguities for narrowband ranging, cf. [17], [18]). Moreover, the portal is probably empty at the same time, so the feedback is at its maximum. For this reason it is imperative to assess the feedback channel inside and outside the gate compared to the backscatter channel to the tag.

Fig. 30 shows the APDPs for monostatic and bistatic setups as well as the APDP of the corresponding backscatter channel to the tag. As can be seen, the feedback always dominates the tag signal, especially outside the gate. A dynamic range of at least 50 dB is needed with in order to be able to separate the backscatter channel from the much stronger feedback inside the gate (average power; without any feedback suppression). The feedback also increases considerably when the pallet is

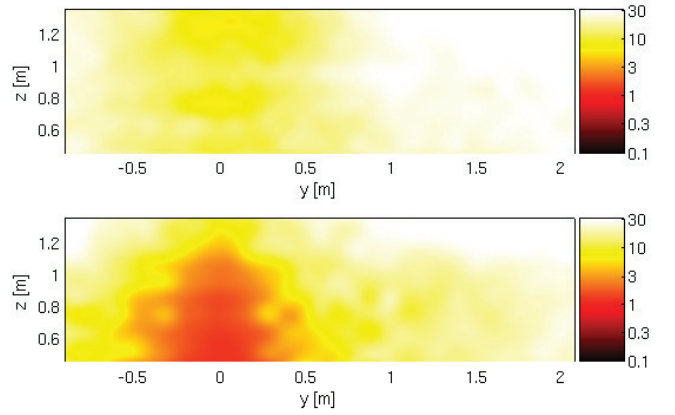


Fig. 29. Standard deviation [m] of a single 2FCW [17] estimate w. $\Delta f = 1$ MHz for bistatic setup TX1-TX2 (top) and monostatic setup TX2-TX2 (bottom); liquids pallet, metal backplanes; view from TX1.

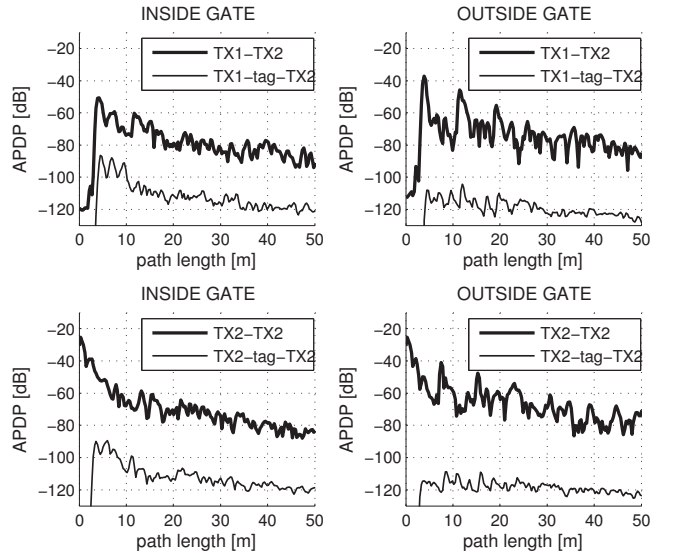


Fig. 30. Average power-delay-profile (APDP) for mono- and bistatic feedback channels in comparison to the APDP of the backscatter channels to the tag.

outside the gate (the pallet blocks some feedback), while at the same time the backscatter channel has an increased attenuation caused by gain patterns and higher distances. A dynamic range of more than 70 dB is needed to still be able to identify the tag reply in this case. A similar dynamic range is also necessary for a UWB system to be able to detect the LOS path of the backscatter channel (peak LOS of backscatter to the same component in the feedback). Note that this does not include any polarization mismatches and modulation depths.

Fig. 31 shows the range of K-factors and RMS delay spreads that should be expected on the feedback channel (on average) while a pallet is moving through the portal.

C. Expected Performance of UWB-based Ranging

Most ranging systems in UHF RFID focus on narrowband signals [1]. Only recently some advances were made into more wideband methods [31], including a proof of concept

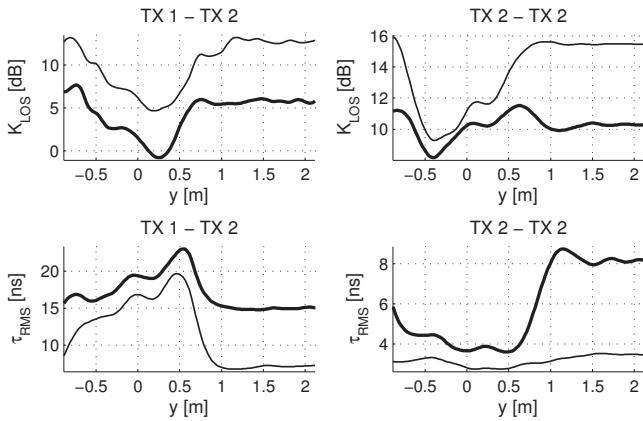


Fig. 31. K_{LOS} and τ_{RMS} of two feedback channels while the pallet is moving through the gate (thin lines: absorber backplanes; bold lines: metal backplanes). For $y=0$ m the pallet is at the center of the gate.

for UWB-based ranging based on measurements in an environment that is comparable to the UHF portal [32]. Even though material properties and free space loss are different in a UWB frequency band, the main channel parameters should at least be comparable to the measurements presented in this paper.

In contrast to narrowband ranging, the strong reflections created by the metal backplanes could be a benefit when combined with ultra-wideband localization. A recently published UWB localization method utilizes strong reflections (clusters) to enhance ranging accuracy by using them as virtual transmitters [33]. Two prerequisites of this method, namely the presence of strong reflectors and a predominantly deterministic (i.e., predictable) nature of the channel are met for UHF portals.

Judging by the measurements, the performance of UWB-based ranging should easily exceed the performance of any narrowband method, cf. [34]. Even when the direct path was obstructed by several hundred liters of packed liquids, the LOS components could be correctly identified in the presented measurements. The attenuation of the LOS path by the liquids (measured between TX1 and TX2) is in the range of 12 dB, cf. Fig. 32. This is consistent with measurements performed using a UHF RFID setup [3]. Although the resulting drop of K_{LOS} will likely be fatal for any narrowband ranging system, the backscatter modulation may still be detectable by a ultra-wideband ranging system⁴.

UWB ranging systems, while being robust to multipath propagation, may be influenced by the channel even if the LOS component was correctly identified, though: The ranging produces a biased estimate if the direct path to the ranged tag is blocked by a pallet due to the reduced group velocity in the denser medium. This effect can be seen in the right plot of Fig. 32: When the LOS path between TX1 and TX2 passes through the pallet, the estimated distance increases by 30 cm. The feedback channel TX1→TX2 is shown here instead of the channel TX1→RX because the effects of the pallet are better

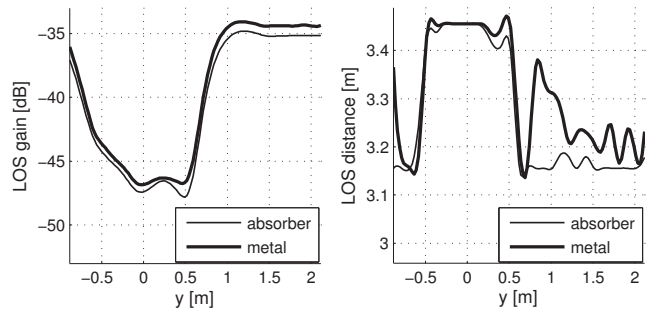


Fig. 32. Line-of-sight gain and estimated distance between TX1 and TX2 (stationary) while the pallet is moving through the gate. For $y=0$ m the pallet is at the center of the gate. Especially note the changing distance estimate.

visible for this link (the receiver plane moves with the pallet); the general results for the channel TX1→RX are identical.

VIII. READER - TAG - READER: BACKSCATTER CHANNEL

All results presented in this paper are based on individual channels, i.e. point-to-point measurements between reader and tag, in order to keep the analysis independent of a used setup (monostatic/bistatic) and to be able to directly use the receiver positions as a virtual array to identify multipath clusters.

UHF RFID, on the other hand, uses backscatter modulation, hence the reader is receiver and transmitter at the same time, while the tag is a time-variant part of the channel, cf. Fig. 1. The individual constituent channels are not accessible.

Backscatter channels in general are degenerate channels, with more pronounced fading than for the individual up- and downlink channels [12], [35]–[39]. The backscatter channel also has lower K_{LOS} and higher τ_{RMS} than each constituent channel [40], [41]. Correlation between the constituent channels, such as in monostatic setups, additionally decreases K_{LOS} and increases τ_{RMS} [41]. While the exact instantaneous shape parameters of the backscatter channel can only be calculated from the backscatter CIR itself due to the random nature of wireless channels, approximations based on the constituent channels' parameters are possible. A complete statistical analysis of the connection between the individual up- and downlink channels and the combined backscatter channel can be found in [41]. The results of this analysis are as follows:

The backscatter K-factor can be approximated independent of the shapes of the single-channel PDPs via

$$K_{LOS,sc} = \left(1 - \frac{\alpha_K}{2}\right) \cdot \frac{K_{LOS,1} \cdot K_{LOS,2}}{1 + K_{LOS,1} + K_{LOS,2}}, \quad (2)$$

where $K_{LOS,1}$ and $K_{LOS,2}$ are the K-factors of the two constituent channels, and $0 \leq \alpha_K \leq 1$ represents correlation between both channels. For uncorrelated channels, α_K equals zero, while for fully correlated constituent channels $\alpha_K = 1$. If the LOS component is not fully isolated, i.e., reflected paths are mapped to the LOS component due to the limited signal bandwidth, α_K is less than one even in monostatic setups, where both channels are identical and thus fully correlated.

⁴The required noise floor may be extremely challenging, though.

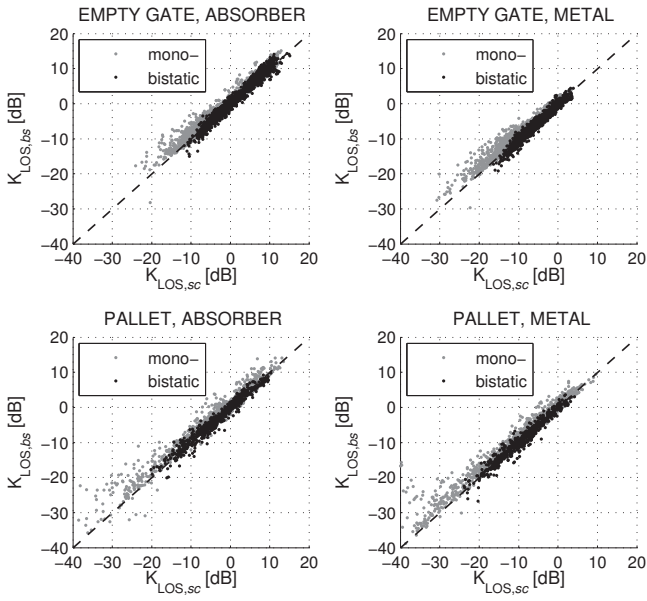


Fig. 33. K-factor w.r.t. LOS: Comparison between single-channel approximation ($K_{LOS,sc}$) and true backscatter parameter ($K_{LOS,bc}$) for mono- and bistatic setup. Values of zero and one are assumed for α_K for the bi- and monostatic case, respectively.

The RMS delay spread of the backscatter channel based on the constituent channel parameters is approximated via

$$\tau_{RMS,sc} = \sqrt{\tau_{RMS,1}^2 + \tau_{RMS,2}^2 + 2 \cdot \alpha_\tau \cdot \tau_{RMS,1} \cdot \tau_{RMS,2}}, \quad (3)$$

where $0 \leq \alpha_\tau \leq 1$ again represents correlation. Unlike for the K-factor, α_τ depends on the shapes of the constituent PDPs for correlated channels, and only approaches $\alpha_\tau = 1$ for high K-factors. For fully correlated up- and downlink channels in monostatic setups, this parameter can be approximated by

$$\alpha_{\tau,monostat.} \approx \frac{K_{LOS,1}}{10 + K_{LOS,1}}, \quad (4)$$

with $K_{LOS,1} = K_{LOS,2}$ due to the full correlation. Although strictly speaking, (4) is only valid for exponential PDPs, the formula works well also for non-exponential PDPs, cf. [40].

Comparisons of the single-channel approximations to measured backscatter parameter statistics are shown in Figs. 33 and 34. Obviously, the backscatter channel parameters can be estimated quite well from the individual ones using the formulas given above. This includes the area inside the portal (PDP: power-law, high correlation) and outside the portal (PDP: exponential, low correlation), as well as LOS and NLOS cases (LOS blocked by pallet). The small positive bias in Fig. 33 for the monostatic setups is caused by reflections that are mapped to the LOS component, thus causing $\alpha_K < 1$ in spite of the full correlation.

Note that the backscatter K-factor rarely exceeds 0 dB for the metal-shielded portal, regardless of its contents. Also the minimum RMS delay spreads inside the metal portal are extremely high, considering that the minimum values of 15 ns (~ 4.5 m) are reached at distances below 1 m. The only exception here is TX2 for the liquids pallet, where the pallet

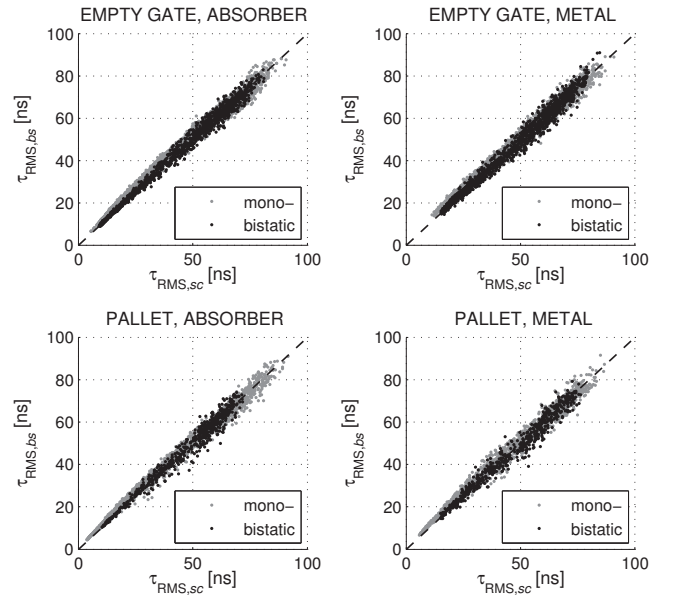


Fig. 34. RMS delay spread: Comparison between single-channel approximation ($\tau_{RMS,sc}$) and true backscatter parameter ($\tau_{RMS,bc}$) for mono- and bistatic setup.

blocks most gate reflections, leading to a considerably lower minimum τ_{RMS} .

IX. CONCLUSION

A comprehensive investigation w.r.t. ranging and localization was presented of the UHF RFID channel, based on measurements inside a warehouse portal. The influence of reflecting/absorbing portals as well as the effects of a reflective pallet on the channel was discussed in detail, including the feedback in mono- and bistatic setups. Furthermore, the channel was analyzed for deterministic components and compared to a number of channel models. A simple relation has been discussed between the individual channels to and from the tag and the combined backscatter channel.

It was found that the UHF RFID backscatter channel features surprisingly low K-factors and high RMS delay spreads due to strong reflections created by the setup. K-factors w.r.t. the LOS component are typically in the range of 0 dB and below for metal-shielded portals and RMS delay spreads are above 15 ns even at very short ranges and when the tag is in direct line-of-sight. As a consequence, the direct path is rarely the dominant path in this typical UHF RFID setup.

It was also found that classical three-path models, which are able to correctly predict the average power distribution inside the portal, are off by factors if calculating any channel parameter that is relevant to ranging, such as the K-factor w.r.t. LOS or the RMS delay spread. Using these models to evaluate the performance of ranging methods in simulations will thus result in overly optimistic predictions of the ranging error. A slightly more complex hybrid channel model combining simplified ray-tracing with a stochastic channel model is able to correctly predict the channel parameters, including the channel impulse response.

X. ACKNOWLEDGMENTS

We would like to express our gratitude to Grzegorz Adamiuk (Karlsruhe Institute of Technology) for designing the antennas used in the measurements, Giuliano Manzi, Martin Rampetsreiter, Gerald Wiednig, and Alexey Nazarov (NXP) for their invaluable help with the measurement setups, as well as Albert Angstenberger (Taconic) for providing the substrates used for the antennas. We would also like to thank NXP Semiconductors, Gratkorn, Austria, for providing the environment for all measurements.

REFERENCES

- [1] P. V. Nikitin, R. Martinez, S. Ramamurthy, H. Leland, G. Spiess, and K. V. S. Rao, "Phase based spatial identification of UHF RFID tags," in *Proc. IEEE Int RFID Conf*, 2010, pp. 102–109.
- [2] Z. Sahinoglu, S. Gezici, and I. Guvenc, *Ultra-wideband Positioning Systems: Theoretical Limits, Ranging Algorithms, and Protocols*. Cambridge University Press, 2008, ISBN-13: 978-0521873093.
- [3] U. Muehlmann, G. Manzi, G. Wiednig, and M. Buchmann, "Modeling and performance characterization of UHF RFID portal applications," *IEEE Trans. Microw. Theory Tech.*, vol. 57, no. 7, pp. 1700–1706, 2009.
- [4] G. Marrocco, E. Di Giampaolo, and R. Aliberti, "Estimation of UHF RFID reading regions in real environments," *IEEE Antennas Propag. Mag.*, vol. 51, no. 6, pp. 44–57, 2009.
- [5] P. Bosselmann, "Planning and analysis of UHF RFID systems for consumer goods logistics using ray tracing predictions," in *Proc. 1st Annual RFID Eurasia*, 2007, pp. 1–7.
- [6] A. F. Molisch, D. Cassioli, C.-C. Chong, S. Emami, A. Fort, B. Kannan, J. Karedal, J. Kunisch, H. G. Schantz, K. Siwiak, and M. Z. Win, "A comprehensive standardized model for ultrawideband propagation channels," *IEEE Trans. Antennas Propag.*, vol. 54, no. 11, pp. 3151–3166, 2006.
- [7] D. Armitz, G. Adamiuk, U. Muehlmann, and K. Witrisal, "UWB channel sounding for ranging and positioning in passive UHF RFID," in *11th COST2100 MCM*, Aalborg, Denmark, Jun. 2010. [Online]. Available: <http://www.spssc.tugraz.at/people/daniel-armitz/ArmitzCOSTMCM10.pdf>
- [8] L. J. Greenstein, S. S. Ghassemzadeh, S.-C. Hong, and V. Tarokh, "Comparison study of UWB indoor channel models," *IEEE Trans. Wireless Commun.*, vol. 6, no. 1, pp. 128–135, 2007.
- [9] M. S. Varela and M. G. Sánchez, "RMS delay and coherence bandwidth measurements in indoor radio channels in the UHF band," *IEEE Trans. Veh. Technol.*, vol. 50, no. 2, pp. 515–525, Mar. 2001, 10.1109/25.923063.
- [10] T. Gigl, T. Buchgraber, A. Adalan, J. Preishuber-Pfluegl, M. Fischer, and K. Witrisal, "UWB channel characterization using IEEE 802.15.4a demonstrator system," in *Proc. IEEE Int. Conf. Ultra-Wideband ICUBW 2009*, 2009, pp. 230–234.
- [11] J. Karedal, S. Wyne, P. Almers, F. Tufvesson, and A. F. Molisch, "A measurement-based statistical model for industrial ultra-wideband channels," *IEEE Trans. Wireless Commun.*, vol. 6, no. 8, pp. 3028–3037, 2007.
- [12] J. D. Griffin and G. D. Durgin, "Multipath fading measurements for multi-antenna backscatter RFID at 5.8 GHz," in *Proc. IEEE Int RFID Conf*, 2009, pp. 322–329.
- [13] Intermec IA39b UHF Reader Antenna. Intermec Technologies Corporation. [Online]. Available: http://www.intermec.com/products/rfid_ant_ia39b/index.aspx
- [14] A. Molisch, *Wireless Communications*, 1st ed. John Wiley & Sons, 2005, ISBN-13: 978-0470848876.
- [15] T. S. Rappaport, *Wireless Communications*, 2nd ed. Prentice Hall International, 2002, ISBN-13: 978-0130422323.
- [16] B. Yanakiev, P. Eggert, G. F. Pedersen, and T. Larsen, "Assessment of the physical interface of UHF passive tags for localization," in *Proc. 1st Int EURASIP RFID Workshop*, 2007, pp. 1–4.
- [17] D. Armitz, K. Witrisal, and U. Muehlmann, "Multi-frequency continuous-wave radar approach to ranging in passive UHF RFID," *IEEE Trans. Microw. Theory Tech.*, vol. 57, no. 5, pp. 1398–1405, Jul. 2009.
- [18] X. Li, Y. Zhang, and M. G. Amin, "Multifrequency-based range estimation of RFID tags," in *Proc. IEEE Int RFID Conf*, 2009, pp. 147–154.
- [19] Y. Zhang, X. Li, and M. G. Amin, "Array processing for RFID tag localization exploiting multi-frequency signals," in *SPIE Symposium on Defense, Security, and Sensing*, 2009.
- [20] The PARIS Simulation Framework. Graz University of Technology / NXP Semiconductors. Open-Source (GNU GPL v3). [Online]. Available: <http://www.spssc.tugraz.at/research-topics/wireless-communications/paris-osf/>
- [21] D. Armitz, U. Muehlmann, T. Gigl, and K. Witrisal, "Wideband system-level simulator for passive UHF RFID," in *Proc. IEEE IEEE Int RFID Conf*, Orlando, Florida, Apr. 2009.
- [22] A. Domazetovic, L. J. Greenstein, N. B. Mandayam, and I. Seskar, "Propagation models for short-range wireless channels with predictable path geometries," *IEEE Trans. Commun.*, vol. 53, no. 7, pp. 1123–1126, 2005.
- [23] K. Witrisal, Y.-H. Kim, and R. Prasad, "A new method to measure parameters of frequency-selective radio channels using power measurements," *IEEE Trans. Commun.*, vol. 49, no. 10, pp. 1788–1800, Oct. 2001, 10.1109/26.957401.
- [24] D. Armitz, U. Muehlmann, and K. Witrisal, "Wideband characterization of UHF RFID channels for ranging and positioning," Poster at IEEE Int RFID Conf, Apr. 2010. [Online]. Available: <http://www.spssc.tugraz.at/people/daniel-armitz/ArmitzRFID10.zip>
- [25] D. C. Hogg, "Fun with the Friis free-space transmission formula," *IEEE Antennas Propag. Mag.*, vol. 35, no. 4, pp. 33–35, 1993.
- [26] C. L. Holloway, M. G. Cotton, and P. McKenna, "A model for predicting the power delay profile characteristics inside a room," *IEEE Trans. Veh. Technol.*, vol. 48, no. 4, pp. 1110–1120, 1999.
- [27] D. M. Dobkin, *The RF in RFID*. Elsevier, 2007, ISBN-13: 978-0750682091.
- [28] S. R. Aroor and D. D. Deavours, "Evaluation of the state of passive UHF RFID: An experimental approach," *IEEE Systems Journal*, vol. 1, no. 2, pp. 168–176, 2007.
- [29] Y. Han and H. Min, "System modeling and simulation of RFID," in *Auto-ID Labs Whitepaper*, 2005. [Online]. Available: <http://www.autoidlabs.org/uploads/media/AUTOIDLABS-WP-HARDWARE-010.pdf>
- [30] A. Paulraj, R. Nabar, and D. Gore, *Introduction to Space-Time Wireless Communications*, 1st ed. Cambridge University Press, 2003, ISBN-13: 9-780521826150.
- [31] J. Heidrich, D. Brenk, J. Essel, S. Schwarzer, K. Seemann, G. Fischer, and R. Weigel, "The roots, rules, and rise of RFID," *IEEE Microw. Mag.*, vol. 11, no. 3, pp. 78–86, 2010.
- [32] D. Armitz, U. Muehlmann, and K. Witrisal, "UWB ranging in passive UHF RFID: Proof of concept," *IET Electron. Letters*, vol. 46, no. 20, pp. 1401–1402, Sep. 2010.
- [33] P. Meissner, C. Steiner, and K. Witrisal, "UWB positioning with virtual anchors and floor plan information," in *Proc. 7th Workshop on Positioning, Navigation and Communication, WPNC 2010*, 2010.
- [34] G. Li, D. Armitz, R. Ebel, U. Muehlmann, K. Witrisal, and M. Vossiek, "Bandwidth dependence of CW ranging to UHF RFID tags in severe multipath environments," submitted to IEEE Int RFID Conf, RFID2011.
- [35] J. D. Griffin and G. D. Durgin, "Complete link budgets for backscatter-radio and RFID systems," *IEEE Antennas Propag. Mag.*, vol. 51, no. 2, pp. 11–25, 2009.
- [36] —, "Gains for RF tags using multiple antennas," *IEEE Trans. Antennas Propag.*, vol. 56, no. 2, pp. 563–570, 2008.
- [37] —, "Link envelope correlation in the backscatter channel," *IEEE Commun. Lett.*, vol. 11, no. 9, pp. 735–737, 2007.
- [38] T. Taniguchi, Y. Karasawa, and M. Tsuruta, "An analysis method of double fading MIMO channels including LOS- environments," in *Proc. IEEE 19th Int. Symp. Personal, Indoor and Mobile Radio Communications PIMRC 2008*, 2008, pp. 1–5.
- [39] D. Kim, M. A. Ingram, and W. W. Smith, "Measurements of small-scale fading and path loss for long range RF tags," *IEEE Trans. Antennas Propag.*, vol. 51, no. 8, pp. 1740–1749, Aug. 2003, 10.1109/TAP.2003.814752.
- [40] D. Armitz, U. Muehlmann, and K. Witrisal, "Wideband characterization of backscatter channels," submitted to Europ. Wireless Conf, EW2011.
- [41] —, "Wideband characterization of backscatter channels: Derivations and theoretical background," submitted to IEEE Trans. Antennas Propag.

Wideband Characterization of Backscatter Channels: Derivations and Theoretical Background

Daniel Arnitz, *Student Member, IEEE*, Ulrich Muehlmann, *Member, IEEE*, and Klaus Witrisal *Member, IEEE*

Abstract—The wireless channel of backscatter radio systems is a two-way pinhole channel, created by the concatenation of two standard wireless channels.

We present a method to calculate wideband channel parameters of backscatter channels based on the parameters of the constituent one-way channels. The focus is on characteristics that are vital for narrowband and wideband ranging, such as the K-factor w.r.t. the direct (line-of-sight) path and the RMS delay spread. The presented analyses include uncorrelated as well as correlated channel pairs, and are thus valid for bistatic and monostatic antenna setups. We also show that the uncorrelated scattering (US) assumption holds for the backscatter channel, provided that the constituent channels are US.

I. INTRODUCTION

Pinhole channels are created by the concatenation of the channel from the transmitter to the pinhole and the channel from the pinhole to the receiver. In (semi-)passive ultra-high frequency radio-frequency identification (UHF RFID), a prime example for backscatter radio systems, the pinhole is formed by the RFID tag, as illustrated in Fig. 1. The overall backscatter channel between TX and RX is composed of the two individual channels to and from the tag, which are both multipath radio channels. Pinhole (a.k.a. keyhole, dyadic, or double fading) channels are quite well-understood in terms of fading statistics for narrowband signals [2]–[5] and channel capacity for multiple-input multiple-output (MIMO) systems [6]–[8]. Even though channel capacity and fading statistics are fully sufficient to analyze the performance of communication over a channel, they are insufficient for the analysis of narrowband and wideband indoor ranging systems (with the exception of receive-power-based methods). The performance of these systems depends on the shape of the power-delay-profile (PDP), and thus on shape parameters like the K-factor w.r.t. the line-of-sight (LOS) and the root-mean-square (RMS) delay spread.

We present a generic expression for the average power-delay-profile (APDP) of pinhole channels based on the APDPs of the constituent channel pair, both for correlated and for uncorrelated individual channels, and a closed-form expression for exponential APDPs. A similar expression for the generic APDP is derived in [9], however this result is limited to orthogonal channels. We also present approximations for common

Parts of this work have been presented at the European Wireless Conference, [1]. This work was funded by NXP Semiconductors, Gratkorn, Austria, and by the Austrian Research Promotion Agency (FFG) under grant 818072.

D. Arnitz and K. Witrisal are with the Signal Processing and Speech Communication Laboratory, Graz University of Technology, Graz, Austria (e-mail: daniel.arnitz@tugraz.at, witrisal@tugraz.at).

U. Muehlmann is with NXP Semiconductors, Gratkorn, Austria (e-mail: ulrich.muehlmann@nxp.com).

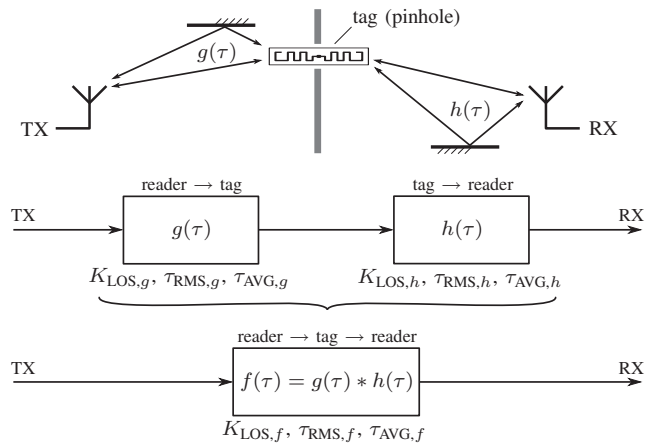


Fig. 1. Combination of individual channels reader→tag (downlink) and tag→reader (uplink) to the backscatter channel reader→tag→reader.

shape parameters of the pinhole APDP, such as K-factor w.r.t. the LOS component (K_{LOS}), RMS delay spread (τ_{RMS}), and average excess delay (τ_{AVG}), based on the parameters of the individual channels, cf. Fig. 1. These formulas can be used to calculate backscatter channel parameters from point-to-point measurements of the constituent channel(s), e.g. [10]–[14].

This paper is organized as follows: A generic expression for the APDPs of backscatter channels is derived in Section II, while a closed-form solution for the typical exponential APDP of short-range indoor channels is introduced in Section III. Section IV deals with the K-factor w.r.t. the LOS path, while expressions for the RMS delay spread and the average excess delay of the backscatter channel are derived in Sections V and VI, respectively. Validation for exponential APDPs and a discussion of robustness w.r.t. non-exponential decays can be found in Section VII, and a measurement-based validation is provided in Section VIII. The appendix contains an investigation of the uncorrelated scattering (US) assumption for the combined backscatter channel.

II. STATISTICAL DERIVATION OF THE BACKSCATTER AVERAGE POWER-DELAY-PROFILE

We define the time-invariant complex equivalent baseband channel impulse responses (CIRs) of the band-limited channels to and from the pinhole by uniformly sampled tapped delay lines [15]

$$g[n] = g(\tau = nT) := g_0\delta[n] + \sum_{i=1}^N g_i\delta[n-i] \quad (1)$$

$$h[n] = h(\tau = nT) := h_0\delta[n] + \sum_{j=1}^M h_j\delta[n-j]. \quad (2)$$

where T is the tap interval, h_0 is the LOS component of $h[n]$, h_i is the i -th reflected (non-line-of-sight, NLOS) component at delay $\tau = iT$, and $\delta[\cdot]$ is the Kronecker delta. All channels are causal, thus $i > 0$ and $j > 0$, and have been normalized to have their LOS component at $n=0$. This normalization has no effect on the results, as the analyzed parameters are shift-invariant¹. Time-invariance is assumed for notational simplicity, although only short-time wide-sense-stationarity (WSS) is required. Also the sampled representation is chosen purely for notational simplicity; we will use continuous-time representations in other parts of this paper. Both representations are equivalent due to the band limitation of the channels.

In the tapped delay line model, each tap represents a large number of physical paths. As a consequence of the central limit theorem [16] each NLOS component in the complex baseband representation can be modeled as zero-mean circular-symmetric complex Gaussian (ZMCSCG) random variable. Also the sampled LOS component will be random to some degree even in direct line of sight, because indirect physical paths close to the LOS path are mapped to the LOS component in the sampled model. In the ideal case, which we will assume for now, the LOS component has a constant amplitude and uniform phase. We will discuss the influence of random LOS amplitudes at the end of this section.

$$|g_0|, |h_0| \sim \text{const.}, \angle g_0, \angle h_0 \sim \mathcal{U}(0, 2\pi) \quad (3)$$

$$g_i \sim \mathcal{CN}(0, \sigma_i^2/2) \quad (4)$$

$$h_j \sim \mathcal{CN}(0, \eta_j^2/2) \quad (5)$$

The individual multipath components are assumed to be uncorrelated (US), cf. [15], [17], [18], i.e.,

$$\mathbb{E}\{g_i g_j^*\} = 0, \quad \mathbb{E}\{h_i h_j^*\} = 0, \quad \mathbb{E}\{g_i h_j^*\} = 0 \quad \forall i \neq j \quad (6)$$

As a first step, the combined channel is obtained by convolution of the two constituent channels,

$$\begin{aligned} f[n] &= g[n] * h[n] = g_0 h_0 \delta[n] + h_0 \sum_{i=1}^N g_i \delta[n-i] \\ &+ g_0 \sum_{j=1}^M h_j \delta[n-j] + \sum_{k=1}^N \sum_{m=1}^M g_k h_m \delta[n-k-m]. \end{aligned} \quad (7)$$

The first term in (7) is the LOS component of the combined pinhole channel. All the other components form the NLOS part. We will focus our derivation on the NLOS part and rewrite it in vector notation in order to remove the delta pulses and further simplify the notation. By defining

$$\tilde{\mathbf{g}} := [g_1 \ g_2 \ \cdots \ g_N \ 0 \ \cdots \ 0]^T \quad (M+N-1) \times 1 \quad (8)$$

$$\tilde{\mathbf{h}} := [h_1 \ h_2 \ \cdots \ h_M \ 0 \ \cdots \ 0]^T \quad (M+N-1) \times 1 \quad (9)$$

$$\tilde{\mathbf{f}} := [f_1 \ f_2 \ \cdots \ f_{N+M-1}]^T \quad (M+N-1) \times 1 \quad (10)$$

¹The K-factor is a power ratio and does not depend on the delay axis at all. The RMS delay spread is a central moment of the APDP, hence the average time shift is irrelevant. The average excess delay is defined relative to the LOS delay and thus shift-invariant.

for the random NLOS part of the channel impulse responses, and the convolution matrix

$$\tilde{\mathbf{H}} := \begin{bmatrix} h_1 & 0 & 0 & \cdots \\ h_2 & h_1 & 0 & \cdots \\ h_3 & h_2 & h_1 & \cdots \\ \vdots & \vdots & \vdots & \ddots \end{bmatrix}, \quad (M+N-1) \times N \quad (11)$$

we can write the NLOS part of the backscatter CIR as

$$\tilde{\mathbf{f}} = g_0 \tilde{\mathbf{h}} + h_0 \tilde{\mathbf{g}} + \tilde{\mathbf{H}} \tilde{\mathbf{g}}. \quad (12)$$

The average power-delay-profile for WSSUS channels is the second moment (autocorrelation) of the channel impulse response, cf. [15], [17], [18]. A proof for the validity of the US assumption for the backscatter channel can be found in the appendix. We will denote the APDP by \mathbf{S} in the vector notation and $S(\tau)$ in the continuous-delay notation, and start by writing down the NLOS part of the backscatter APDP,

$$\begin{aligned} \mathbf{S}_{f,\text{NLOS}} &:= \mathbb{E}\{\tilde{\mathbf{f}} \circ \tilde{\mathbf{f}}^*\} = \mathbb{E}\{g_0 g_0^* \tilde{\mathbf{h}} \circ \tilde{\mathbf{h}}^* + h_0 h_0^* \tilde{\mathbf{g}} \circ \tilde{\mathbf{g}}^*\} \\ &+ \mathbb{E}\{\tilde{\mathbf{H}} \tilde{\mathbf{g}} \circ \tilde{\mathbf{H}}^* \tilde{\mathbf{g}}^*\} + \mathbb{E}\{g_0 h_0^* \tilde{\mathbf{h}} \circ \tilde{\mathbf{g}}^* + g_0^* h_0 \tilde{\mathbf{h}}^* \circ \tilde{\mathbf{g}}\} \\ &+ \mathbb{E}\{g_0 \tilde{\mathbf{h}} \circ \tilde{\mathbf{H}}^* \tilde{\mathbf{g}}^* + g_0^* \tilde{\mathbf{h}}^* \circ \tilde{\mathbf{H}} \tilde{\mathbf{g}}\} \\ &+ \mathbb{E}\{h_0 \tilde{\mathbf{g}} \circ \tilde{\mathbf{H}}^* \tilde{\mathbf{g}}^* + h_0^* \tilde{\mathbf{g}}^* \circ \tilde{\mathbf{H}} \tilde{\mathbf{g}}\}, \end{aligned} \quad (13)$$

where \circ denotes the element-wise multiplication of vectors.

Using the zero-mean property of $\tilde{\mathbf{g}}$ and $\tilde{\mathbf{h}}$, we can define the NLOS APDPs of the individual channels

$$\begin{aligned} \boldsymbol{\sigma}^2 &= \mathbf{S}_{g,\text{NLOS}} := \mathbb{E}\{\tilde{\mathbf{g}} \circ \tilde{\mathbf{g}}^*\} \\ &= [\sigma_1^2 \ \sigma_2^2 \ \cdots \ \sigma_N^2 \ 0 \ \cdots \ 0]^T \quad (M+N-1) \times 1 \end{aligned} \quad (14)$$

$$\begin{aligned} \boldsymbol{\eta}^2 &= \mathbf{S}_{h,\text{NLOS}} := \mathbb{E}\{\tilde{\mathbf{h}} \circ \tilde{\mathbf{h}}^*\} \\ &= [\eta_1^2 \ \eta_2^2 \ \cdots \ \eta_M^2 \ 0 \ \cdots \ 0]^T \quad (M+N-1) \times 1 \end{aligned} \quad (15)$$

and calculate the expected values of the first two summands in (13)

$$\mathbb{E}\{g_0 g_0^* \tilde{\mathbf{h}} \circ \tilde{\mathbf{h}}^* + h_0 h_0^* \tilde{\mathbf{g}} \circ \tilde{\mathbf{g}}^*\} = |g_0|^2 \boldsymbol{\eta}^2 + |h_0|^2 \boldsymbol{\sigma}^2. \quad (16)$$

The next term,

$$\begin{aligned} \mathbb{E}\{\tilde{\mathbf{H}} \tilde{\mathbf{g}} \circ \tilde{\mathbf{H}}^* \tilde{\mathbf{g}}^*\} &= \dots \\ &= \begin{bmatrix} h_1 g_1 \cdot h_1^* g_1^* \\ (g_1 h_2 + g_2 h_1) \cdot (g_1 h_2 + g_2 h_1)^* \\ (g_1 h_3 + g_2 h_2 + g_3 h_1) \cdot (g_1 h_3 + g_2 h_2 + g_3 h_1)^* \\ \vdots \end{bmatrix} \end{aligned} \quad (17)$$

contains fourth-order cross-terms between all channel taps. It can be shown that [19]

$$\mathbb{E}\{x_1 x_2^* x_3 x_4^*\} = \mathbb{E}\{x_1 x_2^*\} \mathbb{E}\{x_3 x_4^*\} + \mathbb{E}\{x_1 x_4^*\} \mathbb{E}\{x_2^* x_3\} \quad (18)$$

for zero-mean complex Gaussian variables $x_1 \dots x_4$. Using (18), we can split the fourth-order terms into auto- and cross-correlation terms of the CIRs

$$E\{g_i g_j^* h_k h_l^*\} = E\{g_i g_j^*\} E\{h_k h_l^*\} + E\{g_i h_l^*\} E\{h_k g_j^*\}. \quad (19)$$

The autocorrelation terms, $E\{g_i g_j^*\}$ and $E\{h_k h_l^*\}$, can easily be obtained from the definitions in (4)–(6). For the two cross-correlation terms we know from the Cauchy-Schwarz-inequality that

$$E\{g_i h_l^*\}^2 \leq E\{g_i g_i^*\} E\{h_l h_l^*\}, \quad (20)$$

and that equality holds if g_i and h_l are fully correlated [20]. We will limit the derivation to zero correlation (ideal bistatic setup) and full correlation (monostatic setup), and thus provide bounds for full/no correlation. Note that full correlation implies that the channels are linearly dependent, and thus in every practical sense $g_i = h_i \forall i$. Hence

$$E\{g_i h_l^*\} = \begin{cases} 0 & i \neq l \\ 0 & i = l \text{ and } g(\tau), h(\tau) \text{ uncorr.} \\ \sigma_i \eta_i & i = l \text{ and } g(\tau), h(\tau) \text{ identical} \end{cases} \quad (21)$$

By applying this approach, it is slightly tedious but straightforward to show that

$$E\{\tilde{\mathbf{H}}\tilde{\mathbf{g}} \circ \tilde{\mathbf{H}}^* \tilde{\mathbf{g}}^*\} = \begin{cases} \Theta^2 \sigma^2 & g(\tau), h(\tau) \text{ uncorr.} \\ 2 \cdot \Theta^2 \sigma^2 & g(\tau), h(\tau) \text{ identical} \end{cases} \quad (22)$$

with

$$\Theta^2 := E\{\tilde{\mathbf{H}} \circ \tilde{\mathbf{H}}^*\} = \begin{bmatrix} \eta_1^2 & 0 & 0 & \dots \\ \eta_2^2 & \eta_1^2 & 0 & \dots \\ \eta_3^2 & \eta_2^2 & \eta_1^2 & \dots \\ \vdots & \vdots & \vdots & \ddots \end{bmatrix}. \quad (23)$$

All the remaining terms in (13) contain as least one of the non-Gaussian RVs g_0 and h_0 , hence (18) does not immediately hold for these terms. However, by extracting the random phase of g_0 and h_0 we can exclude the remaining constant amplitudes from the expectation operators. The phase shifts are absorbed by the NLOS channel taps without any effect due to their circular symmetry. It follows that

$$\begin{aligned} & E\{g_0 h_0^* \tilde{\mathbf{h}} \circ \tilde{\mathbf{g}}^* + g_0^* h_0 \tilde{\mathbf{h}}^* \circ \tilde{\mathbf{g}}\} \\ &= |g_0| |h_0| \cdot E\{\tilde{\mathbf{h}} \circ \tilde{\mathbf{g}}^* + \tilde{\mathbf{h}}^* \circ \tilde{\mathbf{g}}\} \\ &= \begin{cases} [0 \dots 0]^T = \mathbf{0} & g(\tau), h(\tau) \text{ uncorr.} \\ 2|g_0| |h_0| \cdot \sigma \circ \boldsymbol{\eta} & g(\tau), h(\tau) \text{ identical} \end{cases} \end{aligned} \quad (24)$$

Finally, it is straightforward to show that the last remaining terms of (13) are zero due to the zero-mean property of $\tilde{\mathbf{g}}$, $\tilde{\mathbf{h}}$, and $\tilde{\mathbf{H}}$.

$$E\{\tilde{\mathbf{h}} \circ \tilde{\mathbf{H}}^* \tilde{\mathbf{g}}^*\} = E\{\tilde{\mathbf{h}}^* \circ \tilde{\mathbf{H}} \tilde{\mathbf{g}}\} = [0 \dots 0]^T = \mathbf{0} \quad (25)$$

$$E\{\tilde{\mathbf{g}} \circ \tilde{\mathbf{H}}^* \tilde{\mathbf{g}}^*\} = E\{\tilde{\mathbf{g}}^* \circ \tilde{\mathbf{H}} \tilde{\mathbf{g}}\} = [0 \dots 0]^T = \mathbf{0} \quad (26)$$

Hence, the NLOS part of the backscatter APDP is

$$\begin{aligned} S_{f,\text{NLOS}} &= |g_0|^2 \boldsymbol{\eta}^2 + |h_0|^2 \boldsymbol{\sigma}^2 \\ &+ \begin{cases} \Theta^2 \boldsymbol{\sigma}^2 & g(\tau), h(\tau) \text{ uncorr.} \\ 2\Theta^2 \boldsymbol{\sigma}^2 + 2|g_0| |h_0| \cdot \sigma \circ \boldsymbol{\eta} & g(\tau), h(\tau) \text{ identical} \end{cases} \end{aligned} \quad (27)$$

From (27), we can deduce two major conclusions:

- 1) For uncorrelated constituent channels, the backscatter APDP is the convolution of the individual APDPs.

Proof: By separating the APDPs of the channels into LOS and NLOS parts

$$S(\tau) = \begin{cases} 0 & \tau < 0 \\ S_{\text{LOS}} \cdot \delta(\tau) & \tau = 0, \\ S_{\text{NLOS}}(\tau) & \tau > 0 \end{cases}, \quad (28)$$

where $\delta(\tau)$ is the Dirac delta, the convolution of the APDPs of g and h ,

$$S_f(\tau) = S_g(\tau) * S_h(\tau), \quad (29)$$

results in

$$S_{f,\text{LOS}} = S_{g,\text{LOS}} \cdot S_{h,\text{LOS}} \quad (30)$$

and

$$\begin{aligned} S_{f,\text{NLOS}}(\tau) &= S_{g,\text{LOS}} \cdot S_{h,\text{NLOS}}(\tau) + S_{h,\text{LOS}} \cdot S_{g,\text{NLOS}}(\tau) \\ &+ S_{g,\text{NLOS}}(\tau) * S_{h,\text{NLOS}}(\tau). \end{aligned} \quad (31)$$

This decomposition is also illustrated in Fig. 2. Switching to vector notation and inserting (14), (15), and (23) into (31), we obtain $|g_0|^2 \boldsymbol{\eta}^2 + |h_0|^2 \boldsymbol{\sigma}^2 + \Theta^2 \boldsymbol{\sigma}^2$ for the NLOS part of the combined channel, which matches (27) for uncorrelated channels. ■

- 2) For fully correlated constituent channels, the NLOS part of the backscatter APDP is multiplied by a factor of two compared to two independent, but identically parameterized constituent channels.

Proof: With identical constituent channels, $g_i = h_i \forall i$, (27) reduces to

$$S_{f,\text{NLOS},\text{corr.}} = 4|g_0|^2 \boldsymbol{\sigma}^2 + 2\Theta^2 \boldsymbol{\sigma}^2, \quad (32)$$

while for two uncorrelated channels with $\boldsymbol{\sigma}^2 = \boldsymbol{\eta}^2$ and $|h_0| = |g_0|$ we get

$$S_{f,\text{NLOS},\text{uncorr.}} = 2|g_0|^2 \boldsymbol{\sigma}^2 + \Theta^2 \boldsymbol{\sigma}^2. \quad (33)$$

An example is presented in Fig. 3. ■

Summing up, the APDP of the backscatter channel can be calculated via convolution of the APDPs of the individual channels if these channels are uncorrelated. This matches the results in [9], and is also similar to the Kronecker product for the overall correlation matrix in [7]. For fully correlated channels, the NLOS part of the backscatter APDP is merely multiplied by a factor of two; the general shape stays the same. This is not limited to a specific type of APDP and thus applies to all pinhole channels.

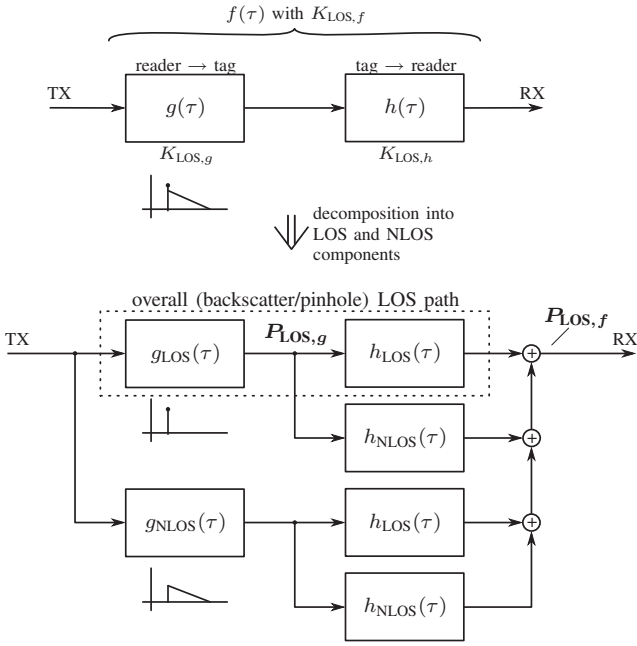


Fig. 2. Decomposition of the constituent channels into LOS and NLOS parts (for uncorrelated channels). This compares to the structure of (30) and (31), as well as (37) and (38), and also illustrates the steps in calculating the pinhole channel's LOS K-factor, $K_{\text{LOS},f}$.

The same reasoning can be applied to the LOS component if the assumption of a constant amplitude does not hold. Due to the linearity of the models the LOS component can be split into a component with constant amplitude and uniform phase and an additive ZMCSCG random variable. Both random variables are uncorrelated due to the US assumption. For fully correlated channels, the power of the Gaussian LOS part will be doubled in the backscatter APDP, just like the NLOS part. As a theoretical limiting case, the entire APDP is doubled if the sampled LOS component is composed entirely of reflected paths. Again, this is not limited to specific shapes of APDPs.

III. BACKSCATTER AVERAGE POWER-DELAY-PROFILE FOR EXPONENTIALLY DECAYING CHANNELS

Indoor average power-delay-profiles are typically exponential due to rich scattering (e.g., [21], [22]). We will now calculate a closed-form indoor backscatter APDP, separated into LOS and NLOS parts

$$S_f(\tau) = S_g(\tau) * S_h(\tau) = \begin{cases} 0 & \tau < 0 \\ S_{f,\text{LOS}} \cdot \delta(\tau) & \tau = 0 \\ S_{f,\text{NLOS}}(\tau) & \tau > 0 \end{cases} \quad (34)$$

For the channels to and from the pinhole, $g(\tau)$ and $h(\tau)$, we assume short-range indoor APDPs [23]

$$S_{g,\text{LOS}} = \rho_g^2, \quad S_{g,\text{NLOS}}(\tau) = \Pi_g e^{-\gamma_g \tau} \quad (35)$$

$$S_{h,\text{LOS}} = \rho_h^2, \quad S_{h,\text{NLOS}}(\tau) = \Pi_h e^{-\gamma_h \tau} \quad (36)$$

where ρ^2 is the LOS power, Π is the NLOS power density, and γ is the NLOS decay constant. Using these definitions,

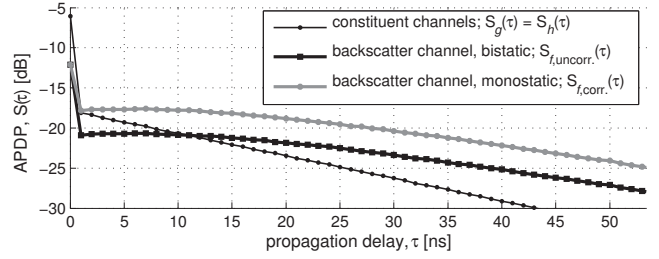


Fig. 3. Simulation-based example showing the doubling of NLOS power due to coherent combining. Both constituent channels are exponentially decaying, with $K_{\text{LOS},g} = K_{\text{LOS},h} = -5$ dB and $\tau_{\text{RMS},g} = \tau_{\text{RMS},h} = 15$ ns, and are either identical (monostatic) or independent (bistatic). The shown APDPs are averaged over 10^4 instantaneous PDPs.

we obtain

$$S_{f,\text{LOS}} = \rho_g^2 \rho_h^2 \quad (\tau = 0) \quad (37)$$

and

$$S_{f,\text{NLOS}}(\tau) = \rho_g^2 \Pi_h e^{-\gamma_h \tau} + \rho_h^2 \Pi_g e^{-\gamma_g \tau} + \frac{\Pi_g \Pi_h}{\gamma_g - \gamma_h} (e^{-\gamma_h \tau} - e^{-\gamma_g \tau}). \quad (\tau > 0) \quad (38)$$

This is the result for uncorrelated channels. Using the conclusions from Section II, we know that coherent combining of the NLOS part will double the power (density) of (38).

Expressions that link K_{LOS} , τ_{RMS} , and the overall power P_0 with ρ , Π , and γ are provided by [23] along with the APDP:

$$\Pi = \frac{P_0 \gamma}{K_{\text{LOS}} + 1} \quad (39)$$

$$\gamma = \frac{1}{\tau_{\text{RMS}}} \cdot \frac{\sqrt{2K_{\text{LOS}} + 1}}{K_{\text{LOS}} + 1} \quad (40)$$

$$\rho^2 = P_0 \frac{K_{\text{LOS}}}{K_{\text{LOS}} + 1} \quad (41)$$

IV. K-FACTOR W.R.T. THE LINE-OF-SIGHT COMPONENT

The K-factor w.r.t. LOS (K_{LOS}) only depends on the ratio between LOS and NLOS power,

$$K_{\text{LOS}} := \frac{P_{\text{LOS}}}{P_{\text{NLOS}}} = \frac{S_{\text{LOS}}}{\int_0^\infty S_{\text{NLOS}}(\tau) d\tau}, \quad (42)$$

and is thus independent of the actual shape of the APDP and the overall power $P_0 = P_{\text{LOS}} + P_{\text{NLOS}} = \int_{-\infty}^\infty S(\tau) d\tau$.

The simplest way to calculate K_{LOS} of the backscatter channel, $K_{\text{LOS},f}$, is based on the decomposition of each individual channel into its LOS and NLOS components, as illustrated in Fig. 2. Using

$$K_{\text{LOS}} = \frac{P_{\text{LOS}}}{P_{\text{NLOS}}} = \frac{P_{\text{LOS}}}{P_0 - P_{\text{LOS}}}, \quad (43)$$

the power of the direct (LOS) path after the first channel is

$$P_{\text{LOS},g} = P_0 \cdot \frac{K_{\text{LOS},g}}{1 + K_{\text{LOS},g}}. \quad (44)$$

At this point, the signal passes the pinhole and is sent over the second channel. It is important to note that both impulse

responses, $g(\tau)$ and $h(\tau)$, are direct representations of physical channels and thus causal per necessity. Hence

$$\begin{aligned} P_{\text{LOS},f} &= P_{\text{LOS},g*h} = P_{\text{LOS},g} \cdot \frac{K_{\text{LOS},h}}{1 + K_{\text{LOS},h}} \\ &= P_0 \cdot \frac{K_{\text{LOS},g}}{1 + K_{\text{LOS},g}} \cdot \frac{K_{\text{LOS},h}}{1 + K_{\text{LOS},h}}. \end{aligned} \quad (45)$$

Using (43) again, the overall K-factor w.r.t. the LOS path is

$$K_{\text{LOS},f} = \frac{P_{\text{LOS},f}}{P_0 - P_{\text{LOS},f}} = \frac{K_{\text{LOS},g} \cdot K_{\text{LOS},h}}{1 + K_{\text{LOS},g} + K_{\text{LOS},h}}. \quad (46)$$

So far, we've treated each channel as an individual, thus implicitly assuming independent channels. According to the results in Section II, full correlation between the channels will add a factor of two to the NLOS power. The LOS component, on the other hand, ideally has constant amplitude and is thus not changed by the coherent combining (see Fig. 3). As a consequence, $K_{\text{LOS},f}$ is reduced by the same factor of two according to (42).

Combining these observations, the K-factor of the combined backscatter channel is

$$K_{\text{LOS},f} = \left(1 - \frac{\alpha_K}{2}\right) \cdot \frac{K_{\text{LOS},g} \cdot K_{\text{LOS},h}}{1 + K_{\text{LOS},g} + K_{\text{LOS},h}}, \quad (47)$$

where $0 \leq \alpha_K \leq 1$ represents correlation between the constituent channels,

$$\alpha_K = \begin{cases} 0 & g(\tau) \text{ and } h(\tau) \text{ uncorr.} \\ 1 & g(\tau) \text{ and } h(\tau) \text{ identical} \end{cases}. \quad (48)$$

Note that a stochastic LOS amplitude will cause $\alpha_K < 1$ even in monostatic setups, see Section II, last paragraph.

From (47) it can be seen that the combined backscatter channel always has a lower K-factor than each individual channel, and that the difference is considerably more severe for low K-factors. Assuming $K_{\text{LOS},g} = K_{\text{LOS},h} = K_{\text{LOS}}$ and uncorrelated channels, for example, $K_{\text{LOS},f}$ asymptotically approaches K_{LOS}^2 for $K_{\text{LOS}} \ll 1$, and $K_{\text{LOS}}/2$ for $K_{\text{LOS}} \gg 1$. As a consequence, the LOS component is only dominant on the backscatter link if both constituent channels have extremely high K-factors. Channel correlation additionally reduces the backscatter K-factor.

V. RMS DELAY SPREAD

Unlike for the K-factor, the RMS delay spread of the backscatter channel cannot be calculated completely independent of the shapes of the APDPs of up- and downlink channel. More precisely, calculating $\tau_{\text{RMS},f}$ solely based on $\tau_{\text{RMS},g}$ and $\tau_{\text{RMS},h}$ works for uncorrelated channels to and from the pinhole, and for correlated channels with low K-factors. For correlated channels with high K-factors though, the individual shapes and K-factors have to be taken into account, as will be shown below.

We will start by formally defining the RMS delay spread, followed by a calculation of $\tau_{\text{RMS},f}$ for uncorrelated channels. We will then extend this result to correlated channels and combine both cases in one equation. Finally, we will specify this equation for exponential APDPs. A discussion of the robustness of these results for non-exponential APDPs and instantaneous PDP can be found in Section VII.

A. General Definitions

The RMS delay spread is the square root of the second central moment of the normalized APDP [15],

$$\tau_{\text{RMS}} := \sqrt{\frac{\int_0^\infty \tau^2 S(\tau) d\tau}{\int_0^\infty S(\tau) d\tau} - \left(\frac{\int_0^\infty \tau S(\tau) d\tau}{\int_0^\infty S(\tau) d\tau}\right)^2}. \quad (49)$$

As the LOS component is at $\tau=0$, its only influence on this formula is via the normalization term $\int_0^\infty S(\tau) d\tau$. We can thus again split the APDP into LOS and NLOS parts and skip the LOS term in the numerators,

$$\tau_{\text{RMS}} = \sqrt{\frac{\int_0^\infty \tau^2 S_{\text{NLOS}}(\tau) d\tau}{S_{\text{LOS}} + \int_0^\infty S_{\text{NLOS}}(\tau) d\tau} - \tau_{\text{AVG}}^2} \quad (50)$$

with the average excess delay

$$\tau_{\text{AVG}} = \frac{\int_0^\infty \tau S_{\text{NLOS}}(\tau) d\tau}{S_{\text{LOS}} + \int_0^\infty S_{\text{NLOS}}(\tau) d\tau}. \quad (51)$$

B. From Uncorrelated to Correlated Channels

The RMS delay spread for uncorrelated constituent channels can easily be obtained using a similarity to statistics: If two independent random variables are added, their distribution functions are convolved and the variances, i.e., second central moments, add up. It is shown in Section II and [9] that the APDPs of two uncorrelated channels are convolved, too. Hence

$$\tau_{\text{RMS},f,\text{uncorr.}} = \sqrt{\tau_{\text{RMS},g}^2 + \tau_{\text{RMS},h}^2}. \quad (52)$$

Extending this analogy, the variance of the sum of two arbitrary random variables x_1 and x_2 is [20]

$$\text{var}\{x_1 + x_2\} = \text{var}\{x_1\} + \text{var}\{x_2\} + 2 \cdot \text{cov}\{x_1, x_2\} \quad (53)$$

where

$$\text{cov}\{x_1, x_2\}^2 \leq \text{var}\{x_1\} \cdot \text{var}\{x_2\} \quad (54)$$

and

$$\text{cov}\{x_1, x_2\}^2 = \begin{cases} 0 & x_1, x_2 \text{ uncorr.} \\ \text{var}\{x_1\} \cdot \text{var}\{x_2\} & x_1, x_2 \text{ identical} \end{cases}. \quad (55)$$

We can thus assume that the RMS delay spread for fully correlated channels will be similar to

$$\tau_{\text{RMS},f,\text{corr.}} \approx \sqrt{\tau_{\text{RMS},g}^2 + \tau_{\text{RMS},h}^2 + 2 \cdot \tau_{\text{RMS},g} \cdot \tau_{\text{RMS},h}}, \quad (56)$$

based on (53) and the analogy of squared RMS delay spreads and variances. Unfortunately, this is as far as the analogy goes. Unlike for uncorrelated channels, the backscatter APDP for correlated channels is not identical to the convolution of the single-channel APDPs, even though the CIRs are still convolved.

As demonstrated in Section II, correlation will lead to increased NLOS power, thus modifying the distribution of power within the backscatter APDP. In the limiting case of identical channels with deterministic LOS amplitudes, the NLOS power is doubled while the LOS component remains untouched, i.e.,

$$S_{f,\text{LOS},\text{corr.}} = S_{f,\text{LOS},\text{uncorr.}} \quad (57)$$

and

$$S_{f,\text{NLOS,corr.}}(\tau) = 2 \cdot S_{f,\text{NLOS,uncorr.}}(\tau). \quad (58)$$

Adapting the definitions of RMS delay spread and average excess delay accordingly, they will contain terms like

$$\frac{2 \int_0^\infty \tau^2 S_{\text{NLOS,uncorr.}}(\tau) d\tau}{S_{\text{LOS,uncorr.}} + 2 \int_0^\infty S_{\text{NLOS,uncorr.}}(\tau) d\tau}. \quad (59)$$

The effect of correlation on the RMS delay spread thus depends on the ratio between LOS and NLOS part. In case of a negligible LOS component, the correlation has no effect on τ_{RMS} at all. Conversely, the maximum effect (56) is reached for an extremely dominant LOS part, i.e., very high K_{LOS} .

This variable influence of channel correlation on $\tau_{\text{RMS},f}$ is taken into account by adding a parameter α_τ to (56), similar (but not identical) to a correlation coefficient,

$$\tau_{\text{RMS},f} = \sqrt{\tau_{\text{RMS},g}^2 + \tau_{\text{RMS},h}^2 + 2 \cdot \alpha_\tau \cdot \tau_{\text{RMS},g} \cdot \tau_{\text{RMS},h}}. \quad (60)$$

The parameter α_τ can be obtained by comparing the results for correlated and uncorrelated channels. Looking at (60) and (52), α_τ obviously has to be zero for uncorrelated channels. In case of full correlation, α_τ has to model the dependence of $\tau_{\text{RMS},f}$ on the K-factor. Assuming uncorrelated channels with identical RMS delay spreads $\tau_{\text{RMS},g} = \tau_{\text{RMS},h}$, the squared RMS delay spread of the pinhole channel is $2\tau_{\text{RMS},g}^2$. For identical channels, which necessarily have identical RMS delay spreads, the result is $2\tau_{\text{RMS},g}^2 \cdot (1 + \alpha_\tau)$. This translates to

$$\tau_{\text{RMS,corr.}}^2 = \tau_{\text{RMS,f,uncorr.}}^2 \cdot (1 + \alpha_\tau). \quad (61)$$

Unfortunately the dependence of α_τ on the shape of the APDP prevents any further specification without the limitation to a specific type of decay. From a generic point of view, some facts are apparent from (60) and (61): Obviously, $\tau_{\text{RMS},f}$ is always larger than $\tau_{\text{RMS},g}$ and $\tau_{\text{RMS},h}$, with an additional factor $1 + \alpha_\tau$ for fully correlated constituent channels. Moreover, $\tau_{\text{RMS},f}$ is dominated by the channel with the higher RMS delay spread due to the geometric sum.

C. Parameter α_τ for Exponential APDPs

For exponential APDPs, the factor α_τ is derived by a rather lengthy, but straightforward derivation from (37) and (38) using the above definitions. For full correlation and thus $K_{\text{LOS},g} = K_{\text{LOS},h}$, we obtain

$$\begin{aligned} \alpha_{\tau,\text{exp.}} &= \frac{K_{\text{LOS},g}^2 \cdot (K_{\text{LOS},g}^2 \cdot (2K_{\text{LOS},g} + 5) - 2)}{(1 + 2K_{\text{LOS},g}) \cdot (K_{\text{LOS},g} \cdot (K_{\text{LOS},g} + 4) + 2)^2} \\ &\approx \frac{K_{\text{LOS},g}}{10 + K_{\text{LOS},g}}. \end{aligned} \quad (62)$$

A comparison between the full formula and the approximation for $\alpha_{\tau,\text{exp.}}$ is shown in Fig. 4. Following this result, correlation between the constituent channels can be ignored as long as K_{LOS} of the individual channels is below 0 dB. For higher K-factors, the correlation term has to be considered. The

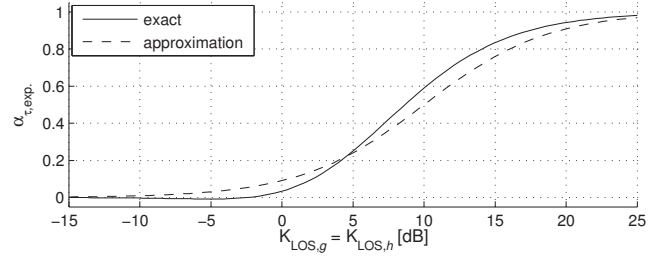


Fig. 4. Correlation factor α_τ in the RMS delay spread approximation for exponentially decaying constituent channels.

approximate version should be sufficiently accurate in these cases (roughly $\pm 5\%$). Hence

$$\alpha_{\tau,\text{exp.}} \approx \begin{cases} 0 & g(\tau) \text{ and } h(\tau) \text{ uncorr.} \\ \frac{K_{\text{LOS},g}}{10 + K_{\text{LOS},g}} & g(\tau) \text{ and } h(\tau) \text{ identical} \end{cases}. \quad (63)$$

VI. AVERAGE EXCESS DELAY

The average excess delay is the first moment of the normalized APDP, cf. (51). As such, and following the same analogy to statistics as for the RMS delay spread, the backscatter parameter for uncorrelated constituent channels can be calculated via

$$\tau_{\text{AVG},f,\text{uncorr.}} = \tau_{\text{AVG},g} + \tau_{\text{AVG},h} \quad (64)$$

independent of the type of decay. Naturally, (64) can also be derived for specific types of APDPs: Calculating (51) for exponential APDPs (35), (36) and substituting (39)–(41) for ρ , Π , and γ leads to same result,

$$\begin{aligned} \tau_{\text{AVG},f,\text{uncorr.,exp.}} &= \frac{\tau_{\text{RMS},g}}{\sqrt{1 + 2K_{\text{LOS},g}}} + \frac{\tau_{\text{RMS},h}}{\sqrt{1 + 2K_{\text{LOS},h}}} \\ &= \tau_{\text{AVG},g} + \tau_{\text{AVG},h}. \end{aligned} \quad (65)$$

For correlated channels with high K-factors and deterministic LOS amplitudes though, the average excess delay of the backscatter channel depends on the shapes of the individual-channels' APDPs. This conclusion can be reached following the same reasoning as for the RMS delay spread above. Again solving (51) for exponential APDPs, but this time doubling the NLOS power (see Section V-B), we obtain

$$\tau_{\text{AVG},f,\text{corr.,exp.}} = \tau_{\text{AVG},f,\text{uncorr.}} \cdot \left(1 + \frac{K_{\text{LOS},g}^2}{2 + 4K_{\text{LOS},g} + K_{\text{LOS},g}^2} \right) \quad (66)$$

with $K_{\text{LOS},g} = K_{\text{LOS},h}$ for identical channels with exponential decays.

VII. VALIDATION FOR EXPONENTIAL APDPs AND DISCUSSION OF ROBUSTNESS TO NON-EXPONENTIAL MULTIPATH DECAYS

Fig. 5 shows a comparison between the backscatter parameters and their respective single-channel approximations for simulated ensembles of CIRs following exponential APDPs. The simulations cover a range of -20 through 20 dB and 3 to 50 ns for the single-channel K-factor and RMS delay

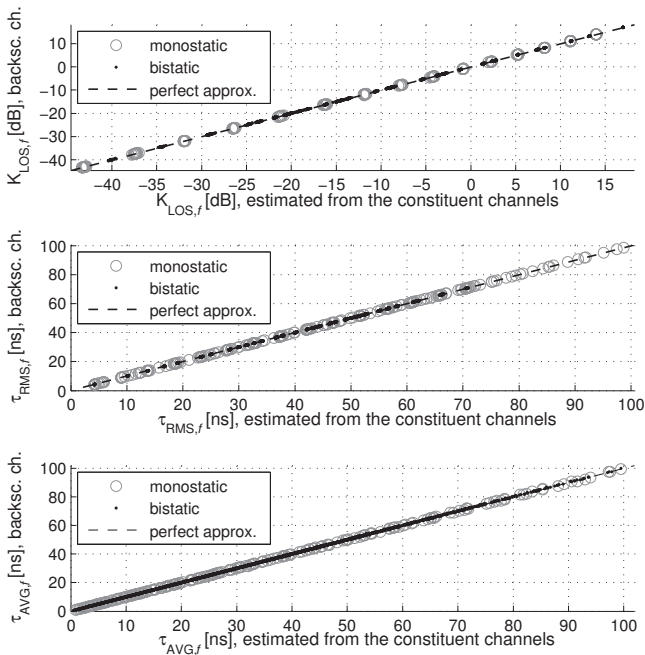


Fig. 5. Comparison between approximation and true backscatter parameter for simulated exponential PDPs. Shown are K-factor (K_{LOS}), RMS delay spread (τ_{RMS}), and average excess delay (τ_{AVG}).

spread, respectively. The results in Fig. 5 were generated using ensemble averages over 100 instantaneous PDPs for each combination of $K_{\text{LOS},g}$, $K_{\text{LOS},h}$, $\tau_{\text{RMS},g}$, and $\tau_{\text{RMS},h}$. Approximations are based on (47) and (48) for K_{LOS} , (60) and the exact version of (62) for τ_{RMS} , and (64) and (66) for the average excess delay, τ_{AVG} .

The single-channel approximation can be expected to match the true backscatter parameters perfectly for exponential APDPs. Fig. 5 reflects and confirms this expectation: All markers are on the dashed line, which marks a perfect match between approximation and true parameter. This validates the approximation formulas for exponentially decaying channels. A more thorough analysis can be found in [1].

The assumption of exponential APDPs for indoor environments is of course a simplification. In reality, clusters will be an issue [24], but also non-exponential decays, especially in industrial environments with large metal reflectors [10], [13]. Moreover, even if the average PDP is exponential, each instantaneous PDP has an arbitrary shape. It is thus important that the approximations are robust to non-exponential APDPs and that they are unbiased when used for instantaneous PDPs. This robustness is discussed below.

The derivations in Section II do not assume a specific type of decay. All results in this section are thus valid for all types of APDPs. This includes the doubling for NLOS power for fully correlated constituent channels, see (27). Also the derivations leading to the final formula for the backscatter K-factor, (47), are independent of the type of multipath decay. The approximation for $K_{\text{LOS},f}$ is thus valid for all types of wireless channels. The same is true for the backscatter RMS delay spread for uncorrelated channels, (52), and also for the

corresponding average excess delay, (64).

In addition, the equations for $\tau_{\text{RMS},f}$ and $\tau_{\text{AVG},f}$ with correlated constituent channels, (60), (63), and (66) also work for non-exponential APDPs with relatively low K-factors. This is demonstrated in Section VIII, where the formulas are used for measured channels with non-exponential decays.

VIII. MEASUREMENT RESULTS

In order to fully validate the above derivations, we compare the single-channel-based approximations to the true backscatter parameters for measured channels.

The used measurements were taken in a UHF RFID warehouse portal with metal backplanes in an industrial environment, see [10], [11]. Portal setup and antenna gain patterns resembled a typical UHF RFID portal, and the channels were recorded in a frequency range of 0.5 through 1.5 GHz [11]. The tag-antennas were mounted on a pallet containing liquids and metal. This environment is characterized by intense and very variable multipath propagation with strong deterministic reflections [10]. The measurements cover exponential and non-exponential APDPs, LOS and NLOS scenarios, channels with heavily correlated components, as well as channels where the LOS component is influenced by spatially close reflections. See [10] for a full analysis of the measurements w.r.t. ranging and localization.

Comparisons between the constituent-channel-based approximations and the corresponding parameters directly estimated from the backscatter channel are shown in Figs. 6 through 8. The parameters here are estimated from instantaneous PDPs. As a consequence, each individual estimate is a random variable, which explains the “noise” in the plots. For an unbiased approximation, the results are clustered around the 45° line, where the constituent-channel-based estimates and the true backscatter parameter are identical. This has been marked as dashed line in all plots. Class averages² are shown as reference for the reader.

The constituent-channel-based estimates generally follow the true backscatter parameters, i.e., the backscatter parameters can be approximated quite well from the single-channel estimates. The approximations use (47) and (48) for K_{LOS} , (60) and (63) for τ_{RMS} , and (64) and (66) for τ_{AVG} . Note that (63) and (66) work well for these largely non-exponential APDPs (cf. [10]), even though they have been calculated specifically for exponential decays.

The slight bias for the monostatic case in Fig. 6, especially for medium to low K-factors, is caused by indirect physical paths that have been mapped to the LOS component. Because the approximation assumes $\alpha_K = 1$, the estimate of $K_{\text{LOS},f}$ from the constituent channels is slightly too low in these cases. Finally, the outliers in Fig. 6 for very low K-factors are created by false-positives in the LOS detection. If the LOS is too weak to be detected, which is increasingly the case for very low K_{LOS} , the detection locks onto the next higher component, thus leading to an almost arbitrary positive error for the backscatter K-factor. RMS delay spread and average

²Averages for ranges of the abscissae, similar to a histogram calculation.

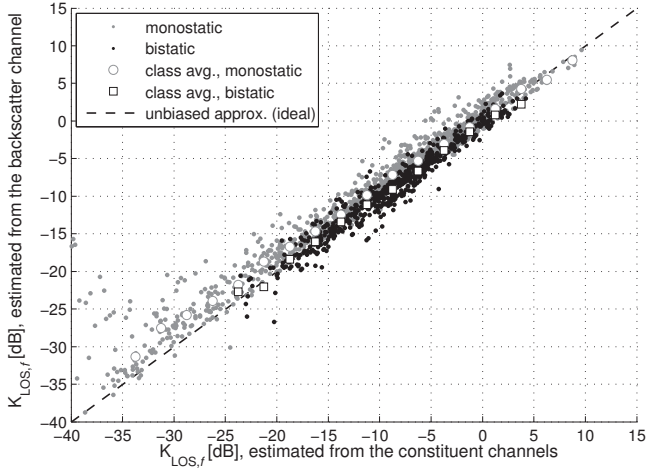


Fig. 6. Approximation of the backscatter K-factor w.r.t. LOS for measured power-delay-profiles. Estimates are based on instantaneous PDPs and assume $\alpha_K = 1$ for the monostatic case.

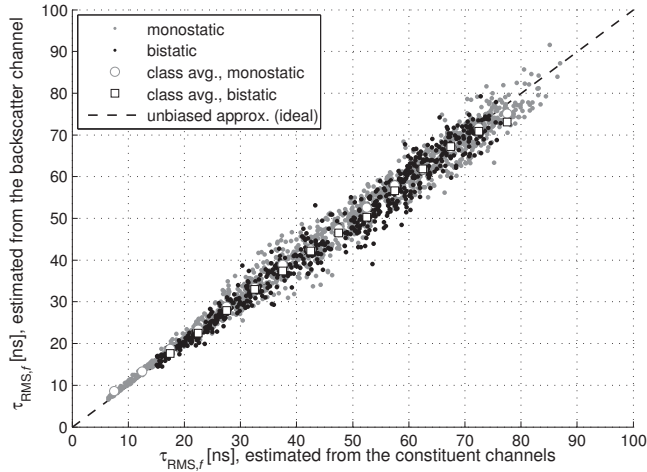


Fig. 7. Approximation of the backscatter RMS delay spread for measured power-delay-profiles. Estimates are based on instantaneous PDPs and use the simplified formula for α_τ with exponentially decaying channels, (63).

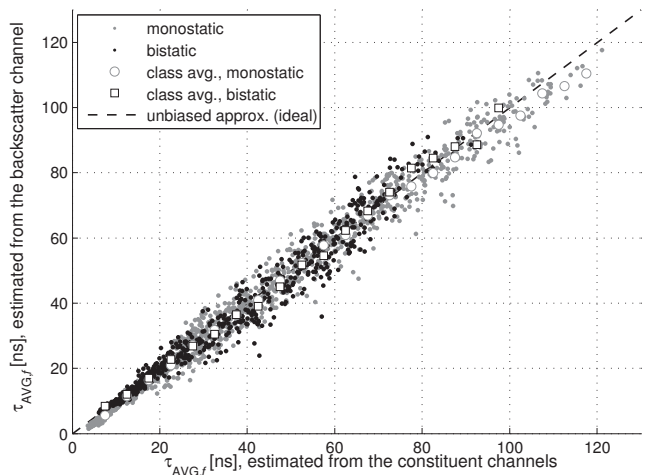


Fig. 8. Approximation of the backscatter average excess delay for measured power-delay-profiles. Estimates are based on instantaneous PDPs and use the formulas for exponentially decaying channels, (66), for the monostatic setup.

delay, on the other hand, are more robust against such errors, hence no such outliers are present in Figs. 7 and 8.

IX. CONCLUSION

A method to compute wideband parameters of wireless backscatter radio channels from the shape parameters of the constituent channel pair was presented. Expressions for the K-factor w.r.t. the LOS path, the RMS delay spread, and the average excess delay of the backscatter channel based on the individual channels' parameters are given. The presented approximations are valid independent of the actual shape of the average power-delay-profile (APDP), with exceptions for fully correlated channels with dominant LOS components. These exceptions are discussed in detail in the paper. It was also shown that the uncorrelated scattering (US) assumption holds for the backscatter channel if both individual channels are US, independent of channel correlation and for all types of APDPs.

As anticipated, the backscatter channel always has a considerably lower K-factor and considerably higher delay spreads than both individual channels. For the K-factor, this is especially true for constituent channels with weak LOS ($K_{LOS} < 0$ dB). All parameters are dominated by the most dispersive constituent channel, i.e., the channel with the lowest K-factor and the highest delay spread.

It was shown that full correlation between up- and downlink channel doubles the NLOS energy compared to uncorrelated constituent channels. Correlation thus additionally decreases the K-factor and increases the delay spread of the backscatter channel.

The presented results have been verified based on simulated and measured indoor channel impulse responses. Although the shape parameters are defined for the average PDP, the presented methods can be readily applied to non-averaged, i.e., instantaneous PDPs, as shown in Figs. 6 through 8.

APPENDIX

A. Uncorrelated Scattering of the Backscatter Channel

It stands to reason that the uncorrelated scattering (US) assumption does not hold for the combined backscatter channel because of the convolution operation, even if the individual channels are US.

Uncorrelated scattering implies uncorrelatedness between the individual paths of a channel impulse response, i.e., the covariance between different taps has to be zero.

$$\text{cov}\{f_i, f_j\} = \text{E}\{f_i f_j^*\} - \text{E}\{f_i\} \text{E}\{f_j^*\} \stackrel{!}{=} 0 \quad \forall i \neq j. \quad (67)$$

The NLOS part of the backscatter CIR was derived in Section II, (12). For convenience, we will repeat this result here:

$$\tilde{\mathbf{f}} = g_0 \tilde{\mathbf{h}} + h_0 \tilde{\mathbf{g}} + \tilde{\mathbf{H}} \tilde{\mathbf{g}}. \quad (68)$$

Clearly, the first two terms in (68) do not create any correlation between the taps of $\tilde{\mathbf{f}}$, because $\tilde{\mathbf{g}}$ and $\tilde{\mathbf{h}}$ have uncorrelated elements. The last term, on the other hand, is the convolution

of $\tilde{\mathbf{g}}$ and $\tilde{\mathbf{h}}$, which might lead to correlation. The structure of this term is

$$\tilde{\mathbf{H}}\tilde{\mathbf{g}} = \begin{bmatrix} h_1 & 0 & 0 & \cdots \\ h_2 & h_1 & 0 & \cdots \\ h_3 & h_2 & h_1 & \cdots \\ \vdots & \vdots & \vdots & \ddots \end{bmatrix} \cdot \begin{bmatrix} g_1 \\ g_2 \\ g_3 \\ \vdots \end{bmatrix} = \begin{bmatrix} g_1 h_1 \\ g_1 h_2 + g_2 h_1 \\ g_1 h_3 + g_2 h_2 + g_3 h_1 \\ \vdots \end{bmatrix} \quad (69)$$

It can easily be shown that

$$\text{cov}\left\{\sum_i x_i, \sum_j y_j\right\} = \sum_i \sum_j \text{cov}\{x_i, y_j\} \quad (70)$$

where x_i and y_j are arbitrary random variables. Inserting the elements of $\tilde{\mathbf{H}}\tilde{\mathbf{g}}$ into (67) and using (70), we end up with covariances between individual terms

$$\text{cov}\{g_i h_k, g_j h_l\} = \text{E}\{g_i h_k g_j^* h_l^*\} - \text{E}\{g_i h_k\} \cdot \text{E}\{g_j^* h_l^*\}, \quad (71)$$

for example

$$\begin{aligned} & \text{cov}\{g_1 h_1, g_1 h_2 + g_2 h_1\} \\ &= \text{cov}\{g_1 h_1, g_1 h_2\} + \text{cov}\{g_1 h_1, g_2 h_1\} \\ &= \text{E}\{g_1 h_1 g_1^* h_2^*\} - \text{E}\{g_1 h_1\} \cdot \text{E}\{g_1^* h_2^*\} \\ & \quad + \text{E}\{g_1 h_1 g_2^* h_1^*\} - \text{E}\{g_1 h_1\} \cdot \text{E}\{g_2^* h_1^*\}. \end{aligned} \quad (72)$$

The second-order terms in (71) are zero for all circular symmetric complex random variables

$$\text{E}\{g_i h_k\} = 0 \quad \forall i, k. \quad (73)$$

and the fourth-order term can be split into second-order terms using (18)

$$\begin{aligned} \text{E}\{g_i h_k g_j^* h_l^*\} &= \text{E}\{g_i g_j^* h_k h_l^*\} \\ &= \text{E}\{g_i g_j^*\} \cdot \text{E}\{h_k h_l^*\} + \text{E}\{g_i h_l^*\} \cdot \text{E}\{h_k g_j^*\}. \end{aligned} \quad (74)$$

The first summand here is zero due to uncorrelated scattering of $\tilde{\mathbf{g}}$ and $\tilde{\mathbf{h}}$, except for the combination $i=j$ and $k=l$. The second summand is always zero for uncorrelated channels, and only nonzero for correlated channels if $i=l$ and $j=k$, cf. (6). Looking at the structure of (69), it is clear that neither combination of indices is present in any cross-covariance. Hence

$$\text{cov}\{g_i h_j, g_k h_l\} = 0 \quad (75)$$

for all combinations between different elements of $\tilde{\mathbf{H}}\tilde{\mathbf{g}}$.

The cross-covariances between the first two terms in (68) and $\tilde{\mathbf{H}}\tilde{\mathbf{g}}$ contain the LOS components of the constituent channels, g_0 and h_0 . These are non-Gaussian random variables³, hence splitting the terms using (18) is not possible. We will instead extract the deterministic amplitude from the expected value. The uniform phase is then absorbed by the remaining ZMCSCG variables, cf. (24). This results in

$$\begin{aligned} \text{cov}\{g_0 h_k, g_j h_l\} \\ = |g_0| \cdot \text{E}\{h_k g_j^* h_l^*\} - |g_0| \cdot \text{E}\{h_k\} \cdot \text{E}\{g_j^* h_l^*\} = 0 \end{aligned} \quad (76)$$

³Any Gaussian fraction in an LOS component is independent from the constant-amplitude part and can thus be modeled as an additive variable (see discussions at the end of Section II). Consequently, (75) applies.

and

$$\begin{aligned} & \text{cov}\{h_0 g_k, g_j h_l\} \\ &= |h_0| \cdot \text{E}\{g_k g_j^* h_l^*\} - |h_0| \cdot \text{E}\{g_k\} \cdot \text{E}\{g_j^* h_l^*\} = 0. \end{aligned} \quad (77)$$

Clearly, the first-order moments here are zero, and it is straightforward to show that also the third-order moments are zero due to the zero-mean properties of the variables. We can thus finally conclude that

$$\text{cov}\{f_i, f_j\} = 0 \quad \forall i \neq j \quad i, j = 1, 2, 3, \dots \quad (78)$$

This leaves possible correlation between the LOS part, $g_0 h_0$ (cf. (7)), and NLOS-components. Such correlations can only be present for terms that either contain g_0 or h_0 , and thus only for the first two terms of (68). Applying (67), and extracting the constant amplitudes of the LOS parts, we obtain for all $i > 0$

$$\text{cov}\{g_0 h_0, g_0 h_i\} = |g_0|^2 |h_0| \cdot \text{E}\{h_i^*\} - |g_0|^2 |h_0| \text{E}\{h_i^*\} = 0 \quad (79)$$

and, following the same reasoning,

$$\text{cov}\{g_0 h_0, h_0 g_i\} = 0 \quad \forall i > 0. \quad (80)$$

Combining (78), (79), and (80) then leads to

$$\text{cov}\{f_i, f_j\} = 0 \quad \forall i \neq j, \quad (81)$$

which proves the uncorrelated scattering assumption for pin-hole channels with correlated or uncorrelated constituent channels.

REFERENCES

- [1] D. Armitz, U. Muehlmann, and K. Witrals, "Wideband characterization of backscatter channels," in *Proc. Europ. Wireless Conf.*, Vienna, Austria, Apr. 2011. [Online]. Available: <http://www.spssc.tugraz.at/publications>
- [2] J. D. Griffin and G. D. Durgin, "Gains for RF tags using multiple antennas," *IEEE Trans. Antennas Propag.*, vol. 56, no. 2, pp. 563–570, 2008.
- [3] T. Taniguchi, Y. Karasawa, and M. Tsuruta, "An analysis method of double fading MIMO channels including LOS environments," in *Proc. IEEE 19th Int. Symp. Personal, Indoor and Mobile Radio Communications PIMRC 2008*, 2008, pp. 1–5.
- [4] J. D. Griffin and G. D. Durgin, "Link envelope correlation in the backscatter channel," *IEEE Commun. Lett.*, vol. 11, no. 9, pp. 735–737, 2007.
- [5] D. Kim, M. A. Ingram, and J. Smith, W. W., "Measurements of small-scale fading and path loss for long range RF tags," *IEEE Trans. Antennas Propag.*, vol. 51, no. 8, pp. 1740–1749, 2003.
- [6] P. L. Kafle, A. Intarapanich, A. B. Sesay, J. McRory, and R. J. Davies, "Spatial correlation and capacity measurements for wideband MIMO channels in indoor office environment," *IEEE Trans. Wireless Commun.*, vol. 7, no. 5, pp. 1560–1571, 2008.
- [7] P. Almers, F. Tufvesson, and A. F. Molisch, "Keyhole effect in MIMO wireless channels: Measurements and theory," *IEEE Trans. Wireless Commun.*, vol. 5, no. 12, pp. 3596–3604, 2006.
- [8] A. Paulraj, R. Nabar, and D. Gore, *Introduction to Space-Time Wireless Communications*. Cambridge University Press, 2003.
- [9] X. Yin, Y. Zhou, and F. Liu, "A generic wideband channel model for keyhole propagation scenarios and experimental evaluation," in *Proc. Fourth Int. Conf. Communications and Networking in China ChinaCOM 2009*, 2009, pp. 1–5.
- [10] D. Armitz, U. Muehlmann, and K. Witrals, "Wideband characterization and modeling of UHF RFID channels for ranging and localization," submitted for publication. [Online]. Available: <http://www.spssc.tugraz.at/publications>

- [11] D. Arnitz, G. Adamiuk, U. Muehlmann, and K. Witrisal, "UWB channel sounding for ranging and positioning in passive UHF RFID," in *11th COST2100 MCM*, Aalborg, Denmark, Jun. 2010. [Online]. Available: <http://www.spsc.tugraz.at/publications>
- [12] M. K. Awad, K. T. Wong, and Z. bin Li, "An integrated overview of the open literature's empirical data on the indoor radiowave channel's delay properties," *IEEE Trans. Antennas Propag.*, vol. 56, no. 5, pp. 1451–1468, 2008.
- [13] J. Karedal, S. Wyne, P. Almers, F. Tufvesson, and A. F. Molisch, "A measurement-based statistical model for industrial ultra-wideband channels," *IEEE Trans. Wireless Commun.*, vol. 6, no. 8, pp. 3028–3037, 2007.
- [14] M. S. Varela and M. G. Sanchez, "RMS delay and coherence bandwidth measurements in indoor radio channels in the UHF band," *IEEE Trans. Veh. Technol.*, vol. 50, no. 2, pp. 515–525, 2001.
- [15] A. Molisch, *Wireless Communications*. John Wiley & Sons, 2005.
- [16] H. Cramér, *Mathematical Methods of Statistics*. Princeton University Press, 1946.
- [17] R. Kattenbach, "Statistical modeling of small-scale fading in directional radio channels," *IEEE J. Sel. Areas Commun.*, vol. 20, no. 3, pp. 584–592, 2002.
- [18] P. Bello, "Characterization of randomly time-variant linear channels," *IEEE Transactions on Communications Systems*, vol. 11, no. 4, pp. 360–393, 1963.
- [19] K. S. Miller, *Complex Stochastic Processes*. Addison-Wesley, 1974.
- [20] A. Papoulis and S. U. Pillai, *Probability, Random Variables, and Stochastic Processes*, 4th ed. McGraw-Hill, 2002.
- [21] L. J. Greenstein, S. S. Ghassemzadeh, S.-C. Hong, and V. Tarokh, "Comparison study of UWB indoor channel models," *IEEE Trans. Wireless Commun.*, vol. 6, no. 1, pp. 128–135, 2007.
- [22] D. Cassioli, M. Z. Win, and A. F. Molisch, "The ultra-wide bandwidth indoor channel: from statistical model to simulations," *IEEE J. Sel. Areas Commun.*, vol. 20, no. 6, pp. 1247–1257, 2002.
- [23] K. Witrisal, Y.-H. Kim, and R. Prasad, "A new method to measure parameters of frequency-selective radio channels using power measurements," *IEEE Trans. Commun.*, vol. 49, no. 10, pp. 1788–1800, Oct. 2001.
- [24] A. Saleh and R. Valenzuela, "A statistical model for indoor multipath propagation," *IEEE J. Sel. Areas Commun.*, vol. 5, no. 2, pp. 128–137, 1987.

Wideband Characterization of Backscatter Channels

Daniel Arnitz*, Ulrich Muehlmann**, and Klaus Witrisal*

* Signal Processing and Speech Communication Laboratory, Graz University of Technology, Austria
{daniel.arnitz, witrisal}@tugraz.at

** NXP Semiconductors, Gratkorn, Austria
ulrich.muehlmann@nxp.com

Abstract—The wireless channel of backscatter radio systems is a two-way pinhole channel, created by the concatenation of two standard wireless channels. Pinhole channels cause higher attenuation and deeper fades than common wireless channels.

Passive ultra-high frequency radio-frequency identification (UHF RFID) is such a backscatter radio system, with the backscattering tag acting as pinhole. While the effects of this type of channel are well-known in terms of fading statistics, the impact of the pinhole channel on wideband parameters is unknown.

We present a method to calculate wideband backscatter channel parameters from the parameters of the constituent channels to and from the pinhole, with a focus on characteristics that are vital for narrowband and wideband ranging. The approximations are verified by simulations and by measurements in a UHF RFID warehouse portal.

I. INTRODUCTION

Pinhole channels are created by the concatenation of the channel from the transmitter to the pinhole and the channel from the pinhole to the receiver. In (semi-)passive ultra-high frequency radio-frequency identification (UHF RFID), a prime example for backscatter radio systems, the pinhole is formed by the backscattering tag, as illustrated in Fig. 1. The overall backscatter channel between transmitter (TX) and receiver (RX) at the reader is composed of the two individual channels to and from the tag. Both constituent channels are multipath radio channels. Pinhole (a.k.a. keyhole, dyadic, double-fading, or relay) channels are quite well-understood in terms of fading statistics for narrowband signals [1]–[4] and channel capacity for multi-input multi-output (MIMO) systems [5]–[7]. Even though channel capacity and fading statistics are fully sufficient to analyze the performance of communications, they are insufficient for the analysis of narrowband and wideband indoor localization systems (with the exception of receive-power based methods). We will thus concentrate on a more general description of the channel, the power-delay-profile (PDP), which is essentially the squared magnitude of the channel impulse response (CIR). The authors of [8] present an expression for the PDP of pinhole channels, but limited to orthogonal constituent channels. Moreover, no further parameterization of the pinhole-PDP is provided.

We present a closed-form expression for the PDP of typical indoor backscatter channels based on the PDPs of the constituent (point-to-point) channels, both for correlated and for uncorrelated point-to-point channels. We also present approximations for common wideband channel parameters, such

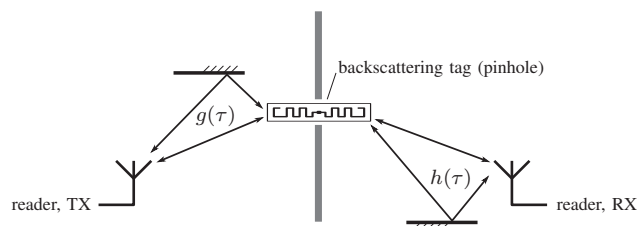


Fig. 1. Illustration of the pinhole effect in (semi)passive UHF RFID systems. In reality, each channel is composed of up to thousands of relevant paths.

as K-factor and root-mean-square (RMS) delay spread. These approximations are valid for exponential and non-exponential PDPs in line-of-sight (LOS) and non-line-of-sight (NLOS) scenarios, correlated and uncorrelated constituent channels, and also for predominantly deterministic channels, as shown below.

The paper is organized as follows: Section II introduces the notation, defines the channel (model) parameters, and discusses their influence on ranging. The following Section III contains closed-form expressions for the channel parameters of the backscatter channel based on the point-to-point channel parameters. These expressions are verified in Section IV using simulated and measured indoor wireless channels.

II. BASICS AND BACKGROUND INFORMATION

A. Wireless Channels

Like any linear system, wireless channels can be represented by their impulse response, the CIR. Wireless CIRs are typically modeled in a random fashion in order to account for the typically unknown and time-variant environment. Similar to the power spectral density for random signals, the power delay profile (PDP) is used to describe the frequency-selective random channel. The PDP (a.k.a. delay power spectrum or multipath intensity profile) is essentially defined as the autocorrelation function of the CIR, and can be estimated by averaging squared CIRs (averaged power delay profile, APDP). More details along with necessary requirements and limitations can for example be found in [9], [10] or textbooks such as [7], [11].

The first arriving component of a wireless CIR corresponds to the direct (line-of-sight, LOS) path and all following components to indirect (reflected, non-line-of-sight, NLOS) paths.

In Fig. 1 the CIR of the channel from the transmitter (TX) to the tag, for example, is denoted by $g(\tau)$, where τ is the propagation delay. For notational simplicity, we will assume that the LOS component is at a delay of $\tau_{\text{LOS}} = 0$ for all channels. This has no influence on the results in this paper, as all analyzed channel parameters are shift-invariant¹. Also note that all CIRs are zero for $\tau < \tau_{\text{LOS}}$ and thus $\tau < 0$, because the LOS is per definition the first nonzero component.

From the PDP, denoted by $S(\tau)$ below, we can calculate several measures that characterize the wireless channel. The power ratio of the direct path to all indirect paths is of vital importance for localization, as it quantifies the influence of the direct path on the CIR. This ratio is provided by the K-factor w.r.t. the LOS path,

$$K_{\text{LOS}} = \frac{P_{\text{LOS}}}{P_{\text{NLOS}}} = \frac{P_{\text{LOS}}}{\int_0^\infty S(\tau) d\tau - P_{\text{LOS}}}, \quad (1)$$

where P_{LOS} and P_{NLOS} are line-of-sight and non-line-of-sight power, respectively. Note that this is not necessarily identical to the definition of the Ricean K-factor, which uses the strongest path instead of the direct path. A second measure relevant for localization is the root-mean-square (RMS) delay spread,

$$\tau_{\text{RMS}} = \sqrt{\frac{\int_0^\infty \tau^2 S(\tau) d\tau}{\int_0^\infty S(\tau) d\tau} - \left(\frac{\int_0^\infty \tau S(\tau) d\tau}{\int_0^\infty S(\tau) d\tau} \right)^2}, \quad (2)$$

which specifies the decay of the CIR over delay.

Although these channel parameters are defined based on the PDP (a fully deterministic function), they can also be calculated from each individual squared CIR, which is often called ‘‘instantaneous PDP’’. Note though, that the squared CIR is a random process, hence all parameters derived from instantaneous PDPs are random variables.

B. Effects of Multipath Propagation on Ranging Errors

The impact of multipath propagation on RF-based ranging (i.e., distance estimation) systems depends on the signal bandwidth and the properties of the channel. Limiting the bandwidth leads to a smoothed CIR due to the uncertainty relation between time- and frequency-domain representations. For narrowband systems, the entire CIR collapses to a single complex gain factor. If the direct path is dominant in the CIR, i.e., the instantaneous K_{LOS} is large, the direct path is also dominant in the complex gain factor, and narrowband ranging will give accurate results. For low K_{LOS} , the gain factor is mainly determined by indirect and thus purely random paths. As a direct consequence, narrowband distance estimates will have a high standard deviation. Moreover, depending on τ_{RMS} and the shape of the PDP, the dominant NLOS results in a bias of the gain factor towards indirect paths, and thus also in a biased distance estimate. Similar considerations apply to all

¹The K-factor is a simple power ratio and does thus not depend on the delay axis at all. The RMS delay spread is a central moment, hence the average time shift is irrelevant.

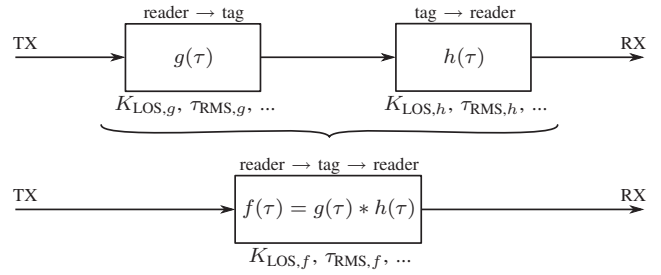


Fig. 2. Combination of individual channels reader→tag (downlink) and tag→reader (uplink) to the backscatter channel reader→tag→reader.

systems that are unable to isolate the LOS component. The PDP, along with shape parameters such as K_{LOS} and τ_{RMS} , can be used to calculate the expected distance errors of such ranging systems (bias and std. deviation). However, if the LOS component is correctly identified and extracted, the shape of the PDP loses its influence on the ranging error. This usually requires a large signal bandwidth, though.

Passive UHF RFID is one of the most challenging scenarios for backscatter-based localization. The system is typically used indoors and in industrial or industrial-like environments [12]–[14], with massive reflections close to the backscattering tag. These features, along with the pinhole properties of the channel, create a severe multipath environment, where the direct path is rarely dominant and very large bandwidths are required to properly resolve the closely spaced components [12], [13]. Conventional wideband approaches such as multi-carrier or frequency-modulated continuous-wave radar (e.g., [15], [16]) suffer from biased and high-variance estimates in such environments [12], [17]. Ultra-wideband methods such as [18] are able to correctly identify the LOS path, but suffer from the massive channel attenuation due to the backscatter nature and the low signal-to-self-interference ratios, cf. [12].

C. Pinhole and Backscatter Wireless Channels

As mentioned in the introduction and illustrated in Figs. 1 and 2, the backscatter channel is the concatenation of two wireless channels and as such always a pinhole channel. In the terminology of RFID, the channel from the reader to the tag is called ‘‘downlink channel’’, while the channel from the tag to the reader is called ‘‘uplink channel’’, cf. [19]. Up- and downlink channel are identical for monostatic setups, where the reader uses only one antenna for simultaneous transmission and reception. For bistatic reader setups, on the other hand, they can be (almost) independent, since TX- and RX-antenna are spatially distinct, cf. [20].

The individual channels to and from the pinhole, represented by their respective CIRs $g(\tau)$ and $h(\tau)$, each have their own set of channel parameters (K_{LOS} , τ_{RMS} , ...). It is straightforward to see from Fig. 2 that the backscatter CIR $f(\tau)$ can be calculated by the convolution of $g(\tau)$ and $h(\tau)$. The connection between the channel parameters of the backscatter channel and their counterparts of the individual channels, on the other hand, is less obvious. Apart from the mathematical point of

view, which can be found below, we can make some basic observations regarding the backscatter channel. For this, we refer to a channel with low K_{LOS} and high τ_{RMS} as a “bad” channel, while a channel with high K_{LOS} and/or low τ_{RMS} is “better” in comparison, i.e., a “good” channel.

- The combined channel is always worse than both individual channels. This follows directly from the convolution, which results in a longer channel impulse response and dispersed peaks (also affecting the LOS peak).
- Correlation between up- and downlink channel has an adverse effect on the backscatter channel, because coherent combining of the random NLOS-parts increases the NLOS energy².
- The statistics of the worse channel dominate the statistics of the backscatter channel. Hence in bistatic setups, both reader antennas need to have a clear line-of-sight to the tag in order to obtain a good backscatter channel. Also this fact can be inferred from the convolution operation: The convolution of an ideal CIR w.r.t. ranging (a dirac) with any dispersive CIR, for example, results in the dispersive (i.e. bad) one for the overall channel.

III. APPROXIMATION FORMULAS

A. Power-Delay-Profile

It has been shown in [8] that the PDP of a pinhole channel can be obtained by a convolution of the PDPs of up- and downlink channel, provided that these channels are uncorrelated.

By separating the power-delay-profiles of the channels to and from the tag, $S_g(\tau)$ and $S_h(\tau)$, into LOS and NLOS parts

$$S_g(\tau) = S_{g,\text{LOS}} \cdot \delta(\tau) + S_{g,\text{NLOS}}(\tau) \cdot \sigma(\tau) \quad (3)$$

$$S_h(\tau) = S_{h,\text{LOS}} \cdot \delta(\tau) + S_{h,\text{NLOS}}(\tau) \cdot \sigma(\tau) \quad (4)$$

the convolution of the PDPs can be written as

$$\begin{aligned} S_{f,\text{uncorr}}(\tau) &= S_g(\tau) * S_h(\tau) = S_{g,\text{LOS}} \cdot S_{h,\text{LOS}} \cdot \delta(\tau) \\ &+ \sigma(\tau) \cdot [S_{g,\text{LOS}} \cdot S_{h,\text{NLOS}}(\tau) + S_{h,\text{LOS}} \cdot S_{g,\text{NLOS}}(\tau) \\ &+ S_{g,\text{NLOS}}(\tau) * S_{h,\text{NLOS}}(\tau)]. \end{aligned} \quad (5)$$

where $*$ denotes the convolution, $\delta(\tau)$ is the Dirac delta, and $\sigma(\tau)$ is the step function

$$\sigma(\tau) = \begin{cases} 1 & \tau > 0 \\ 0 & \text{otherwise} \end{cases}. \quad (6)$$

$S_{f,\text{uncorr}}(\tau)$ is the backscatter PDP for uncorrelated constituent channels, cf. [8], [21]. Splitting this PDP into LOS and NLOS parts, we obtain

$$S_{f,\text{LOS}} = S_{g,\text{LOS}} \cdot S_{h,\text{LOS}} \quad (7)$$

and

$$\begin{aligned} S_{f,\text{NLOS,uncorr}}(\tau) &= S_{g,\text{LOS}} \cdot S_{h,\text{NLOS}}(\tau) + S_{h,\text{LOS}} \cdot S_{g,\text{NLOS}}(\tau) \\ &+ S_{g,\text{NLOS}}(\tau) * S_{h,\text{NLOS}}(\tau). \end{aligned} \quad (8)$$

²An effect that can also be seen for the variance of two additive random variables.

Coherent combining of the stochastic NLOS part in case of fully correlated up- and downlink channels doubles the NLOS power without changing the shape of the NLOS part [21], hence

$$S_{f,\text{NLOS,corr}}(\tau) = 2 \cdot S_{f,\text{NLOS,uncorr}}(\tau). \quad (9)$$

Full correlation between the constituent channels also implies that their K-factors and RMS delay spreads are identical [21], i.e., $\tau_{\text{RMS},g} = \tau_{\text{RMS},h}$ and $K_{\text{LOS},g} = K_{\text{LOS},h}$.

Passive UHF RFID is typically used indoors, where the rich scattering leads to exponential PDPs (e.g., [22], [23]). For the following derivations we thus assume exponential short-range indoor PDPs for the two individual channels g and h ,

$$S_g(\tau) = \begin{cases} 0 & \tau < 0 \\ \rho_g^2 & \tau = 0 \\ \Pi_g e^{-\gamma_g \tau} & \tau > 0 \end{cases} \quad \text{and} \quad (10)$$

$$S_h(\tau) = \begin{cases} 0 & \tau < 0 \\ \rho_h^2 & \tau = 0, \\ \Pi_h e^{-\gamma_h \tau} & \tau > 0 \end{cases}, \quad (11)$$

where ρ_g^2 and ρ_h^2 are the LOS power levels of channels g and h , respectively, Π_g and Π_h are the NLOS power densities, and γ_g and γ_h are the decay constants of the channels, cf. [24].

Using these definitions, we calculate the closed-form PDP of short-range indoor backscatter channels. The LOS component of this PDP is

$$S_{f,\text{LOS}} = \rho_g^2 \rho_h^2, \quad (12)$$

and the NLOS part for uncorrelated channels is

$$\begin{aligned} S_{f,\text{NLOS,uncorr}}(\tau) &= \rho_g^2 \Pi_h e^{-\gamma_h \tau} + \rho_h^2 \Pi_g e^{-\gamma_g \tau} \\ &+ \frac{\Pi_g \Pi_h}{\gamma_g - \gamma_h} (e^{-\gamma_h \tau} - e^{-\gamma_g \tau}). \end{aligned} \quad (13)$$

The NLOS-part is multiplied by a factor of two for correlated constituent channels, see (9).

From this we will calculate K-factor and the RMS delay spread of the combined backscatter channel. Formulas linking ρ , Π , and γ with K_{LOS} and τ_{RMS} for the exponential PDPs are readily provided by [24],

$$\Pi = \frac{P_0}{K_{\text{LOS}} + 1} \gamma, \quad (14)$$

$$\gamma = \frac{1}{\tau_{\text{RMS}}} \frac{\sqrt{2K_{\text{LOS}} + 1}}{K_{\text{LOS}} + 1}, \quad (15)$$

$$\rho^2 = P_0 \frac{K_{\text{LOS}}}{K_{\text{LOS}} + 1}, \quad (16)$$

where the overall power $P_{\text{LOS}} + P_{\text{NLOS}}$ is denoted by P_0 .

B. K-Factor w.r.t. the Line-of-Sight Component

The K-factor can be directly calculated from (1) by inserting (12) and (13). Substituting (14)–(16) then leads to

$$\begin{aligned} K_{\text{LOS},f} &= \frac{S_{f,\text{LOS}}}{\int_0^\infty S_{f,\text{NLOS}}(\tau) d\tau} \\ &= \left(1 - \frac{\alpha_K}{2}\right) \cdot \frac{K_{\text{LOS},g} \cdot K_{\text{LOS},h}}{1 + K_{\text{LOS},g} + K_{\text{LOS},h}}. \end{aligned} \quad (17)$$

where the parameter $0 \leq \alpha_K \leq 1$ represents correlation between the channels g and h . Due to the doubling of the NLOS energy for correlated up- and downlink, cf. (9), we obtain

$$\alpha_K = \begin{cases} 0 & g(\tau) \text{ and } h(\tau) \text{ uncorr.} \\ 1 & g(\tau) \text{ and } h(\tau) \text{ fully corr.} \end{cases} \quad (18)$$

C. RMS Delay Spread

The RMS delay spread is calculated from the backscatter PDP via

$$\tau_{\text{RMS},f} = \sqrt{\frac{\int_0^\infty \tau^2 S_{f,\text{NLOS}}(\tau) d\tau}{S_{f,\text{LOS}} + \int_0^\infty S_{f,\text{NLOS}}(\tau) d\tau}} - \tau_{\text{AVG},f}^2, \quad (19)$$

cf. (2), where

$$\tau_{\text{AVG},f} = \frac{\int_0^\infty \tau S_{f,\text{NLOS}}(\tau) d\tau}{S_{f,\text{LOS}} + \int_0^\infty S_{f,\text{NLOS}}(\tau) d\tau} \quad (20)$$

is the average delay. By solving these equations for (12) and (13) we obtain the RMS delay spread for uncorrelated channels,

$$\tau_{\text{RMS},f,\text{uncorr.}} = \sqrt{\tau_{\text{RMS},g}^2 + \tau_{\text{RMS},h}^2}, \quad (21)$$

with (14)–(16). The same result can also be reached by using a similarity to statistics: Just like the PDPs of uncorrelated constituent channels the density functions of two added uncorrelated random variables are convolved and the variances add up. From this observation it is straightforward to see that (21) holds for arbitrary types of PDPs.

For correlated channels though, things are more complicated. Looking at the structure of (19) and (20), the doubling of NLOS-power for correlated channels, cf. (9), will lead to an imbalance in the denominators. As a consequence, the ratio between LOS- and NLOS-power—and thus K_{LOS} —has an influence on the result. Following the same derivation as for (21) with doubled NLOS-power we obtain

$$\begin{aligned} \tau_{\text{RMS},f,\text{corr.}} &= \sqrt{\frac{2 \int_0^\infty \tau^2 S_{f,\text{NLOS}}(\tau) d\tau}{S_{f,\text{LOS}} + 2 \int_0^\infty S_{f,\text{NLOS}}(\tau) d\tau}} - \dots \\ &= \tau_{\text{RMS},g} \sqrt{2 + 2\alpha_\tau} \end{aligned} \quad (22)$$

for fully correlated channels and with $\tau_{\text{RMS},g} = \tau_{\text{RMS},h}$ (full correlation). The parameter α_τ here represents the correlation and is also obtained from the above calculations,

$$\begin{aligned} \alpha_\tau &= \frac{K_{\text{LOS},g}^2 \cdot (K_{\text{LOS},g}^2 \cdot (2K_{\text{LOS},g} + 5) - 2)}{(1 + 2K_{\text{LOS},g}) \cdot (K_{\text{LOS},g} \cdot (K_{\text{LOS},g} + 4) + 2)^2} \\ &\approx \frac{K_{\text{LOS},g}}{10 + K_{\text{LOS},g}} \end{aligned} \quad (23)$$

with $K_{\text{LOS},g} = K_{\text{LOS},h}$ due to the full correlation.

While it can again be shown that (22) holds for arbitrary PDPs [21], (23) is derived specifically for exponential ones. However, the PDPs of all wireless channels have a similar shape due to the fact that they decay for increasing delay. Hence (23) is a suitable approximation even for channels with non-exponential PDPs, as can be seen from the measurement

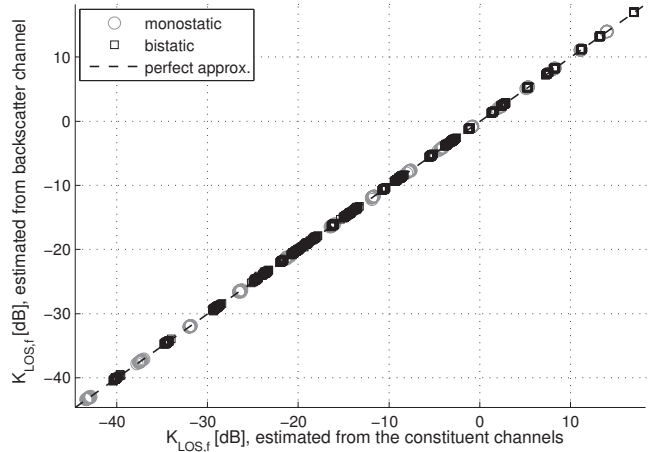


Fig. 3. Approximation of the backscatter K-factor w.r.t. LOS for simulated exponential power-delay-profiles. Estimates are based on averaged PDPs.

results in Section IV-B. Finally, α_τ vanishes for low K-factors, hence correlation between the constituent channels can be ignored if the NLOS component is dominant on the backscatter link, and the result again becomes independent of the type of PDP.

IV. VALIDATION BASED ON SIMULATIONS AND MEASUREMENTS

The above approximations are tested with simulated and measured channel impulse responses in this section. To this end, we compare the approximations based on parameters estimated from the PDPs of the constituent channels, $S_g(\tau)$ and $S_h(\tau)$, to parameters directly estimated from the backscatter PDP (channel f). Both estimates match in the ideal case, resulting in a 45° line in the plots.

The simulated channels with known expected values for all parameters are used to verify the estimates in controlled environments, while the validation with measured channel impulse responses ensures robustness in realistic propagation environments. The measurements cover exponential and non-exponential PDPs, LOS and NLOS scenarios, as well as channels where the LOS component is massively influenced by spatially close reflections.

A. Simulated Exponential Power-Delay-Profiles

The simulated random CIRs have been generated by the smallscale model of the PARIS framework [25], [26], which implements a sampled version of the exponential PDP in [24] and is thus fully defined by K_{LOS} and τ_{RMS} . K-factor and RMS delay spread in the simulations were swept from -20 to 20 dB and from 3 through 50 ns, respectively, for the average PDP of both constituent channels. This should cover most typical indoor scenarios, cf. [12], [13], [27], [28]. An ensemble of 100 instantaneous PDPs is averaged for each combination of $K_{\text{LOS},g}$, $K_{\text{LOS},h}$, $\tau_{\text{RMS},g}$, and $\tau_{\text{RMS},h}$. Some residual “noise” can thus be expected in the estimates.

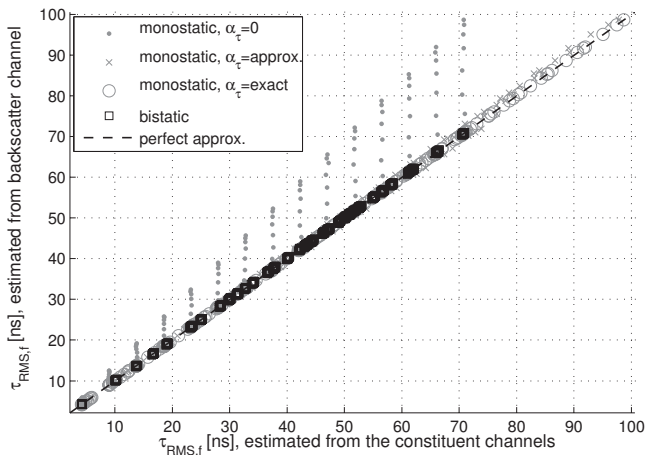


Fig. 4. Approximation of the backscatter RMS delay spread for simulated exponential power-delay-profiles. Estimates are based on averaged PDPs.

The results of this Monte-Carlo-simulation are shown in Fig. 3 for the K-Factor and Fig. 4 for the RMS delay spread. The K-factor calculated from the constituent channel parameters using (17) matches the K-factor of the combined pinhole channel throughout the simulated range, both for the monostatic (fully correlated) and the bistatic (uncorrelated) setup. The RMS delay spreads for the bistatic setup and the exact monostatic approximation according to (22) and (23) show a perfect match, too. Using the simplified formula for α_τ leads to a nonperfect but nonetheless quite good approximation of the RMS delay spread for the monostatic case. If correlation is completely ignored though ($\alpha_\tau = 0$), the approximation is increasingly off for $K_{LOS,g} = K_{LOS,h} > -3$ dB.

B. Measured Power-Delay-Profiles

The used measurements were taken in a UHF RFID warehouse portal with metal backplanes, in an industrial environment, and with directive reader antennas, see [12], [13]. The tag-antennas were mounted on a pallet containing liquids and metal. This creates an intense and very variable multipath environment with strong deterministic reflections. A photograph of this setup can be found in Fig. 5; details are presented in [12] and [13].

The channels inside the portal have a multipath decay according to a power-law, while the channels outside the portal feature an exponential decay [12]. The direct path between transmitter, tag, and receiver (backscatter channel) is blocked by the pallet for 43% of the measured channels. The measurements thus not only cover “typical” exponential PDPs and LOS scenarios, but also differently shaped delay-profiles and NLOS scenarios. Mounting the tag-antennas directly on the pallet also causes indirect (NLOS) paths to be part of the LOS component due to the necessarily limited measurement bandwidth. Moreover, multiple deterministic reflections inside the gate cause correlation within the CIRs of up- and downlink. This violates one of the basic assumptions underlying the theory behind the approximation formulas given in this paper,

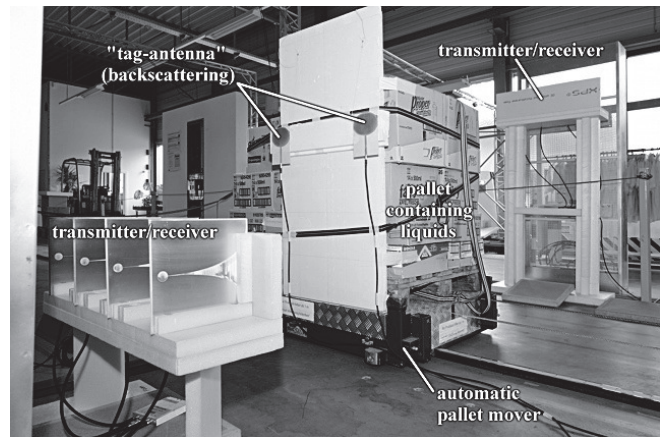


Fig. 5. Photograph of the warehouse gate with metal backplanes (directly behind the transmitter/receiver arrays) and the pallet with packed liquids/metals.

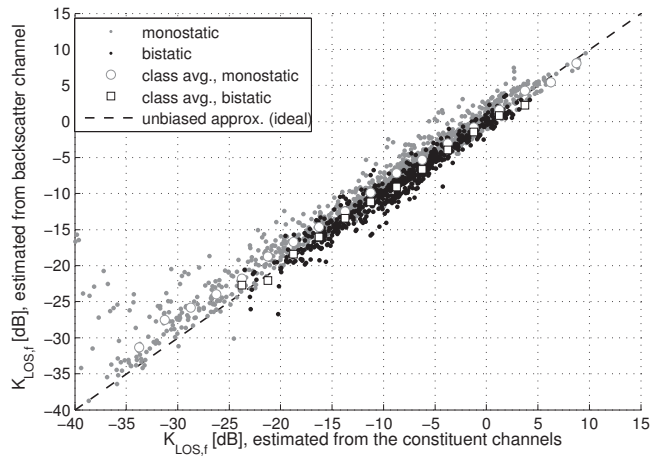


Fig. 6. Approximation of the backscatter K-factor w.r.t. LOS for measured power-delay-profiles (UHF RFID warehouse portal, metal portal, liquids/metal pallet). Estimates are based on individual (instantaneous) power-delay-profiles; averages are shown for comparison.

cf. [21]. The portal scenario is thus not only a challenging example for backscatter-based localization, but also for the approximation methods presented in this paper.

The results for the measured channels can be found in Figs. 6 and 7, respectively. Note that the noise level in these estimates is considerably higher than for the simulations in Figs. 3 and 4. This is because the simulated PDPs are averaged before estimating $K_{LOS,f}$ and $\tau_{RMS,f}$, while the measured parameters are calculated from individual (instantaneous) PDPs in order to show that the above equations can also be used as estimators for instantaneous PDPs. Averages are shown in the plots for comparison.

The backscatter channel parameters can obviously be predicted quite well from the individual ones. This includes the area inside the portal, where the PDP follows a power-law, and the area outside the portal, which features an exponential PDP, cf. [12]. The slight bias in $K_{LOS,f}$ for the monostatic

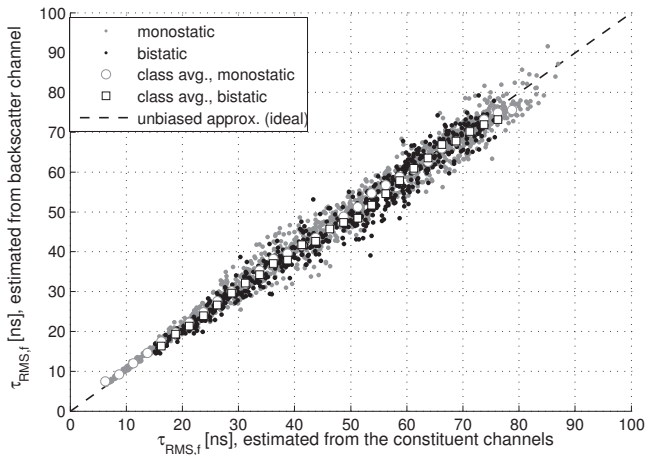


Fig. 7. Approximation of the backscatter RMS delay spread for measured power-delay-profiles (UHF RFID warehouse portal, metal portal, liquids/metal pallet). Estimates are based on individual (instantaneous) power-delay-profiles and use the simplified formula for α_τ in (23). Averages are shown for comparison.

setup is caused by reflections that could not be isolated from the LOS component with the given bandwidth. This leads to $\alpha_K < 1$ even though the constituent channels are fully correlated, cf. [21]. Naturally, this effect increases for weaker LOS, i.e., lower K_{LOS} . The outliers for very low K-factors in Fig. 6 are caused by false-positives in the LOS detection for the backscatter channel due to the weak LOS. For these points, the LOS component of the backscatter channel is close to or below the noise floor of the measurements and cannot be detected reliably any more. The estimated K-factor then depends on which component the LOS-detection locks onto, but is always larger than the true $K_{LOS,f}$, explaining why all outliers are above the 45° line.

V. CONCLUSION

Backscatter-based localization systems operate on the combined backscatter channel and thus have to deal with its pinhole nature. Detailed information regarding the backscatter channel is crucial to the analyses of such systems, yet the vast majority of characterizations and measurements are performed for point-to-point wireless channels, e.g., [12], [13], [28]–[30].

We presented a method to combine wideband parameters of wireless indoor radio channels to the parameters of the backscatter channel. Expressions for the K-factor w.r.t. the LOS path and the RMS delay spread of the backscatter channel based on the individual channels' parameters are given and validated using simulated and measured wireless indoor channel impulse responses. It is shown that these approximations are applicable and useful even in critical environments, where several of the theoretical assumptions do not hold.

The approximations can for example be used to estimate the performance of backscatter indoor localization systems based on point-to-point measurements of the channel. Although they are derived for the average PDP, they can be readily applied to squared CIRs, as shown in Figs. 6 and 7.

VI. ACKNOWLEDGMENTS

The authors wish to thank the anonymous reviewers whose comments helped to substantially improve this contribution.

This work was funded by NXP Semiconductors, Gratkorn, Austria, and the Austrian Research Promotion Agency (FFG) under the grant number 818072.

REFERENCES

- [1] J. D. Griffin and G. D. Durgin, "Gains for RF tags using multiple antennas," *IEEE Trans. Antennas Propag.*, vol. 56, no. 2, pp. 563–570, 2008.
- [2] T. Taniguchi, Y. Karasawa, and M. Tsuruta, "An analysis method of double fading MIMO channels including LOS environments," in *Proc. IEEE 19th Int. Symp. Personal, Indoor and Mobile Radio Communications PIMRC 2008*, 2008, pp. 1–5.
- [3] J. D. Griffin and G. D. Durgin, "Link envelope correlation in the backscatter channel," *IEEE Commun. Lett.*, vol. 11, no. 9, pp. 735–737, 2007.
- [4] D. Kim, M. A. Ingram, and J. Smith, W. W., "Measurements of small-scale fading and path loss for long range RF tags," *IEEE Trans. Antennas Propag.*, vol. 51, no. 8, pp. 1740–1749, 2003.
- [5] P. L. Kafle, A. Intarapanich, A. B. Sesay, J. McRory, and R. J. Davies, "Spatial correlation and capacity measurements for wideband MIMO channels in indoor office environment," *IEEE Trans. Wireless Commun.*, vol. 7, no. 5, pp. 1560–1571, 2008.
- [6] P. Almers, F. Tufvesson, and A. F. Molisch, "Keyhole effect in MIMO wireless channels: Measurements and theory," *IEEE Trans. Wireless Commun.*, vol. 5, no. 12, pp. 3596–3604, 2006.
- [7] A. Paulraj, R. Nabar, and D. Gore, *Introduction to Space-Time Wireless Communications*. Cambridge University Press, 2003, ISBN-13: 9-780521826150.
- [8] X. Yin, Y. Zhou, and F. Liu, "A generic wideband channel model for keyhole propagation scenarios and experimental evaluation," in *Proc. Fourth Int. Conf. Communications and Networking in China ChinaCOM 2009*, 2009, pp. 1–5.
- [9] R. Kattenbach, "Statistical modeling of small-scale fading in directional radio channels," *IEEE J. Sel. Areas Commun.*, vol. 20, no. 3, pp. 584–592, 2002.
- [10] P. Bello, "Characterization of randomly time-variant linear channels," *IEEE Transactions on Communications Systems*, vol. 11, no. 4, pp. 360–393, 1963.
- [11] A. Molisch, *Wireless Communications*. John Wiley & Sons, 2005, ISBN-13: 978-0470848876.
- [12] D. Arnitz, U. Muehlmann, and K. Witrisal, "Wideband characterization and modeling of UHF RFID channels for ranging and positioning," submitted to *IEEE Trans. Antennas Propag.*
- [13] D. Arnitz, G. Adamiuk, U. Muehlmann, and K. Witrisal, "UWB channel sounding for ranging and positioning in passive UHF RFID," in *11th COST2100 MCM*, Aalborg, Denmark, Jun. 2010. [Online]. Available: <http://www.spsc.tugraz.at/people/daniel-arnitz/ArnitzCOSTMCM10.pdf>
- [14] U. Muehlmann, G. Manzi, G. Wiednig, and M. Buchmann, "Modeling and performance characterization of UHF RFID portal applications," *IEEE Trans. Microw. Theory Tech.*, vol. 57, no. 7, pp. 1700–1706, 2009.
- [15] S. Kunkel, M.-S. Huang, R. Bieber, and M. Vossiek, "SAR-like localization of RFID tags for non-uniform trajectory," in *Proc. European Wireless Technology Conf. (EuWIT)*, 2010, pp. 281–284.
- [16] D. Arnitz, U. Muehlmann, and K. Witrisal, "Multi-frequency continuous-wave radar approach to ranging in passive UHF RFID," *IEEE Trans. Microw. Theory Tech.*, vol. 57, no. 5, pp. 1398–1405, Jul. 2009.
- [17] G. Li, D. Arnitz, R. Ebel, U. Muehlmann, K. Witrisal, and M. Vossiek, "Bandwidth dependence of CW ranging to UHF RFID tags in severe multipath environments," in *Proc. IEEE Int RFID Conf*, Orlando, Florida, Apr. 2011.
- [18] D. Arnitz, U. Muehlmann, and K. Witrisal, "UWB ranging in passive UHF RFID: Proof of concept," *IET Electron. Letters*, vol. 46, no. 20, pp. 1401–1402, Sep. 2010.
- [19] K. Finkenzeller, *RFID Handbook: Fundamentals and Applications in Contactless Smart Cards and Identification*, 2nd ed. Wiley & Sons, 2003, ISBN-13: 978-0470844021.

- [20] J. D. Griffin and G. D. Durgin, "Complete link budgets for backscatter-radio and RFID systems," *IEEE Antennas Propag. Mag.*, vol. 51, no. 2, pp. 11–25, 2009.
- [21] D. Armitz, U. Muehlmann, and K. Witrissal, "Wideband characterization of backscatter channels: Derivations and theoretical background," submitted to *IEEE Trans. Antennas Propag.*
- [22] L. J. Greenstein, S. S. Ghassemzadeh, S.-C. Hong, and V. Tarokh, "Comparison study of UWB indoor channel models," *IEEE Trans. Wireless Commun.*, vol. 6, no. 1, pp. 128–135, 2007.
- [23] D. Cassioli, M. Z. Win, and A. F. Molisch, "The ultra-wide bandwidth indoor channel: from statistical model to simulations," *IEEE J. Sel. Areas Commun.*, vol. 20, no. 6, pp. 1247–1257, 2002.
- [24] K. Witrissal, Y.-H. Kim, and R. Prasad, "A new method to measure parameters of frequency-selective radio channels using power measurements," *IEEE Trans. Commun.*, vol. 49, no. 10, pp. 1788–1800, Oct. 2001.
- [25] The PARIS Simulation Framework. Graz University of Technology / NXP Semiconductors. Open-Source (GNU GPL v3). [Online]. Available: <http://tinyurl.com/paris-osf/>
- [26] D. Armitz, U. Muehlmann, T. Gigl, and K. Witrissal, "Wideband system-level simulator for passive UHF RFID," in *Proc. IEEE Int. Conf. on RFID*, Orlando, Florida, Apr. 2009.
- [27] D. Armitz, U. Muehlmann, and K. Witrissal, "Wideband characterization of UHF RFID channels for ranging and positioning," Poster at *IEEE Int. Conf. on RFID*, Apr. 2010. [Online]. Available: <http://www.spsc.tugraz.at/people/daniel-armitz/ArmitzRFID10.zip>
- [28] M. K. Awad, K. T. Wong, and Z.-b. Li, "An integrated overview of the open literature's empirical data on the indoor radiowave channel's delay properties," *IEEE Trans. Antennas Propag.*, vol. 56, no. 5, pp. 1451–1468, 2008.
- [29] J. Karedal, S. Wyne, P. Almers, F. Tufvesson, and A. F. Molisch, "A measurement-based statistical model for industrial ultra-wideband channels," *IEEE Trans. Wireless Commun.*, vol. 6, no. 8, pp. 3028–3037, 2007.
- [30] M. S. Varela and M. G. Sanchez, "RMS delay and coherence bandwidth measurements in indoor radio channels in the UHF band," *IEEE Trans. Veh. Technol.*, vol. 50, no. 2, pp. 515–525, 2001.

Multifrequency Continuous-Wave Radar Approach to Ranging in Passive UHF RFID

Daniel Arnitz, *Student Member, IEEE*, Klaus Witrisal, *Member, IEEE*, and Ulrich Muehlmann, *Member, IEEE*

Abstract—In this paper, we present the extension of a recently published two-frequency continuous-wave (CW) ultra-high-frequency RF identification ranging technique to multiple carriers. The proposed system concept relies on exact phase information; hence, the passive tag cannot be accurately modeled as a frequency-flat linear device. A linearized model of the tag's reflection coefficient is devised to bridge the gap between the nonlinear reality and the linear CW radar theory. Estimation error bounds are derived and effects caused by noise and multipath propagation are analyzed in detail. It has been found that systematic errors introduced by the tag's reflection characteristic cannot be compensated by using multiple carriers due to large variations caused by detuning. Nonetheless the system, while being vulnerable to multipath propagation effects, still performs well under line-of-sight conditions; mean average errors below 15% of the true distance are possible in typical fading environments.

Index Terms—Continuous-wave (CW) radar, detuning, multipath channel, narrowband, ranging, system modeling, ultra-high-frequency (UHF) RF identification (RFID).

I. INTRODUCTION

THE AUTOMATIC and simultaneous identification, localization, and tracking of targets using electromagnetic radiation started mainly as a military application in radar systems. In the early 1970s, commercial tracking of large and expensive goods emerged, followed by smaller items by the end of the 20th Century [1]. Since then, RF identification (RFID) became almost ubiquitous in commercial applications, e.g., tracking and identification of goods or electronic article surveillance.

Although estimating distances to tagged items is not a new idea in itself, it is a relatively new field of interest in passive ultra-high-frequency (UHF) RFID. Recent work combines the need for a continuous carrier (to power the tag) with range estimation, employing well-known principles like continuous-wave (CW) radar [2], [3]. The application of multiple carriers is also not a new idea in UHF RFID [4].

The restrictive spectral masks enforced by existing regulations are a major reason for using narrowband systems like amplitude modulation CW radar for ranging (cf. [5]). Wideband systems like frequency modulation CW radar and ultra-wideband (UWB) systems [6], [7] would require considerable modifications to existing regulations.

Manuscript received June 03, 2008; revised December 29, 2008. First published April 07, 2009; current version published May 06, 2009. This work was supported by NXP Semiconductors, Gratkorn, Austria, and by the Austrian Research Promotion Agency (FFG) under Grant 818072.

D. Arnitz and K. Witrisal are with the Signal Processing and Speech Communication Laboratory, Graz University of Technology, A-8010 Graz, Austria (e-mail: daniel.arnitz@tugraz.at; witrisal@tugraz.at).

U. Muehlmann is with NXP Semiconductors, A-8101 Gratkorn, Austria (e-mail: ulrich.muehlmann@nxp.com).

Digital Object Identifier 10.1109/TMTT.2009.2017320

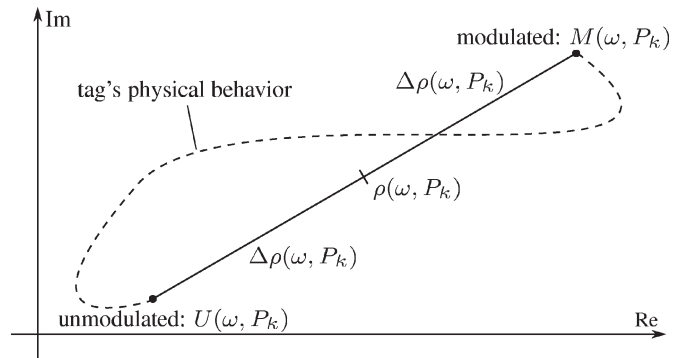


Fig. 1. Tag reflection coefficient linearization: the tag's physical behavior during modulation is a nonlinear, time-variant, frequency-dependent, and power-dependent curve. The linearized model assumes a fictive center value $\rho(\omega, P_\kappa)$ and a difference value $\Delta\rho(\omega, P_\kappa)$; only the endpoints are identical to the original curve. The assumption of short-time stationary power $P(\kappa) = P_\kappa$ completes the linearization.

This study completes the theoretical background of the recently published two-frequency continuous wave (2FCW) radar approach for passive UHF RFID [2]. This ranging system is also extended to multiple carriers in an effort to minimize errors introduced by noise, multipath propagation, and tag variations. The resulting multifrequency continuous-wave (MFCW) ranging approach is evaluated under typical UHF RFID environmental conditions.

In Section II, a linearized model of the tag's reflection coefficient during backscatter modulation is introduced. This model is applied in Section III to derive the signals used for MFCW ranging, followed by the derivation of a distance estimate out of multiple carriers and a discussion of detuning effects in Section IV. Section V contains detailed noise and multipath propagation influence analyses. The ranging system concept is verified using a wideband UHF RFID system-level simulator [8] in Section VI. Finally, the findings are summarized in Section VII.

II. LINEAR MODEL OF THE TAG MODULATION

On the physical level, a tag modulates data by varying a modulation impedance. The reflection coefficient during this process depends on the chip impedance, which itself depends on the chip input power. This dependence causes the reflection coefficient to be nonlinear. Moreover, the interaction between the time-variant impedances creates a curved transition trajectory in the complex plane (cf. Fig. 1). Tag detuning can be interpreted as additional impedance, thus having a direct influence on the reflection coefficient as well.

As a first step, the linearization neglects everything but the end points of this curve, introducing a center value $\rho(\omega, P)$ and

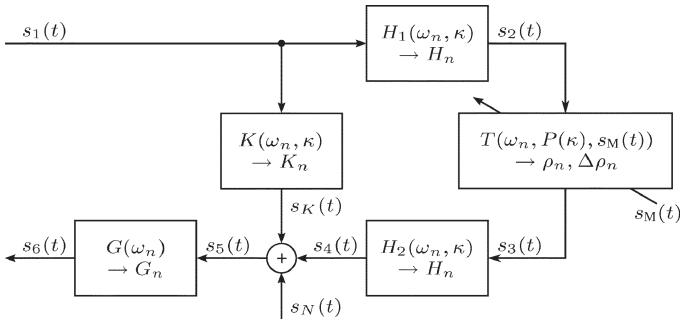


Fig. 2. Used signal model: reader to reader channel $K(\omega, \kappa)$, reader to tag channels $H_1(\omega, \kappa)$ and $H_2(\omega, \kappa)$, tag reflection coefficient $T(\omega, P, s_M)$, reader input stage $G(\omega)$, modulation signal $s_M(t)$, carrier level signals $s_1(t)$ through $s_6(t)$, noise $s_N(t)$; κ is a time index for short-time stationary variables, ω is the angular frequency, t is the time variable, and n is the carrier index.

a difference value $\Delta\rho(\omega, P)$ where ω and P are the angular frequency and the available tag power, respectively. The end points are more important here than the trajectory itself due to the nearly square tag modulation (either modulated or unmodulated)

$$\begin{aligned} \text{modulated : } & M(\omega, P) = \rho(\omega, P) + \Delta\rho(\omega, P) \\ \text{unmodulated : } & U(\omega, P) = \rho(\omega, P) - \Delta\rho(\omega, P). \end{aligned} \quad (1)$$

Assuming an arbitrary modulation signal $s_M(t)$ satisfying $-1 \leq s_M(t) \leq 1$, we can approximate the time-variant tag reflection coefficient $T(\omega, P, t)$ by

$$T(\omega, P, s_M(t)) \approx \rho(\omega, P) + s_M(t) \cdot \Delta\rho(\omega, P) \quad (2)$$

which is a simplified trajectory, but still power dependent, and thus, nonlinear. Under the assumption of short-time stationary power P_κ for some time period with index κ , the linearization is complete as follows:

$$T(\omega, P_\kappa, s_M(t)) \approx \rho_\kappa(\omega) + s_M(t) \cdot \Delta\rho_\kappa(\omega). \quad (3)$$

Note that ρ_κ and $\Delta\rho_\kappa$ still depend on carrier power, frequency, and detuning—they are merely linearized for one time instant.

As complex sinusoids are eigenfunctions of linear systems, we can finally write

$$e^{j\omega_n t} \cdot [\rho(\omega_n) + s_M(t) \cdot \Delta\rho(\omega_n)] \quad (4)$$

for the modulation of a sinusoid of frequency ω_n . The superposition principle is also applicable due to the linearity of this model, which will be exploited to calculate the backscattered signal for multiple carriers in Section III.

III. DERIVATION OF AMPLITUDE AND PHASE RELATIONS

The derivations outlined in this section are based on the signal model shown in Fig. 2 and done in the complex baseband. The entire derivation assumes short-time stationarity.

The interrogator sends $s_1(t)$ and receives $s_5(t)$. The sent signal is composed of N_c carriers at different frequency offsets ω_n from the center carrier. Phase relationships between the

carriers and the demodulation signal are implicitly considered in the carrier amplitudes A_n

$$s_1(t) = \sum_{n=1}^{N_c} A_n e^{j\omega_n t}. \quad (5)$$

Downlink and uplink channels are assumed to be linear filter channels, modeled by frequency-dependent gain factors H_n for purely sinusoidal signals

$$s_2(t) = \sum_{n=1}^{N_c} A_n H_n e^{j\omega_n t}. \quad (6)$$

Modulation on tag is performed using the linear model introduced in Section II. We assume a cosine modulation signal

$$s_M(t) = \cos(\omega_M t + \phi_M) = \frac{1}{2} e^{j(\omega_M t + \phi_M)} + \frac{1}{2} e^{-j(\omega_M t + \phi_M)} \quad (7)$$

where ω_M is the modulation frequency and ϕ_M is an arbitrary phase shift. We use the superposition principle to calculate the backscattered signal

$$\begin{aligned} s_3(t) = & \sum_{n=1}^{N_c} A_n H_n \rho_n e^{j\omega_n t} + \frac{1}{2} \sum_{n=1}^{N_c} A_n H_n \Delta\rho_n e^{j((\omega_n + \omega_M)t + \phi_M)} \\ & + \frac{1}{2} \sum_{n=1}^{N_c} A_n H_n \Delta\rho_n e^{j((\omega_n - \omega_M)t - \phi_M)}. \end{aligned} \quad (8)$$

Uplink and downlink channels are assumed to be identical for simplicity, but can easily be separated in the results. If the channels are not identical [distinct transmit and receive antennas (cf. [9])], only the average distance can be estimated.

The feedback term $s_K(t)$ models direct coupling caused by parasitics and nonideal devices, as well as reflections by the channel. Like uplink and a downlink channels, it is modeled as linear filter channel that decomposes into frequency-dependent gain factors K_n for sinusoidal signals

$$s_K(t) = \sum_{n=1}^{N_c} A_n K_n e^{j\omega_n t}. \quad (9)$$

The received signal $s_5(t)$ consists of modulated carriers $s_4(t)$, unmodulated carriers $s_K(t)$, and additive noise $s_N(t)$. We will denote the n th carrier's upper sideband by index $n + M$, while the lower sideband is denoted $n - M$. For example, the channel gain H_{4+M} is the gain for the upper sideband of carrier $n = 4$. Finally, the reader frontend introduces an additional frequency-dependent gain factor G . Hence,

$$\begin{aligned} s_6(t) = & s_N(t) + \sum_{n=1}^{N_c} A_n G_n (K_n + H_n^2 \rho_n) e^{j\omega_n t} \\ & + \frac{1}{2} \sum_{n=1}^{N_c} A_n H_n H_{n+M} G_{n+M} \Delta\rho_n e^{j[(\omega_n + \omega_M)t + \phi_M]} \\ & + \frac{1}{2} \sum_{n=1}^{N_c} A_n H_n H_{n-M} G_{n-M} \Delta\rho_n e^{j[(\omega_n - \omega_M)t - \phi_M]}. \end{aligned} \quad (10)$$

We extract the deterministic channel delay τ from the channel gains, e.g.,

$$H_{n+M} = \tilde{H}_{n+M} \cdot e^{-j(\omega_c + \omega_n + \omega_M)\tau} \quad (11)$$

with ω_c being the carrier frequency. The phase of the remaining channel gain \tilde{H}_{n+M} is completely stochastic, reflecting multipath propagation.

The frequency components of $s_6(t)$ are separated by shifting each component to dc and applying a low-pass filter (direct conversion receiver). We define the complex amplitude of the n th carrier's upper sideband as

$$c_{n+M} := \frac{1}{2} A_n \tilde{H}_n \tilde{H}_{n+M} G_{n+M} \Delta \rho_n e^{j[\phi_M - \tau \cdot (2\omega_c + 2\omega_n + \omega_M)]} \quad (12)$$

and the amplitude of the corresponding lower sideband as

$$c_{n-M} := \frac{1}{2} A_n \tilde{H}_n \tilde{H}_{n-M} G_{n-M} \Delta \rho_n e^{-j[\phi_M + \tau \cdot (2\omega_c + 2\omega_n - \omega_M)]} \quad (13)$$

for $n = 1, \dots, N_c$. Estimates of these amplitudes are used by MFCW ranging to determine the distance to the tag.

IV. MFCW DISTANCE ESTIMATE

The set of lower and upper sideband phases $\angle c_{n+M}$ and $\angle c_{n-M}$ form a system of equations that is solved for the desired delay τ . Estimation based on the received signal strength (RSS) is also possible, but not in the scope of this paper.

The tag modulation phase shift ϕ_M is typically unknown and cannot be controlled by an interrogator or tag. It is thus assumed to be uniformly distributed between $-\pi$ and π . Since $\omega_c \gg \omega_n \gg \omega_M$, a direct solution of this system of equations leads to an ill-conditioned problem. Therefore, we subtract the phase shifts in order to eliminate ϕ_M and ω_c beforehand. This cannot be achieved by combining upper and lower sidebands, hence, c_{n+M} and c_{n-M} are used separately.

A phase comparison between two different components $i+M$ and $j+M$ in (12) or $i-M$ and $j-M$ in (13) leads to the following result; in short notation,

$$\begin{aligned} \angle c_{i\pm M} c_{j\pm M}^* &= \angle c_{i\pm M} - \angle c_{j\pm M} \\ &= 2\tau(\omega_j - \omega_i) + \angle \Delta \rho_i \Delta \rho_j^* \\ &\quad + \angle \tilde{H}_i \tilde{H}_{i\pm M} \tilde{H}_j^* \tilde{H}_{j\pm M}^* + \angle A_i A_j^* \\ &\quad + \angle G_{i\pm M} G_{j\pm M}^*. \end{aligned} \quad (14)$$

The last two terms $\angle A_i A_j^*$ and $\angle G_{i\pm M} G_{j\pm M}^*$ are systematic influences and can be compensated. Fading channels are represented by $\angle \tilde{H}_i \tilde{H}_{i\pm M} \tilde{H}_j^* \tilde{H}_{j\pm M}^*$. The effect of this term will be discussed in Section V; it is zero for additive white Gaussian noise (AWGN) channels. The differential phase shift caused by the tag $\angle \Delta \rho_i \Delta \rho_j^*$ is another error term and will be discussed below.

A distance estimate can be obtained from each comparison (14) by

$$\hat{d}_{i,j,\pm} = \frac{c}{2(\omega_j - \omega_i)} \angle \hat{c}_{i\pm M} \hat{c}_{j\pm M}^*, \quad i, j = 1, \dots, N_c, i \neq j \quad (15)$$

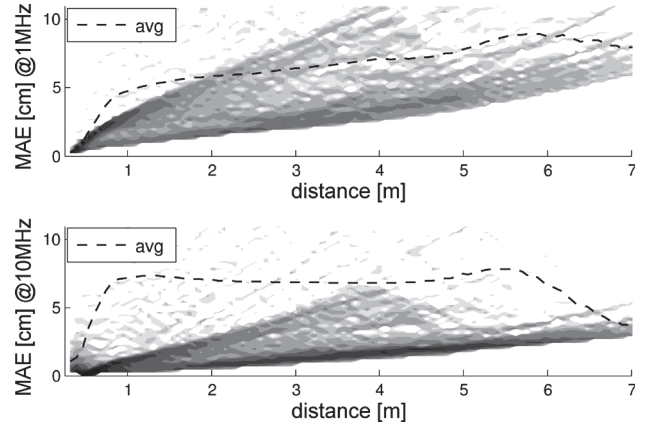


Fig. 3. Influence of detuning on the MAE for 2FCW ranging at frequency offsets of 1 and 10 MHz.

where c is the speed of light and $\hat{c}_{n\pm M}$ denotes an estimate of $c_{n\pm M}$. These estimates are averaged to obtain the desired overall distance.

A. Example: 2FCW Radar ($N_c = 2$)

Using two carriers and assuming perfectly compensated systematic errors, the phase shifts between the two upper and lower sidebands are identical

$$\angle c_{1+M} c_{2+M}^* = \angle c_{1-M} c_{2-M}^* = 2\tau(\omega_2 - \omega_1) + \angle \Delta \rho_1 \Delta \rho_2^* \quad (16)$$

and the distance estimate is

$$\hat{d} = \underbrace{\tau c}_d + \underbrace{\frac{c \cdot \angle \Delta \rho_1 \Delta \rho_2^*}{2(\omega_2 - \omega_1)}}_{\text{error caused by tag}}. \quad (17)$$

The error term introduced by the tag causes the distance estimate \hat{d} to be biased.

B. On Mitigation of the Systematic Error Caused by the Tag

The bias in (17) depends on frequency, power, and detuning. Exemplarily, this influence on the mean absolute error (MAE) of 2FCW ranging is shown in Fig. 3. Detuning plus assembly impedance is varied from -70% to 400% from the optimal value for this plot. We used an AWGN channel with single-sided noise density $N_0 = -82$ dBm/Hz and an estimation window size of $N = 144432$ samples. The carriers were set to 3.2 W/32 mW effective isotropic radiated power (EIRP) at a center frequency of $\omega_c = 910$ MHz with 0-Hz offset for the primary (energy) carrier. Note that the maximum range of detuned tags is considerably lower than 7 m; only functional tags are taken into account. The background of Fig. 3 contains a histogram of the MAE, while the foreground shows the average MAE. We have chosen a strong secondary carrier to minimize the influence of noise in these plots.

While noise is still an issue compared to the systematic bias for a frequency offset of 1 MHz and distances of >2 m, it is almost negligible for 10-MHz offset. The maximum MAE was approximately 40–50 cm for both plots, while the average MAE does not exceed 10 cm.

Effective removal of this error is a nontrivial task and yet unresolved. The tag is designed to work for a frequency range of 860–960 MHz specified in the EPCglobal Class-1 Gen-2 standard [10]. Consequently, its spectral characteristic is a smooth function and a Taylor-series expansion of the phase shift $\angle \Delta \rho_i \Delta \rho_j^*$ is approximately linear subject to the frequency difference $(\omega_j - \omega_i)$ for reasonably small carrier offset frequencies. Since the phase shift caused by wave propagation $2\tau(\omega_j - \omega_i)$ is also linear with frequency difference, the effects of tag and distance cannot be separated using multiple carriers.

A characterization of the labels after manufacture and/or after application to the tagged items would tremendously increase costs and is thus not practicable. Moreover, such a characterization would lose its validity if the items are placed near other objects due to changes in the state of detuning. For the same reasons, i.e., the dependence of the error on individual incident power levels and on detuning, reference estimates based on tags at known ranges can only be used to compensate for an approximate average value, not for the true value. If the range of detuning is known, at least an expected average error can be compensated.

It shall be noted that typical UHF RFID channels are fading channels. The MAE is dominated by multipath propagation effects even in moderate multipath environments, not by detuning (cf. Fig. 9).

V. INFLUENCE OF NOISE AND MULTIPATH PROPAGATION

A. Influence of White Noise

Analogous to other phase estimators [11] and under the assumption of independent real and imaginary parts, i.e., circular symmetric noise, we can write

$$\text{var}\{\hat{\varphi}_i\} = \frac{1}{N \text{SNR}_i} = \frac{N_0}{N|c_i|^2} \quad (18)$$

for the variance of one phase estimate. N is the length of the estimation window in samples, N_0 is the single-sided noise density, and $|c_i|$ is the signal (component) amplitude. For the phase difference between two components, we obtain

$$\text{var}\{\hat{\varphi}_{ij}\} = \frac{1}{N \text{SNR}_i} + \frac{1}{N \text{SNR}_j} + \frac{r_{ij}}{N^2 \text{SNR}_i \text{SNR}_j} \quad (19)$$

where r_{ij} is the cross covariance between components i and j . Typically passive RFID systems are forward-link-limited [1] so signal-to-noise (SNR) values are high. It follows that the quadratic cross correlation term is negligible. Using (15) to obtain the distance results in

$$\text{var}\{\hat{d}_{ij}\} = \frac{c^2}{4(\omega_j - \omega_i)^2} \text{var}\{\hat{\varphi}_{ij}\}. \quad (20)$$

There are $N_c(N_c - 1)$ feasible combinations of phase differences between the sidebands of N_c carriers. Averaging all these combinations comes at the cost of correlation between the components. For the conservative approach of using each sideband only once, $\lfloor N_c \rfloor_e$ combinations remain, where $\lfloor N_c \rfloor_e$ denotes

the rounding to the next lower even integer value. For this case, we obtain

$$\begin{aligned} \text{var}\{\hat{d}\} = & \frac{c^2 N_0}{4N \lfloor N_c \rfloor_e^2} \sum_{i=1}^{N_c/2} \frac{|\hat{c}_{2i-1+M}|^2 + |\hat{c}_{2i+M}|^2}{|\hat{c}_{2i+1+M}|^2 |\hat{c}_{2i+M}|^2 (\omega_{2i} - \omega_{2i-1})^2} \\ & + \frac{c^2 N_0}{4N \lfloor N_c \rfloor_e^2} \sum_{i=1}^{N_c/2} \frac{|\hat{c}_{2i-1-M}|^2 + |\hat{c}_{2i-M}|^2}{|\hat{c}_{2i+1-M}|^2 |\hat{c}_{2i-M}|^2 (\omega_{2i} - \omega_{2i-1})^2} \end{aligned} \quad (21)$$

for the overall variance. Remarkably, we can ignore the correlation between \hat{d}_{ij} and combine all sidebands in case of equal carrier amplitudes A_2, \dots, A_{N_c} (A_1 can be arbitrary) and equal frequency spacings, obtaining an approximation

$$\text{var}\{\hat{d}\} \approx \frac{1}{N_c^2 (N_c - 1)^2} \sum_{i=1}^{N_c} \sum_{\substack{j=1 \\ j \neq i}}^{N_c} \text{var}\{\hat{d}_{ij}\} \quad (22)$$

with

$$\hat{d}_{ij}|_{i>j} = \frac{c}{2} \cdot \frac{\angle \hat{c}_{i+M} \hat{c}_{j+M}^*}{(\omega_j - \omega_i)} \quad \hat{d}_{ij}|_{i<j} = \frac{c}{2} \cdot \frac{\angle \hat{c}_{i-M} \hat{c}_{j-M}^*}{(\omega_j - \omega_i)}. \quad (23)$$

Clearly, $N_c^2 (N_c - 1)^2 \gg \lfloor N_c \rfloor_e^2$ for $N_c > 2$, thus the resulting variance is considerable lower if all sidebands are combined and the correlation can be neglected. The average component variance in such a system is approximately equal to the individual secondary carrier variances because of the strong primary (energy) carrier

$$\begin{aligned} \text{var}\{\hat{d}_{23}\} = \text{var}\{\hat{d}_{32}\} = \text{var}\{\hat{d}_{34}\} = \dots \\ \approx \overline{\text{var}\{\hat{d}_{ij}\}} = \frac{1}{N_c(N_c - 1)} \sum_{i=1}^{N_c} \sum_{\substack{j=1 \\ j \neq i}}^{N_c} \text{var}\{\hat{d}_{ij}\} \end{aligned} \quad (24)$$

It follows that the best achievable variance scaling for multiple carriers is

$$\text{var}\{\hat{d}\}|_{\text{MFCW}} \approx \frac{\overline{\text{var}\{\hat{d}_{ij}\}}}{N_c(N_c - 1)}. \quad (25)$$

while the largest possible frequency offset is $N_c \Delta \omega$ with $\Delta \omega$ being the frequency spacing. If this offset is chosen for 2FCW, according to (15), its variance scales with

$$\text{var}\{\hat{d}\}|_{\text{2FCW}} \approx \frac{\overline{\text{var}\{\hat{d}_{ij}\}}}{N_c^2}. \quad (26)$$

which is lower than the multicarrier's variance. Simulations have shown that the correlation can be used to reduce the variance caused by noise slightly below this level for multicarrier systems.

B. Influence of Multipath Propagation

In case of multipath propagation, the stochastic channel phase term $\angle \tilde{H}_i \tilde{H}_{i \pm M} \tilde{H}_j^* \tilde{H}_{j \pm M}^*$ in (14) is nonzero. We start our analysis with one channel, assuming given channel gains $\tilde{H}_i, \tilde{H}_j \sim \mathcal{CN}(m, \sigma^2)$, circular symmetric around the mean value. This assumption implies a Ricean fading channel with line-of-sight

(LOS) amplitude m and is valid for a small frequency spacing. We assume a pure smallscale channel here to strip the tilde and define the covariance matrix

$$\mathbb{E}\{\underline{h}\underline{h}^H\} - \mathbb{E}\{\underline{h}\}\mathbb{E}\{\underline{h}\}^H = \begin{bmatrix} \sigma^2 & \beta \\ \beta^* & \sigma^2 \end{bmatrix} \quad (27)$$

with $\underline{h} = [H_i \ H_j]^T$. The superscript H denotes the Hermitian transpose.

We are evaluating $\angle H_i - \angle H_j = \angle H_i H_j^*$ for the distance estimate, which is approximately

$$\angle H_i H_j^* = \arctan\left(\frac{\text{Im}\{H_i H_j^*\}}{\text{Re}\{H_i H_j^*\}}\right) \approx \frac{\text{Im}\{H_i H_j^*\}}{\text{E}\{\text{Re}\{H_i H_j^*\}\}} \quad (28)$$

for LOS scenarios with a high Ricean K-factor. Thus,

$$\text{var}\{\angle H_i H_j^*\} \approx \frac{\text{var}\{\text{Im}\{H_i H_j^*\}\}}{\text{E}\{\text{Re}\{H_i H_j^*\}\}^2}. \quad (29)$$

After some short derivations using the properties of complex Gaussian processes [12], we obtain

$$\mathbb{E}\{H_i H_j^*\} = \beta + |m|^2 \quad (30)$$

$$\text{var}\{\text{Im}\{H_i H_j^*\}\} = \frac{1}{2} \text{Re}\{\sigma^4 - \beta^2 + 2|m|^2(\sigma^2 - \beta)\} \quad (31)$$

and, thus,

$$\text{var}\{\angle H_i H_j^*\} \approx \frac{\text{Re}\{\sigma^4 - \beta^2 + 2|m|^2(\sigma^2 - \beta)\}}{2\text{Re}\{\beta + |m|^2\}^2} \quad (32)$$

which is the variance caused by one channel.

Introducing a second channel, we have to deal with $\angle H_i H_{i\pm M} H_j^* H_{j\pm M}^*$ instead of $\angle H_i H_{j\pm M}^*$, which is a lot more complicated to handle. The problem becomes simple if we assume that the product $H_i H_{i\pm M}$ is also approximately Gaussian with new variance and mean value $H_i H_{i\pm M} \sim \mathcal{CN}(\tilde{m}, \tilde{\sigma}^2)$. In this case, the above derivations apply to $H_i H_{i\pm M}$ as well. This assumption of Gaussianity holds for LOS scenarios with a high K-factor $K \gtrsim 10$ dB. Exploiting the properties of complex Gaussian processes again, it can easily be shown that

$$\tilde{m} = m^2 \quad \tilde{\sigma}^2 = 2\sigma^2(\sigma^2 + 2|m|^2) \quad \tilde{\beta} = 2\beta(\beta + 2|m|^2) \quad (33)$$

for identical uplink and downlink channels and

$$\tilde{m} = m^2 \quad \tilde{\sigma}^2 = \sigma^2(\sigma^2 + 2|m|^2) \quad \tilde{\beta} = \beta(\beta + 2|m|^2) \quad (34)$$

for distinct channels under this assumption.

The simplest way to obtain the variance for the combination of multiple carriers is to use the average frequency shift to calculate the covariance matrix. This approach is possible because of the small frequency spacings up to a few megahertz. Direct application of (21) is not possible due to heavy correlation between the phase estimates.

C. MAE

The expected MAE of the proposed ranging system concept can be expressed by mean and standard deviation of the calcu-

lated estimate. We assume a Gaussian distribution for the distance estimate \hat{d} , which is approximately true for LOS scenarios, i.e., high Ricean K-factors. Applying this assumption, the deviation from the true value d is also Gaussian with mean value $\mu := \mathbb{E}\{\hat{d}\} - d$ and the MAE is

$$\begin{aligned} \text{MAE}\{\hat{d}\} &= \mathbb{E}\{|\hat{d} - d|\} \\ &= \frac{1}{\sigma\sqrt{2\pi}} \int_{-\infty}^{\infty} |x - \mu| e^{-\frac{x^2}{2\sigma^2}} dx \\ &= \sqrt{\frac{2}{\pi}} \sigma e^{-\frac{\mu^2}{2\sigma^2}} + \mu \text{erf}\left\{\frac{\mu}{\sqrt{2}\sigma}\right\} \end{aligned} \quad (35)$$

where $\text{erf}\{\alpha\}$ is the error function [13]

$$\text{erf}\{\alpha\} = \frac{2}{\sqrt{\pi}} \int_0^{\alpha} e^{-x^2} dx. \quad (36)$$

VI. SIMULATIONS

A. Simulator Setup

The theoretical results given in this paper have been verified by simulations using a wideband interrogator/tag simulation tool [8]. It is based on behavioral models of tag and interrogator building blocks and partially implements the EPCglobal Class-1 Gen-2 protocol [10].

The simulator was configured as follows: carrier frequency $f_c = 910$ MHz, tag clock frequency $f_{\text{clk}} = 1.92$ MHz, and modulation frequency $f_M = 48$ kHz with an unknown uniformly distributed phase shift $\varphi_M \in [-\pi, \pi]$. Unless otherwise stated, transmit power of the primary (energy) carrier $n = 1$ was set to 3.2 W EIRP at a frequency offset of $f_1 = 0$ Hz, while secondary (ranging) carriers were set to 320 μ W EIRP. The average direct feedback gain was chosen to be $\mathbb{E}\{K_n\} = -30$ dB with an average delay of 3 ns; the sampling window size was set to $N = 144432$ samples for all simulations. Systematic errors that could be corrected by the interrogator in real-world applications are perfectly compensated.

The simulator results in Figs. 5–9 were calculated by averaging 250 independent estimates per marker. Four-frequency continuous-wave (4FCW) ranging was performed by comparing the phases of carriers 1/2 and 3/4 (each carrier used only once).

All simulated multipath channels are based on a short-range indoor smallscale channel model [14], resulting in Ricean fading. Uplink and downlink channels were chosen to be identical (worst case, cf. Fig. 8). All multipath simulations, except for Figs. 4 and 9, where a light fading channel was desired, used a logarithmically dropping Ricean K-factor with 30 dB at 0 m and 10 dB at 5 m. The root mean square (rms) delay spread increased logarithmically from 1 to 20 ns in the same range. This channel setup reflects the values given in the literature for the UHF RFID frequency band (cf. [9] and [15]). We extended the range to 7 m for the light fading channel, approximately resulting in an rms delay spread of 1–10 ns and a Ricean K-factor of 30–15 dB within 0–5 m. Additive white noise was set to -82 dBm/Hz after sampling at the reader input stage.

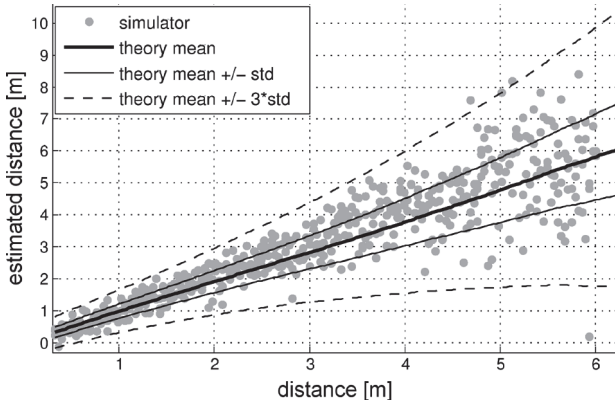


Fig. 4. Example comparison between analytical and simulation results for a weakly fading channel.

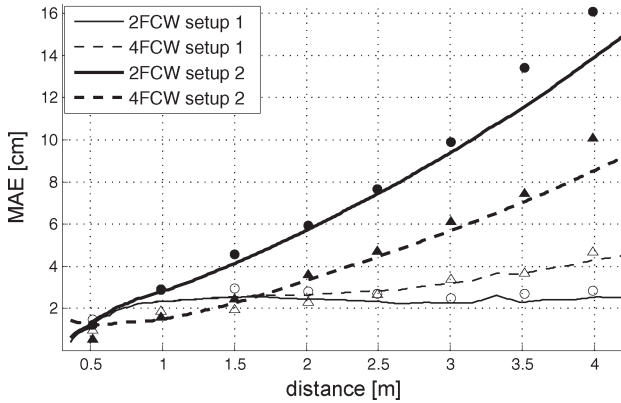


Fig. 5. Mean absolute distance error caused by **noise and the bias introduced by the tag** for 2FCW ($N_c = 2$) and 4FCW ($N_c = 4$): analytical results versus simulation for two different carrier setups. Carrier offset frequencies $f_n = 0, 3, 1, 2$ MHz (setup 1) and $f_n = 0, 4, 2, 10$ MHz (setup 2).

B. Simulation Results

The proposed ranging method was tested under various conditions of which only a small selection of simulations can be presented here.

Fig. 4 shows a comparison of theory and simulations for 2FCW radar using a frequency spacing of 8 MHz. In this simulation a detuned tag (+100% of the optimal impedance) moves from 30 cm to 6 m in the light multipath environment, while the interrogator continuously estimates its range. The expected average deviation using (17) and 68/99.7% intervals applying the results in Section V are also displayed for comparison. As can be seen, the ranging performs within expected parameters.

The MAE in AWGN and fading environments for different carrier setups is depicted in Figs. 5 and 6, respectively. Setup 2 uses the standard power setup, while the secondary carrier power is increased to $P_{2...4} = 32$ mW for Setup 1. All simulations assume a well-tuned tag; frequency setups are given in the captions. The small deviations from the expected analytical values given in this paper are caused by overlapping harmonics due to nonideal filters and residual filter transients. The results

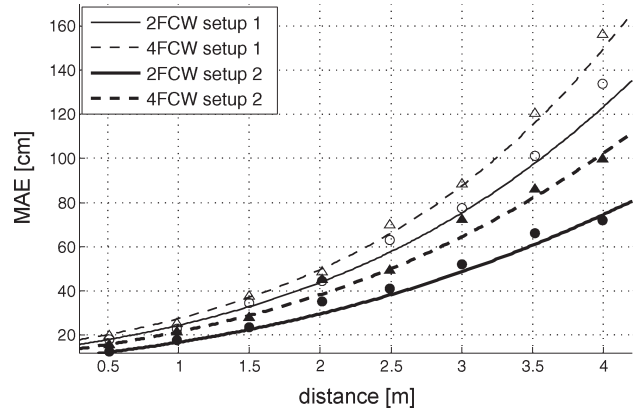


Fig. 6. Mean absolute distance error caused by **multipath propagation** for 2FCW ($N_c = 2$) and 4FCW ($N_c = 4$): analytical results versus simulation for two different carrier setups. Carrier offset frequencies $f_n = 0, 6, 2, 4$ MHz (setup 1) and $f_n = 0, 12, 2, 6$ MHz (setup 2).

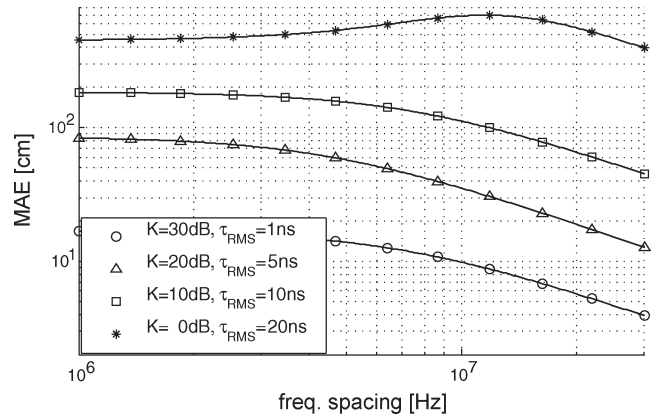


Fig. 7. Analytical mean absolute distance error caused by multipath propagation for 2FCW ($N_c = 2$) versus frequency spacing $f_2 - f_1$ for four different channels. Uplink/downlink channels are identical (worst case).

show that the performance depends primarily on the largest frequency offset. Moreover, noise is negligible compared to the errors caused by multipath propagation.

A special property of the proposed ranging system is shown in Fig. 7. The MAE for multipath propagation drops for an increased frequency spacing, as long as the channel features a significant LOS component. The maximum frequency offset is bounded by phase ambiguities at one quarter of the wavelength. We thus suggest to select the frequency offset of a 2FCW system such that

$$f_2 - f_1 \lesssim \frac{c}{4(d_{\max} + 3\sigma)} \quad (37)$$

where c is the speed of light, d_{\max} is the maximum distance, and σ is the standard deviation caused by the channel. This minimizes the influence of noise and multipath propagation while still avoiding phase ambiguities.

An undesired effect is caused by the combination of backscatter communication with identical receive/transmit (RX/TX) antenna at the interrogator. This combination creates identical uplink and downlink channels, increasing the fading range and the error rate of MFCW ranging, as shown in Fig. 8.

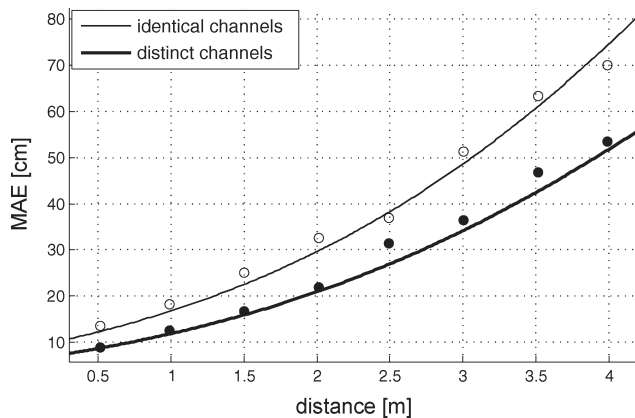


Fig. 8. Mean absolute distance error caused by **multipath propagation** for 2FCW ($N_c = 2$) using a well-tuned tag: analytical results versus simulation for identical and independent uplink/downlink channels.

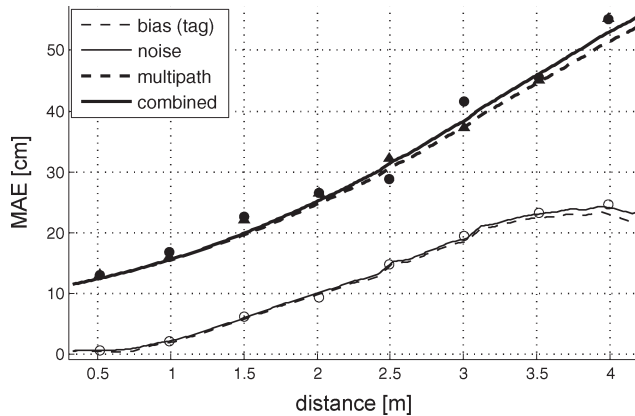


Fig. 9. Mean absolute distance error caused by **noise and multipath propagation** for 2FCW ($N_c = 2$): tag detuned by +100% of the optimal impedance, light multipath channel; carrier offset frequencies $f_n = 0, 10$ MHz.

This simulation uses offset frequencies of $f_n = 0, 12$ MHz and identical parameters per uplink and downlink channel. Analytical results are given in Section V.

A direct comparison between the errors caused by noise, multipath propagation, and the bias introduced by the tag's phase shift can be found in Fig. 9. We set up a simulation using only a moderate multipath channel with high K-factor and low rms delay spread for this plot. The tag is detuned by +100% of the optimal impedance, which approximately maximizes the influence of the bias on the MAE. Further detuning flattens the reflection coefficient and thus reduces the introduced error. It can be seen that the bias is dominant in the AWGN case, while it is almost negligible in the presence of multipath propagation.

VII. CONCLUSION

A linearized model of the time-variant nonlinear reflection coefficient of a passive UHF RFID tag was introduced in this paper. This model was designed for the EPCglobal Class-1 Gen-2 protocol standard [10], but is also applicable to other types of RFID transponders using backscatter modulation. The 2FCW radar ranging approach for UHF RFID presented in [2] was generalized to an arbitrary amount of carriers, utilizing an improved method of component selection. The resulting system

was analyzed for vulnerabilities to systematic and stochastic errors. Performance bounds for AWGN and multipath propagation channels were derived accordingly. The theoretical results were verified by extensive simulations using a wideband UHF RFID simulator [8].

It has been found that the system, while being vulnerable to multipath propagation (like any narrowband system), still performs well for typical RFID channels. The mean average error can be kept below 20% at distances from 0.75 m up to 4 m in such channels for the worst case of identical reader RX/TX-antennas. Using distinct antennas, the error can be kept well below 15% within the same range.

Detuning is a problem at short ranges and in nonfading channels. Simulations have shown that the MAE can exceed 50 cm for "unlucky" detuning, shifting the resonance exactly to the tag's operating point. The mean MAE for detuning in the range of -70% to 400% of the optimal impedance does not exceed 10 cm. Compensation of this error is not possible due to large variations caused by the detuning.

Finally, it has also been found that there is no gain in using more than one secondary carrier within the coherence bandwidth of the channel. As mentioned above, the systematic error caused by detuning could not be compensated using multiple carriers. Additionally, the estimate's variance cannot be improved using multiple secondary carriers inside the coherence bandwidth: In this case, the error caused by multipath propagation solely depends on the average carrier spacing, with smaller errors for larger offsets. If the 2FCW system uses the largest spacing, the variance for higher order systems is always greater than the 2FCW's variance. For AWGN channels, a similar relationship has been shown in Section V. Thus, the best achievable MAE is obtained when using 2FCW ranging with the highest possible frequency offset. Consequently, 2FCW radar is the recommended choice for narrowband ranging. Placing 2FCW carrier pairs well outside the respective coherence bandwidths will create independent fading and, thus, mitigate multipath propagation effects—at the cost of a considerably larger overall bandwidth.

REFERENCES

- [1] D. M. Dobkin, *The RF in RFID*. New York: Elsevier, 2007, 13: 978-0750682091.
- [2] U. Muehlmann and A. Salfelner, "Two-frequency CW RADAR approach to ranging in UHF RFID systems," in *Proc. Eur. Microw. Assoc.*, Dec. 2007, vol. 4, pp. 317–322.
- [3] M. Vossiek and P. Gulden, "The switched injection-locked oscillator: A novel versatile concept for wireless transponder and localization systems," *IEEE Trans. Microw. Theory Tech.*, vol. 56, no. 4, pp. 859–866, Apr. 2008.
- [4] H.-C. Liu, Y.-T. Chen, and W.-S. Tzeng, "A multi-carrier UHF passive RFID system," in *Int. Appl. Symp. and Internet Workshops*, Munich, Germany, Jan. 2007, p. 21.
- [5] K. Finkenzeller, *RFID Handbook: Fundamentals and Applications in Contactless Smart Cards and Identification*, 2nd ed. New York: Wiley, 2003, 13: 978-0470844021.
- [6] I. Oppermann, M. Hämmäläinen, and J. Iinatti, *UWB Theory and Applications*. New York: Wiley, 2004, 13: 978-0470869178.
- [7] Z. Sahinoglu, S. Gezici, and I. Guvenc, *Ultra-Wideband Positioning Systems: Theoretical Limits, Ranging Algorithms, and Protocols*. Cambridge, U.K.: Cambridge Univ. Press, 2008, 13: 978-0521873093.
- [8] D. Arnitz, U. Muehlmann, T. Gigl, and K. Witrisal, "Wideband system-level simulator for passive UHF RFID," in *Proc. IEEE Int. RFID Conf.*, Orlando, FL, Apr. 2009, to be published.

- [9] D. Kim, M. A. Ingram, and W. W. Smith, "Measurements of small-scale fading and path loss for long range RF tags," *IEEE Trans. Antennas Propag.*, vol. 51, no. 8, pp. 1740–1749, Aug. 2003.
- [10] *EPCglobal Class 1 Gen 2*, ISO/IEC 18000-6C, ISO Standard, 2004.
- [11] S. M. Kay, *Fundamentals of Statistical Signal Processing—Estimation Theory*. New York: Prentice-Hall, 1993, vol. 1, 13: 978-0133457117.
- [12] K. S. Miller, *Complex Stochastic Processes*. Reading, MA: Addison-Wesley, 1974.
- [13] I. N. Bronstein, K. A. Semendjajew, G. Musiol, and H. Muehlig, *Taschenbuch der Mathematik* (in German), 5th ed. Berlin, Germany: Harri Deutsch, 2005, 10: 978-3817120154.
- [14] K. Witrals, Y.-H. Kim, and R. Prasad, "A new method to measure parameters of frequency-selective radio channels using power measurements," *IEEE Trans. Commun.*, vol. 49, no. 10, pp. 1788–1800, Oct. 2001.
- [15] M. S. Varela and M. G. Sánchez, "RMS delay and coherence bandwidth measurements in indoor radio channels in the UHF band," *IEEE Trans. Veh. Technol.*, vol. 50, no. 2, pp. 515–525, Mar. 2001.



Daniel Arnitz (S'08) received the Master degree Dipl.-Ing.(FH) in electrical engineering from the University of Applied Sciences FH Joanneum Kapfenberg, Styria, Austria, in 2005. His diploma thesis focused on a feasibility study of (burst) error correcting codes for long-range RFID systems. He is currently working toward the Ph.D. degree at Graz University of Technology, Graz, Austria.

He is currently with the Signal Processing and Speech Communication Laboratory (SPSC), Graz University of Technology.



Klaus Witrals (S'98–M'03) received the Dipl.-Ing. degree in electrical engineering from the Technical University of Graz, Graz, Austria, in 1997, and the Ph.D. degree (*cum laude*) from the Delft University of Technology, Delft, The Netherlands, in 2002. His doctoral thesis concerned frequency-domain channel characterization and orthogonal frequency division multiplexing (OFDM) transmission technology.

He is currently an Assistant Professor with the Signal Processing and Speech Communication Laboratory (SPSC), Graz University of Technology, Graz, Austria. His current research interests concern broadband wireless communications, in particular UWB technology, propagation channel modeling, and multiple-input–multiple-output (MIMO) systems.

Dr. Witrals is co-chair of the Austria chapter of the IEEE Communications (COM)/Microwave Theory and Techniques (MTT) societies.



Ulrich Muehlmann (M'05) received the Dipl.-Ing. degree (Master) in telematics and Ph.D. degree (with honors) from the Graz University of Technology, Graz, Austria, in 2000 and 2005, respectively.

In 2001, he began research in optical tracking with the Department of Electrical Measurement and Measurement Signal Processing, Technical University of Graz, Graz, Austria). Since 2005, he has been with NXP Semiconductors (formerly Philips Semiconductors), Gratkorn, Austria, where he is involved with the field of UHF RFID technology focused on systems

and analog innovation. He has authored or coauthored several publications in the field of optical tracking, machine vision, and RFID.

UWB ranging in passive UHF RFID: proof of concept

D. Armitz, U. Muehlmann and K. Witrisal

A proof of concept for ultra-wideband (UWB)-based ranging in passive UHF RF identification (RFID) is presented. The proposed method uses the tag's backscatter modulation and thus does not require processing of the UWB signal by the tag. It is evaluated using measurements in an indoor environment similar to a warehouse portal in terms of channel impulse responses. The ranging accuracy is comparable to classical UWB ranging and thus inherently robust to multipath propagation.

Introduction and motivation: Even though passive UHF RFID is now a widespread technology, reliable positioning is a feature that is not yet available. Foremost in the list of reasons for this are the need to keep the tag simple (power consumption, costs) and the bandwidth limits of the UHF RFID frequency bands. As a consequence, currently used ranging methods are based on narrowband parameters such as return link phases [1], which rely on a very dominant direct path in multipath environments. Channel measurements in a warehouse portal [2] have shown that UHF RFID channels are typically dominated by the indirect (non-line-of-sight, NLOS) paths and not the direct line-of-sight (LOS) path. This leads to large errors and biased estimates in narrowband ranging methods, which in general cannot extract the LOS signal (see [2]). It is well known that ultra-wideband systems are able to overcome this problem and are thus able to provide accurate ranging in dense multipath environments. A related FMCW-based ultra-wideband ranging method has recently been published [3].

Discussion of ranging method: Setup description: The proposed method augments conventional passive UHF RFID by adding a UWB radar system. The radar system operates in parallel to the UHF system, see Figs. 1 and 2. As in conventional UHF RFID systems, tag power supply and communication is performed by the UHF reader and protocol. The radar setup emits an ultra-wideband signal, which is reflected by the tag during normal operation. Separation from the generally time-variant environment (decluttering) is performed by detecting the backscatter modulation in the received UWB signal. This modulation in the UWB frequency range can for example be achieved by creating a second match of chip and antenna impedance in the UWB band or by using two distinct antennas and modulation transistors for UHF and UWB.

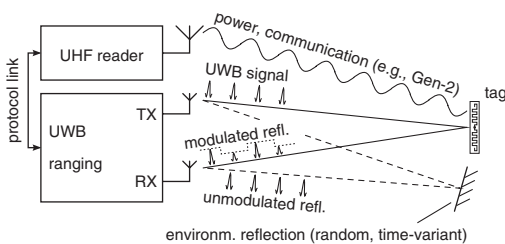


Fig. 1 Basic principle of operation

UWB radar determines tag range during normal tag operation by detecting shortest path that shows modulation

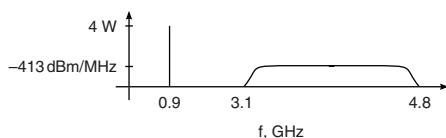


Fig. 2 Example spectrum

Parallel operation of conventional UHF RFID at 900 MHz and UWB radar in UWB frequency band

It is important to note that the tag does not process the UWB signal in any way except for backscattering it during normal operation. Thus the system requires only minimal changes in tag design and does not require any power supply by the tag. As the UWB transmitter and the receiver are within the same unit, coherent processing of the UWB signal can be achieved without the complexity of synchronisation.

Range detection: The radar base station uses estimates of the channel impulse response (CIR) over time to estimate the range to the tag. During modulation, the tag essentially switches between match (little reflection) and mismatch (large reflection). As a consequence of this backscatter modulation, the tap of the CIR that corresponds to the shortest path to the tag and many subsequent taps (multipath propagation on the return link) will show the modulation. This can be detected by evaluating the time-variance of each component of the CIR over time. The protocol link to the reader ensures that the tag reply is known to the UWB radar and thus can be used for the detection of the backscatter modulation in the CIR.

Proof of concept: This concept has been evaluated in the frequency range 3–6 GHz using time-variant transmission coefficient measurements between TX and RX antennas by a network analyser. The measurements were taken in an enclosed room (approx. 3 × 6 m) with steel-reinforced concrete floor and walls, reflective windows, and large metal surfaces on walls and ceiling. This makes it a relatively dense multipath environment. The channel TX → tag → RX fits classical short-range wireless indoor channel models with K-factors in the range of 0 dB and RMS delay spreads in the range of 20 ns. This is comparable to the inside of a warehouse gate with metal reflectors [2].

As UWB-band antennas matched to the chip are not yet available, the modulation was emulated by measuring match and short independently using omnidirectional UWB patch antennas. Time-variant transmission coefficient measurements using a standard UHF tag have confirmed that the modulation is detectable using this setup if the antenna is matched to the chip. We have also confirmed that passive backscatter modulation above 3 GHz is feasible during normal tag operation using an NXP UCODE G2XM chip attached to an omnidirectional UWB antenna [2]. However, as chip and antenna are not matched for this setup, the modulation is too unstable and weak to be detectable by the NWA setup. Therefore manual switching between short and match has been chosen for this evaluation.

Range estimates were taken at several positions in this room; the channel impulse responses were estimated out of 30000 modulation cycles for each position. The power-delay-profiles (PDP) for a position with a path length TX → tag → RX of 2.8 m are presented in Fig. 3. The upper plot shows the difference between the PDPs for matched and unmatched states. Note that the difference between the delay-profiles in this plot has been amplified for better visibility. The lower plot shows the extraction of this difference (not amplified). As can be seen, the profiles start to differ at the shortest path to the tag.

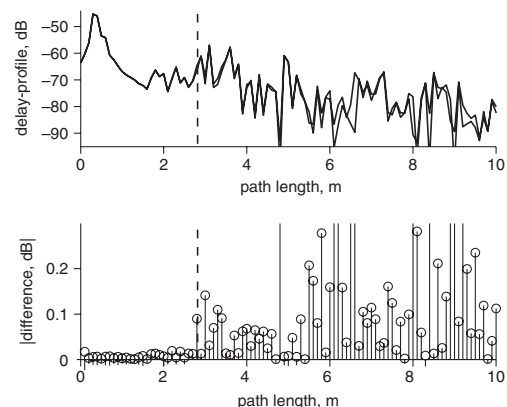


Fig. 3 Measured PDP for matched/unmatched modulation state (top) and extracted differences (bottom)

Note that difference in upper plot has been increased by factor of 20 to increase visibility; lower plot shows true difference

Conclusions and discussion: We have presented a proof of concept for UWB radar based ranging in conventional UHF RFID. The system does not require any processing of the UWB signal by the tag or synchronisation at the RF level. Ranging accuracy can be expected to be similar to coherent ultra-wideband ranging. The ranging method relies on the ability of the tag to reflect signals with sufficient modulation depth in an ultra-wideband frequency range. Commercially available UHF RFID chips are only designed for operation in frequency ranges up to 2.5 GHz (e.g. UCODE HSL). Additional research is required to assess

the feasibility of ultra-wideband matching of an antenna to state-of-the-art UHF RFID chips in the frequency range above 3 GHz. This might prove a nontrivial task owing to the power- and frequency-dependence of the chip and modulation impedance. Integrating a second modulation transistor on the chip that short-circuits a UWB antenna port might be a feasible alternative here: as the power levels in the UWB band are very low and the tag power supply is maintained by the UHF link, the UWB modulation transistor can be built as a very small structure and completely short-circuit a perfectly matched impedance for modulation. This switching between (close to) ideal loads would ensure an optimal modulation depth and match the measurements presented in this Letter.

Acknowledgments: The authors thank NXP Semiconductors, Gratkorn, Austria, for supporting and funding this project. This work was supported by the Austrian Research Promotion Agency (FFG) under the grant number 818072.

© The Institution of Engineering and Technology 2010
22 June 2010
doi: 10.1049/el.2010.1703

D. Arnitz and K. Witrisal (*Signal Processing and Speech Communication Laboratory, Graz University of Technology, Austria*)

E-mail: daniel.arnitz@tugraz.at

U. Muehlmann (*NXP Semiconductors, Mikronweg 1, 8101, Gratkorn, Austria*)

References

- 1 Nikitin, P.V., Martinez, R., Ramamurthy, S., Leland, H., Spiess, G., and Rao, K.V.S.: 'Phase based spatial identification of UHF RFID tags'. Proc. IEEE Int. conf. on RFID, Orlando, FL, USA, 2010, pp. 102–109
- 2 Arnitz, D., Adamiuk, G., Muehlmann, U., and Witrisal, K.: 'UWB channel sounding for ranging and positioning in passive UHF RFID'. 11th COST2100 MCM, Aalborg, Denmark, 2010 ([Online]. Available: <http://www.spsc.tugraz.at/people/daniel-arnitz/ArnitzCOSTMCM10.pdf>)
- 3 Heidrich, J., Brenk, D., Essel, J., Schwarzer, S., Seemann, K., Fischer, G., and Weigel, R.: 'The roots, rules, and rise of RFID', *IEEE Microw. Mag.*, 2010, **11**, (3), pp. 78–86

Bandwidth Dependence of CW Ranging to UHF RFID Tags in Severe Multipath Environments

Gang Li[‡], Daniel Arnitz[†], Randolph Ebelt[‡], Ulrich Muehlmann^{*}, Klaus Witrisal[†], Martin Vossiek[‡]

[‡] Clausthal University of Technology, Institute of Electrical Information Technology, Clausthal-Zellerfeld, Germany
 {li, ebelt, vossiek}@iei.tu-clausthal.de

[†] Signal Processing and Speech Communication Laboratory, Graz University of Technology, Graz, Austria
 {daniel.arnitz, witrisal}@tugraz.at

^{*}NXP Semiconductors, Gratkorn, Austria
 ulrich.muehlmann@nxp.com

Abstract— In this paper the impact of the signal bandwidth on the performance of frequency modulated continuous wave (FMCW) radar based ranging to ultra high frequency (UHF) radio frequency identification (RFID) tags is investigated. The analyses are based on ultra-wideband (UWB) channel measurements performed in a warehouse portal, which is a severe multipath environment. It is illustrated that the available bandwidth of the usual ISM bands at 900 MHz, 2.5 GHz and 5.8 GHz is only sufficient for a precise RFID tag localization if moderate or low multipath conditions are given. However, in severe multipath channels the ISM bands are unsuited and UWB signals are needed. The results can be considered a lower bound for signal time of flight (TOF) based localization approaches that utilize Fourier or correlation methods for the signal travel time estimation.

Keywords—UHF RFID, multipath channels, channel sounding, FM radar, distance measurement.

I. INTRODUCTION

The increased reading range of modern UHF RFID systems comes along with an increasing uncertainty of the actual spatial and situational context during the reading event. This stimulates an increasing interest in distance measurements to RFID tags and direct range bounding.

The basic principles to identify and localize a cooperative target such as an RFID backscatter transponder with the use of secondary radar have been known for a long time [1]-[3]. In [4] and [5], several CW secondary radar based transponder systems are presented that allow localizing and tracking amplitude- or phase-modulated backscatter transponders by phase or frequency evaluation of the radar beat signal. The principles of single-carrier CW, multi-frequency or stepped-frequency, and FMCW radar systems and their related evaluation approaches can be found in the above mentioned publications. Recently, several research groups have utilized these CW approaches for the UHF and microwave RFID tag localization problem and extended them by new features or established new applications [6]-[10].

The application of a CW radar system for UHF RFID localization is attractive because the design of RFID reader and backscatter tag required for ranging is very similar or even identical to general UHF RFID systems. Merely the tag

modulation, the RF synthesizer, and the reader signal evaluation have to be adapted.

Even though passive UHF RFID is now a widespread technology, reliable positioning in real-life scenarios is a feature that is not yet available. Beside the constraints of the power supply, the reading range, and the system complexity, also the bandwidth limit of the UHF RFID frequency band poses a major challenge. The channel sounding in a warehouse portal [11] has shown that UHF RFID channels are often dominated by indirect (non-line-of-sight, NLOS) paths and not by the direct (line-of-sight, LOS) path. This leads to large ranging errors and biased distance estimates for narrowband radar signals, since an extraction of the LOS signal is rarely possible with low bandwidths. Ultra wideband (UWB) systems have the potential to overcome this problem and make accurate ranging in dense multipath environments feasible [12], [13], but have strict power emission limits and a considerably higher system complexity.

In a preceding measurement campaign ([11],[14]), a representative set of the UWB channel transfer functions in a UHF RFID warehouse gate has been acquired. These measurements are utilized in this paper to analyze the impact of the chosen signal bandwidth on the ranging uncertainty in multipath channels. The analysis covers bandwidths ranging from narrowband to ultra-wideband.

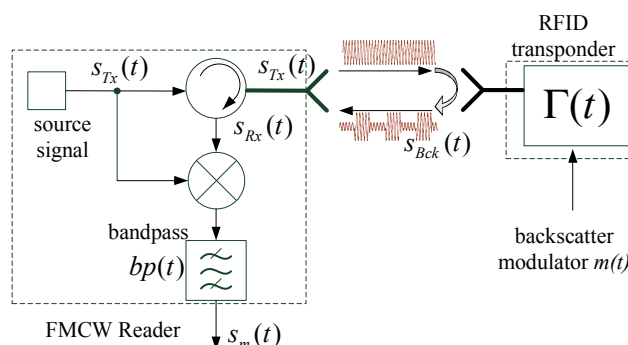


Figure 1. Setup of the FMCW radar based RFID localization system.

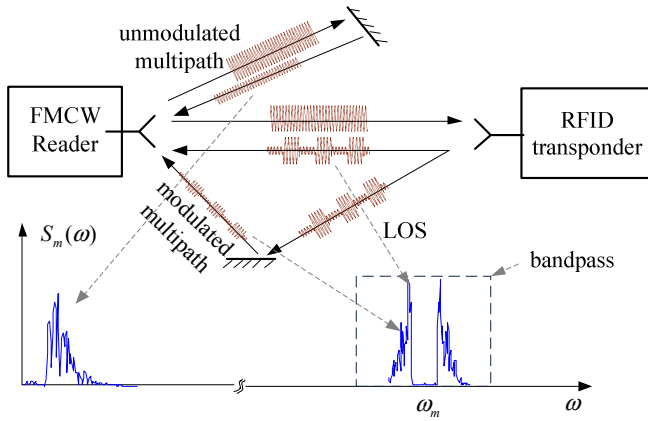


Figure 2. Exemplary radar echo profile of a FMCW secondary radar measurement to a RFID backscatter transponder in a multipath environment.

II. CW RADAR BASED UHF RFID TAG LOCALIZATION

A. System Setup and Localization Approach

The setup of the considered FMCW radar based RFID localization system is depicted in Fig. 1. The radar unit emits a transmit signal $s_{Tx}(t)$ that will be reflected by the RFID transponder and additional passive objects located in the environment. If we assume that the transponder reflectivity $\Gamma(t)$ is a periodical modulation with a period $T_m = 2\pi/\omega_m$, where $1/T_m$ is the modulation frequency and let φ_m denote the phase shift, we can write:

$$\Gamma(t) = \Gamma_0 \cdot \cos(\omega_m \cdot t + \varphi_m). \quad (1)$$

Note that this analysis concentrates on the effects of the channel, hence the modulation is assumed to be stable, i.e., the frequency variation is assumed to be negligible inside the measurement window. For simplicity, we also presume a frequency-independent reflection coefficient.

The radar will receive two kinds of echoes from the channel: a) the echoes of the passive objects that are the time delayed replicas of the transmitted signal and b) the echoes caused by the transponder that are delayed and superimposed by the amplitude modulation given by (1). Both kinds of echoes can either be transmitted directly over the LOS path or via multipath reflections. In a FMCW radar, the frequency of the down-converted radar beat signal $s_m(t)$ is proportional to the signal roundtrip-time-of-flight (RTOF) of a given echo. The modulation (1) shifts the complete echo profile related to the backscattered transponder signal from the center frequency $\omega = 0$ to the radian modulation frequency $\omega = \omega_m$, i.e., to larger distance values well separated from the echoes of the passive objects. A typical echo profile is shown in Fig. 2. Since the transponder signal components are amplitude modulated, we obtain an echo profile with two sidebands centered around ω_m . In [4]-[6] and [8] it is shown that the RTOF of a transponder echo can be determined by the frequency and/or phase difference between the two spectral lines – which are symmetrically located around ω_m . By identifying the LOS echoes, i.e., the two spectral lines with the closest distance to

the left and right of ω_m , the distance between the reader and the backscatter RFID tag can be determined.

B. Range resolution

The minimal width of an echo and thus the range resolution δ_{rad} quantifies the ability of a FMCW radar to separate two closely spaced echoes. It is directly linked with the radar signal bandwidth B via

$$\delta_{rad} \approx \frac{c_0}{2B}, \quad (2)$$

where c_0 is the free space RF signal phase velocity.

C. Transmission model

For identical up- and downlink channel impulse responses $h(t)$ and given a transmit-signal $s_{Tx}(t)$ the measured beat signal $s_m(t)$ is given as follows:

$$s_m(t) = \left(\left(\left(s_{Tx}(t) * h(t) \right) \cdot \Gamma(t) \right) * h(t) \right) \cdot s_{Tx}(t) * bp(t), \quad (3)$$

This transmission model is applied for the investigation below.

III. IMPACT OF THE SIGNAL BANDWIDTH ON RANGING ACCURACY

A. Experimental Setup

Our investigation is based on (3) and on a measurement campaign that yielded a set of channel transfer functions in a UHF RFID warehouse gate.

The modulation and band-pass are known and assumed to be ideal. The modulation frequency was set to 320 kHz and the band-pass / IF filter was adjusted to the expected distance range of the FMCW radar beat signal (see Fig. 2). The selection of the modulation frequency has no effect on the ranging uncertainty provided that the backscattered signals are well separated from the echoes of passively reflecting objects. For this scenario, 320 kHz is sufficient to achieve this separation.

The transmitted radar signal is assumed to be a linearly frequency modulated signal and given as:

$$s_{Tx}(t) = A_{Tx} \cos\left(\omega_c t + \pi \cdot \frac{B}{T} \cdot t^2\right) \quad \text{for } 0 < t < T, \quad (4)$$

where A_{Tx} , ω_c , B and T denote the Amplitude, the RF center frequency, the sweep bandwidth, and the sweep duration, respectively (s. [4]-[6]). The RF center frequency was set to 800 MHz, and the sweep duration T was set to 1 ms. The bandwidth B of the transmitted signal, and thus the bandwidth of the measurements, are varied in the range from 10 MHz to 500 MHz.

Our investigation is focused on the impact of a lifelike channel. Other system impairments such as receiver noise, phase noise of the RF synthesizer, instabilities of the

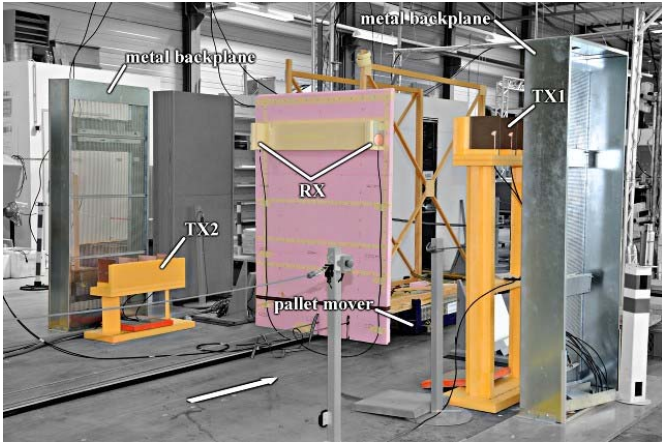


Figure 3. Photograph of the measurement setup for the “empty gate” measurements (EGM). The receivers are mounted on electromagnetically inert polyurethane slabs.

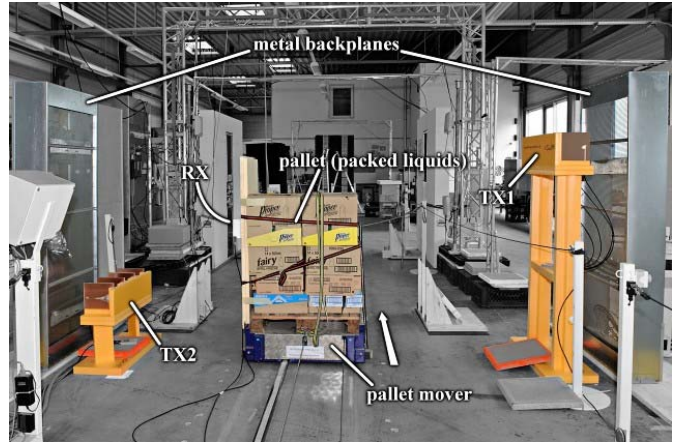


Figure 4. Photograph of the measurements setup for the “liquids pallet” measurements (LPM). Receivers are mounted on the left side of the pallet and move with the pallet, which contains mostly liquids and thus serves as a challenging example for ranging.

modulation, as well as phase and amplitude distortion of the antenna and the RF system were ignored. However, based on practical experience with CW radar based RFID localization [6,8,9,13,15], most of these distortions can be kept small by careful system design, so multipath propagation is very often the dominating cause for ranging errors. The channel inside a UHF RFID portal is a severe multipath environment, providing a challenge even for ultra-wideband localization, as will be shown below.

B. Channel Characterization

Passive UHF RFID is mostly used in logistics, with main applications in supply chain management and product tracking. Consequentially, typical application environments are industrial, i.e., constructed of highly reflective materials. A common supply-chain scenario employing UHF RFID are portals registering tagged objects while they are moving through. These portals are often constructed with metal surfaces for mechanical stability and in order to concentrate energy to the interior of the portal. In combination with the unavoidable backscatter nature of passive UHF RFID, this creates a severe multipath scenario.

The presented investigations use channel impulse responses recorded in such a portal. The recordings were taken in NXP’s Application and System Center, a large hall with corrugated metal walls and ceiling, and a steel-reinforced concrete floor. The portal itself was constructed using two bare steel portal chassis, forming the metal backplanes behind the transmitter antennas (“reader”). The receiver antennas (“tags”) were mounted on pallets and hauled through the portal by an automated pallet mover. Photographs of this setup are shown in Figs. 3 and 4.

Channel impulse responses were recorded in a frequency range of 0.5-1.5 GHz for two scenarios: An empty gate simulated by an electromagnetically inert pallet (Fig. 3), and a challenging product pallet containing packed liquids (Fig. 4). These two scenarios are denoted EGM (empty gate measurement) and LPM (liquids pallet measurements) below. A detailed description of the measurement setup has been

published in [11], and an in-depth channel analysis w.r.t. ranging can be found in [14].

In essence, the entire setup can easily be characterized as the worst case with respect to ranging. The high attenuation of backscatter radio requires highly sensitive receivers. At the same time, signal-to-interference ratios can reach -70 dB and below [14]. The relatively small dimensions of the gate cause major reflections to be spatially close to the LOS component. Large signal bandwidths are required to resolve these multipath components and separate them from the LOS. Tags are also often mounted on reflecting materials such as liquids, thus creating multipath components that are within a few cm of the LOS and thus mostly inseparable. These conditions make the LOS-detection and thus ranging quite challenging.

Moreover, reader antennas used in such portals are directive (cf. Fig. 5), with the main-lobe pointed at the opposite side of the portal. This creates massive reflections at the gate’s walls, while at the same time causing a weak LOS path if the

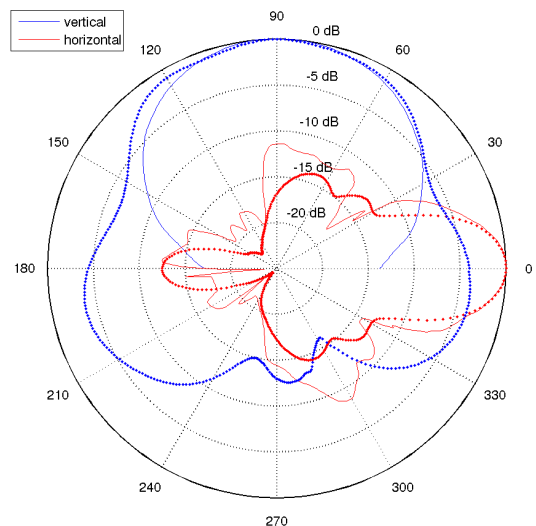


Figure 5. Gain pattern of the used transmitter arrays (dots) compared to an Intermecc IA39B UHF RFID portal antenna (line). The UWB gain pattern of the transmitter array is averaged over 500 MHz bandwidth around the center frequency of 800 MHz.

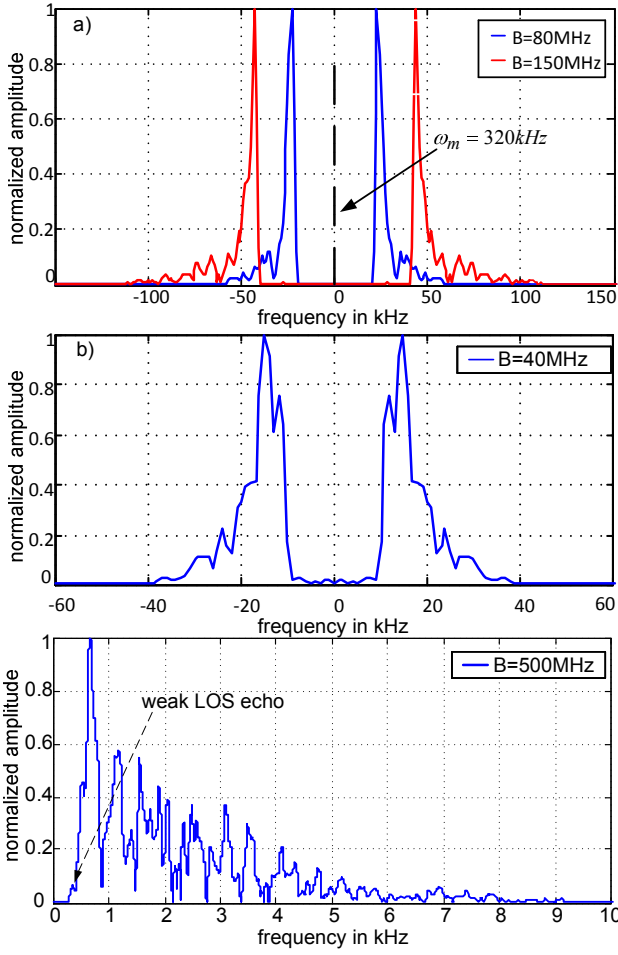


Figure 6. Example echo profiles: a) low multipath distortion, b) considerable multipath components, but strong LOS, c) weak LOS in zoomed profile.

tag is outside the main-lobe (see [16] for an RFID-specific analysis of this portal).

C. Results

In the presented analysis, the ranging accuracy is quantified via the root mean square error (RMSE):

$$\sigma_r = \sqrt{\frac{1}{M} \sum_{m=1}^M (d'_m - d_m)^2}, \quad (5)$$

where d'_m and d_m denote the measured and true distance between the RFID reader and tag.

As depicted in Fig. 6a, the echo profiles $S_m(f)$ are located around the modulation frequency ω_m . We took the frequency difference of the sidebands for RFID ranging (cf. [4]-[6]):

$$d = \frac{\Delta f \cdot T \cdot c_0}{4B}. \quad (6)$$

In Fig. 6a the echo profiles were not notably disturbed by multipath propagation. Thus, the distance estimation of (6) even with an 80 MHz bandwidth matched the true distance

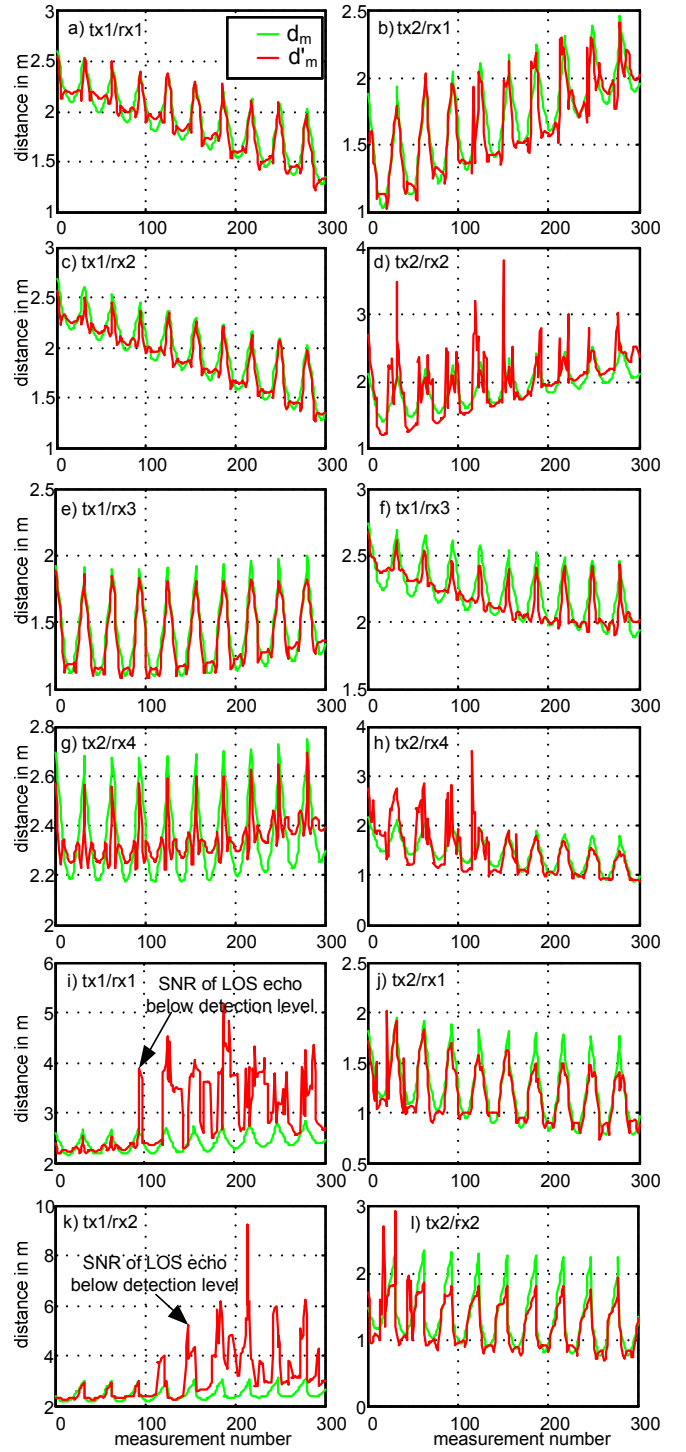


Figure 7. Ranging results calculated from the measured channel transfer functions for multiple passes of the receivers through the portal. The measurements are from different receiver positions in situation EGM (a-h) and LPM (i-l). The FMCW sweep bandwidth here is 500 MHz.

well. However, in most other cases the measured channel transfer functions and the resulting echo profiles were strongly corrupted by multipath distortions.

According to (2) it is known that the replicas of the echo profile with different time delays have the same width δ_{rad} as the LOS component. These multipath echoes can shift the

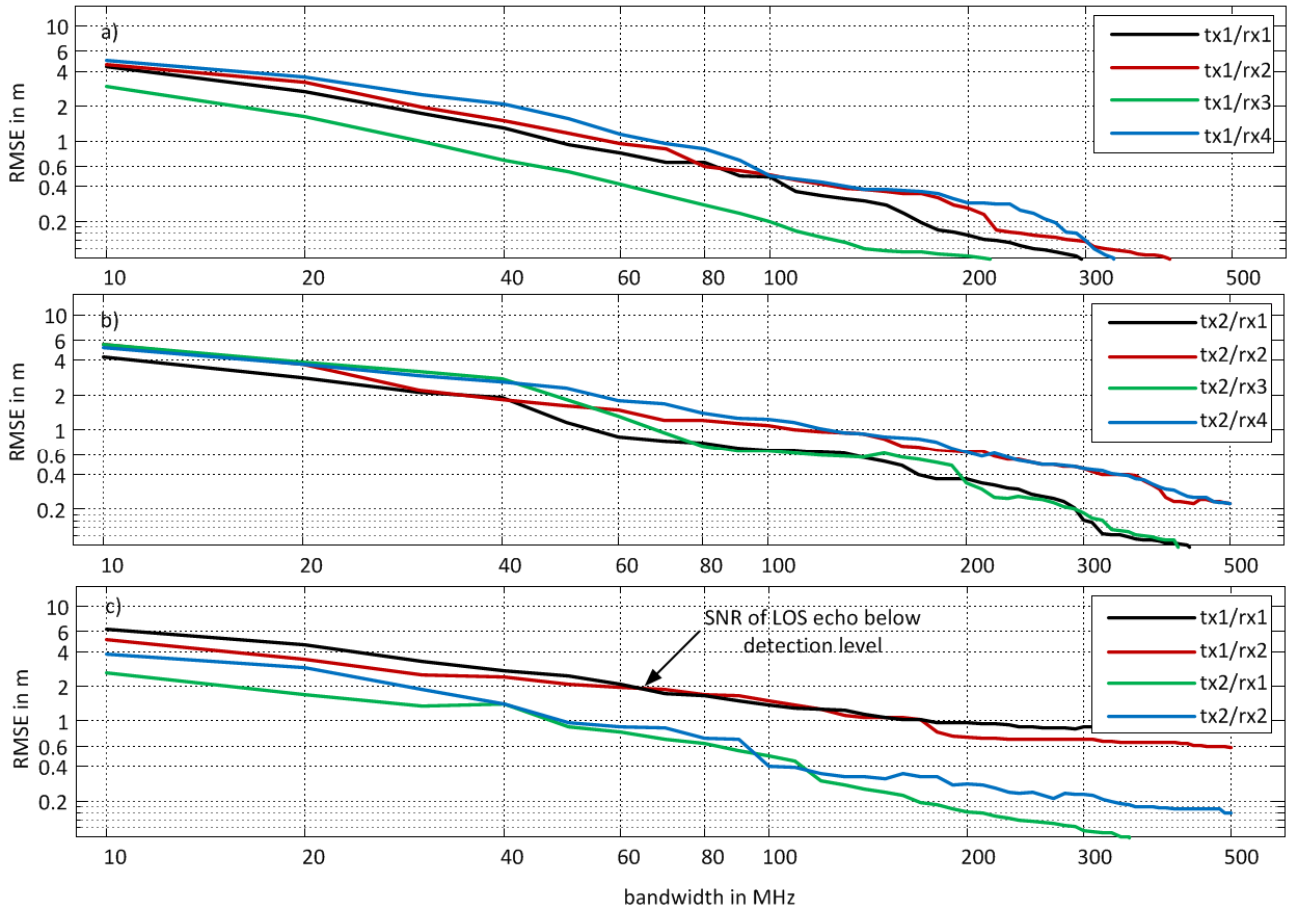


Figure 8. Logarithmic representation of the FMCW radar based ranging performance in the gate environment. In the data processing runs, the FMCW sweep bandwidth was varied from 10 MHz to 500 MHz. The measured channel transfer functions are taken from a) RFID reader tx1, b) tx2 of “EGM” and c) “LPM”.

maximum of the LOS echo, if they are close enough. Examples of echo profiles with strong multipath distortions are shown in Figs. 6b and 6c.

The results of the ranging experiments for each RFID reader and tag can be found in Fig. 7. The results in Fig. 7a-h match our assumption well that the distance of the passive UHF RFID tag can be determined accurately with wideband FMCW signals. The huge ranging errors – as depicted in Fig. 7d and 7h of “EGM” and 7i and 7k of “LPM” – were caused by a very weak LOS-component with an amplitude below the detection level. The system thus falsely identifies a reflected component as LOS, which causes large ranging errors. This is especially true for the LPM and tx1, where the pallet completely blocks the LOS path, but not the gate-reflection. It is obvious that a very good SNR is required to detect the correct LOS echo in such a scenario. If the LOS signal is masked by noise, a strong echo at a larger distance can easily be mistaken for the LOS echo and an erroneous distance is determined, as shown in Fig. 7d, 7i and 7k.

The impact of the radar signal bandwidth on the ranging uncertainty is depicted in Fig. 8. In our investigation we calculated the ranging uncertainty based on 300 measured channel transfer functions of EGM and LPM for each chosen radar sweep bandwidth B , which was varied from 10 MHz to

500 MHz. Fig. 8a shows the ranging uncertainty of the RFID reader tx1 and tags rx1-4, while Fig. 8b corresponds to tx2. Our investigations illustrate that the FMCW radar based ranging uncertainty in this severe multipath environment is around 1 m for the 80 MHz ISM bandwidth. Not considering the NLOS cases, which may have arbitrary errors per definition, this meets the expected ranging resolution of $\delta_{rad,80MHz} = c/\nu/2B = 1.9$ m. From the results in Fig. 8 we conclude that the ranging uncertainty in the severe multipath channel is about half the minimal width δ_{rad} of an echo – if the low SNR situations in Fig. 8c are not considered. As visible, the ranging uncertainty is inversely proportional to the radar sweep bandwidth B . This assumption provides a lower bound of the RFID ranging error in severe multipath environments, because many possible error sources such as phase noise of the RF synthesizer, phase noise of the modulation oscillator and phase and amplitude distortion of the antenna and the RF system have been ignored.

In Section III.D we present a theoretical justification of this assumption. According to this assumption, the ranging uncertainty should be around 0.5 m in the shown severe multipath environments when using the 5.8 GHz FMCW radar based UHF RFID system with a bandwidth of 150 MHz. The results in Fig. 8 matched this estimation well. We can also conclude that accurate ranging in the cm-range is not possible

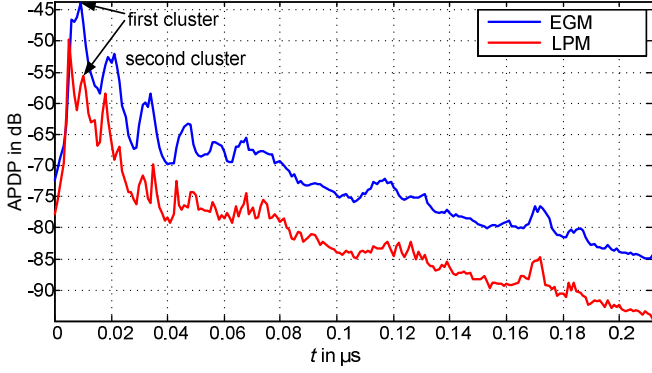


Figure 9. The average power delay profile of the measured channel transfer functions in [11].

with a 5.8 GHz ISM-band UHF RFID localization system in the given measurement scenarios. To improve the localization precision an increased bandwidth and/or diversity or synthetic aperture techniques (cf. e.g. [9, 20]) are required.

D. Interpretation of the Results

In our experiments we observed that the ranging uncertainty in severe multipath channels is inversely proportional to the bandwidth, provided that the LOS component can be correctly identified. Subsequently we want to present a qualitative theoretical justification of this identified behavior.

Provided that there is a discernable LOS component in the measured signal, we can conclude that the multipath reflection that has a RTOF that exceeds the RTOF of the LOS signal by more than the resolution limit can be resolved and does not disturb the range estimation. Based on (2) we can define this critical RTOF difference that is required to resolve the multipath reflections as:

$$\Delta d_c > \frac{c_0}{2B}. \quad (7)$$

Below this limit the LOS echo is superimposed by the echoes of multipath components and the ranging performance will be degraded. It is reasonable to assume that this degradation will be increased with an increasing number of multipath reflections and increasing amplitudes of the reflections. For the sake of simplicity we don't consider the phase effects in the subsequent derivation, even though they are crucial for the precision of each individual range measurement in multipath scenarios. Our assumption is that the phase constellations are randomly distributed for a larger set of measurements taken for arbitrarily distributed distance between reader and tag and that the amplitude consideration is sufficient for a qualitative, averaged /statistical consideration.

Based on the explanation above we define a multipath distortion measure $\sigma'_r(\Delta d_c)$ based on the average PDP (power delay profile) as:

$$\sigma'_r(\Delta d_c) = \sigma'_r(B) = \frac{\int_{\zeta=0}^{\Delta d_c} |P_{mp}(\zeta)| d\zeta}{P_{LOS}} = \frac{\int_{\zeta=0}^{c_0/2B} |P_{mp}(\zeta)| d\zeta}{P_{LOS}}, \quad (8)$$

where ζ denotes the RTOF difference of a multipath echo w.r.t. to the LOS signal. The power of the LOS signal is denoted as P_{LOS} . The integral sums up the power $P_{mp}(\zeta)$ of all multipath echoes with RTOF difference ζ that fall below the resolution limit (7) and disturb the LOS echo. Thus the definition of (7) describes a kind of signal to multipath distortion measure.

Many channel models assume an exponential decay of the multipath components in the PDP [18, 19]. The PDP of our measured channel transfer functions is shown in Fig. 9. The time delay of the first cluster is about 10 ns for this given profile.

If we provide such an exponential decay during the delay time interval defined by (7), we can write:

$$|P_{mp}(\zeta)| \cong P_{max} e^{-\frac{\zeta}{\gamma}}, \quad (9)$$

where the RTOF difference is denoted by ζ , the term γ is the delay constant of the channel and the amplitude of P_{max} is assumed to be the power of the strongest echo of the signal.

Now we insert (9) into (8), solve the integral and obtain the following relation:

$$\sigma'_r(B) \cong \frac{\int_{\zeta=0}^{c_0/2B} P_{max} e^{-\frac{\zeta}{\gamma}} d\zeta}{P_{LOS}} = \gamma \frac{P_{max}}{P_{LOS}} (1 - e^{-\frac{c_0}{2\gamma B}}). \quad (10)$$

Given a time delay constant of γ in the order of several nanoseconds and given a radar sweep bandwidth range from 10 MHz to 500 MHz and provided that the LOS echo is the strongest echo within Δd_c , expression (10) can be approximated by:

$$\sigma'_r(B) \approx \frac{c_0}{2B}. \quad (11)$$

As visible, the experimental results shown in Fig. 8 and (10) and (11) are congruent. Unsurprisingly, the relation of (11) equals the range resolution definition given in (2). Hence, both the FMCW radar range resolution and the ranging performance in severe multipath scenarios are approximately inversely proportional to the radar sweep bandwidth B .

Note that the presented rules of thumb (10) and (11) are only valid to estimate the effect of multipath distortions. Other possible error sources that may degrade the ranging results were not considered. On the other hand, a well designed system operating in an environment with low multipath distortion can provide a ranging precision that is much better than indicated by (10) and (11). An expression for the lower bound of precision in ideal situations, where multipath and all other

distortions except noise are negligible, can be derived from the Cramér-Rao Lower Bound (CRLB). The CRLB for a two-way ranging system is given as [21]:

$$\sigma_r'(B, E_s, N_0) \geq \frac{c_0}{2B} \sqrt{\frac{1}{\pi^2 E_s / N_0} \left(1 + \frac{1}{E_s / N_0}\right)}, \quad (12)$$

where E_s and N_0 denote the signal and noise power. Provided that the bandwidth is fixed by legal spectrum regulations, expression (12) shows that the signal-to-noise ratio is the limiting factor in ideal measuring conditions.

IV. CONCLUSION

In this paper the impact of the signal bandwidth on the performance of CW radar based ranging to UHF RFID tags was studied. It has been shown that the ranging performance in severe multipath scenarios is approximately inversely proportional to the radar bandwidth B as long as the LOS echo is detectable. The results are of course not only valid for the presented CW radar approaches but for all localization approaches that utilize Fourier or correlation methods for the signal travel time estimation. In a following step we want to verify our findings by measurements with a broadband FMCW radar based RFID localization system. Parallel to and in conjunction with these measurements the effect of other distortion parameters, e.g. noise, phase noise of the RF synthesizer and the modulation oscillator as well as phase and amplitude distortion of the antenna and the RF system, will be considered.

TABLE OF ACRONYMS

| | |
|------|---|
| CW | continuous wave |
| EGM | empty gate measurement test set-up |
| FMCW | frequency modulated continuous wave |
| ISM | industrial, scientific and medical (frequency band) |
| LOS | line of sight |
| LPM | liquids pallet measurement test set-up |
| NLOS | non line of sight |
| PDP | power delay profile |
| RMSE | root mean square error |
| RFID | radio frequency identification |
| CRLB | Cramér-Rao lower bound |
| RTOF | roundtrip time of flight |
| TOF | time of flight |
| UHF | ultra high frequency |
| UWB | ultra-wideband |

REFERENCES

[1] H. Stockman, "Communication by Means of Reflected Power," *Proceedings of the IRE*, vol. 36, pp. 1196-1204, 1948.
 [2] A. Koelle, S. Depp, and R. Freyman, "Short-range radio-telemetry for electronic identification using modulated backscatter," *Proceedings of the IEEE*, vol. 63, no. 8, pp. 1260-1260, 1975.

[3] R. J. King, "Microwave Homodyne Systems," Peregrinus, London, England, 1978.
 [4] P. Heide, M. Vossiek, German Patent Application DE 19946161 A1, 27.9.1999
 [5] P. Heide, J. Ilg, R. Roskosch, K. Hofbeck, W. Piesch, and M. Vossiek, "US Patent US6946949B2," 30.11.2000.
 [6] J. Heidrich, et al., "Local positioning with passive UHF RFID transponders," in *Wireless Sensing, Local Positioning, and RFID*, 2009. IMWS 2009. IEEE MTT-S International Microwave Workshop on, 2009, pp. 1-4.
 [7] P. Nikitin, et al., "Phase Based Spatial Identification of UHF RFID Tags," 2010 IEEE International Conference on RFID, pp. 102-109, 14-16 April 2010.
 [8] M. Vossiek and P. Gulden, "Switched Injection Locked Oscillator: A Novel Versatile Concept for Wireless Transponder and Localization Systems," *IEEE Transactions on Microwave Theory and Techniques*, vol. 56, pp. 859-866, Apr. 2008.
 [9] S. Kunkel, M.-S. Huang, R. Bieber, and M. Vossiek, "SAR-like Localization of RFID Tags for Non-uniform Trajectory," in *40th European Microwave Conference*, Paris, France, Sept. 2010, pp. 1758-1761.
 [10] D. Arnitz, U. Muehlmann, and K. Witrissal, "Multi-Frequency Continuous-Wave Radar Approach to Ranging in Passive UHF RFID," *IEEE Trans. Microwave Theory Tech.*, vol. 57, no. 5, pp. 1398-1405, May 2009.
 [11] D. Arnitz, G. Adamiuk, U. Muehlmann, and K. Witrissal, "UWB Channel Sounding for Ranging and Positioning in Passive UHF RFID," *11th COST2100 MCM*, Denmark, 2010.
 [12] D. Arnitz, U. Muehlmann, and K. Witrissal, "UWB Ranging in passive UHF RFID: A Proof of Concept," *IET Electron. Letters*, vol. 46, no. 20, pp. 1401-1402, Sept 2010.
 [13] Heidrich, J., Brenk, D., Essel, J., Schwarzer, S., Seemann, K., Fischer, G., and Weigel, R.: "The roots, rules, and rise of RFID", *IEEE Microw.Mag.*, 2010, 11, (3), pp. 78-86
 [14] D. Arnitz, U. Muehlmann, and K. Witrissal, "Wideband Characterization and Modeling of UHF RFID channels for Ranging and Localization", 2011, submitted for publication.
 [15] A. Aleksieieva and M. Vossiek, "Design and Optimization of Amplitude-Modulated Microwave Backscatter Transponders," in *5th German Microwave Conference (GeMiC2010)*, Berlin, Germany, Mar. 2010, pp. 134-137.
 [16] U. Muehlmann, G. Manzi, G. Wiednig, and M. Buchmann, "Modeling and Performance Characterization of UHF RFID Portal Applications," *Microwave Theory and Techniques*, *IEEE Transactions on*, vol. 57, pp. 1700-1706, 2009.
 [17] D. M. Dobkin, *The RF in RFID*. Elsevier, 2007.
 [18] A. Saleh and R. Valenzuela, "A statistical model for indoor multipath propagation," *IEEE Journal on selected areas in communications*, vol. 5, pp. 128-137, 1987.
 [19] A. Molisch, et al., "A comprehensive standardized model for ultrawideband propagation channels," *IEEE Transactions on Antennas and Propagation*, vol. 54, p. 3151, 2006.
 [20] M. Vossiek, A. Urban, S. Max and P. Gulden, "Inverse Synthetic Aperture Secondary Radar Concept for Precise Wireless Positioning," *IEEE Transactions on Microwave Theory and Techniques*, vol. 55, pp. 2447-2453, Nov. 2007.
 [21] S. Lanzisera and K. S. J. Pister, "Burst Mode Two-Way Ranging with Cramer-Rao Bound Noise Performance," in *Global Telecommunications Conference*, 2008. IEEE Globecom 2008. IEEE, 2008, p. 1-5.